Initiation and propagation of rebar corrosion in carbonated and cracked concrete

Rita Maria Ghantous

THÈSE

En vue de l'obtention du

DOCTORAT DE L'UNIVERSITÉ DE TOULOUSE

Délivré par :

Institut National des Sciences Appliquées de Toulouse (INSA Toulouse)

Présentée et soutenue par :
Rita Maria Ghantous
Le Vendredi 30 Septembre 2016

Identification des phases d'initiation et de propagation de la corrosion des armatures enrobées dans un béton fissuré et carbonaté

École doctorale MEGEP : Génie Civil

Unité de recherche :

Laboratoire d'Études du Comportement des Bétons et des Argiles, CEA Saclay
Laboratoire Matériaux et Durabilité des Constructions, INSA Toulouse

Directeur de Thèse : Raoul FRANÇOIS
Co-Directrice de Thèse : Valérie L'HOSTIS

Jury

Ueli ANGST	Professeur, ETH IfB Zürich	Examinateur
Bernhard ELSENER	Professeur, ETH IfB Zürich	Président
Raoul FRANÇOIS	Professeur, INSA Toulouse	Directeur
Mette Rica GEIKER	Professeur, NTNU	Rapporteuse
Valérie L'HOSTIS	Ingénieur chercheur, CEA Saclay	Co-directrice
Stéphane POYET	Ingénieur chercheur, CEA Saclay	Encadrant
Michael RAUPACH	Professeur, RWTH Aachen University	Rapporteur
Nhu-Cuong TRAN	Ingénieur chercheur, EDF Renardières	Examinateur

ACKNOWLEDGMENT

The scientific work that I present in this manuscript could not have been achieved if I were not supported humanely and scientifically.

I had the opportunity to meet a person who impressed me by his wealth of humanity. It is with such a quality of benevolentce and attentive presence, that Raoul François supervised my thesis. He has always shown complete confidence, invaluable support and constant kindness to me, which enabled me to carry out and complete my research work during these three years. I am very happy that I had him as a thesis director and benefited on a scientific and human level from his great experience and his immense culture. Finding strong words to say "Thank you" is a difficult task, especially in a language that is not my mother tongue.

I would also like to express my warmest thanks to Valérie L'Hostis, the co-director of my PhD thesis, for having believed in my skills and given me the chance to accomplish this work. Working with Valerie was a pleasure, first of all because of her very humane, welcoming and modest attitude, and of course her scientific skills.

Many thanks to Stéphane Poyet for his support and encouragement that motivated me to circumvent the many difficulties I encountered during my thesis. I deeply appreciate his creativity and constructive criticism and I will not forget his remarks and contribution in the achievement of this work.

My acknowledgements for Nhu-Cuong Tran, the industrial partner, for welcoming me at EDF and assisting me during the progress of the work.

I would like also to acknowledge Delphine Neff for her help in the interpretation of the Raman Spectroscopy results.

I would like also to address my acknowledgement to Alain Millard who accepted to help me in the modeling part despite his busy schedule. He was always ready to answer my questions and try to find solutions with a notable sympathy.

I would also like to thank the members of the LMDC laboratory for having me in their premises for a couple of months during my PhD.

I was welcomed at the LECBA laboratory with good humor and conviviality. I will never forget the awesome and touching moments spent with the LECBA team and would like to thank you all for everything.

A special thanks to the professors who agreed to examine my work and who gave me the honor to have them as a member of the jury: Professor Ueli Angst, Bernhard Elsener, Mette Rica Geiker and Mickaël Raupach.

Moving away from the sphere of science, I extend my gratitude and much more to all my friends for their support. Without them I would not have had the joy of continuing on this long, studious path. This "success" is also somewhat theirs.

Finally, I thank my parents for their love, encouragement, support and sacrifices that allowed me to go to the end of my dreams. It is impossible for me to find words to say how much I am Proud of them, and how much I love them. Many thanks also to you my brother.

TABLE OF CONTENTS

LIST OF TABLES

LIST OF FIGURES

ABSTRACT

This thesis aims to study the carbonation-induced corrosion initiation and propagation in cracked concrete under different conditions. It is performed in the framework of concrete ageing management of cooling towers of Electricity of France (EDF) nuclear power plants. Indeed some of them can be affected by cracks which may promote the carbonation of the concrete surrounding the cracks and induce a rapid reinforcement corrosion initiation in the carbonated area.

Firstly, cracks representative of those encountered in the cooling towers concrete are reproduced on laboratory specimens using the three point bending test. Three crack openings are obtained (100 µm, 300 µm and 500 µm). Cracked specimens are thereafter exposed to accelerated carbonation for two aims. First for the acceleration of the concrete neutralization phase which ensure the suitable thermodynamic conditions for active corrosion initiation. Second, for the estimation of the length of the mechanically damaged steel/binder interface supposed to be comparable to the carbonated length along the rebar on both sides of the crack. It is found that carbonation at 50% CO2 is not suitable here because it overestimated the damaged zone length, maybe due to enhanced carbonation shrinkage.

The second part aims to investigate the corrosion initiation and propagation phases while varying several parameters. For this purpose, cracked and carbonated specimens are subjected to corrosion under different exposure conditions. Specimens showing different crack widths and different types of binder are corroded in a reference test in which 30 minutes of rain occurs each 3 days at 20°C. Additionally, some corrosion tests are realized under raining/drying cycles for 3 minutes rain, other at 40°C and other in natural environmental conditions. Moreover, some cracked specimens are exposed in different orientations with respect to rain. Furthermore, specimens with different bars locations are prepared in order to investigate the influence of the steel/binder interface quality on the corrosion products layer distribution.
A decrease in the iron mass dissolution rate is a common observation for all the above mentioned conditions. This traduces the decrease of corrosion kinetics with time. Additionally, when performed, free corrosion potentials drops down at the beginning of the corrosion test then increases to reach the potential of a passivated rebar. Moreover, the corrosion products fill the de-passivated (carbonated) area and remain localized around the crack. All these observations lead to predict that carbonation-induced corrosion deep in the crack is not the most harmful parameter for the structure sustainability due to a possible rebar repassivation. Additionally, the position of the rebar impacts significantly the corrosion process. The highest rebar with respect to casting direction shows the highest corrosion thickness on its lower part due to the voids and defects induced by the materials settlement and bleeding (Top bar effect).

Finally, it is deduced that the corrosion conditions have an influence on the crystallinity state of the corrosion products. Corrosion products with a good crystallinity state are detected for the conditions having the lowest saturation degree (40°C, 3 min rain, natural environment). This is important to note because the mechanical resistance of corrosion products is dependent from their crystallinity

Based on these conclusions, a phenomenological corrosion model is proposed for steels located in cracked and carbonated concrete in this study based on the obtained results and on the literature review.

Keywords: Reinforced concrete, cracks, carbonation-induced corrosion, environmental conditions.

RÉSUMÉ

Contexte et objectif

Dans cette étude, nous nous intéressons à la durabilité des tours aéroréfrigérantes des centrales nucléaires d'EDF. Ces ouvrages peuvent présenter des états de fissuration plus ou moins prononcés. Ceux-ci peuvent être dus au retrait empêché ayant pour origine des phénomènes physiques (cycles d'humidification / séchage, dilatation thermique différentielle due à l'écart thermique entre les parois internes et externes de l'aéroréfrigérant) et/ou des aspects mécaniques (action du vent et sollicitations résultantes des tassements différentiels).

Les fissures facilitent la pénétration dans le béton du dioxyde de carbone présent dans l'atmosphère. Ce phénomène favorise la carbonatation qui par la suite conduit à la dépassivation puis à la corrosion active des armatures en fond de fissure. L'expansion de la couche de rouille peut provoquer le développement de nouvelles fissures dans la structure, menaçant ainsi sa durabilité.

Le but de cette thèse est de déterminer l'influence des fissures préexistantes ainsi que l'effet des conditions environnementales (ensoleillement, précipitations, humidité relative de l'air ambiant) sur l'initiation et la propagation de la corrosion induite par la carbonatation du béton d'enrobage des tours aéroréfrigérantes. Les résultats obtenus seront utilisés par la suite afin de développer un modèle opérationnel prenant en compte les paramètres précédents (action EDF). Le modèle serait utilisé *in fine* par EDF pour évaluer la cinétique de dégradation des tours du parc nucléaire dans le but d'optimiser le programme de suivi et de maintenance.

Méthodes

Pour cette étude, un protocole de fissuration permettant de reproduire les fissures observées sur les tours a été défini et consiste en une flexion trois points sur des éprouvettes prismatiques de dimension 70×70×280 mm. Une armature de haute adhérence (HA) et de diamètre de 6 mm est localisée au centre de chaque éprouvette. Différentes ouvertures de fissures peuvent être obtenues en contrôlant le chargement appliqué. Trois ouvertures de fissures résiduelles après déchargement ont été choisies : 100, 300 et 500 µm et ont été mesurées par l'intermédiaire d'un capteur de déplacement fixé dans la zone de fissuration (Figure 1). De plus, la corrélation d'image ainsi que la tomographie aux rayons X ont été utilisées pour déterminer l'ouverture de la fissure sur toute la hauteur de l'échantillon ainsi qu'au niveau de l'armature.

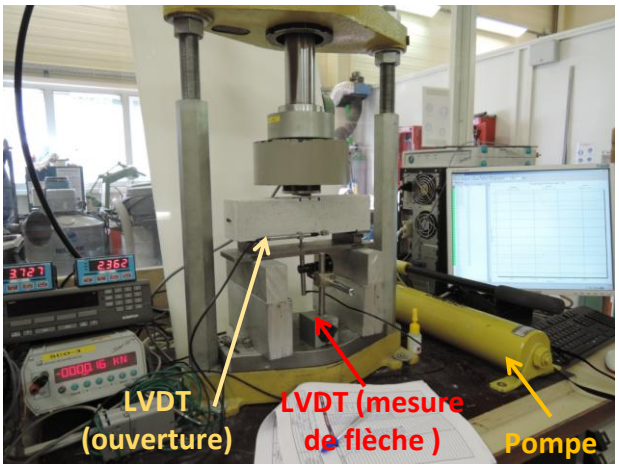

(a)

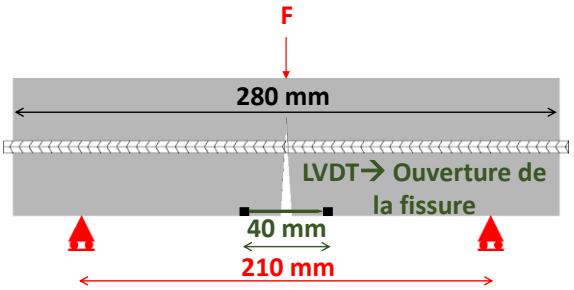

(b)

Figure 1 : Flexion trois points sur une éprouvette de 70×70×280 mm

Une attention particulière a été portée à la limitation de l'endommagement de l'interface acier/liant afin de pouvoir étudier la phase de la propagation de la corrosion. Dans la littérature, il est déduit que le dioxyde de carbone est capable de carbonater les fronts d'une fissure indépendamment de son ouverture. En se basant sur cette conclusion, il a été supposé dans cette étude que la longueur endommagée pourrait être estimée en mesurant la longueur carbonatée de l'interface acier/liant. Par conséquent, les éprouvettes fissurées ont été carbonatées (de manière accélérée) dans le double but de mesurer la longueur de la zone de d'interface altérée et de dépassiver l'armature en fond de fissure pour permettre l'initiation de la corrosion (Figure 2).

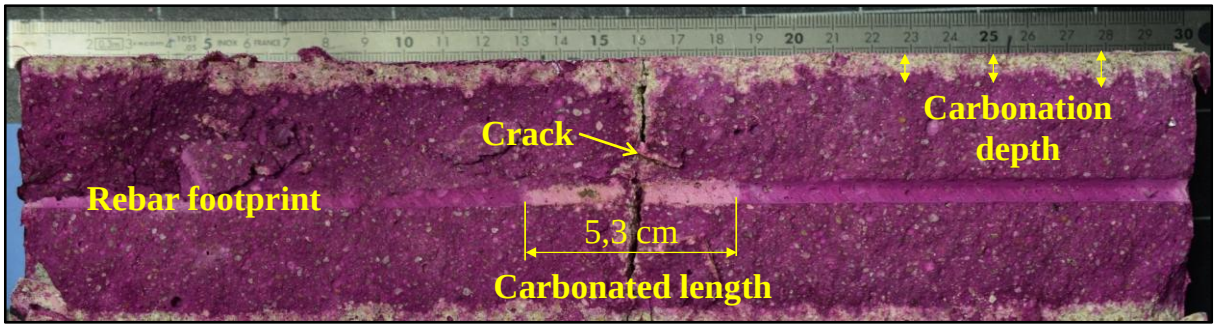

Figure 2 : Estimation de la longueur d'endommagement de l'interface acier/liant

Une étude préliminaire a été menée afin de définir les conditions de carbonatation convenables (%CO_2 et durée de carbonatation).

Après carbonatation, et par l'intermédiaire du dispositif ARIEL (Figure 3) développé et mis en place au cours de cette étude, les éprouvettes ont été soumises à la corrosion au moyen de cycles de pluie/séchage en conditions contrôlées.

Différentes configurations représentatives des conditions de service des tours aéroréfrigérantes ont été testées (ouvertures, orientations de fissures, effet du liant, qualité de l'interface acier/liant, durée de pluie, température, conditions environnementales naturelles, etc.).
Dans cette optique, différents types de cycles de pluie/séchage ont été appliqués. Les échantillons dédiés à l'étude de l'effet du liant, des ouvertures des fissures et de leurs orientations ont été exposés à un cycle de référence de 30 minutes de pluie tous les 3 jours, à 20°C. En particulier, deux orientations de la fissure par rapport à la pluie ont été testées : fissure orientée verticalement et horizontalement. Trois types de liants ont été fabriqués : mortier à base de CEM I, mortier à base de (CEM I + 50 % laitier) et béton (CEM I). L'effet de la durée d'exposition à la pluie a été étudié en imposant une durée de 3 minutes sur d'autres échantillons. Celui de la température a été cerné en augmentant celle du cycle de référence à 40°C. Des échantillons supplémentaires conservés dans les conditions extérieures ont été testés afin de valider si la corrosion obtenue en laboratoire est représentative de celle développée naturellement. De plus, afin d'étudier l'influence de la qualité de l'interface acier/béton sur la distribution de la couche de produits de corrosion, des échantillons décimétriques de 550×150×300 mm contenant des armatures à différentes hauteurs ont été analysés (Figure 4).

Figure 3: le dispositif ARIEL (simulAting RaInfall for concrEte durabiLity) pour corrosion accélérée par cycles de pluie en laboratoire

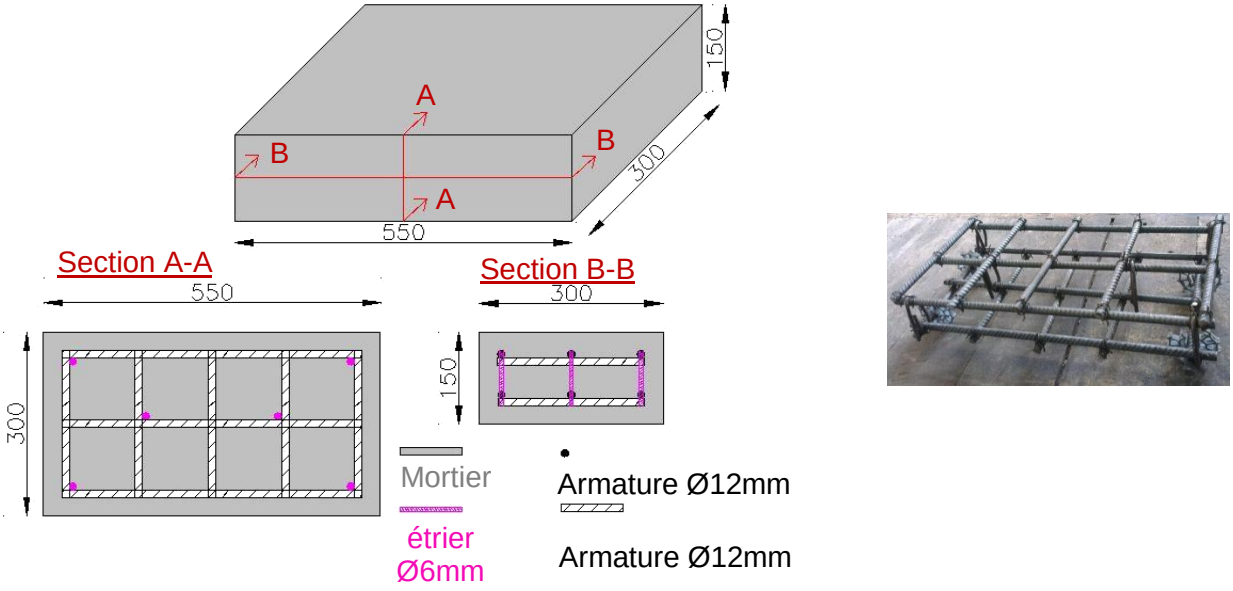

Figure 4: Schéma des échantillons métriques

Des éprouvettes ont été récupérées après différentes durées de corrosion, allant de 18 jours à 12 mois. Pour chacune de ces échéances, 4 éprouvettes de chaque condition d'exposition ont été analysées. La masse de fer perdue a été quantifiée à l'aide de mesures gravimétriques (desquamation de l'armature selon la norme NF ISO 8407). Finalement, la cinétique de corrosion a été déduite pour chaque condition de corrosion.
Par ailleurs, la répartition de la couche de corrosion de part et d'autre de la fissure a été déterminée par l'intermédiaire du microscope optique et la nature des produits de corrosion a été identifiée par la micro-spectroscopie Raman. En parallèle, des mesures en continu du potentiel de corrosion libre ont été menées sur quelques éprouvettes afin d'avoir une indication qualitative de l'état de corrosion.

Le programme expérimental est résumé dans la Table 1.

Conditions	Caractéristiques des échantillons	Ouverture de fissure (mm)	Orientation de la fissure	Nombre d'échantillons	Date d'analyse	Méthode d'analyse
Ouverture de la fissure	70×70×280 mm (mortier (CEM I))	0.1 0.3 0.5	Vertical	60	0, 1.5, 3, 6, 12 mois	1) Mesures gravimétriques 2) Microscope Optique 3) Spectroscopie Raman 4) Potentiel de corrosion libre
Orientation de la fissure			Horizontal	48	1.5, 3, 6, 12 mois	
Duré de la pluie			Vertical	18	1.5, 3, 6, 12 mois	
Humidité relative				15	3, 6, 12 mois	
Nombre de cycle de pluie/séchage	40×40×160 mm (mortier (CEM I))	0.1		2	Durée totale de 2 mois	1) Spectroscopie Raman 2) Fluorescence aux rayons X
Température	70×70×280 mm (mortier (CEM I))	0.1 0.3	Vertical	30	1.5, 3, 6, 12 mois	1) Mesures gravimétriques 2) Microscope Optique 3) Spectroscopie Raman
Conditions naturelles (Saclay)		0.3		12	3, 6, 12 mois	
Type de liant	70×70×280 mm (mortier (CEM I + laitier))	0.3	Vertical	15	0, 3, 6, 12 mois	
	70×70×280 mm (béton (CEM I))			15		
Dimensions de l'échantillon	550×300×150 mm (béton (CEM I))	0.1	Vertical	7	0, 3, 6 mois	Microscope Optique
Effet du %CO_2 et de la durée de carbonatation	70×70×280 mm + anneaux (mortier (CEM I))	0.1 0.3 0.5		42 + 3	3, 7, 15, 21, 30, 49, 61, 89 jours de carbonatation	Pulvérisation de Phénolphtaléine (indicateur de pH)

Table 1 : Résumé du programme expérimental

Résultats et discussions

Concernant les caractéristiques de la fissure, il a été déduit que dans un plan donné, l'ouverture de la fissure au niveau de l'armature est approximativement égale à celle mesurée sur le parement extérieur de l'éprouvette. En plus, le théorème de Thalès pourrait être appliqué pour déterminer l'ouverture de la fissure au niveau de l'armature par rapport à sa valeur maximale mesurée par le capteur de déplacement. Le ratio entre ces deux valeurs de l'ouverture de la fissure est 44 ± 5 %.

Il a été déduit que la carbonatation accélérée à 50% CO_2 (habituellement appliquée) n'est pas convenable parce qu'elle induit un retrait de carbonatation tout au long de l'interface acier / mortier. Par conséquent, la longueur d'endommagement de l'interface acier/liant supposée égale à la longueur carbonatée de l'interface sera surestimée. Les conditions de carbonatation convenables pour l'estimation de la zone endommagée sont 3% CO_2, 25°C et 55% humidité relative pendant 1 mois. En appliquant ce protocole de carbonatation sur 145 éprouvettes, il a été déduit que la longueur de l'interface acier/liant endommagée reste limitée à quelques centimètres de part et d'autre de la fissure induite par la flexion trois points.

Dans la suite, l'effet des différents paramètres testés sur la corrosion est présenté.

Les résultats montrent que la masse de fer perdue augmente avec l'ouverture de la fissure. En revanche, la cinétique de corrosion reste constante quelle que soit l'ouverture en raison de l'extension de la zone corrodée qui augmente elle-aussi avec l'ouverture de la fissure. D'autre part, après un certain nombre de cycles de pluie / séchage, la cinétique de corrosion diminue pour atteindre un palier avec une pente très faible entre 60 et 120 cycles correspondant à 6 et 12 mois d'expositions aux cycles de pluie / séchage. Cette diminution dans la cinétique de corrosion est liée aux produits de corrosion qui sont développés en fond de la fissure et qui jouent le rôle d'une barrière protectrice pour l'armature en limitant la diffusion des agents agressifs jusqu'à cette dernière.

De plus, il a été déduit que la cinétique de corrosion est indépendante de l'orientation de la fissure par rapport à la pluie ainsi que de la durée de pluie pendant chaque cycle. Cela est aussi dû aux produits de corrosion qui se développent en fond de fissure et contrôlent par leurs propriétés de diffusion la cinétique de corrosion. Les deux durées de pluie testées sont supposées être représentatives de deux faces opposées de la tour aéroréfrigérante ne recevant pas la même quantité de pluie. D'après les résultats de cette thèse, il pourrait être conclu que toutes les faces de la tour doivent être traitées de la même façon au cours du programme de maintenance.

La cinétique de corrosion mesurée sur des échantillons exposés à 20°C et 40°C est similaire.
Cela est dû à l'augmentation de la résistivité du mortier pendant la phase de séchage supérieure à 40°C qu'à 20°C. Cette augmentation de la résistivité limite la corrosion par macropile et masque ainsi la possible augmentation de la cinétique de corrosion à 40°C par la thermo-activation des réactions anodiques et cathodiques. Par conséquent, les tours aéroréfrigérantes devront être examinées lors de la maintenance indépendamment de leur localisation en France.

Les cinétiques de corrosion mesurées sur les échantillons exposés aux conditions environnementales de Saclay montrent la même tendance que celles obtenues sur les échantillons corrodés dans l'essai de référence. Les résultats obtenus sur les échantillons corrodés dans l'environnement de Saclay peuvent être un outil de validation du modèle empirique qui va être développé ultérieurement par EDF.

Les résultats ne montrent pas d'influence significative du type du liant utilisé sur la cinétique de corrosion. Cela est aussi justifié par les produits de corrosion qui se développent en fond de fissure et contrôlent la cinétique de corrosion indépendamment du liant. Par contre, il devra être noté que les longueurs de corrosion mesurées sur les armatures enrobées dans un béton à base de CEM I et dans un mortier à base de CEM I et du laitier sont plus faibles que celles mesurées lorsque le liant est un mortier à base de CEM I.
En effet, les longueurs d'endommagement mesurées sur l'interface acier/béton sont plus faibles que celles mesurées sur l'interface acier/mortier. Cette différence explique la différence observée dans les longueurs de corrosion.
Le mortier à base de (CEM I + laitier) a une plus grande résistivité que le mortier à base de (CEM I). Pour cette raison, la corrosion par macropile pourrait être limitée dans les liants contenant du laitier induisant ainsi une limitation dans la longueur de la zone corrodée. D'un autre côté, les réactions cathodiques peuvent aussi être limitées dans le mortier à base de (CEM I +50% laitier) en raison de la faible porosité de ces matériaux réduisant ainsi la présence d'oxygène.

L'épaisseur de la couche de corrosion est fortement liée à la qualité de l'interface. Cette différence dans l'épaisseur de corrosion est due au tassement et au ressuage du béton ou mortier, plus important sous l'armature supérieure par rapport au sens de coulage, induisant la création de vide et de défauts sous cette dernière. La plus importante conclusion est que dans le cas d'un enrobage fissuré (<500 µm), la qualité de l'interface acier/liant conditionne la corrosion plus que l'ouverture de la fissure. Opérationnellement, concernant les tours, on peut déduire que les armatures localisées dans la partie supérieure de chaque levée de béton coulée sont sujettes à une corrosion plus développée que les autres armatures et doivent être inspectées en premier.

La Figure 5 récapitule tous les résultats et montre que la cinétique de corrosion est similaire pour tous les paramètres testés (l'ouverture de la fissure et son orientation, le type du liant et des différentes conditions environnementales).

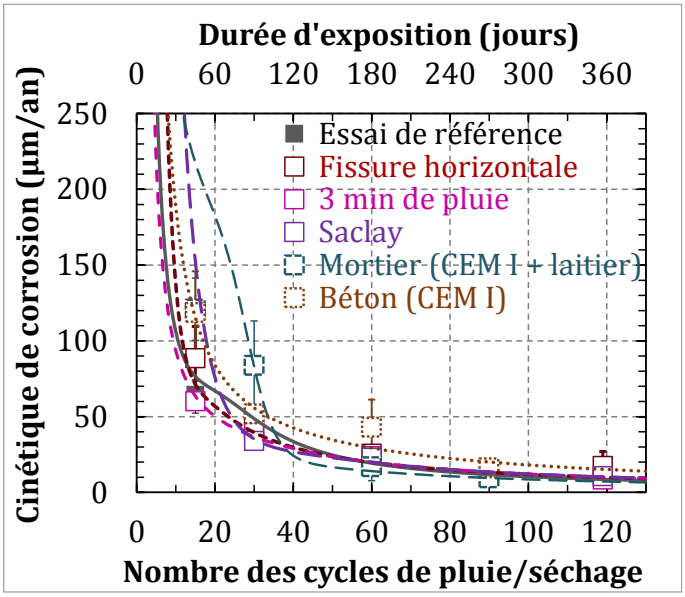

Figure 5 : Cinétique de corrosion en fonction de différents paramètres et du nombre de cycles de pluie/séchage

La nature des produits de corrosion développés dans les expériences décrites ci-dessus a été analysée par la spectroscopie Raman. Il a été déduit que le degré de saturation a un impact sur le degré de cristallisation des produits de corrosion. Dans le cas des échantillons ayant une faible saturation (cycles sous 40°C, cycles à 3 minutes de pluie, environnement de Saclay), les produits de corrosion amorphes se déshydratent et recristallisent en des phases mieux cristallisées, plus stables et ayant une faible réactivité. Ce qui n'est pas le cas dans les conditions d'expositions induisant un degré de saturation important dans les échantillons (cycles à 30 minutes de pluie, 90% d'humidité relative). Dans ces dernières conditions de corrosion, les produits de corrosion identifiés semblent être plus réactifs en ayant un degré de cristallisation faible. Il a aussi été déduit que pour chaque condition la nature des produits de corrosion n'a pas changé durant la durée de cette étude (12 mois).

Les valeurs du potentiel de corrosion libre diminuent pendant les 10 premiers cycles de pluie/séchage. Ensuite, le potentiel de corrosion augmente et rejoint celui d'une armature passive (Figure 6). Ces mesures de potentiel marquent l'existence de deux mécanismes de corrosion. Le premier mécanisme est la corrosion par macropile puis lorsque le potentiel de corrosion augmente et rejoint celui d'une armature passive, le mécanisme de corrosion par micropile devient prépondérant.

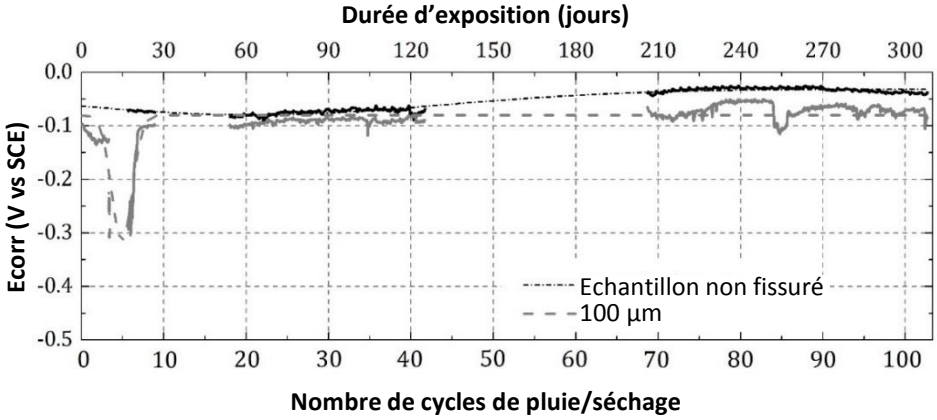

Figure 6 : Un exemple d'un cas de mesure du potentiel de corrosion libre

Conclusions et perspectives

Cette thèse répond à une demande opérationnelle d'EDF ayant pour but de rationaliser sa politique de surveillance et de maintenance des tours aéroréfrigérantes. L'objectif de ce travail est de caractériser l'influence de la fissuration sur la corrosion par carbonatation des armatures.
Pour cela des essais spécifiques ont été développés et les résultats montrent une diminution dans la cinétique de corrosion en fonction du temps, une absence de fissure de corrosion et une augmentation dans le potentiel de corrosion après un certain nombre de cycles. De plus, la cinétique de corrosion apparaît peu impactée par l'ouverture de la fissure, l'orientation de la fissure, le type du liant et les différentes conditions environnementales. Ces résultats confirment que des produits de corrosion remplissent le fond de la fissure et limitent la propagation de la corrosion. Par conséquent, il pourrait être déduit que la fissure favorise l'initiation de la corrosion mais pas sa propagation. Pour cette raison, les structures fissurées (ouverture < 500 µm) peuvent être traitées comme celles non fissurées. Ce point est important car il facilitera l'évaluation de la durabilité des tours aéroréfrigérantes (EDF).

La corrosion à très long terme n'a pas pu être investiguée dans cette thèse en raison de la contrainte de temps. Par contre, un modèle prédisant la propagation de la corrosion à long terme a été proposé (Figure 7). Ce modèle est basé sur quatre phases :

1. L'incubation : le temps nécessaire pour le dioxyde de carbone pour pénétrer dans la fissure et accéder à l'interface acier/liant.

2. L'initiation : cette période correspond à la période pendant laquelle la corrosion s'initie le long de l'armature interceptant un matériau carbonaté

3. L'induction : cette période commence lorsque la cinétique de corrosion diminue et sera contrôlée par les produits de corrosion développés en fond de fissure

4. La propagation : la période pendant laquelle la cinétique de corrosion augmente de nouveau et la corrosion se propage jusqu'à atteindre un degré limite acceptable.

En se basant sur les résultats obtenus dans cette thèse, il pourrait être supposé que la phase de propagation ne sera pas induite par la corrosion en fond des fissures mécaniques mais plutôt par la carbonatation totale du béton d'enrobage. Ce modèle a été proposé dans l'étude [1] discutant la corrosion induite par les chlorures dans un béton fissuré. Dans cette thèse, on prouve que le même modèle est applicable aussi en cas de corrosion par carbonatation dans un matériau fissuré.

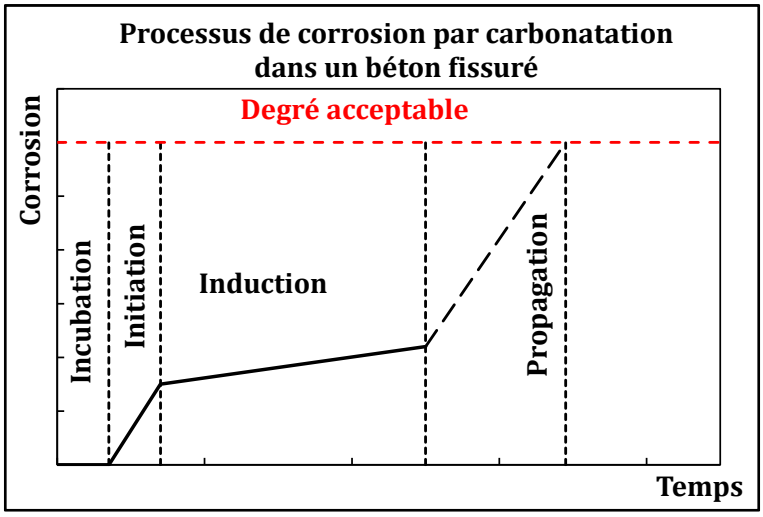

Figure 7 : Modèle de corrosion par carbonatation dans un béton fissuré

Il est important de noter que ces conclusions ne s'appliquent pas sur les structures :

- Exposées au gel-dégel ou à des attaques chimiques pouvant être décisives pour la durabilité de la structure plus que la corrosion induite par carbonatation en fond d'une fissure.

- Exposées à des chargements dynamiques induisant une variation dans l'ouverture de la fissure et pouvant éventuellement annuler la protection de l'armature par les produits de corrosion.

Du fait que les tours aéroréfrigérantes peuvent être exposées à des chargements mécaniques et à des variations dans l'ouverture de la fissure, il serait intéressant dans les futurs travaux de contrôler l'évolution de la cinétique de corrosion sous ces conditions. Pour simuler la variation de la fissure en laboratoire, des chargements cycliques peuvent être réalisés sur des échantillons exposés à la corrosion à des intervalles de temps constant. Une

représentation schématique du protocole expérimental qui pourrait être utilisé pour cet objectif est donnée dans la Figure 8. Par l'intermédiaire d'une clé dynamométrique, le chargement pourrait être contrôlé et modifié. La mesure du potentiel de corrosion libre pourrait être suffisante pour avoir une indication sur l'évolution de l'état de la corrosion sous les cycles de chargement.

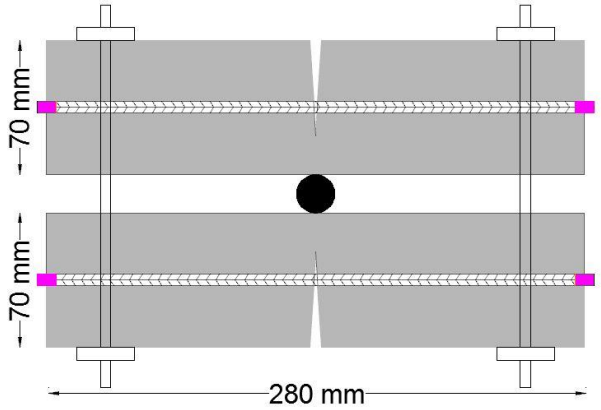

Figure 8 : Système de chargement

D'un autre côté, il serait intéressant d'analyser certains échantillons des tours aéroréfrigérantes pour deux raisons. La première est d'avoir une estimation de l'état réel de corrosion dans les tours. La deuxième est de valider les résultats obtenus en laboratoire. En particulier, ces échantillons pourront être prélevés des armatures localisées sur la partie supérieure d'une levée de béton coulée en une seule fois parce qu'elles seront représentatives de l'état le plus critique.
En fonction des résultats, il pourrait être confirmé si la durabilité des tours est menacée par la corrosion en fond de fissure ou plutôt par la carbonatation du béton d'enrobage. Ainsi, il pourrait être décidé si un traitement de corrosion ou une protection du béton d'enrobage contre les dégradations est nécessaire.

GENERAL INTRODUCTION

Steel reinforced concrete is a composite material combining the compression strength of concrete and the high tensile properties of reinforcement steel and has a wide range of applications in structural engineering. Concrete plays a protective role against reinforcement corrosion. Indeed, the alkalinity of the concrete pore solution ensures to the steel rebars a passive state in which the corrosion rate is negligible. Additionally, the concrete cover acts as a barrier for aggressive agents and delays their time of arrival to the rebar. However, this protection may be weakened by the presence of cracks in the concrete.

Cracks are unavoidable because of the low tensile strength of concrete. They can occur as a result of shrinkage, loads, deformations, etc. However, independently from their origin, the presence of cracks compromises the protective characteristics of the concrete cover by changing the permeability of the materials in the cracked zone. Indeed, various substances such as carbon dioxide, chloride, moisture and oxygen can therefore reach the rebar through the cracks much faster than through the pore system of the concrete cover. Consequently, a marked increase in the corrosion initiation rate takes place in the cracked areas.

The propagation phase of chloride-induced corrosion along reinforcement steel intercepting cracked concrete is widely studied in the literature while the propagation of carbonation-induced corrosion is still a subject of debate. The propagation of corrosion may be dependent from several factors:

- Crack direction with respect to the rebar: the corrosion process is different in cracks perpendicular to the reinforcement and in cracks parallel to the reinforcement.

- Crack width which may be a conditioning factor for the accessibility of aggressive agents to the rebar.

- Dimension of the slip zone (i.e. damaged zone) induced by the mechanical loading along the steel/concrete interface surrounding the mechanical crack.

- Location of the rebar in the structure which could impact the steel/concrete quality.

- Environmental factors such as temperature, rain duration, etc.

Concerning the consequence of this propagation phase, two hypotheses shall be examined:

- Corrosion will be stopped after a certain time due to the repassivation of steel induced by the corrosion products that may seal the crack. This is supposed since all the structures are cracked and continue to function acceptably for a long periods of time.

- The expansive action of corrosion products may induces corrosion cracking. The latter cracks start at the rebar and reach the outer surface of the concrete cover. They are generally parallel to the rebar. Therefore, these corrosion cracks allow a direct access for aggressive agents, water, and oxygen to reinforcement which leads to an atmospheric corrosion process. The consequence of this phenomenon is the reduction in the adhesion between concrete and steel and a probable delamination of concrete which will threaten the durability of structures in advance stages.

The main objective of this study is to identify the carbonation-induced corrosion initiation and propagation in cracked concrete under different conditions.

Additionally, an industrial application is behind this project. In fact, the obtained results will be used thereafter to estimate the corrosion kinetics in the cooling towers of Electricity of France (EDF) nuclear power plants. Actually, some of them can be affected by cracks and EDF implements a maintenance program to extend their service life to over than 40 years. For a better control of cooling towers concrete damage evolution, it is necessary to apprehend the development of corrosion due to carbonation in cracked concrete structures which is thus the main interest of this project. The results obtained during this study will be used later to develop an empirical model aiming to estimate the carbonation-induced corrosion kinetics in the cooling towers. Thereafter, this will be implemented into numerical tools developed by EDF aiming to evaluate the degradation of cooling towers in order to optimize the maintenance program.

Consequently, the experimental campaign is defined in a way to make results useful for the industrial objective. Cracks perpendicular to the rebar will only be performed with different widths chosen accordingly to those existing on the cooling towers. Moreover, the influence of several environmental conditions representative of those surrounding the cooling towers on the corrosion development are also tested (raining/drying cycles, temperature, etc.). Additionally, several materials type will be performed in this study. Furthermore, different specimen's dimensions are also realized to simulate the structure dimension and determine the impact of the steel/binder interface quality on the corrosion spread.

The realization of the above mentioned experiments requires a specific and suitable cracking protocol in addition to the development of several equipments in the laboratory in order to simulate the environmental conditions (raining/drying cycles).

In the following, a brief description of each chapter in this thesis is given:

The first chapter presents a literature review on carbonation and corrosion processes. First, a brief description of the carbonation process is given. Then, its occurrence with respect to different factors and its impact on the structure are presented. In a second step, the corrosion process is presented and the influence of several factors on its development is also given. Finally, the impact of the corrosion process on the structure is also discussed.

The second chapter describes the program implemented and conducted at CEA Saclay and LMDC Toulouse. First the specimen's characteristics will be given. Thereafter, equipments developed to perform the required experiments for the accomplishment of this project are presented. Then the cracking protocol, the carbonation procedure and the corrosion tests are detailed in addition to the method of analyses chosen.

The remaining chapters going from the third one to the seven one aim to present and discuss results.

Chapter 3 is dedicated to the presentation and discussion of the cracking protocol. In detail, the methods used to control the crack width and to quantify the length of the damaged zone from either side of the crack.

Chapter 4 discusses the influence of the crack opening on the carbonation-induced corrosion and propose a long term behavior for the corrosion development.

Chapter 5 presents the corrosion results obtained under the different exposure conditions tested in this study which consist of varying the orientation of the crack with respect to rain, the rain duration, the temperature, etc.

Chapter 6 presents the impact of the material type on the rebars corrosion. Three cracked cementitious materials type are considered: CEM I mortar, (CEM I + slag) mortar and CEM I concrete.

Chapter 7 aims to discuss the impact of the steel/mortar interface quality on the corrosion development.

Finally, general conclusions are introduced and prospects are proposed.

CHAPTER 1. BIBLIOGRAPHIC REVIEW

1.1 INTRODUCTION

Corrosion of reinforcement in cracked and carbonated concrete is the focus of this study. Therefore, the aim of this bibliographic review is to present first the cementitious materials in general. Then the carbonation process in cementitious materials will be discussed. At the end, literature works studying corrosion by carbonation are exposed.

1.2 CEMENTITIOUS MATERIALS

90 % of cement contains four chemical compounds which are:

- Two types of calcium silicate: dicalcium silicate (*C_2S)* and tricalcium silicate (*C_3S).* These chemical compounds, constituting 75% of the chemical composition of Portland cement, essentially ensure the mechanical strength of the hydrated cement,
- Tricalcium aluminate (*C_3A),*
- Tetracalcium aluminoferrite (*C_4AF*).

The hydration process of both calcium silicates leads to the formation of calcium hydroxide *$Ca(OH)_2$* symbolized by "*CH* " known as portlandite. The alkalinity of the latter compound ensures to the pore solution a high pH value of 12.45 at 25°C. The presence of alkalis (Na(OH) and K(OH)) increases the value of the pH up to 13 or 13.5. This high pH inhibits the corrosion of steel reinforcement [2]. Consequently, the CH compound has an important role in the durability of concrete.

On the other hand, the calcium-silicate-hydrate (C-S-H), second compound of the hydration reaction of silicates, is determining in the mechanical strength of a structure [3]. Na_2O and K_2O increase the pore solution pH.

Following Tennis and Jennings [4], the chemical hydration reaction can be summarized as follows:

Dicalcium silicate is :

$$2C_2S + 8.6H \rightarrow C_{3.4}S_2H_8 + 0.6CH \quad (1.1)$$

Tricalcium silicate is:

$$2C_3S + 10.6H \rightarrow C_{3.4}S_2H_8 + 0.6CH \quad (1.2)$$

Tricalcium aluminates is:

$$C_3A + 3C\bar{S}H_2 + 26H \rightarrow C_6A\bar{S}_3H_{32} \quad (1.3)$$

Tetracalcium aluminoferrite is:

$$C_4AF + 2CH + 10H \rightarrow 2C_3(A,F)H_6 \quad (1.4)$$

According to the diagram shown in Figure 1-1 taken from the study [4], at the final stage of hydration, C-S-H constitutes 50% to 60% of the volume of the hydrated cement paste while portlandite form 10% to 15% of this volume. During the hydration reaction, ettringite ($C_6A\bar{S}_3H_{32}$) may be consumed in order to form monosulfoaluminate ($C_4A\bar{S}H_{12}$). This diagram is for a cement paste with water to cement ratio of 0.5 based on a type I cement composition.

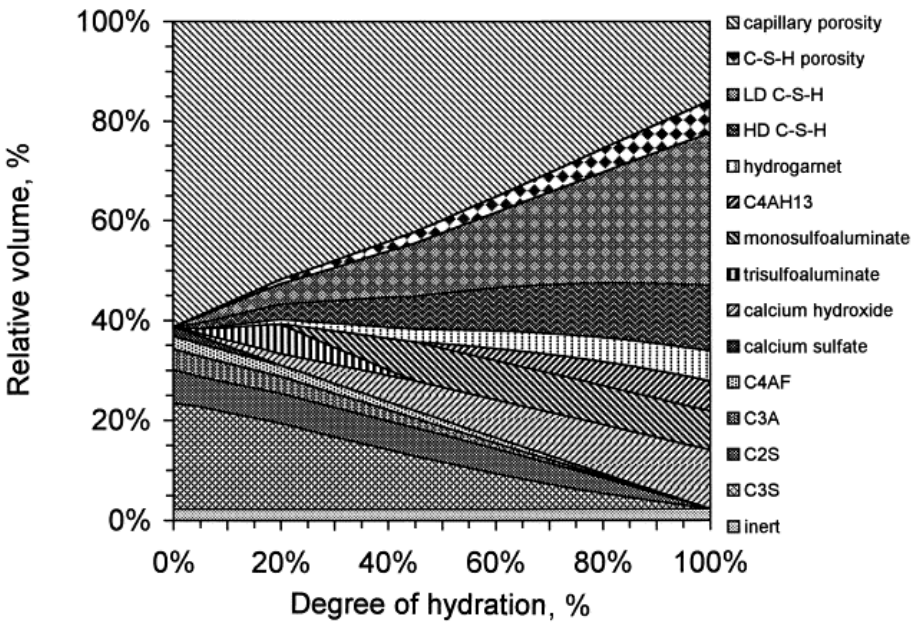

Figure 1-1: Relative volume of each phase of the cement composition as a function of the degree of hydration [4]

Figure 1-2 obtained using scanning electron microscopy (SEM) shows the major phases present in the microstructure of a hydrated cement paste. It is obvious that the morphology and the size of these phases is not uniform. The C-S-H morphology vary from poorly crystalline fibers to reticular network. The exact structure of C-S-H still subject to debate [5]. In contrast to the C-S-H, portlandite is well crystallized and forms large crystals with a distinctive hexagonal-prism morphology. Ettringite shows a needle-shaped prismatic crystal. The monosulfate hydrate obtained from ettringite has an hexagonal-plate crystals [5].

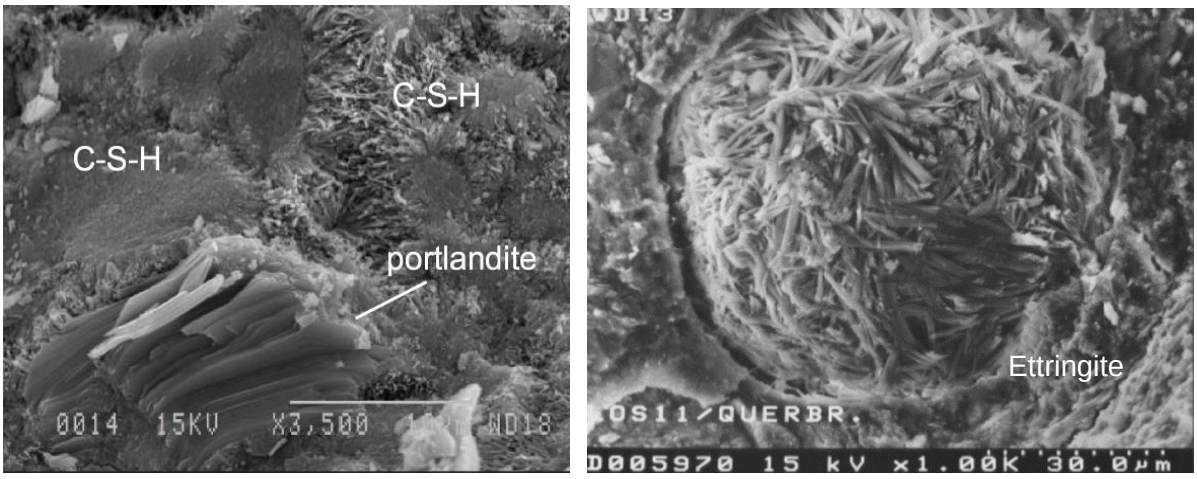

Figure 1-2: Scanning electron microscope (SEM) images of hydrates[6], [7]

In addition to solids, the hydrated cement paste contains different type of voids (pores). The size of voids and solid is given in Figure 1-3. Concerning the void size in cementitious materials, it varies from nanometric scale to millimetric scale.

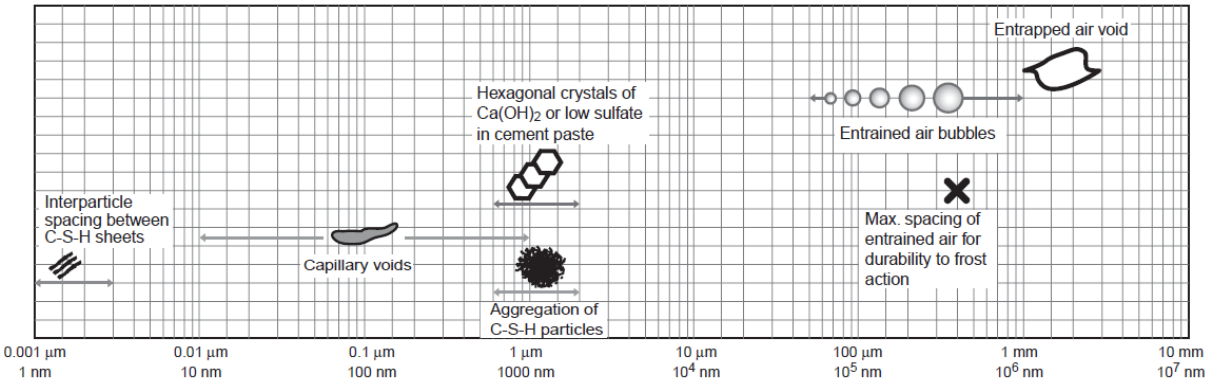

Figure 1-3 : Dimensional range of solids and pores in hydrated cement paste [5]

Nanoporosity is generally associated to spacing between the C-S-H sheets which is dependent from the materials type and the hydration degree [4]. In this study, it is considered to range from 0.3 nm to 10 nm.

Capillary voids correspond to the irregular space not filled by the solid components of the hydrated cement paste. The volume and the size of the capillary pores decreases with hydration. In this study, their size is considered to be from 10 nm to 1mm.

Air voids are generally spherical [5] and corresponds to the air entrapped in the cement paste during the mixing and to entrained air voids. The entrained air bubbles usually range from 50 to 200 µm and do not exist in the cementitious materials performed in this study. While the entrapped air voids can be as large as 3 mm.

The hydrated phases in cementitious matrix are able to interact with the environmental components like the carbon dioxide and this reaction is detailed in the following section.

1.3 CARBONATION PHENOMENON

1.3.1 Carbon dioxide concentration

Since the industrial revolution, the CO_2 concentration continues increasing in the atmosphere [8]. Since 1950, this concentration starts increasing by a relative value of 0.5% per year on a global scale and particularly in urban areas [3] . Due to these climatic changes, the carbonation of reinforced concrete is getting worst through the time. The percentage of carbon dioxide can reach a value of 1% in poorly ventilated environment such as tunnels. In large cities, the CO_2 volume fraction is about 0.3%. This is not the case for the rural environment surrounding the cooling towers, where the volume fraction of CO_2 is about 0.03-0.04% [9].

1.3.2 Dissolution of carbon dioxide in an aqueous solution

When a solution is exposed to a partial pressure of carbon dioxide, the latter dissolves in the water and it hydrates in the form of carbonic acid according to Henry's law [10]:

$$CO_{2(g)} + H_2O \leftrightarrow H_2CO_3 \quad (1.5)$$

Following the autoprotolysis of water (equation (1.6)), carbonic acid H_2CO_3 dissociates in water into two phases (HCO_3^- and CO_3^{2-}) as shown in the two equations (1.7) and (1.8).

$$H_2O + H_2O \leftrightarrow OH^- + H_3O^+ \quad (1.6)$$

$$H_2CO_3 + OH^- \leftrightarrow HCO_3^- + H_2O \quad (1.7)$$

$$HCO_3^- + OH^- \leftrightarrow CO_3^{2-} + H_2O \quad (1.8)$$

The reaction shown in the equation (1.7) releases the hydrogen carbonate (HCO_3^-), a predominant acid for a pH between 6.3 and 10.3. The dissociation of the bicarbonate ion according to equation (1.8) allows the formation of carbonate ion which is predominant for a pH greater than 10.3.

1.3.3 Carbonation process in reinforced concrete structures

Atmospheric carbon dioxide is able to diffuse through the unsaturated pore network and/or through the cracks existing in the reinforced concrete structures. A portion of the carbon dioxide dissolves in the pore solution and induces a decrease in the pH to a value of about 8. The acidification of the pore solution induces the dissolution of the hydrates, especially the portlandite $Ca(OH)_2$. This neutralization reaction of hydrates by the carbon dioxide is called carbonation and is presented below for each hydrate.

The steps of the **portlandite** carbonation mechanism as indicated in [11] are shown below :

$$Ca(OH)_2 \leftrightarrow Ca_2^+ + 2OH^- \quad (1.9)$$

The calcium ions, obtained from the reaction (1.9), react with the carbonate ions, released from the reaction (1.8), according to equation (1.10).

$$Ca_2^+ + CO_3^{2-} \leftrightarrow CaCO_3 \quad (1.10)$$

Figure 1-4 illustrates the portlandite carbonation mechanism showing the transition of CO_2 from a gaseous phase to a solid phase through an aqueous phase.

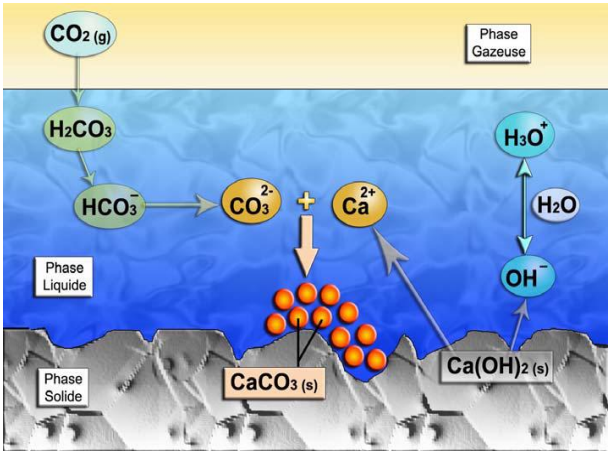

Figure 1-4: Portlandite carbonation mechanism [11]

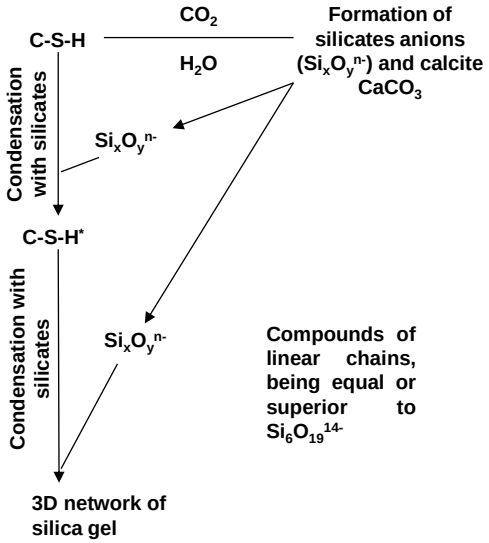

Figure 1-5 : C-S-H carbonation mechanism and formation of silica gel [12]

C-S-H can also be carbonated according to reaction (1.11). The dissolved CO_2 decalcifies C-S-H releasing silicate anions. These silicates react with other silicates in C-S-H. That leads eventually to the formation of a silicate chain increasingly longer and low in calcium. The product formed has an amorphous structure, which is similar to silica gel (Figure 1-5).

According to Dunster [12], the carbonation of C-S-H refers to a polymerization process of silicate forming product that are not representative of the initial silicates.

$$(CaO)_x - (SiO_2)_y - (H_2O)_z + xH_2CO_3 \rightarrow xCaCO_3 + ySiO_2.tH_2O + (x - t + z)H_2O \quad (1.11)$$

Groves et al. [13] shows that accelerated carbonation is not always representative to natural carbonation where calcium hydrated silicate (C-S-H) polymerizes without forming silica gel. While in accelerated carbonation, silica gel is obtained as shown in the results of Castellote et al. [14], which investigated the effect of the carbon dioxide concentration on the changes in Portland cement due to its carbonation.

Other hydrates are also sensitive to carbonation such as **hydrated calcium aluminates** resulting from the C_3A hydration reaction. Their amount in conventional cementitious materials containing moderate sulfate and/or aluminates quantities is small. Moreover their carbonation and the carbonation of the alkalis Na_2O and K_2O are fast.

1.3.4 Carbonation front in concrete

The carbonation of cementitious materials is driven by the diffusion of CO_2. The kinetics of carbonation through the concrete cover is proportional to the square root of time [15]. Most finite element models express the carbonation front (mm) "x" as equal to "$K\sqrt{t}$" where K is the carbonation constant (mm/yr$^{0.5}$) and t is the exposition time (yr). The value of K is an indicative of the concrete quality as proposed in Table 1-1.

Table 1-1: concrete quality depending on the K values [16]

	Poor concrete	Average concrete	Good concrete
K (mm/yr$^{0.5}$)	>9	9>K>6	<6

1.3.5 Parameters affecting carbonation

Carbonation of concrete is a slow process. Several factors affect its kinetic. Some of them are related to the concrete itself (cement type, water to cement ratio w/c, cracking), to the atmosphere surrounding the concrete (concentration of carbon dioxide in the air, relative humidity, temperature) and to the fabrication process (cure, casting, heat treatment).

1.3.5.1 Parameters related to the concrete

a) Cement type:

Concrete including composite cements showed a greater carbonation depth than concrete based only on CEM I according to [17]–[19]. This result is linked to the fact that in alternative cements, calcium carbonate is formed in smaller amounts which facilitates the progression of carbonation through the concrete cover. On the opposite, Drouet [20] showed that the permeability of CEM V and low pH cement paste is lower than the one of CEM I and CEM II cement paste. But this difference is not sufficient to compete the effect of the carbonatable materials amount.

In this study, the effect of two cement type is tested: CEM I and CEM I + 50% slag.

b) Water/cement ratio:

In the absence of cracks, carbonation rate is affected by the water to cement ratio. In fact, in such a case, carbonation requires that carbon dioxide penetrates from the concrete surface to the reinforcement. Low porosity and permeability are two major factors that can inhibit the penetration of the carbon dioxide. Literature studies [21], [22] show that the higher w/c, the higher the permeability and porosity. In fact, high water to cement ratio leads to a high

evaporable water quantity. Once evaporated, pores become accessible to carbon dioxide diffusion. This justifies the increase in the kinetics of carbonation with the increase in the water to cement ratio. In the same context, a high cement contents leads to a small carbonation depth since it reduces the concrete porosity and enhances its density which reduces the CO_2 access to the carbonatable products [10].

In the presence of cracks, the w/c ratio has a negligible effect. The carbon dioxide reaches the reinforcement through the crack with a speed clearly higher compared to its penetration from the cover to the reinforcement in the absence of cracks. **That is why, the w/c ratio effect is not studied in this project and is chosen as a value equal to that observed in the concrete composing cooling towers.**

c) Pre-cracks:

Cracking is an adventitious phenomenon that can be due to different physical, chemical and mechanical factors. Concrete cracking is common and inevitable [23]. This is why, several works aim at studying its effect on structures durability.

Cracks offer an easy path for the penetration of different aggressive agents (carbon dioxide, chloride ion, oxygen, water, etc.) to the reinforcement, and thus accelerate the carbonation of the concrete in cracked zone.

In case of cracked specimens, loading affects significantly the carbonation process. In fact, and as illustrated by [24], the carbonation front is thicker in the areas subjected to tension (Figure 1-6) than in those subjected to compression. This study reveals also that loading may induce micro-cracks between the cement and the reinforcement as well as between the cement and the aggregates, which increases the porosity and facilitates the penetration of the carbon dioxide. The development of these microcracks is dependent from the loading rate and from the resulting crack opening. This is also confirmed by Castel et al. [25].

On the other hand and concerning carbonation deep in the crack, Alahmad et al. [26] showed that carbonation in the crack path of crack surface occurs independently from the crack opening, but diffusion perpendicular to the crack path occurs only for crack opening higher than 9 µm. Alahmad et al. [26] relates that to the interaction between the two sides of the crack. Moreover, the same study shows that for a crack opening between 9 and 41 µm, the carbonation depth perpendicular to the crack side is limited.

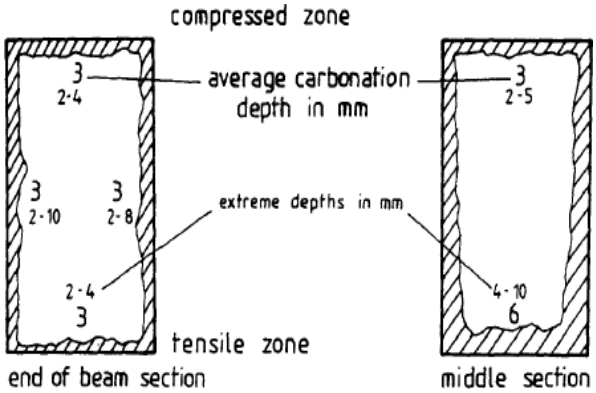

Figure 1-6: Depth of carbonation in two sections: one in the middle of the beam and one at the end of the beam (40 weeks after carbonation) [24]

The effect of different crack openings on the carbon dioxide penetration along the steel/mortar interface is chosen to be tested in this study.

1.3.5.2 Parameters related to the atmosphere:

a) Temperature:

On one hand, the solubility of reagents (C-S-H, CO_2 and $Ca(OH)_2$) decreases with the increase in temperature [18]. Moreover, several studies prove the existence of an optimal carbonation temperature above which the solubility of the hydrates decreases and therefore the kinetics of carbonation decreases [27], [28], [20].

On the other hand, transport properties (gas (CO_2) and ion diffusion (CO_3^{2-}, Ca^{2+})) increase with temperature due to the thermal – activation according to Arrhenius law (1.12) and the water evaporation [29], [30] (Table 1-2).

$$D = D^0 \exp\left(\frac{-E_a}{RT}\right) \quad (1.12)$$

Table 1-2: Effect of the temperature on the carbonation depth [20]

Author's name	Reference	Year	Temperature	Carbonation
Mori et al	[31]	1972	20°C to 40°C	Depth multiplied by 2
Yanagi&Tomosawa	[32]	1987	10°C to 30°C	Kinetics multiplied by 1.7
Papadakis et al	[33]	1991	22°C to 42°C	Depth multiplied by 1.2
Villain et al	[34]	2000	20°C to 40°C	Depth multiplied by 2.8
Drouet	[20]	2010	20°C to 80°C	Depth multiplied by 3.9

Since the optimal carbonation temperature is still unknown, a constant temperature, equal to the ambient one (25°C), is chosen for our study.

b) Relative humidity:

The relative humidity (RH) is a major factor influencing the kinetics of the carbonation.

Carbonation reaction does not occur neither in a completely dry concrete nor in a saturated one. In fact, at low RH, chemical reactions are inhibited because of the lack of water while at high RH, CO_2 diffusion is limited due to the concrete pores saturation (the diffusion coefficient of carbon dioxide in aqueous solution is 10^4 times lower than in the gas phase [35]).

The optimal relative humidity for the carbonation reaction at a temperature of 20°C is between 50% and 70% (Figure 1-7) [36].This result is consistent with that of Galan et al. [37], showing that the total weight gain after 1 year of carbonation depends on RH and follows a parabolic behavior having a maximum around 55% of RH (Figure 1-8).

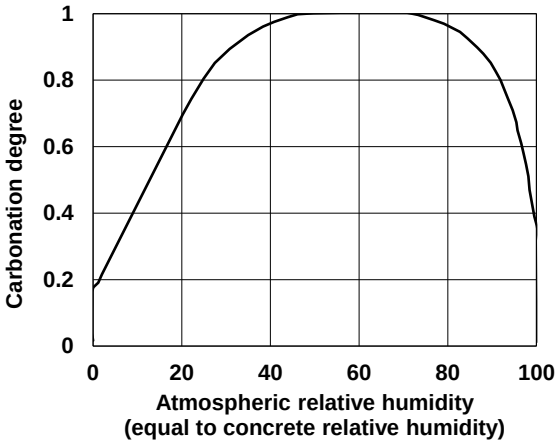

Figure 1-7: Kinetics of the carbonation with respect to the relative humidity [36]

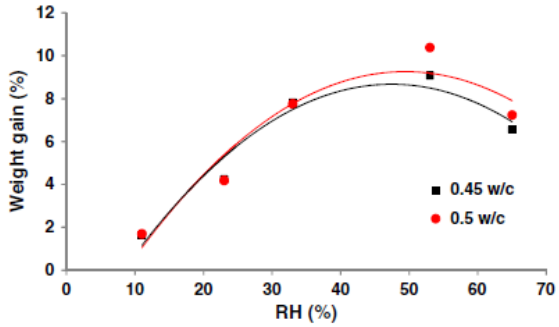

Figure 1-8: Weight gain induced by one year of carbonation with respect to relative humidity [37]

In our study, the carbonation is used in order to initiate corrosion. So a high kinetics of carbonation reaction is needed. For this reason, based on the results of the literature, specimens are carbonated in a climatic chamber regulated at 55% RH.

c) Carbon dioxide concentration :

The carbonation rate increases with the carbon dioxide concentration [14]. This result was deduced by monitoring the evolution of the specimen's weight during accelerated carbonation experiments realized at different carbon dioxide concentrations (Figure 1-9). In these experiments, the measured mass stabilizes earlier for carbonation at 10% and 100% of CO_2 than for carbonation at 3% of CO_2.

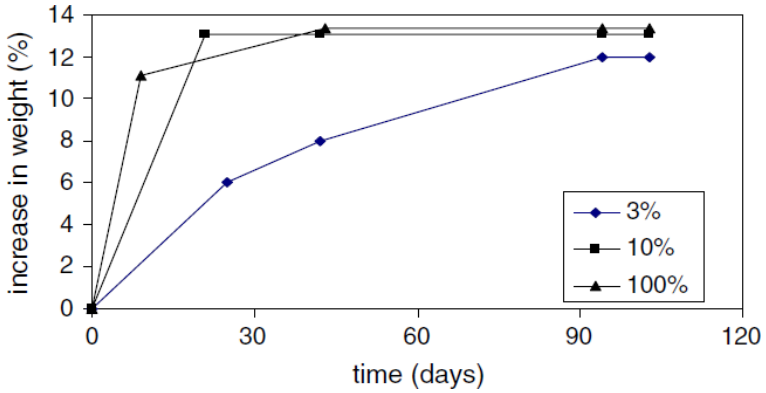

Figure 1-9: Evolution of the specimen's weight in an accelerated carbonation according to different carbon dioxide concentrations [14]

In addition, the carbonation depth (x) is linearly proportional to the square root of the carbon dioxide concentration (1.13).

$$x_c = \frac{\sqrt{2.D_{CO_2}.P_{CO_2}.t}}{QRT} \quad (1.13)$$

With:

- D_{CO_2}: coefficient of CO_2 diffusion in carbonated zones (m^2/s)
- P_{CO_2}: pressure of CO_2 at the concrete surface (Pa)
- t: time (s)
- Q: quantity of carbonatable materials (mol/m^3 of material)
- R: constant of perfect gases (J/mol/K)
- T: temperature (K)

This law remains valid for carbon dioxide concentration lower than 50% [38]. Matsushita [39] showed also that the carbonation degree increases with increasing the carbon dioxide concentration.

Consequently, high carbon dioxide concentration proves its beneficial effect in accelerating carbonation in laboratory tests. However, it has an important drawback that should not be forgotten which is the lack in the representativity of the natural carbonation. In this field and regarding C-S-H carbonation, Castellote et al. [14] showed that carbon dioxide concentrations greater than 3% give results that are not representative of natural carbonation. This is due to the fact that at higher concentration, the carbon dioxide induces a strong decalcification and polymerization in the silicate chain, which can cause the C-S-H disappearance and this is not the case at lower CO_2 concentrations. Moreover, the studies [13], [40] showed that during the carbonation reaction at a high carbon dioxide concentration, an impermeable $CaCO_3$ layer surrounds portlandite. Therefore, the C-S-H will provide more Ca than portlandite which would induce a strong decalcification of C-S-H. In the study [40], it was indicated that the carbonation shrinkage is directly related to the decalcification of C-S-H. This is also confirmed by the studies [36], [41], [42] and [43]. Faucon et al. [44] observed, after leaching tests of a Portland cement paste, the formation of cracks in the region subjected to the greatest Ca/Si gradient ratio. According to [44], these cracks are due to the decalcification of C-S-H and precipitation of silica gel. Therefore, the carbonation reaction at a high carbon dioxide concentration may induce damage for the cement paste.
In this study, we will pay attention to this phenomenon while determining the carbonation propagation along the steel/mortar interface.

d) Rainfall

The surfaces of a structure exposed directly to rainfall are less carbonated than that away from the rainfall. This can be explained by the fact that the rain increases the saturation of the samples and thus prevents the diffusion of carbon dioxide [45].

However, in presence of cracks, carbonation may be capable to occur deep in the crack independently from the rain. **This is taken as hypothesis in this study and the effect of the rain on the carbonation is not studied.**

1.3.5.3 Parameters related to the fabrication:

a) Wall effects:

During the concrete casting, several gravels are localized near the mold walls. In this zone, the location of the gravels is determining in the microstructure of the concrete. During vibration, the center of large aggregates cannot be close to the mold surface more than their radius "r". This phenomenon is the cause of the wall effect (Figure 1-10). During the study [46], it was observed that areas subjected to the wall effect have a porosity volume 21% larger than that existing in the concrete mass. Therefore, the penetration of aggressive agents and water through the face of concrete suffering from wall effect is easier and thus the chemical reaction, including the carbonation reaction, is the most advanced in this zone. The wall effects are also observed in several other studies [47]–[49].

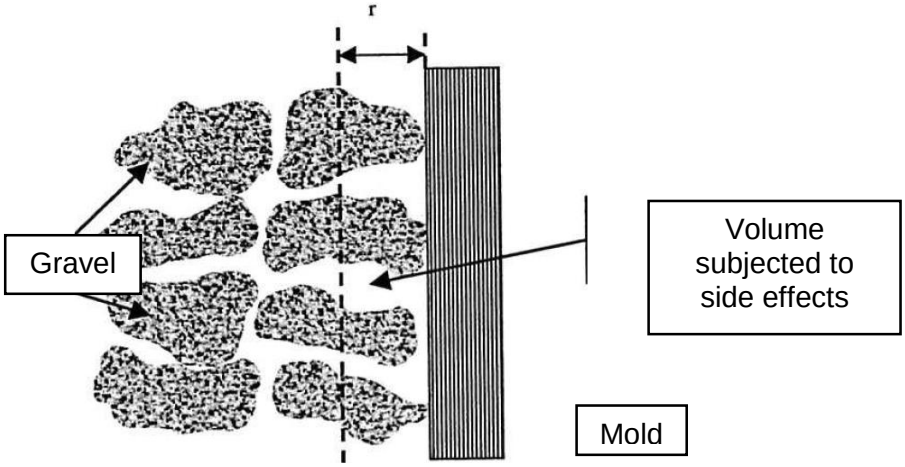

Figure 1-10: Gravels disposition near the mold wall [46]

b) Curing duration:

During the first hours after casting, concrete may be subjected to desiccation. This induces a lack of water that is required for the complete hydration of concrete. Thus, the concrete porosity increases. As a consequence, carbonation rate increases also. Hence, a minimum duration of concrete curing is needed in order to obtain sufficient maturity of the concrete surface. That is how, the sensitivity of concrete to drying becomes lower. Moreover, the required water for the cement hydration and the microstructure development is ensured. Therefore, a well cured concrete is known to have a high performance in terms of durability (resistance to the penetration of aggressive agents…). The higher the concrete cure duration, the higher the carbonation resistance [50]. This is also seen in the Figure 1-11, which shows the compressive strength of the concrete according to different curing time (if the compressive strength is high, the pore size is small; therefore, the resistance to carbonation is high). Moreover, it is mentioned in [10] that a curing time of three days in the laboratory is representative of that on the worksite, the increase in the cure time from one day to three days decreases the carbonation front by 40%. The latter observation corresponds well with what was found in the studies [51], [52] and [53] (Figure 1-12). .

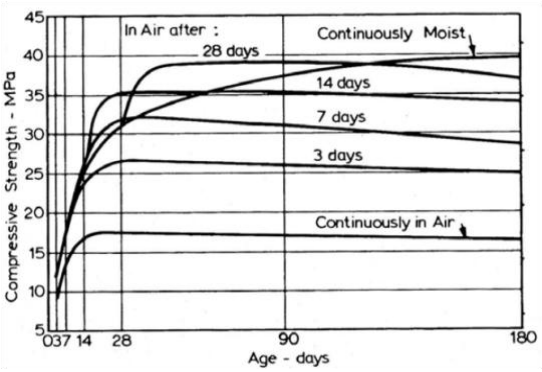

Figure 1-11: compression strength of the concrete having a water to cement ratio of 0.5 with respect to the curing time [54]

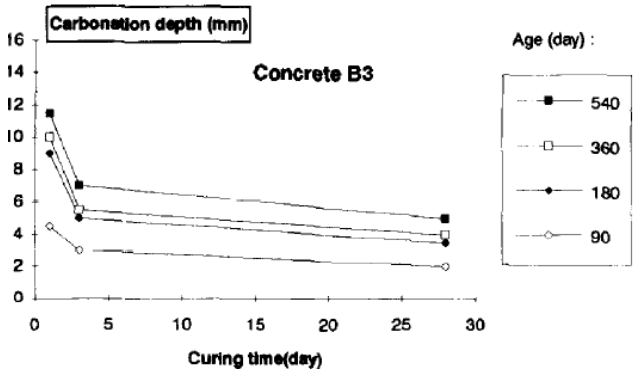

Figure 1-12: Effect of curing on carbonation (cement used CPJ 45) [51]

In our study, standardized curing time of 28 days for concrete is chosen

1.3.6 Consequences of carbonation

Carbonation changes several characteristics of concrete. The most important factors are the microstructure of the concrete, its mechanical performance, its transport properties, its water content and change in its pH value.

Apart from pH decrease, carbonation also impacts microstructure. The molecular volume of calcium carbonate is higher than that of calcium hydroxide [55]. For concrete, this increase in volume is beneficial because it partially seals the pores of the concrete and increases its mechanical strength. Moreover, calcium carbonate is an excellent binder. So the carbonation reaction is not harmful to the concrete itself and helps improving its mechanical properties [56]. But the decrease of the interstitial solution pH, induced by carbonation, reduces the protective role of concrete to the reinforcement steel. That is why, carbon dioxide is identified as an aggressive agent.

Moreover, it was found in [57] that the carbonation modifies the transport properties of water. This has been linked to the mineralogical and microstructural variation registered in the carbonated cementitious materials. These changes induced by carbonation in the transport properties of water and in the microstructure of cementitious materials may have a direct influence on the oxygen concentration and on the saturation degree in the concrete. It is known that the latter factors are determining in the kinetics of the steel corrosion in the un-cracked concrete. As consequence, the carbonation may have a significant impact on the durability of structures.

1.4 CORROSION OF REINFORCEMENTS

1.4.1 Generality on the corrosion induced by carbonation

The heat treatment, applied on iron during its fabrication, results in the creation of a nanometric layer of magnetite Fe_3O_4 on its surface. In the construction sites, the magnetite layer extends and forms a calamine layer. This latter consists mostly of magnetite in addition to some hematite Fe_2O_3 and Wüstite (FeO), called WMaH layer [58]. In the study [59], it was indicated that the casting steps after concrete fabrication are sufficiently slow allowing the transformation of the Wüstite to Hematite and Magnetite. As already mentioned, the pH of the interstitial solution of the sound concrete is around 13. It is obvious in the Pourbaix diagram (Figure 1-13), that for a pH equal to 13, the iron oxides (Fe_3O_4, Fe_2O_3) are stable and the concrete-embedded steel is in a passive state. So in this environment, the developed layer of iron oxides is called a passivation layer. A high alkalinity and an appropriate electrochemical potential ensure the protective role of the latter layer [60]. When in passive state, the corrosion rate of steel reinforcement is very low. Its value is approximately equal to 0.1 µm / year [61], [62].

After carbonation, pH pore solution drops down from 12.5 to 8.5 approximately which makes the iron unstable. The depassivation of the steel by the carbon dioxide cannot alone induce the initiation of the active corrosion. It can only provide the thermodynamic conditions required to induce the corrosion in an active state [63]. Other factors are needed and are divided in two types: primary factors (oxygen, water, electrolyte availability) and secondary factors (differential pH, differential aeration cells…).
Once the depassivation factors (carbon dioxide, chloride …) and the accelerating factors are ensured together, the corrosion could be in its active state.

In this corrosion state, the steel is attacked by electrochemical reactions that lead to electron-ion transfer at the steel-concrete interface due to a differential potential existing between these two phases.
The electrochemical reaction is composed of four partial processes Figure 1-14.

1. Iron Anodic reaction:

The oxidation of iron (anodic process) liberates electrons and gives rise to iron ions.

$$Fe \rightarrow Fe^{2+} + 2e^{-} \tag{1.14}$$

2. Cathodic reaction:

The reduction of oxygen (cathodic process) consumes the electrons released from the anodic reaction.
In the presence of oxygen, the cathodic reaction that will occur is:

$$O_2 + 2H_2O + 4e^{-} \rightarrow 4OH^{-} \tag{1.15}$$

This reaction is the most frequent in the case of carbonated non saturated concretes.

Without oxygen in the environment:

$$2H_2O + 2e^{-} \rightarrow 2OH^{-} + 2H^{+} \tag{1.16}$$

$$2H^{+} + 2e^{-} \rightarrow H_2 \tag{1.17}$$

3. Transport of current (I_{con}) within concrete:
   This is ensured by the ion movement in pore solution from the cathodic regions to the anodic ones.

4. Transport of current in the metal (I_m):
   The transport of electrons within the metal from the anodic regions to the cathodic regions induces an electrical current in the opposite direction because electrons carry a negative charge.

This process allows a reaction between products released from the anodic and the cathodic reaction. And thus, corrosion rust develops as shown in the equation (1.18).

$$Fe^{n+} + nOH^- \rightarrow Fe(OH)_n \quad (1.18)$$

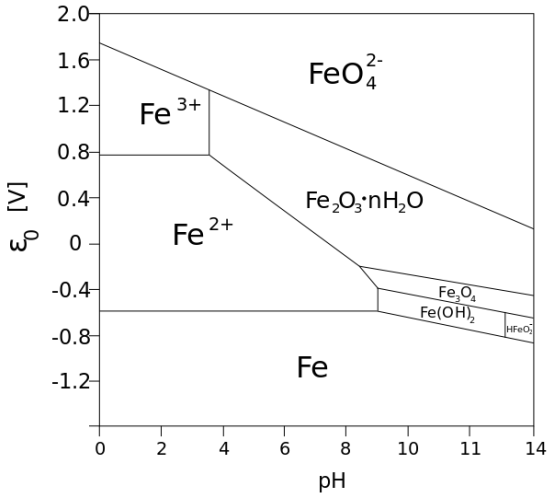

Figure 1-13: Pourbaix diagram for steel [63]

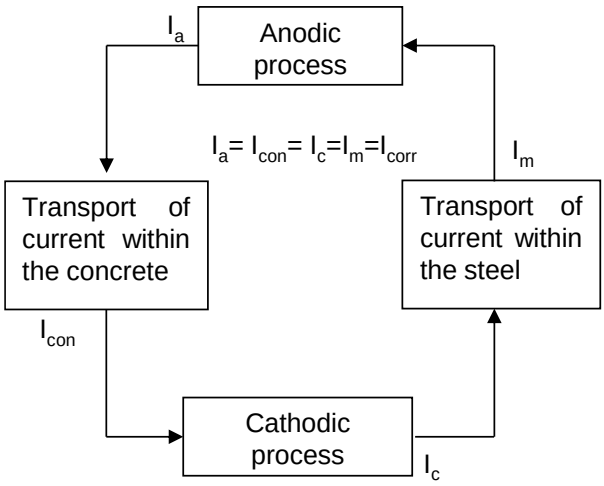

Figure 1-14: Electrochemical mechanism of steel corrosion in concrete (in [64])

1.4.2 Evolution of the corrosion products induced by carbonation

Normally, the iron (II) hydroxide is obtained and has a bright green color in the solution (1.19). This product is not stable generally. It transforms to hydrated iron (III) oxide due to a partial oxidation (1.20).

$$Fe^{2+} + 2OH^- \rightarrow Fe(OH)_2 \quad (1.19)$$

$$2Fe(OH)_2 + H_2O + \frac{1}{2}O_2 \rightarrow 2Fe(OH)_3 \quad (1.20)$$

According to Huet et al. [65], these corrosion products appear at the active corrosion state where the pH is approximately equal to 9.4. When the pH continues decreasing, the corrosion products continue developing. Iron oxyhydroxide appears, mainly the Goethite α-FeO(OH) and Lepidocrocite γ–FeO(OH). After a long period of corrosion by carbonation, some blotches of iron oxides (Ferrihydrite/Maghemite and/or Maghemite/magnetite) are identified. Ferrihydrite precipitates initially and then Maghemite appears.

In some cases, a residual of the passivation WMaH layer (Wüstite-Magnetite-Hematite layer) can be observed. Moreover, Demoulin et al. [59] indicates that the structural evolution of the corrosion pattern is lined to wetting/drying cycles and/or pH evolution during the corrosion process. A schematic of this scenario is shown in Figure 1-15. In the same study [59], it was

found that irrespective of the binder and concrete-embedded steel, the nature of the corrosion pattern in the long term have the same characteristics.

Duffó et al. [66] indicate the presence of two corrosion layers: the inner one composed mainly of magnetite and the outer one composed of Goethite and Lepidocrocite called as a final corrosion products in the case of carbonation-induced corrosion.

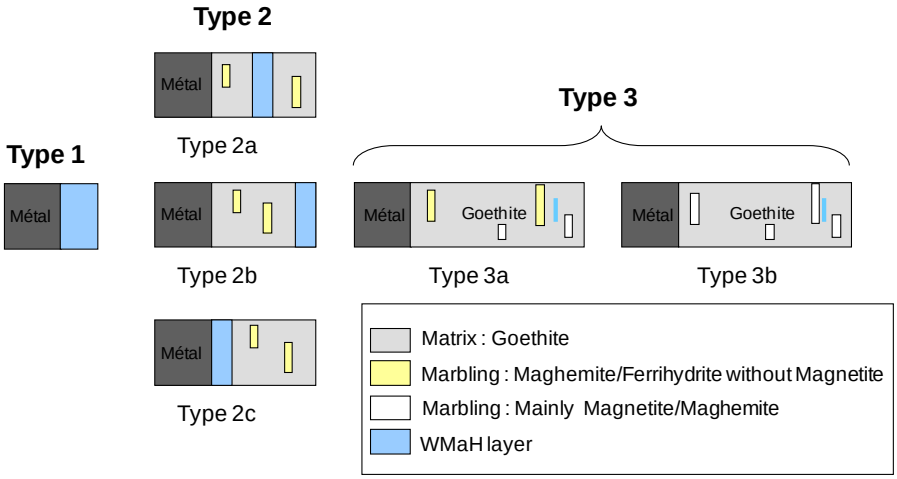

Figure 1-15: Hypothetical scenarios for the formation of long-term corrosion by carbonation patterns [59]

1.4.3 Parameters affecting the corrosion

1.4.3.1 Cracks

The existence of cracks influences the initiation of corrosion process and its propagation.

Corrosion at crack location takes place through two principal mechanisms: microcell and macrocell corrosion (Figure 1-16). In the case of the micro-cell corrosion, the anodic and cathodic reactions take place in the adjacent sub-areas on the cracked zone. The oxygen required for the cathodic reactions is supplied through the crack.

In contrast, in the case of the macro-cell corrosion, the anodic dissolution occurs in the cracked area but cathodic reaction occurs at the passive reinforcement being in non-cracked concrete. In this type, the oxygen penetrates mainly through un-cracked zone of concrete. It seems that the mechanism of macro-cell dominates [67]. The corroded steel surface area in this case is larger than that obtained by the micro-cell corrosion.

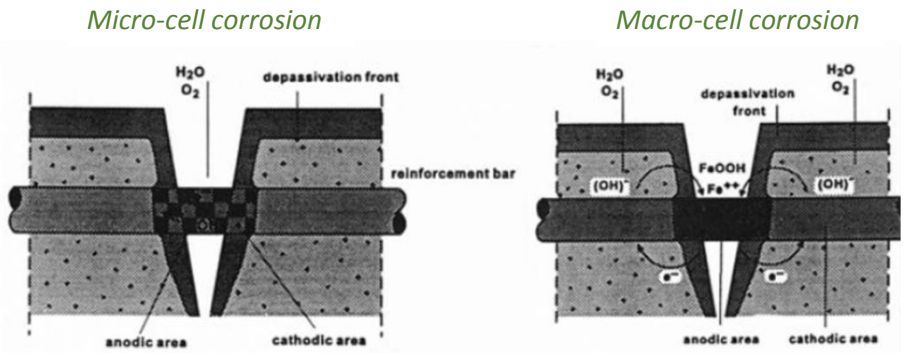

Figure 1-16: Schematic representation of the two corrosion mechanisms in cracked zone [67]

The characteristics of the cracks, such as its width, frequency, location and orientation with respect to steel reinforcement, have also an effect on the corrosion. In the following, the effect of the pre-crack on the corrosion initiation and the corrosion propagation will be explained separately.

a) Effect of crack on the corrosion initiation state:

Pre-cracks promote rapid penetration of aggressive agents such as carbon dioxide, chloride and may thereby accelerate the corrosion initiation. Therefore, the time to depassivation decreases in the presence of cracks [68]. Both laboratory studies [1], [69]–[73] and *in situ* observations [74]–[78] have noted an expedited corrosion initiation in cracked concrete compared to un-cracked concrete. In a conceptual approach, [67] assesses that the time to depassivation is dependent from the crack opening as shown in Figure 1-17. It is supposed that the time to depassivation might be inversely dependent from the crack opening. The scatter visible in the same figure is related to the effect of other factors such as concrete cover properties or climatic conditions on the time to depassivation.

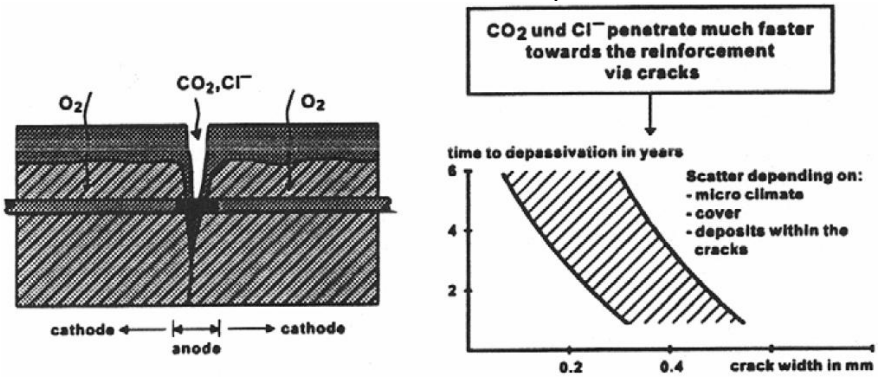

Figure 1-17: Schematic illustration of the influence of cracks on the initiation period [67]

b) Effect of pre-crack on the corrosion propagation state:

Concerning the propagation of chloride-induced corrosion in cracked concrete structures, François and Arliguie [79] propose a model for corrosion process (Figure 1-18). Four periods are proposed to take place: the incubation period, the initiation period, the induction period and the propagation period. During the first period, the aggressive agent (chloride in their study) penetrates through the crack easily leading promptly to the beginning of the initiation period. Thereafter, the corrosion rate is reduced during the induction period due to the corrosion products that fill the crack. The duration of this period is dependent from the exposure conditions. Corrosion products will continue to develop along the steel/concrete interface which may or may not lead to the formation of corrosion cracks. If corrosion cracks appear, the propagation phase begins. Even if corrosion cracks are a hairline cracks, they

will give to aggressive agents, humidity and oxygen access to the rebar inducing thereby an increase in the corrosion rate. During this corrosion propagation phase, the corrosion cracks interconnect between them progressively and increase in width also. In the structure, some zones will be in the induction phase while others can be in the propagation phase because the corrosion is known to be very heterogeneous. It is therefore indicated in the same study that an accurate separation between the end of the induction and the beginning of the propagation phase is not easy.

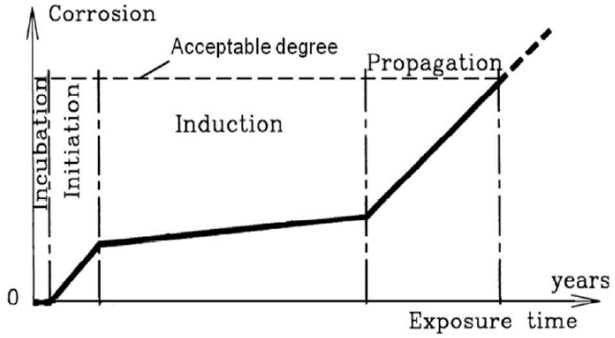

Figure 1-18 : Corrosion process in cracked concrete [79]

However, only few laboratory works exist in the literature on the propagation of corrosion by carbonation environment. [80], [24], [81], [82] had reported that the corrosion developed in a zone of few millimeters around the bars at the crack location and does not show serious consequence for the structure sustainability. The study [83] proposing a more quantitative approach, is among the most recent research in this domain. In the latter study, specimens was first cracked then carbonated and subjected thereafter to immersion/drying cycles. It was found that the pre-cracks favor the corrosion propagation. As a matter of fact, new corrosion cracks appeared from the micro-cracks created during the mechanical crack. The lack in this study is that the entire steel/concrete interface was damaged, i.e. micro-cracks exist on whole steel length. This condition is not representative of real structures and inhibits the study of the corrosion propagation deep in the crack.

In this project, the cracking protocol should be well chosen in order to avoid an entire damage in the steel/concrete interface. After choosing the suitable cracking protocol, corrosion tests will be conducted to deduce if the same corrosion process found in chloride environment will take place in the carbonation-induced corrosion.
Moreover, an interest is also given to the crack width in order to detect a possible repassivation induced by the corrosion products that seal the crack and limit the access of aggressive agents to the rebar.

1.4.3.2 Parameters related to the atmosphere

Several environmental parameters may influence the corrosion rate. This is a complex subject and is still in debate in the research community. The influence of each parameter is not sufficiently known and this is made worst if the combination of several parameters is considered. An effort is made in [84] and [85] to list and summarize the effect of different environmental conditions that have shown to have an influence on corrosion. The presence of water and oxygen is a must for the corrosion to start. The main parameters therefore are rainfall, temperature, relative humidity. These latter are detailed in the following.

a) Wetting/drying cycles

Studies show that the worst corrosion induced by carbonation is in structures subjected to alternating periods of low relative humidity (RH) and high RH. In fact, if the RH is around 60%, the carbonation rate is maximal (Figure 1-19). At this RH, corrosion rate is very low

because the water-saturation level of the concrete cover is not sufficient to ensure its development. So during drying period, the carbon dioxide and the oxygen diffuse through the structure and during humid stage, corrosion reactions are enhanced. Therefore, the duration and frequency of wetting/drying cycles is determinant in the development of corrosion [64].

Moreover, [86] indicates that the wetting/drying cycles affect also cathodic reactions. In fact, as shown in Figure 1-20, during the wetting stage and the drying stage (for relative humidity between 100 and 60%), oxygen diffuse through concrete cover and is reduced (equation (1.15)). During the drying stage (for relative humidity lower than 60%), the corrosion process cannot develop because the water-saturation level of the concrete cover is too low and the concrete resistivity increases. Changes in the cathodic reaction occur during the first wetting stage (for RH lower than 60%). At this stage, the reduction of active phases contained in the corrosion product *(Fe^{3+})* layer occurs instead of oxygen reduction. The oxide III reduction may lead to the formation of iron II species, which are more soluble and could be transferred through concrete creating a zone called “transform medium” by the authors.

It is well known in the literature how wetting/drying cycles influence the corrosion rate. Nevertheless, there is no study in the literature quantifying the effect of the humid phase duration and of the number of wetting/drying cycles on the kinetics of corrosion in cracked concrete. This is among the most important objective of this study.

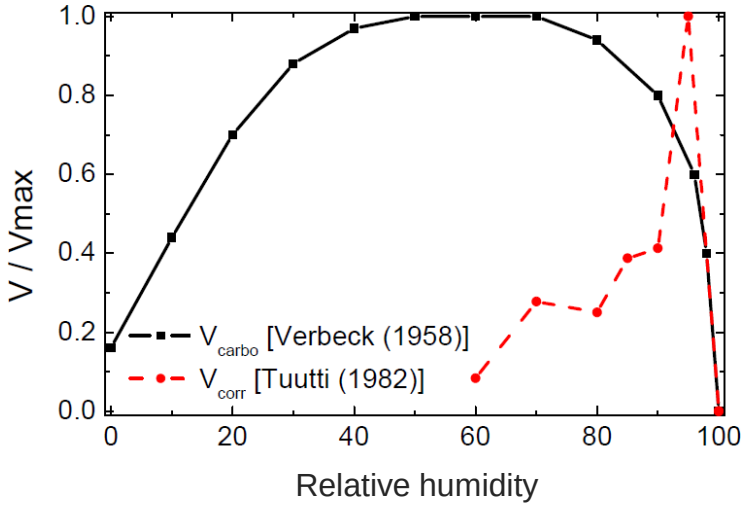

Figure 1-19: Kinetics of corrosion and carbonation with respect to relative humidity [87]

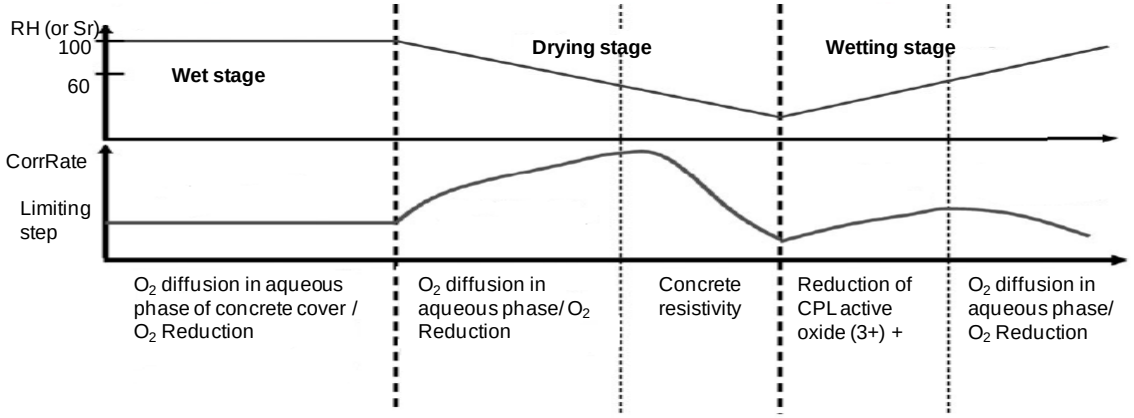

Figure 1-20: Corrosion of steel-embedded concrete in case of humidity/drying cycles [88]

b) Temperature

In general, one should borne in mind that an increase in the ambient temperature leads to an increase in the corrosion rate [89]. This increase is significant and it can double for a 10°C temperature increase. This is true for low ambient temperature. However, when the ambient temperature is above 40°C, the dependency between the corrosion rate and the temperature is more complex. In fact the saturation degree and the concrete resistivity change at high temperatures and combined phenomena are to be considered [90]. At high temperatures (>40°C), the oxygen is less soluble in water and, therefore, the corrosion rate drops down with the increase in temperature [91], [84]. However, in a ventilated environment, this conclusion is not reliable. Moreover, temperature may have other consequences on corrosion such as changing the nature of corrosion products [92].

The effect of the temperature on the corrosion rate is studied during this project.

c) Relative humidity

The influence of the relative humidity on the corrosion rate is the subject of multiple research studies in the literature. The latter show that there is a critical RH needed for the corrosion to start. Goni et al. [93] identified a humidity threshold of about 60%. They claim that below this value no corrosion is possible. Moreover, [68] determined a maximum relative humidity value of about 90-95% above which no corrosion is possible. In fact, a higher relative humidity value limits the oxygen diffusion and reduces the corrosion rate considerably. In Figure 1-21, the corrosion rate of carbonated concrete is shown as a function of the environmental relative humidity; these data are based on thousands of reading taken mainly in Spain [94]. It can be seen that the maximum corrosion rates, on the order of 100 µm/year (100 mA/m^2), will be reached in a very wet environment.

Andrade et al. [95] discussed the influence of humidity variations on the corrosion rate. They claim that variation in the relative humidity with seasons affects the corrosion rate. However, this is not the case for daily relative humidity changes since the humidity at the reinforcement zone is approximately constant because the water transport by capillarity is a slow phenomenon [96].

To enhance concrete protection against corrosion, Weydert [97] proposes to dry the carbonated concrete coating.

In this project, a comparison between the effect of relative humidity and raining/drying cycles on the corrosion rate of steel in a cracked reinforced mortar is performed.

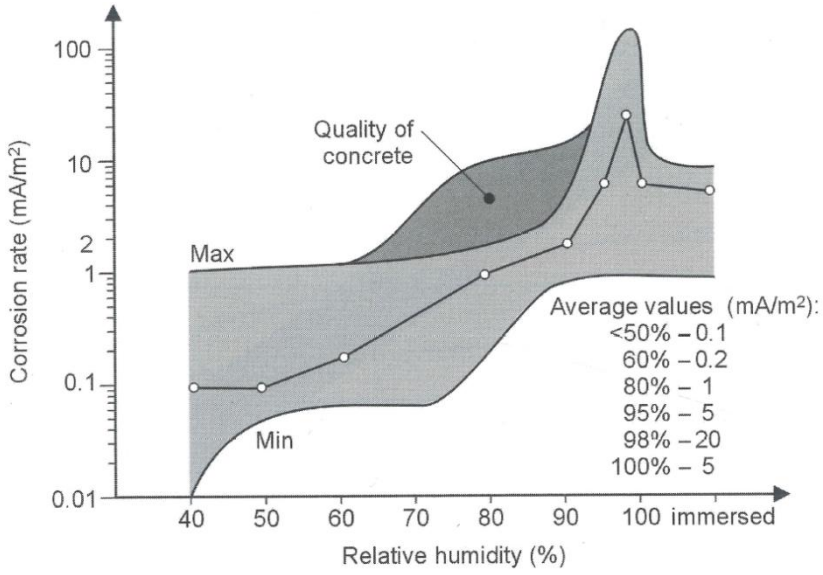

Figure 1-21: Maximum and minimum values of the corrosion rate in carbonate concrete as a function of environmental humidity [94] cited in [64]

1.4.3.3 Concrete cover properties

There are several concrete cover properties which affect the corrosion rate of steel reinforcement. At least four factors may influence the corrosion rate. These factors are the concrete quality (w/c ratio), concrete cover depth, electrical resistivity of concrete and cement type. In this paragraph the effect of each factor is presented.

a) Water to cement ratio of concrete cover:

Permeability is mainly affected by water/cement ratio. The increase of this ratio reduces the strength of concrete and also leads to a high diffusivity of oxygen and thus an easier penetration of aggressive agent like chloride and carbon dioxide [98]. [99] confirms this effect and add that the permeability is substantially reduced for a water to cement ratio lower than 0.45. The distribution of the pore network, which is a determining factor in the rate of saturation of the material at certain relative humidity, is also sensitive to porosity and thus to water to cement ratio. Ryu et al. [96] confirm these observations by showing that rainfall affects the relative moisture of uncracked concrete for bigger depth in materials having a coarse microstructure (w/c 0.6) than those having a dense microstructure (w/c 0.3). They add that for cracked concrete, under a dry environment, the effect of crack opening on the reduction in the relative moisture in specimens is more visible for materials having dense microstructure than those having coarse microstructures. This is attributed to the fact that in coarse microstructure, the escape of moisture is not only through the crack faces but also through percolated capillary pores. Furthermore, It was experimentally observed in the study of [100] that the corrosion rate increase with the water to cement ratio. Balabanić et al. [101] analyzed the influence of concrete quality (w/c ratio) on the corrosion current density using a mathematical model for the chloride-induced corrosion of reinforcing steel in concrete. They deduced that the reduction in w/c ratio influences much more the corrosion current density value than an increase in the thickness (from 5 to 10 cm) of the concrete cover with the same quality. Mangat et al. [102] show that w/c ratio is the dominant factor which controls corrosion in uncracked concrete.

Water to cement ratio of reinforced concrete specimens should be representative of the cooling tower's concrete composition.

b) Concrete cover depth

The concrete cover ensures the protection of the steel reinforcement. It constitutes the diffusion path for the oxygen, water, and other aggressive agents from the surface to the steel reinforcement interface. It was found in the study of [103] that for a given water to cement ratio, the corrosion rate decreases with increasing cover thickness. Furthermore, the thickness of the concrete cover is one of the factors affecting the cracking and spalling of concrete as a result of the corrosion development [61].

Standards such as Eurocode 2 specify for each environmental condition a corresponding concrete cover depth.

Reinforced concrete specimens of this study should be the most representative of the cooling towers; that is why a 30 mm cover thickness will be used in the laboratory tests.

c) Concrete resistivity

Once carbonation front has reached the steel reinforcement, the latter is depassivated and active corrosion can occur if the accelerating factors (oxygen, water…) are ensured. Despite the fact that researchers often assume that carbonation-induced corrosion is uniform they could argue that concrete resistivity is a parameter of the corrosion process. Alonso et al. [104] stated that the corrosion rate is governed by the resistivity of the concrete. While, when steel is passivated, the corrosion rate is not affected by resistivity

In the study of [104], where the steel reinforcement was depassivated by carbonation, a relation between the corrosion rate and the electrical resistivity has been proposed (Figure 1-22). This relation could make from the on-site measurement of resistance an indicator of the corrosion rate of the reinforcement. In real structures the carbonation may not be uniform and some zone of the steel may remain passivated inducing macro-cells. The action of these cells could not be detected measuring the local electrical resistivity [104].

Different authors propose for each corrosion state a corresponding interval value for the resistivity. In the study [68], it was indicated that concrete resistivity is very dependent from temperature, relative humidity, water to cement ratio, cement type… This was confirmed in the thesis of Lataste [105]. In the latter study, it was also indicated that the dependency of the resistivity from the listed factors, especially from temperature and relative humidity, makes the determination of a "corrosion risk" based on the values of resistivity proposed not reliable.

For example, in the studies [104], [106] and [107], it was indicated that a change in RH induces a change in the type of the factor controlling the corrosion. More precisely, in aerated carbonated specimens (HR<80%), the corrosion process is controlled by the resistivity. While for saturated carbonated specimens (HR>80%), the corrosion rate is under the cathodic control (O_2 availability) (Figure 1-23).

The effect of temperature on the electrical resistivity is described by the Arrhenius law (equation (1.21)) [108] cited in [61]. In this equation, ρ is the resistivity at the temperature T, and E_a is the activation energy. It is visible that an increase in the temperature until certain value induces a decrease in the resistivity. This could be related to an increase in the activation energy of dissolution reaction with increasing temperature.

$$\Delta\rho = \rho . exp\left(\frac{E_a}{R}\left(\frac{1}{T+\Delta T} - \frac{1}{T}\right)\right) \quad (\mathbf{1.21})$$

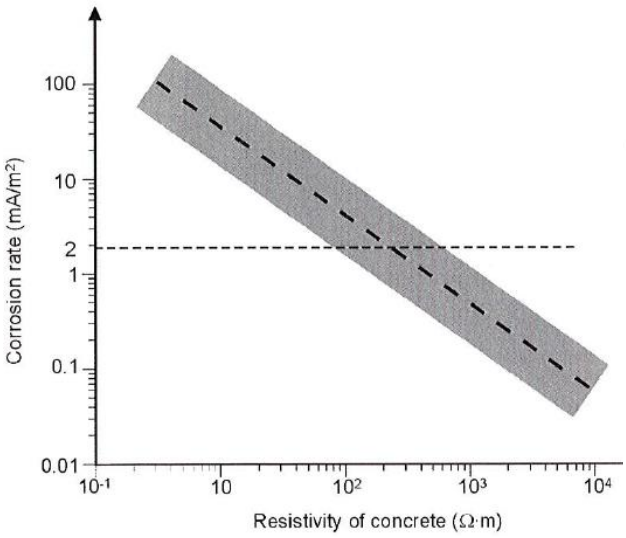

Figure 1-22: Schematic representation of the corrosion rate in carbonated concrete as a function of the resistivity of concrete [64]

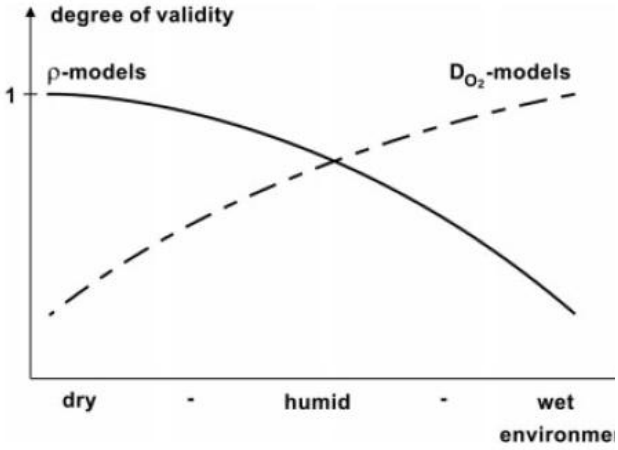

Figure 1-23: The controlling factors for the corrosion rate with regard to relative humidity [106]

d) Cement type

The influence of cement type on corrosion exists in two levels. The first level is the penetration of carbon dioxide. Since the carbonation neutralize cement hydrates, the cement type influence the nature of hydrates and thus the carbonation propagation. The second level is the stability of the corrosion products associated with the composition of the pore solution and its pH [87].

In order to detect the effect of cement type, 6 types of carbonated cement paste were tested in the study [104] and the relation between the corrosion rate and the resistivity was quite similar in all the cases. Despite that, in [67], it was indicated that cement type influences the carbonation resistance and thus the corrosion resistance as shown in Table 1-3 and Table 1-4. In these tables, the '+' sign indicates that the corresponding parameter leads to an improvement in the durability. The converse is indicated by the sign '-'. The symbol 'NSE' means 'no significant effect'. Since the resistivity influences directly the corrosion rate as shown above, each improvement in resistivity induces decrease in corrosion rate.

Table 1-3: Carbonation resistance [67]

	Carbon dioxide diffusion Coefficient (D_{eff})	Binding capacity (a)	Overall effect on carbonation rate
Inclusion of pulverised fuel ash (PFA)	+	-	-
Inclusion of ground granulated blast-furnace slag (GGBS)	+	-	-
Inclusion of silica fume (SF)	+++	---	NSE
Reduction in water/binder ratio	+	+	+
Increase in binder content	+	+	+
Presence of air entrainment	NSE	-/NSE	NSE

Table 1-4: Electrical resistivity [67]

	Electrical resistivity - ρ_0	Ageing factor n
Inclusion of pulverised fuel ash (PFA)	+	+++
Inclusion of ground granulated blastfurnace slag (GGBS)	++	+++
Inclusion of silica fume (SF)	+++	++
Reduction in water/binder ratio	+	NSE
Increase in binder content	+	NSE
Presence of air entrainment	NSE	NSE

In this project, the corrosion rate of steel reinforcement embedded in two cement types is quantified.

1.4.3.4 Steel/mortar interface quality

In paragraph 1.4.3.1, it is noted that several studies shows that the corrosion initiation and propagation is related to surface crack width. Therefore in structural design codes and recommendations [109]–[111], controlling concrete surface crack widths become the norm to minimize the effect of crack on reinforcement corrosion. However, recent research investigations show that steel/mortar interface quality is more important to reinforcement corrosion issues than the surface crack width. In fact, defects exist always along the steel/mortar interface. Mix design and concrete casting procedure may induce entrapped air voids. Moreover, settlement and water bleeding under horizontal reinforcement with respect to casting direction create gaps along the steel/mortar interface [112]. The study [113] confirms the presence of those defects by showing a higher porosity under the horizontal steel bars. This is confirmed in the study [114] in which a comparison of interfacial transition zone (ITZ) thickness between vertical and horizontal bars is performed. Kenny and Katz [114] deduce that a large void exist under horizontal bars which is not the case in the vertical

bars. Furthermore, mechanical cracks that reach reinforcement induce slip and separation along steel/concrete interface which participate in creating voids among this interface. Since gaps are induced by concrete settlement and water bleeding, it is important to note that the location of horizontal bars in reinforced concrete element is determinant in the steel/concrete interface quality. This is confirmed in the study [115] showing that the interfacial quality decreases with depth of concrete under the steel and depend on the bleeding capacity of concrete mixture. Mohammed et al. [116] reports also that gaps are more present under the top horizontal bars than under the bars located at lower section with respect to casting direction.

The effect of the gaps, entrapped air voids and higher porosity on the chloride-induced corrosion initiation is demonstrated in several studies ([113], [117]–[119]). Ryou and Ann [120] confirm this observation by proving that corrosion starts in the voids in contact with the steel bar regardless chloride origin. Some research investigations show that the size of defect along steel/mortar interface is a factor to consider while studying the corrosion initiation. For example, Hartt and Nam [121] indicate that corrosion initiates preferentially at entrapped air voids with a diameter bigger than 2.5 mm. Söylev and François [122] divide defect in two groups : macrodefects (resulting from bleeding, settlement) and microdefects (same origin as macrodefects but no identifiable by visual inspection). And they find that macrodefects have a direct effect on corrosion when microdefects have no significant effect on corrosion. Furthermore, interfacial defects affect also the corrosion pattern. Yu and al. [123] prove that corrosion cracks appear quickly on the top cast-steel bars where the interfacial defects are much more developed than on the low cast steel bars.

To our knowledge, the effect of the steel/mortar interface quality on carbonation-induced corrosion propagation was only studied by Dang et al. [83]. In this study, ring-shaped mortar specimens with pre-cracks induced by internal pressure were carbonated in accelerated conditions (50% CO_2-65% RH). Therefore, these mortar specimens were subjected to immersion/drying cycles to promote corrosion development. It was observed that the carbon dioxide spread along the total length of steel/mortar interface. Moreover, corrosion product layer is observed all around the perimeter of the carbonated rebar. Corrosion initiation on the entire perimeter of the rebar is related to the totally carbonated interface. It is indicated that mechanical loading led to damage at the steel/mortar interface characterized by microcracks. The latter facilitates the spread of the carbon dioxide all around the steel/concrete interface. In large structures, mechanical loading induces partial steel/concrete interface damage. The length of the steel/concrete interface damage could be a key parameter in the initiation and the propagation processes of the carbonation induced corrosion. It is also deduced that the corrosion layer is thicker in the lower half surface of the steel reinforcement than that observed on its upper half. This observation is justified by the presence of higher porosity and lower $Ca(OH)_2$ amount at the bottom surface of reinforcement [113].

To summarize, it can be deduced that the corrosion is more developed in the lower surface of the steel reinforcement located at the higher section in each block of concrete with respect to casting direction. This is a point to take into account while inspecting corrosion in the cooling towers. Moreover, to complete the study [83], and understand the effect of cracking, both in terms of corrosion initiation and propagation, a cracking protocol leading to cracks and steel-interface damage representative of those existing in real structures should be found.

For this reason, the effect of steel/mortar interface quality on carbonation spread and corrosion development is considered in this study.

1.4.4 Consequence of corrosion process on the materials

a) Concrete

The corrosion reaction transforms the metallic iron to a ferric oxide (rust). The corrosion products begin precipitating in the connected porosity available in the concrete surrounding the steel bar. At the beginning, small product volume fills the pores without creating negative side effects on the concrete. However, for an advanced state of corrosion, the volume of corrosion products increases. That can even reach six times the metallic iron volume [124]. This increase in volume causes pressure on the steel/concrete interface that can lead to cracking of the concrete once the tensile strain capacity of the concrete is exceeded. A small volume growth may lead to cracks in the concrete cover along the line of bars. A more severe volume growth can lead to delamination or even to spalling if this volume growth is excessive. These phenomena are illustrated in Figure 1-24.

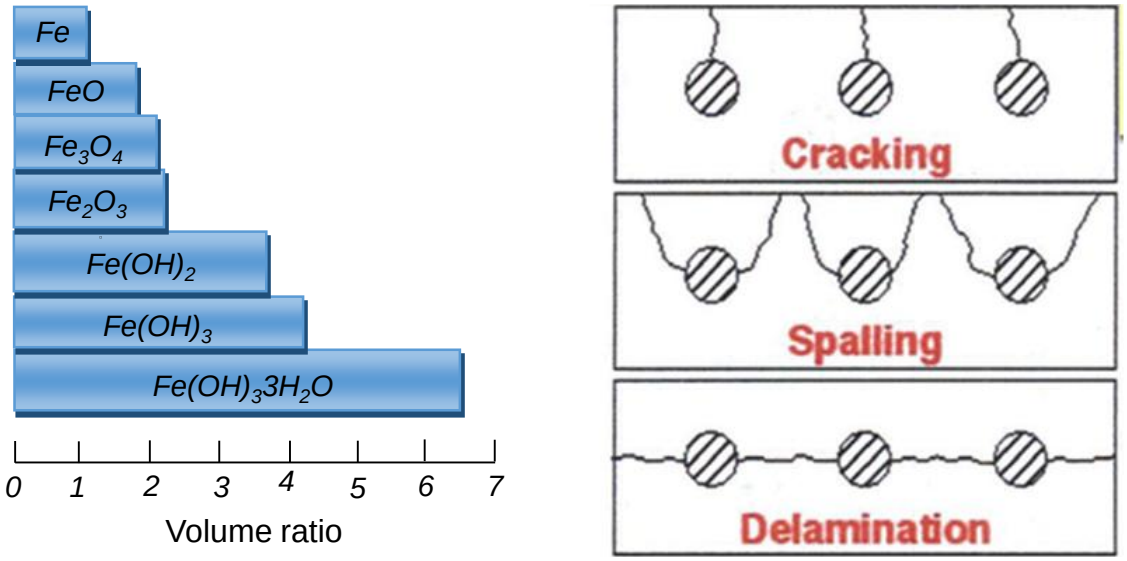

Figure 1-24: Effect of corrosion products volume on concrete([89] cited in [84])

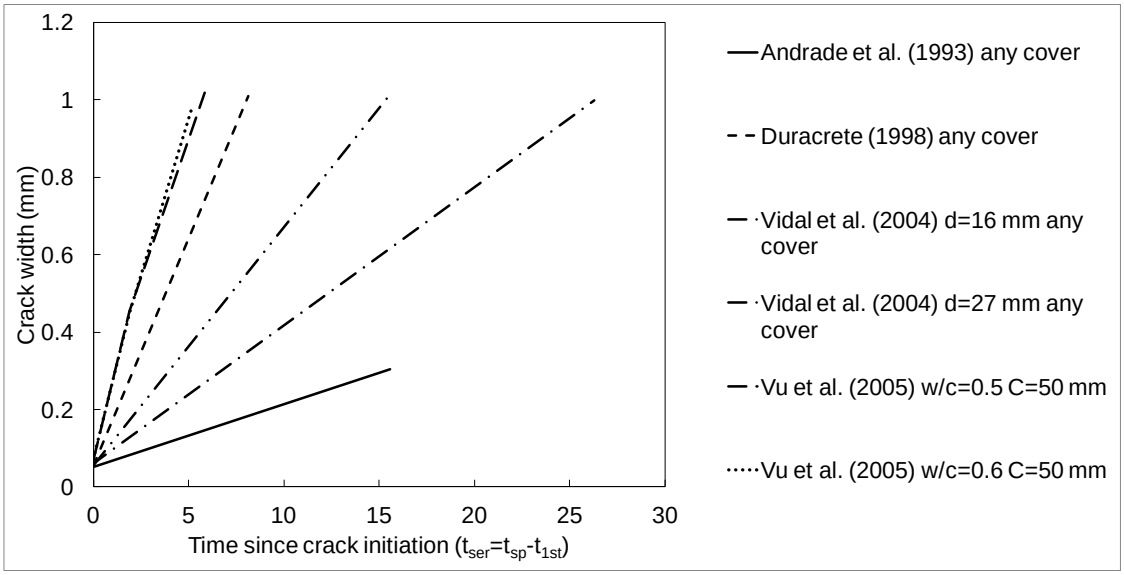

Figure 1-25: Comparison between different empirical models for estimating the crack width due to corrosion propagation in the case of chloride-induced corrosion [125]

[126], [127] discussed the main factors that are behind the different effects of corrosion on concrete. They claim that this phenomenon depend on the length of the corroded section, the thickness of the concrete cover, as well as, the rebar diameter.

Several numerical models were developed in the literature to predict when the concrete cover is cracked according to the chlorination-induced-corrosion [128], [129].

Moreover, many other empirical models propose a relationship between the corrosion-induced crack opening and the corrosion propagation [130] cited in [84], [67]. However, depending on the experiment procedures, assumptions, and parameters, important differences are found between the models as shown by [125] who set a comparison between different empirical crack propagation models (Figure 1-25). In this figure, t_{ser} is the number of years since crack initiation and is calculated by $t_{ser} = t_{sp} - t_{1st}$, where *tsp* is the crack propagation time measured from the beginning of the experiment, and t_{1st} is the time to crack initiation. In addition, Khan et al. [131] were interested in the same thematic and compared different models with experimental results in order to determine if it is possible to predict the evolution of corrosion induced cracks width with respect to time. They deduced that an accurate prediction of the time needed to achieve a certain crack width is difficult due to the complexity of the corrosion crack initiation and propagation phenomenon.

Therefore generally, the different studies in the literature agree on the dangerous effect that chloride-induced corrosion has on concrete.

While very few attempts in the literature were made to produce a numerical model allowing predicting the development of the cracks due to the carbonation-induced-corrosion. One of the most recent model in this domain is the “CORDOBA” model developed by A. Millard [132], [88]. The evolution of the cracks pattern induced by the growth of the corrosion products layer is predicted as shown in Figure 1-26. A section of the studied structure is presented, P_{ext} is the point closest to the external atmosphere and P_{int} is the point at the internal part of the specimen. The white semi-circle is the steel bar reinforcement. The damaged zones in red simulate the cracks. The difference images from 1 to 9 show the progressive development of the cracks due to the corrosion layer growth. It is obvious that cracks initiate around the rebar due to the high orthoradial stresses induced by the corrosion products development. These results are obtained by coupling different multi-physics models, described in the studies [107], [133], to the mechanical damaging model CORDOBA. According to the concrete cover depth, the final crack patterns will be different. Moreover, in the case of the studied structure, the non-uniformity of the corrosion layer which is more developed on the outer part than on the inner part of the steel/concrete interface may have an influence on the times at which the various cracks appear. This effect of the non-uniformity on the final crack pattern has been checked in this study, and no influence was detected. Note that the CORDOBA model is used only for the estimation of the active corrosion period. It was assumed that no mechanical damages are induced by the passive layer growth.

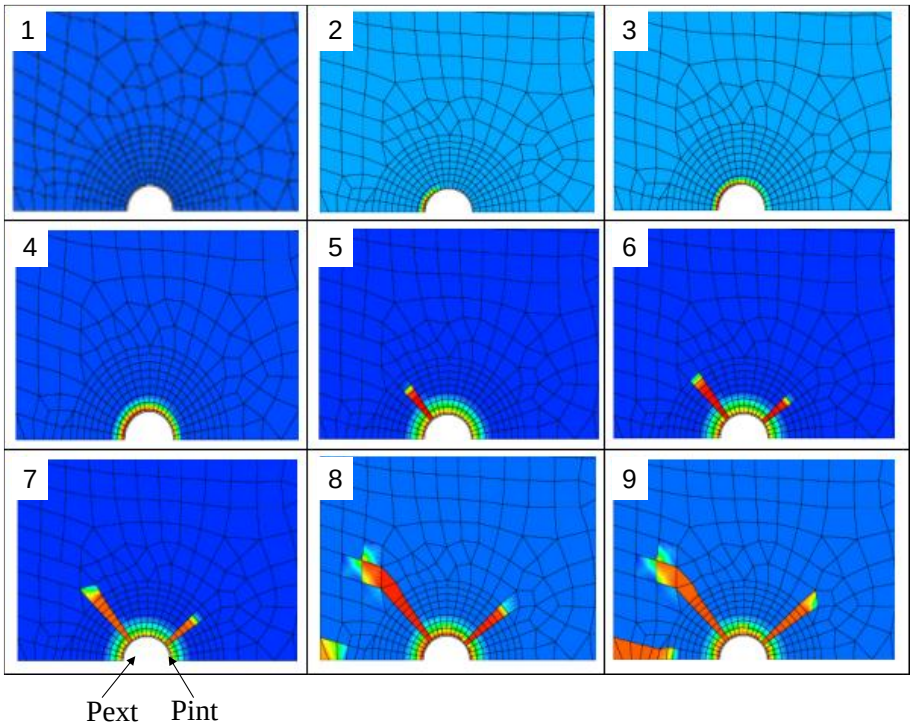

Figure 1-26: Evolution of the cracks pattern with time [132]

b) Cracked concrete

Millard and L'Hostis [132] have used the CORDOBA model on a pre-cracked specimen in order to take into account the influence of the pre-existing cracks on the development of corrosion. It was found that the corrosion rate reaches high values at the crack tip in a few hours (Figure 1-27). With time, the corrosion rate at the crack tip has dropped down; the highest value of the corrosion rate was found a little further than the crack tip location (Figure 1-28). This phenomenon was related to the oxygen concentration and to the saturation degree in the concrete at the crack tip. It was found that the very beginning, *i.e.* few days, the oxygen concentration is quickly high at the crack tip, while the saturation degree has not yet much diminished. After one month, the saturation degree decreases at the crack tip while the oxygen concentration remains high. That can explain the observed decrease in the corrosion rate at the crack tip with time.

Moreover, as shown in the Figure 1-29, the thickness of the corrosion products has the highest value near the crack. Millard and L'Hostis in this same study [132] found that this thicker layer at the crack tip may lead to the formation of rust plug deep in the crack, which tends to slow down the corrosion process by acting as a barrier to the oxygen diffusion. This has been found in an experimental research developed by François and Arliguie [1] who studied the effect of cracking and micro-cracking on the development of corrosion induced by chlorination.

In our study, we are interested in the propagation of the corrosion induced by carbonation in pre-cracked concrete. To our knowledge, no research work in the literature study the development of a rust plug deep in the crack in case of corrosion induced by carbonation. Since a rust plug could inhibit the development of the corrosion process, this phenomena will be studied in this thesis.

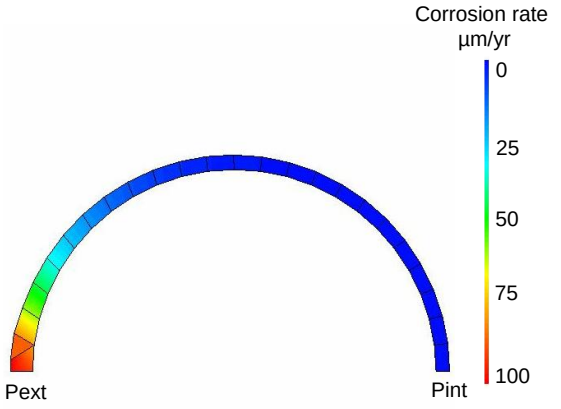

Figure 1-27: Average corrosion rate calculated at the steel concrete interface after four hours [132]

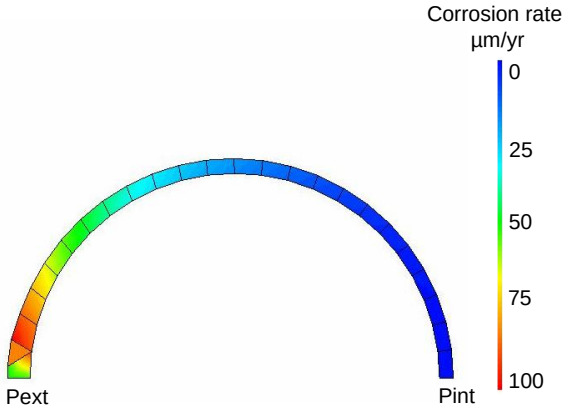

Figure 1-28: Average corrosion rate calculated at the steel concrete interface after four days [132]

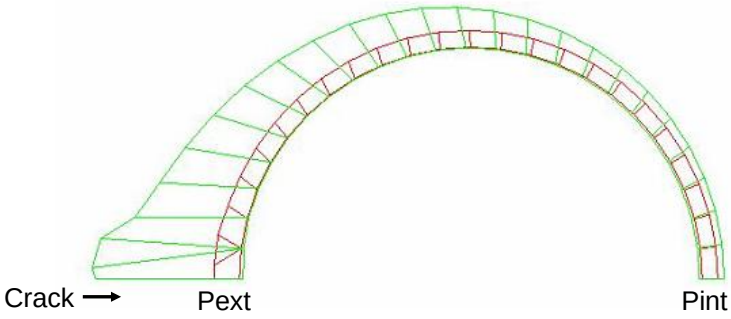

Figure 1-29: Initial and deformed shape of the rust layer after one year [132]

c) Steel

Basing on the model of Rodriguez et al. [130] cited in [131], the residual bar diameter can be obtained from the equation (1.22).

$$\phi_t = \phi_0 - \alpha x \qquad \textbf{(1.22)}$$

Where,

Φ_t Residual diameter at time t [mm]

Φ_0 Initial bar diameter [mm]

α Attack penetration parameter.

For homogeneous corrosion: $\alpha=2$

For localized corrosion: $4<\alpha<8$ [130]

x Attack penetration in case of pitting corrosion (Figure 1-31)

Radius loss in case of homogeneous corrosion (Figure 1-30)

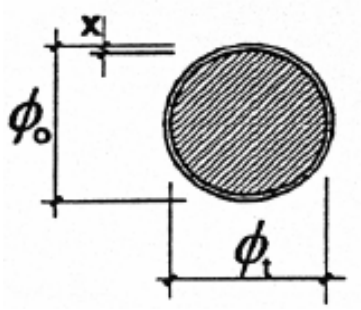

Figure 1-30: Residual reinforcing bar section for homogeneous corrosion [67]

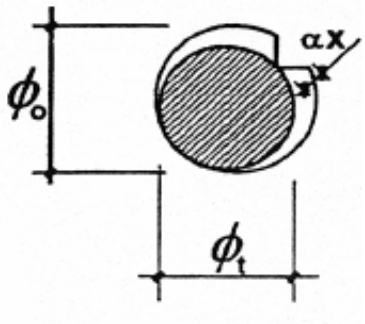

Figure 1-31: Residual reinforcing bar section for pitting corrosion [67]

Several studies in the literature were interested in the influence of the reduction in cross section of the steel on its mechanical properties. For example, in the study [134], [135], it was found that the cross section loss in the case of the corrosion by chlorination leads to a decrease in the yield strength, to a significant degradation in elongation under tensile load and in deflections under flexion. This results corresponds with the results described in the study [67]. The latest study explain this phenomena by the fact that the reinforcing bar normally fails at the pit locations due to the local reduction of the cross-section when, perhaps the strain of the bar in zones outside the pit is still well below the maximum potential elongation of the corroded steel.

Since the reduction in the cross section of the rebar is not local but uniform, no significant variation in the mechanical properties of the rebar corroded by carbonation should be detected.

d) Steel/concrete interface

The bond between reinforcement and concrete enables a force transfer between concrete and rebar that enables the structure to sustain both the traction and the compression forces. At the steel/concrete interface, tensile resistance is created by this bonding. When the reinforcement is corroded, the increase in volume starts generating stresses at the interface. Studies realized on this subject such as [128], [129], [136], [137], [138] agree on the following conclusions.
When the corrosion products lead to a small volume increase (less than 0.4%), the steel/concrete bonding is enhanced by the increase in the bar diameter. However, for higher corrosion levels, the increase in volume generates an important pressure at the steel/concrete interface which causes splitting cracks and a loss of bonding. [139], [140] found that this loss of bonding increases with the increase in the corrosion level. This implies a decrease in the overall rigidity of the structure [141] without necessarily changing the ultimate failure stress of the beam subjected to flexion forces.

1.5 SUMMARY

Corrosion has a harmful effect on concrete structures, thus considerably shortening its lifetime. For structures exposed to the atmosphere (buildings, tunnels, parking, towers…), corrosion is mainly induced by carbonation (reaction of carbon dioxide with hydration products), while chloride plays a major role in corrosion kinetics of structures located in a marine environment or exposed to deicing salts. The industrial application of this thesis is to estimate the corrosion kinetics of the reinforcement in the cracked concrete of EDF cooling towers in France located far from the marine environment. For this reason, only the carbonation-induced corrosion of reinforcement embedded in concrete and intercepting a

crack is studied. A general agreement exists in the literature on the effect of cracks in inducing interfacial slip and separation between steel and concrete and in accelerating the corrosion initiation deep in the crack and a few millimeters around the rebar intercepting the crack. However, the propagation of reinforcement corrosion induced by carbonation deep in the crack is stills a subject in debate. For this reason, the propagation of carbonation-induced corrosion of steel in cracked concrete is in the focus of this project.
The objective is therefore to give answers for two main questions:

- Will carbonation-induced-corrosion deep in the crack induce the development of corrosion cracks facilitating the corrosion propagation it will form a “corrosion plug” in the crack and slow down the corrosion propagation?
- How the kinetics of the carbonation-induced corrosion in reinforcement will be impacted by several parameters like the width and the orientation of the crack with respect to the rain, the rain duration, the temperature, the relative humidity?

Several parameters must be defined in order to achieve the objective. For instance, the corrosion propagation may directly be related to the crack opening and to the length of the steel/mortar interface slip. Therefore, a suitable cracking protocol allowing obtaining controllable crack opening should be found. Moreover, the load-induced damages along the steel/mortar interface should also be limited around the crack. Thereafter, a protocol that allows quantification of load induced damage length should also be determined.

All the parameters tested in this study are chosen to be the most representative for those surrounding the cooling towers.

CHAPTER 2. PROGRAM DESCRIPTION

2.1 INTRODUCTION

In this chapter, the mixture of each material tested and the dimensions of specimens are presented. Afterward, the equipments developed for carbonation and corrosion experiments are presented. Thereafter, required cracks characteristics and suitable cracking protocol are detailed. Then, the corrosion conditions chosen to be tested are presented. At the end, method of corrosion analyzes are described.

2.2 MATERIALS

2.2.1 Cementitious materials

2.2.1.1 Composition

Three different cementitious materials formulations are used and are given in Table 2-1. A reference mortar mixture based on CEM I cement is used to prepare most of the laboratory specimens. Some specimens are prepared using a mortar mixture based on (CEM I + slag) in order to determine the effect of slag on the corrosion kinetics. Moreover, some other concrete specimens are prepared using a CEM I cement in order to test if concrete aggregates have an impact the corrosion kinetics.

- Mortar mix based on CEM I cement:

A standardized mortar mix which uses three parts sand, two parts cement and one part water, is used (NF EN 196-1 [142]).

- Mortar mix based on (CEM I + Slag):

The cement is made manually by substituting 50% of cement by slag (by mass). The mortar composition is similar to the one used for the mortar based on CEM I.

- Concrete mix :

The formulation of concrete used in this study is inspired from the one used in the thesis of Witasse [143]. This is because the latter study has the same industrial context which is the durability and the maintenance of the cooling towers.

Table 2-1: cementitious materials formulations

CEM I Mortar mixture	
Materials	Quantity (kg/m^3)
Siliceous sand (EN 196-1)	1543
CEM I 52.5 N	514
Water	257

(CEM I + slag) Mortar mixture	
Materials	Quantity (kg/m^3)
Siliceous sand (EN 196-1)	1529
Slag	254
CEM I 52.5 N	254
Water	254

CEM I Concrete mixture	
Materials	Quantity (kg/m^3)
Calcareous sand 0/2	225
Calcareous sand 0/4	525
Rounded Gravel 4/10	1110
CEM I 52.5 N	350
Water	175

The origin of the Calcia cement used for these three formulations is the Couvrot factory. The slag used is from Ecocem. The chemical composition of these two materials is given in Table

2-2 (a, b). The provenance of sand 0/2 and 0/4 is Saint Dizier (S1). The limestone gravels 4/10 are from Lafarge industry.
It is important to note that some concrete specimens are prepared and studied in LMDC (Toulouse) laboratory. Their composition is the same as the one shown in Table 2-1. Nevertheless, the materials origin is not the same. The rounded gravel 4/10, the sand 0/2 and the sand 0/4 are from the Portet-sur-Garonne quarry. The cement used is CEM I 52.5 R from Le Teil factory. Its chemical composition is given in Table 2-2(c).

Table 2-2: Elementary composition of cement and slag used (% by mass)

SiO_2	Al_2O_3	Fe_2O_3	TiO_2	MnO	CaO	MgO	SO_3	K_2O	Na_2O	P_2O_5	S^{2-}	Cl^-
19.5	5.2	2.3	0.3	0.0	64.2	0.9	3.5	1.07	0.07	0.2	<0.02	0.01

(a) CEM I, 52.5 N, Couvrot

SiO_2	Al_2O_3	Fe_2O_3	TiO_2	MnO	CaO	MgO	SO_3	K_2O	Na_2O	P_2O_5	S^{2-}	Cl^-
37.1	10.8	0.6	0.5	0.3	43.4	6.7	0.1		0.5		0.9	0.01

(b) Slag, Ecocem

SiO_2	Al_2O_3	Fe_2O_3	TiO_2	MnO	CaO	MgO	SO_3	K_2O	Na_2O	P_2O_5	S^{2-}	Cl^-
20.34	4.53	2.47			65.35	1.01	3.38	0.14	0.13	0.08	<0.1	<0.1

(c) CEM I, 52.5 R, Teil

2.2.1.2 Preparation

Firstly, cement and sand are mixed together for three minutes. Then water is added gradually while mixing for another minute. Then, the material is mixed supplementary three minutes. For concrete mixtures, the same procedure is applied despite that at the beginning gravel is mixed with cement and sand for three minutes and the duration of mixing after addition water lasts for five minutes instead of three. The fresh cementitious materials viscosity is controlled by Abrams test (NF EN 12350-2 [144]) and the three materials mixtures have a common S3 consistence class.

Once prepared, the fresh cementitious materials are poured in the corresponding mold in two layers, each of them is vibrated in order to eliminate air voids. The required time of vibration at each layer is approximately 30 seconds. After casting, the surface of the specimens is covered with a plastic film to inhibit the evaporation of water. The specimens are placed in a curing room where the relative humidity is approximately equal to ninety five percent. After 24 hours, the specimens are unmolded and therefore cured for 28 days in cure solution (water with calcium hydroxide in excess). The specimens tested in this project are fabricated from 12 consecutive batches of approximately 55 liters of cementitious materials each.

2.2.1.3 Mechanical characteristics

The compressive and tensile strengths of CEM I mortar are obtained using 8 cylindrical mortar specimens (110 × 220 mm) according to the European Standards (NF EN 12390-3 [145] and NF EN 12390-6 [146] respectively). 4 other specimens are used to determine the Young's modulus and Poisson ratio of mortar mixture (NF EN 12390-13 [147]). The steel/mortar interface bond is obtained by the pull-out test [148] realized on two cubic specimens (150 x 150 x 150 mm) containing a 14 mm embedded ribbed rebar. The cracking energy is obtained from a three-point bending test realized on two 70 × 70 × 280 mm specimen containing a central notch according to [149] .

Each of the mechanical properties of concrete mixture realized in Toulouse (compressive strength, Young's modulus and Poisson ratio) is obtained using 2 cylindrical concrete specimens (110 × 220 mm).

The mortar specimens based on (CEM I + 50% slag) are not characterized mechanically.

The obtained mechanical characteristics are shown in Table 2-3

Table 2-3: Mechanical characteristics of the cementitious materials mixture

Materials	Compressive strength f_c (MPa)	Tensile strength f_{ctk} (MPa)	Young's Modulus E (GPa)	Poisson ratio ν	Steel/mortar bond C (MPa)	Cracking energy Gf(N/m)
Mortar (CEM I)	55 ± 1.4	3.5 ± 0.5	33.3 ± 2.6	0.21 ± 0.03	16.2 ± 1.9	96.7 ± 38
Concrete (CEM I)	56 ± 5.0		35.7 ± 0.2	0.22 ± 0.01		

2.2.1.4 Microstructure

The results presented in this section are obtained on cementitious mixtures prepared in CEA Saclay laboratory. The specimens characterized have the same age (12 months). The objective of these characterizations is to compare the microstructures of the three cementitious materials cast in this study.

- Intrudable pore diameter using mercury intrusion porosimeter (MIP)

The characterization of the materials structure from the nanometric scale to the macroscopic scale is obtained using the MIP method. Micromeritics' AutoPore IV 9500 is used for these measurements. During the test, incremental levels of pressure P_{Hg} are applied on a dried sample immersed in mercury. The cumulative volume of mercury V penetrating the pores is measured at each applied pressure level: $V = V(P_{Hg})$. The Washburn law [150] allows to estimate for each level of pressure the intrudable pore diameter (supposed to have cylindrical form). The Washburn law is shown in equation 2.1.

$$D = \frac{-4\sigma_{Hg}\cos\theta_{Hg}}{P_{Hg}} \qquad 2.1$$

θ_{Hg} is the contact angle between the mercury and solid phase. Depending on the solid properties, θ_{Hg} can be equal to a value between 117º and 145º. Basing on the study [6], the value of θ_{Hg} is 141º.
σ_{Hg} is the surface tension of mercury which is equal to 0.475 N/m.
This apparatus allows applying a maximum pressure equal to 414 MPa and therefore the minimal diameter pore detected by this mercury porosimeter is 0.003 µm.
It is indicated in the study [151] that the MIP do not allow to determine pore sizes distribution. Indeed, in some cases, big pore diameter can only be accessible by fine pore. Therefore, mercury will not be able to fill this big pore before reaching a threshold pressure sufficient to fill the fine pore. Then, this big pore is considered in calculation as a fine one. Moreover, the Washburn law supposes that the pore is in a cylindrical shape which is not the case in the reality. In addition, the high mercury pressure may induce cracks in the cementitious matrix and thus falsify results. For all these reasons, the MIP serves only to determine the pore entry diameter and not the pore size distribution.

For a better penetration of mercury in the cementitious matrix, all the capillary water should be thrown out of the specimens before the MIP test. In this study, the chosen drying method consists on lyophilizing the specimens in a vacuum for 5 days after immersion in a liquid nitrogen.

Four samples from each cementitious materials mixture are subjected to MIP test. The average curve for each cementitious mixture is given in Figure 2-1.

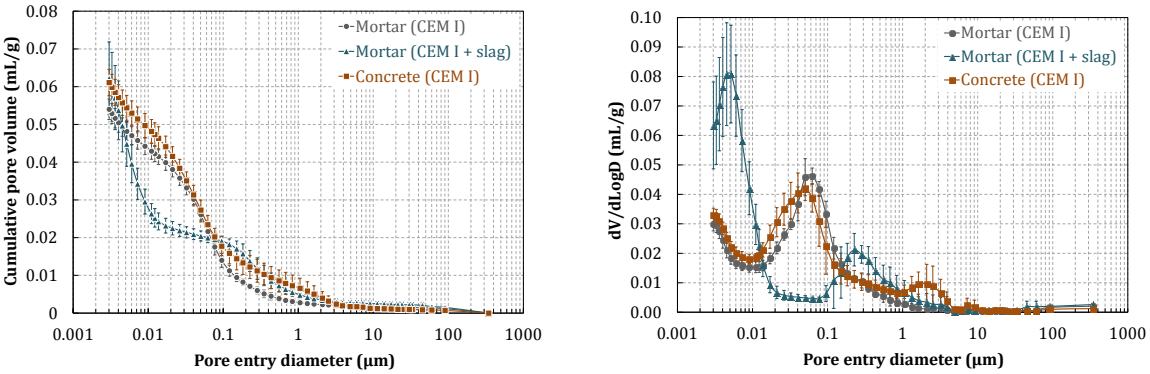

Figure 2-1 : Pore entry diameter of three different compositions

In this study, the critical entry diameter corresponds to the inflection point of the cumulative pore volume curve with respect to pore entry diameter [152].

While comparing (CEM I + slag) mortar mixture with CEM I mortar mixture and concrete, it can be deduced that (CEM I+ slag) mortar mixture shows the biggest critical entry diameter of nanometric pores. This difference in the entry diameter can be attributed to a lower C-S-H density in the (CEM I + slag) mixture than in the mixture based on CEM I [153], [154].

The critical entry diameter of capillary pores in (CEM I + slag) mixture (0.226 µm) is bigger than the one observed in mixtures based on CEM I (0.056 µm). Nevertheless, the volume of the capillary pores is equal to 0.043 ± 0.002 $mL.g^{-1}$ in CEM I mortar mixture, 0.048 ± 0.003 $mL.g^{-1}$ in CEM I concrete mixture and 0.026 ± 0.003 $mL.g^{-1}$ in (CEM I + slag) mortar mixture. Therefore, the latter mixture shows the lowest volume of capillary pores accessible to mercury.

No significant difference can be noted between CEM I mortar mixture and CEM I concrete mixture.

- Porosity

The porosity of the three cementitious materials is determined using two protocols:

(a) Porosity accessible to water:

For each cementitious materials mixture, 4 disks of approximately 20 mm thickness and 50 mm diameter are cut using a diamond saw. Then, these specimens are re-saturated under water in a vacuum following the recommended protocol (GranDuBé [155]).
The porosity is equal to the ratio between the volume of water inside the specimen and the specimen volume.
To determine the volume of each specimen, the buoyancy method is applied. Then, according to the French norm NF P18-459, to measure the amount of water, the specimen is dried in an oven at 105°C temperature until reaching a mass variation lower than 0.05% after 24 hours of drying. The porosity of water is determined using the equation 2.2, where $M_{atmospher}$ is the mass of the saturated specimen, M_{water} is the apparent mass of the specimen when submerged and M_{dry} is the mass of the specimen at its drying state.

$$\emptyset = \frac{M_{atmospher} - M_{dry}}{M_{atmospher} - M_{water}} \times 100 \qquad 2.2$$

This protocol allows also determining the density of the materials using the equation 2.3, where ρ_{water} is the water density.

$$\rho = \frac{M_{atmospher}}{(M_{atmospher} - M_{water})/\rho_{water}} \quad 2.3$$

(b) Porosity accessible to mercury:

In order to determine the porosity by the MIP, it is sufficient to note the value of the intruded mercury volume at the end of the test (V_{tm}) and divide it by the specimen volume. The latter is determined by making the subtraction between the penetrometer volume (V_p) and the volume of mercury injected at low pressure (V_m). This is summarized in the equation 2.4. It should be noted that the total porosity determined using this method concerns only the pores with an entry diameter bigger than 3 nm.

$$\emptyset = \frac{V_{tm}}{V_p - V_m} \times 100 \quad 2.4$$

It is also possible to determine the materials density by the main of MIP according to equation 2.5.

$$\rho_{Hg} = \frac{M_{specimen\ before\ test}}{V_p - V_m} \times 100 \quad 2.5$$

The results obtained are given in Table 2-4.

Table 2-4 : Total porosity and density of cementitious materials obtained by MIP and water porosity tests

Material composition	Porosity (Hg) %	Density (Hg) ($g.mL^{-1}$)	Porosity (H_2O) %	Density (H_2O) ($g.mL^{-1}$)
CEM I mortar mixture	11.84 ± 0.64	2.19 ± 0.02	18.7 ± 0.2	2.30 ± 0.00
(CEM I + slag) mortar mixture	13.29 ± 2.01	2.14 ± 0.02	18.4 ± 0.1	2.29 ± 0.01
CEM I concrete mixture	13.17 ± 0.82	2.19 ± 0.05	16.9 ± 0.7	2.40 ± 0.01

It is possible to determine the volume of the nanometric pores ($V_{nanometric\ pores}$) (even those having an entry diameter lower than 3 nm) by combining the water porosity test and the MIP test (equation 2.6). Equation 2.7 allows quantifying the nanometric volume of pores having an entry diameter lower than 3nm. The results are given in Table 2-5.

$$V_{nanometric\ pores} = \frac{M_{atmospher} - M_{dry}}{\rho_{water}} - V_{capillary\ pores\ (MIP)} \quad 2.6$$

$$V_{nanometric\ pores<3nm} = V_{nanometric\ pores} - V_{nanometric\ pores\ (MIP)}$$
$$V_{nanometric\ pores\ (MIP)} = V_{tm} - V_{capillary\ pores\ (MIP)} \quad 2.7$$

Table 2-5: nanometric pore volume of cementitious materials

Material composition	Total Nanometric pores volume (<10nm) ($mL.g^{-1}$)	Nanometric pores volume > 3nm (MIP) ($mL.g^{-1}$)	Nanometric pores volume < 3nm ($mL.g^{-1}$)
CEM I mortar mixture	0.039	0.011	0.028
(CEM I + slag) mortar mixture	0.054	0.036	0.018
CEM I concrete mixture	0.022	0.013	0.009

The (CEM I+ slag) mortar and the CEM I mortar seem to have the same total porosity accessible to water. While, the porosity of (CEM I + slag) mortar accessible to mercury is higher than that of CEM I mortar mixture. This is due to the existence of higher volume of nanometric pores with an entry diameter lower than 3nm in CEM I mortar mixture than in (CEM I + slag) mortar.

The concrete mixture shows the lowest porosity accessible to water. This is because the volume fraction of cement paste in the concrete is lower than the one in the mortar mixture. Therefore, this mixture shows the lowest nanometric pores volume and thus the lowest porosity accessible to water.

- Resistivity

Several authors use the electrical resistivity as an indicator for the transport properties of cementitious materials [156]–[158]. In this study, the estimation of the electrical resistance of the three cementitious mixture is performed by the electrochemical impedance spectroscopy (EIS).

EIS measurements are performed using the potentiostat/galvanostat/ZRA reference 600 with a frequency domain ranging from 10^{-3} Hz to 10^{5} Hz, 7 points per decade. The potential amplitude of the perturbation signal is 10 mV peak-to-peak. For each cementitious materials mixture, 1 disk of approximately 20 mm thickness and 50 mm diameter is cut using a diamond saw. Then, it is saturated by the same method used for the water porosity test (recommended protocol in GranDuBe). After saturation, 2 stainless steel plate electrodes are placed at the end of the specimen. Between the electrodes and the specimen surface, a wet sponge acts as a conductive medium. Plastic ties are used to tighten the electrodes against the specimen (Figure 2-2). The latter is covered by a plastic wrap to avoid drying during measurements. During the EIS test, the specimen is put in a desiccator where the relative humidity is regulated at 95% using potassium nitrate salt [159]. Using a geometrical factor, it is possible to calculate the material resistivity (ρ) from the electrical resistance (R) calculated basing on the EIS measurements (equation 2.8).

$$\rho = R \times \frac{A}{L} \qquad 2.8$$

Where A is the cross sectional area of the specimen and L is its length.
The electrical resistance (R) of the sample is equal to the average value of the real impedance values measured at high frequency (horizontal line). The domain of frequency used to calculate the electrolyte resistance is shown in Figure 2-3 by two vertical blue lines.

Table 2-6 shows the electrical resistivity obtained on the three cementitious materials. It can be noted that (CEM I + slag) mortar mixture shows the highest electrical resistivity.

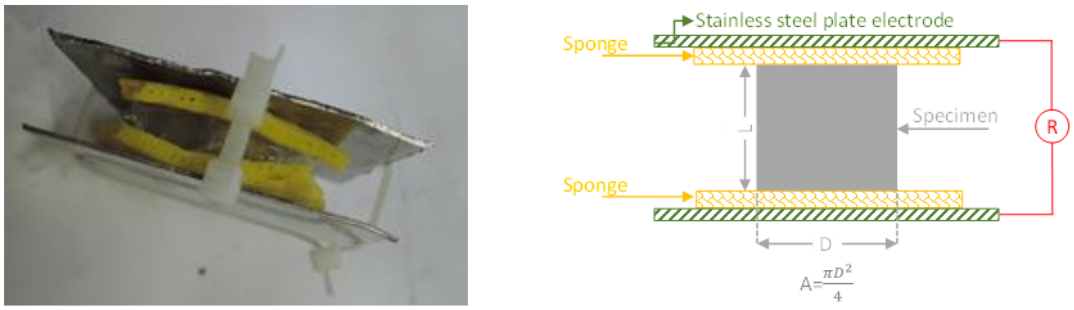

Figure 2-2: Uniaxial measurement of the specimen resistance

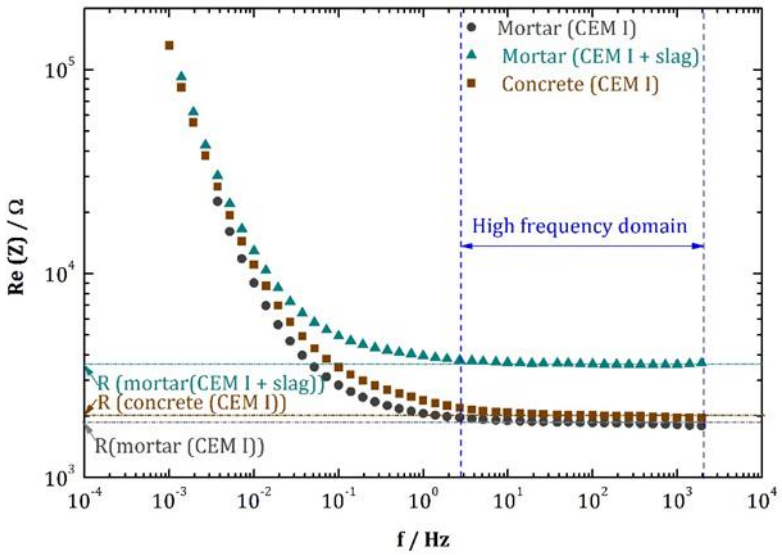

Figure 2-3: Real impedance values measured in different materials at different frequencies

Table 2-6: Resistivity measurements on the three cementitious materials

Material composition	Resistivity (EIS) (KΩcm)
CEM I mortar mixture	20
(CEM I + slag) mortar mixture	36
CEM I concrete mixture	20

- Specific surface area

The specific surface area can also be obtained from the MIP tests. As indicated above, from this test, the volume of mercury (Vmercury) is linked to the pore entry diameter (D). Assuming that the pore has a cylindrical shape, it is possible to determine its surface (S) (equation 2.9). The surface calculation should be performed for each entry pore diameter. The sum of all surfaces provides the specific surface area. The obtained results are shown in Table 2-7.

$$V_{mercury} = \frac{\pi D^2}{4} \times L$$

$$S = \pi DL$$

$$\rightarrow \quad S = \frac{4V_{mercury}}{D} \qquad 2.9$$

Table 2-7: Specific surface area of the three cementitious materials

Material composition	Specific surface area (m^2/g)
CEM I mortar mixture	13 ± 1
(CEM I + slag) mortar mixture	30 ± 6
CEM I concrete mixture	14 ± 2

Once again, the (CEM I + slag) mortar mixture shows the highest specific surface area this is directly linked to the presence of high nanometric pores volume.

- Summary

According to the above cementitious materials characterization, it can be summarized that the (CEM I + slag) mortar mixture shows the lowest capillary pores volume, highest nanometric pores volume, highest resistivity and highest specific surface area. From these observations, it can be deduced that the (CEM I + slag) mortar mixture has the lowest transport properties [153]. As a conclusion, steel reinforcement embedded in this type of cementitious material may show a different corrosion development than the steel embedded in cementitious mixtures based on CEM I.

2.2.2 Steel bar reinforcement

2.2.2.1 Steel characteristics

A 6 mm ribbed steel rebar FeE500 is used in this study. Its nominal yield strength is 500 MPa. An elementary analysis of this rebar is performed using energy dispersive spectrometry (EDS). A minor presence of some elements is detected (Table 2-8). Their presence is neglected in this study.

Table 2-8: Elementary composition of steel rebar obtained by EDS analysis

Element	**Fe**	**Mn**	**Cu**	**Si**	**S**	**Cr**	**Co**
% by mass	Reference	1.39	0.37	0.3	2.95	0.16	0.51

To determine the steel microstructure, 3 samples of the same rebar are etched with 3% Nital after polishing. Then, photos are captured using an optical microscope with an objective 100x (Figure 2-4). The small dimension of the perlite grain (mixture of ferrite and cementite) present next to the ferrite grains indicates a low percentage of carbon (approximately 0.1 - 0.2% by mass) [160]–[162]. The microstructure of the three samples is homogenous with a grain size equal to 8.9 µm ± 0.5 µm. A homogenous microstructure is also visible between the center and the surface of the steel (Figure 2-5) which means that these rebars are not subjected to a hardening process.

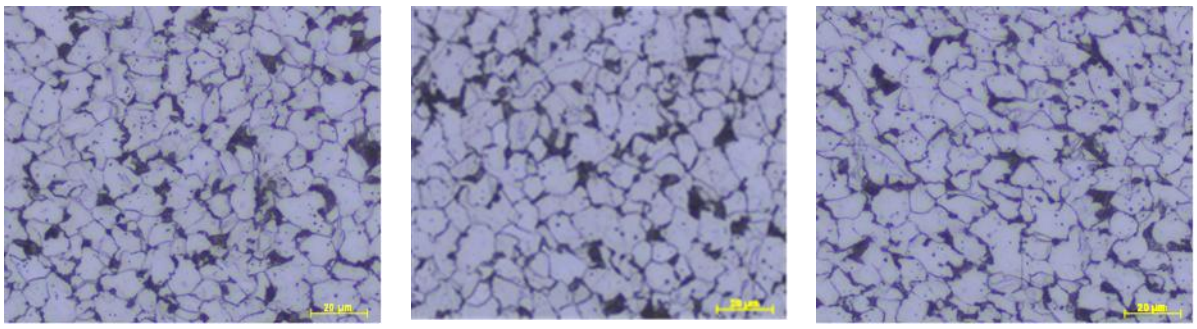

Grain size= 8.43 µm Grain size= 9.47 µm Grain size= 8.8 µm

Figure 2-4: optical microscopy photos of the steel center microstructure

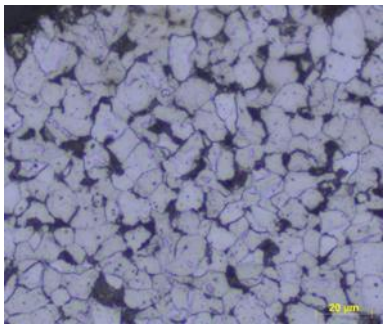

Figure 2-5 : optical microscopy photo of the steel surface microsctructure

The three samples etched by Nital are repolished. Then, the Vickers hardness of the steel rebar is measured using DuraScan equipment with a diamond square-based pyramid indenter. The latter leaves a square imprint on the sample. By a micrometric microscope linked to the machine, the length of the square diagonals can be measured and thus the average diagonal length can be calculated (Figure 2-6). The load applied is 9.8 N (HV1). The Vickers hardness is obtained using equation 2.10:

$$\mathrm{HV} = 0.102\left[\frac{2Fsin\left(\frac{136^2}{2}\right)}{d^2}\right] = 0.1891\frac{F}{d^2} \qquad 2.10$$

Where, F is the load applied (N) and d is the average length of the square diagonals (mm).

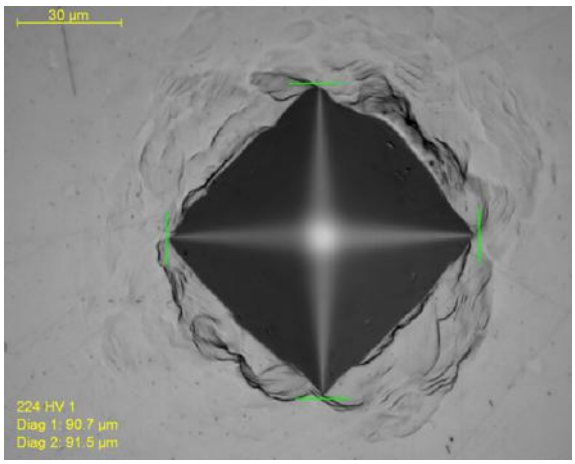

Figure 2-6: square footprint on the steel surface

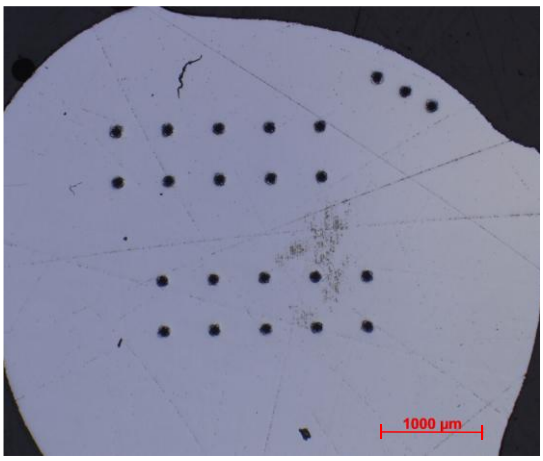

Figure 2-7: steel hardness measurements location

For each sample, the steel hardness is measured at different locations (Figure 2-7). The Vickers hardness of the steel is homogenous between the center of the sample and its edge. Moreover, it is also uniform along the steel rebar because the same hardness value is obtained on the three samples Table 2-9. The average Vickers hardness value of the steel rebar is 226 ± 10.

Table 2-9 : Vickers hardness values obtained at different measurements locations

Test location	Center of specimen 1	Edge of specimen 1	Center of specimen 2	Edge of specimen 2	Center of specimen 3
Vickers hardness value	228 ± 5	217 ± 4	229 ± 9	211 ± 3	222 ± 13

According to [163], the ultimate tensile strength of steel can be deduced from its Vickers Hardness value using equation 2.11.

$$\mathrm{HV} = \mathrm{a}R_m \qquad 2.11$$

Where, R_m is the ultimate tensile strength and “a” is a constant depending from the material. Basing on the European Standards (NF EN ISO 18265 [164]), it can be concluded that the tensile strength of the steel used in this study is around to 708 MPa.

2.2.2.2 Surface preparation

The time needed for the corrosion to initiate is determining in this study. It is well known that the steel surface state affects the initiation of corrosion. That is why; the ideal is to have a uniform surface state throughout the steel bar.

Different steel surfaces are tested in the literature. It is determined that steel preparation by wire brushing leaves in place a defect cracked layer of calamine with a thickness less than 75 µm [165]. Defects are, therefore, points of weakness that may facilitate the initiation of corrosion in the calamine layer. This can skew the experimental results. Indeed, if the defect in the calamine layer is localized at the crack tip of one sample but not in the other, the comparison between them is not accurate. Thus, the wire brushing is eliminated.

The preparation of steel surface by sandblasting is also tested in [165]. This method allows obtaining a uniform surface. However, the disadvantage of this method is the absence of the calamine layer leading to a lack in the representativity of the experimental test. On the other hand, according to the results of [165] and [166], cleaning steel surface by sandblasting slows the initiation of corrosion. These results are also supported by [167], [168]. Moreover, [169] indicates that sandblasting could inhibit the spread of corrosion. [168] Indicates that the sandblasting changes the atomic composition of the steel bar. For all these reasons, the sandblasting method is rejected in this study.

Since all the preparation methods of steel surface are rejected, it is chosen in this study to use the steel as received without any action at its surface.

2.2.2.3 Measurement of the steel reinforcement active surface.

X-ray Computed Tomography (X-ray CT) is performed on the deformed steel rebar in order to determine its external surface. A 6 mm deformed rebar is examined using the industrial 3D µCT scanner at BAM[1] (Federal Institute for Materials Research and Testing in Berlin) (Figure 2-8). This scanner is equipped with a 225 kV micro focus X-ray tube and a flat panel detector with 2048 × 2048 pixels. The spatial resolution is approximately 3 µm special voxel (volumetric picture element) size for the scanning of the 6 mm twisted rebar. The surface obtained by the µCT is equal to 19.54 ± 0.08 mm^2/mm

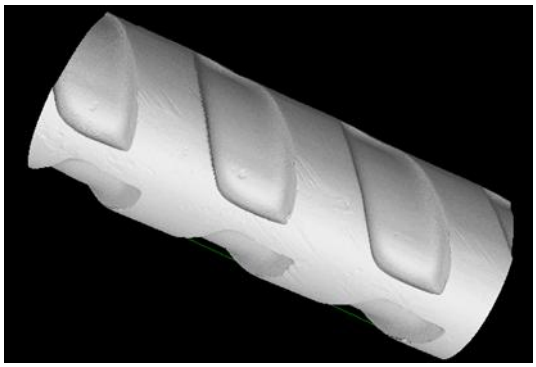

Figure 2-8: CT – 3D visualization of the 6 mm deformed rebar

2.3 SPECIMENS CHARACTERISTICS

2.3.1 Metric specimens: slabs

Most of the laboratory tests are performed on centimetric scale specimens. However, it is important to perform some experiments on specimens representative of the cooling towers. That is why in this study, some concrete slabs having a prismatic shape of 550 × 300 × 150 mm are cast. They are reinforced by two steel bars layers of Ø 12mm. The reinforcement layers are connected with Ø 6mm stirrups. Concrete cover is equal to 30 mm (Figure 2-9). The first advantage of using two layers of reinforcement is to represent a real structure and to test the effect of the “top bar effect” on the corrosion development. Indeed, upper bars according to casting direction are sensitive to casting defects due to fresh concrete settlement and bleeding.

[1] https://www.bam.de/

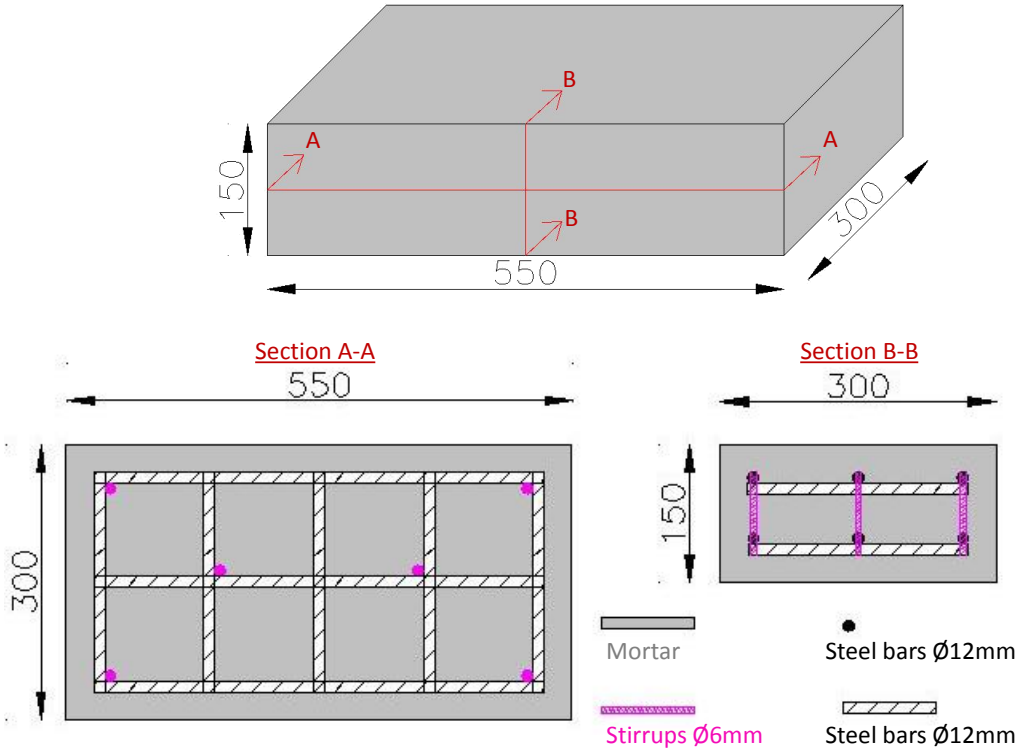

Figure 2-9: Dimensions of the metric specimens (mm)

2.3.2 Centimetric specimens: prisms and rings

The specimens have a prismatic shape of 70 × 70 × 280 mm. For each specimen, a 6 mm deformed rebar is used and positioned in the middle of the specimen as shown in Figure 2-10.

Two ways are used in this study in order to maintain the rebar in the middle of the specimen. The first one is by the means of plastic wedges as shown in Figure 2-11. The second way is retaining the rebar by two holes performed in the middle of vertical walls in the plastic molds (Figure 2-13). In the latter configuration, the steel rebar passes through the specimen dimensions of about 5 mm.

The specimens containing plastic wedges are used to study the effect of the carbon dioxide concentration and the carbonation time on the carbonated length of the steel mortar interface. Moreover, for the same objective, 3 mortar specimens in a ring shape of 50 mm high, 50 mm internal diameter and 150 mm external diameter are also casted. For these mortar specimens, 8 mm deformed steel bars having the shape of a circle with 100 mm diameter are used as reinforcement. They are positioned in the middle of the mold by the main of three fixed metal wires (Figure 2-12).

The specimens having the steel rebar kept in the middle by the means of holes are used for the corrosion kinetics study (Figure 2-13). The steel not embedded in mortar is subjected to atmospheric corrosion which distorts the corrosion kinetics estimation. To avoid this phenomenon, this part of steel should be protected against corrosion. Several materials were been tested to perform this protection, and it is found that the “Lacomit” varnish is the most adapted for this study (resists to high pH solution, can be removed easily). To prevent any crevice corrosion, the varnish was not limited to the steel reinforcement exposed to the atmosphere but also extended to the embedded region. Therefore, the steel reinforcement surpassing the specimen is varnished on a length of 25 mm. It means all the steel reinforcement length (5 mm) subjected to the atmosphere are varnished and the varnish is

extended to the steel reinforcement embedded in the concrete (20 mm length from each side) (Figure 2-13).

To estimate the corrosion kinetics, the iron mass loss induced by corrosion is needed to be determined. For this reason, the initial mass of each non-corroded steel rebar should be measured before casting of concrete and before putting the varnish on the edge of the rebar. Moreover, in the case of rebars passing through the specimens, additional precautions are taken into account. In fact, it is important to avoid penetration of water and carbon dioxide through the steel bar extremities. Otherwise, the corrosion may initiate at the steel bar extremities which is not the objective of this study. Therefore, the two vertical faces (70 × 70 mm) of the mortar specimen are also protected by “Lacomit” varnish (Figure 2-14). This double protection of the steel may limit the initiation of corrosion by carbonation, from each either sides of the rebar, leaving a preferential corrosion in the zone intercepting the crack

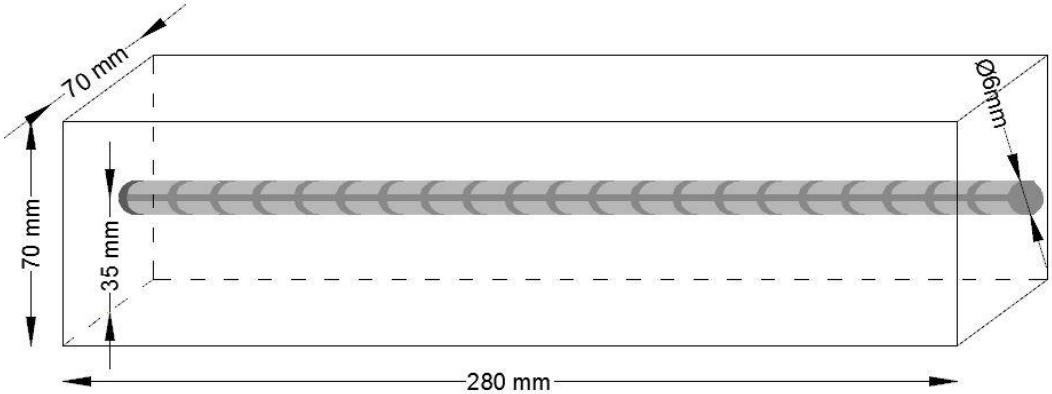

Figure 2-10: Schematic of the reinforced mortar specimens

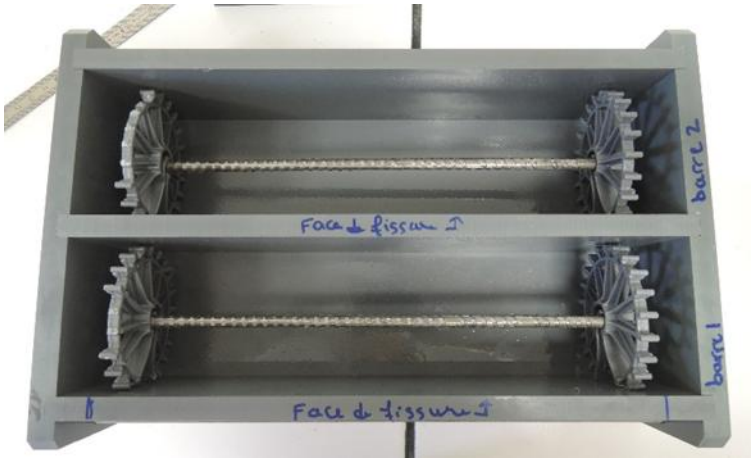

Figure 2-11: Steel centered in the mold by two plastic wedges

Figure 2-12: Ring shape mortar specimens

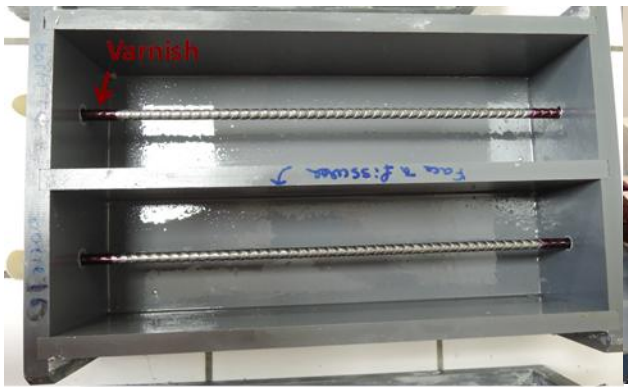

Figure 2-13: Steel centered by holes in the vertical wall of the mold

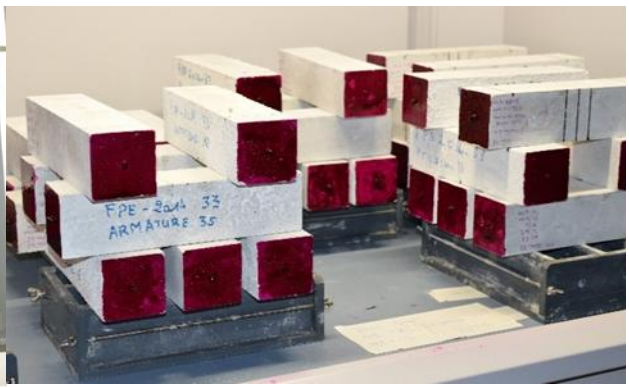

Figure 2-14: Varnished ends of specimens

2.3.3 Millimetric specimens

Some experiments are performed at a millimetric scale in order to determine the type of the early-age corrosion products. Cubic samples of 20 × 20 × 10 mm dedicated to this aim are extracted from a prismatic shape specimen of 40 × 40 × 160 mm. For each specimen, a 6 mm deformed rebar is used and positioned in its middle as shown in Figure 2-15. Once cubic samples are cut, they are polished according to the direction indicated in Figure 2-15 until reaching the mid-section of the steel rebar. Then the surface of this section is polished by grinding (SiC, 80 to 4000 grades) and by 3-µm diamond paste under ethanol. A photo of an obtained sample is given in Figure 2-16. The pre-crack is perpendicular to the rebar, this is not visible in the photo because the crack width is micrometric. Thereafter in order to avoid atmospheric corrosion, the surface of the polished section is protected by the main of a kapton film before exposing the specimen to corrosion condition (humidification/drying cycles).

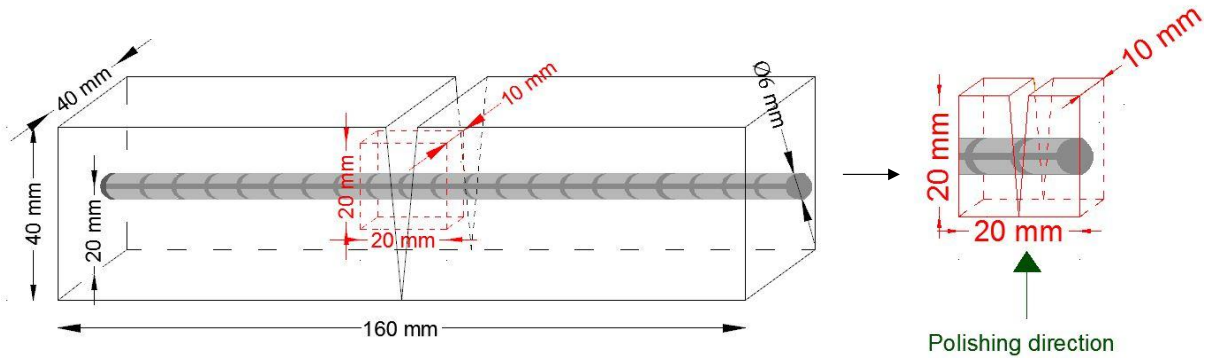

Figure 2-15: Schematic of the reinforced mortar specimen

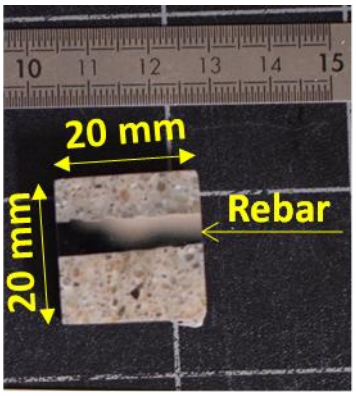

Figure 2-16: 20 × 20 ×10 mm sample configuration

2.3.4 Processing of specimens

Whatever the dimension, after the curing phase, each specimen is cracked using a suitable cracking protocol. Once cracked, the specimens are pre-conditioned. Thereafter, specimens dedicated to the study of the carbonation parameter are subjected to different conditions of carbonations. While specimens dedicated to corrosion study are carbonated then subjected to corrosion environment. To accelerate corrosion in laboratory, cracked and carbonated specimens are subjected to several raining/drying cycles. Several parameters that may affect the corrosion kinetics are tested in this study, such as cracks, rain duration, relative humidity, temperature, cementitious materials type and specimen's dimension. These parameters are chosen in such a way to be the most representative of the cooling towers (Figure 2-17).

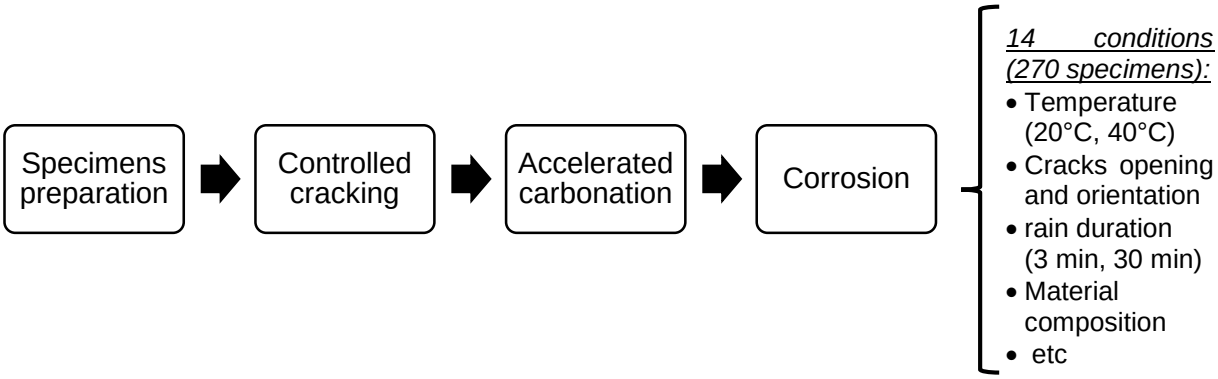

Figure 2-17 : Schematic representation of the specimen processing

The realization of this experimental campaign requires development of specific equipments: first for the carbonation test and second for the corrosion test.
In the forthcoming paragraphs, the developed experimental equipments are presented then each step of the specimen processing is detailed.

2.4 DEVELOPMENT OF SPECIFIC EXPERIMENTAL EQUIPMENTS

2.4.1 Carbonation climatic chamber

To ensure place for the huge number of specimens needed for this study, a new climatic chamber Vötsch VC^3 0060 of 600 liters was adapted during this study for carbonation experiments (Figure 2-18) according to the plans of another carbonation chamber implemented by Drouet [20].
In this climatic chamber, the temperature and the relative humidity are continuously controlled. As indicated in the study [20], the standard deviations in the temperature and in the relative humidity are respectively equal to 0.05˚C and 0.2%.

Figure 2-18: Carbonation climatic chamber

Figure 2-19: Siemens cabinet of CO_2 analysis and control

The carbon dioxide rate inside the climatic chamber is regulated using a SIEMENS cabinet of analysis and control (Figure 2-19). This cabinet contains a CO_2 analyzer (measure by absorption of infrared radiation) and a regulation system (pumps and servo-electro valves). Gas is continuously sampled from the climatic chamber and analyzed by the analyzer. Once the CO_2 concentration inside the climatic chamber drops below the set value, the regulation system inject CO_2 inside the climatic chamber in order to maintain the required carbon dioxide pressure. The standard deviation detected in the CO_2 pressure value is equal to 0.05% for an operating range from 0 to 100%.
The water vapor that may exist in the CO_2 may disturb the analysis. Moreover, its condensation in the measurement system may damage it. For these reasons, the CO_2 gas should be dry before its analysis. A gas cooler is added in order to drop down relative humidity when the analyzed gas is charged with water vapor (for experiments performed with a relative humidity higher than 50%) (Figure 2-19). This gas cooler maintain a temperature lower than 5˚C. A peristaltic pump was also added to remove the condensate.

The communication between the SIEMENS cabinet and the climate chamber is achieved by means of flexible tubes and sealed fittings (Figure 2-21). A schematic of the complete system is shown in Figure 2-20. Three flexural tubes are used to set this connection. Two of these

tubes are used for the measurement of the CO_2 pressure inside the chamber. The first one is used to take out of the climatic chamber a gas sample for analysis. While the other is used to return back the analyzed gas sample inside the climatic chamber. The third tube is used for the injection of CO_2 inside the climatic chamber for the regulation. The evacuation of the CO_2 out of the climatic chamber before its opening is also obtained using a supplementary tube.

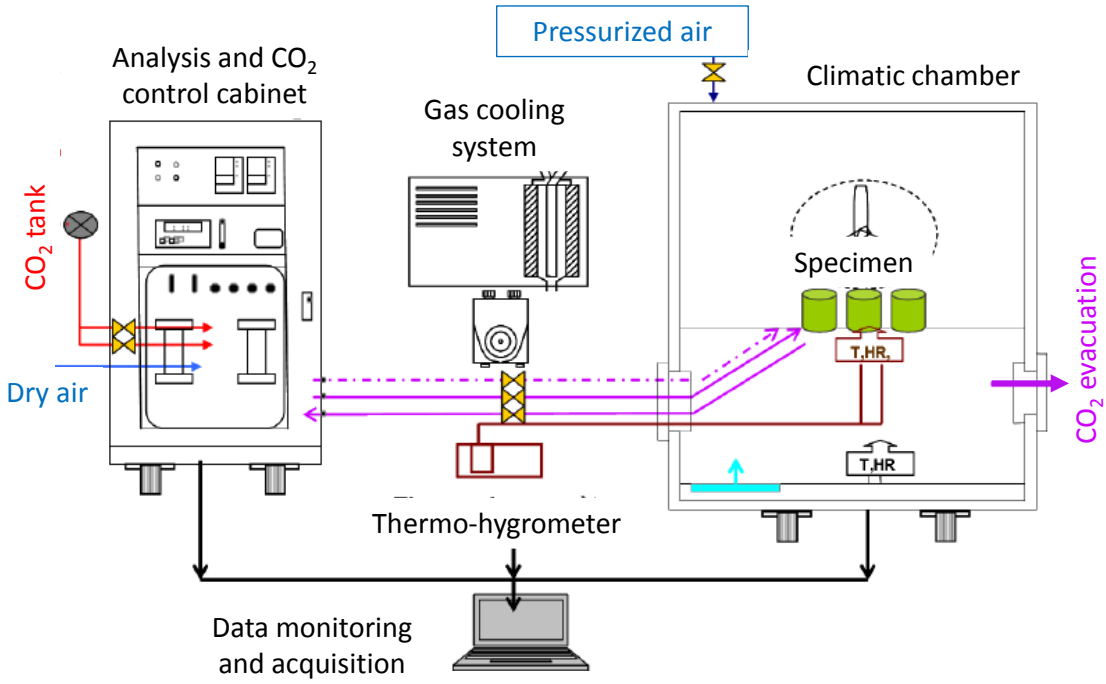

Figure 2-20: Schematic of the carbonation system [20]

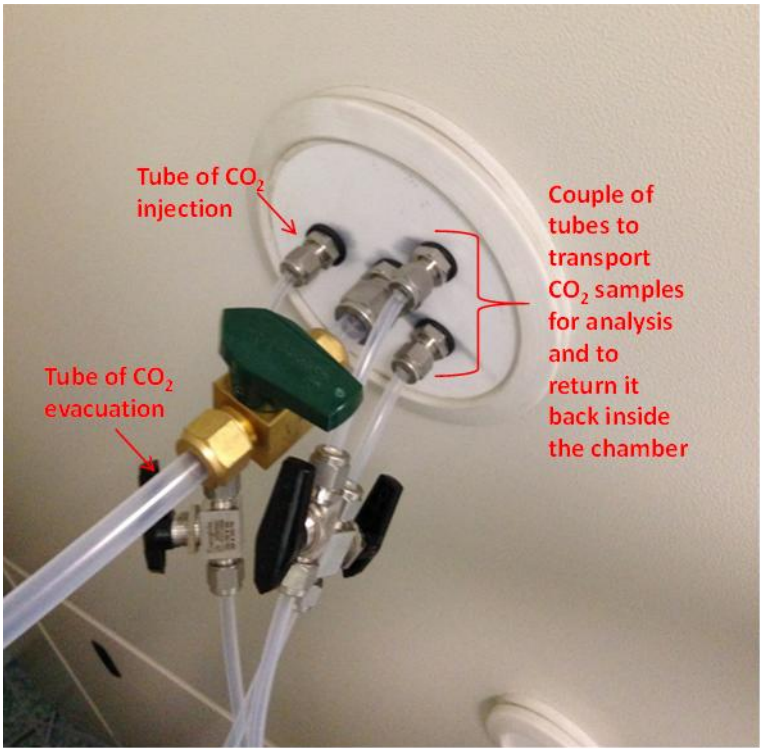

Figure 2-21: Flexible tube used to communicate between the Siemens cabinet and the climatic chamber

2.4.2 Experiments that require rainfall

As indicated in Figure 2-17, some prismatic specimens should be subjected to 30 minutes of rainfall in each raining/drying cycle, while others should only be exposed to three minutes of rainfall. That requires two independent equipments allowing to perform two rainfall durations. That is why two custom raining chambers are designed and manufactured during this study. These devices are called ARIEL: simulAting RaInfall for concrEte durabiLity.

Each raining chamber is equipped with three rows, in order to settle the required number of specimens. The rain is ensured using a micro drip system (Figure 2-24). The latter supports a maximum pressure of 1.5 bar. To ensure homogeneous rain on the specimens, a preliminary test is performed. It is concluded that, with the existing distance between the sprinkler and the specimen's surface in the raining chamber, one sprinkler is needed for two specimens. For an accurate experiment, the specimens should be subjected to the same water. Therefore, it is important to inhibit the flow of water from the highest row to the lowest one. For this reason, at each row, water is collected (yellow color in the Figure 2-22) and is evacuated through a common pipe for the three rows (grey pipe linked to the yellow collector in the Figure 2-22)

Tap water is used to ensure rainfall. To avoid clogging of sprinklers due to limestone, water is filtered using a duo decalcification and anti-impurities station (green color in the Figure 2-22. The pH of the water is 7.5 and its chemical composition is given in Table 2-10.

The big raining chamber (thirty minutes raining), contains a big amount of water that is why, one water purification station is used for each row. While one water purification station is used to the small raining chamber subjected to a small amount of water (Figure 2-22).
Inside these raining chambers, raining/drying cycles are programmed by an automated control unit. In each row of each raining chamber, a hygrometer is continuously recording the temperature and the relative humidity. Moreover, since this experience is performed in an air-conditioned laboratory in which the temperature is regulated at 20° C ± 1°C and relative humidity should be 60 ±5%, an hygrometer is also continuously measuring the hygrometric conditions inside the laboratory room. Dedicated software is registering hygrometric data each minute. A real view of the raining chambers is visible in Figure 2-23.

Moreover, some experiments are conducted at 40°C; to that end a specific climatic chamber is needed. This latter is adapted in order to perform rainfall inside. The same system explained above for the raining chamber is also implemented in the climatic chamber (Figure 2-25). In this climatic chamber, wetting/drying cycles are also programmed using the same automatic control unit. Hygrometric conditions are also registered each minute.

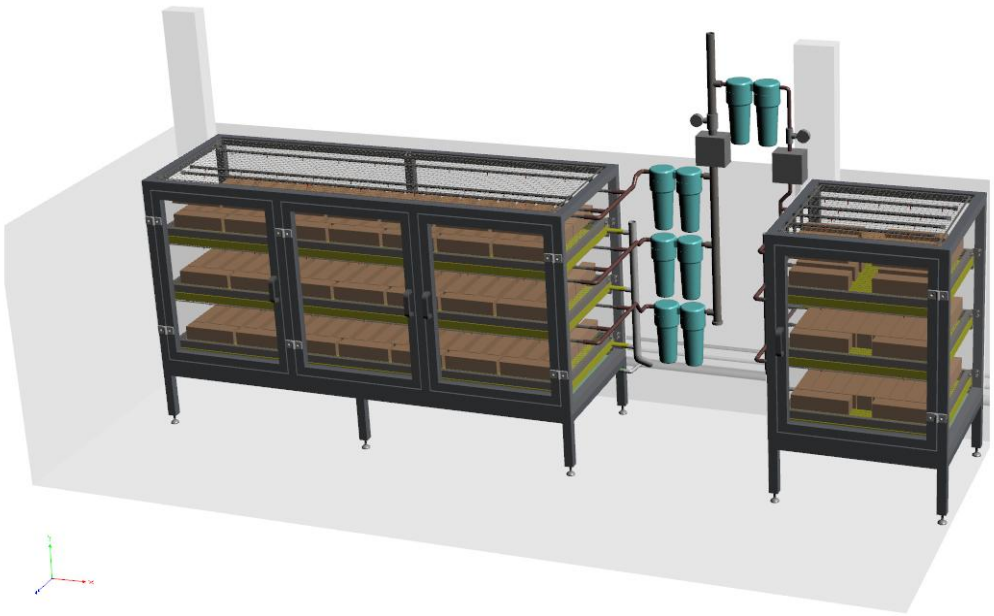

Figure 2-22: Plans for custom raining chambers

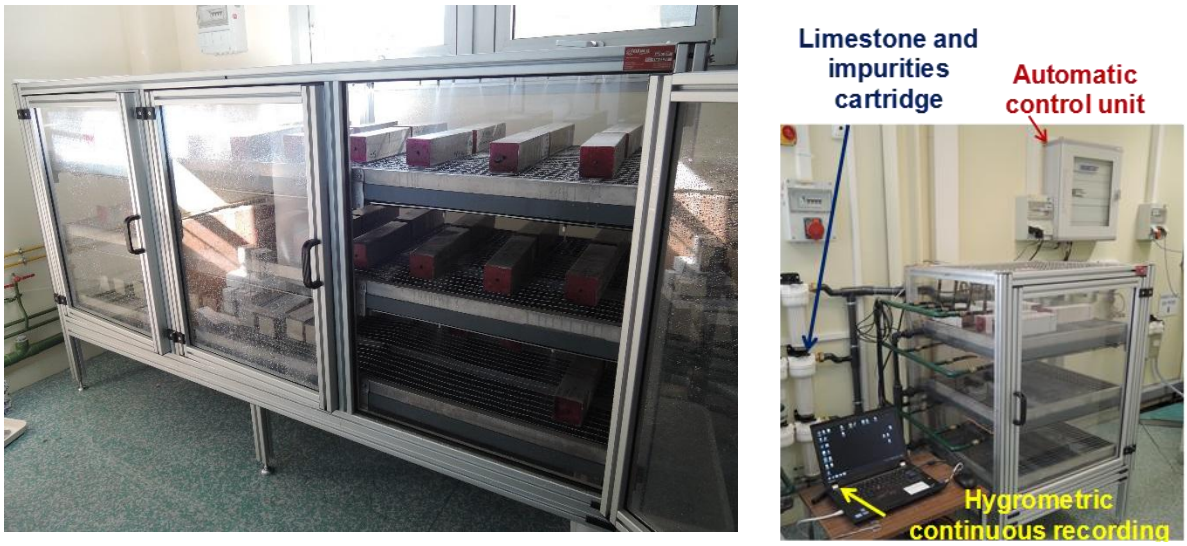

Figure 2-23: Real atomized device for humidification/drying cycles

Table 2-10 : Elements present in tap water

Element	NH_4-N (mg/L)	NH_4 (mg/L)	NO_2 (mg/L)	HCO_3 (mg/L)	Cl (mg/L)	NO_3 (mg/L)	SO_4 (mg/L)	CO_3 (mg/L)
Amount	<0.039	<0.05	<0.01	200	12	17	45	<1

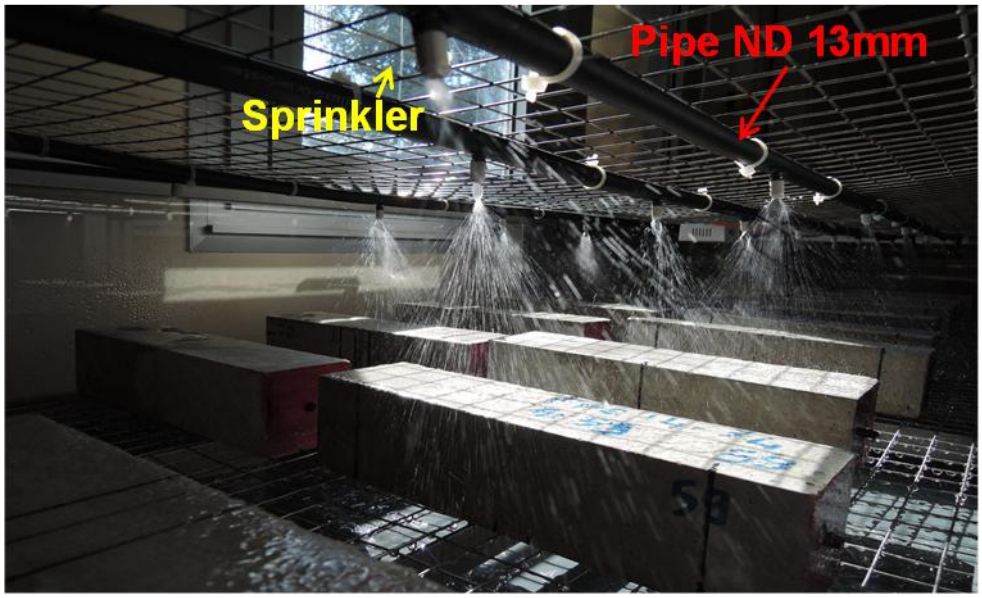

Figure 2-24: A view inside the raining chamber

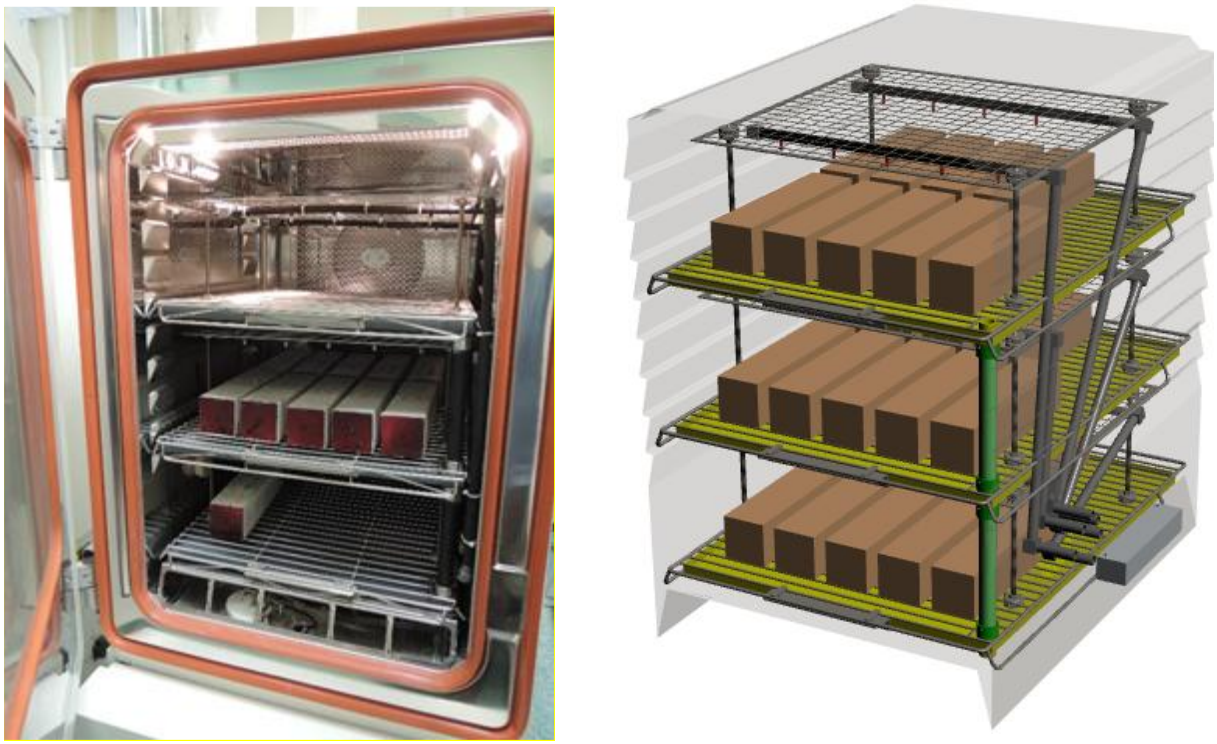

Figure 2-25 : Plans and real view of the adapted climatic raining chamber

2.5 CRACKING

All the parameters in this study are chosen to be representative of the cooling towers characteristics including the cracks properties. For this reason, in the forthcoming paragraphs, a description of the cracks visible on the cooling towers is presented. Then a suitable cracking protocol that induces similarly cracks on the laboratory specimens is also exposed.

2.5.1 Characteristics of cracks visible on the cooling towers

According to [143], when the cooling towers are put into operation, several factors can induce cracking like the desiccation shrinkage of the concrete that occurs on the cooling towers parts subjected to a highest humidity and/or temperature gradient. These cracks are vertical (meridian) and intercept the reinforcement bars.

The width of some cracks could be variable once the cooling towers are operational due to thermohydric phenomena, the wind effect and the differential settlement.
To summarize, the cracks are almost exclusively meridian with small series of horizontal cracks.

The crack openings communicated by EDF span between 0.1 and 0.5 mm.

2.5.2 Definition of a suitable cracking protocol

It should be born in mind that the cracking protocol has to be chosen in such a way that the cracks obtained are representative of those found on the cooling towers.

The most important characteristic is obtaining cracks opening between 0.1 and 0.5 mm. Three crack openings (W) are targeted in this study: 0.1; 0.3; 0.5 mm. Moreover, the crucial parameter is the length of the steel/mortar interface damage induced by the cracking protocol. It is very important to avoid cracking protocols which lead to total steel/concrete interface damage. Otherwise, it will be impossible to study the steel corrosion propagation deep in the crack because in this case the corrosion will initiate along the total length of the steel/mortar interface [134].
In this study several crack openings need to be tested in order to determine the effect of the crack opening on the length of the load-induced damage zone at the steel/mortar interface and thereafter on the corrosion initiation and propagation along this interface.

Because several specimens are needed for this study, the reproducibility of the crack width on the different test specimens should be ensured.

None of the big amount of cracking protocols of cementitious materials that could be found in the literature meets the above mentioned criteria. For example, cracking by compression tests [170] as well as freezing/thawing cracking methods [171] generate diffuse cracks. The tensile test performed by imposing a direct traction on a steel bar embedded in concrete [172] leads to a transversal crack on the whole diameter of the specimen which is not representative of that found on cooling towers. For these reasons, these methods cannot be retained.
The expansive core method is already used to crack ring shaped mortar specimens ([26]; [173]). During the carbonation of the cracked specimens at 50% CO_2, carbon dioxide spread along the total length of the steel/mortar interface which inhibit the study of the corrosion propagation deep in the crack. To justify, this protocol leads to cracks which are close to each other and this may induce an overlap in the length of damaged steel/mortar interface and lead therefore to a spread of the carbon dioxide along the total length of the interface. On the other hand, this total carbonation may be due to the high carbon dioxide concentration used and not to the mechanical cracking protocol.

Despite that this protocol is not retained for the corrosion study in this project, it is used to crack ring shape mortar specimens in the frame of the carbonation study in order to determine if the total carbonation is linked to the carbon dioxide concentration.

Two main cracking protocols possibilities remain: shrinkage cracking and three points bending tests.
During the search of a suitable cracking protocol, three different shrinkage protocols are tested, namely, the humidity gradient test, the heat treatment test and the carbonation shrinkage test. The specimen dimensions for these tests are (40 × 40 × 160 mm).

These preliminary tests were performed on two different materials: cement paste and mortar. Cement paste fails the competition in front of the mortar. This is because, in cement paste, there is no gravel, thus energy of cracking cannot be absorbed by any component and the propagation of the crack cannot be stopped. Therefore, in all tests performed on cement paste, cracks appear in a mosaic form which is not the case on the cooling towers. For this reason, the use of the cement paste is rejected. In the following, cracking protocols are discussed only for mortar specimens.

Concerning the humidity gradient test, it consists in subjecting the specimens immediately after curing to a low humidity level. The humidity in the specimens taken out of the cure is equal to 100%. Once they are subjected to a lower humidity value, they tend to be in equilibrium with the new environmental condition. This requires water to diffuse out of the specimen, thus leading to shrinkage. The latter is characterized by a decrease in the material volume which induces stresses that lead to cracking. Once tested on mortar specimens, no cracks were detected after one month long experience independently of the humidity gradient level applied. **Therefore, humidity gradient cracking protocol was rejected.**

Regarding the heat treatment, it consists on heating the samples from ambient temperature to 90°C. Similarly to the humidity gradient test, water evaporates from inside the sample leading to cracking by shrinkage. This cracking protocol leads to crack that fulfills the required characteristics (crack opening; steel/mortar interface damage). The inconvenient of this test is the impossibility to manage the crack opening. As a consequence, a range of crack opening could not be performed. Moreover, it was indicated in the studies [174], [175] that in some concrete the decomposition of the ettringite starts at 50°C. This induces mineralogical alteration.
For these reasons, the heat treatment protocol on mortar specimen is also rejected.

Concerning the carbonation shrinkage cracking protocol, according to [41], the carbonation shrinkage is mostly due to the loss of the water chemically linked to the C-S-H. However, [42], [43] propose that this shrinkage is caused by the decalcification of C-S-H and the polymerization of the silica gel formed during the carbonation reaction. To use this phenomenon in order to create cracks on our specimens, after curing, several mortar specimens were preconditioned at 55% RH and 25°C temperature for two months. Afterwards, they were carbonated at 3% CO_2, 55% RH and 25°C temperature for 37 days. Close cracks were detected and crack openings were not controllable; hence **the carbonation shrinkage cracking protocol was also rejected.**

Only by the three point bending test of the **mechanical cracking protocol** (see after), all the crack characteristics are very well managed and fulfilled. In the following, this cracking protocol will be presented and discussed.

2.5.3 Three point bending test and crack opening control

After curing, controlled cracking of prismatic specimens are obtained using three point bending test. This cracking protocol consists in applying the load in the mid span of a simply supported specimen using a hydraulic pump as shown in Figure 2-26(a). The load direction

is perpendicular to the casting direction in order to apply the same mechanical loading on the upper surface and the lower surface of the specimen with respect to casting direction The crack is usually obtained in the cross section subjected to the greatest tensile stress. In order to quantify the crack opening, a Linear Variable Differential Transformer (LVDT) is placed where the crack was expected to appear, as shown in Figure 2-26(b). This LVDT measures the horizontal displacement between two points located 20 mm on either side of the specimen center. Throughout the test, the applied load and the displacement measured by the LVDT are registered continuously at a frequency of 50 Hz. Note that the displacements registered by the LVDT before the appearance of the crack are due to the flexural deformation of the beam and cannot be considered as a crack opening. Therefore, to calculate the crack opening, these initial deformations are set equal to zero.
At the beginning, the load is increased slowly until cracking starts. Then, by performing loading\unloading cycles and by increasing the maximum applied load from one cycle to another, the residual crack opening (that is to say after unloading) increases. Therefore, the crack opening could be controlled and a range of crack opening could be obtained.

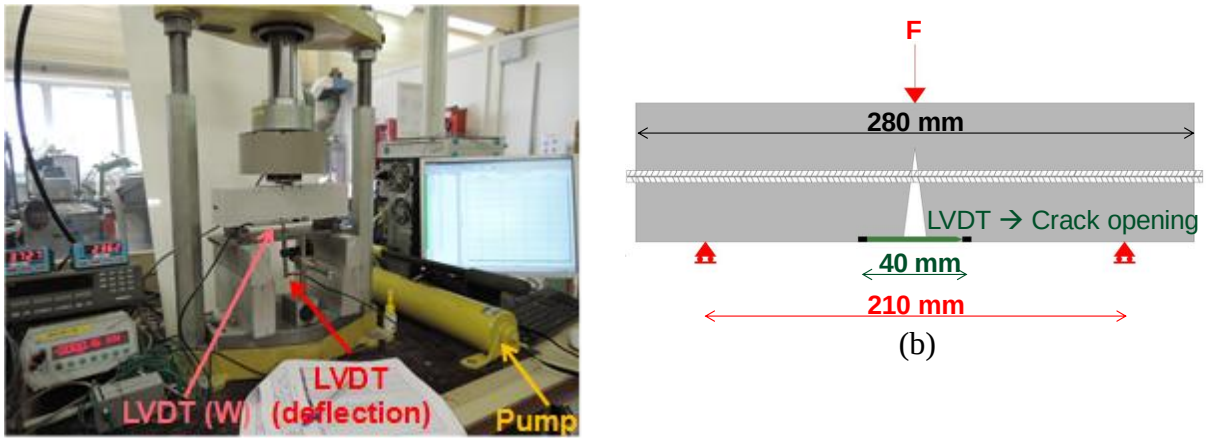

(a) (b)

Figure 2-26: 3-points bending test on a 70 × 70 × 280 mm specimen

By the means of the LVDT, the crack opening is measured on one point of the specimen. Digital image correlation (DIC) is used to obtain the crack opening profile over the entire sample height and to obtain its evolution with respect to loading/unloading cycles. The set-up of the digital image correlation equipment is illustrated in Figure 2-27 (a) consisting of digital charge coupled device (CCD) camera positioned around the center of the specimen and parallel to its surface during the three point bending test. The distance between the specimen surface and the camera determines the area monitored which is approximately equal to 150 × 230 mm^2 (height × width) in this study. Reproducible small ink stains are performed using a toothbrush and a black ink in order to increase the local contrast and allow a better definition of the reference points (Figure 2-27 (b)). It is know that the size of the speckles in a given speckle pattern is an important parameter in the correlation process [176], [177] and should not be bigger than the correlation window (20 × 20 pixels in this study). The size of the speckles obtained varies between 261 and 750 µm and cover a few pixels. In this study, the pixel corresponds to approximately 120 µm. The mesh chosen is shown in Figure 2-27 (c) and induces 120 × 40 points of correlations. To compare the results obtained by the DIC with the LVDT measurements, an LVDT is placed as explained above on the second vertical surface which is not directly exposed to the CCD camera.
A first image of the specimen is taken before the loading, then images with the CCD camera are recorded every 1.5 second until the end of the test. Each captured image corresponds to a different load step. The load applied and the displacements measured by the LVDT are recorded at a frequency of 20 Hz.

Captured images are subsequently processed by a “CMV code” developed by Bornert et al. [178] in order to measure a displacement field of the mesh chosen on the specimen surface (Figure 2-28(b)). The crack opening is equal to the difference of the displacements between two points chosen at the same height (blue crosses in Figure 2-28 (a)) from either side of the crack.

The cracks obtained by the three point bending test are monitored by the DIC on two specimens only.

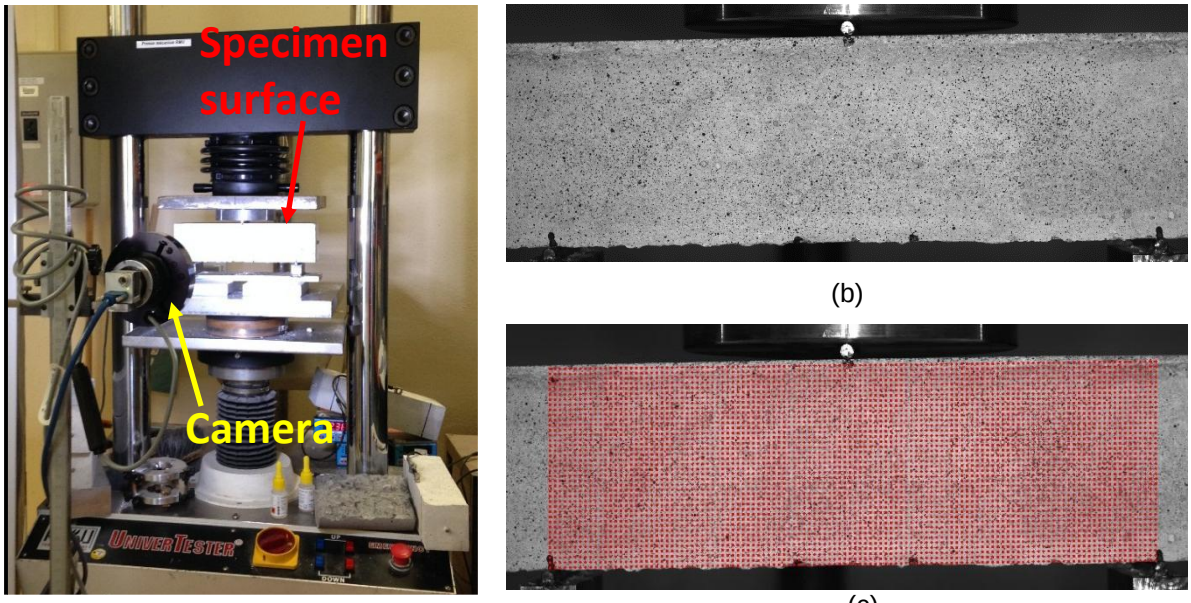

(a) (b) (c)

Figure 2-27: Set-up of digital image correlation equipment

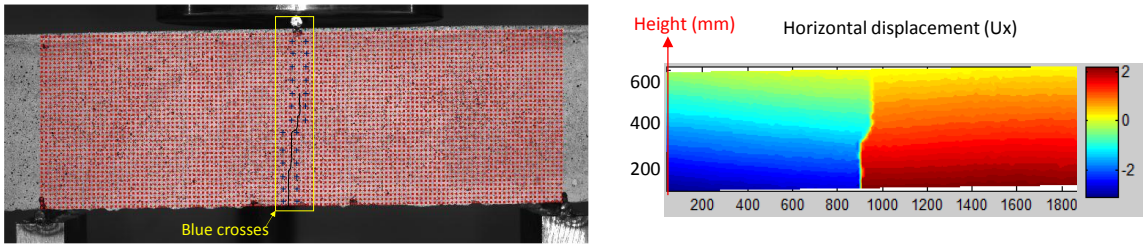

(a) (b)

Figure 2-28: horizontal displacement field of the specimen

The information obtained by the DIC on the crack opening remains in a 2D plan. The results are extended to 3D using X-ray Computed Tomography. Three crack openings (100 µm; 300 µm and 500 µm) are realized on three 70 × 70 × 280 mm specimens using the three point bending test. The same 3D µCT scanner of the BAM detailed in § 2.2.2.3 is used for this three cracked specimens. For technical specifications, cubic shape samples of 70 × 70 × 70 mm are cut from the prismatic one before scanning (Figure 2-29). To avoid variation in the cracks characteristics during the cut of the sample, a diamond wire saw is used. The spatial resolution is approximately 35 µm special voxel (volumetric picture element) size for the scanning of the 70 × 70 × 70 mm sample.

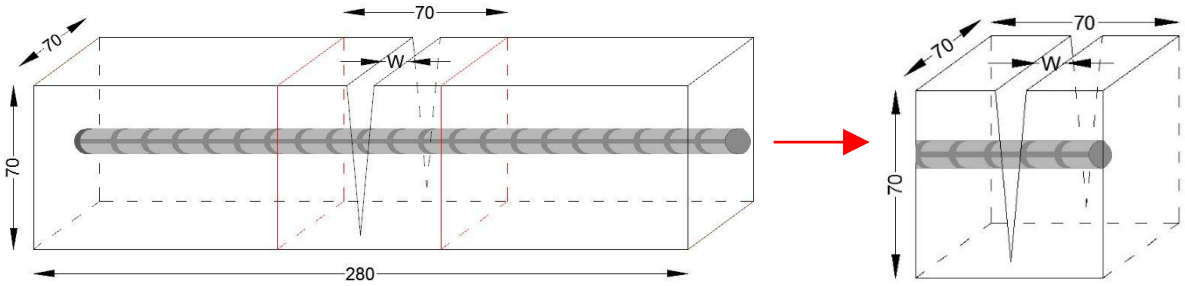

Figure 2-29: Samples cut for X-ray CT test

The three point bending test is also used to crack the metric specimens (concrete slabs) as shown in Figure 2-30. In this case, to measure the crack opening, a video microscope is used instead of the LVDT. The same cracking protocol is used for the 40 × 40 × 160 mm mortar specimen and the crack openings are monitored using an LVDT (Figure 2-31). For these prismatic specimens, one small crack opening (0.1 mm) is needed.

Figure 2-30: Cracking protocol of the concrete slabs

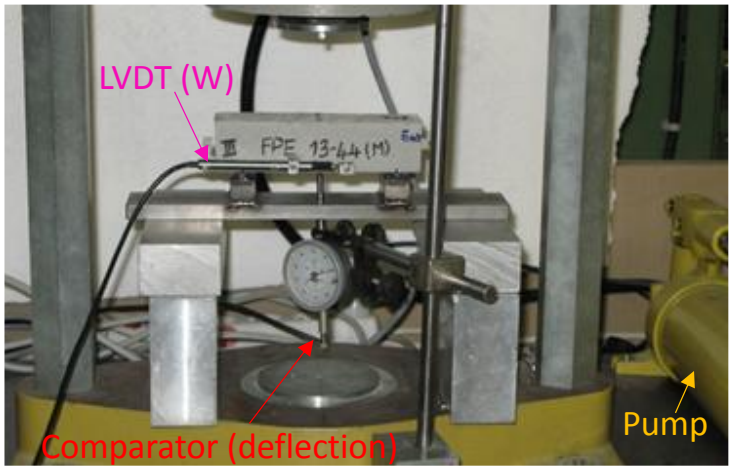

Figure 2-31: three point bending test on a 40×40×160 mm specimen

Cracks in the ring shape mortar specimens are controlled by the expansive core method used in the studies [26], [179] (Figure 2-32). The expansive core is a conical hardened-steel cylinder and is inserted in a set of six conical hardened-steel petals held around the expansive core by a thin cylindrical PVC jacket. The PVC jacket holding the petals and the expansive core is inserted inside the internal diameter of the ring shape specimen. The conical cylinder is forced against the petals by the means of steel bolt and nut as shown in Figure 2-32 (b). The strength applied on the petals induces an increase in the PVC jacket diameter which induces a tensile strength among the internal diameter of the mortar specimen. Since mortar is known to have a low tensile strength resistance, cracks appear. Their number and width is directly dependent on the applied load. A video microscope is used to monitor the crack opening. As indicated above, this cracking protocol and the ring shape specimens are not used for the corrosion propagation study because of the possible overlay in the damaged steel/mortar interface. It is performed in order to study the effect of the carbon dioxide concentration and duration on the length of the steel/mortar interface

damage. This shape is chosen in order to make a comparison with Dang [83] who detects a total damage of the steel/mortar interface in ring shape specimens carbonated at a high carbon dioxide concentration.

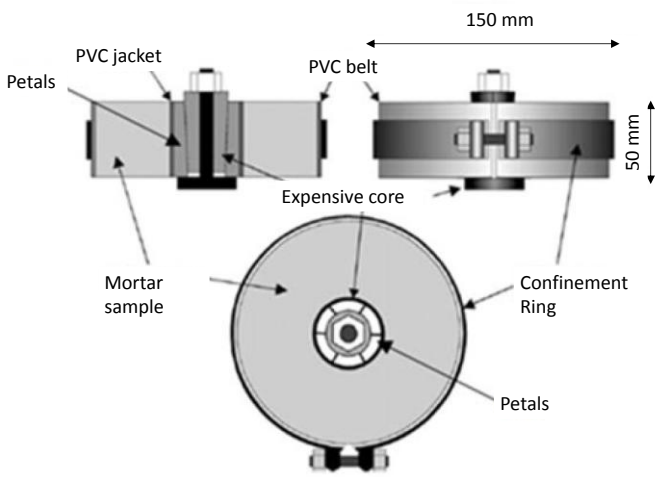

(a) From [179]

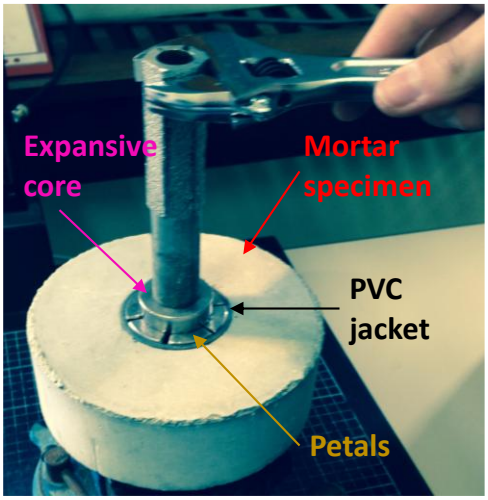

(b)

Figure 2-32: expansive core method

2.5.4 Measuring the steel/mortar interface damage

It was shown in [26] that the carbonation of a steel/mortar interface intercepting a crack occurs regardless of the crack opening. Therefore, carbon dioxide is able to penetrate through load-induced damages at the steel/mortar interface whatever the crack opening. As a conclusion, after a suitable accelerated carbonation duration of specimens, the length of the carbonated interface could be an indication of the length of the load-induced damaged zone. To determine the carbonated interface length, carbonated specimens are split in two parts (Figure 2-33) and rebars are extracted. Afterwards, a dilute solution of phenolphthalein is sprayed on the mortar surface. Noting that the phenolphthalein is a pH indicator test that stays colorless in carbonated zone (pH < 9-10) and becomes purple in non-carbonated zone (pH>9-10). Therefore, carbonated length measurements can be performed as shown in Figure 2-34.

In this study, first of all, carbonation conditions (carbon dioxide concentration, carbonation duration) should be defined in order to obtain reliable carbonated length measurements.
The environmental conditions (temperature and relative humidity) are chosen according to literature review in order to obtain the maximum carbonation rate: 25°C temperature and 55% relative humidity [36], [37].

Cracked specimens are pre-conditioned at (25 ± 2˚C – 55 ± 5% RH) for one month duration before carbonation. This step is important in order to reduce the water content of the cementitious materials and to get as close as possible to equilibrium near the cracks and thus ensure CO_2 diffusion in this materials during the carbonation test.

Figure 2-33: Splitting test

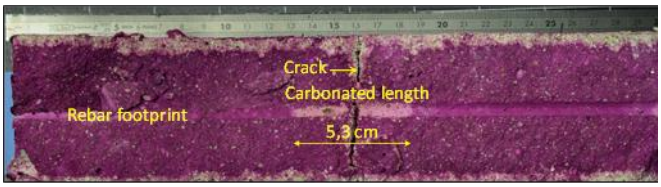

Figure 2-34: Alteration length of the steel/mortar interface for a cracked and carbonated specimen with a residual crack opening of 500 µm

2.5.4.1 Effect of the carbon dioxide concentration

In the previous studies [26], [83] and in French standard procedure XP P18-458 [180], accelerated carbonation tests are performed at a high carbon dioxide concentration (50% CO_2). The advantage of this high CO_2 concentration is the high carbonation rate. Nevertheless, as explained in paragraph 1.3.5.2, carbon dioxide concentrations greater than 3% induce a significant mineralogical change in the hydrates which does not occur during natural carbonation. It was found that 3% CO_2 concentration offer compromise between the carbonation duration needed for the experiments and the representativity to the natural carbonation phenomenon [14], [181], [182]. For this reason, the specimens dedicated to the study of the corrosion kinetics are carbonated at 3% carbon dioxide concentration. However, the effect of the carbon dioxide concentration on the carbonation propagation along the steel/mortar interface is considered in this study. For that, prismatic shape specimens of 70 × 70 × 280 mm showing a 300 µm residual crack opening are carbonated at (50 % CO_2 – 55% RH – 25°C) for (3, 7, 15 and 30 days). The rate of the carbonation propagation along the steel/mortar interface is compared with the one obtained from specimens carbonated at 3% carbon dioxide concentrations for a similar carbonation duration.
Moreover, 3 ring shaped cracked mortar specimens are carbonated at (3 % CO_2 – 55% RH – 25°C) in order to compare the length of the carbonated steel/mortar interface with the one observed in [173]. In the latter study, an initiation of carbonation on the whole steel/mortar interface is detected after 7 days of carbonation at (50 % CO_2 – 55% RH – 25°C). The aim of this comparison, it is to determine whether the totally carbonated interface detected in [173] is due to microcracks induced by the expansive core cracking protocol along the entire interface or to microcracks created due to carbonation shrinkage induced by the high concentration of the carbon dioxide. Note that the ring shaped mortar specimens in this study are prepared with the same formulation and the same materials used in [173].

2.5.4.2 Suitable carbonation duration

It is very important to determine the carbonation duration that is sufficient to give a reliable estimation of the damaged zone length. If specimens are kept for a long carbonation duration, carbon dioxide will propagate along the steel/mortar interface by diffusing through its porosity and this will not give any information about the damaged zone. To this end, different durations (7, 14, 21, 30, 49, 60, 90 days) are tested in accelerated conditions (3% CO_2 - 55% RH - 25°C). The carbonation duration after which the rate of carbonation propagation along the steel/mortar interface decreases is considered as a suitable carbonation duration and is used to carbonate specimens prepared for the corrosion kinetics study.

2.5.5 Modeling of the three point bending test

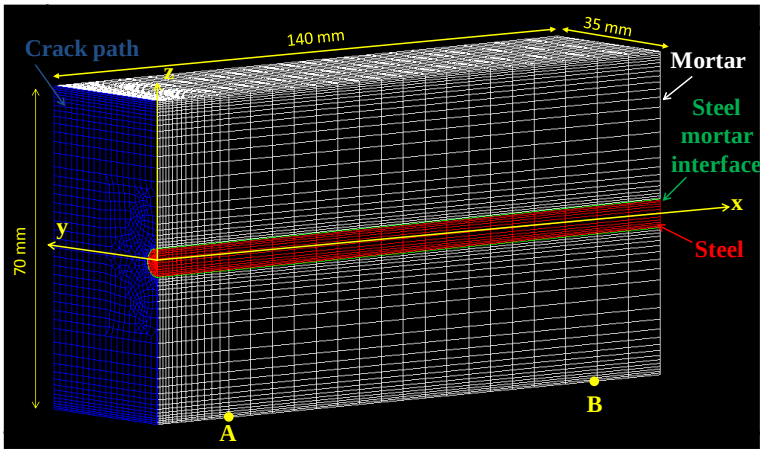

Figure 2-35: Mesh of the quarter of the 70×70×280 mm specimen

The symmetry conditions make it possible to account for the quarter of the 70×70×280 mm specimen. The boundary conditions inhibit the displacement along the x-axis of the surface passing by the points (0; 0; 0), (0; 35 mm; 0), (0; 0; 35 mm). The displacement along the y-axis of the surface passing by the points A (20mm; 0; -35 mm), B (105 mm; 0; -35 mm) and (0; 0; 0) is not permitted. The quarter of the beam is simply supported on the line linking point B (105 mm; 0; -35 mm) with point (105 mm; 35 mm; -35 mm). The loading/unloading cycles are conditioned by applying displacement at the surface linking points (0; 0; 35 mm), (0; 35 mm; 35 mm), (2 mm; 35 mm; 35 mm) and (2 mm; 0; 35 mm). By this means, the displacement is not applied on a segment but rather on a small surface avoiding localization of numerical artifacts.
The thickness of the crack path is of 2 mm. The model used for this part of mortar is characterized by a damaged-elastic mechanical behavior. The steel/mortar interface is also a 2mm thick mortar. The model used for this part is Drucker Prager model characterized by an elasto-plastic mechanical behavior. The steel and the remaining part of mortar (presented with a white color in Figure 2-35) are considered to have elastic mechanical behavior. The strength in the steel remains lower than 500 MPa. The input parameters for materials are those given in Table 2-3.

The crack opening is calculated in the same way as in the experiments: by subtracting the horizontal displacement between two points located at 20 mm from either sides of the specimen center. Point A is located at 20 mm from the specimen center. A' is the symmetric point of A with respect to the specimen mid-span. According to the symmetry conditions, the displacement of point A' along the x-axis ($U_x(A')$) is equal to the opposite of point A displacement along the x-axis ($U_x(A)$). The calculation of the crack opening (W) is done by equation 2.12 where U'_x indicates the displacement along the x-axis of points A and A' before the crack appearance. This is also performed in the experimental procedure as explained before.

$$W = [U_x(A) - U_x(A')] - [U'_x(A) - U'_x(A')]$$
$$W = 2U_x(A) - 2U'_x(A') \qquad 2.12$$

The length of the load-induced damage at the steel/mortar interface is equal to the length of the zone where plastic deformation is non-zero along the steel/mortar interface.

2.6 CORROSION

In each corrosion test, only one environmental factor is tested (rain duration, crack effect, temperature...). The aim of these experiments is to propose an empirical model describing the effect of the environmental conditions on the corrosion kinetics. In order to verify the accuracy of this model, it is important to test corrosion development under arbitrary environmental conditions which will be those of Saclay.

2.6.1 Reference protocol

To compare the effect of all these parameters on the corrosion kinetics, it is important to define a reference protocol. In this protocol, the rain duration is 30 minutes at each cycle while the drying phase lasts 72 hours following each rainfall period. During the rainfall period, the relative humidity in the chamber increases to 95% ± 5%. After the raining period, the drying phase starts and in this phase relative humidity value takes around 12 hours to drop down to approximately 60% ± 5% (Figure 2-36). The temperature in the reference protocol is regulated at 20°C. During the raining period temperature decreases from 4 to 6 degrees and this is due to the lower temperature of water injected inside the rain chamber (Figure 2-36). At each cycle, the precipitation is approximately equal to 190 mm.

The residual crack openings of the specimens in the reference protocol are 100, 300 and 500 µm and cracks are orientated vertically with respect to rain as shown in Figure 2-37. The type of cementitious materials is CEM I mortar. Moreover, the corrosion analyses are globally performed at five time periods (1.5, 3, 6, 12 months). For each parameter tested, the time periods of the corrosion analysis are summarized later in Table 2-12.

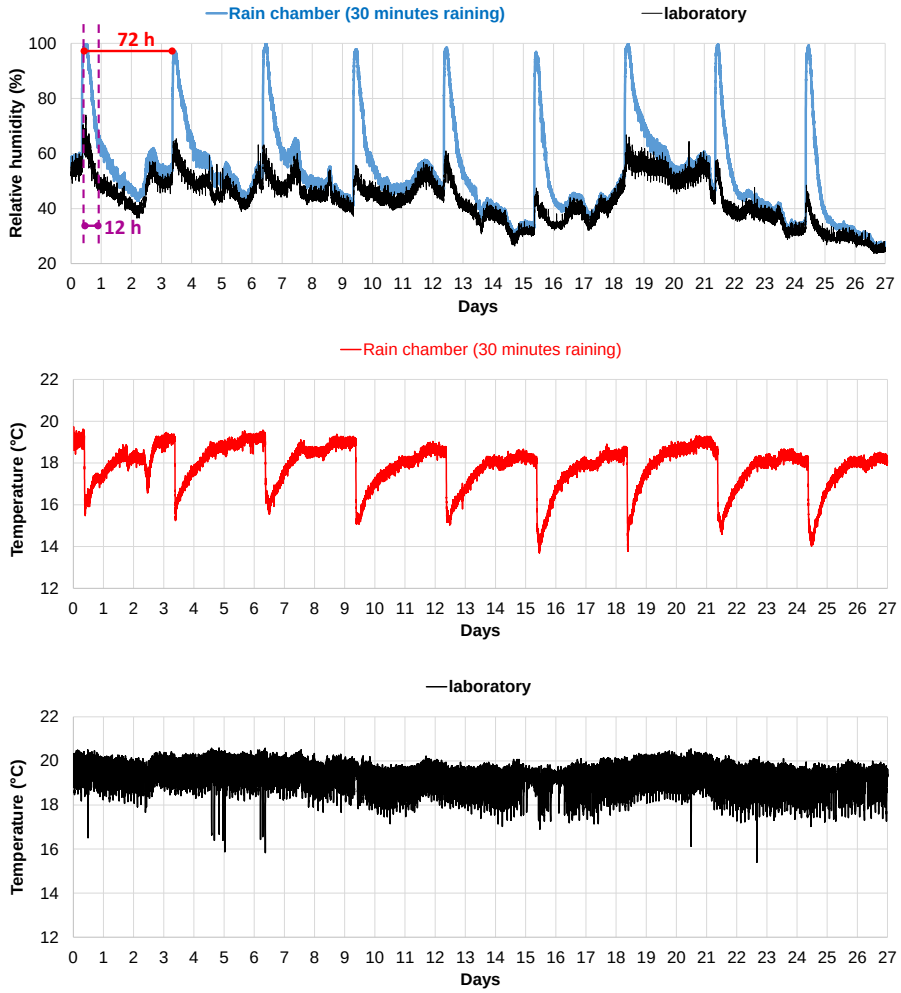

Figure 2-36: Relative humidity and temperature variation during raining/drying cycles in the reference protocol

2.6.2 Influence of parameters related to the cracks

The effect of two pre-cracks characteristics on the corrosion development are tested: the crack opening and the crack orientation with respect to rain. CEM I mortar specimens of 70 × 70 × 280 mm dedicated to this aim are subjected to same accelerated corrosion conditions as the reference protocol.

2.6.2.1 Crack opening

The effect of the crack opening on the corrosion development is deduced from the reference protocol experiments. Therefore, the corrosion propagation in specimens showing three residual crack openings (100, 300 and 500 µm) is tested.

2.6.2.2 Crack orientation

The corrosion propagation is also studied in specimens having a horizontal crack orientation with respect to rain (Figure 2-38). Three residual crack opening are tested: 100, 300 and 500 µm. Results will be compared with those obtained in specimens having vertically oriented cracks in the aim of deducing the influence of the crack orientation on the corrosion development.

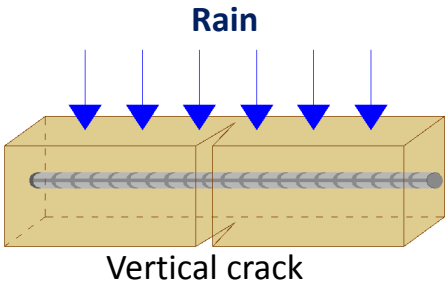

Figure 2-37: Cracks oriented vertically with respect to rain direction

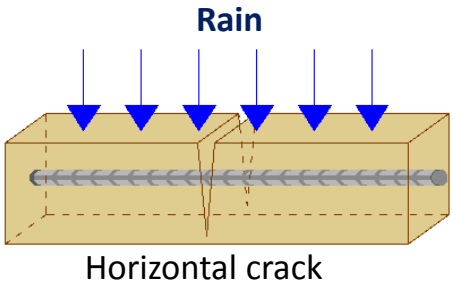

Figure 2-38: Cracks oriented horizontally with respect to rain direction

2.6.3 Influence of the parameters related to the atmosphere

2.6.3.1 Raining/drying cycles number

The effect of the number of raining/drying cycles on the corrosion development is deduced from the specimens corroded in the reference protocol. Nevertheless, the corrosion analysis of these specimens is performed punctually at a determined time intervals (Table 2-12). The number of raining/drying cycles between each corrosion analysis varies from 15 to 119. In fact, millimetric samples were prepared in this project basically in order to test the corrosion initiation and its evolution more frequently using the X-ray fluorescence spectroscopy. Nevertheless, results were not exploitable because the amount of iron present in the first corrosion products may be small and under the detection limit of the X-ray fluorescence detector (details of this experiments can be found in appendix I.1). For this reason, these millimetric samples are especially used to identify the nature of the early age corrosion products using Raman micro-spectroscopy.

The humidification/drying cycles are performed by immersing the sample to the half of its thickness in water (Figure 2-39). In this configuration, the access of oxygen and the rise of water by capillarity are simultaneously possible, which optimize the corrosion rate. Moreover this configuration is representative to the real situation were the oxygen and water diffuse through the pores network and the cracks of the cementitious materials before reaching the metal surface. The sample is kept immersed in water for 30 minutes then it is subjected to 24 hours drying at 55% RH and 25°C temperature. The total number of humidification/drying cycles realized is 48 cycles.

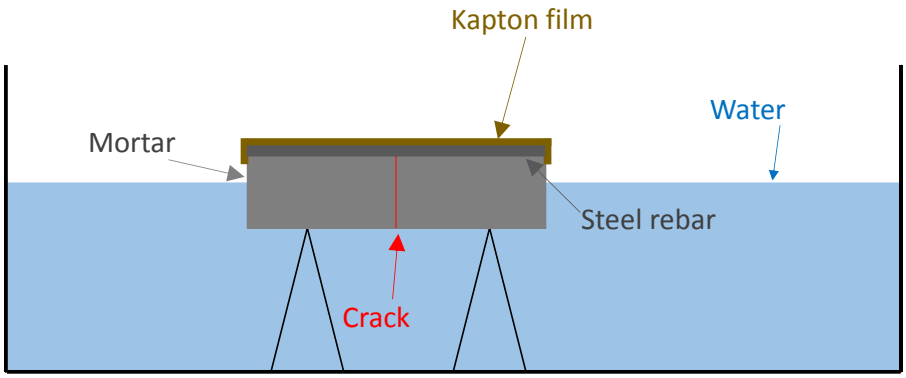

Figure 2-39: Schematic of the humidification/drying cycles for the millimetric sample

2.6.3.2 Raining/drying cycles duration

In this study, the wind is supposed to be unidirectional as shown in the Figure 2-40. That implies that the side of the cooling towers facing the wind (0°) receives most of the rain, while sides parallel to the wind direction (90°, 270°) receive less rainfall.

On the other hand, the air saturated with water vapor produces a cloud, visible at the exit of the cooling towers. This uprising plume is pushed by the unidirectional wind, and therefore induces high relative humidity on the side of the cooling towers located below this plume (180°). This latter side is not directly exposed to precipitation.

In the laboratory test, in order to compare the kinetics of corrosion in the different sides of the cooling tower, series of experimental tests are performed based on the “reference protocol” using CEM I mortar specimens of 70 × 70 × 280mm.

The reference protocol (30 minutes rain per cycle) aims at being representative of the 0° side.

To simulate the 90° and 270° sides, the same conditions of the reference protocol are used except the rain duration which is only 3 minutes at each cycle (1/10 of the wet time on the 0° side). During the rainfall period, the relative humidity value increases to 80% ± 5%. After the raining period, the drying phase starts and in this phase relative humidity value takes around 6 hours to drop down to approximately 60% ± 5% (Figure 2-41). The temperature is like in the reference protocol regulated at 20°C. During the raining period temperature decreases from 2 to 4 degrees and this is also due to the temperature of water injected inside the rain chamber (Figure 2-41). Specimens subjected to these conditions present a 300 µm residual crack opening oriented vertically with respect to rain.

To determine the corrosion development in the cracked specimen not directly exposed to rain (180° side), specimens having a 300 µm residual crack opening are put in a climatic chamber regulated at 90% RH, 20°C temperature.

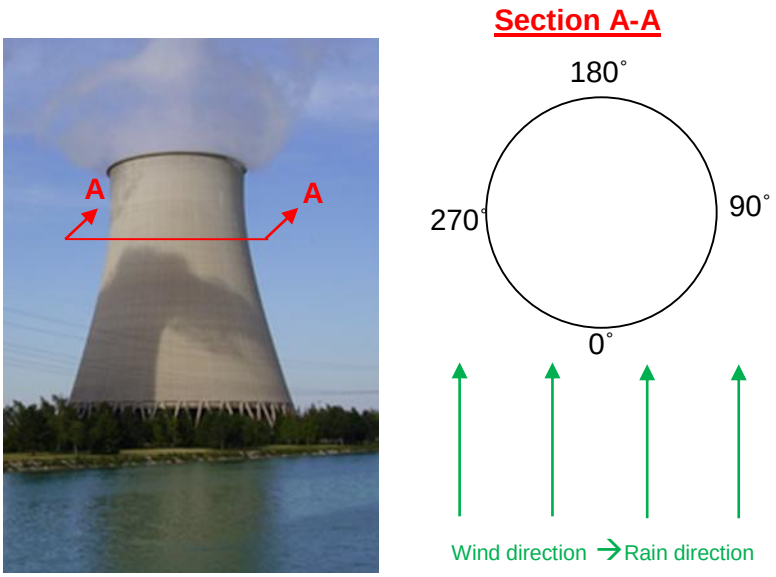

Figure 2-40: Different sides of a cooling tower

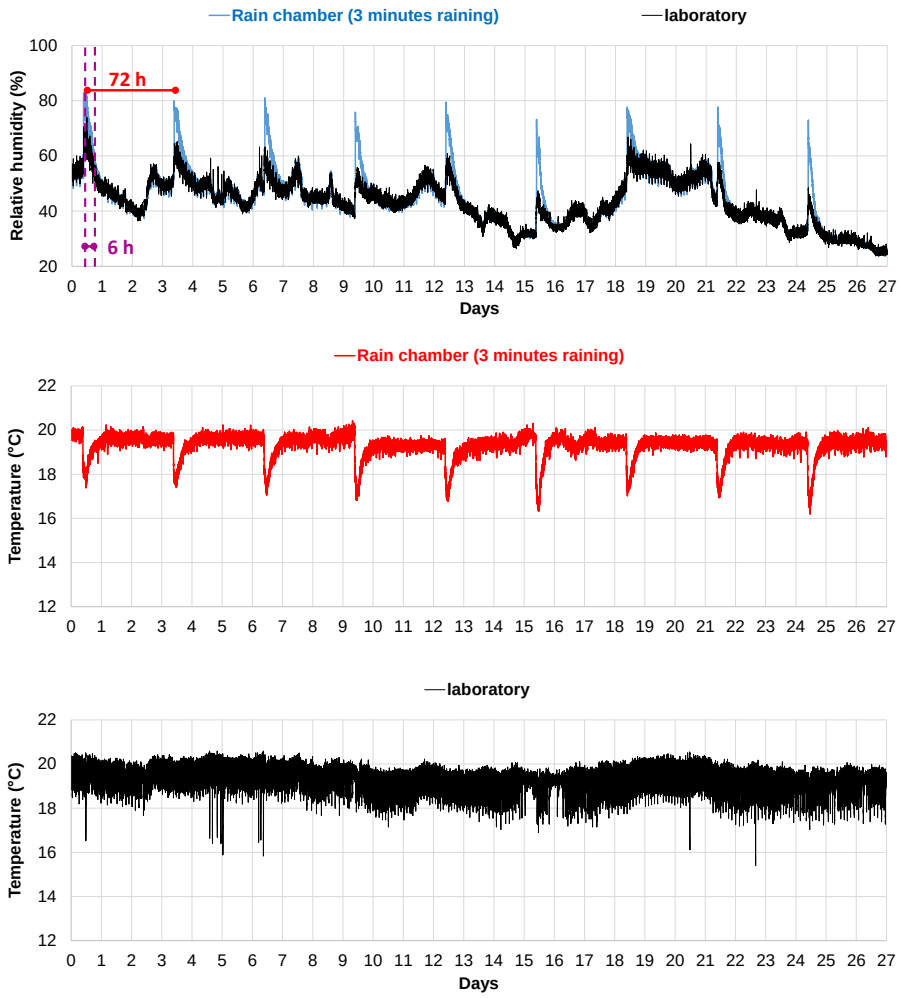

Figure 2-41: Relative humidity and temperature variation during raining/drying cycles in the 3minutes raining duration protocol

2.6.3.3 Temperature

The effect of the temperature is tested by subjecting CEM I mortar specimens of 70 × 70 × 280 mm to the same raining/drying cycles of the reference protocol but the temperature is regulated at 40°C instead of 20°C. During the rainfall period, the relative humidity value increases to 100%. After the raining period, the drying phase starts and in this phase relative humidity value takes around 2 hours to drop down to approximately 40% (Figure 2-42). The temperature is regulated at 40°C but the one obtained is not more than 35°C. During the raining period temperature decreases from 8 to 10 degrees and this is also due to the lower temperature of water injected inside the rain chamber (Figure 2-42).Two residual crack opening are tested 100 µm and 300 µm. These cracks are oriented vertically with respect to rain.

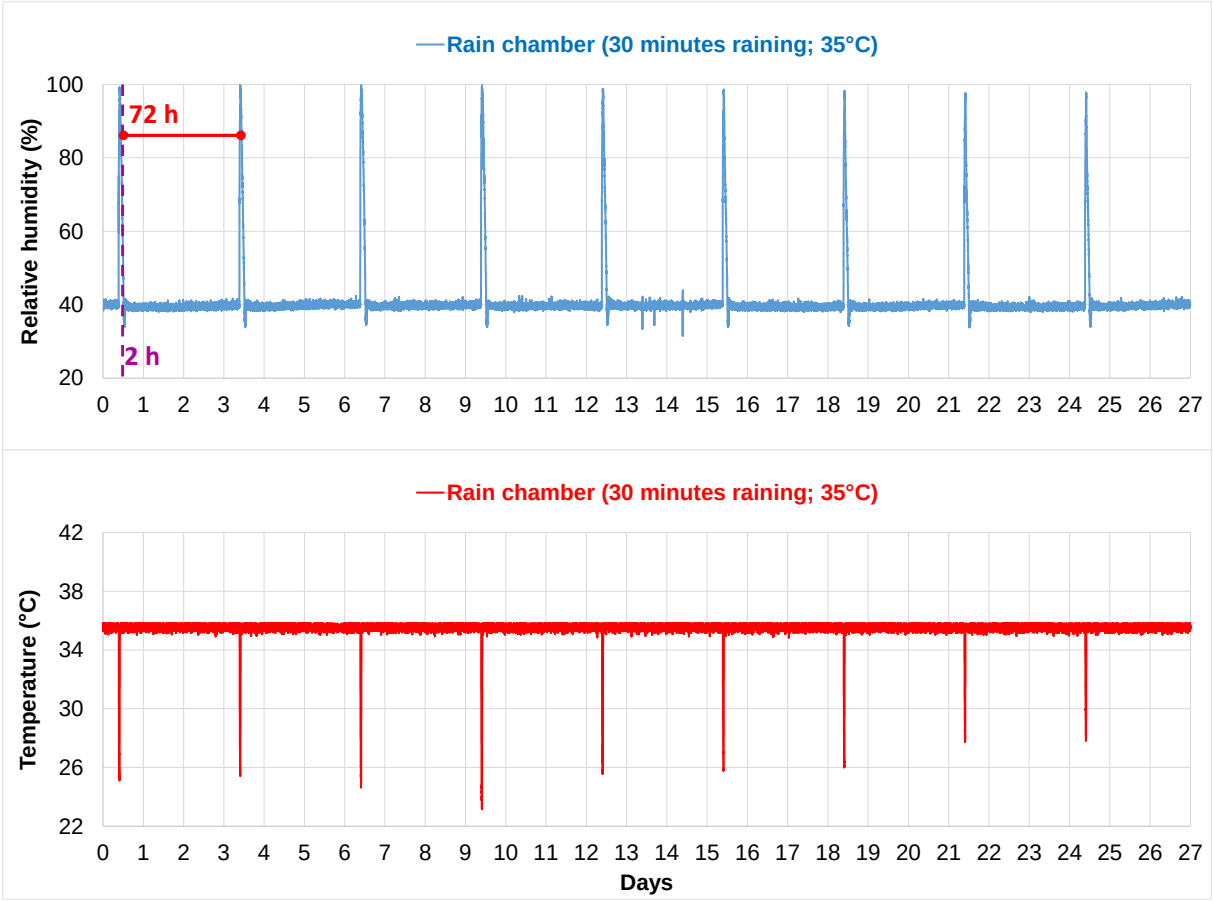

Figure 2-42: Relative humidity and temperature variation during raining/drying cycles in the 40°C temperature corrosion protocol

2.6.3.4 Natural conditions

For that, some CEM I mortar specimens of 70 × 70 × 280 mm, cracked with a 300 µm residual vertical crack, are subjected to the corrosion after carbonation in the environmental conditions of Saclay. In these conditions, all the above environmental factors (temperature, rainfall duration and humidity) vary at the same time (Figure 2-43). Relative humidity and temperature are registered continuously by a hygrometer and the amount of precipitation is picked from the meteorological station of CEA Saclay.

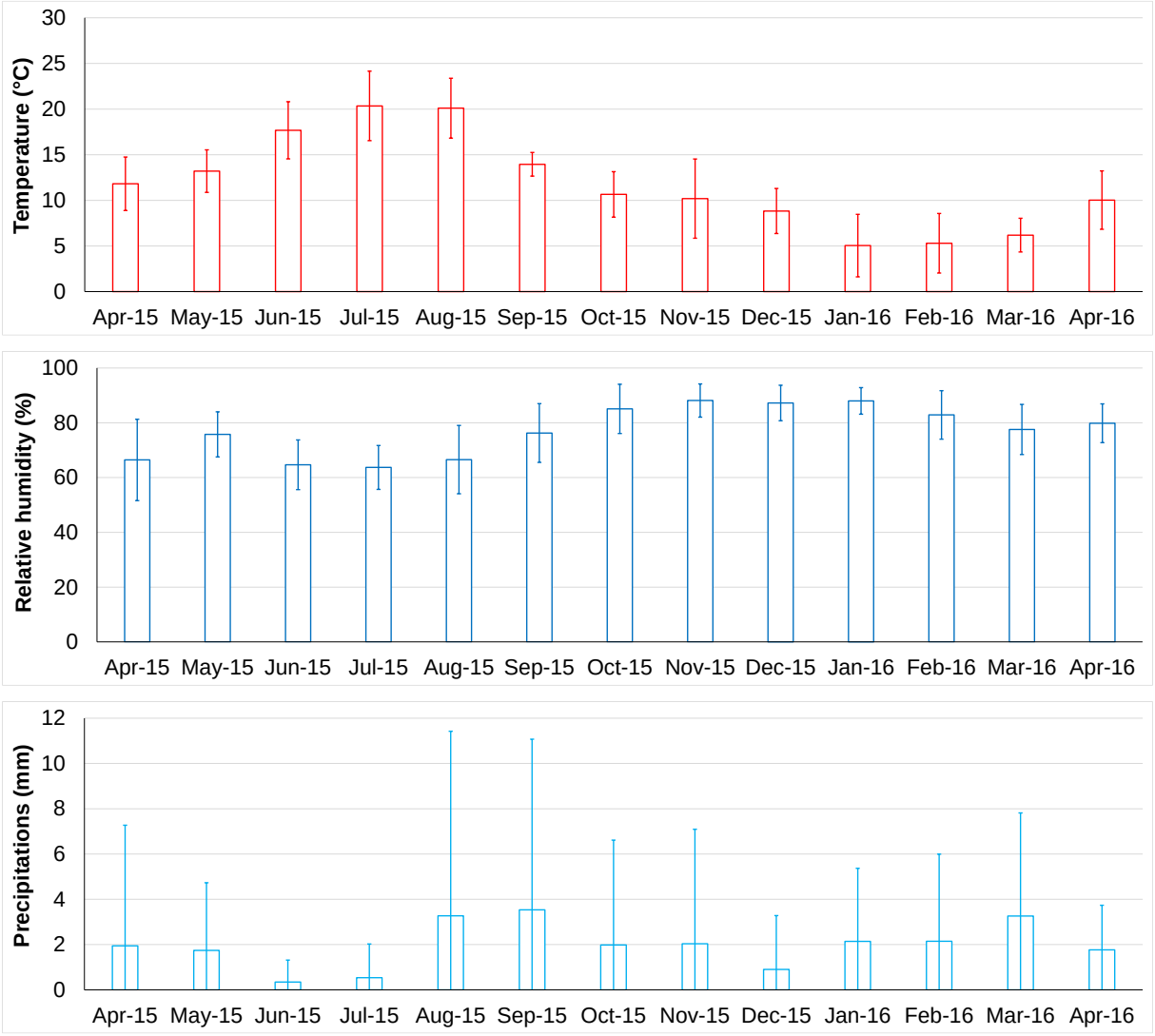

Figure 2-43: Hygrometric conditions in Saclay environment during experiments

2.6.4 Parameters related to specimens preparation

0.1.1.1 Cementitious material composition

The comparison of corrosion kinetics in the three cementitious compositions tested in this project is performed on specimens showing 300 µm residual crack openings oriented vertically with respect to rain and exposed to the accelerated corrosion conditions of the reference protocol.

2.6.4.1 Specimens

It is important to perform experiments on specimens which are representative of the cooling towers. Concrete slabs of 550 × 300 × 150 mm reinforced by two steel bars layers of Ø12mm are used for this aim. After cracking, these slabs are carbonated at 50% carbon dioxide concentration (restriction due to other experiments conducted at this concentration in the same carbonation chamber of the LMDC Toulouse), 55% relative humidity and 25°C temperature. Afterwards, they are subject to 30 minutes raining per week. They are put in a laboratory where the temperature is 20°C ± 5°C and 60% ± 10%. The residual crack opening is around 100 µm.

To perform raining cycles for the concrete slabs, specimens are moved in a curing chamber for 30 minutes once per week. In this curing chamber, water is ejected continuously by the means of sprinklers (Figure 2-44). Thereafter, specimens are moved out this room and put in a laboratory where humidity is around 60%.

Figure 2-44: Raining chamber in LMDC laboratory

2.7 METHODS FOR CORROSION ANALYSIS

For each maturity date of corrosion analyses, some specimens are used for physico-chemical analysis and others for surface analyses. Moreover, in some corrosion conditions, the free corrosion potential of the rebars is monitored continuously during the experiments (Figure 2-45). In Figure 2-45, some abbreviations are used and their meaning is given here:

- CPL: corrosion products layer
- Ecorr: free corrosion potential

Each of the analysis methods is detailed below.

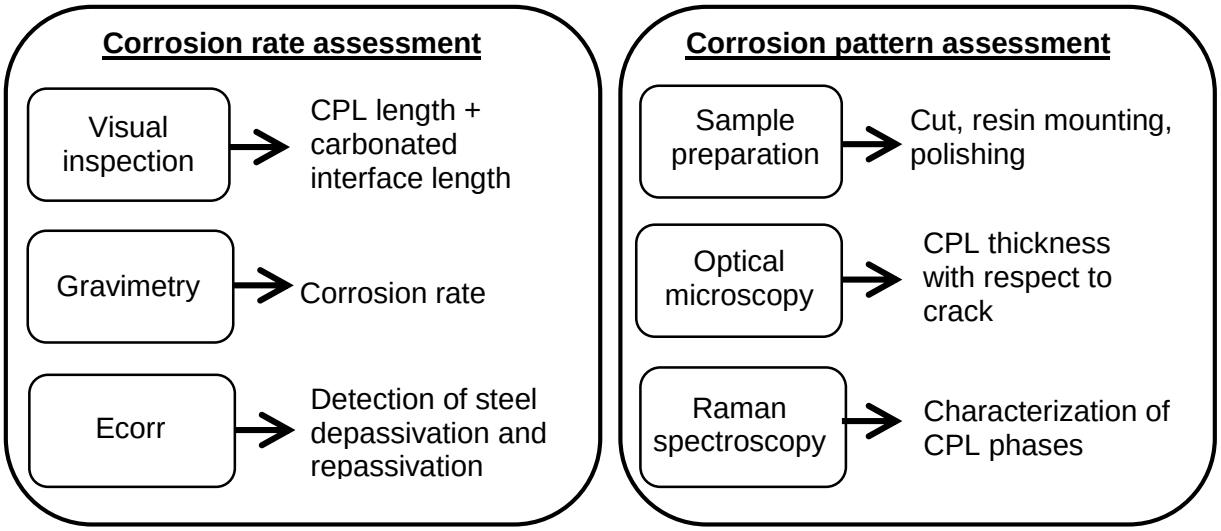

Figure 2-45: Summary of the corrosion analysis method used

2.7.1 Physico-chemical analysis

2.7.1.1 Rebar extraction and visual inspection

Centimetric specimen is first split in two parts. Before extracting the reinforcement, visual inspection of the corrosion products distribution along the steel rebar is performed. Corroded lengths measured on its upper and lower part with respect to casting direction are noted. These corroded lengths measurements are crucial for the calculation of the corrosion kinetics (§2.7.1.3).
After steel extraction, phenolphthalein is pulverized on the split surface to measure the carbonated length along the steel mortar interface and compare it to the corroded length (Figure 2-46).

Furthermore, before splitting specimens in two parts, a visual examination of their external surface is performed using a digital scanner in order to verify if new cracks induced by corrosion appear with time.

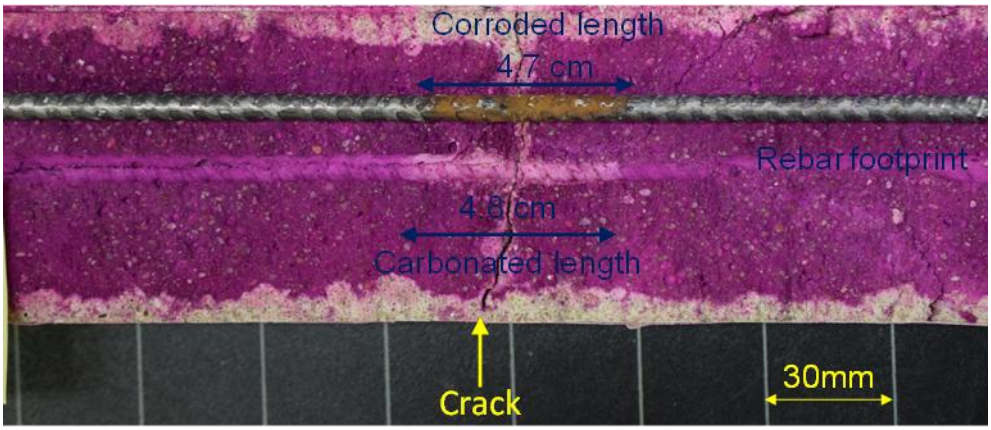

Figure 2-46: Measurement of the corrosion length and carbonation length

2.7.1.2 Gravimetric measurements

The corrosion products attached to the extracted rebar are removed from the steel surface by chemical attack (Sb_2O_3 + $SnCl_2$ + HCl) following the standard ISO 8407 [183]. The difference between the initial mass of the steel (before corrosion) and its final mass (after chemical treatment) gives the steel mass loss (Δm_S).

In our study, each gravimetric measurement is repeated on two rebars corroded in the same conditions for the analysis periods: 0, 1.5 and 3 months. While for the two last analysis periods (6 and 12 months), three rebars corroded in the same conditions are used for gravimetric measurements.

2.7.1.3 Corrosion kinetics estimation

The carbonation-induced corrosion process does not induce a pitting morphology like the chloride-induced corrosion one. The corrosion products layer is known to be more homogenous in carbonation-induced corrosion and this allow to suppose that the thickness of the steel lost during this corrosion process is uniform along the steel corroded length (Figure 2-47). Therefore, the volume of the steel lost (V_{SL}) during the corrosion process can be calculated using equation 2.13, where S_{SL} is the surface of the corroded ribbed rebar. The determination of this surface is directly dependent from the average of the corrosion length (L_C) measured during the visual inspection as explained in §2.7.1.1. This surface is

calculated using equation 2.14 basing on the X-ray CT measurement shown in 2.2.2.3. In equation 2.14, D is supposed to be equal to 6 mm. Introducing the volume of steel lost in equation 2.15 in which ρ_S is the density of steel equal to 7860 Kg/m^3, the thickness of the steel lost during corrosion (T_{SL}) can be calculated as shown in equation 2.16. T_{SL} is obtained at each maturity date of the corrosion analysis and thus the kinetics of corrosion can be calculated using equation 2.17 and its unit is µm/year. This equation is adequate to the one proposed in the study [184].

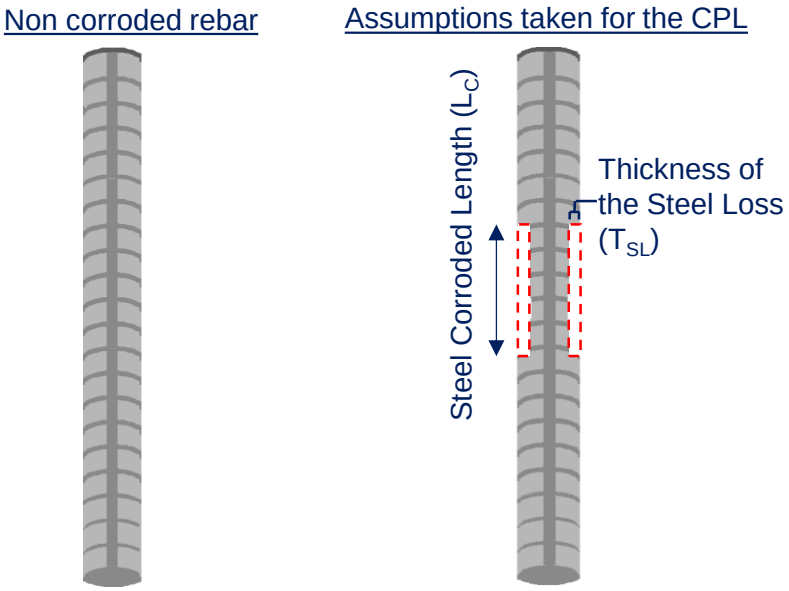

Figure 2-47: Assumption taken in the corrosion kinetics calculation

$$V_{SL} = S_{SL} \times T_{SL} \quad (2.13)$$

$$S_{SL} = 19.54 \times L_C \quad (2.14)$$

$$V_{SL} = \frac{\Delta m_S}{\rho_S} \quad (2.15)$$

$$T_{SL} = \frac{\Delta m_S}{\rho_S \times S_{SL}} \quad (2.16)$$

$$\text{Corrosion kinetics} = \frac{T_{SL}}{\text{Corrosion duration (month)}} \times 12 \quad (2.17)$$

2.7.2 Surface analyses

Optical microscopy, Raman micro-spectroscopy are used to identify and to measure the thickness of the corrosion products formed at various locations of specimens.
First of all, a protocol for samples preparation should be defined to be used on all the specimens that are dedicated to surface analysis. This is discussed in the following paragraphs.

2.7.2.1 Samples preparation

The first and most important step in defining the samples preparation protocol is to determine the cutting direction of the specimen. Two possible cutting directions exist.

The first one is the “transversal cutting”, it consists on cutting the specimen into different slices perpendicular to the steel reinforcement as shown in Figure 2-48 (a). Therefore, in this protocol, several samples are generated from one specimen. An example of the sample generated after this cutting way is showed in Figure 2-48 (c).
The second one is the “longitudinal cutting”, it consists in extracting a 120 x 70 x 15 mm block including the steel reinforcement from the specimen as shown in Figure 2-48 (b). In this method, the steel reinforcement is still covered by concrete after the cutting step. To analyze the steel/mortar interface, the cementitious materials and the steel are removed by polishing until reaching the mid-section of the steel as described in the following. An example of the sample generated after this cutting and polishing procedure is showed in Figure 2-48 (d). The pros and cons for each cutting direction are discussed hereafter.

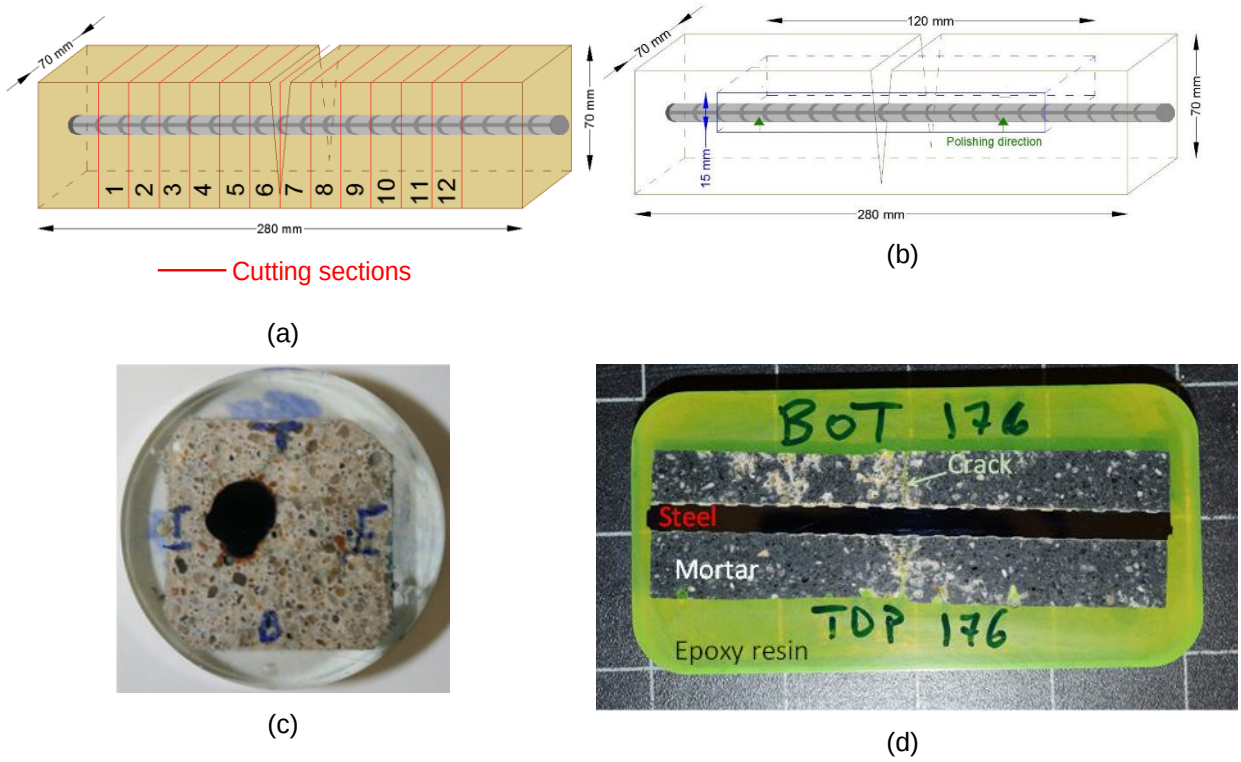

Figure 2-48: Cutting direction possibilities

The major advantage of transversal cutting is the possibility to measure the corrosion thickness all around the steel rebar. One inconvenient is the number of samples that are generated which is much greater than that obtained by the longitudinal cutting. The most important one is the difficulty in localizing the section of the steel/mortar interface that exactly intercepts the crack which is not planar. The last inconvenient is the inability of having an accurate information about the distribution of corrosion over the entire length of the steel from either sides of the crack.

On the contrary, the longitudinal cutting allows obtaining this information very easily. Nevertheless, by the longitudinal cutting, only the upper and the lower part of the steel/mortar interface with respect to casting direction can be analyzed. The information concerning the other sides of the steel/mortar interface are lost. In [83], it is indicated that the corrosion thickness showed to be more developed on the lower part of the steel/mortar interface than on the other part of this interface. This corresponds well with the observations obtained in this study during the preliminary tests as shown in Figure 2-49. This figure shows that the corrosion products are mainly developed at the lower part of the steel/mortar interface. Therefore, by choosing the longitudinal cutting, a focus on the most corroded and the less

corroded steel/mortar interface are performed. The amount of information lost concerning the corrosion in the longitudinal cutting is lower than that lost choosing the transversal cutting. Consequently, a longitudinal cutting is chosen to be used for all the specimens' preparations.

Once the sample is cut, it is embedded into fluorescent epoxy resin (fluorescent color allows the visualization of the crack). The resin takes around 24 hours to polymerize and become resistant. Thereafter, the sample is polished until reaching the mid-section of the steel/reinforcement (according to the polishing direction shown in Figure 2-48(b). Then, the surface of this section is polished by grinding (SiC, 80 to 4000 grades) and by 3-µm diamond paste under ethanol. Once the specimen is prepared, the surface analyses are performed using Optical Microscopy and Raman micro-spectroscopy.

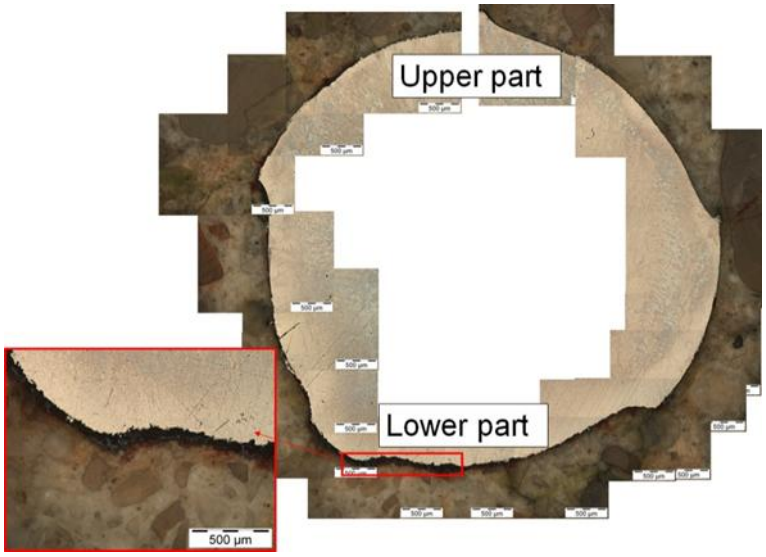

Figure 2-49: Optical microscopy analysis on a specimen subjected to transversal cracking

The same protocol is applied to prepare samples from concrete slabs for the surface analysis. At each maturity date, a sample is cut from the concrete slab as shown in Figure 2-50. Then a prismatic sample of 550 × 100 × 150 mm containing two longitudinal steel rebars and 10 transversal steel rebars is obtained. From this sample, small samples should be cut according to the red lines in Figure 2-51. Then the obtained samples are covered by fluorescent epoxy resin before longitudinal polishing. A photo of a final sample ready to surface analysis is given in Figure 2-52.

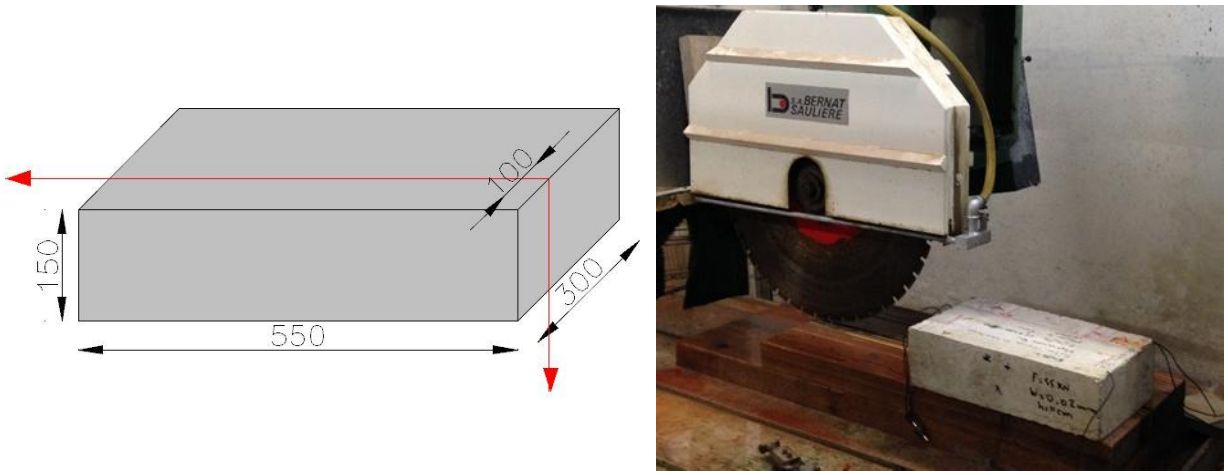

Figure 2-50: Way of cutting a part from concrete slabs

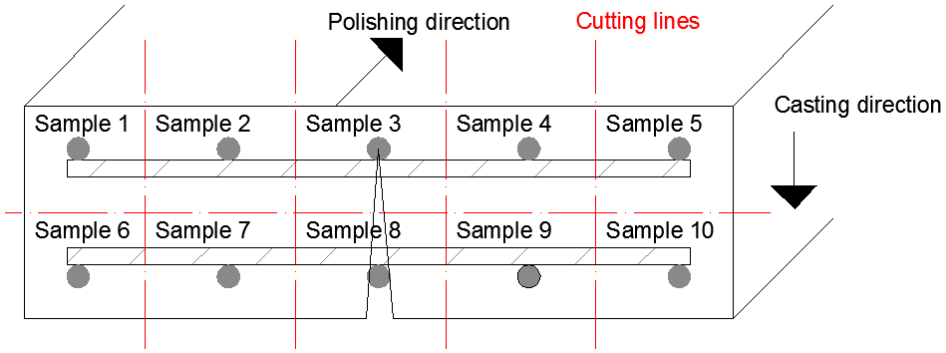

Figure 2-51: Way of cutting samples from the prismatic part cut from the concrete slab (Figure 2-50)

Figure 2-52: sample obtained from a concrete slab

Concerning the millimetric samples, there is no preparation needed before surface analysis.

2.7.2.2 Optical microscopy

Optical microscopy is a method which uses visible light and a system of lenses to magnify images. This analysis allows determining the morphology of the corrosion (general or local corrosion) and the thickness of the corrosion product layer. Results are plotted in a graph representing the evolution of the layer depending on the localization relative to the crack (Figure 2-53).

It is important to note that the thickness of the corrosion products layer measured is submitted to optical microscopy variability. When samples are analyzed, a blurred zone can be observed (Figure 2-54), at the steel mortar interface, corresponding to void (mainly at the bottom part due to top bar effect). The blurred zone is especially visible for the first corrosion analyses date and disappears when corrosion layer is developed. Thus, a first assumption is made by rejecting all blurred area in the measurement of the thickness.
Another assumption is also made and is related to the calamine layer which is created during the rebar manufacturing. The thickness of this layer is determined and is between 10 to 20 µm. During the measurements of the corrosion layer, it is not easy to eliminate the preexisting calamine layer because it cannot be differentiate from the other corrosion products only by the optical microscopy. Consequently, the corrosion thickness measured using the optical microscopy can have a variability around 15 µm. For a corrosion layer measured between 50 µm and 200 µm, an uncertainty from 7.5% to 30% is considered.

Optical microscopy analyses are realized on samples obtained from metric, centimetric samples and on millimetric samples.

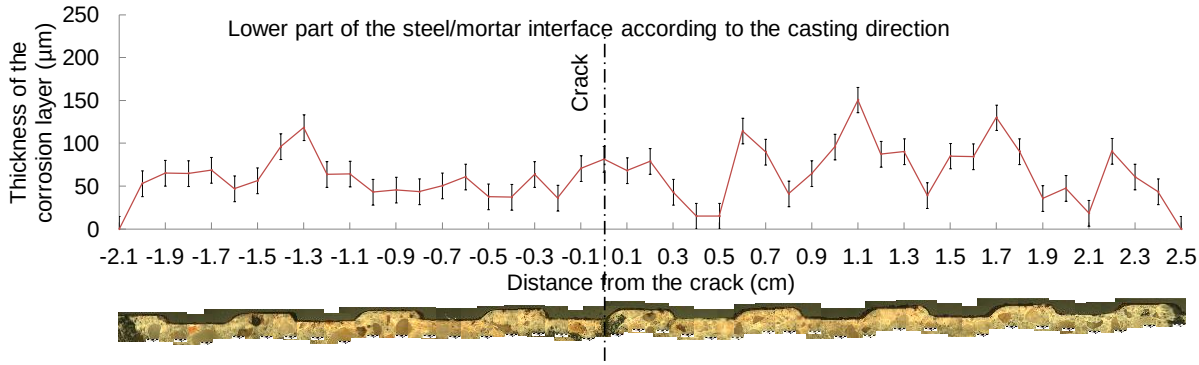

Figure 2-53: Graphic representing the thickness of the corrosion layer depending on the localization along the rebar

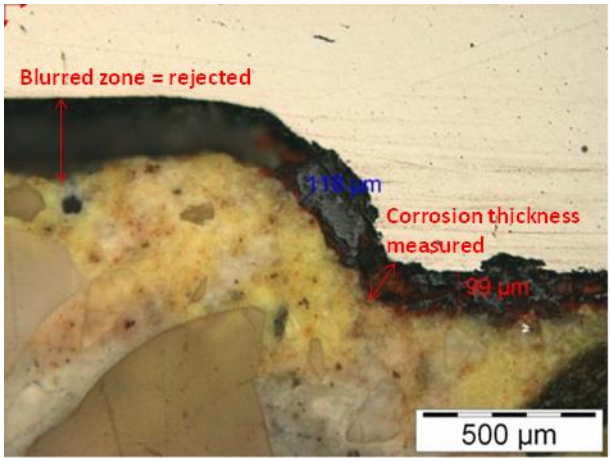

(a) Bottom part of a steel mortar interface (with respect to casting direction) after 1 month of corrosion

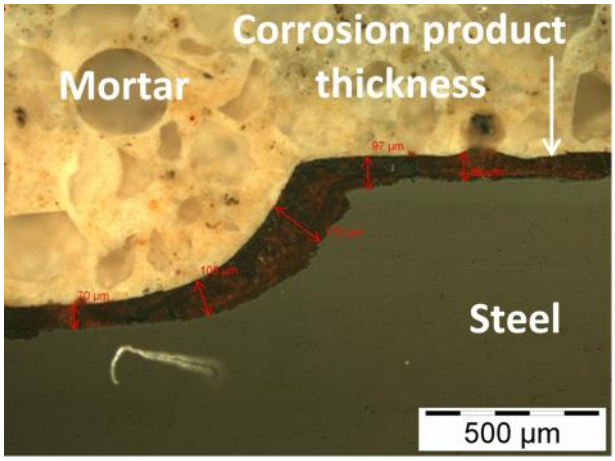

(b) Upper part of a steel mortar interface (with respect to casting direction) after 6 month of corrosion

Figure 2-54 : Thickness of the corrosion layer measured with optical microscopy (Magn: ×10)

2.7.2.3 Raman micro-spectroscopy

Raman micro-spectroscopy is used to identify the corrosion products present at the polished steel/mortar interface. This equipment includes an optical microscope with four objectives (×5, ×10, ×50 and ×100). The microscope allows visualizing the sample and focusing on zones of interest. The sample is illuminated with a thin laser beam that interacts with constituting molecules of the sample. This results in the energy of the laser photons being shifted up or down. The shift in energy gives information about the vibrational modes in the system. The excitation laser power are filtered below 0.6mW in order to avoid thermal effects on sensitive iron oxides and (oxy)hydroxide [185]. The spectral resolution of that setup is $2cm^{-1}$ due to the entire optical path and the detection system. The energy calibration of the spectrometer is performed by means of a silicon crystal. The experiments are realized in this study using the visible wavelength 532 nm.
Finally, the phases are identified by comparison with spectra detected in the literature. Based on [185]–[187]. Table 2-11 gives a list of wavenumber that characterizes different iron oxides and (oxy)hydroxides. In this table, the wavenumbers showing the biggest intensity in each corrosion product type are shown in bold.

Table 2-11: List of wavenumber characterizing iron oxides and (oxy) hydroxides in Raman spectroscopy analysis

Corrosion product type	Wavenumbers
Goethite	247, **301**, **388,** 416, 482, 552, 685, 1003
Lepidocrocite	223, **257,** 284, 310, 355, 380, 532, 657, 1300
Maghemite	350, 512, **670, 710,** 1400
Magnetite	308, 542, **669**
Hematite	**223,** 241, **289,** 404, 494, 604, 1310
Ferrihydrite	370, 510, **710**

Raman analyses are realized on millimetric samples and on samples obtained from centimetric specimens.

In each specimen three zones are inspected: two of them are located far from the crack at the extremities of the corrosion products layer and one zone corresponds to the corrosion products developed deep in the crack as shown in Figure 2-55. In this figure, the number “1” corresponds to the zones located far from the crack while the zone intercepting the crack is called by the number “2”. This designation is applicable for the entire Raman micro-spectroscopy analyses performed in this project.

In order to compare the effect of different corrosion conditions on the corrosion products type, it has been chosen to perform Raman micro-spectroscopy analyses only on the upper part of the steel/mortar interface of specimens. A comparison between the corrosion products type developed along the upper part of the steel/mortar interface and its lower part is performed on one specimen corroded in the reference protocol.

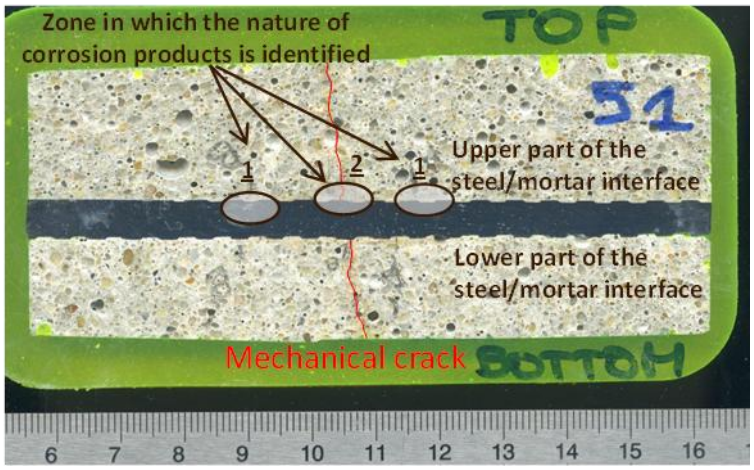

Figure 2-55 : Zones of corrosion in which the nature of the corrosion products is determined using Raman micro-spectroscopy

A schematic representation is performed for each analyzed specimen to summarize the identified corrosion products in the zone “1” and the zone “2”. A template of this schematic representation is given in (Figure 2-56). In this figure, “a” is the distance between the zone “1” and the zone “2” and “e” is the average thickness of the corrosion products layer developed along the analyzed interface.

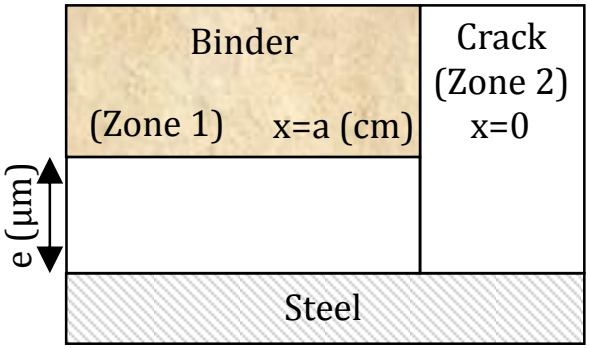

Figure 2-56 : Template for the schematic representation used to summarize the identified corrosion products

2.7.3 Electrochemical analysis (Free corrosion potential evolution)

To study the depassivation and the eventual repassivation of steel close to the cracks during the experiment, an embedded Manganese Dioxide reference electrode (ERE 20) for potential reading is cast into the mortar cover of some specimens and it is positioned at 50 mm from the crack (Figure 2-57 (a)). In this configuration, the reference electrode measures a coupled corrosion potential (between active and passive parts of steel bar) which is continuously registered using a data acquisition switch unit.
These measurements are used to check whether the free corrosion potential tends to stabilize or increase after corrosion initiation. The interpretation of this variation in the free corrosion potential could be due to a repassivation induced by the creation of a corrosion products that seal the crack. If the natural potential continues decreasing that means that repassivation of the rebar does not occur.

Corrosion potential measurements are performed on specimens having three residual crack openings (Figure 2-57 (a)) (100; 300; 500 µm) with vertical (Figure 2-37) and horizontal crack orientation (Figure 2-38) with respect to rain. They are also realized on specimens not directly exposed to rain (Figure 2-57 (b)). These specimens are corroded with the reference protocol. Measurements are also performed on specimens having three residual crack openings oriented vertically with respect to rain in the protocol developed to be representative of the 90˚ and 270˚ cooling tower sides (3 minutes rain).

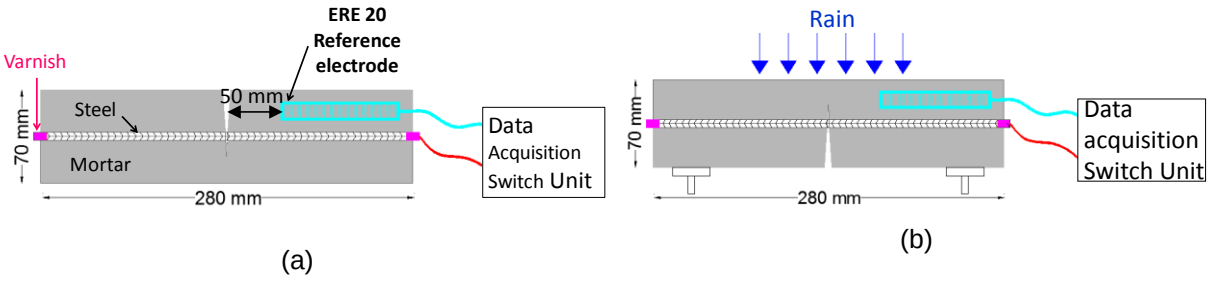

Figure 2-57: Electrochemical measurement

2.8 SUMMARY OF THE EXPERIMENTAL PROGRAM

The realization of the above experiments requires approximately 270 specimens of 70 × 70 × 280 mm in addition to the seven concrete slabs, two specimens of 40 × 40 × 160 mm and 3 ring shape mortar specimens. The experimental program is summarized in Table 2-12 keeping in view the parameters that are studied during this project and the corrosion analyses methods.

Table 2-12: Summary of the experimental program

Conditions	Specimens characteristics	Crack opening (mm)	Crack orientation	Number of specimens	Time period for corrosion analyses	Method of analyses
Crack opening	70×70×280 mm (CEM I mortar)	0.1 0.3 0.5	Vertical	60	0, 1.5, 3, 6, 12 months	1) Gravimetric measurements 2) optical microscopy 3) Raman spectroscopy 4) Free corrosion potential
Crack orientation			Horizontal	48	1.5, 3, 6, 12 months	
Raining/drying cycles duration			Vertical	18	1.5, 3, 6, 12 months	
Relative humidity				15	3, 6, 12 months	
Raining/drying cycles number (early age corrosion)	40×40×160 mm (CEM I mortar)	0.1		2	For a total duration of two months	1) Raman micro-spectroscopy
Temperature	70×70×280 mm (CEM I mortar)	0.1 0.3	Vertical	30	1.5, 3, 6, 12 months	1) Gravimetric measurements 2) optical microscopy 3) Raman spectroscopy
Natural conditions (Saclay environment)		0.3		12	3, 6, 12 months	
Cementitious material composition	70×70×280 mm (CEM I + slag) mortar	0.3	Vertical	15	0, 3, 6, 12 months	
	70×70×280 mm (CEM I concrete)			15		
Dimension of the specimens	550×300×150 mm (CEM I concrete)	0.1	Vertical	7	0, 3, 6 months	Optical microscopy
Effect of the CO_2 concentration and carbonation duration	70×70×280 mm + ring shaped (CEM I mortar)	0.1 0.3 0.5		42 + 3	3, 7, 15, 21, 30, 49, 61, 89 days of carbonation	Phenolphthalein pH indicator test

CHAPTER 3. CRACKS CHARACTERISTICS

3.1 INTRODUCTION

This chapter presents the experimental results of the crack opening obtained on 145 specimens and then compares them to a numerical analysis performed using the finite element code, CAST3M, developed by the CEA. Moreover, a suitable experimental protocol allowing quantification of the load-induced damage length along the steel / mortar interface is defined and results are compared with the numerical ones.

3.2 CRACK OPENINGS

3.2.1 Determination of the maximal crack opening experimentally and numerically

The three points bending test enables obtaining cracks located in the midspan of the prismatic specimen (70 × 70 × 280 mm). The crack width is controllable and monitored by loading/unloading cycles as illustrated in Figure 3-1. Figure 3-1(a) shows the curve obtained experimentally while Figure 3-1(b) shows the numerical curve. The numerical curve is representative to the experimental one despite that the numerical model is not able to present the same hysteretic behavior visible in the experimental curve.

Figure 3-2 shows the loading force over the cracking force with respect to the residual crack opening. The cracking force is the load at which the crack appears while the loading force corresponds to the maximum load applied at the cycle that gives the desired residual crack opening (Figure 3-1 (a)). After testing 145 specimens, it is visible that the residual crack openings have a tendency to increase with the reload ratio despite an important scatter as shown in Figure 3-2. This observed scatter can be due to a possible difference in the specimens properties that were prepared from 12 different batches. Moreover, this scatter may also be partly attributed to some variability in the rebar position (± 1 mm from one specimen to another one). Additionally, the loading is applied manually during the three point bending test. This fact may also participate in the observed scatter.
Nevertheless, the scatter observed on the residual crack opening remains limited. Therefore, obtaining a specific residual crack opening is possible using this loading protocol.
On the other hand, numerical results also follow the same trend as experimental one which allows validating the numerical model.

Figure 3-3 illustrates the crack pattern on two sides of a cracked specimen. It can be noted that the maximum residual crack opening value is uniform on the side subjected to the maximum tensile stress. Moreover, on the vertical side it can be seen that the residual crack opening values decreases from sections subjected to maximum tensile stress to sections subjected to lower tensile stress value.

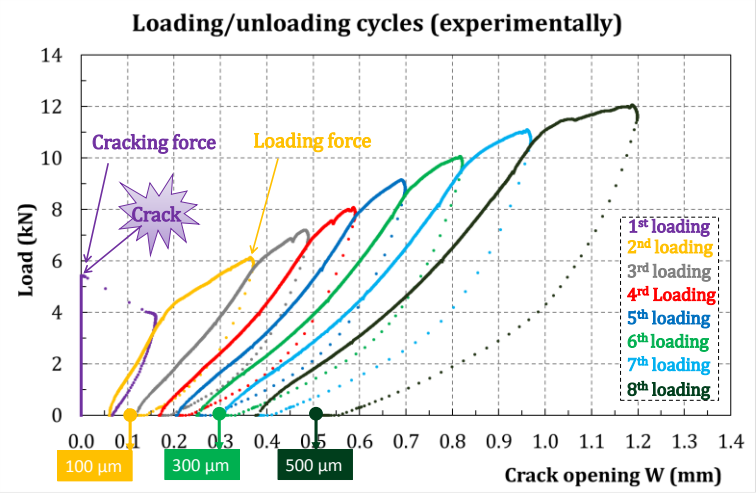

(a)

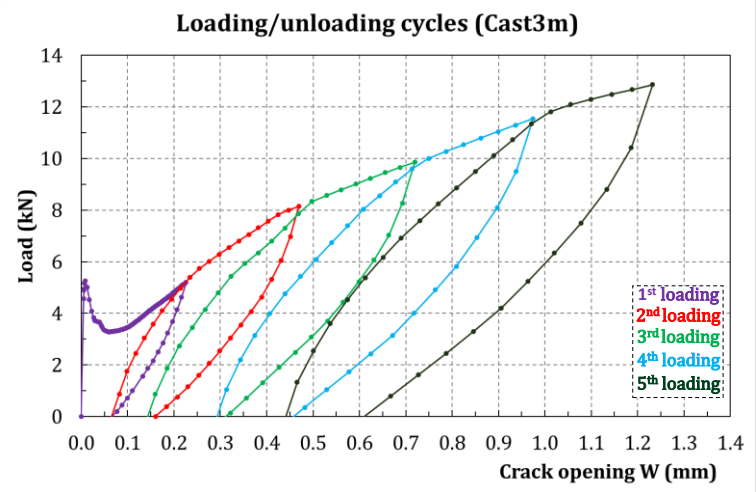

(b)

Figure 3-1: Experimental (a) and numerical (b) range of the residual crack opening obtained by the three point bending test

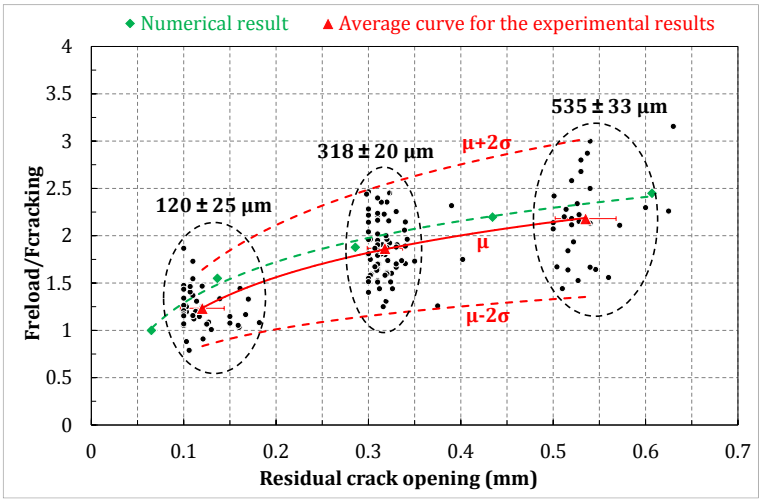

Figure 3-2 : Experimental (145 specimens) and numerical results showing loading ratio versus residual crack openings

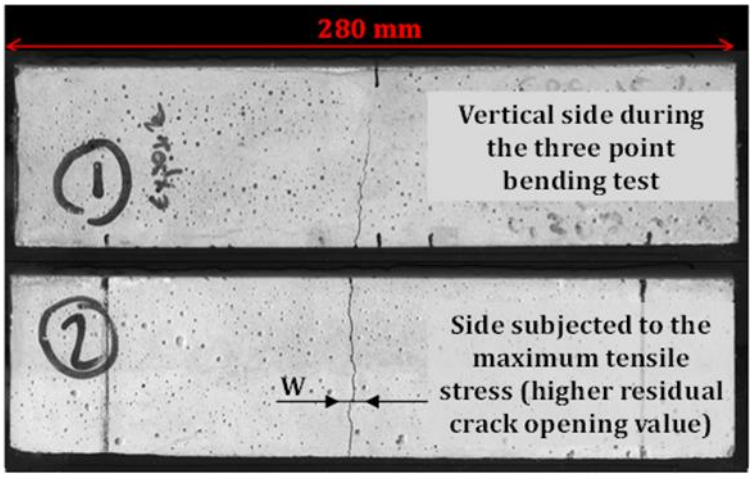

Figure 3-3: Illustration of a cracked specimen

3.2.2 Crack opening profile over the entire height of the specimen

Figure 3-4 presents the evolution of the residual crack openings on the entire height of two prismatic specimens (70 × 70 × 280 mm) with respect to loading steps. The value of the crack openings are obtained basing on the displacements measured by DIC images treatment using CMV code (see §2.5.3 for more details). Similarly to the LVDT measurements, an increase in the crack width with respect to loading is notable over the entire height of the specimen. The evolution of the crack width with the loading is not similar between both specimens. This is in agreement with the variability detected in Figure 3-2. Moreover, it is plain to see that once the crack appears, it spreads over 90% of the specimen height with a bigger crack width in the region subjected to the higher tensile stress. The crack opening on the outer surface of the specimen at the steel rebar position (3.5 cm height) has an average value of 44% ± 5% of the biggest crack width measured on the lower part of the specimen (around 0.5 cm height) as shown in Figure 3-5.

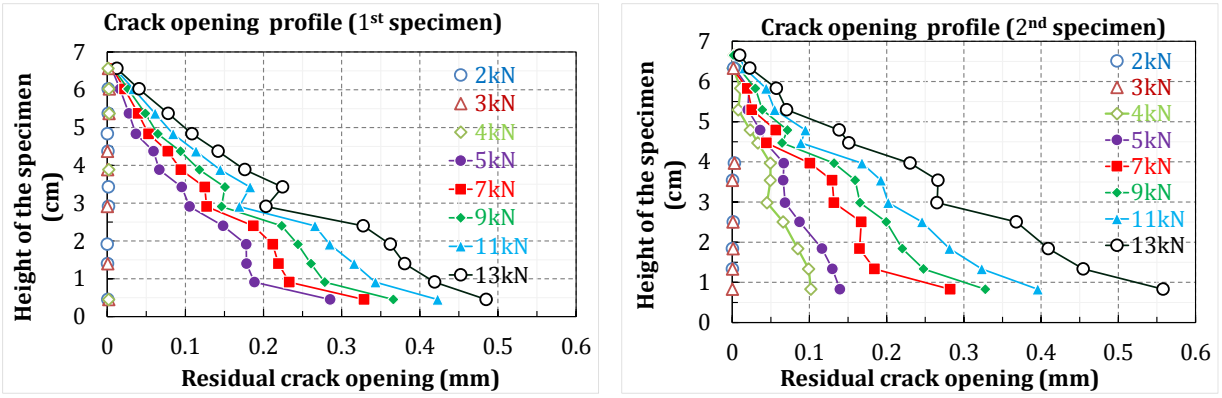

Figure 3-4: Crack opening profile over the entire height of two specimens

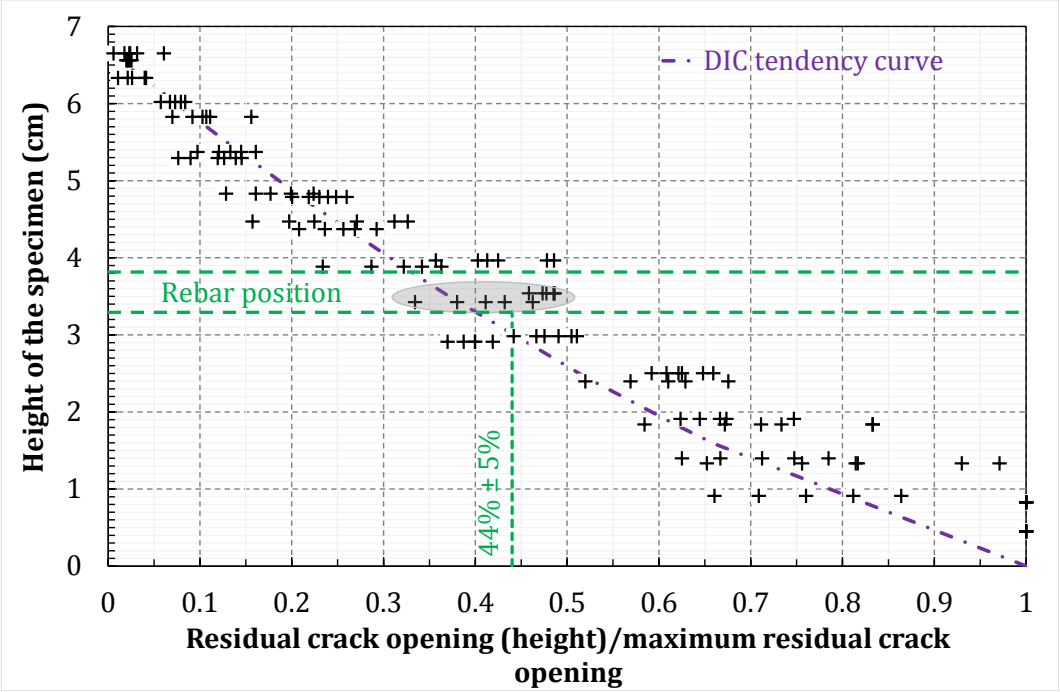

Figure 3-5 : Evolution of the crack opening on the entire height of the specimen with respect to the maximum crack opening

3.2.3 3D aspect of the crack

Figure 3-6 shows a visualization of the cracked specimen tested using the x-ray CT (see §2.5.3 for more details) and defines the axes orientation that is used in the following graphs.

A 3D visualization of the crack is given in Figure 3-7. This separation of cementitious materials from the crack and the rebar is performed by thresholding the grey level distribution. In this figure, some big pores are also visible because they have the same grey level as the crack.

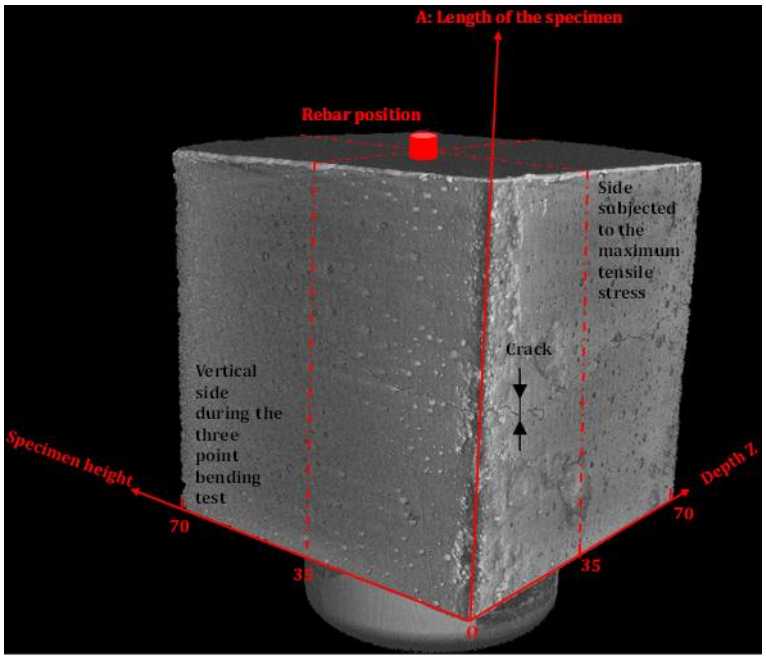

Figure 3-6 : CT - 3D visualization of a cracked prismatic mortar specimen

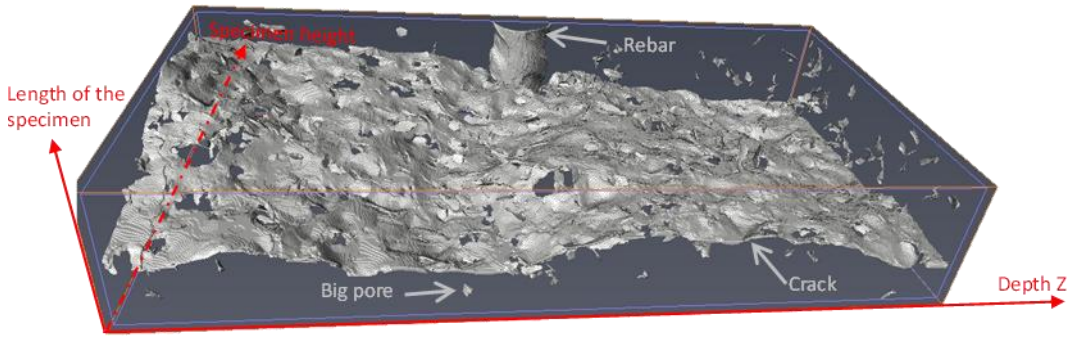

Figure 3-7 : CT-3D visualization of the crack in a prismatic specimen

The evolution of the residual crack width in the specimens is given in Figure 3-8. The evolution of the residual crack width with respect to the maximal residual crack width value is shown in Figure 3-9. It can be noted that the crack opening decreases with the specimen height but at a given specimen height, the crack opening values seems to be close to each other even at the rebar position level.

In addition the DIC tendency curve shown in Figure 3-5 is drawn in Figure 3-9. It can be seen that this tendency curve describes very well the crack evolution on the entire height of the specimen independently from the depth. Therefore, it can be deduced that surface measurements of the crack width can be sufficient to deduce its value inside the specimen especially near the rebar.

For specimen showing 100 µm residual crack opening, the crack openings at the rebar position (specimen height = 30 mm approximately) range between 0.25 and 0.4 of the maximum residual crack opening with an average of 0.3 ± 0.06. While the average residual crack opening at the rebar position for specimens showing 300 and 500 µm residual crack opening is 0.36 ± 0.11 and 0.37 ± 0.02 respectively. No difference can be noted between the three residual crack openings and thus the residual crack opening at rebar position is 35 ± 7% of the maximum residual crack opening. This value is in agreement with the one obtained from the DIC test (44%±5%) and not far from the one that could be obtained by

applying Thales theorem (43%). Therefore, the crack width values near the rebar corresponding to the maximum residual crack width of 100, 300 and 500 µm measured by the LVDT range around 35, 105 and 175 µm respectively.

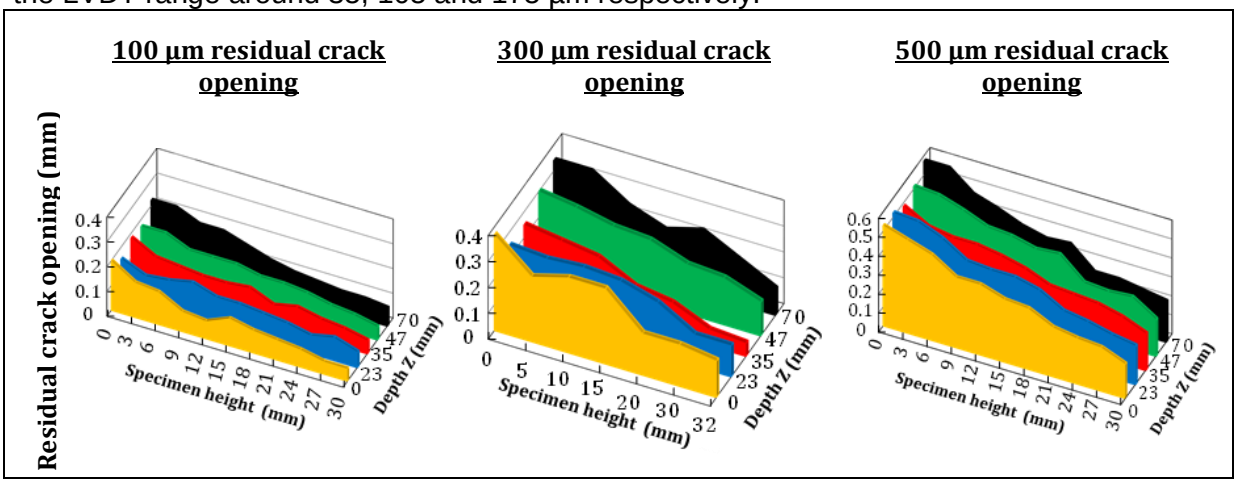

Figure 3-8: Evolution of the residual crack opening on the height of the specimen at different depths

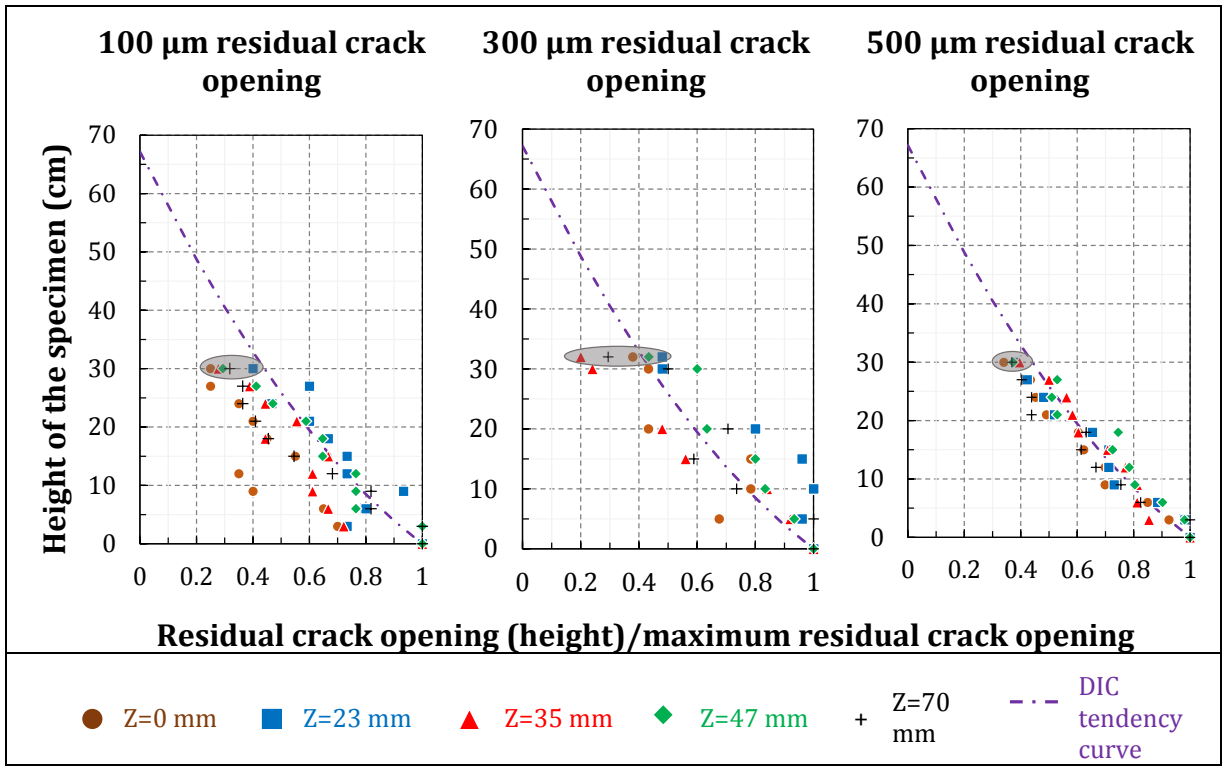

Figure 3-9 : Evolution of the crack opening on the entire height of the specimen with respect to the maximum crack opening at different depths

3.3 STEEL/MORTAR INTERFACE DAMAGE

3.3.1 Determination of the suitable accelerated carbonation protocol

3.3.1.1 Carbon dioxide concentration

Figure 3-10 shows the carbonation depth measured according to the European standard [180] on prismatic specimens (70 × 70 × 280 mm) carbonated for different durations at two carbon dioxide concentrations (50% CO_2 and 3% CO_2). The carbonation rate measured on the outer surface of the specimen carbonated at 50% CO_2 is 2.45 times the rate measured on specimens carbonated at 3% CO_2 (Figure 3-10). To validate the experimental results, the carbonation depths measured at 50% CO_2 in this study are compared with the one measured in the study of Hyvert [10]. In fact, Hyvert results [10] are chosen because they were measured in similar conditions to this study (50% CO_2, same mortar composition). According to Figure 3-11, carbonation depths obtained in these two studies follow the same trend.

On the other hand, the carbonated length along the steel mortar interface is also measured on the same specimen and is given in Figure 3-12. In fact, the carbonation rate of the steel/mortar interface intercepting a mechanical crack in specimens carbonated at 50% CO_2 is 4.75 times higher than the rate measured in specimens carbonated at 3% CO_2 (Figure 3-12).

Therefore, it is evident that the ratio between the carbonation rates measured along the steel/mortar interface carbonated at 50%CO_2 and 3% CO_2 is approximately two times higher than the carbonation ratio obtained on the outer surface of the specimen (4.75 / 2.45).

The difference noticed between the ratio of carbonation rates measured at the surface and that measured at the steel/mortar interface for the two carbon dioxide concentrations tested lead the author to deduce that 50% CO_2 may not be suitable for the measurements of the load/induced damage length. This high carbon dioxide concentration induces a high carbonation shrinkage which allows the CO_2 to spread for a greater length than the damaged one. This hypothesis is in agreement with the study of Castellote et al. [14], [43], [55].
As a conclusion, to determine the length of the load/induced damage zone by the mean of carbonation, cracked specimens should be carbonated at low carbon dioxide concentration (3% CO_2 for example) and not at 50% CO_2 which is conventionally used for this kind of measurement in France ([83], [172], [180]).

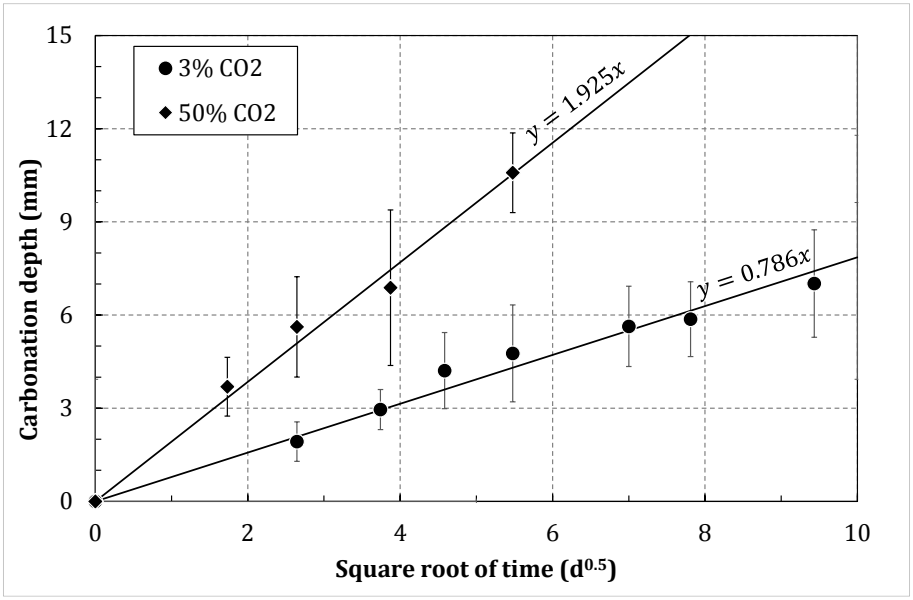

Figure 3-10: Carbonation depth with respect to square root of time for two carbon dioxide concentrations (3% CO_2; 50% CO_2)

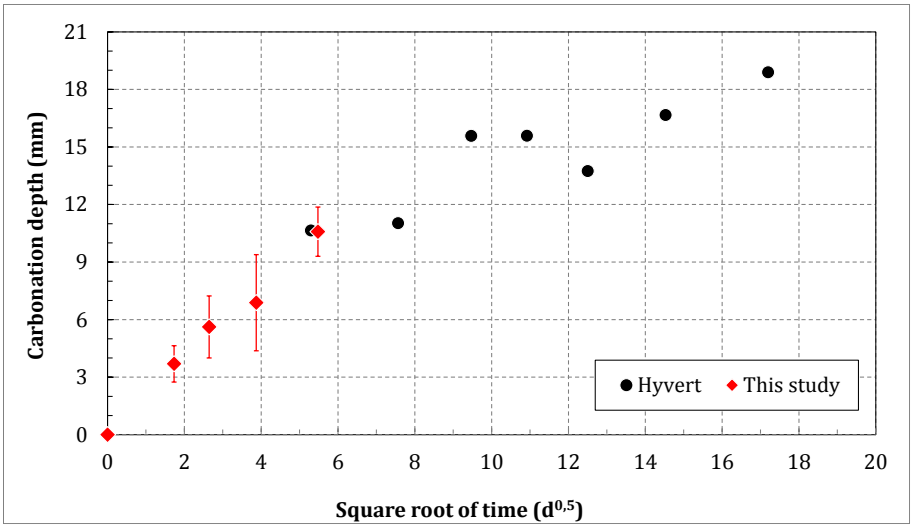

Figure 3-11: Comparison of the carbonation rate calculated at 50%CO_2 in this study with those found in the study of Hyvert [10]

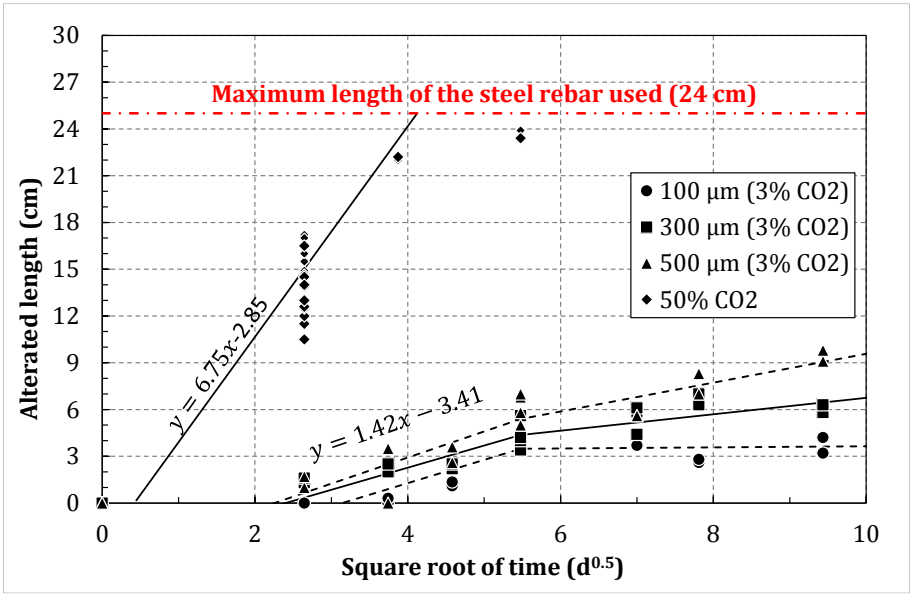

Figure 3-12: Carbonation length along the steel/mortar interface with respect to square root of time for two carbon dioxide concentrations (3% CO_2; 50% CO_2)

3.3.1.2 Carbonation duration

According to Figure 3-13, a shift in the carbonation rate of the steel/mortar interface intercepting a crack is visible after 30 days of carbonation at (3% CO_2 concentration, 55% RH and 25°C). Therefore, two regimes of carbonation can be detected. The first one occurs during the first 30 days of carbonation and thereafter a second carbonation regime takes place.

The following mechanism can be proposed: during the first carbonation regime, carbon dioxide fills the microcracks induced mechanically along the steel/mortar interface from either side of the crack and may diffuse a little further than this damaged area. While during the second carbonation regime showing a lower carbonation kinetics than the first one, diffusion plays the major role in the carbonation propagation along the steel/mortar interface. It can be noted that the carbonation kinetics during this second carbonation regime increases with the increase in the residual crack opening.

Consequently, 30 days of carbonation at (3% CO_2, 55% RH and 25°C temperature) is sufficient to estimate the length of the load-induced damage along the steel/mortar interface.

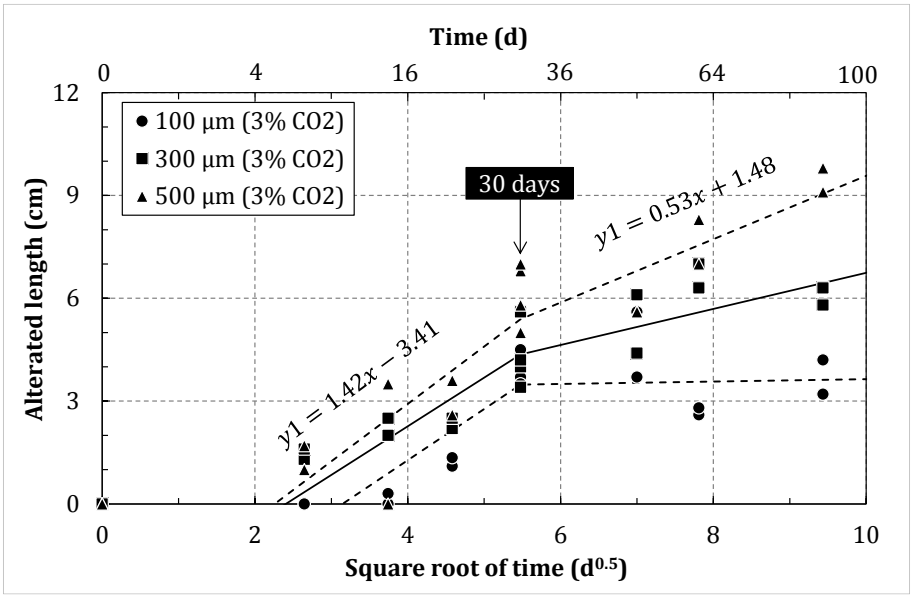

Figure 3-13: Carbonation length along the steel/mortar interface with respect to square root of time for three residual crack openings (100; 300; 500 µm)

3.3.2 Validation of the proposed accelerated carbonation protocol

The carbon dioxide concentration recommended in France [180] (50% CO_2) may induce a carbonation shrinkage that may lead to progressive damage along the steel/mortar interface allowing the carbon dioxide to spread further than the mechanically damaged zone. This result may explain the total carbonation of the steel/mortar interface detected after exposing cracked ring shape mortar specimens to 50% CO2, 65% RH and 23°C temperature for 7 days in the study of Dang et al. [173] (Figure 3-15). However, cracks are close to each other in the case of ring shape mortar specimens and therefore an overlay of damaged zone may also occur and induce a spread of the CO_2 along the total steel/mortar interface.

To validate whether the proposed carbonation protocol (3% CO_2, 30 days) remains applicable in this configuration, it was tested on ring shape mortar specimens fabricated similarly to those performed in the study [173]. Figure 3-14 (a) shows that the carbonated steel/mortar interface remains limited from either side of the crack and does not spread along the total steel/mortar interface despite that this specimen shows five cracks (numbered in Figure 3-15 (a)) having different crack width given in Figure 3-14(b). One can recognize that the color change of the phenolphthalein solution is not the same on the outer surface of the specimen and on its core. This is directly linked to the way used to split the specimen in two parts. In fact a notch is realized under water using a diamond saw thus the lower pH of water alter the pore solution pH in this zone and induce this variation.

The determination of the length of the load-induced damaged zone using carbonation can be realized by exposing cracked specimens at 3% CO_2, 25°C temperature and 55% relative humidity for 30 days.

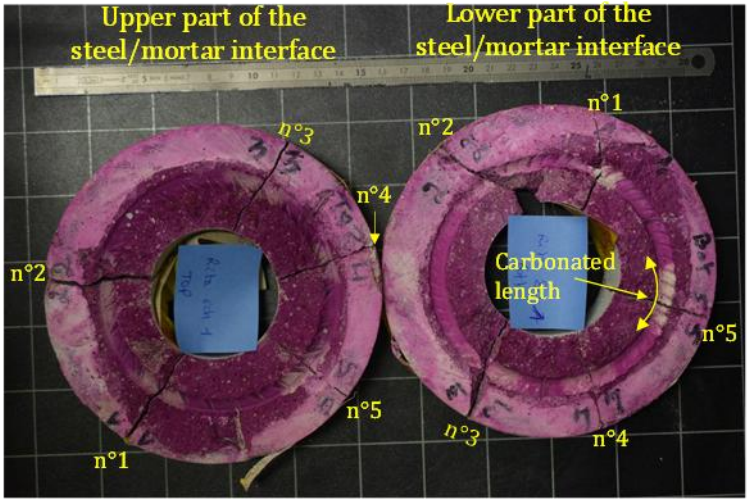

(a)

Crack number	Crack opening on the upper part of the steel/mortar interface (µm)	Crack opening on the lower part of the steel/mortar interface (µm)
1	57.5	57.5
2	70.3	74.5
3	74.5	80.2
4	30.9	30.9
5	114.0	150.0

(b)

Figure 3-14 : (a) Phenolphthalein test on a ring shape mortar specimen carbonated at 3% CO_2 for 30 days; (b) Crack openings value measured on the upper and the lower surfaces of this specimen

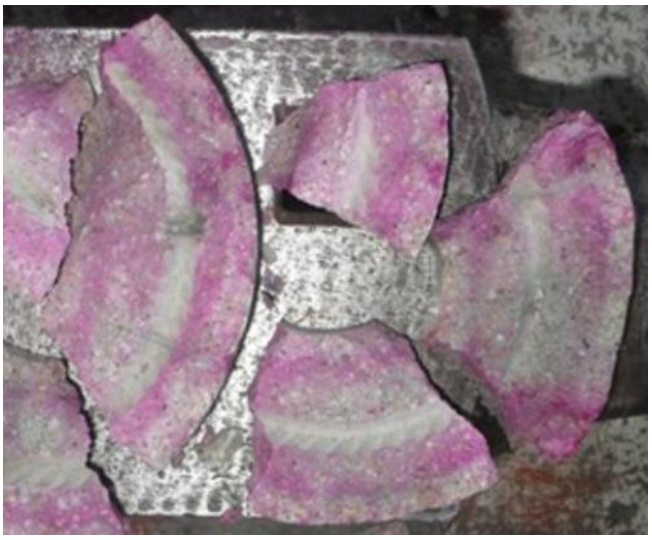

Figure 3-15: Phenolphtalein pH test on a ring shape mortar specimen carbonated at 50% CO_2 for 7 days [173]

3.3.3 Quantification of the load-induced steel/mortar interface damage

3.3.3.1 Experimental and numerical values

Figure 3-16 shows the length of carbonated steel/mortar interface measured on 79 prismatic specimens (70 × 70 × 280 mm) with respect to the residual crack openings after 30 days of accelerated carbonation at (3% CO_2, 55% RH and 25°C). An increase in the carbonation length is notable with the increase in the residual crack opening. However, it is evident that the carbonation length remains limited to several centimeters from either side of the crack.

In Figure 3-17 (a), the numerical results show a total damage of the steel mortar interface for value of the residual crack opening greater than 0.1 mm. This could be due to the fact that too small plastic deformations could not physically correspond to significant damage at the steel mortar interface. Therefore, a physical threshold for the plastic slip between the steel and the mortar surrounding the steel could be found. This is performed based on the experimental results. In fact, a series of computations are done with different values for the plastic slip threshold (arbitrary chosen: 0.17; 0.28; 0.38; 0.52 mm) and the results are shown in Figure 3-17 (b). Comparing these results with the one obtained experimentally (Figure 3-16) allows to determine that the suitable threshold is 0.28 mm. It should be important to indicate that the numerical length of the damaged steel/mortar interface does not have the same trend of the experimental one. It is also important to highlight that applying a threshold for the plastic slip is a simplified empirical approach of a crack initiation criterion. The model should be improved: first, by a better calibration of the plastic model parameters, based on pull-out test results; second, by using a more refined mechanical model to describe the steel/mortar interface behavior.

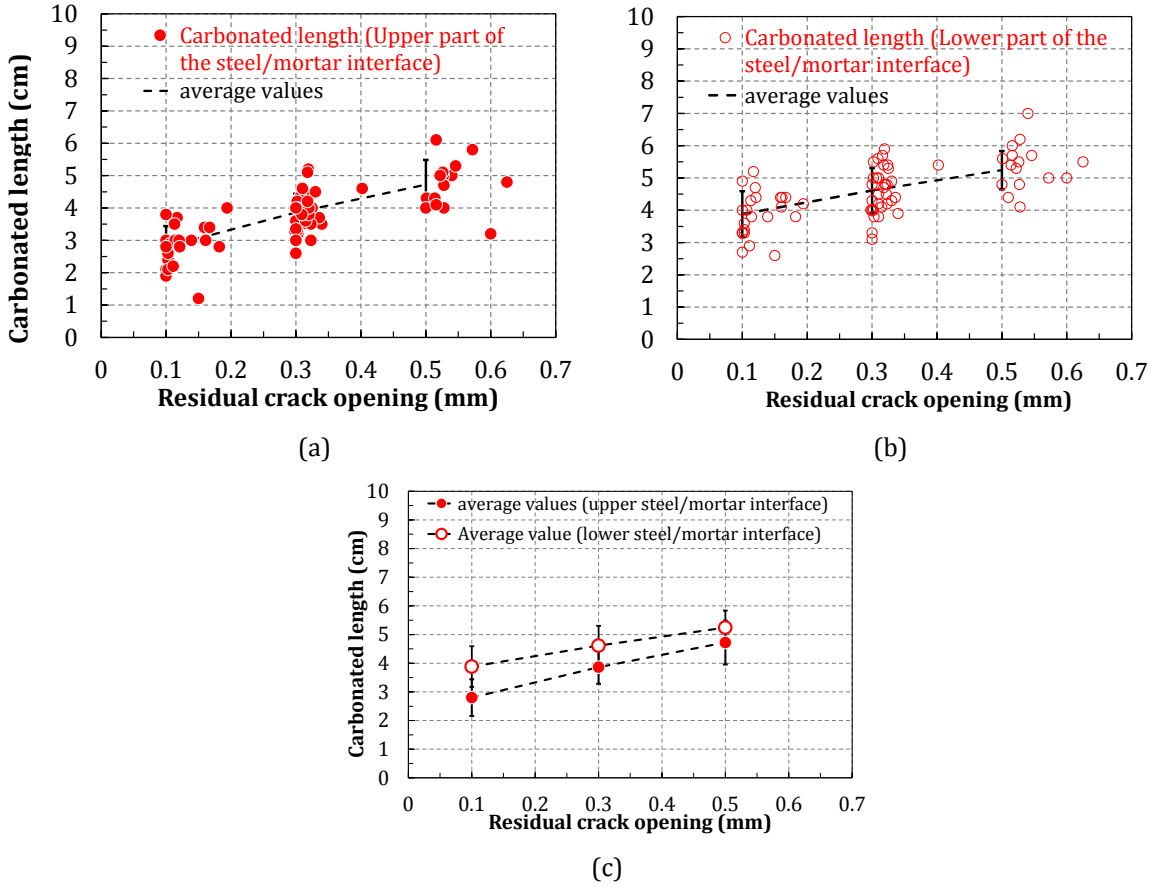

Figure 3-16: Experimental (79 samples) carbonated length of steel/mortar interface

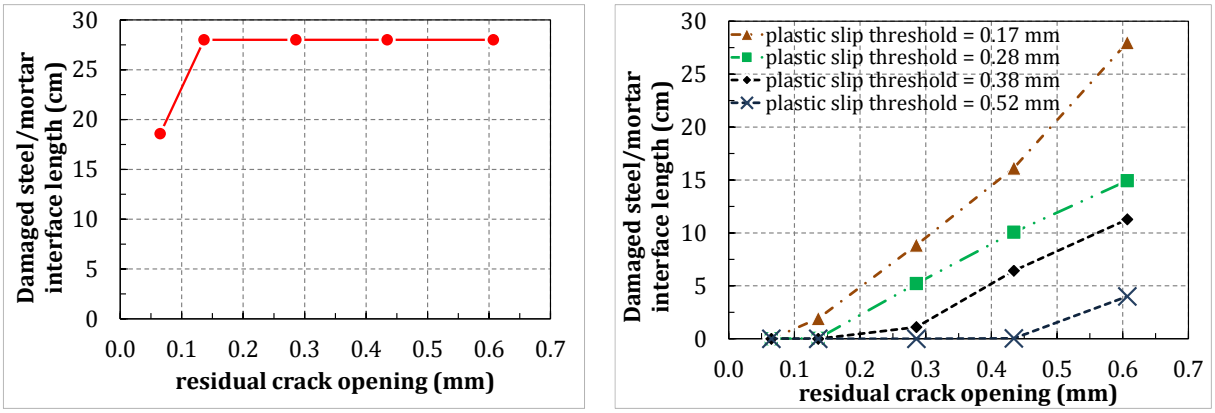

(a) (b)

Figure 3-17 : Numerical length of damaged steel/mortar interface with respect to residual crack opening: (a) without a threshold on the plastic deformation; (b) with a threshold on the plastic deformation

3.3.3.2 Effect of the steel/mortar quality on the carbonation propagation

Figure 3-16 (c) shows also that for the same residual crack opening the carbonation length along the steel/mortar interface is higher on the bottom side than on the upper side despite that they are both exposed to the same mechanical loading during the three point bending test. Moreover, Figure 3-18 shows the difference noted between the carbonation length measured on the upper and the lower part of the steel/mortar interface with respect to square root of carbonation duration for three residual crack openings (100, 300 and 500 µm). An average ratio between these carbonation lengths is also given in Figure 3-18. Additionally, Figure 3-19 shows the spread of carbon dioxide along the steel/mortar interface intercepting artificial holes and cracks. It can be noticed that the carbon dioxide spread for a greater length on the lower part of the steel/mortar interface than on the upper part. Moreover, it can be visible that once the carbon dioxide reaches the rebar on one side, it is able to access to the circumference of the reinforcement.

Two causes may explain this notable difference. In fact, the casting direction leads to a poorer quality in the lower part of the steel/mortar interface than on the upper part. Indeed, the porosity of the lower steel/mortar interface is higher than that on the upper steel mortar interface [113]. Moreover, Horne et al. [113] shows in the same study that the Portlandite exists in lower amount on the bottom part of the steel/mortar interface comparing with its upper side. All these factors allow carbon dioxide to spread for a greater length on the bottom side of the steel/mortar interface with respect to the upper side.

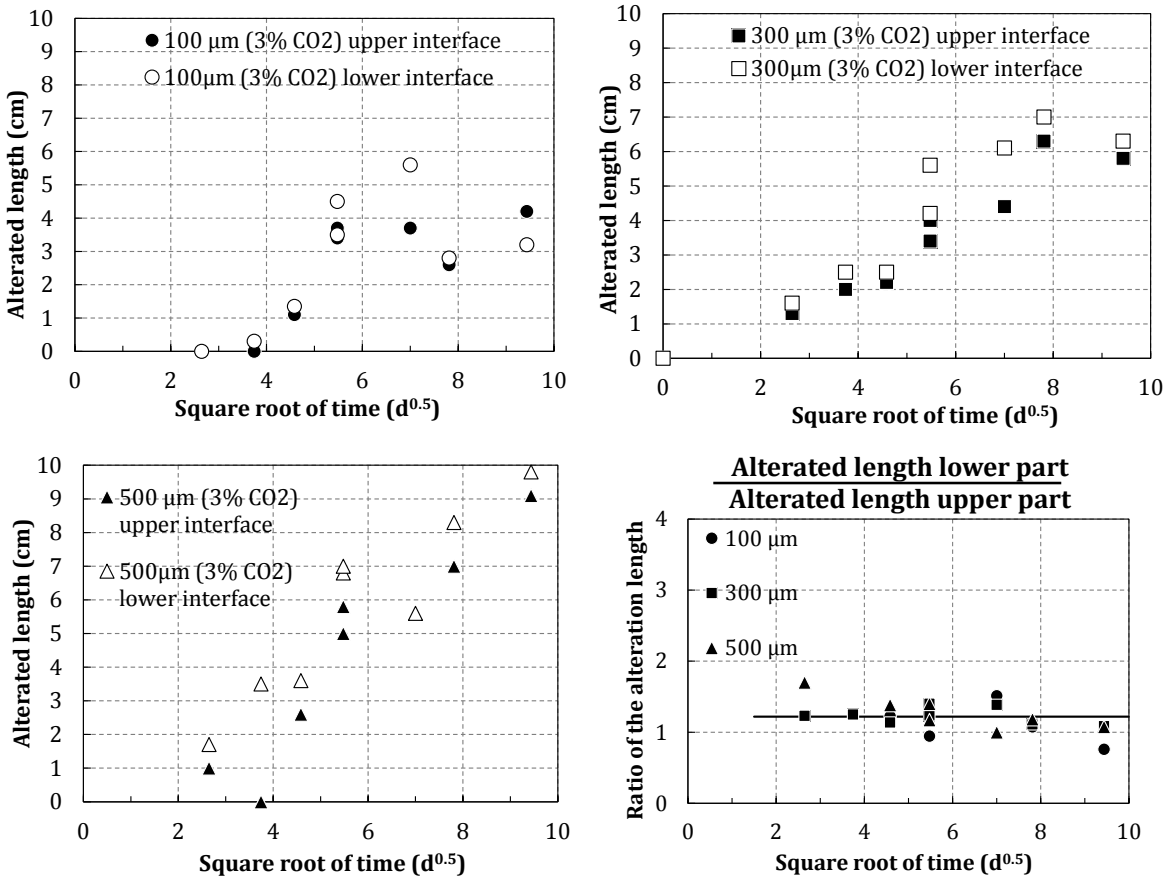

Figure 3-18: Comparison of the carbonated length between the upper and the lower part of the steel/mortar interface

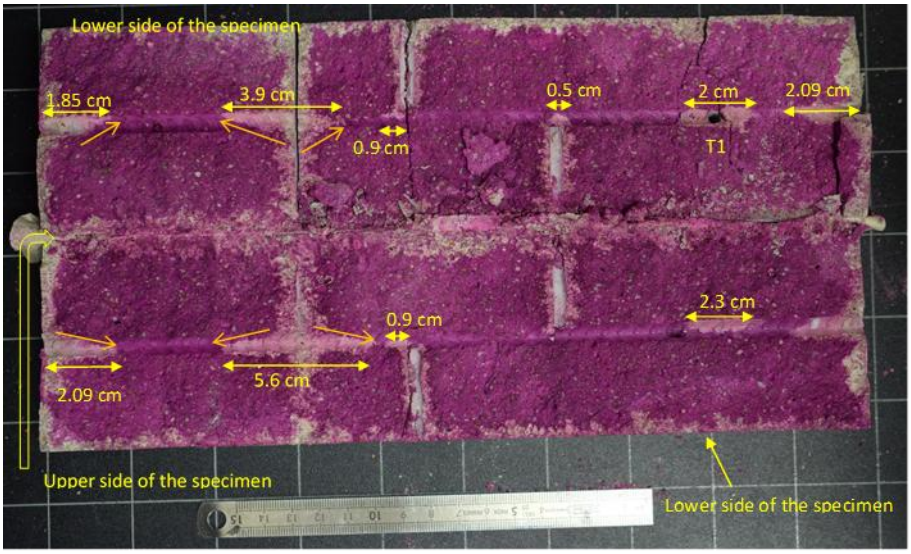

Figure 3-19: Spread of the carbon dioxide along the upper and the lower part of steel/mortar interface from either side of artificial crack and holes

3.4 SUMMARY

The results indicate that there is a correlation between load/unload cycles performed on prismatic specimens during the three point bending test and the residual crack opening. The correlation found numerically catch well the experimental results. The crack opening shows the higher value in the zone subjected to maximum tensile stress and decreases with the decrease in the tensile stress. Furthermore, the crack opening is (35 ± 7 %) smaller near the rebar comparing with the maximal residual crack opening value.
On the other hand, an experimental protocol allowing the estimation of the load-induced damage zone is improved. It consists on carbonating cracked specimens for 30 days at 3% CO_2, 55% RH and 25°C temperature instead of 50% CO_2. In fact, the high carbon dioxide concentration may induce carbonation shrinkage along the steel/mortar interface and thus overestimate the length of the damaged zone.
Using this protocol, the damaged steel / mortar interface observed after the three-point bending test, is quantified experimentally and is shown to be limited around the mechanical crack. In addition, it was shown that the casting direction promotes the carbonation at the lower part of steel bars. Modelling of the size of the damaged zone at steel-concrete interface by FEM approach need to be improved in the future.

CHAPTER 4. EFFECT OF CRACK WIDTH ON THE CORROSION DEVELOPMENT

4.1 INTRODUCTION

This chapter aims to study the effect of crack opening value on the carbonation-induced corrosion development. First of all, the distribution of the corrosion products layer with respect to crack openings is presented. Thereafter, the iron mass loss, the corrosion kinetics and the free corrosion potential measurements are exposed. Furthermore, the corrosion products type are analyzed. Finally, the results are discussed and conclusion is drawn.

4.2 DISTRIBUTION OF THE CORROSION PRODUCTS LAYER

4.2.1 Length of corrosion products layer

Evolutions of the corrosion length on the upper and the lower part of the steel/mortar interface[2] with respect to the number of raining/drying cycles are presented in Figure 4-1(a, b, c) for specimens showing 100, 300 and 500 µm residual crack openings respectively. One can see that corrosion in specimens subjected to the same corrosion conditions for the same exposure duration is heterogeneous. Therefore, a certain variability on the corrosion results exits in this study and should not be neglected during the results interpretations.
Furthermore, in the same figures, it is visible that whatever the crack width, corrosion length seems to be similar on the upper and the lower interface. This is not only observed for this specific corrosion condition but also for all the exposures conditions tested in this project (Appendix I). As a consequence, these two corrosion lengths will not be distinguished again in this study and the term corrosion length is used in this entire document to indicate the average value of these two corrosion lengths and is also used for the corrosion kinetics calculation detailed in (§ 2.7.1.3).

Therefore, Figure 4-2 is the template chosen to be used for the forthcoming similar figures. It shows the evolution of the average corrosion length measured on three replicates corroded similarly for the same duration with respect to the number of raining/drying cycles. In this figure, it is visible that the corrosion length increases with the residual crack opening and trend to stabilize after 30-60 raining/drying cycles. This observation corresponds to the one found in the study of Tremper [81] stating an increase in the size of the corroded area with an increase in the crack width.

In fact, it is proven in Figure 3-16 that the length of the carbonated steel/mortar interface increases with the residual crack opening. On the other hand, the length of the de-passivated steel is directly linked to the carbonated length. Consequently, the difference in the measured carbonation length could justify the difference in the corrosion length measured for different crack openings.

In these figures, cracks are oriented vertically with respect to rain, the same trend in the corrosion length is visible for cracks oriented horizontally with respect to rain (Appendix I.3).

[2] The upper and the lower part of the steel/mortar interface are defined accordingly to the casting direction.

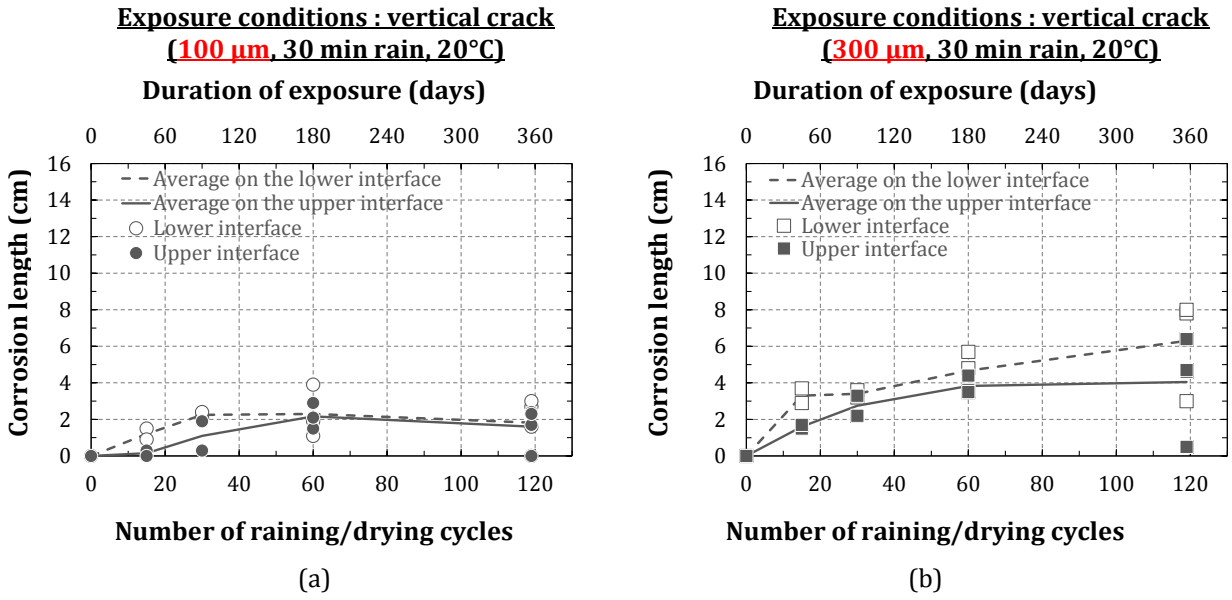

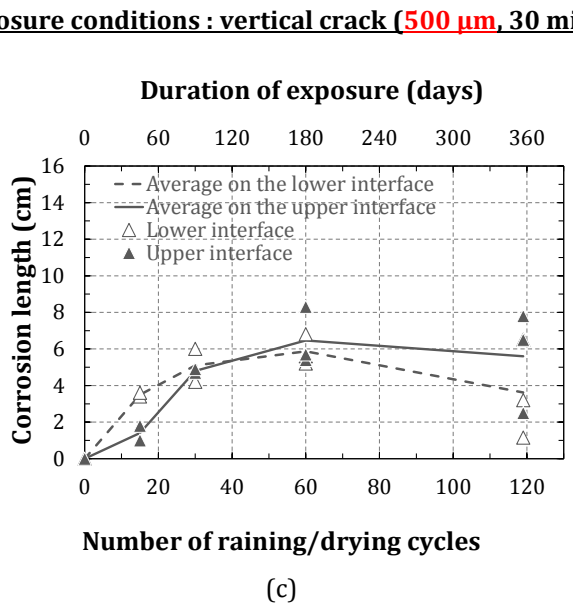

Figure 4-1 : Corrosion length along the upper and the lower steel/mortar interfaces measured during the visual inspection (naked eye)

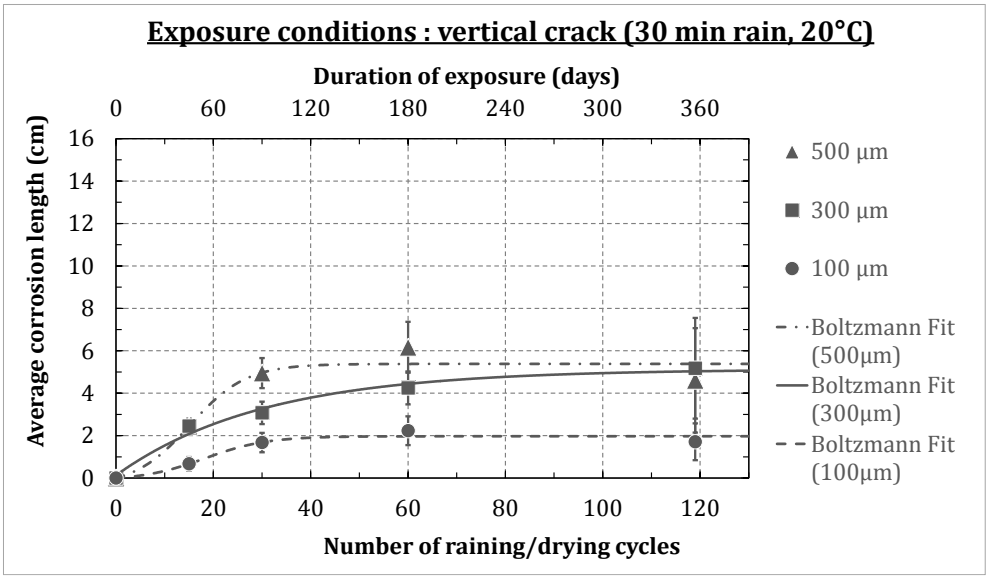

Figure 4-2 : Corrosion length evolution with respect to raining/drying cycles and residual crack width (visual inspection)

4.2.2 Corrosion products evolution

Figure 4-3 (a, b, c) shows the corrosion over carbonation length ratios measured on the upper and the lower part of the steel/mortar interfaces with respect to raining/drying cycles applied on specimens showing 100, 300 and 500 µm residual crack openings respectively. Similarly, for the corrosion length, no difference can be noted between the upper and the lower steel/mortar interfaces. Consequently, the mode of presentation adopted for these type of results is given in Figure 4-4. In this figure, the average corrosion over carbonation length ratio corresponds to the average of the ratios measured on the upper and lower steel/mortar interfaces of different specimens subjected to the same exposure conditions and duration.

It can be seen that the corrosion products fill the carbonated steel/mortar interface zone at the first thirty raining/drying cycles and do not spread for a greater length. Moreover, some ratios are greater than 1 and reach a value of 1.6 which may be related to the accuracy of the phenolphthalein pH indicator test and not to corrosion propagation. Indeed, according to Glasser and Matschei [188] cited in [20], the carbonated area detected by the phenolphthalein test is limited to the totally carbonated zone where the pH is lower than 8 and where no more portlandite and C-S-H remain. This pH is lower than the one needed to depassivate the steel and which is between 9.4 and 10 [59]. On the other hand, Parrott et al. [189] divided the carbonated depth in two zones: the first is totally carbonated and the second is a mixed zone where calcium carbonate and portlandite exist. A color change in the phenolphthalein solution is visible in the first zone and cover only the half of the mixed zone. Moreover, Demoulin et al. [59] confirm the limitation of the phenolphthalein test in detecting the carbonation especially at its beginning and this by detecting carbonation products in zones where phenolphthalein result is negative.

Therefore, in this study the carbonation length measured using the phenolphthalein test may underestimate the real carbonated length and this could explain the presence of some corrosion to carbonation ratios lightly higher than 1. Moreover, the measurement variability of the corrosion and the carbonation lengths may also have a small impact on the measured corrosion over carbonation ratios.

Moreover, digital scanning of each specimen is realized after each exposure duration and before the corrosion analysis and no corrosion cracks are visible on the outer surface of the

prismatic specimen which could confirm the absence of corrosion propagation far from the carbonated area.

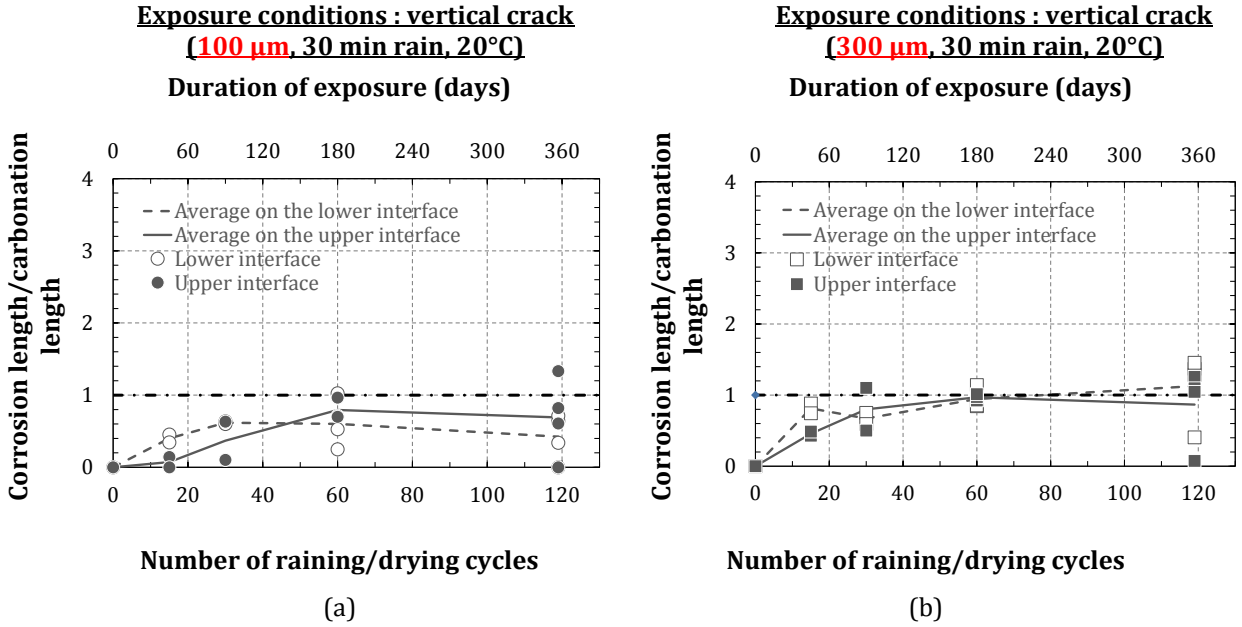

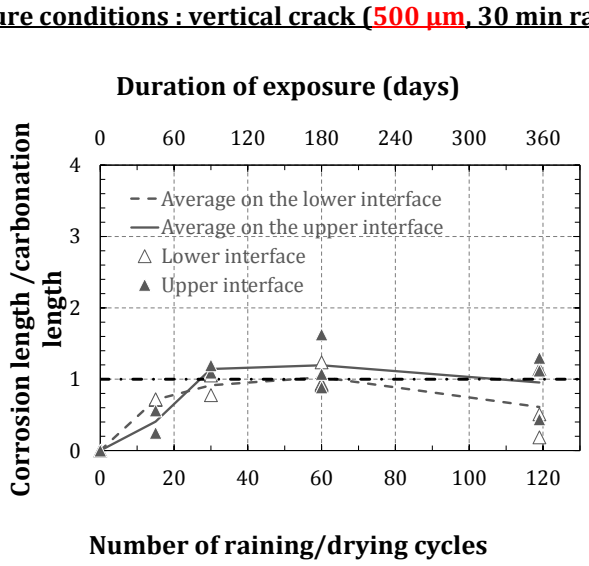

Figure 4-3 : Evolution of the corrosion over carbonation length ratio measured on the upper and the lower steel/mortar interfaces with respect to raining/drying cycles and residual crack widths (visual inspection)

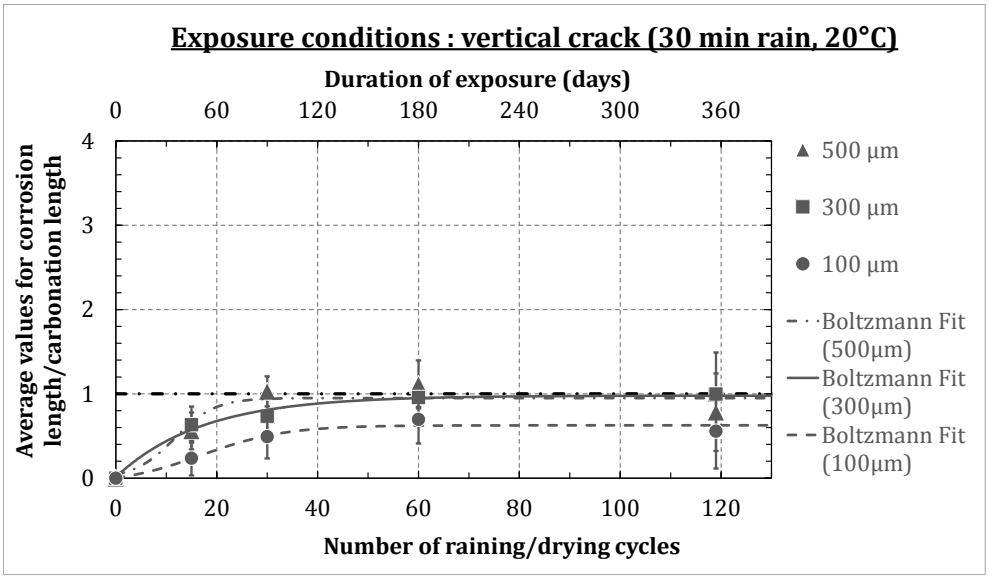

Figure 4-4 : Evolution of the corrosion over carbonation length ratio with respect to raining/drying cycles and residual crack widths (visual inspection)

4.2.3 Thickness of the corrosion products layer

Figure 4-5 provides information on the corrosion layer thickness from either side of the crack in specimens showing different residual crack openings (100, 300 and 500 µm) and subjected to different number of raining/drying cycles (30, 60 cycles). The letter “S” on each graph represents the area between the curve and the x-axis. It corresponds to the overall corroded surface measured on the upper part of the steel/mortar interface and could be used as an indicator of the corrosion products amount developed at this part of the interface.

It can be noted that the corrosion layer thickness measured on the upper steel/mortar interface increases with the increase in the residual crack opening.

It is obvious that the length of the corrosion products layer increases also with the residual crack opening which is in agreement with Figure 4-2. Moreover, the amount of corrosion products increases with the residual crack opening. Concerning the corrosion evolution, no significant evolution in the corrosion length is noticed between 30 and 60 cycles for the three residual crack openings which is in agreement with Figure 4-2 and Figure 4-4.

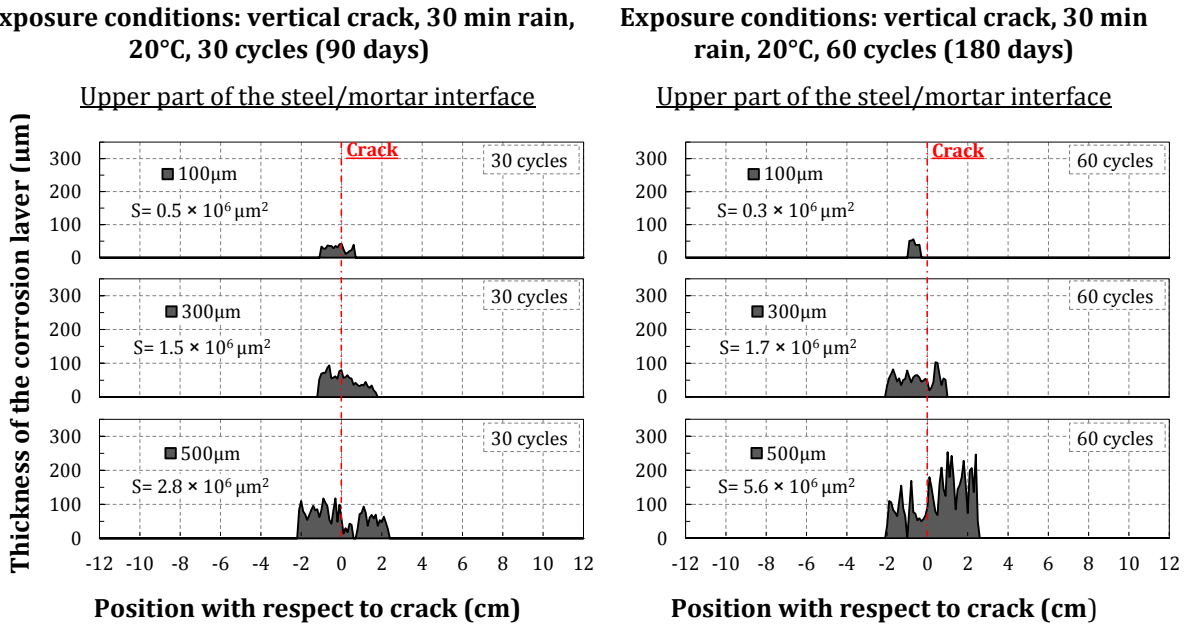

Figure 4-5 : Corrosion products repartition obtained on specimens showing different residual crack openings (optical microscopy)

4.3 GRAVIMETRIC MEASUREMENTS

4.3.1 Iron mass loss

Figure 4-6 presents the results of the gravimetric measurements. Each point in this figure is an average value of iron mass loss measured on triplicates subjected to the same conditions. An increase in the iron mass loss with the number of cycles and with crack opening is obvious. Whatever the crack opening, the iron mass loss tends to stabilize after 30-60 raining/drying cycles. This stabilization in the iron mass loss corresponds to the one found in the study of Tuutti [68] where cracked specimens were exposed to corrosion at different relative humidity. In this study, a quick corrosion attack occurs at the beginning of the corrosion process then a stabilization is visible after this time and remains valid till the end of their test which last 2 years.

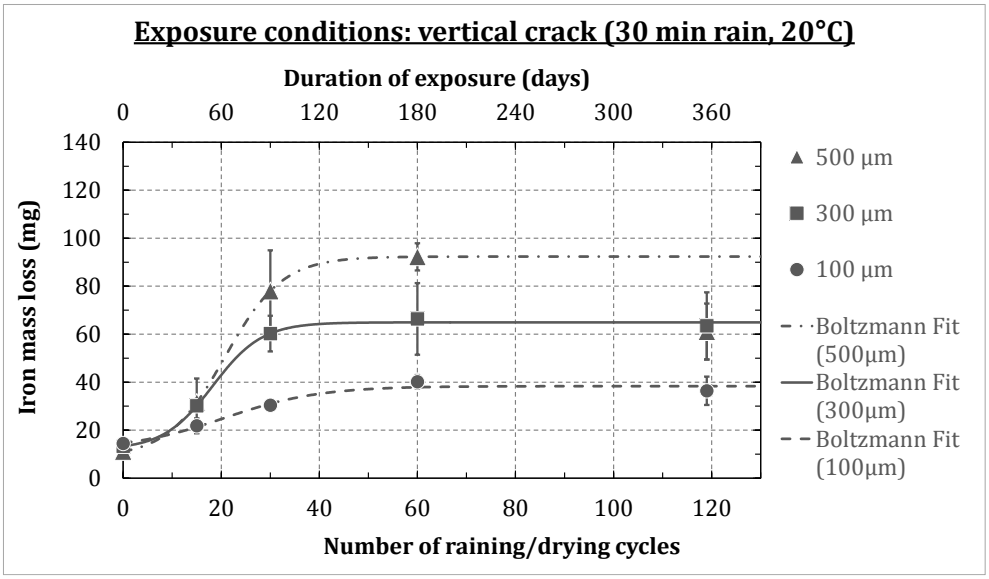

Figure 4-6: Iron mass losses in specimens having different residual crack openings with respect to raining/drying cycles

4.3.2 Corrosion rate

It is plain to see in Figure 4-7 that the corrosion kinetics decreases with the number of cycles for the three residual crack openings. This is due to the formation of porous oxide layer at the steel surface. It can also be noted that, near 60 cycles, the corrosion rate seems to be independent from the residual crack opening and is around 10 µm/year after 119 cycles. In addition, the difference between the corrosion kinetics measured at 6 and 12 months is negligible. Consequently, an estimation of the corrosion kinetics at 12 months relative to that at 6 months should logically give a value comparable to the passive corrosion kinetics (0.1-1 µm/year [190], [191]). However, it is not possible in this study to determine its exact value because specimens analyzed at 6 months are not the same at 12 months. The same trends for the iron mass loss and the corrosion rate are also obtained on cracks exposed horizontally with respect to rain (Appendix I.34).

The observed decrease in the corrosion kinetics corresponds to the one proposed in the model of Tuutti [68]. According to Tuutti, this decrease is linked to the repassivation and he assumes that the corrosion products seal cracks and inhibit the access of carbon dioxide to the rebar. However, substances that increase the pH value can diffuse from the mortar to the steel, leading to a repassivation. This assumption is also proposed by Schießl [77]. The phenomenon is verified here by monitoring the evolution of the carbonated steel/mortar interface length at different times during the corrosion test. It is found that the carbonated length remains unchanged for the entire exposure duration and does not decrease (Figure 4-8)[3]. This does not exactly fit the theory of Tuutti and Schießl and the explanation could be linked to the neutral water that fills the cracked area every three days, during the raining phase. The absorption of water by the mortar may inhibit a possible increase in its pH in the cracked zone surrounding the rebar. In addition, this could also be related to the macrocell process that leads to the creation of hydroxyl ions outside the carbonated (and corroded) area. Nevertheless, despite all these assumptions, an increase in pH cannot be totally discounted because it could occur without bringing the pH above 9, which would

[3] A change in the length of the carbonated interface is not detected in all the exposure conditions tested in this project (Appendix I.7).

make it undetectable by the phenolphthalein pH indicator test. The theory of Tuutti and Schießl would probably apply for long exposure durations (more than 12 months).

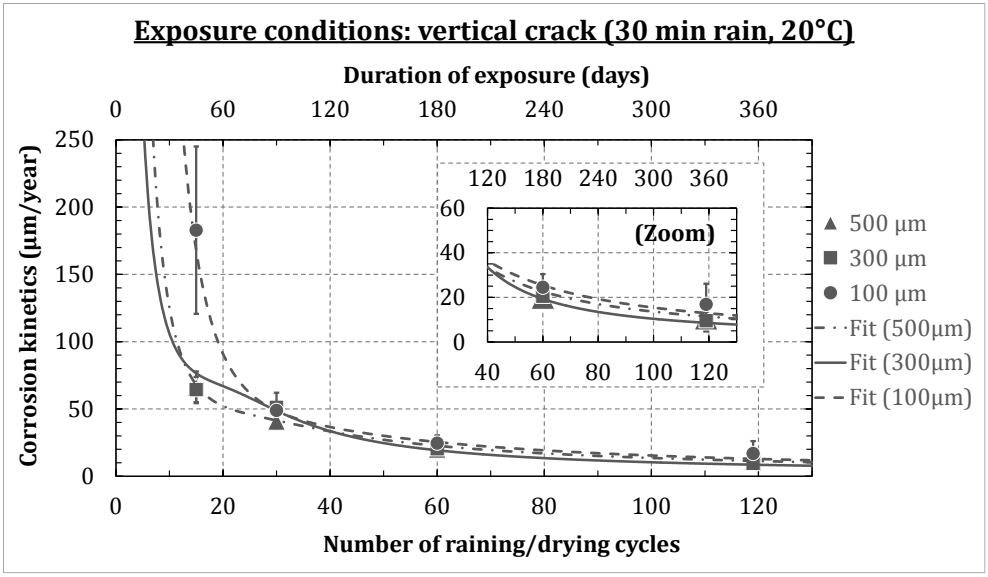

Figure 4-7: Corrosion rate evolution in specimens having different residual crack openings with respect to raining/drying cycles

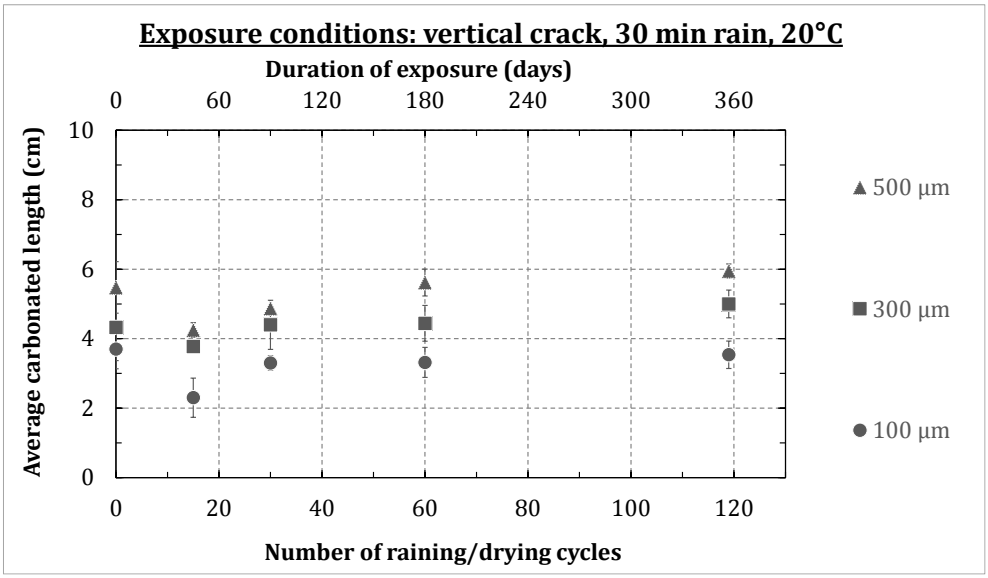

Figure 4-8: Evolution of the carbonated steel/mortar interface length in specimens having different residual crack openings and corroded in the reference test

4.4 FREE CORROSION POTENTIAL MEASUREMENTS

The evolution of the measured corrosion potentials is given in Figure 4-9. Two distinct periods can be observed in the corrosion process.

- The first period, during the first month of exposure, corresponds to the initiation of corrosion, in which a drop in the corrosion potential from -70 mV/SCE to -350 mV/SCE indicates corrosion initiation at the crack location.

At the beginning of the corrosion test, the steel deep in the crack intercepts carbonated mortar. Therefore, this part of the steel was able to be oxidized and the corrosion potential thus fell.
In this project, the rebar is surrounded by a heterogeneous mortar (carbonated and non-carbonated). This heterogeneity induces a difference in the potential and lead to the formation of a cell between these two zones. The passivated steel intercepting a noncarbonated mortar and located far from the crack could act as a cathode while the steel intercepting a carbonated mortar and located deep in the crack could act as an anode. Therefore, during corrosion initiation, in addition to the microcell mechanism, a macrocell corrosion mechanism directly dependent on the chemical characteristics of the surrounding electrolyte (pH of the mortar) also come into play. According to [67], it is likely that macrocell corrosion would predominate.

- The second part of the process concerns corrosion propagation deep in the crack. In this process, the corrosion potential starts to increase from - 350 mV/SCE and almost reaches the corrosion potential of the uncracked specimen (around -70 mV/SCE), which is an indication of the reduction of the macro-cell process of corrosion. This increase in the corrosion potential could be related to the limitation of the anodic process at the crack location due to the oxide layer developed deep in the crack. The difference in the potential between the zone of the steel intercepting a carbonated mortar and the one intercepting a non-carbonated mortar would then be strongly reduced. At this moment, the macrocell corrosion process would be limited and the microcell corrosion process would dominate.

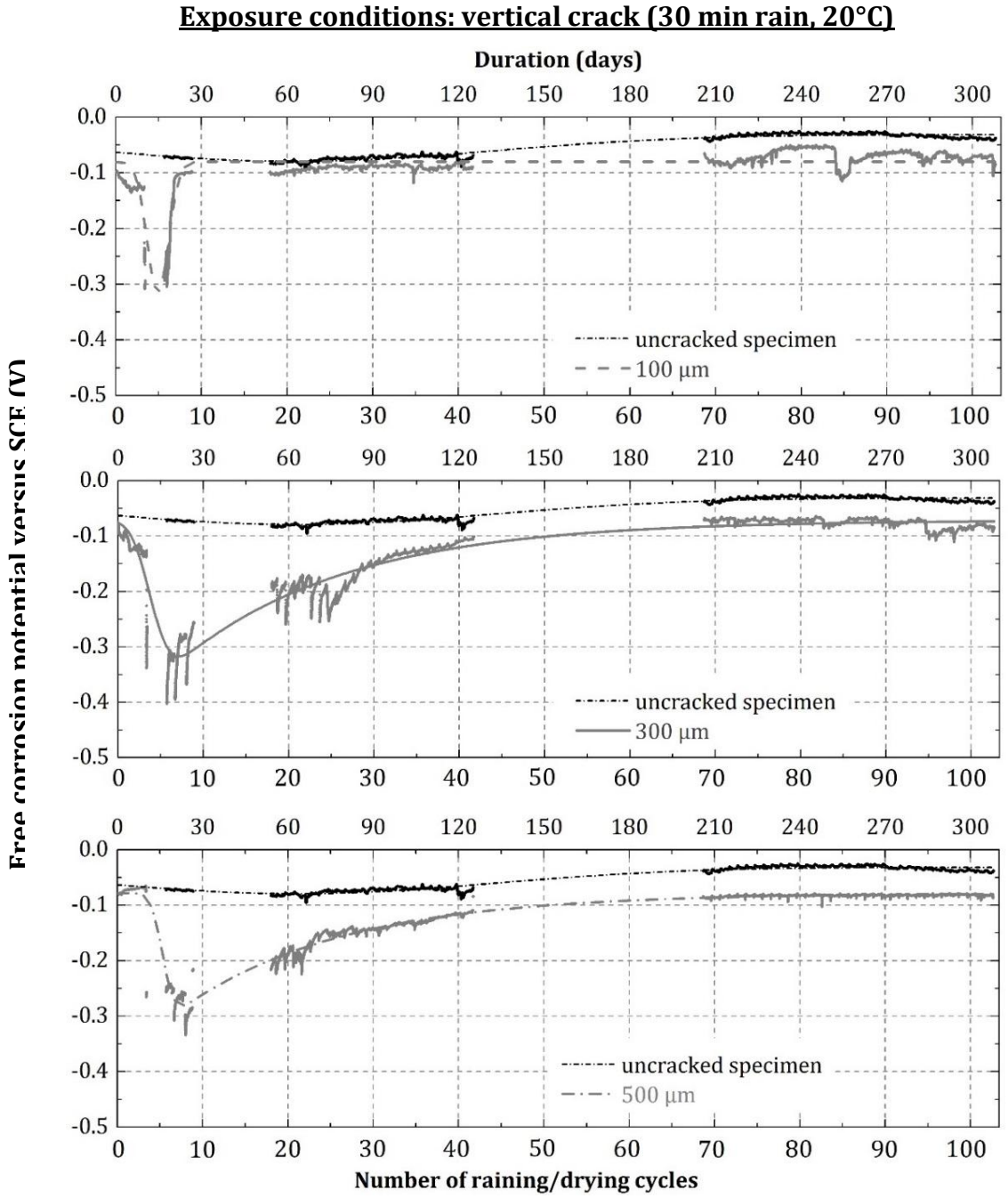

Figure 4-9 : Free corrosion potential (versus SCE) evolution in specimens showing different residual crack openings and exposed to raining cycles for 310 days

4.5 CORROSION PRODUCTS TYPE

Corrosion products type developed on the upper part of the steel/mortar interface of specimens having three different residual crack openings oriented vertically with respect to rain are analyzed.

Figure 4-10, Figure 4-11 and Figure 4-12 show the corrosion layer developed along the steel/mortar interface of specimens having 100, 300 and 500 µm residual crack openings respectively. Representative Raman spectra obtained in each analyzed zone are given in Figure 4-13. One can find all the obtained Raman spectra in Appendix I.6.1. A schematic representation summarizing the corrosion products type identified is given in Figure 4-14.

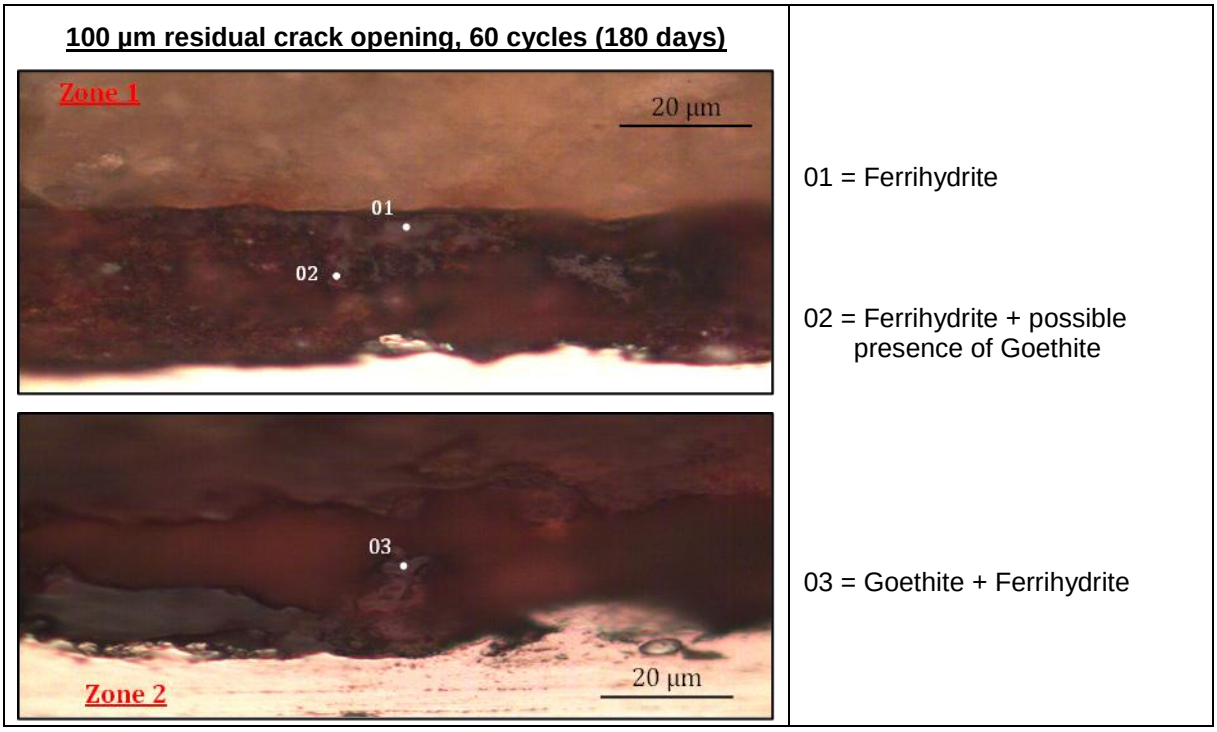

Figure 4-10 : Corrosion layer observed at the steel/mortar interfaces located far from the crack and deep in the crack in specimen having 100 µm residual crack opening

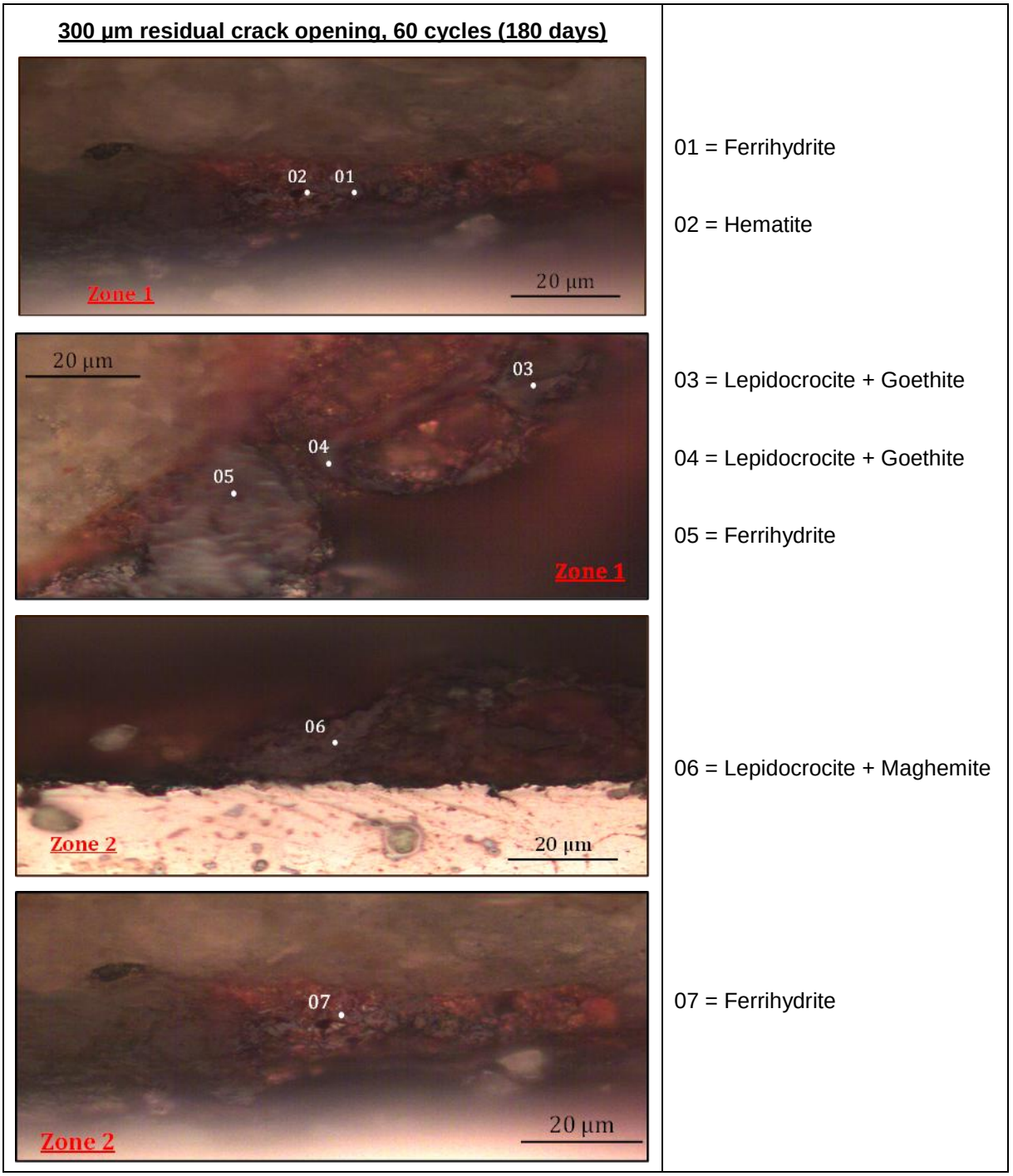

Figure 4-11 : Corrosion layer observed at the steel/mortar interfaces located far from the crack and deep in the crack in specimen having 300 µm residual crack opening

500 µm residual crack opening, 60 cycles (180 days)

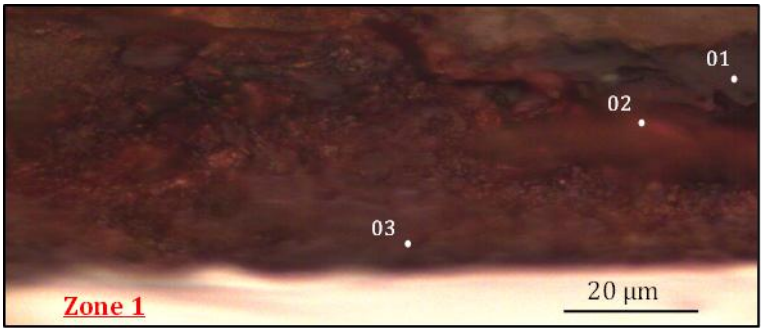

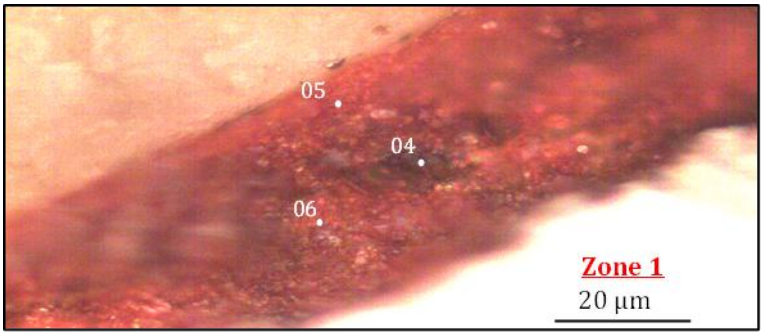

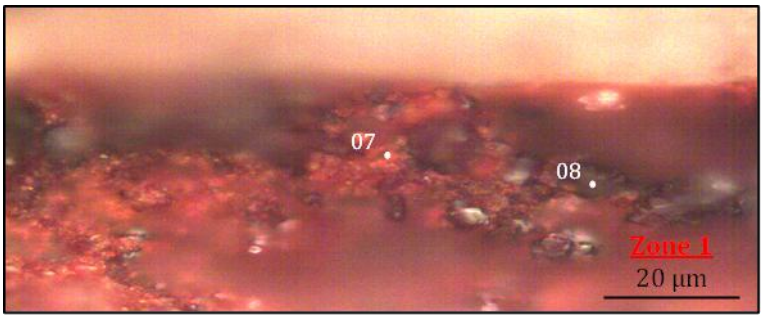

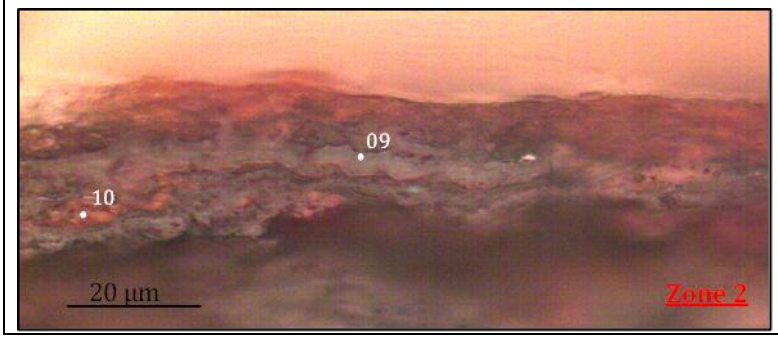

01 = Ferrihydrite + possible presence of Goethite

02 = Ferrihydrite + undetermined phase

03 = Ferrihydrite

04 = Ferrihydrite

05 = Ferrihydrite + undetermined phase

06 = Ferrihydrite + undetermined phase

07 = Ferrihydrite + undetermined phase

08 = Ferrihydrite + undetermined phase

09 = Goethite + Ferrihydrite

10 = Lepidocrocite + Ferrihydrite

Figure 4-12 : Corrosion layer observed at the steel/mortar interfaces located far from the crack and deep in the crack in specimen having 500 µm residual crack opening

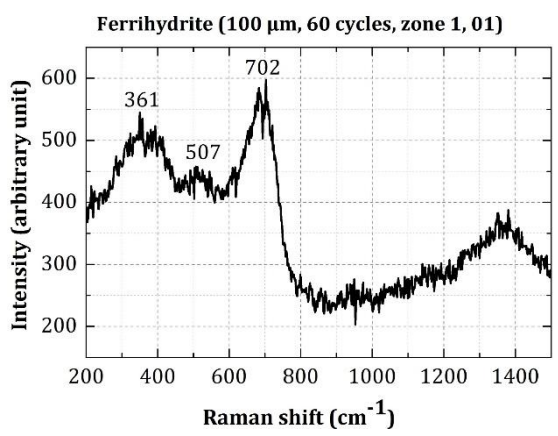
Ferrihydrite (100 µm, 60 cycles, zone 1, 01)
Intensity (arbitrary unit)
Raman shift (cm-1)
361
507
702

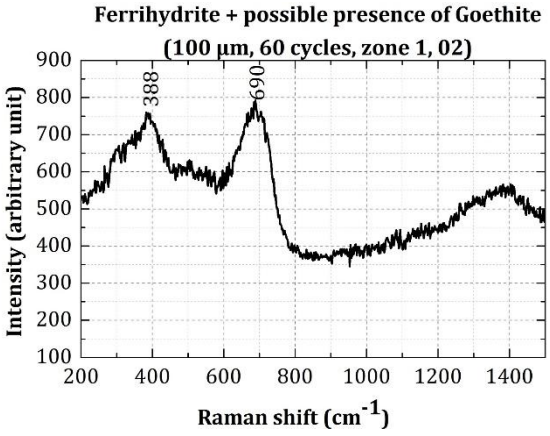
Ferrihydrite + possible presence of Goethite
(100 µm, 60 cycles, zone 1, 02)
Intensity (arbitrary unit)
Raman shift (cm-1)
388
690

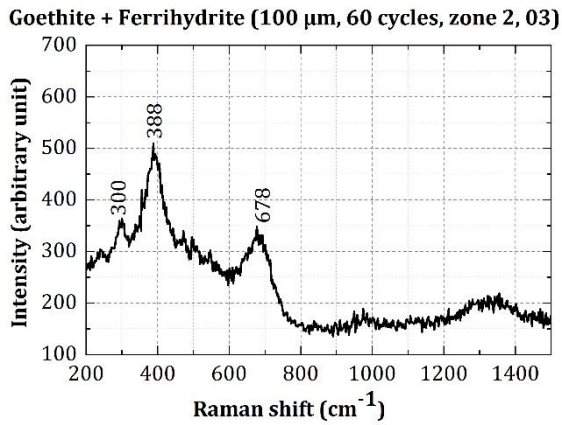
Goethite + Ferrihydrite (100 µm, 60 cycles, zone 2, 03)
Intensity (arbitrary unit)
Raman shift (cm-1)
300
388
678

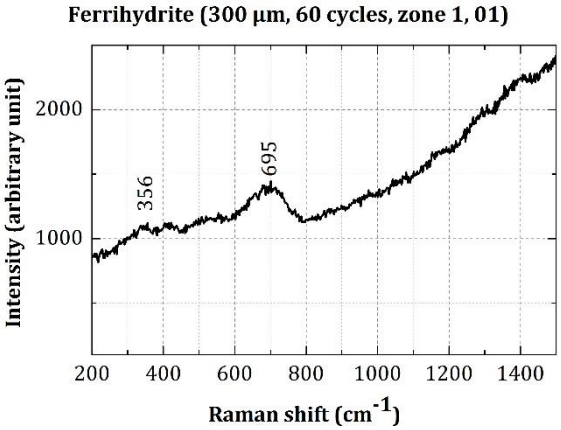
Ferrihydrite (300 µm, 60 cycles, zone 1, 01)
Intensity (arbitrary unit)
Raman shift (cm-1)
356
695

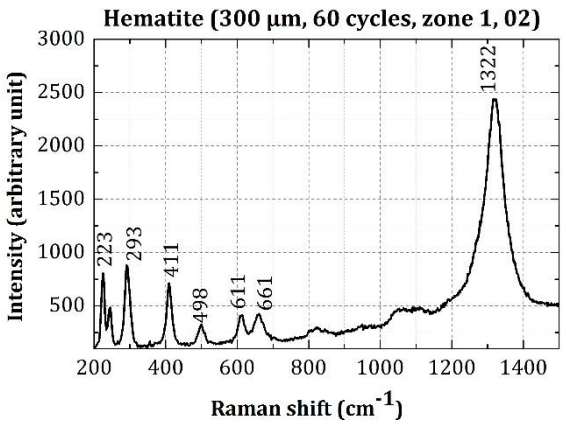
Hematite (300 µm, 60 cycles, zone 1, 02)
Intensity (arbitrary unit)
Raman shift (cm-1)
223
293
411
498
611
661
1322

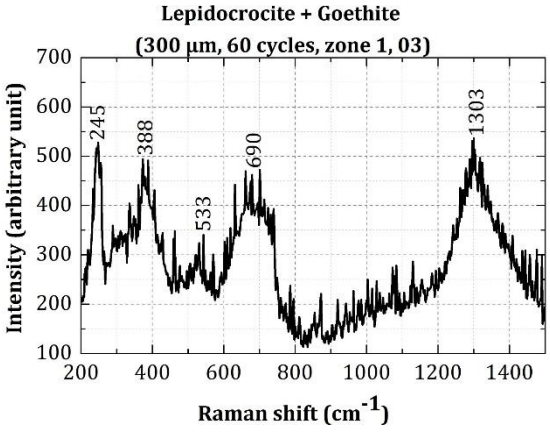
Lepidocrocite + Goethite
(300 µm, 60 cycles, zone 1, 03)
Intensity (arbitrary unit)
Raman shift (cm-1)
245
388
533
690
1303

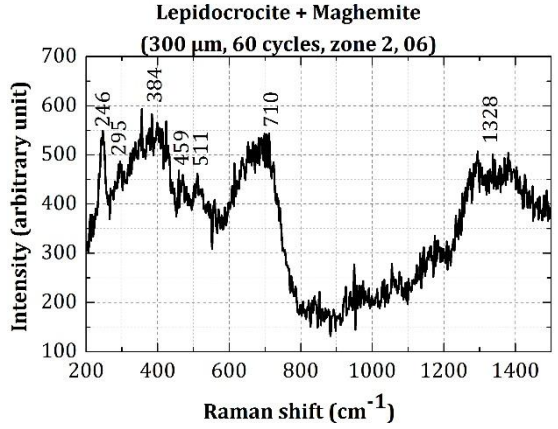
Lepidocrocite + Maghemite
(300 µm, 60 cycles, zone 2, 06)
Intensity (arbitrary unit)
Raman shift (cm-1)
246
295
384
459
511
710
1328

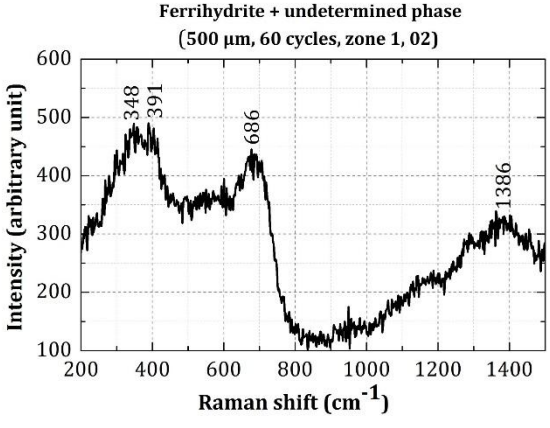
Ferrihydrite + undetermined phase
(500 µm, 60 cycles, zone 1, 02)
Intensity (arbitrary unit)
Raman shift (cm-1)
348
391
686
1386

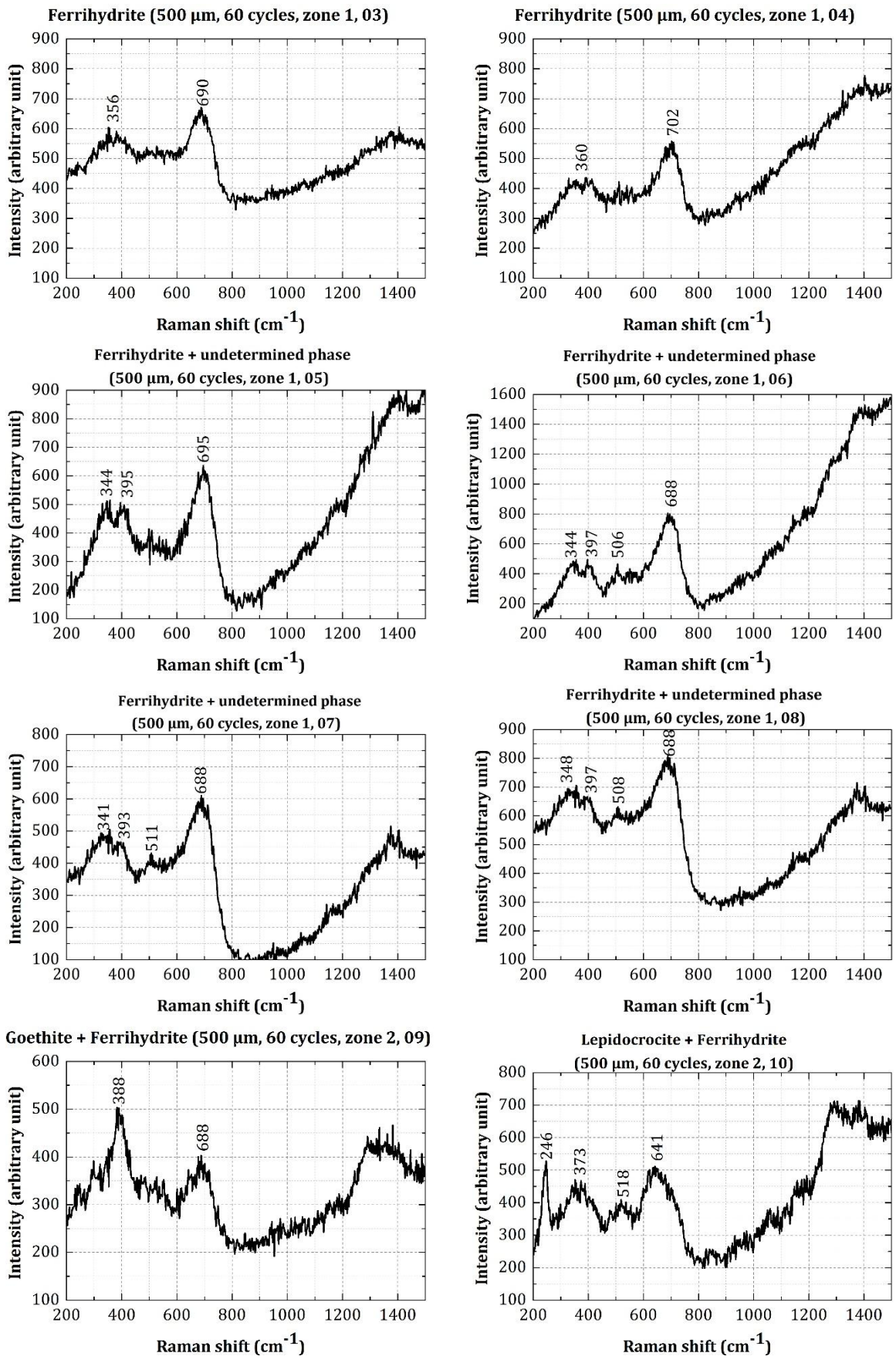

Figure 4-13 : Raman spectra of corrosion products obtained on specimens showing three different residual crack openings

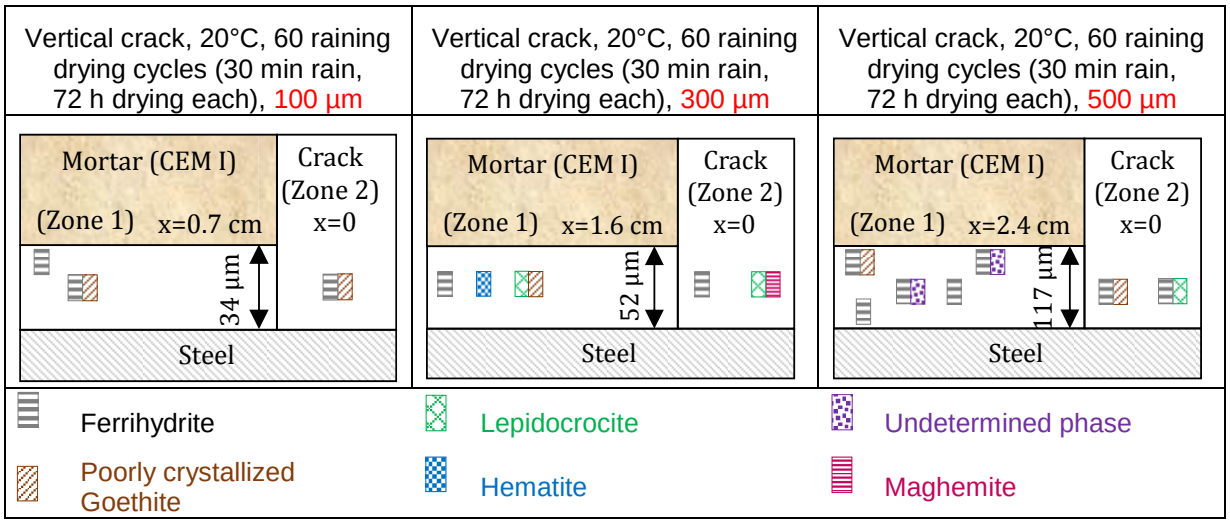

Figure 4-14 : Summary of the corrosion products identified in different zones of specimens showing different residual crack openings

Ferrihydrite ($5Fe_2O_3.9H_2O$), a poorly crystallized phase whose chemical formula is still under discussion [192], [193], is always present.
In addition to ferrihydrite, maghemite is also detected. These phases are known to be chemically and electrochemically reactive[4] [92] especially in the condition of atmospheric corrosion [194], [195].
Poorly crystallized Goethite is also detected and as pointed out in the study of Monnier et al. [196], the electrochemical reactivity of this phase is linked to its crystallinity. Therefore, the goethite detected in the corroded specimens can also be a reactive phase.
Lepidocrocite is also detected in the corroded specimens and according to Misawa et al. [197], this phase appears in more aerated conditions. Despite that this phase is not usually shown in the corrosion of steel in concrete [59], [87], it is detected in long term corrosion layer developed on rebars embedded in concrete only where the steel/concrete interface contains air bubbles [198]. The presence of these voids may increase the aeration which may justify the appearance of Lepidocrocite in [198]. Its presence in this study could be correlated with the presence of cracks in concrete. It may also be due to an artefact during the preparation of the sample. The cause of the Lepidocrocite detection could not be confirmed but independently from its origin during the wetting stages of a wetting/drying cycles, it can be reduced and be involved in the following cycle as proven in [199]. Antony et al. [194], [195] confirm that Lepidocrocite can be one of the reactive phases but they add that ferrihydrite is much more reactive.

In some Raman spectra, a double pic is visible at 340, 395 cm^{-1} Raman band. Basing on the literature review, it was impossible to determine the phase that corresponds to this double pic. It appears usually with ferrihydrite and it may be a precursor phase that may develop during the ferrihydrite formation or the ferrihydrite transformation.

4.6 Discussion and conclusions

In this research study, the effect of the crack opening on the initiation and propagation of carbonation-induced corrosion is tested and analyzed. The results indicate a decrease in the corrosion kinetics with the number of raining/drying cycles. The effect of the crack opening on the corrosion kinetics is masked after several raining/drying cycles. Moreover, the corrosion products do not spread beyond the carbonated zone limits. In addition, no

[4] In this case, reactivity means the ability of reduction of identified phases constituting the rust layer

corrosion cracks are visible on the outside surface of the specimens. Furthermore, an increase in the free corrosion potential is noticed after several raining/drying cycles. All these results allow the author to deduce that the corrosion products seal the cracks and limit the access of oxygen and water to the rebar which slows down the corrosion propagation and may lead to repassivation of steel rebar. This result is in agreement with the one obtained by a numerical simulation in the study of Millard et al. [132].

It should be highlighted that the term repassivation used in this study is due to the corrosion products that protect the rebar and limit the access of water to the rebar and not to the recovery of the initial pH (before carbonation) of the carbonated mortar surrounding the corroded rebar

Additionally, based on the curve of the free corrosion potential measurements, two corrosion mechanisms may occur consecutively. The first mechanism is globally a macrocell corrosion that occurs during the initiation phase. Afterwards, the second mechanism comes during the propagation phase and corresponds to a microcell corrosion.

The corrosion rate measured in this study decreases with time and in the duration of this study, the corrosion is in its induction phase (reduction in the corrosion rate induced by the development of a porous corrosion layer on the steel surface). The duration of this phase cannot be predicted and in the long term, two possibilities exist:

- The first is that the corrosion will not have any detrimental effect on the durability of the structures (Figure 4-15(a)).

  In this case, the most harmful parameter on the structure sustainability is the concrete cover carbonation. The model proposed by Tuutti [68] to describe the steel corrosion sequence in un-cracked concrete could be applicable in the un-cracked zones. It is presented in Figure 4-15(b) and consists of two phases (initiation, propagation). During the initiation phase, the carbon dioxide penetrates the concrete cover, leading eventually at a certain depth of carbonation to a situation wherein corrosion initiation is thermodynamically favored. Thereafter, corrosion propagation phase begins and is marked by an acceleration in the corrosion rate and consequently in the deterioration rate. The duration of the initiation and the propagation phases are dependent from the concrete cover properties (thickness, w/c ratio) [73], [77], [78], [81], [200].

  By combining, the corrosion process deep in the crack and far from the crack, it can be deduced that the corrosion model proposed in the study of François & Arliguie [79] may describe the global behavior of structure (Figure 4-15 (c)). A similar corrosion model for cracked and carbonated concrete is also proposed by Tuutti [68].

  The results drawn in the study of Schießl [77] supports this first hypothesis concerning the corrosion propagation. The author investigated cracked specimens after four and ten years of exposure and reported the presence of corrosion in the un-cracked zones due to the penetration of the carbonation front to the steel. However, Tremper [81] investigated cracked specimens after 10 years of outside exposure and identified the presence of corrosion attacks only in the zones of cracks and their immediate surroundings. Tremper added also that the corrosion detected does not have serious consequence because of its minor degree. Additionally, Vesikari [82] investigated the corrosion development in cracked concrete of 50 years old bridges and found that very few cracks had given rise to serious corrosion damage. This observation approve that the corrosion process is retarded after the first initiation phase. Therefore, several authors agree that the carbonation-induced corrosion deep in the crack is not the most harmful parameter for the structure durability.

- The second possibility aims to suppose a creation of corrosion cracks before the total carbonation of the concrete cover. In this condition, the corrosion cracks may be behind the corrosion propagation process. However, it should be noted that the new corrosion cracks intercept rebar embedded in an alkaline medium. Therefore, a certain duration of carbonation is needed in order to ensure the corrosion propagation along the rebar. In fact, corrosion cracks are generally parallel to the rebar and this promotes a homogenous carbonation deep in the crack. Therefore, a microcell corrosion mechanism may take place during the propagation phase. A schematic sketch of steel corrosion development in this second possibility is given in Figure 4-16. It should be noted that this second possibility has a small probability to occur especially in structures not subjected to dynamic loading.

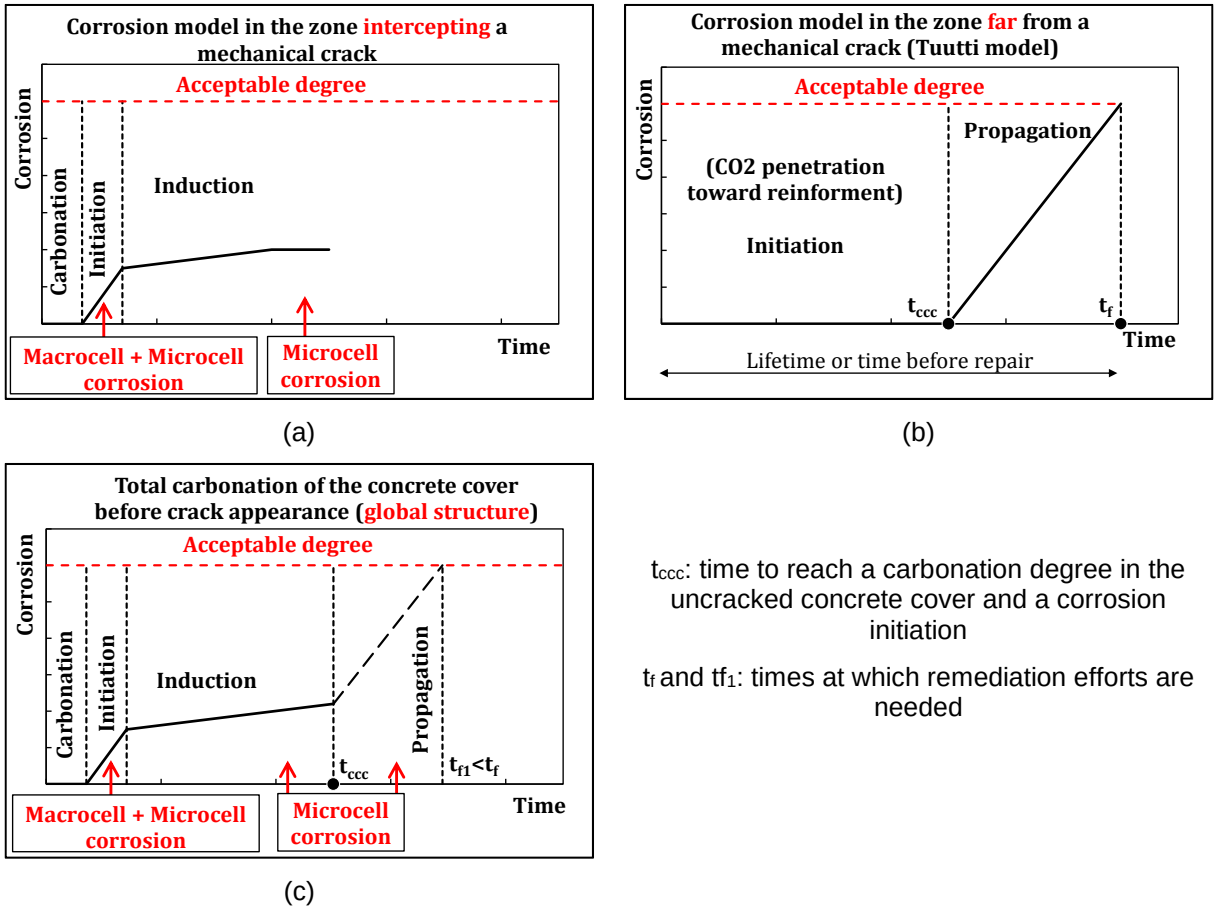

t_{ccc}: time to reach a carbonation degree in the uncracked concrete cover and a corrosion initiation

t_f and tf_1: times at which remediation efforts are needed

Figure 4-15: Corrosion model supposing a corrosion propagation induced by a total carbonation of the concrete cover (corresponding to the corrosion model proposed by François & Arliguie [79])

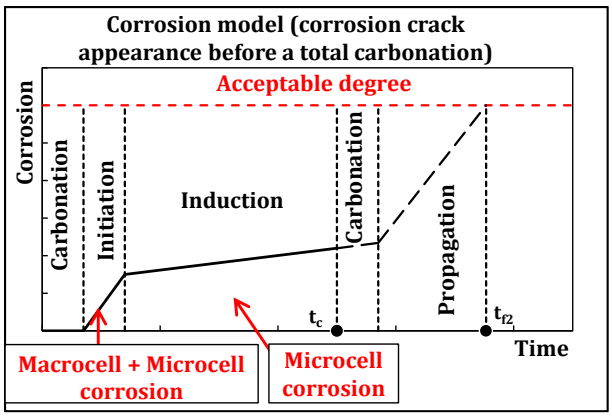

tc: time of the corrosion cracks appearance

tf: times at which remediation efforts are needed

Figure 4-16 : Corrosion model supposing a corrosion propagation induced by a corrosion crack

Finally, concerning the corrosion products type, it can be deduced that there is no influence of the crack opening on the corrosion products type. The main observation is that the corrosion products developed are known to be reactive phases which are electrochemically and chemically unstable and have tendency to be reduced (Lepidocrocite, ferrihydrite, poorly crystallized goethite, etc). Therefore, these phases may act as a cathode during the microcell mechanism corrosion in which the iron is the anode.

CHAPTER 5. EFFECT OF CRACK ORIENTATION AND ENVIRONMENTAL CONDITIONS ON THE CORROSION DEVELOPMENT

Chapter 5. Effect of crack orientation and environmental conditions on corrosion development

5.1 INTRODUCTION

The effect of several exposure conditions on the corrosion development is examined in this chapter by comparing results with those obtained from the reference test and presented in chapter 4. The exposure conditions tested here corresponds to different crack orientations with respect to rain, various environmental conditions (rain duration, temperature, relative humidity, etc…). At the end of this chapter, the evolution in the corrosion products type with respect to time is presented.

For each exposure condition, the order of the results presentation is similar to chapter 4. Distribution of the corrosion products layer will be firstly given. Then the gravimetric and the free corrosion potential measurements will be argued. Afterward, the identified corrosion products type will figure. Finally, results are discussed and conclusions are drawn.

5.2 CRACK ORIENTATION

Three configurations are tested in this study. In the first one, cracks are oriented vertically with respect to rain (reference test). While in the second, they are horizontally oriented with respect to rain. The third configuration corresponds to cracks not directly exposed to rain. For this last configuration, only free corrosion measurements are performed. Accordingly, the distribution of the corrosion layer, the gravimetric measurements and the nature of the corrosion products developed are only given for the vertically and horizontally oriented cracks.

The effect of the crack orientation on corrosion is tested on specimens showing three residual crack openings (100, 300 and 500 µm). Considering the results given in chapter 4 that do not report significant difference between the 300 and 500 µm residual crack openings, it has been chosen in this section not to present the results obtained in the case of 500 µm residual crack opening. However, they can be found in appendix I.4.1.

5.2.1 Distribution of the corrosion products

In this section, the corrosion developed in vertically and horizontally oriented cracks is compared based on the corrosion products layer length, its evolution with respect to carbonation steel/mortar interface length and its thickness from either sides of the crack.

Figure 5-1 shows the evolution of the corrosion length with respect to the number of raining/drying cycles for cracks oriented vertically and horizontally with respect to rain and having two widths: 100 µm (Figure 5-1(a)) and 300 µm (Figure 5-1(b)). For both crack orientations, the corrosion length increases with the number of raining/drying cycles and tends to stabilize after 30-60 raining/drying cycles. The stabilization of the corrosion length appears earlier in cracks oriented horizontally than in those oriented vertically with respect to rain. However, it is visible that the variability on the corrosion developed between specimens is important and this may be the only reason behind this difference in corrosion evolution trend. Moreover, this difference is not observed in the case of specimens showing 500 µm residual crack opening (Appendix I.4.11).

Therefore, it can be deduced that crack orientation does not impact the corrosion length evolution independently from the crack opening.

The evolution of corroded length with respect to the carbonated one is given in Figure 5-2 for the two cracks orientations and the two residual cracks openings (100, 300 µm). Similarly to the observations drawn for the corrosion length evolution, no difference can be noted between the cracks oriented differently with respect to rain. This is also valid for specimens showing 500 µm residual crack opening (Appendix I.4.12).

Concerning the thickness of the corrosion products layer, only results obtained after 60 raining/drying cycles are given for the two residual crack openings 100 and 300 µm in Figure 5-3 (a and b) respectively.

For the two residual crack openings, the corrosion products amount (S) is very marginally greater for cracks oriented horizontally than those oriented vertically with respect to rain. In fact, the thickness of the corrosion products layer is very close between the two orientations. However, the length of the corrosion products layer is higher in cracks oriented horizontally. Nevertheless, this is not at all in accordance with corrosion length obtained on other replicates inspected visually (Figure 5-1). Moreover, for the specimens showing 500 µm residual crack opening, the corrosion length observed by the optical microscopy is similar for both of the cracks orientations (Appendix I.4.13). Once again the heterogeneity is the only reason behind the observed difference. A simple examination of similar graphs obtained also by the optical microscopy at different number of raining/drying cycles could confirm that crack orientation do not have any impact on the corrosion products layer repartition (Appendix I.5.2).

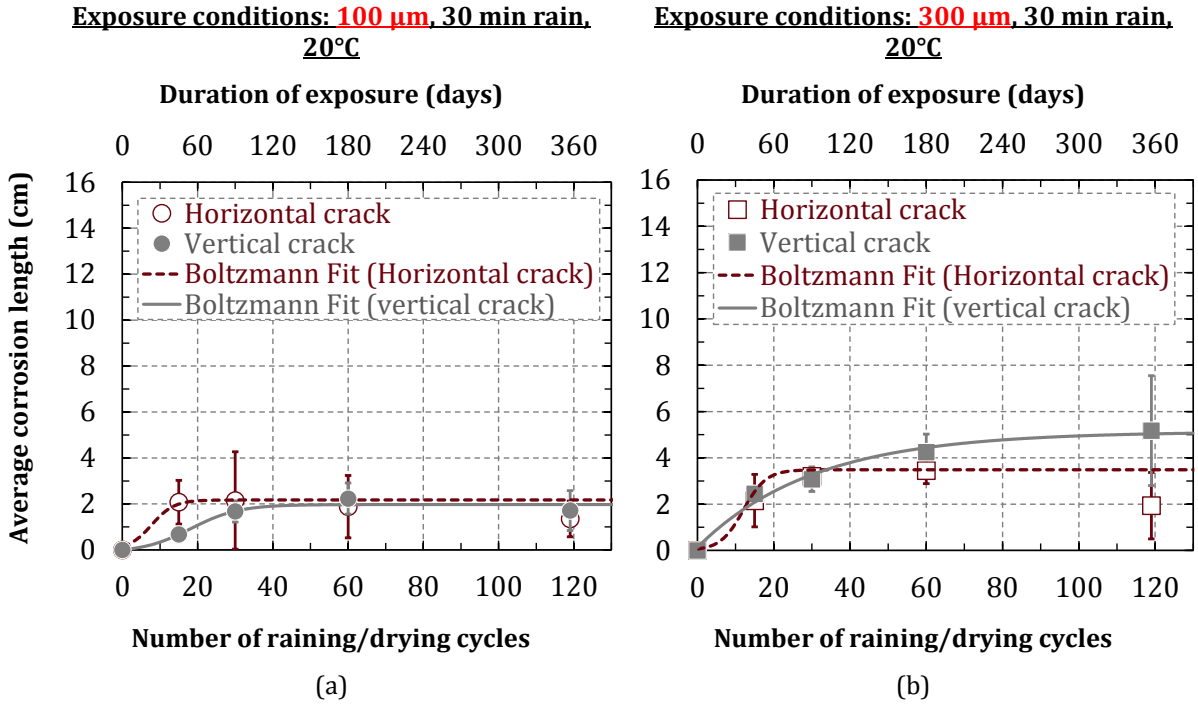

Figure 5-1: Corrosion length evolution with respect to raining/drying cycles and crack orientations (visual inspection)

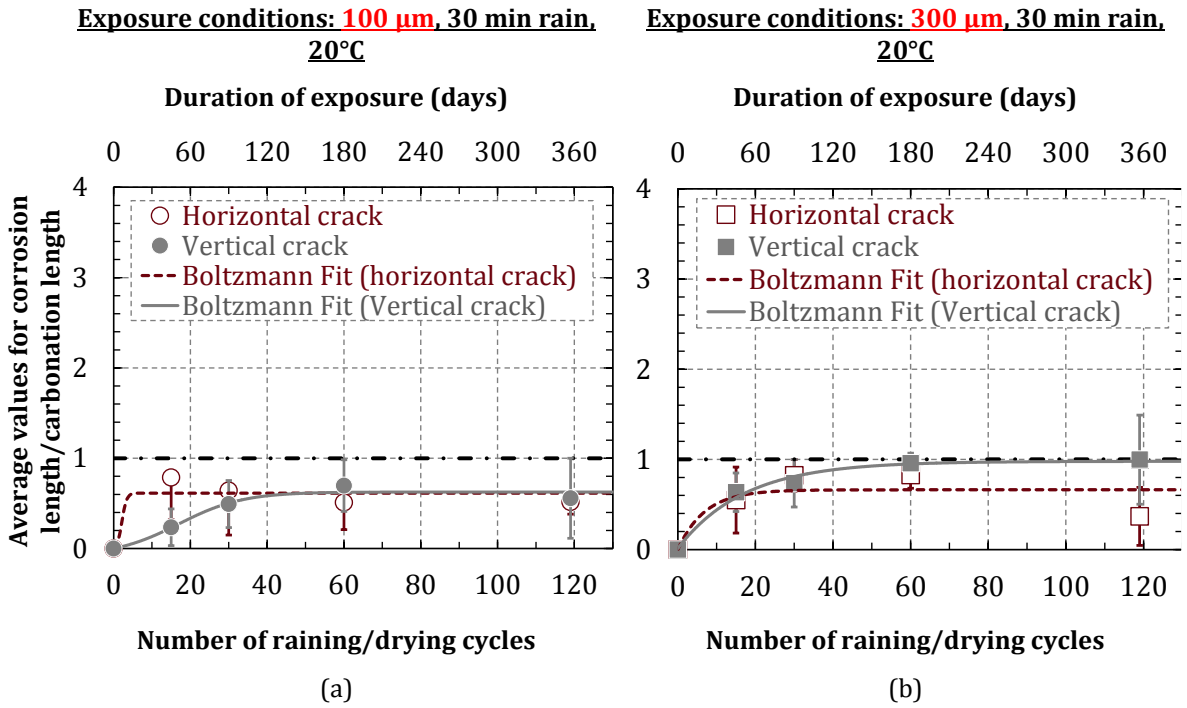

Figure 5-2: Evolution of the corrosion over carbonation length ratio with respect to raining/drying cycles and crack orientations (visual inspection)

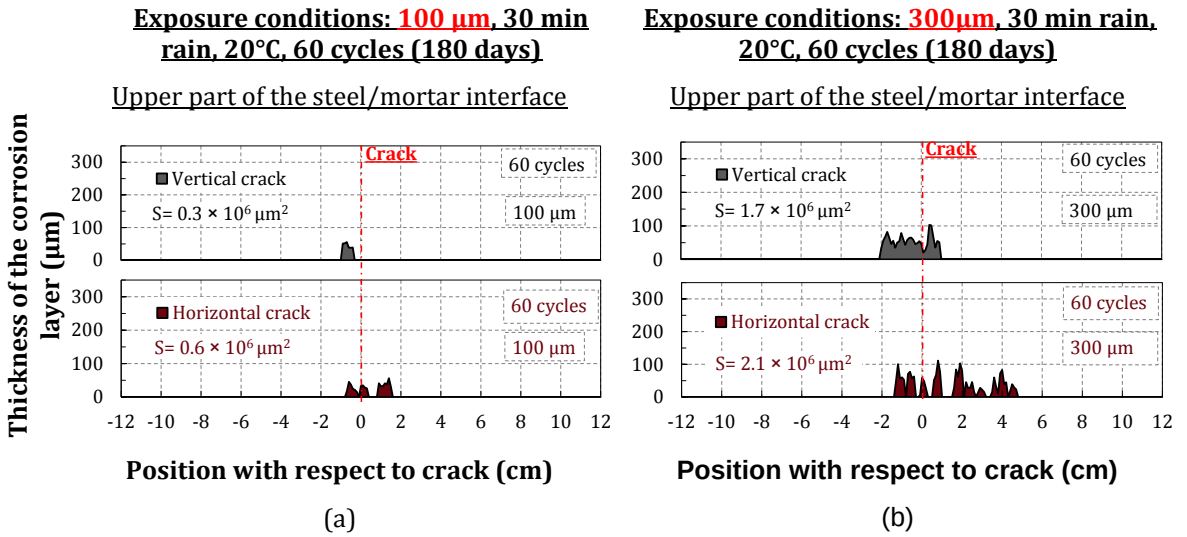

Figure 5-3: Corrosion products repartition obtained on specimens oriented differently with respect to rain (optical microscopy)

5.2.2 Gravimetric measurements

Figure 5-4 compares the iron mass losses in specimens showing different residual crack openings and oriented differently with respect to rain. It is evident that crack orientation does not alter the measured iron mass losses.

The corrosion kinetics is also not impacted by the crack orientation independently from the residual crack openings (Figure 5-5). This is also the same for specimens showing 500 µm residual crack opening (Appendix I.4.14).

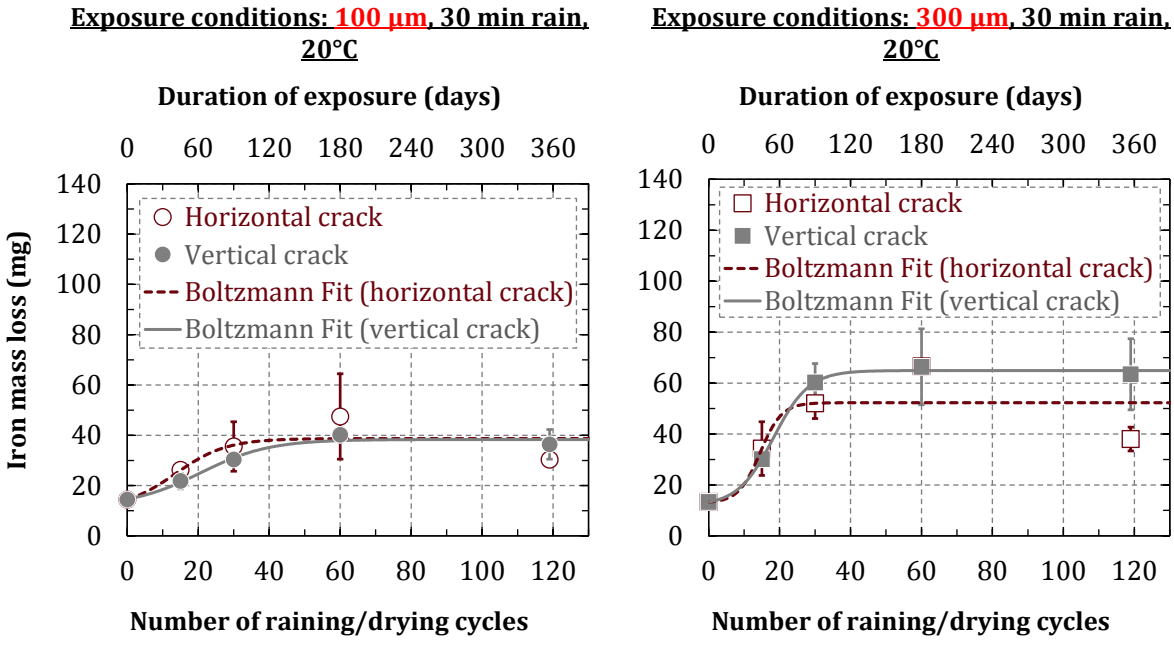

Figure 5-4: Iron mass losses in specimens having different crack orientations with respect to raining/drying cycles

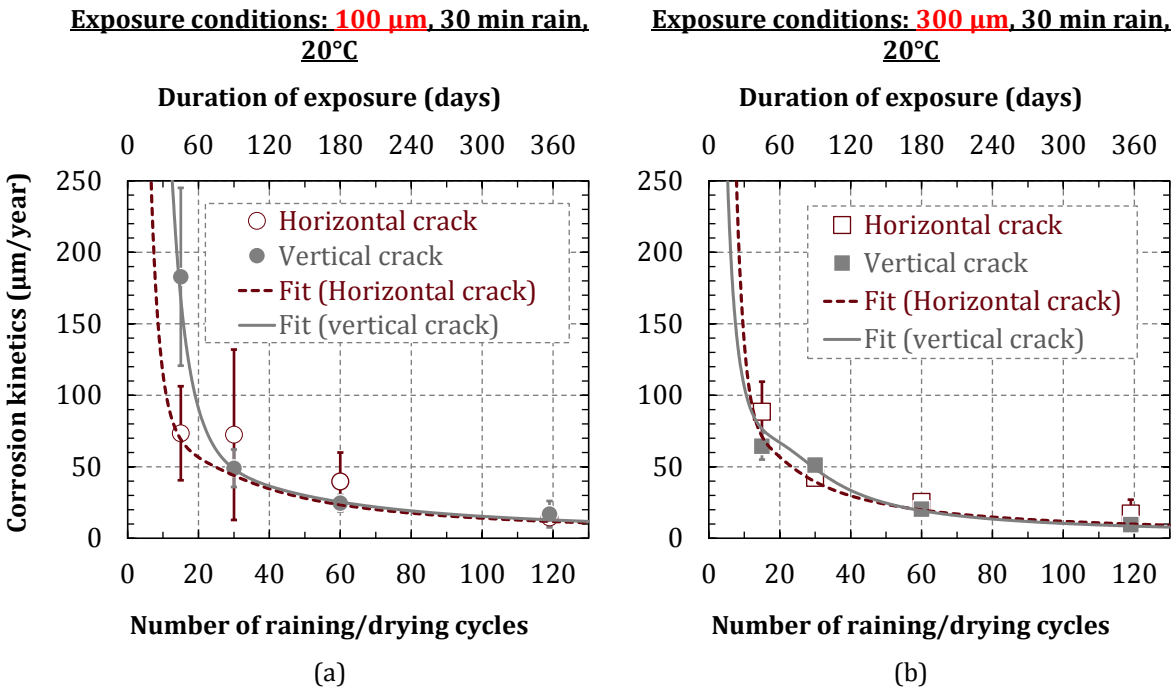

Figure 5-5: Corrosion rate evolution in specimens having different crack orientations with respect to raining/drying cycles.

5.2.3 Free corrosion potential measurements

The evolution of the measured free corrosion potentials for specimens having 100 µm and 300 µm are given in Figure 5-6 and Figure 5-7 respectively. The two periods of corrosion process detailed in (§ 4.4) exist for the three crack orientations. Once again, there is no notable difference between the free corrosion potentials tendency obtained in specimens exposed differently with respect to rain.

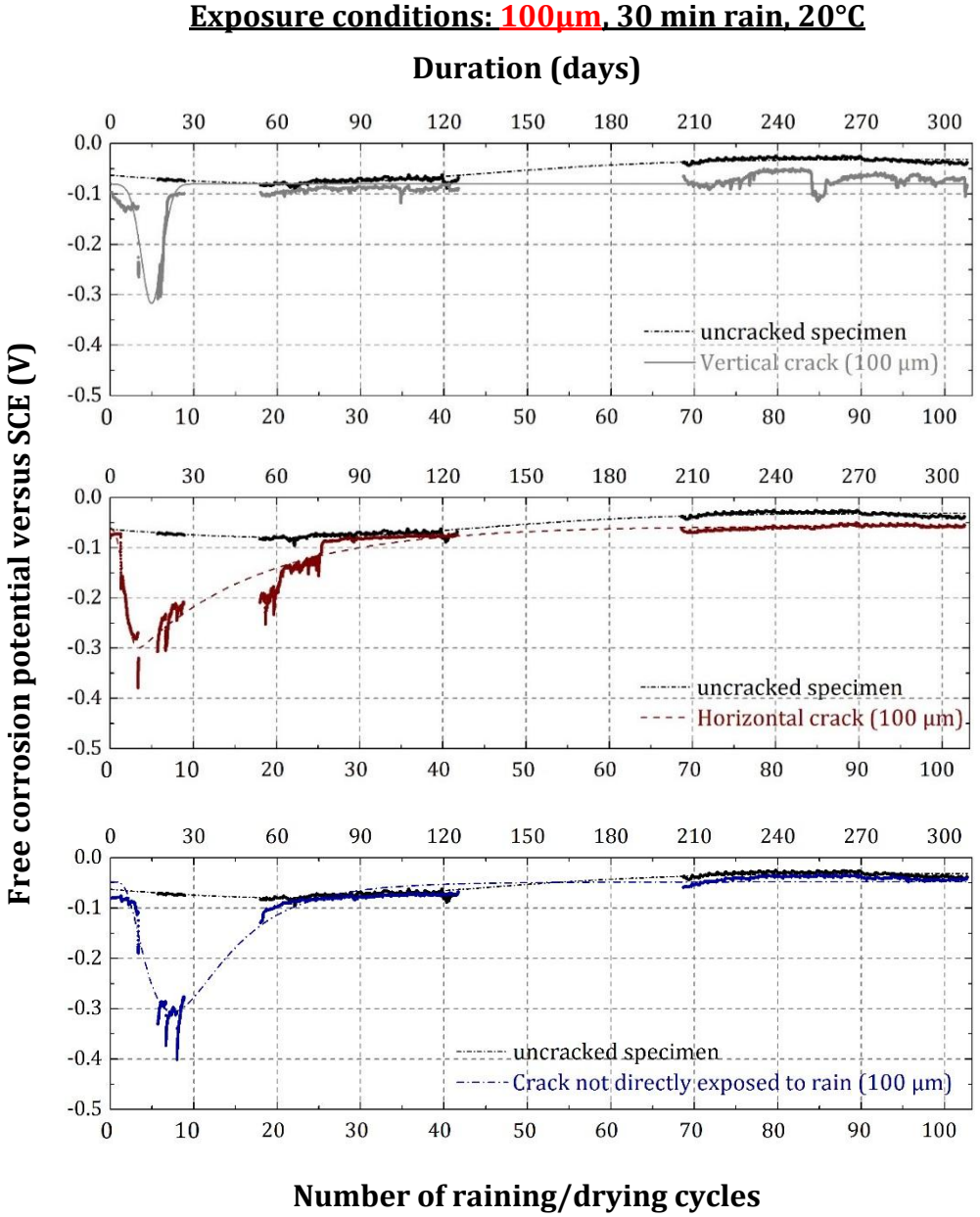

Figure 5-6: Free corrosion potential (versus SCE) measured in specimens showing 100 µm residual crack exposed in different directions with respect to rain

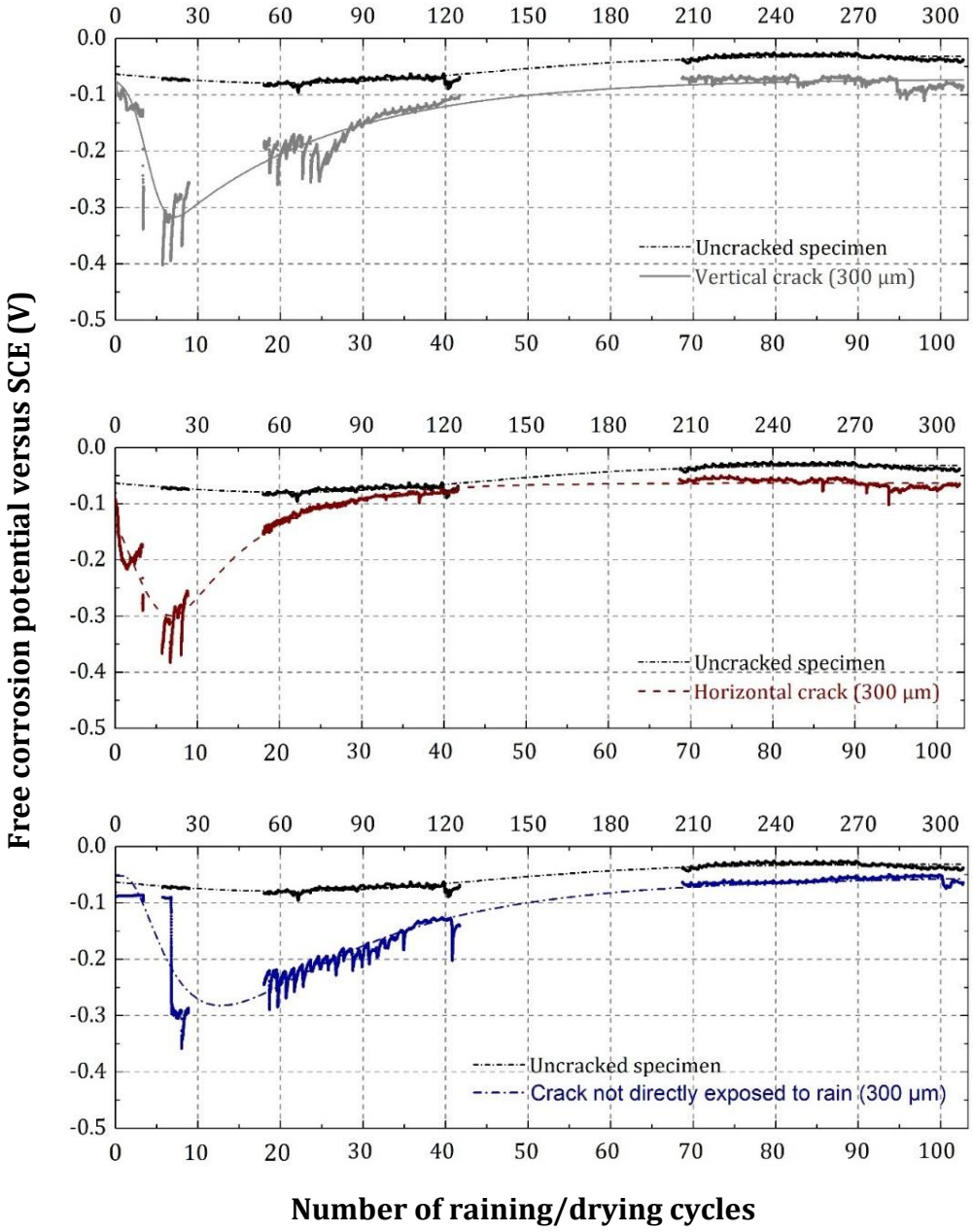

Figure 5-7: Free corrosion potential (versus SCE) measured in specimens showing 300 µm residual crack exposed in different directions with respect to rain

5.2.4 Corrosion products type

Figure 5-8 shows the corrosion layer developed along the upper part of the steel/mortar interface of specimens showing 300 µm residual crack oriented horizontally with respect to rain. Representative Raman spectra are given in Figure 5-9.

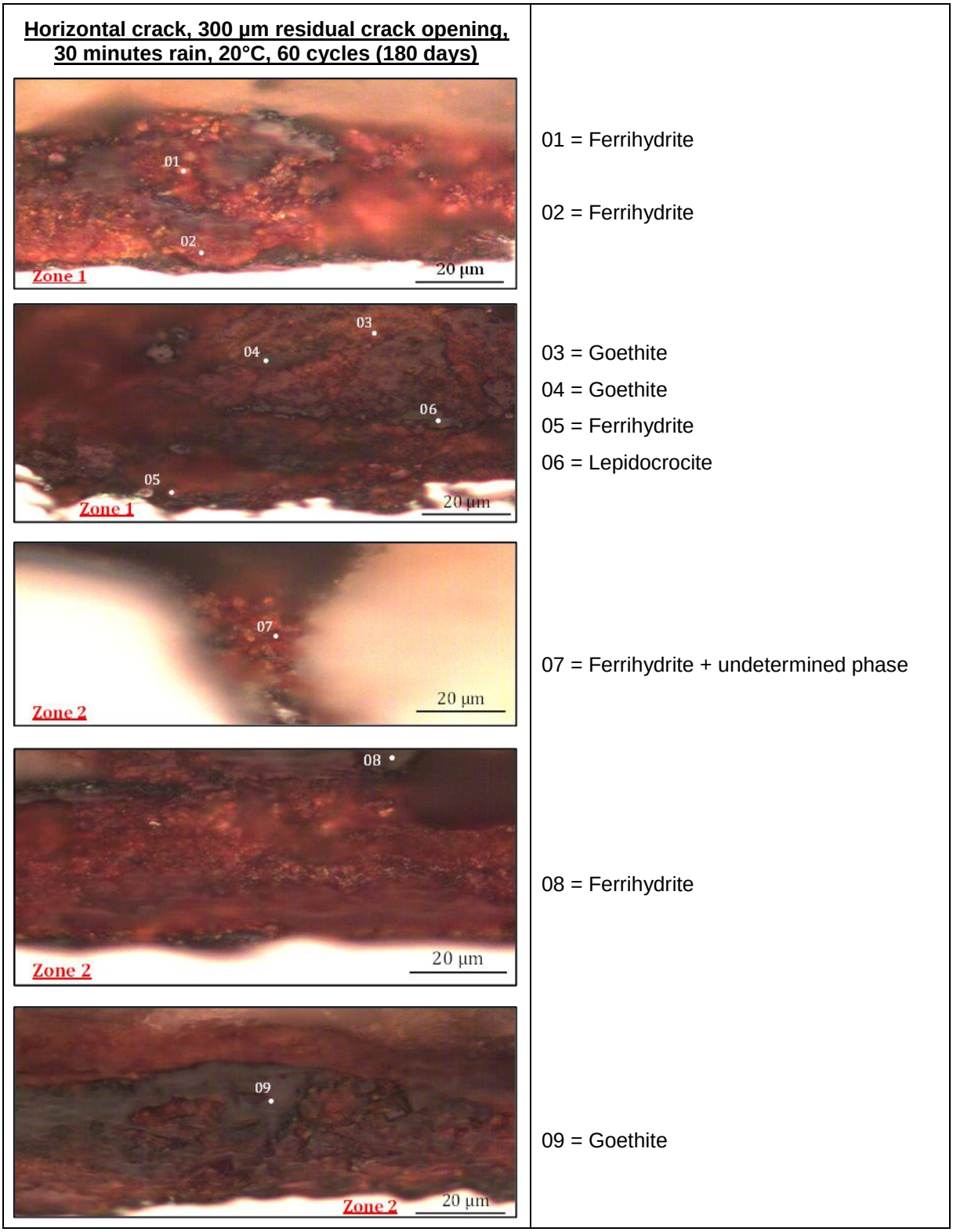

Figure 5-8: Corrosion layer observed at steel/mortar interfaces located far from the crack and deep in the crack in specimens having 300 µm crack oriented horizontally with respect to rain

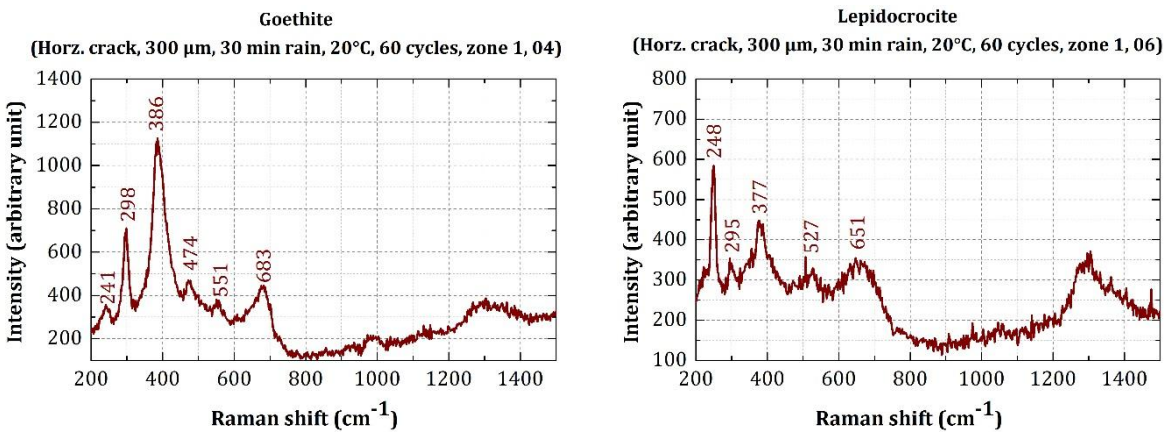

Figure 5-9: Raman spectra of corrosion products obtained on specimens having 300 µm residual crack width oriented horizontally with respect to rain

Figure 5-10 summarizes schematically the corrosion products type identified in specimens showing cracks oriented vertically and horizontally with respect to rain. The main phases identified are the ferrihydrite in addition to poorly crystallized goethite and Lepidocrocite

A comparison between the corrosion products developed in this two corrosion conditions leads to deduce that corrosion products are similar and are not impacted by the crack orientation.

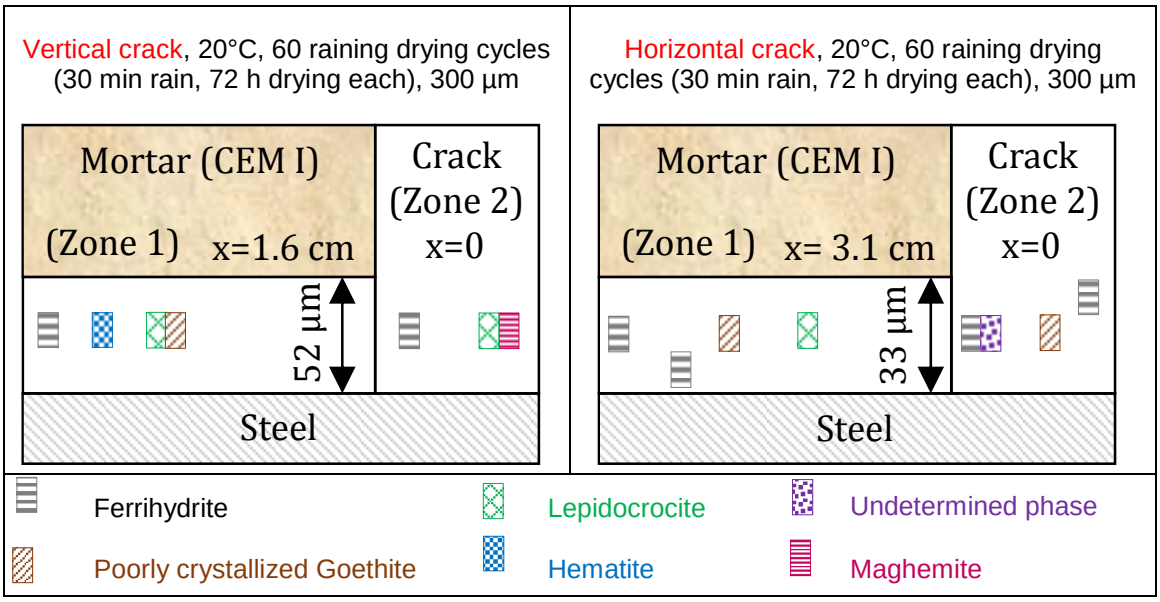

Figure 5-10: Summary of the corrosion products identified in different zones of specimens oriented differently with respect to rain

5.2.5 Discussion and conclusion

From all the above results, it can be deduced that the corrosion layer evolution is not impacted by the crack orientation. A steel repassivation is observed in the three orientations. Additionally corrosion rates decreases with raining/drying cycles for horizontally and vertically oriented cracks. Moreover, the corrosion products type is similar for both specimens tested oriented vertically and horizontally with respect to rain.

At the beginning of this study, this test was performed because it was supposed that water may accumulate deep in horizontally oriented cracks more than in vertically oriented cracks. Since the same corrosion kinetics are found for these two crack orientations, it can be deduced that the saturation and the drying rates of vertically and horizontally oriented cracks are similar for these two crack orientations. Consequently, it can be deduced that the corrosion propagation phase is not impacted by the crack orientation.

5.3 RAIN DURATION

The quantity of electrolyte in the concrete is one of the factors which control the corrosion process. Therefore in this section, the influence of rain duration on the corrosion development is tested. The first rain duration corresponds to the reference test (30 minutes raining, 72 hours drying). The second corresponds to (3 minutes raining, 72 hours drying). Additionally, some specimens are exposed continuously to 90% RH and are supposed to be representative of cooling tower's side where cracks do not receive water directly (180° side in §2.6.3.2). For the latter configuration, free corrosion potential measurements are not performed.

It should be noted that only one residual crack opening of 300 µm is chosen to be considered to test the impact of rain duration on the corrosion.

5.3.1 Distribution of the corrosion products

The average lengths of corroded steel embedded in specimens subjected to 30 and 3 minutes rain duration evolve similarly with respect to raining/drying cycles (Figure 5-11(a)). Similar observation can be noted concerning the evolution of the corrosion length over carbonation length ratios measured for these two exposure conditions (Figure 5-12(a)). In addition, the amount of the corrosion products (S) is similar between specimens subjected to 3 and 30 minutes of rain duration (Figure 5-13). In the same figure, it can be seen that corrosion length and thickness measured on the specimen exposed to 30 minutes rain are close to those measured in specimens exposed to 3 minutes rain duration. This is also the case for the other optical microscopy results obtained after a different number of raining/drying cycles (Appendix I.5.3).

The corrosion products layer developed in specimens exposed continuously to 90% RH is not similar to the one measured in specimens subjected to raining/drying cycles. In fact, the average corrosion lengths measured in the 90% RH exposure condition is higher than the one quantified in specimens subjected to raining/drying cycles (Figure 5-11(b)). The second observation noted at 90% RH is that steel does not corrode only in the zone intercepting the carbonated mortar but corrosion spreads also in the zone where mortar is not carbonated. This is illustrated in Figure 5-12(b) showing corrosion over carbonation length ratio higher than one for the 90% RH. This is inexplicable because steel intercepting a non-carbonated mortar is covered by a passive layer due to the high alkalinity of the surrounding medium and corrosion should not initiate before the depassivation of the steel. Nevertheless, it should be noted that the corrosion in this non-carbonated zone is not as dense as the one developed inside the carbonated area (Figure 5-14). A discussion about this observation is performed at the end of this section in §5.3.5. On the other hand, contrary to the corrosion length, the thickness of the corrosion products layer developed in specimens subjected to 90% RH for 180 days is lower than the one measured under raining/drying cycles conditions (Figure 5-13).

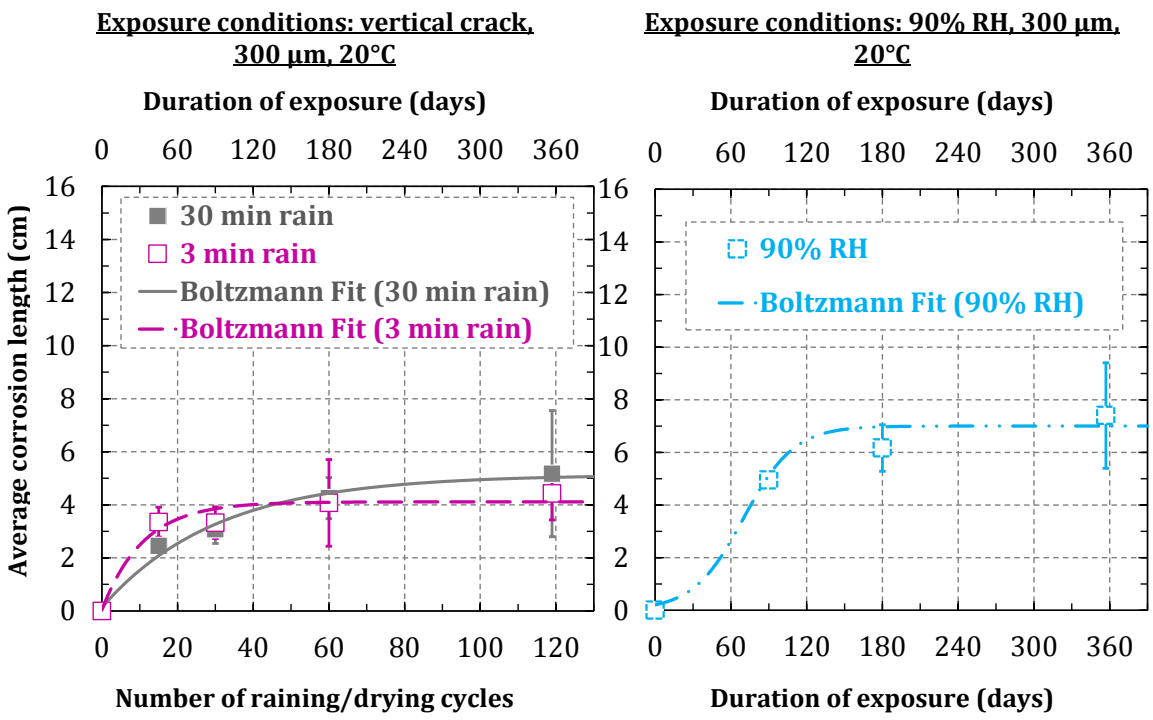

(a) (b)

Figure 5-11: Corrosion length evolution with respect to raining/drying cycles and rain durations (visual inspection)

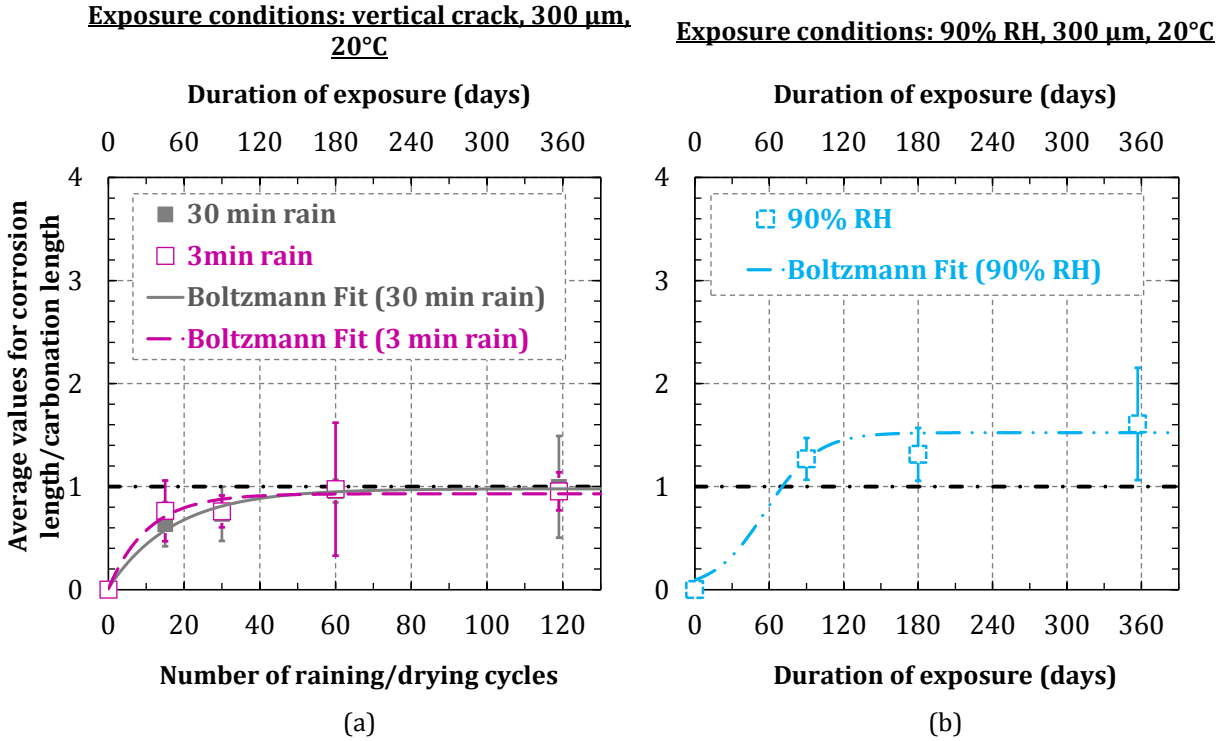

(a) (b)

Figure 5-12: Evolution of the corrosion over carbonation length ratio with respect to raining/drying cycles and rain durations (visual inspection)

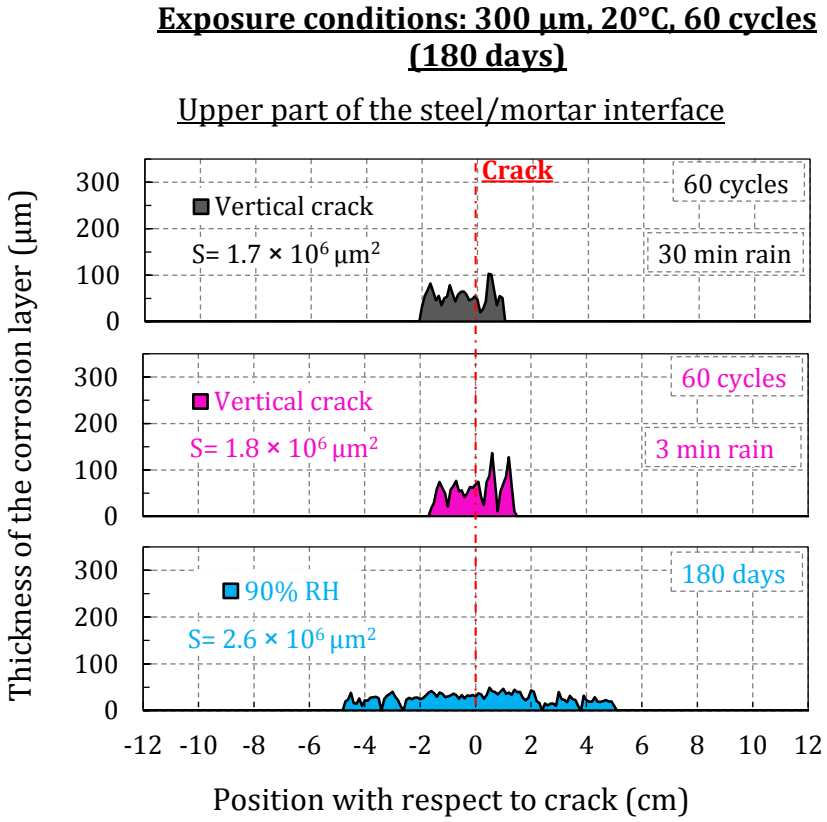

Figure 5-13: Corrosion products repartition obtained on specimens subjected to different rain durations (optical microscopy)

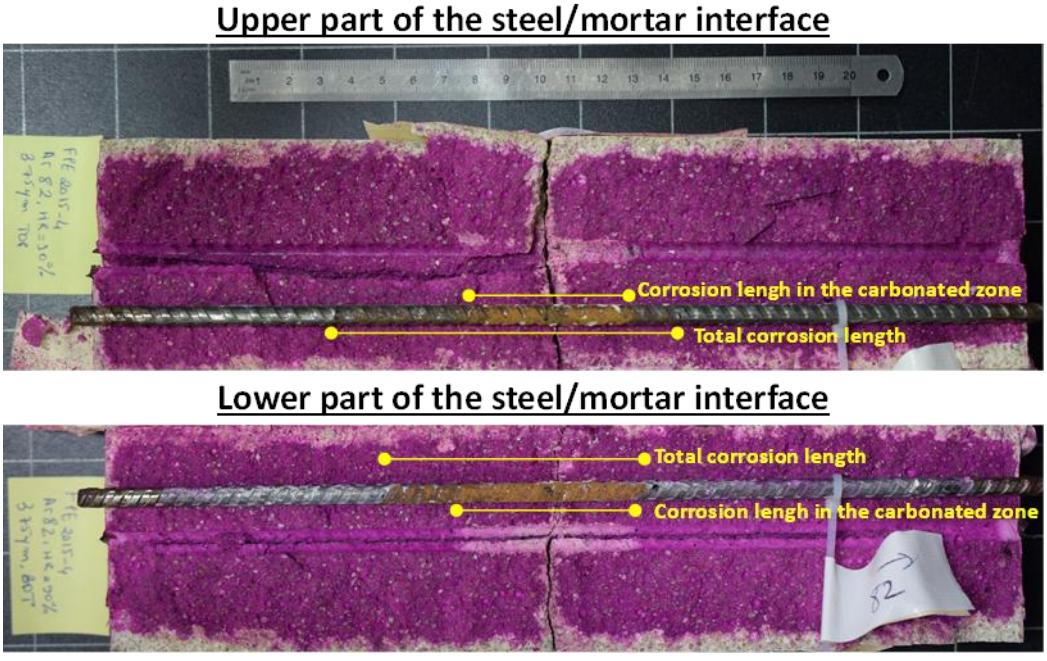

Figure 5-14: Photo comparing the steel corrosion length with the length of the carbonated steel/mortar interface for a specimen exposed 357 days at 90% RH

5.3.2 Gravimetric measurements

The evolution of the iron mass loss and the corrosion kinetics in specimens subjected to different raining durations with respect to the raining/drying cycle's number are given in Figure 5-15 (a) and Figure 5-16 (a) respectively. It is visible that the two raining durations tested (30 and 3 minutes rain) do not have any influence neither on the iron mass loss nor on the corrosion kinetics.

Figure 5-15 (b) and Figure 5-16 (b) give the evolution of the iron mass loss and the corrosion kinetics measured on specimens exposed to 90% RH respectively. It is plain to see that these curves have the same trend as the one obtained on specimens subjected to raining/drying cycles despite that these two corrosion conditions do not show similar corrosion layer distributions.

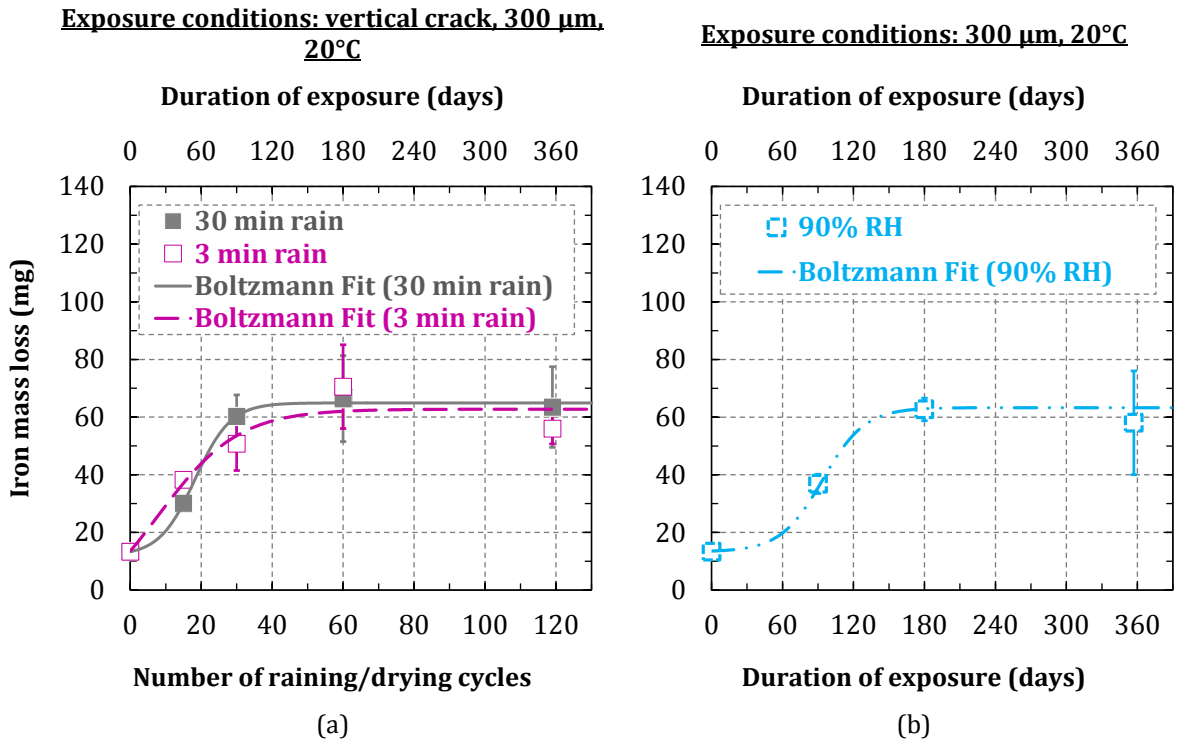

Figure 5-15: Iron mass losses in specimens subject to different durations of rainfall with respect to raining/drying cycles

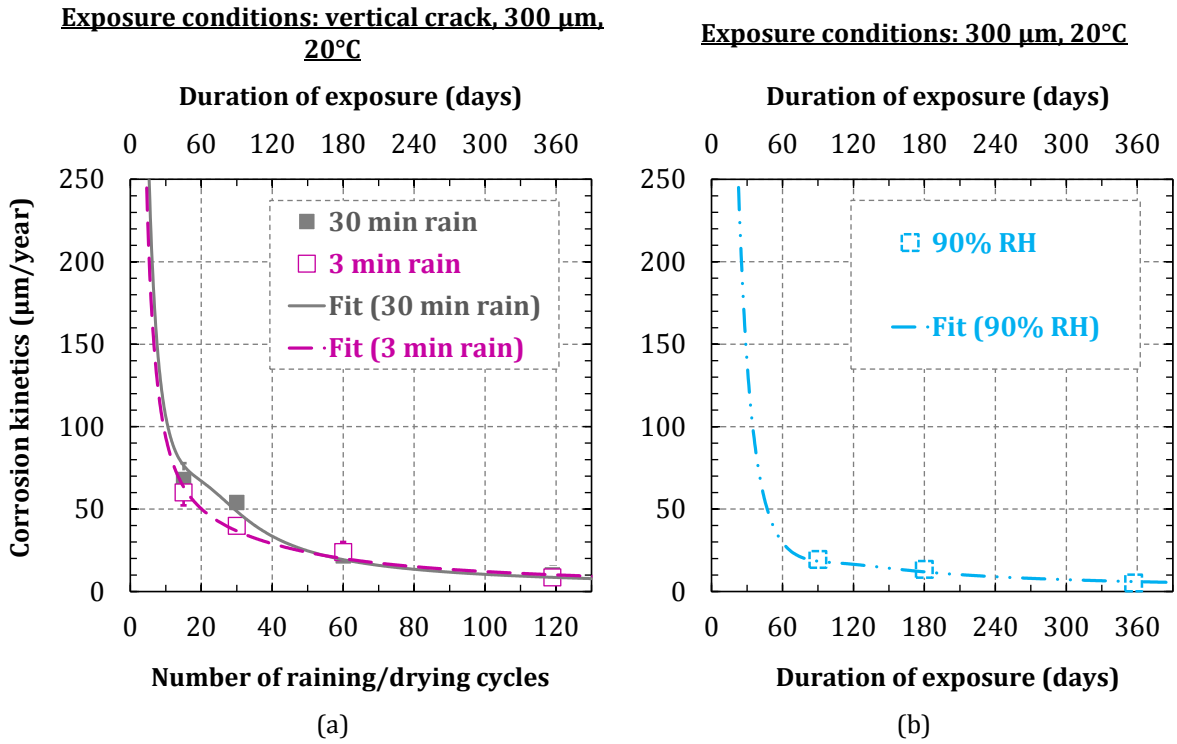

Figure 5-16: Corrosion rate evolution in specimens subject to different durations of rainfall with respect to raining/drying cycles

5.3.3 Free corrosion potential measurements

The evolution of the measured free corrosion potential for specimens having 300 µm residual crack opening and exposed to 3 and 30 minutes rain durations in each raining/drying cycle are given in Figure 5-17. The tendency of the free corrosion potential evolution is the same for the two raining durations. An increase in the recorded corrosion potential is noted after several raining/drying cycles independently from the rain duration. This could be the result of a repassivation of the corroded steel in these two corrosion conditions. This same conclusion can be drawn in specimens having 100 and 500 µm residual crack openings (Appendix I.4.2). Therefore, once again, no influence of the rain duration on the corrosion evolution is noted.

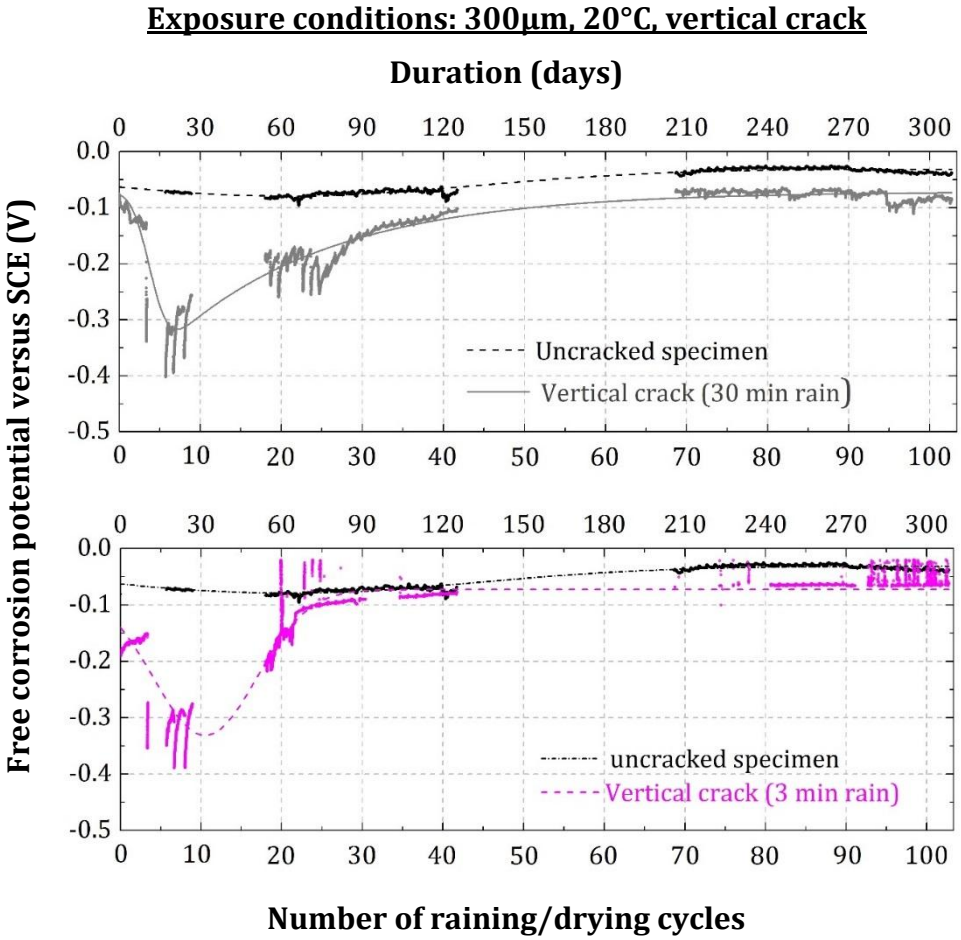

Figure 5-17: : Free corrosion potential (versus SCE) measured in specimens showing 300 µm residual crack width and exposed to different raining durations

5.3.4 Corrosion products type

The corrosion layers developed along the upper part of the steel/mortar interface of specimens showing 300 µm residual crack exposed to 3 min rain and 90% RH are given in Figure 5-18 and Figure 5-19 respectively. Some Raman spectra are given in Figure 5-20 and Figure 5-21 for the 3 min rain and 90% RH conditions respectively.

Figure 5-22 summarizes the corrosion products type developed under different raining duration. In this figure, it can be seen that mostly reactive phases are developed in 30 minutes rain duration and 90% RH conditions. However, for the small rain duration (3 minutes rain), less reactive phase are detected (well crystallized goethite [196]) .

Vertical crack, 300 µm residual crack opening, 3 minutes rain, 20°C, 60 cycles (180 days)

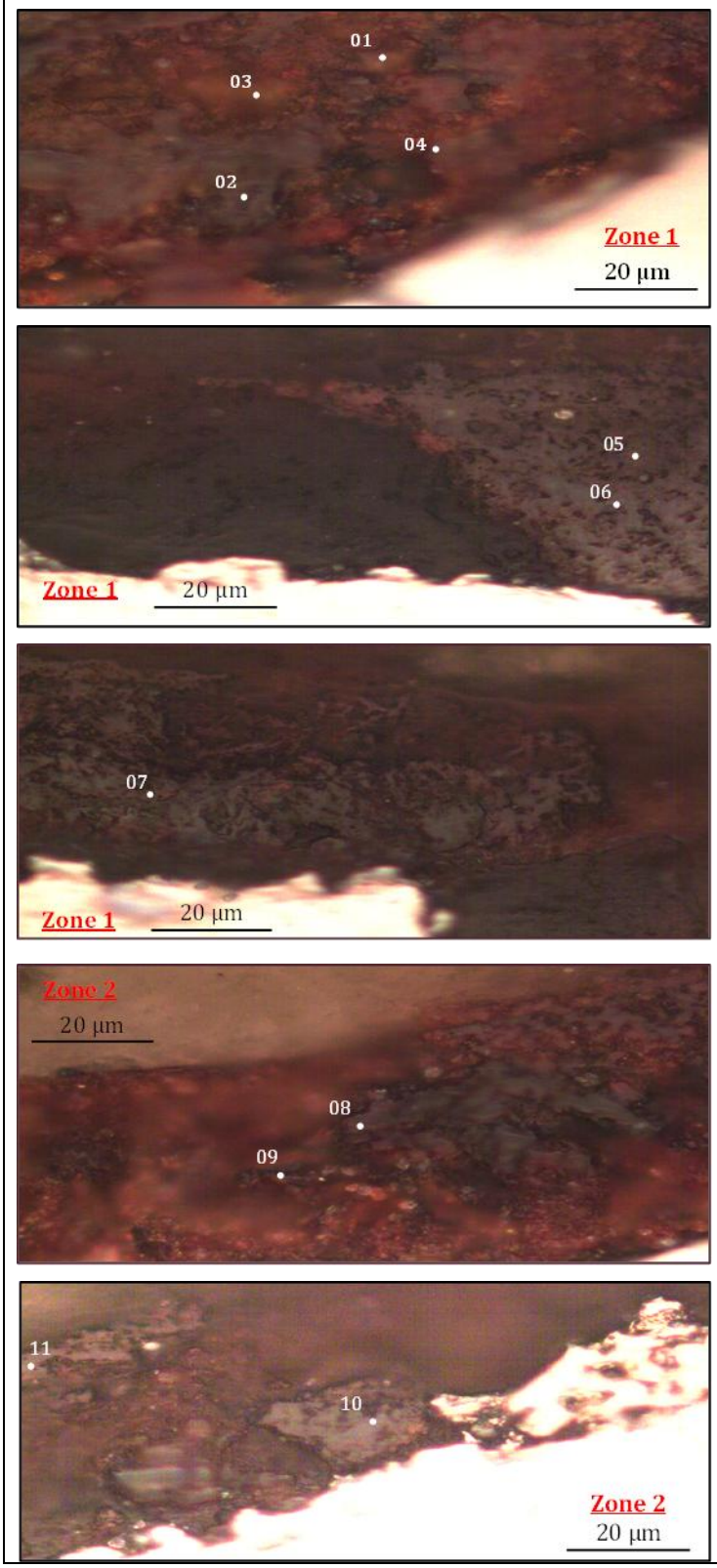

01 = Ferrihydrite + Goethite (well crystallized)

02 = Ferrihydrite + Goethite (well crystallized)

03 = Goethite (well crystallized)

04 = Goethite + Ferrihydrite

05 = Lepidocrocite + Goethite (well crystallized)

06 = Ferrihydrite + Goethite (well crystallized)

07 = Goethite + Ferrihydrite

08 = Ferrihydrite + undetermined phase

09 = Ferrihydrite + possible presence of Goethite

10 = Goethite + Ferrihydrite

11 = Lepidocrocite + Ferrihydrite

Figure 5-18: Corrosion layer observed at steel/mortar interfaces located far from the crack and deep in the crack in specimens having 300 µm residual crack width and exposed to 3 minutes rain in each raining/drying cycle.

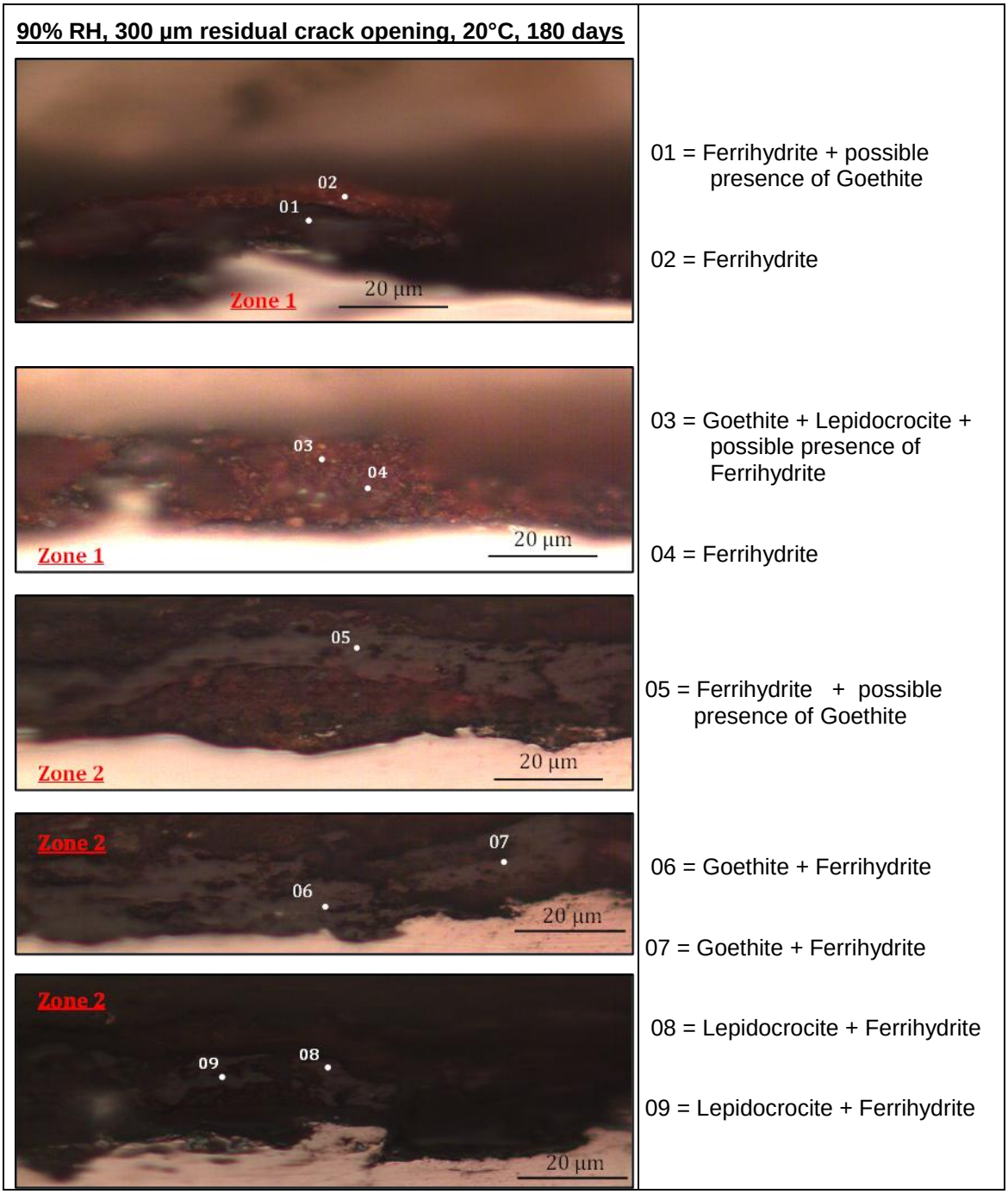

Figure 5-19: Corrosion layer observed at steel/mortar interfaces located far from the crack and deep in the crack in specimens having 300 µm residual crack width and exposed continuously to 90% RH.

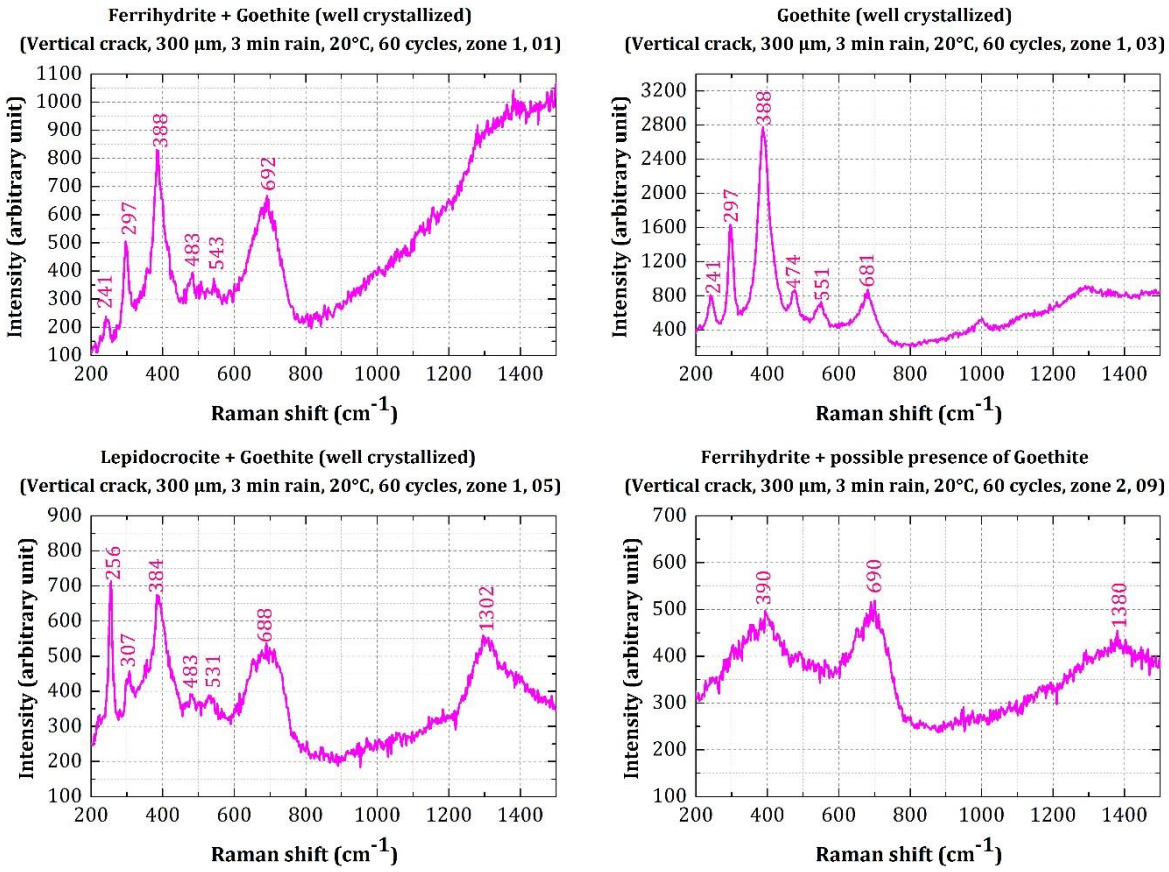

Figure 5-20: Raman spectra of corrosion products obtained on specimens having 300 µm residual crack width and subjected to 3 minutes rain at each raining/drying cycle.

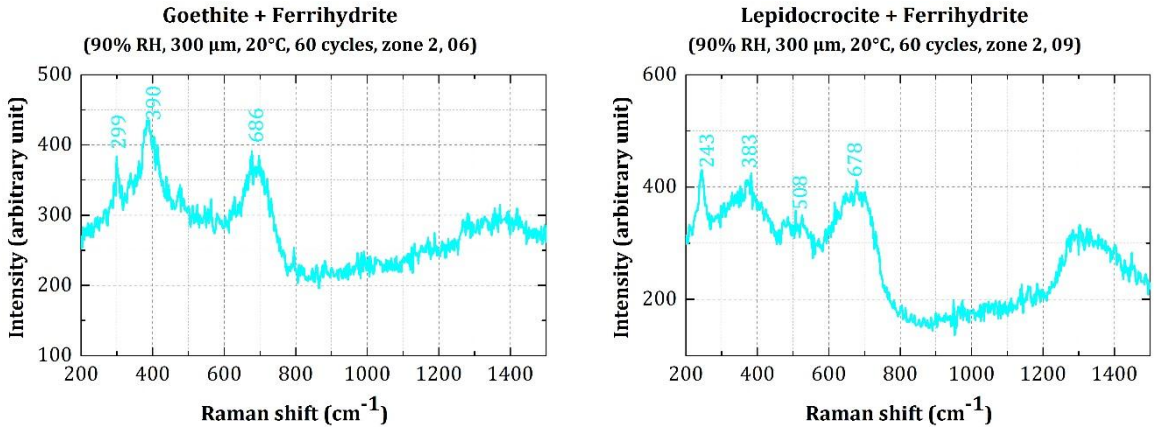

Figure 5-21: Raman spectra of corrosion products obtained on specimens having 300 µm residual crack width and subjected continuously to 90% RH

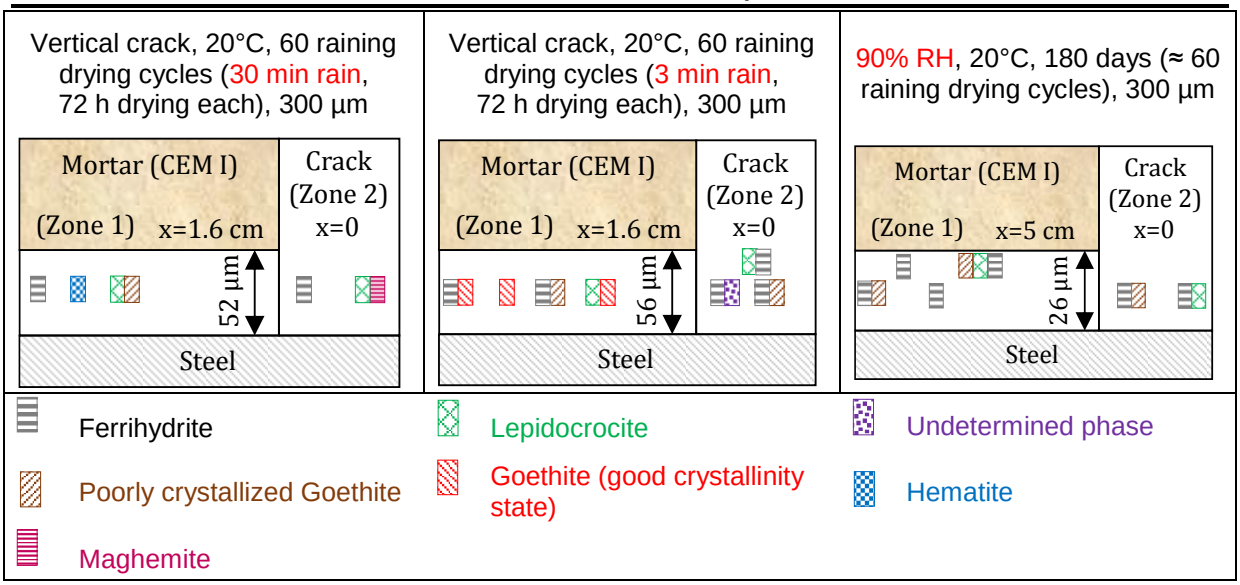

Figure 5-22: Summary of the corrosion products identified in different zones of specimens subjected to different rain durations

5.3.5 Discussion and conclusion

In this section, the influence of the rain duration on the corrosion development is experimented. The results indicate that the same corrosion products layer distribution (corrosion length, corrosion over carbonation length ratios, corrosion thickness) and the same gravimetric measurements (iron mass loss and corrosion kinetics) are visible for the two tested rain durations (30 and 3 minutes rain at each raining/drying cycle). Moreover, for this two exposure conditions, the same tendency for the free corrosion potential measurements is also observed. Thus, one can deduce that the corrosion development is similar between the two raining durations.

In fact, cracks are rapidly filled with water during the raining phase. Therefore, the iron oxidation is possible to occur for the both tested raining durations. On the other hand, independently from the raining duration, moist concrete is able to behave as an electrolyte allowing thus the transfer of hydroxyl ions from the passive zone (cathode) to the carbonated zone (anode). Consequently, the macrocell corrosion process that dominate during the first 30 raining/drying cycles (§4.4) is able to occur independently from the rain duration. In addition, during the second corrosion phase, it is proven that corrosion products seal the crack and limit the access of water to the rebar. This occurs for the two tested rain durations and may mask the influence of the raining/drying cycles on the corrosion process in this second phase also.

For all these reasons, the rain duration does not impact the whole corrosion process.

A third exposure condition is tested in this section and corresponds to specimens exposed continuously to 90% RH. The corrosion length developed under this condition is higher than the one developed under raining/drying cycles and higher than the carbonation length measured along the steel/mortar interface of these specimens. However, the thickness of the corrosion products layer is lower than the one measured under raining/drying cycle's exposure condition. Despite these differences, the iron mass loss and the corrosion kinetics values under 90% RH are close to those obtained for specimens subjected to raining/drying cycles.

Concerning the corrosion over carbonation ratio higher than one, one possible hypothesis is that the corrosion products visible in the non-carbonated area corresponds to a corrosion deposition and not to real corrosion with iron mass loss. If this hypothesis is right, no loss in the steel section should be encountered in the corroded zone intercepting a non-carbonated mortar. Figure 5-23 shows optical microscopy photos taken at different distances from the crack (x in cm). Figure 5-23 (a) corresponds to corroded steel in a non-carbonated zone. Figure 5-23(b) corresponds to non-corroded steel and Figure 5-23 (c) corresponds to the corroded steel developed in the carbonated zone. A loss in the steel cross section is visible for the two corroded zones either intercepting a carbonated mortar or intercepting a non-carbonated mortar. The non-corroded steel does not show loss in the steel cross section. Therefore, it can be concluded that the corrosion in the non-carbonated mortar results from electrochemical reactions and is not a simple deposit of corrosion products.

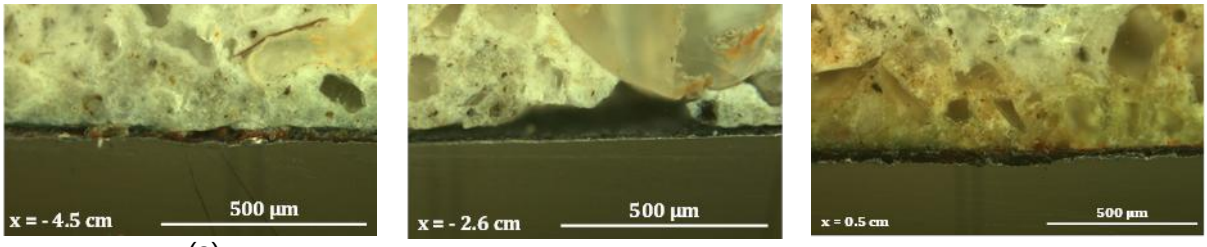

(a) (b) (c)

Figure 5-23: Loss section in the steel at different distances from the crack in a specimens exposed continuously to 90% RH for 180 days (optical microscopy)

An hypothesis is proposed thereafter in order to understand the phenomenon that could happen at 90% RH and lead to a corrosion over carbonation length ratio higher than 1. After a certain exposure duration at 90% RH, the saturation degree should almost be the same along the entire length of the rebar which is not the case for specimens subjected to raining/drying cycles. In addition, according to several studies ([201]–[203]) summarized in [204], the coefficient of diffusion of dissolved ions increases with the increase in the saturation degree. Consequently, the high saturation degree of specimens exposed to 90% RH may increase the diffusion of the dissolved hydroxyl ions from the cathodic area to the anodic area where they will be consumed by the iron ions. Therefore, at the extremities of the carbonated area (anodic zone), a high amount of hydroxyl may be consumed rapidly leading to a small decrease in the pH of the medium. This decrease may not be detectable by the phenolphthalein pH indicator test for two reasons. The first reason corresponds to the accuracy of the phenolphthalein test discussed in §4.2.2. The second reason is that the pH may decrease but remain higher than 9 which can not be detectable by the phenolphthalein test. Consequently, due to the slight decrease in the pH at the extremities of the carbonated zone, the rebar may lose its passivity and may corrode for a greater length than the initially carbonated area. It should not be forgotten that the corrosion products formed outside the initially carbonated area are not very dense (Figure 5-14). This indicates that the kinetics of corrosion in this zone is small which justify the non-detection of its influence on the corrosion

kinetics curve (Figure 5-16 (b)). The similarity in the mass losses determined in specimens exposed to 90% RH and subject to raining/drying cycles (Figure 5-15) may be due to the fact that under raining/drying cycles, the iron dissolution may be more active deep in the crack (higher amount of water) while in the 90% RH condition, the iron dissolution is similar in all the carbonated area due to a probable uniformity in the saturation degree.

Despite the fact that the corrosion evolution is shown to be similar in specimens subjected to 3 min rain and 30 min rain at each raining/drying cycles, the corrosion products type identified in the exposure condition corresponding to raining/drying cycles having 3 minutes rain and 72 hours drying are different than those detected in the two other exposure conditions tested in this study (continuous exposure to 90% RH, 30 minutes rain exposure at each raining/drying cycles). Figure 5-22 summarizes the corrosion products type developed under these three exposure conditions. In this figure, it can be seen that mostly reactive phases are developed in 30 minutes rain duration and 90% RH conditions. However, for the small rain duration (3 minutes rain) and far from the crack position, a less reactive phase are detected (well crystallized goethite). While, deep in the crack of specimens subjected to (3 minutes rain), a reactive phases are detected.

The corrosion products are exposed to water for a higher duration in the 30 minutes condition than in the 3 minutes rain condition. Moreover, the relative humidity inside the specimens exposed continuously to 90% RH is higher than its value inside specimens receiving 3 minutes of water each 3 days (72 hours). Therefore, it can be deduced that the stability of the corrosion products is dependent from the rain duration phase.

At 30 minutes rain, water reaches the rebar in a zone located far from the crack and a rust reduction from Fe(III) to Fe(II) may occur. While, at 3 minutes rain, the access of water to the zone far from the crack may be lower than at 30 minutes rain especially after the development of corrosion in the crack tip. This will ensure to amorphous corrosion products developed in these zones at 3 minutes rain the suitable conditions to dehydrate and recrystallized to a more crystallized phase. However, this is not the case for corrosion products developed deep in the crack of specimens exposed to 3 minutes rain because they are directly exposed to water at each raining/drying cycles.

At 90% RH, the saturation degree of the mortar surrounding the rebar is high and this inhibit the recrystallization of amorphous phases into other phases having a high crystallinity state. This could explain the detection of reactive phases in specimens subjected continuously to 90% RH.

These observations are consistent with the hypothesis suggested by Antony et al. [194], [195] saying that the reactivity is dependent from synthesis protocol that may lead to different grain sizes and crystallinity states. Authors indicate that the poorly crystallized goethite obtained from the precipitation and oxidation of Fe(II) to Fe(III) shows a higher reactivity than the well crystallized one formed from direct precipitation of Fe(III). Moreover, Monnier et al. [196] shows that the specific surface of the well crystallized goethite is 9 times lower than the poorly crystallized goethite. They add that the grain size diameter of poorly crystallized goethite is lower than the grain size diameter of a well crystallized goethite. They confirm that different factors may influence the chemical stability of the corrosion products like the grain size and the crystallinity.

5.4 TEMPERATURE

The influence of the temperature on the carbonation-induced corrosion in cracked specimens is tested in this section. Specimens showing 100 µm and 300 µm residual crack openings are subjected to corrosion at 40°C under raining drying cycles of 30 min rain each. Conclusions are drawn by comparing results obtained at 40°C with the one obtained in the reference test performed at 20°C.

5.4.1 Distribution of the corrosion products

This section discusses the results concerning the length of the corrosion products layer, its evolution with respect to the length of the carbonated steel/mortar interface and its thickness.

The evolution of the corrosion products layer length and the corrosion over carbonation length ratio with respect to the number of raining/drying cycles performed at 20°C and 40°C on specimens showing two residual crack openings (100 µm and 300 µm) are given in Figure 5-24 and Figure 5-25 respectively. The length of the corrosion products layer is higher at 40°C than 20°C either for 100 µm or 300 µm cracks. Additionally, for specimens corroded at 40°C, the length of the corrosion products layer is higher than the length of the carbonated steel/mortar interface. Nevertheless, after 119 raining/drying cycles, this observation does not remain valid and the corrosion over carbonation length ratio is lower than 1 for the two residual crack openings (Figure 5-25). This fact illustrates the big discrepancy observed in this condition. Rebars corroded at 40°C condition and showing the biggest corrosion length are shown in Figure 5-26. In the same figure, the length of the carbonated interface in each specimen is also visible. According to Figure 5-26, the corrosion layer appearance is uniform in the carbonated and the non-carbonated interface contrary to the 90% RH condition (Figure 5-14). The corrosion over carbonation length ratio higher than one is an unpredictable result and will be discussed later (§ 5.4.4).

The thickness of the corrosion products layer with respect to crack is given in Figure 5-27 for specimens corroded at 40°C and 20°C temperature (60 cycles). Optical microscopy results obtained after 15 and 30 raining/drying cycles are not given in this chapter but can be found in the (Appendix I.5.4). It can be seen in Figure 5-27 that the amount of corrosion products developed under 40°C temperature is higher than the one developed under 20°C for both tested residual crack openings, due to a bigger corrosion length and not to a difference in the corrosion thickness (Figure 5-27). These observations remains valid for optical microscopy analysis performed after a different number of raining/drying cycles (Appendix I.5.4).

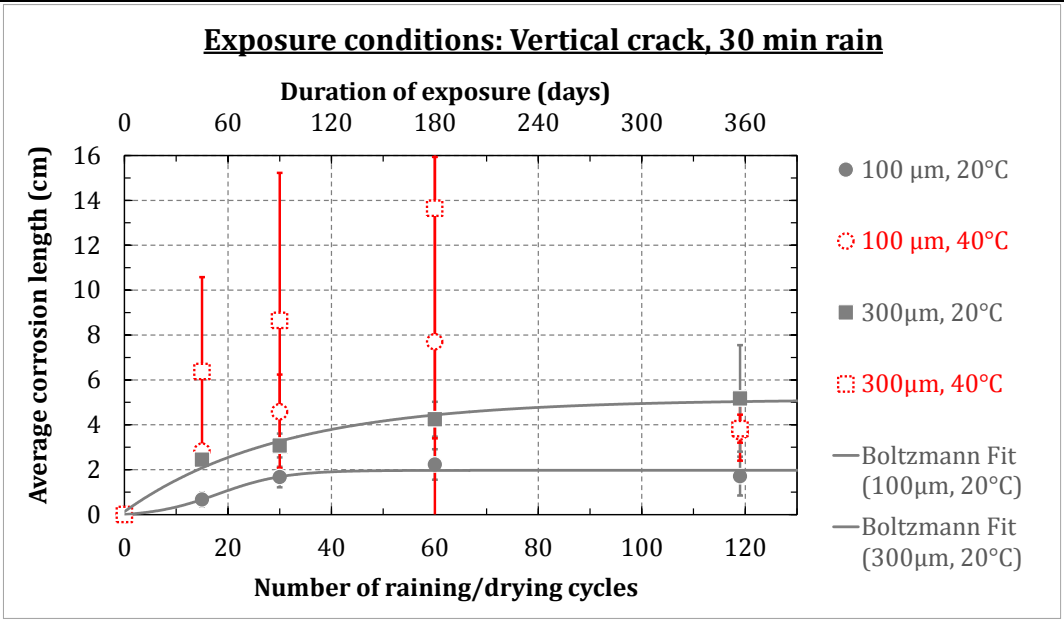

Figure 5-24: Corrosion length evolution with respect to raining/drying cycles and different temperatures (visual inspection)

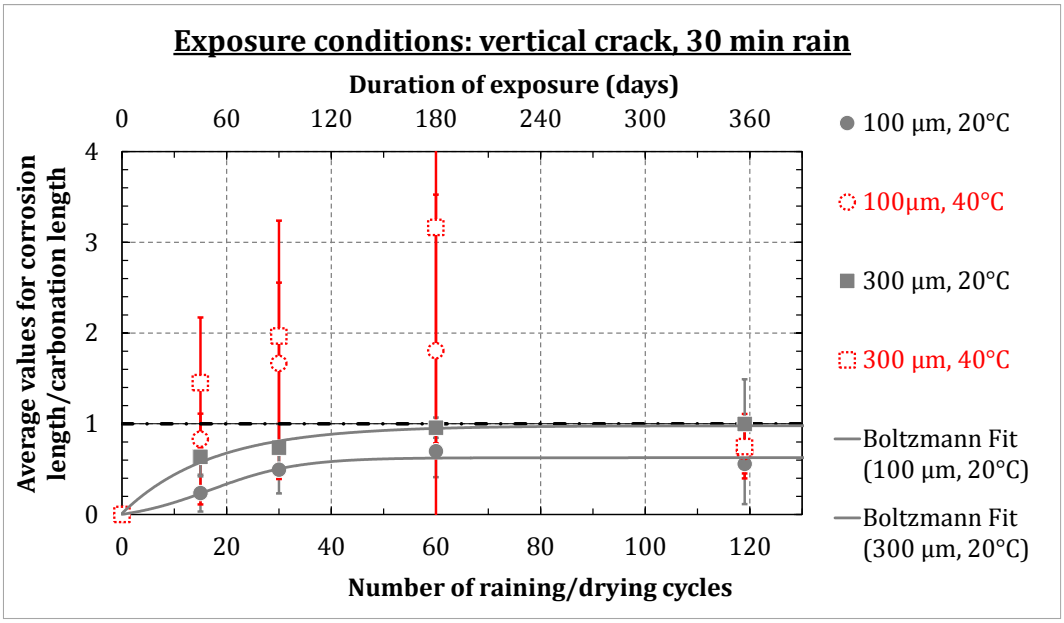

Figure 5-25: Evolution of the corrosion over carbonation length ratio with respect to raining/drying cycles and different temperatures (visual inspection)

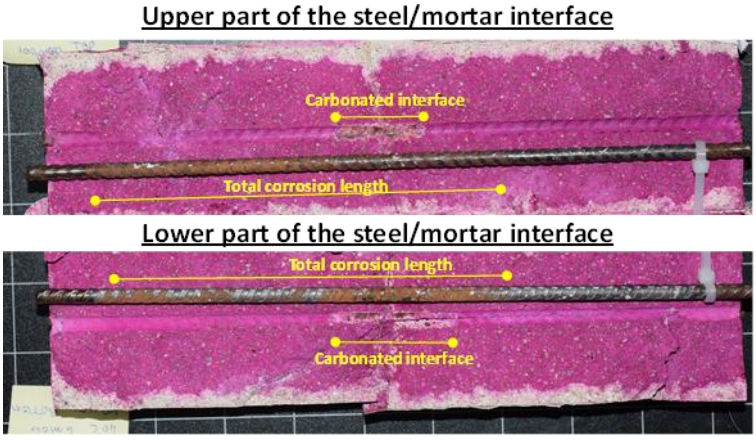

(a): W_r= 100 µm

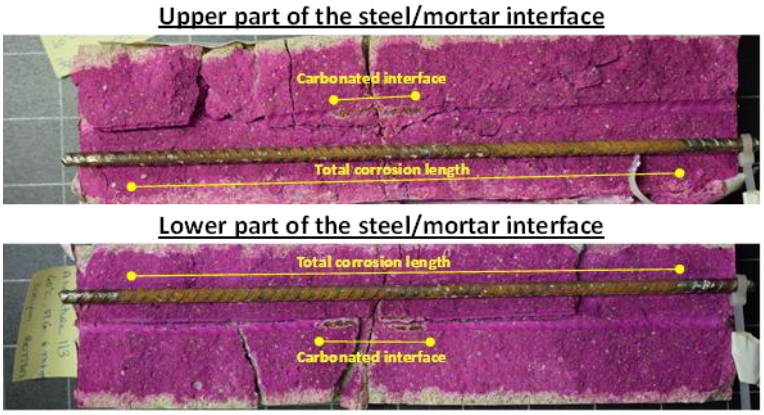

(b): W_r = 300 µm

Figure 5-26: Photo comparing the steel corrosion length with the length of the carbonated steel/mortar interface for a specimen exposed to 60 raining/drying cycles at 40°C

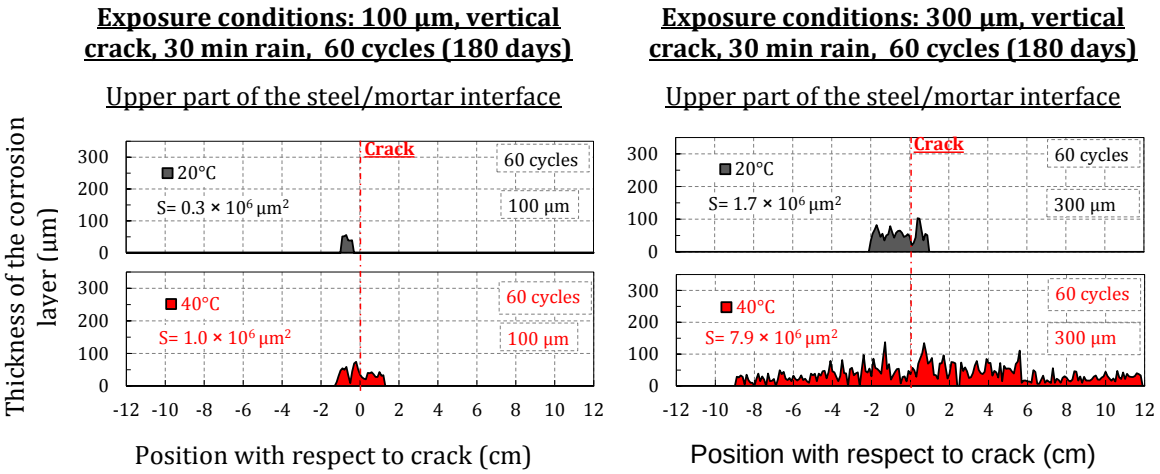

Figure 5-27: Corrosion products repartition obtained on specimens subjected to different temperatures (optical microscopy)

5.4.2 Gravimetric measurements

The evolution of the iron mass loss and corrosion kinetics measured in specimens subjected to raining/drying cycles under different temperatures and showing different residual crack openings are examined in this section.

The iron mass losses increase with the residual crack opening and with the number of raining/drying cycles and tends to stabilize after a certain number of cycles for the two temperatures tested: 40°C and 20°C (Figure 5-28). However, the iron mass loss measured in the specimens corroded at 40°C is higher than the one measured in specimens corroded at 20°C.

Iron mass losses measured on specimens corroded at 40°C temperature decrease between 60 and 119 cycles especially for specimens showing 300 µm residual crack opening. This decrease corresponds very well to that of observed in the measured corrosion lengths (Figure 5-24).

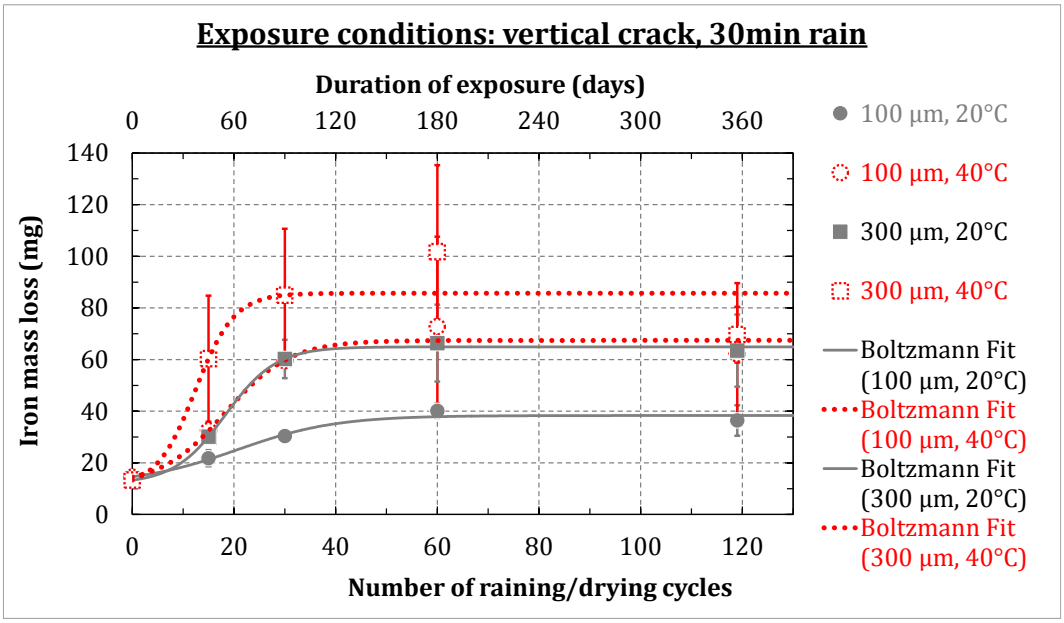

Figure 5-28: Iron mass losses in specimens subjected to different temperatures during the corrosion test and showing two different residual crack openings

The corrosion kinetics measured on specimens showing 100 µm and 300 µm residual crack openings and exposed to raining/drying cycles at different temperatures are given in Figure 5-29 and Figure 5-30 respectively. Corrosion kinetics measured at 40°C are close to those measured at 20°C and at both temperature a decrease in the corrosion kinetics can be noted.

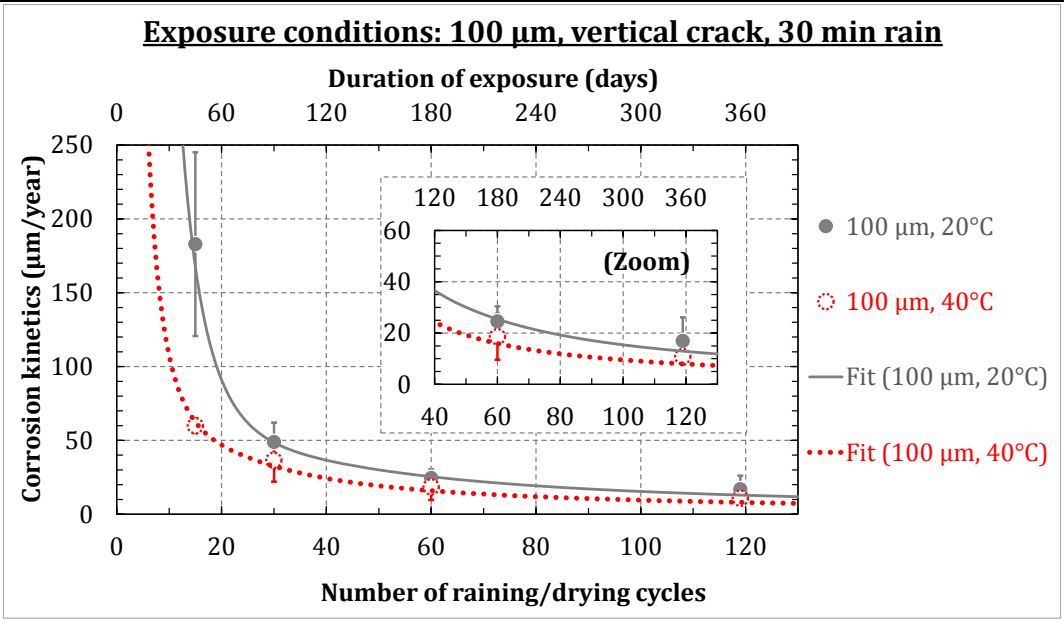

Figure 5-29: Corrosion rate evolution in specimens subjected to different temperatures during the corrosion test and showing 100 µm residual crack opening

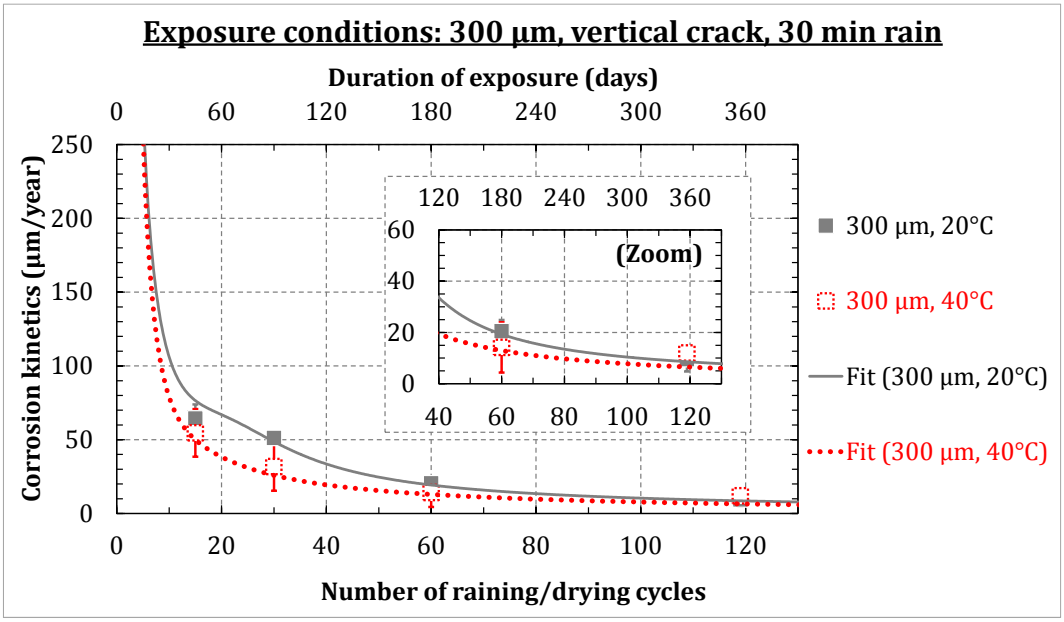

Figure 5-30: Corrosion rate evolution in specimens subjected to different temperatures during the corrosion test and showing 300 µm residual crack opening

5.4.3 Corrosion products type

The corrosion products are analyzed on a specific specimen showing 300 µm residual crack opening corroded at 40°C temperature (Figure 5-27). This specimen is chosen because it shows corrosion products on the steel intercepting the non-carbonated interface. This allows to determine whether these corrosion products have the same nature as the one developed in the steel intercepting the carbonated interface. Figure 5-31 presents the corrosion layer and the corresponding nature of the corrosion products developed deep in the crack (i.e. in

the carbonated interface). Figure 5-32 give some Raman spectra obtained in both zones tested: deep in the crack and far from the crack (i.e. non-carbonated interface). Figure 5-33 summarizes the corrosion products found in these two zones. It can be concluded that the corrosion products developed in the steel intercepting the non-carbonated interface are similar to those developed deep in the carbonated interface.

Ferrihydrite exists also in the corrosion products developed under the corrosion test realized at 40°C temperature. Moreover, a well crystallized goethite is detectable under this corrosion condition at both analyzed zones. It should be pointed out that this phase was not found in the corrosion products developed in specimens corroded in the reference test. This is consistent with the observation noted in §5.3.5 highlighting that well crystallized goethite appears for the low saturation degree (3 min rain). Moreover, at 40°C, the drying phase is aggressive which will enable recrystallization of amorphous phase into more crystallized one.

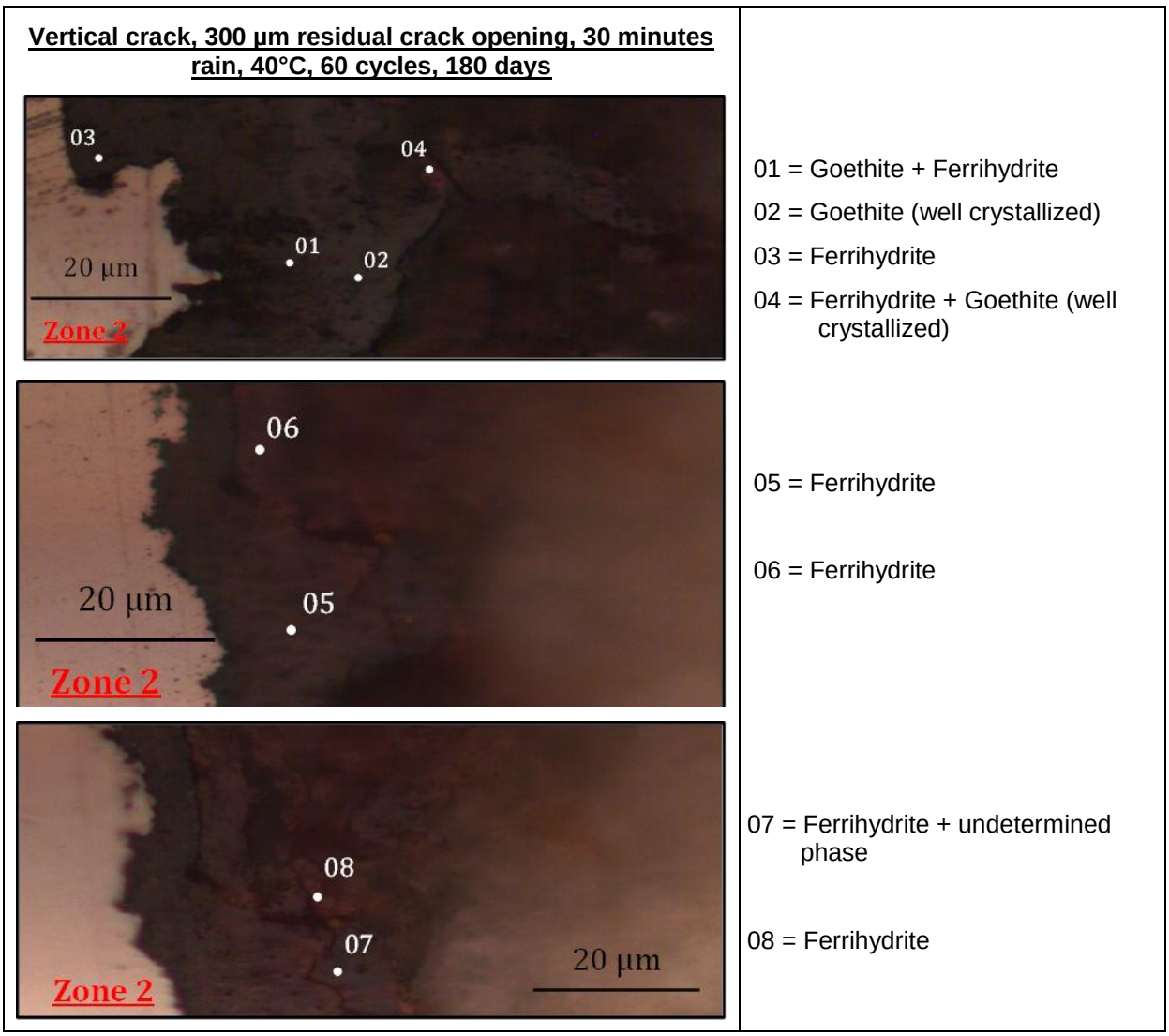

Figure 5-31: Corrosion layer observed at steel/mortar interface located deep in the crack in a specimen having 300 µm residual crack width and corroded under raining/drying cycles at 40°C

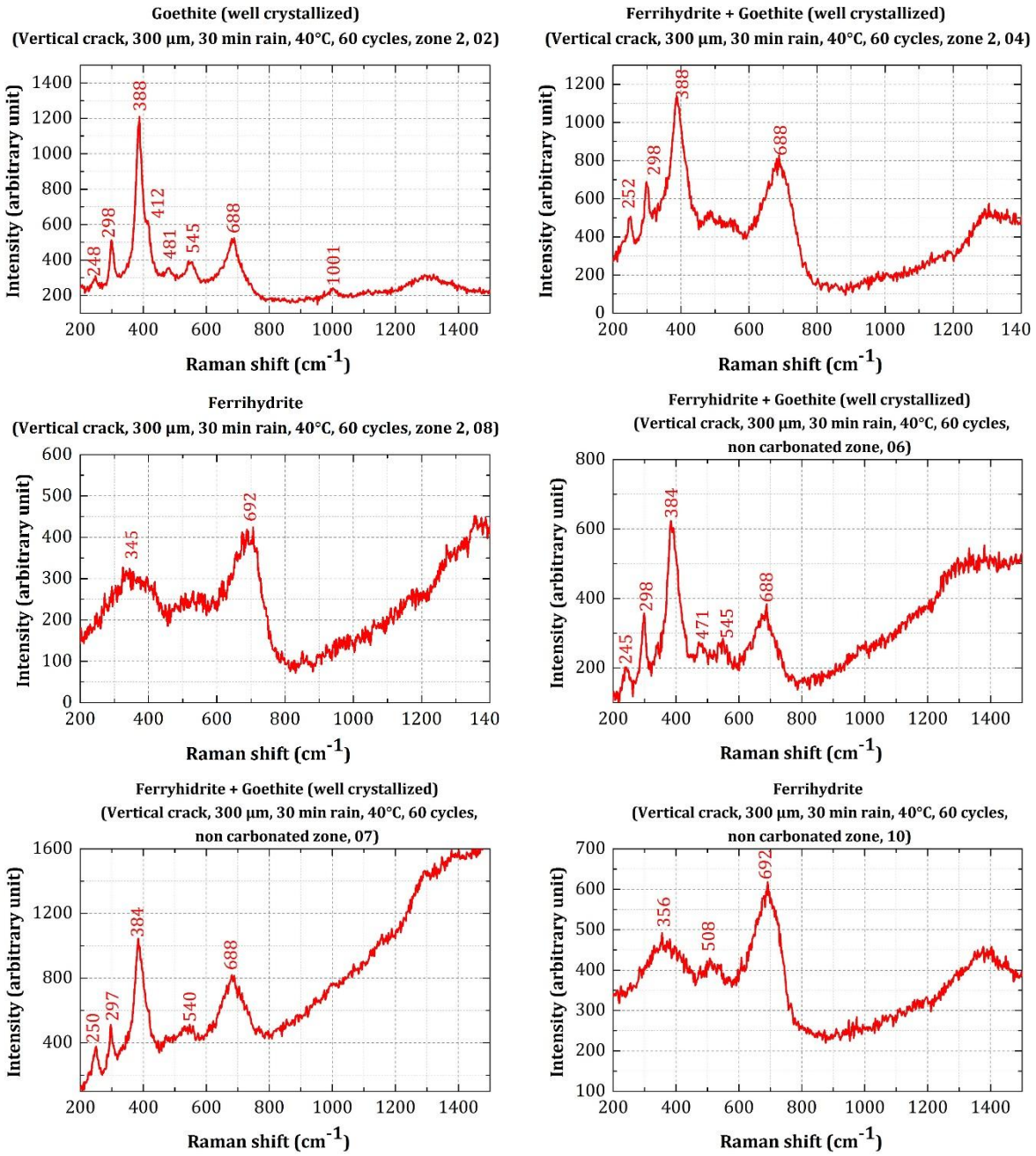

Figure 5-32: Some Raman spectra of corrosion products obtained on specimens having 300µm residual crack width corroded at 40°C under raining/drying cycles of 30 minutes rain each.

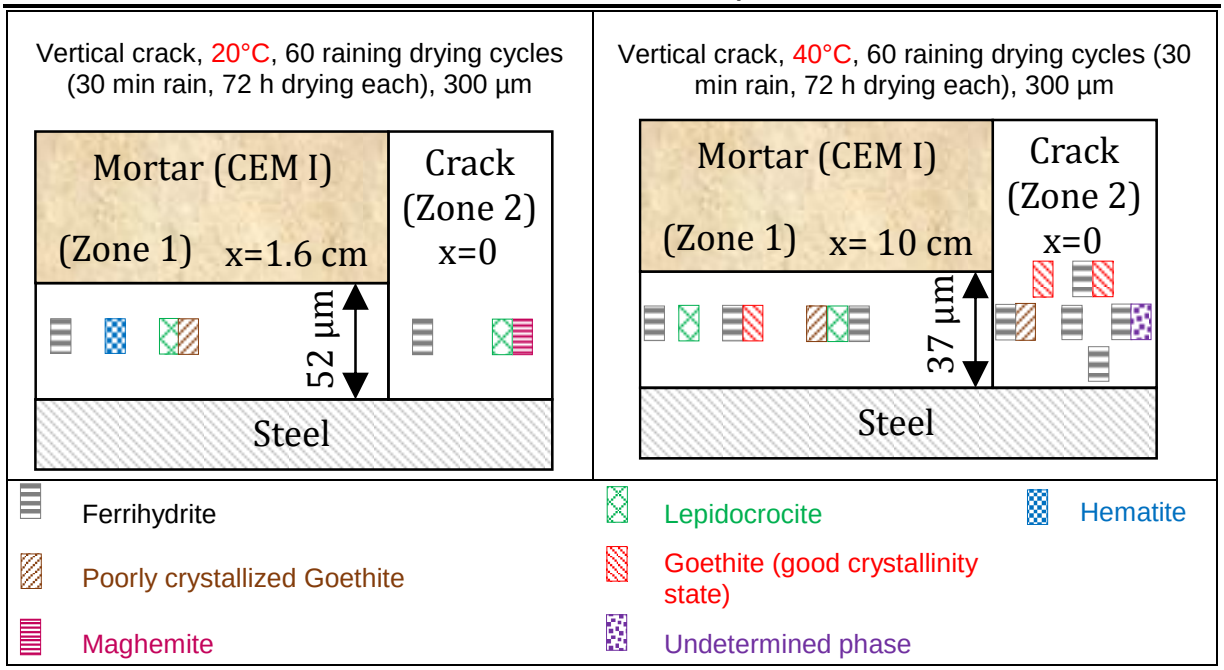

Figure 5-33: Summary of the corrosion products identified in different zones of specimens subjected to raining/drying cycles at different temperatures

5.4.4 Discussion and conclusion

The aim of this section is to test the influence of the temperature on the corrosion development (20°C and 40°C). The results indicate that the corrosion lengths and the iron mass losses increase with temperature independently from the crack opening tested. The corrosion kinetics deduced from these two measurements decreases with the number of raining/drying cycles and is close to the one measured in specimens corroded in the reference test at 20°C for 100 and 300 µm residual crack openings.

Accordingly to Arrhenius law, the increase in temperature could lead to an increase in the rate of anodic and cathodic processes which are known to be thermally activated. Therefore, the temperature may increase the corrosion rate by increasing the electrochemical reactions. Nevertheless, it should not be forgotten that temperature increases also the drying rate during the drying phase of each raining/drying cycle. Consequently, the increase in temperature induces a decrease in the concrete electrical resistivity [205] which will limit the macrocell corrosion process. From this point of view the corrosion rate should decreased with temperature.

In each raining/drying cycle, the drying phase at 40°C is faster than at 20°C. Consequently, during the 72 hours of drying, the corrosion process may be limited by resistivity earlier at 40°C than at 20°C. This will lead therefore to comparable corrosion kinetics at these two temperatures.

Results indicate also that the corrosion products layer lengths are higher than the carbonated lengths measured along the corresponding steel/mortar interfaces except those obtained after 119 raining/drying cycles. The results obtained after 119 cycles are the most logical. However, the reason behind the decrease in the corrosion over carbonation ratios between 60 and 119 cycles could not be explained. Consequently, it cannot be confirmed how the corrosion will spread at 40°C. Supplementary analysis for a higher exposure durations are needed in this case but due to time constraint it was not performed in the frame of this study.

In the forthcoming paragraphs, several hypotheses are proposed in order to try understanding the phenomena that may lead to a corrosion over carbonation lengths higher than one. However, it should be borne in mind that the results of this study do not confirm the occurrence of a corrosion spread out of the carbonated area at 40°C.

The first hypothesis assumes the presence of corrosion cracks that may expose the steel to the atmosphere and give to the water a direct access to the rebar along its entire length inducing therefore an atmospheric corrosion process. However, all the mortar specimens' surfaces have been examined before each corrosion analyses and no corrosion cracks were visible (Figure 5-34). On the other hand, one can imagine that if this corrosion crack exists, its opening on the outer surface may be very small and not detectable neither by the naked eye nor by the scanning performed. For this aim, the specimen used to perform optical microscopy observations given in Figure 5-27 and showing a 300 µm residual crack opening is used. This specimen is already embedded in a fluorescent epoxy resin and this will help visualizing the presence of corrosion cracks in case they exist. To do that, the specimen is polished according to the direction shown in (Figure 5-35(a)) and thereafter a photo of the polished section is taken under UV light (Figure 5-35(b)). The thickness of the materials remaining before reaching the rebar is 2 mm. Therefore, basing on this photo, the presence of corrosion cracks is omitted and the proposed hypothesis is thus rejected.

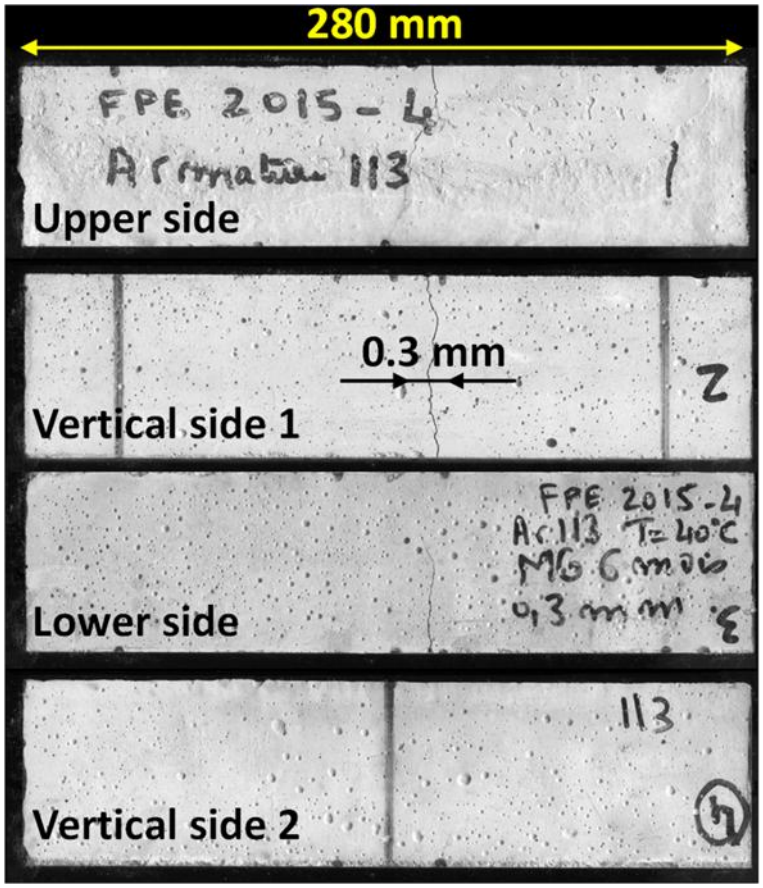

Figure 5-34: External sides of a prismatic specimen after 60 raining/drying cycles (30 min rain, 72 hours drying) at 40°C temperature

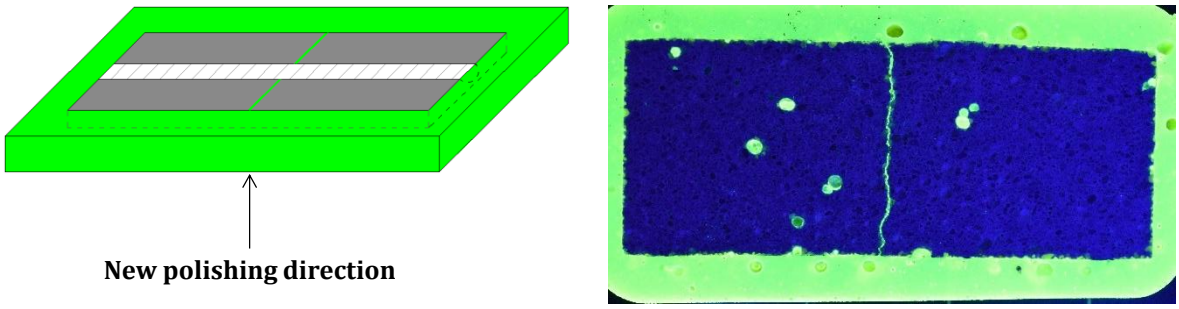

(a) (b)

Figure 5-35: Trying to detect the presence of corrosion cracks by the mean of fluorescent epoxy resin

The second hypothesis assumes that corrosion products at 40°C may induce tensile stress along the steel/mortar interface and may extend the alteration zone for a greater length than the initially quantified one. Thus, water during the raining phase may have access to this new damaged steel/mortar interface area and may induce corrosion. Consequently, there is two points needed to be verified in order to conclude if this second hypothesis is right. The first point is verifying the existence of a new damaged zone along the steel/mortar. The second point is verifying if water could induce corrosion in a steel zone surrounded by an alkaline material.

In order to verify the presence of a new damaged zone, one specimen subjected to corrosion under raining/drying cycles at 40°C and another exposed to corrosion in the reference test (20°C) are taken out of the raining chambers after 119 cycles and are subjected again to carbonation at 3% CO_2, 25°C temperature and 55% RH during 30 days. Thereafter, they are split in two parts and a phenolphthalein test is performed to estimate the damaged length similarly to the procedure detailed in chapter 3. An increase in the carbonated length along the steel/mortar interface of the two carbonated specimens could be noted after the supplementary carbonation month (Figure 5-36). In this figure, it is obvious that the specimens corroded at 40°C do not show a different behavior than those corroded at 20°C. Consequently, it can be deduced that there is no exceptional damage along the steel/mortar interface of specimens corroded at 40°C.

On the other hand, one can think that corrosion may induce an increase in the damaged steel/mortar interface at the both exposure conditions (20°C and 40°C). However, this cannot be confirmed because the noted increase in the carbonation length may only be linked to the diffusion of carbon dioxide along the interface. In fact, it is notable in Figure 5-36 that the carbonation length does not evolve during the corrosion length duration (357 days). It should be also reminded that all the specimens are carbonated from 30 days before the corrosion test. Based on that, it can be supposed that the specimens carbonated for 30 days after 357 days of corrosion corresponds to specimens carbonated to 60 days at 3% CO2, 55% RH and 25°C. In 3.3.1.2, an evolution of the carbonation length with respect to time is given. Comparing results of carbonation length obtained after the post carbonation test with those given in 3.3.1.2 may lead to deduce that diffusion process may be responsible of this carbonation spread (Figure 5-37). Consequently, an extra damage induced by corrosion could not be confirmed.

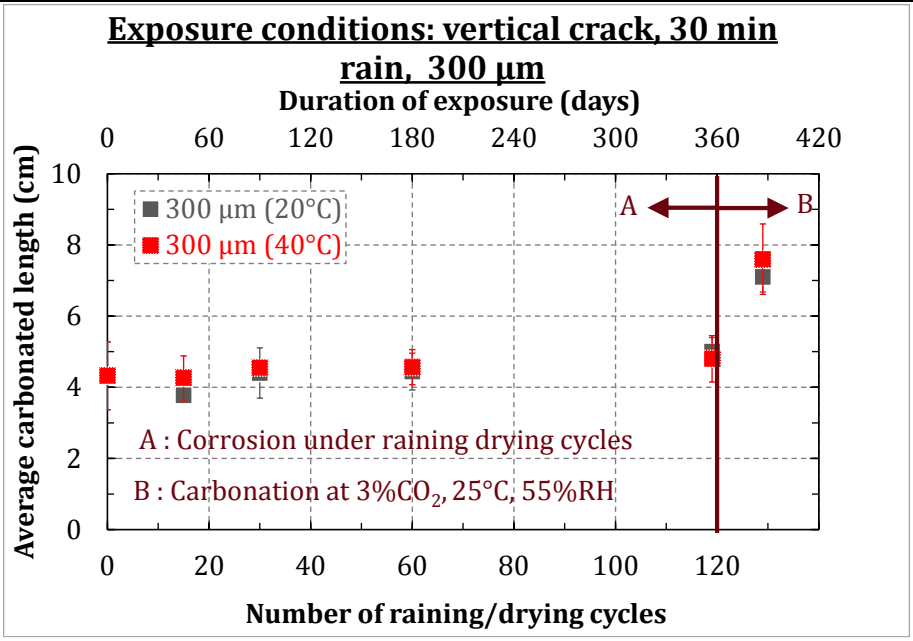

Figure 5-36: Evolution of the carbonated steel/mortar interface length in specimens corroded at 20°C and 40°C

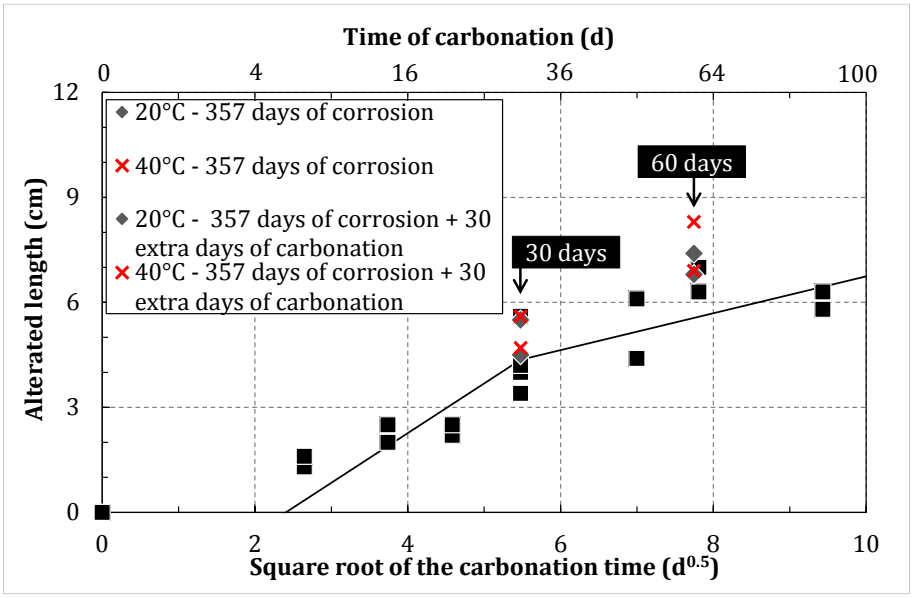

Figure 5-37: Evolution of the carbonation length along the steel/mortar interface with respect to the carbonation duration at 3%CO_2 of specimens showing 300 µm residual crack opening.

On the other hand, in order to test if a pure atmospheric corrosion process may occur independently from the electrolyte pH, one cracked specimen is subjected to raining/drying cycles at 40°C and another is subjected to corrosion in the reference test without any previous carbonation. After 30 cycles, no corrosion products are visible along the rebar intercepting a non-carbonated mortar which is still able to keep the rebar in its passive state (Figure 5-38). Therefore, this second hypothesis is rejected.

Corrosion in the reference test (20°C) for 30 raining/drying cycles

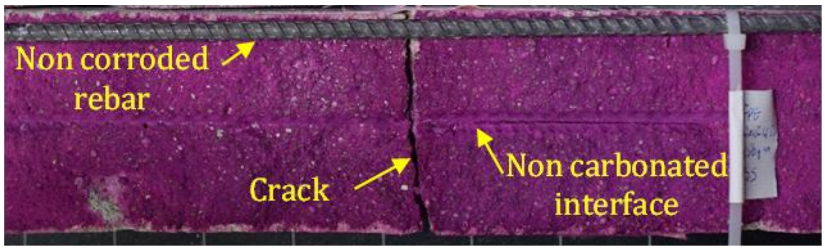

(a)

Corrosion at 40°C for 30 raining/drying cycles

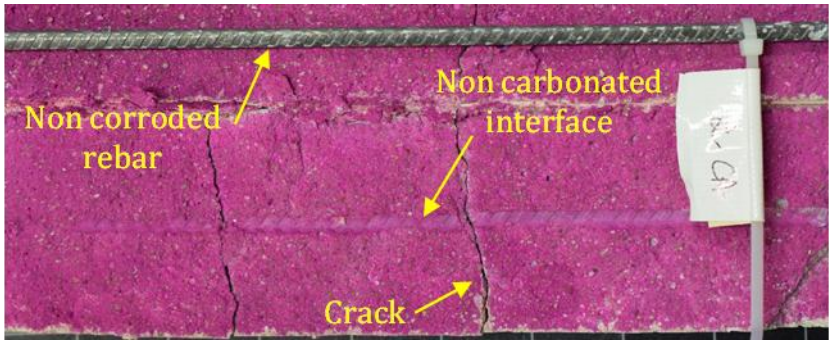

(b)

Figure 5-38: Corrosion development in cracked and non-carbonated specimens

The third hypothesis assumes that the corrosion products developed along the non-carbonated steel/mortar interface corresponds to a corrosion deposit. However, loss in the steel section is visible along the corroded zone either intercepting a carbonated mortar (Figure 5-39 (c)) or intercepting a non-carbonated mortar (Figure 5-39 (b)). The non-corroded steel does not exhibit loss in the steel cross section (Figure 5-39 (a)).

Another approach is performed to confirm the presence of the steel cross section loss in the non-carbonated zone and corresponds to measure the length of the roughness in the steel reinforcement after the gravimetric measurements. The roughness may be an indicator of a loss in the steel section. It is visible that this length was higher than the carbonated length which means that the corrosion develops for a higher length than the carbonated one. In Figure 5-40 (a), a visual comparison between roughness length (i.e. corroded length) and the carbonated length is shown. It is visible that the corrosion length is bigger than the carbonated one. Optical microscopy images of point 1, 2 and 3 shown in the Figure 5-40 (b, c and d). These photos indicate that the part of the steel located outside the considered corroded length present a smooth surface (Figure 5-40 (b)) which is not the case inside the corroded length (Figure 5-40 (c) and (d)). These observations confirm the presence of steel cross section loss even in the rebar intercepting a non-carbonated interface. Consequently, corrosion developed in the non-carbonated interface is due to a local electrochemical mechanism.

The fourth hypothesis is similar to the one given for 90%RH exposure condition. At 40°C, during the humid phase, the anodic and cathodic reactions are thermoactivated. In addition, the flow of hydroxyl ions in the electrolyte from the cathode to the anode is also increased with temperature [206]. The hydroxyl ions may be rapidly consumed by the iron ions in the anodic zone. This could lead to a light drop down in the pH at the extremities of the anodic

area. Consequently, a loss of rebar passivity may occur step by step at the anode extremities leading to an extension of the anodic area.

It should be highlighted that all these propositions remains hypothesis that need to be confirmed in future works and that they may not correspond to what really happen in the reality since a corrosion over carbonation length ratio lower than one is visible after 119 raining/drying cycles.

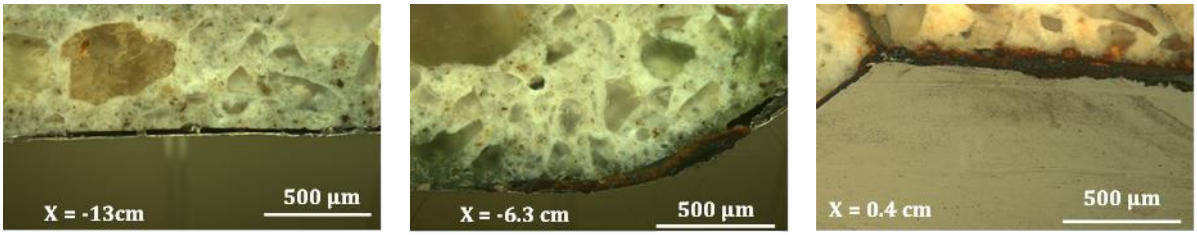

(a) (b) (c)

Figure 5-39: Loss section in the steel located in the non-carbonated and carbonated steel/mortar interface of a specimen corroded at 40°C for 60 raining/drying cycles (optical microscopy) (x = distance from the crack)

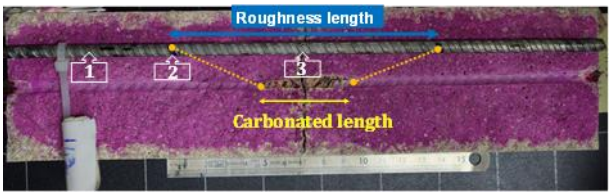

(a)

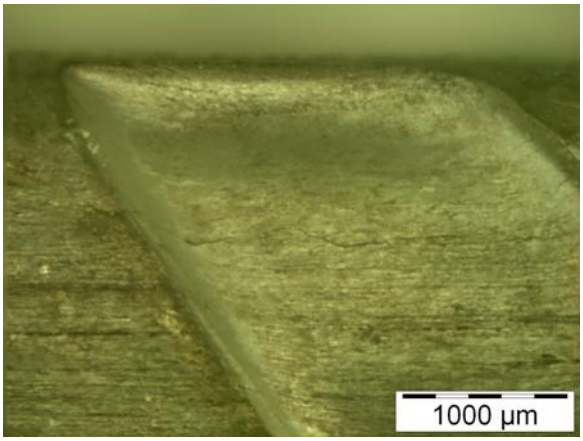

(b) → point 1 (no corrosion)

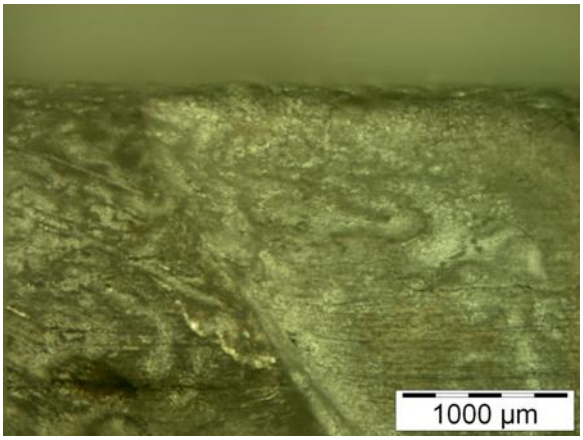

(c) → point 2 (corrosion)

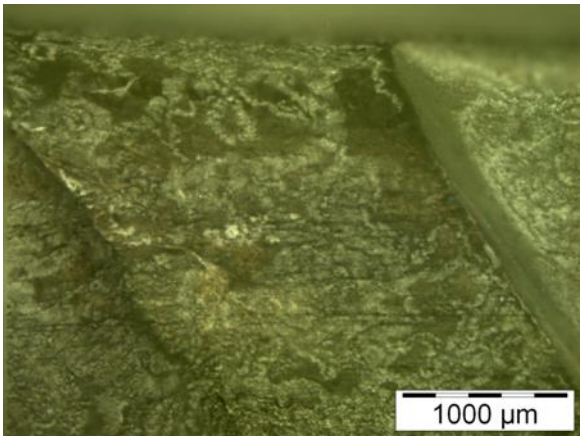

(d) → point 3 (corrosion)

Figure 5-40: Surface roughness of the corroded steel after removing the corrosion products by the acid solution

5.5 ENVIRONMENTAL CONDITIONS OF SACLAY

Specimens subjected to corrosion in the natural environment of Saclay are analyzed in this section. In this configuration test, specimens have 300 µm cracks exposed vertically with respect to rain.

5.5.1 Rain/dry cycles in Saclay

It should be noted that the number and the conditions of raining/drying cycles are not similar between Saclay and the reference test for the same exposure duration. This section aims to compare raining/drying cycles between these two corrosion conditions. This comparison is realized on the number of cycles and on the amount of precipitations (Table 5-1). It should be indicated that the data communicated by the weather station of Saclay gives information on the amount of precipitation per day. It does not rain continuously all the day outside and several raining/drying cycles of short duration may occur in the same day. However; it is not possible to obtain information on the number of raining phases per day for this reason all the cycles that may occur in one day are considered as one cycle.

Since, it has been concluded previously that the drying phase has an influence on the corrosion kinetics (limitation of macrocell), the drying duration is estimated for specimens corroded in Saclay environment (Figure 5-41).

Table 5-1: Comparison of raining/drying cycle's number and precipitation between Saclay and the reference test

Analysis date	Exposure duration (days)	Precipitation (Saclay)	Precipitation (reference test)	Cycles number (Saclay)	Cycles number (reference test)
04/15	0	0	0	0	0
07/15	90	118.7	5808	11	30
10/15	180	342.7	11616	23	60
04/16	357	674.1	23232	60	119

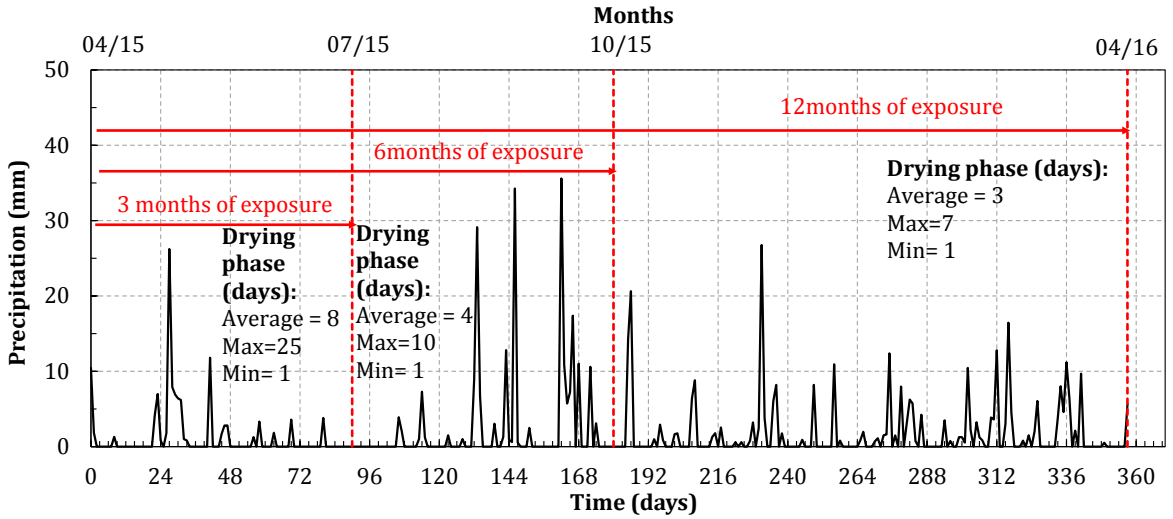

Figure 5-41: precipitations in Saclay with respect to time

The number of raining/drying cycles and the precipitations in the raining chamber is much higher than those in Saclay environment (Table 5-1). However the drying phase can last longer in Saclay than in the raining chamber (Figure 5-41). But during the drying phase in Saclay, the outside relative humidity is higher than the one in the raining chamber (Figure 2-43 and Figure 2-36). It cannot be therefore confirmed if the degree of saturation in specimens exposed to Saclay is higher or lower than the one in the reference test. Moreover, the temperature in Saclay is not continuously equal to 20°C as in the reference test.

For all these reasons, corrosion developed in specimens corroded in Saclay environment cannot be directly compared with those developed in the reference test.

This corrosion test (Saclay environment) will be used to validate the empirical model that will be developed later by EDF in order to estimate the corrosion kinetics while all the environmental conditions vary simultaneously.

5.5.2 Distribution of the corrosion products

The averages of the corrosion products layer lengths increase at the first months of exposure then it does not evolve significantly between 11 and 60 cycles equivalent to 12 months of exposure (Figure 5-42). It can also be noted basing on Figure 5-43 that the corrosion length is less than that of the total carbonated steel/mortar interface area. It can also be observed that the thickness of the corrosion product layer does not increase significantly between 11 and 23 cycles (Figure 5-44).

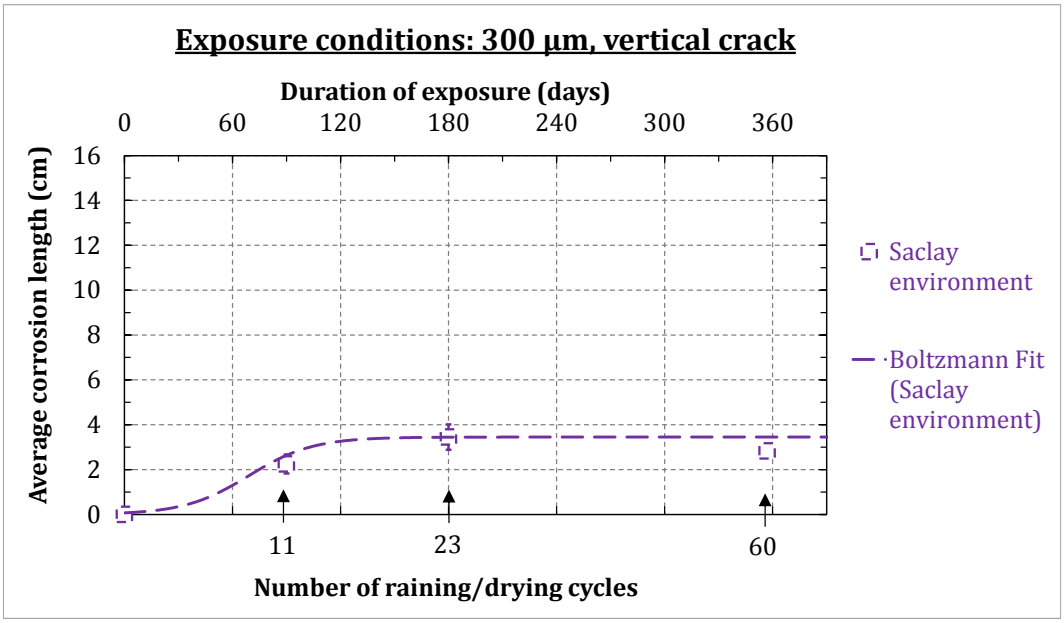

Figure 5-42: Corrosion length evolution with respect to raining/drying cycles in specimens corroded in Saclay environment (visual inspection)

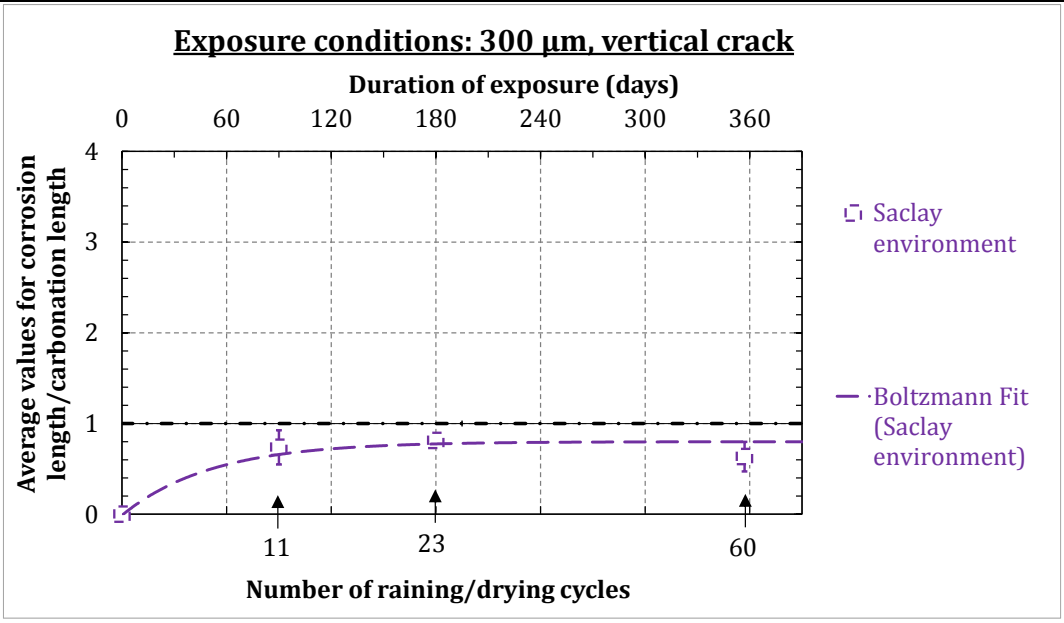

Figure 5-43: Evolution of the corrosion over carbonation length ratio in specimens corroded in Saclay environment with respect to the exposure duration (visual inspection)

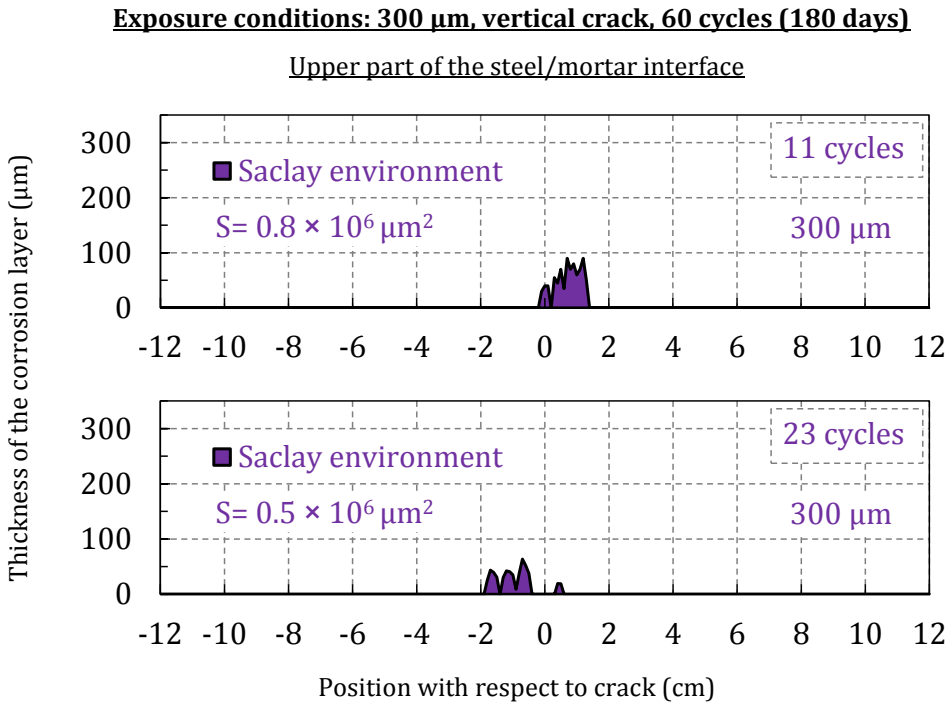

Figure 5-44: Corrosion products repartition obtained on specimens exposed to Saclay environment (optical microscopy)

5.5.3 Gravimetric measurements

An increase in the iron mass losses with the increase in the exposure duration to Saclay environment is visible at the first 6 months of exposure then the iron mass loss in the steel tends to stabilize between 6 and 12 months duration of exposure (Figure 5-45). The corrosion kinetics evolution with respect to the exposure duration of specimens in Saclay is shown in Figure 5-46. A tendency of decrease in the corrosion kinetics can be noted with respect to the exposure duration.

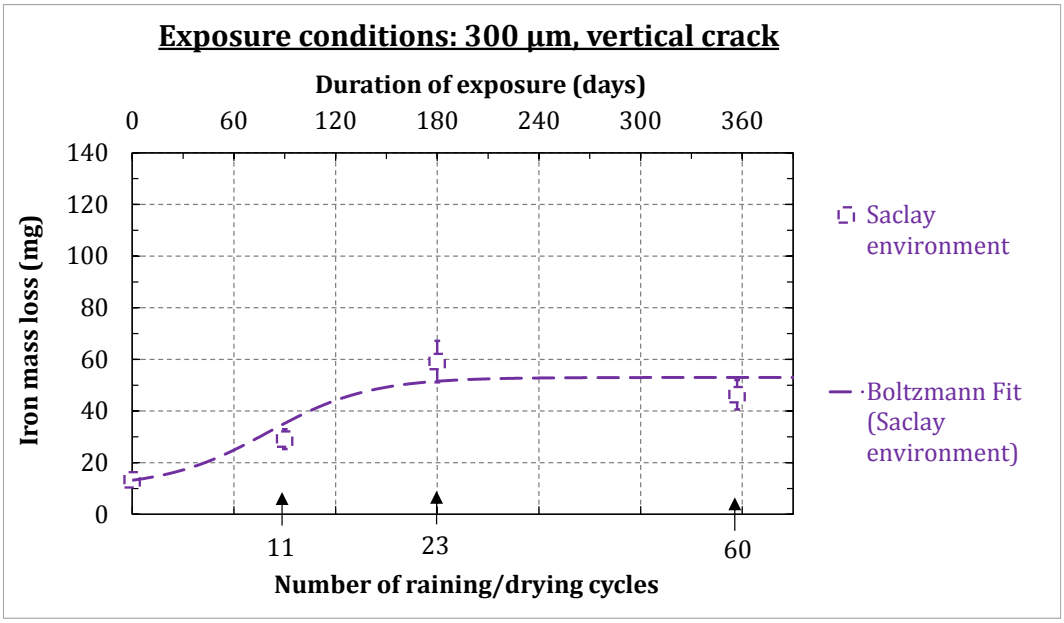

Figure 5-45: Iron mass losses in specimens exposed to Saclay environment with respect to the exposure duration

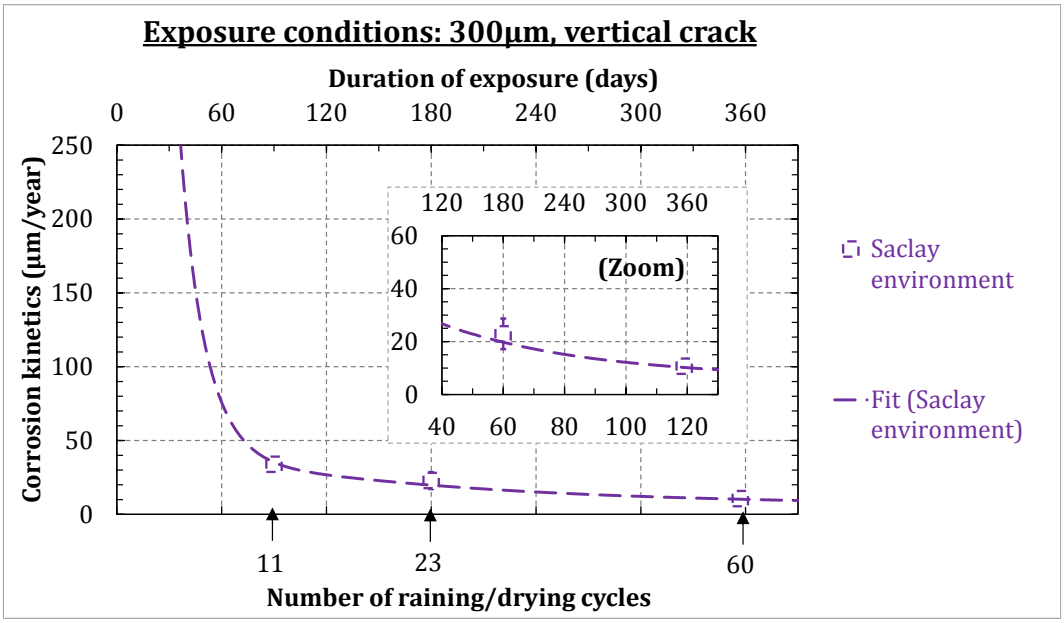

Figure 5-46: Corrosion rate evolution in specimens exposed to Saclay environment with respect to the exposure duration

5.5.4 Corrosion products type

The corrosion layer developed along the upper part of the steel/mortar interface of a specimen exposed to Saclay environment for 180 days is shown in Figure 5-47. In this same figure, the nature of the corrosion products identified is also visible. Some representative Raman spectra are given in Figure 5-48.

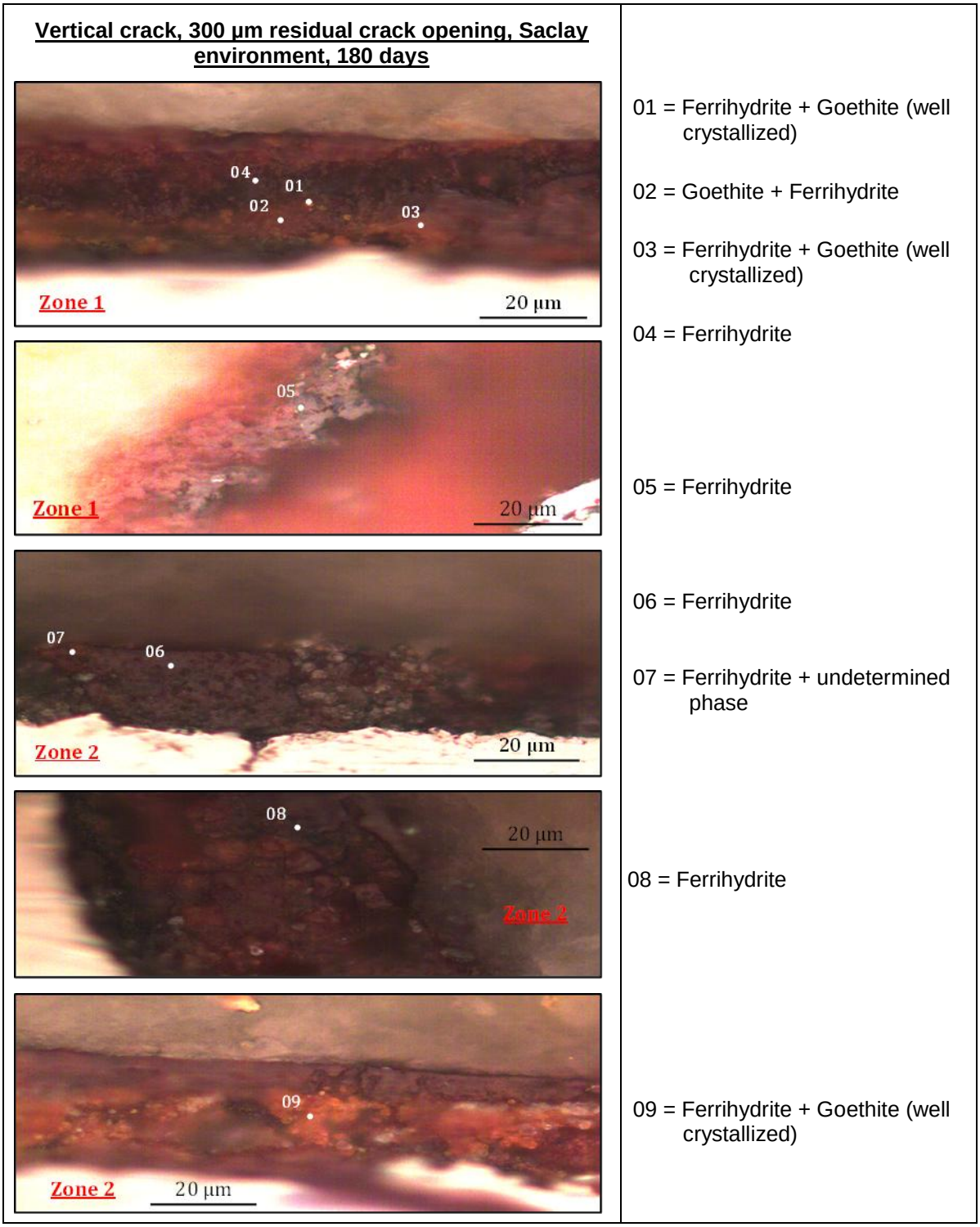

Figure 5-47: Corrosion layer observed at steel/mortar interfaces located far from the crack and deep in the crack in specimens exposed to Saclay environment

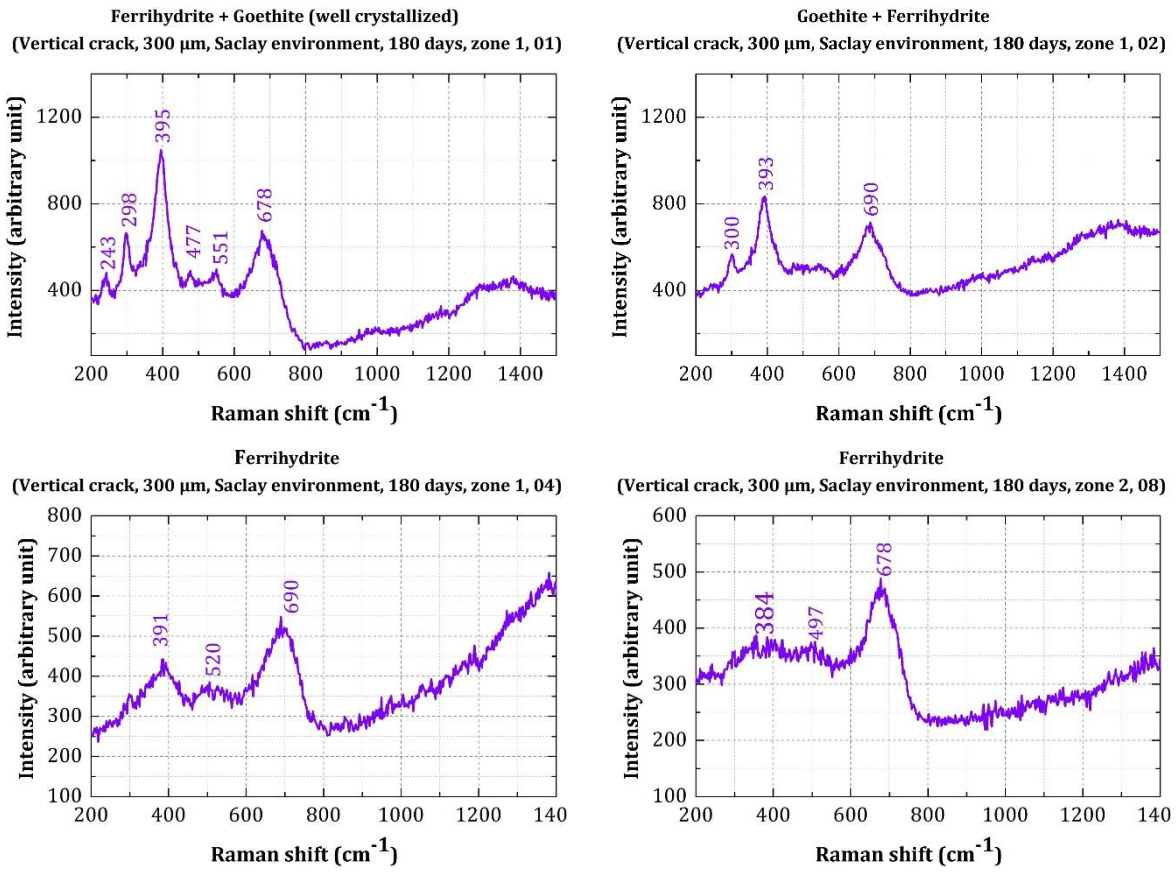

Figure 5-48: Some Raman spectra of corrosion products obtained on specimens having 300µm residual crack width and corroded in Saclay environment

A schematic representation of the corrosion products type developed in specimens corroded in Saclay environment is given in Figure 5-49. A goethite with a good crystallinity state is detected under this condition. According to conclusion drawn in §5.3.5, the corrosion products type is dependent from the duration of the raining phase and phases are more crystallized when specimens are subjected to lower raining duration or to aggressive drying phase. In fact, it is proved in § 5.5.1 that the amount of water received by specimens subjected to Saclay is much lower than the one in the reference test. Moreover, the drying phases may last much longer in Saclay then in the reference test. This could explain the presence of well crystallized phase in Saclay environment.

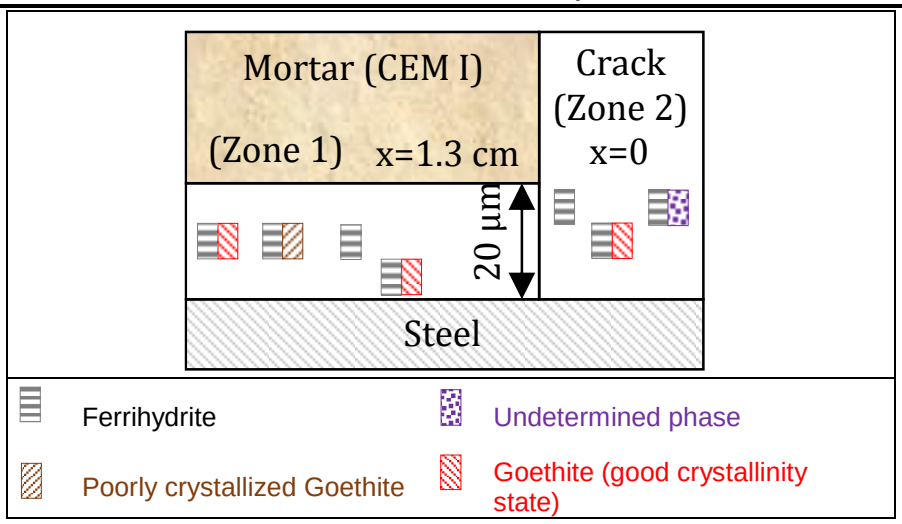

Figure 5-49: Summary of the corrosion products identified in different zones of specimens exposed to Saclay environment

5.5.5 Discussion and conclusion

In this section, corrosion development in specimens subjected to Saclay environment are examined. It is observed that the corrosion length stabilizes after a certain exposure duration and does not spread for a greater length than the carbonated one. Moreover, the corrosion kinetics tends to decrease with time. All these observations lead the author to deduce that corrosion of rebar in specimens exposed to natural environmental conditions of Saclay follow the same mechanism than specimens corroded in the reference test (laboratory conditions). The observed results will be used later to validate the empirical model that will be developed by EDF to predict the corrosion kinetics.

5.6 EVOLUTION OF THE CORROSION PRODUCTS TYPE

This section aims first to determine the evolution of the corrosion products type with respect to the number of raining/drying cycles.

Millimetric samples described in §2.3.3 are used to determine the corrosion products type at the first wetting/drying cycles. Thereafter, centimetric samples are used to identify the corrosion products type for higher number of raining/drying cycles. It can be noticed that two different terms are used to describe the cycles performed at millimetric samples and centimetric ones. This is because they are not performed similarly on these two samples dimensions (see §2.6.3.1 for more details).

Raman analyses are performed after 6 and 9 wetting/drying cycles realized on millimetric samples. Figure 5-50 and Figure 5-51 show the respective corrosion products type developed. In these figures, it is not easy to see the corrosion layer because specimens were covered by a scotch during Raman analyses. The Raman spectrum of the scotch and of some corrosion products are given in Figure 5-52.

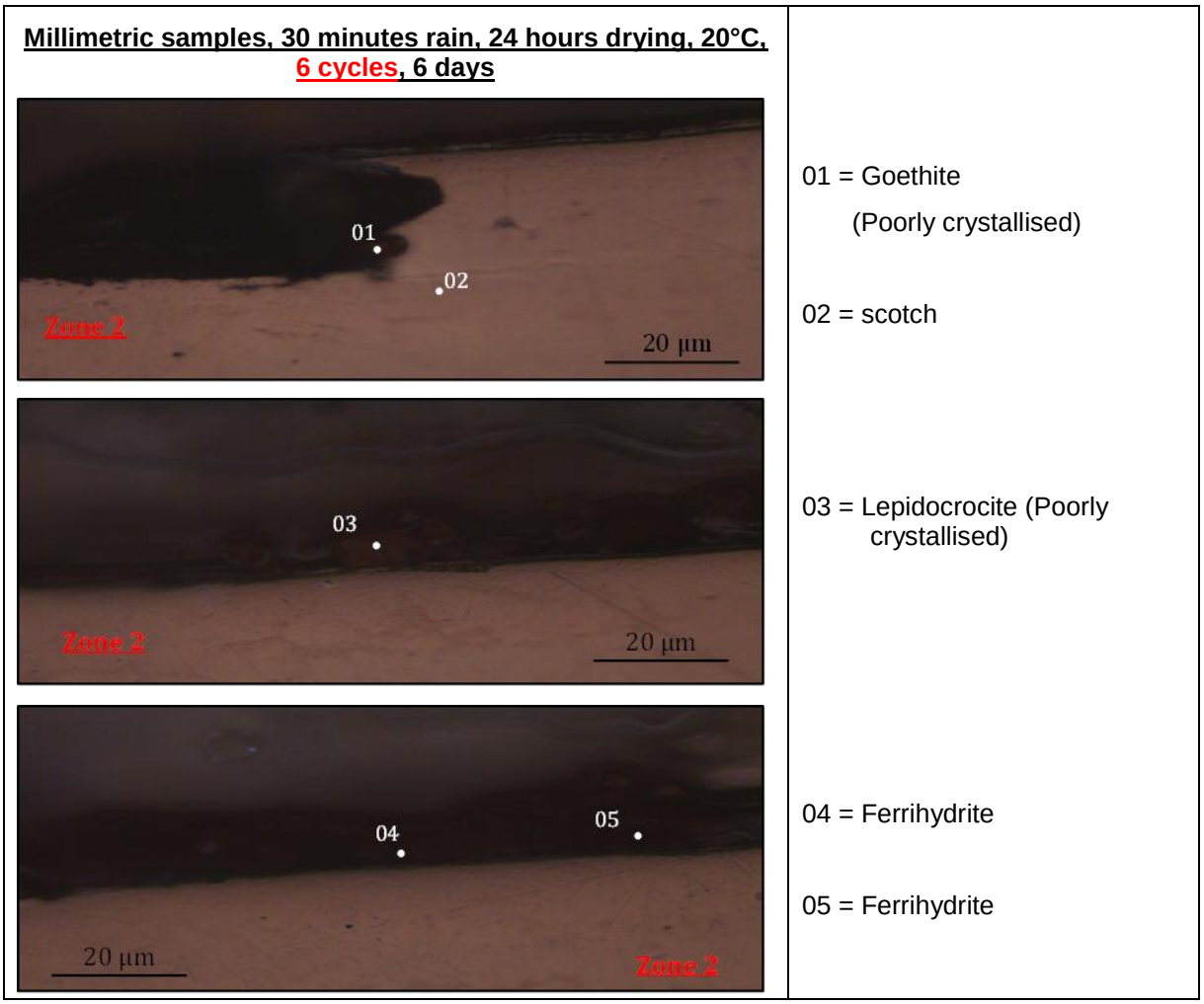

Figure 5-50: Corrosion layer observed at the upper part of the steel/mortar interface of millimetric sample subjected to 6 wetting/drying cycles

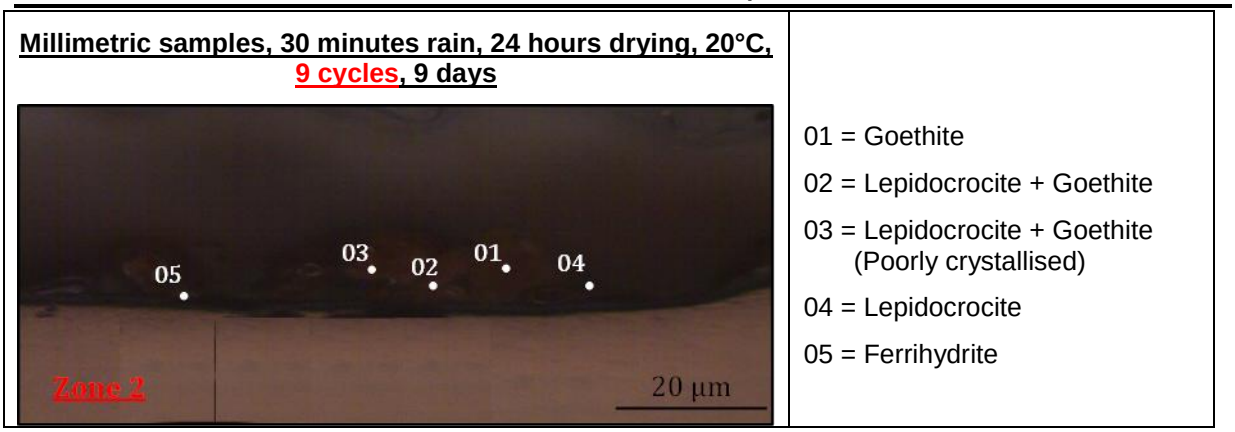

Figure 5-51: Corrosion layer observed at the upper part of the steel/mortar interface of millimetric sample subjected to 9 wetting/drying cycles

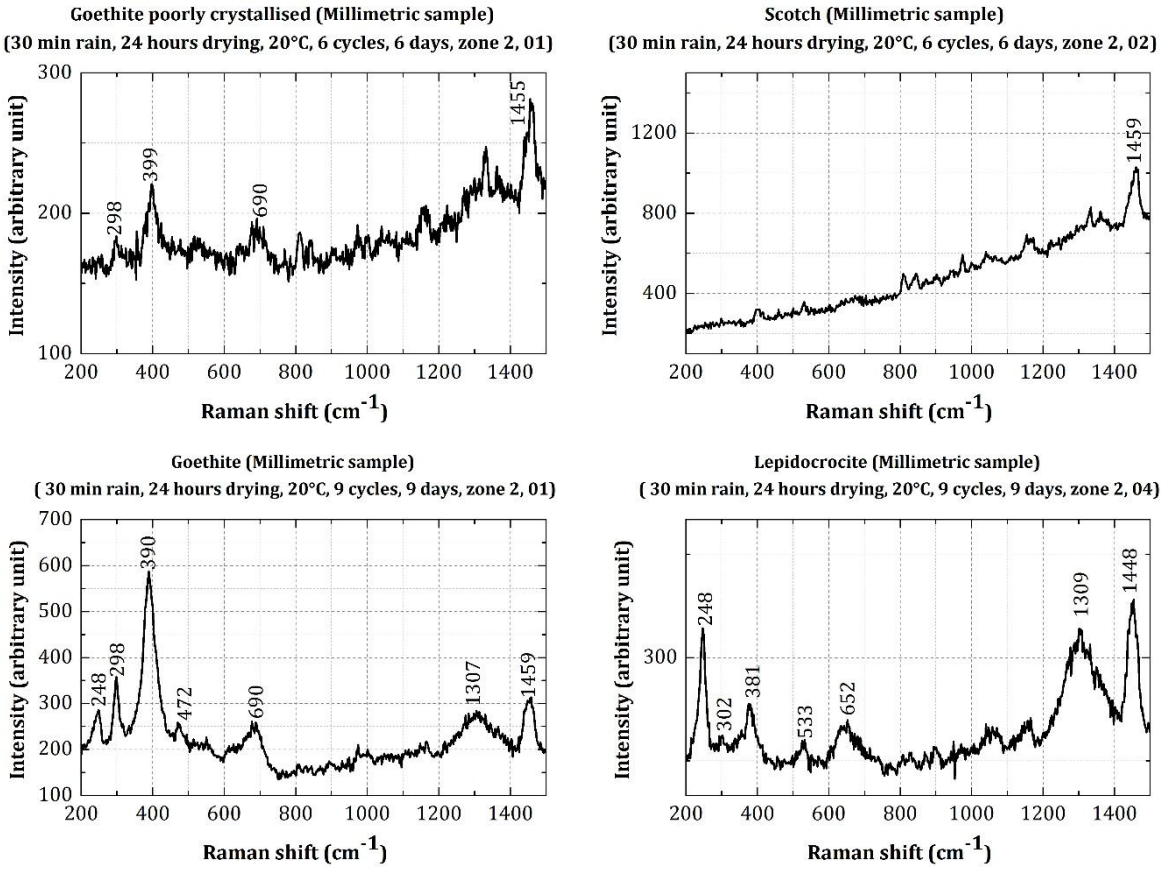

Figure 5-52: Some Raman spectra of corrosion products obtained on millimetric samples after 6 and 9 wetting/drying cycles

Corrosion products type identified after 15 and 30 raining/drying cycles on the upper steel/mortar interface of centimetric specimens are shown in Figure 5-53, Figure 5-54 respectively. Some Raman spectrum for the corrosion products are given in Figure 5-55. To remind, all the Raman spectrum obtained in this study can be found in Appendix I.6.7. Concerning the 60 raining/drying cycles, corrosion products types are given in §4.5 for specimens showing 300 µm residual crack openings.

Vertical crack, 30 minutes rain, 72 hours drying, 20°C, 15 cycles, 45 days, 300 µm

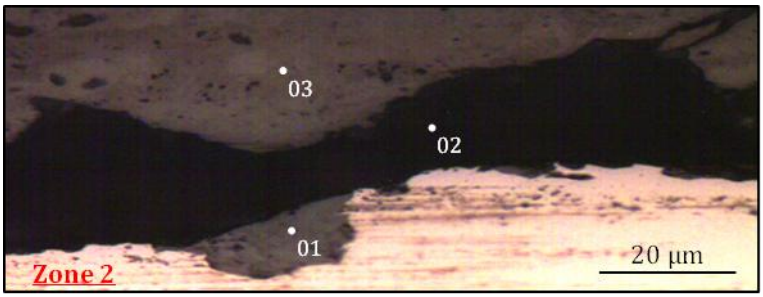

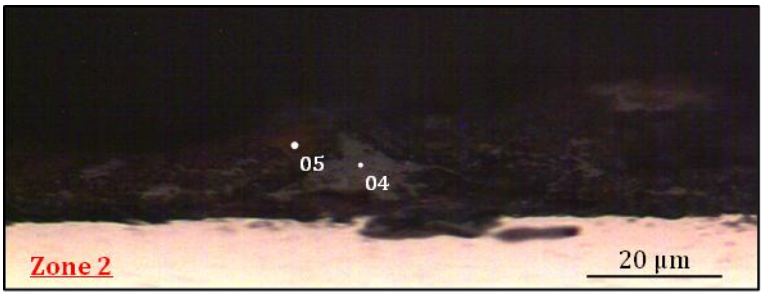

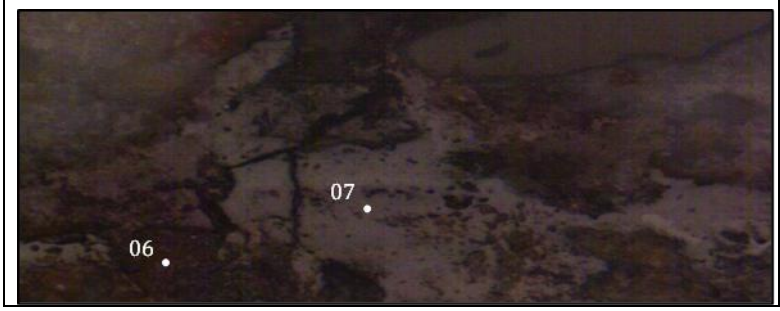

01 = Lepidocrocite

02 = void

03 = Goethite

04 = Lepidocrocite

05 = Lepidocrocite + Goethite + possible presence of Ferrihydrite

06 = Goethite + possible presence of Ferrihydrite

07 = Magnetite + possible presence of poorly crystallised Goethite

Figure 5-53: Corrosion layer observed at the upper part of the steel/mortar interface of centimetric sample subjected to 15 raining/drying cycles

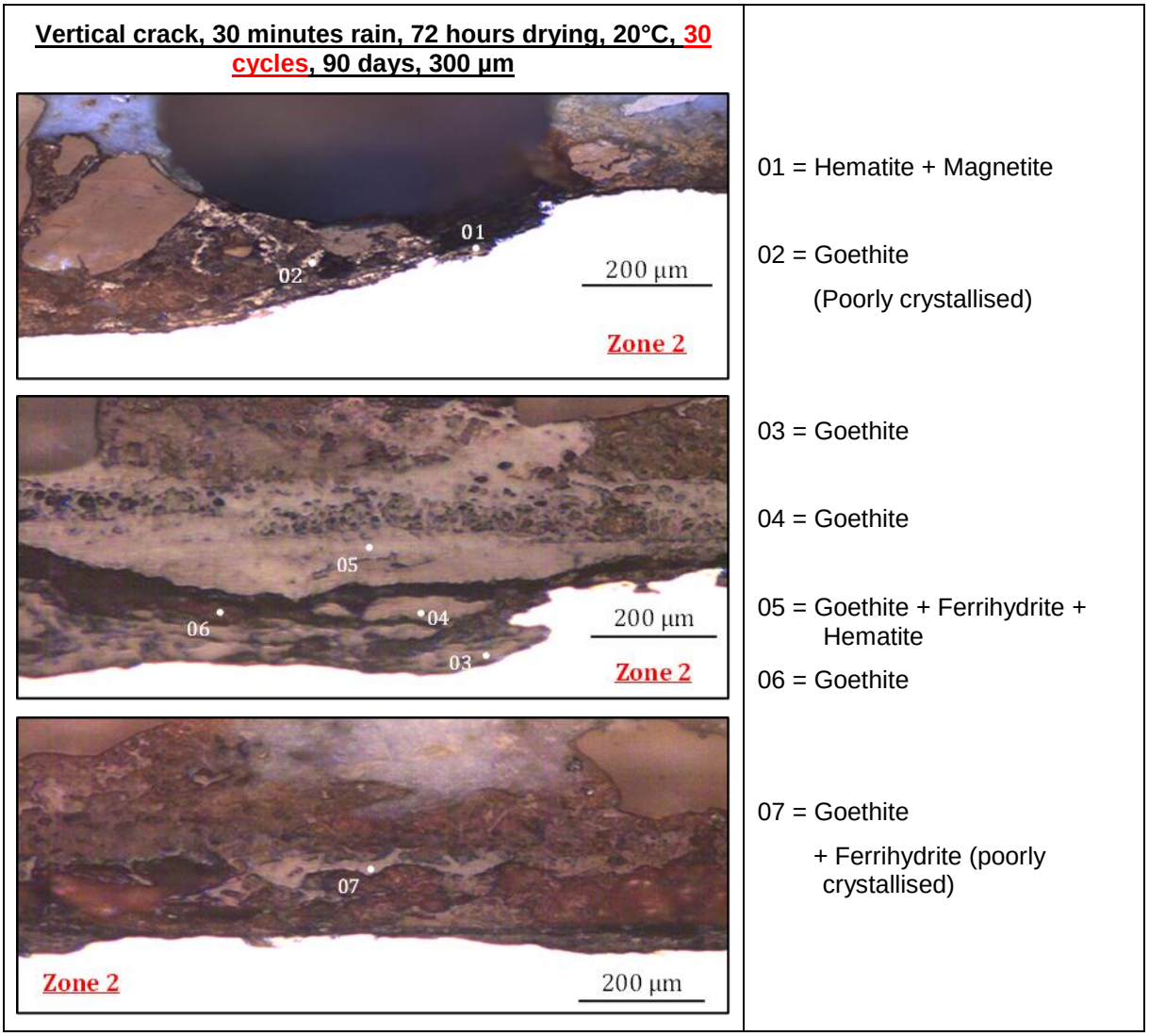

Figure 5-54: Corrosion layer observed at the upper part of the steel/mortar interface of centimetric sample subjected to 30 raining/drying cycles

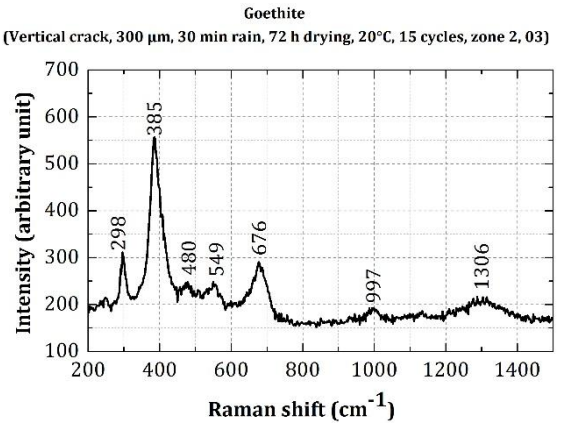

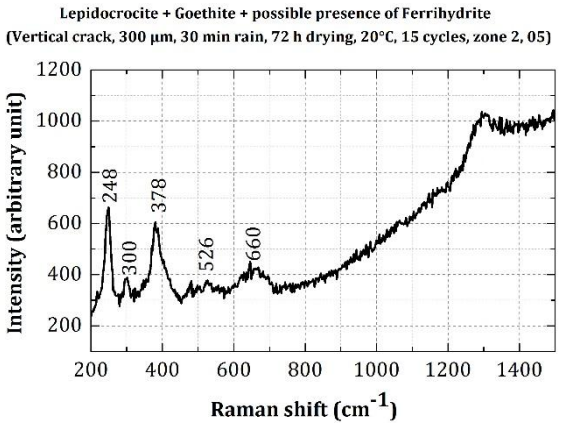

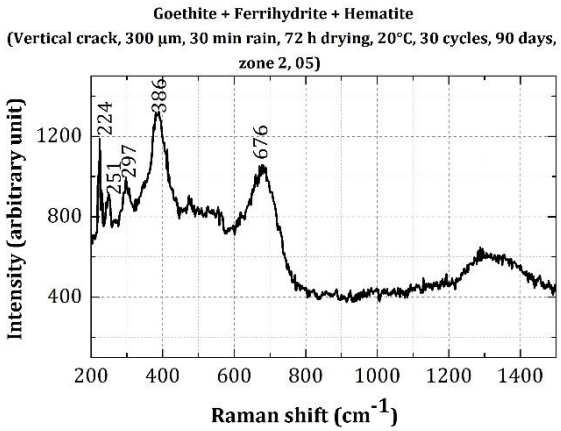

Figure 5-55: Some Raman spectra of corrosion products obtained on centimetric samples after 15 and 30 raining/drying cycles

Figure 5-56 summarizes all the corrosion products type identified with respect to the number of raining/drying cycles. From the first cycles, goethite, Lepidocrocite and ferrihydrite are present. And these phases persist for higher raining/drying cycle's number. Therefore, it is not evident to detect the precursor element in this project and no difference is noted on the corrosion products type with the number of cycles. However, the quantity of each corrosion phase could evolve with the number of cycles. Due to time constraint, corrosion products type quantification is not performed in the frame of this study but it could be interesting to test it in the future

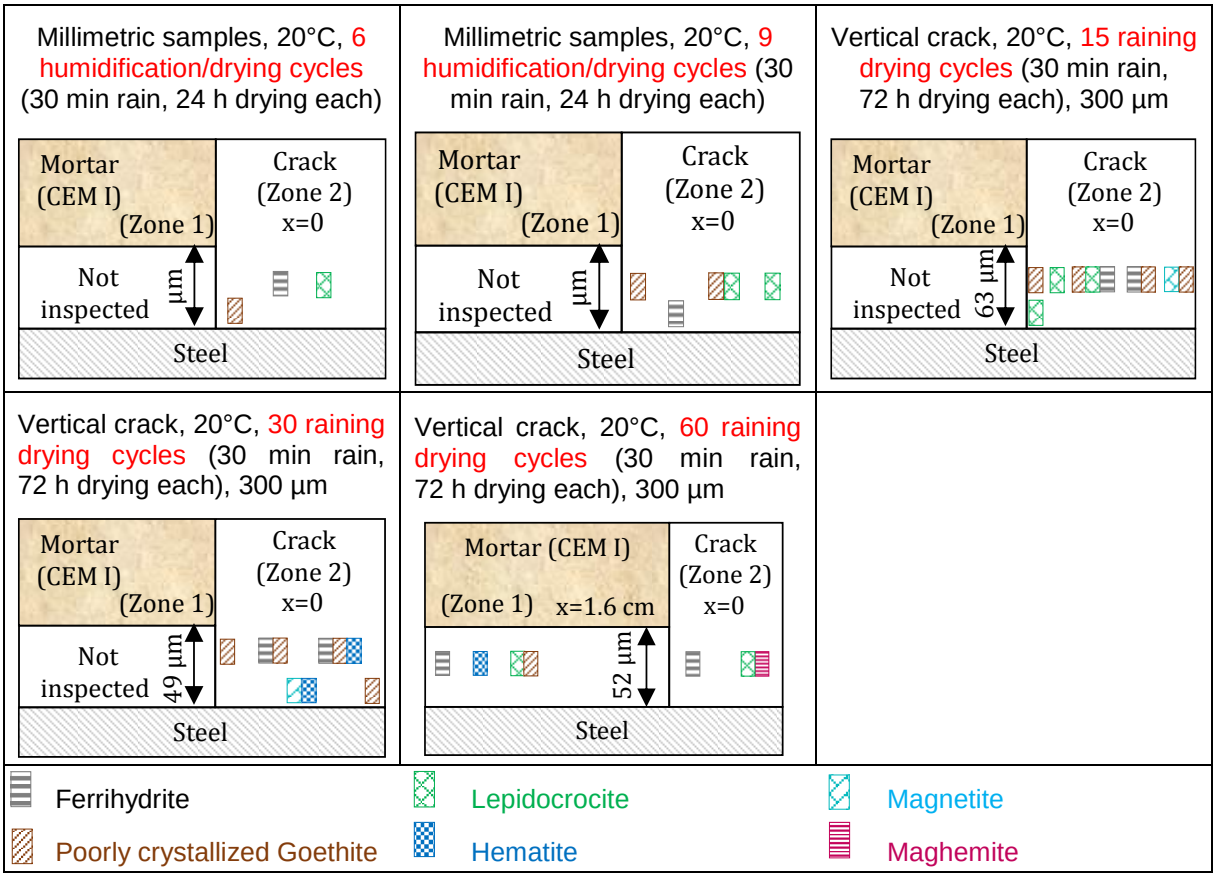

Figure 5-56: Summary of the corrosion products identified on the upper part of the steel/mortar interface of specimens subjected to corrosion for different number of raining/drying cycles

5.7 GENERAL CONCLUSION

In this chapter, the influence of several exposure conditions on the carbonation-induced corrosion is tested. It can be seen that the corrosion kinetics tendency is the same independently from the exposure conditions and it decreases after several number of raining/drying cycles. This is an indicator for the presence of a retardation phase in the corrosion process.

It should be noted that the crack orientation and the rain duration do not have influence on the carbonation-induced corrosion development.

Additionally, the corrosion products type in a low saturation degree conditions are more crystallized than those developed in conditions showing a higher saturation degree. Corrosion products layer lengths show an unexpected behavior either for specimens exposed continuously to 90% RH or for those corroded under raining/drying cycles at 40°C. This may be related to a slight decrease in the pH at the extremities of the anodic zone leading to its extension.

The corrosion process in the natural environment of Saclay is similar to the one obtained in specimens corroded in the reference test which valid the representativity of the laboratory corrosion protocol. In addition, the corrosion products types do not change with the number of raining/drying cycles going from 6 to 60.

CHAPTER 6. EFFECT OF MATERIALS TYPE ON THE CORROSION DEVELOPMENT

6.1 INTRODUCTION

The influence of the materials type on the corrosion development is presented in this chapter. One residual crack opening of 300 µm is chosen to compare the three tested materials: CEM I mortar, (CEM I + slag) mortar and CEM I concrete.

6.2 DISTRIBUTION OF THE CORROSION PRODUCTS

Figure 6-1 compares the corrosion length evolution for the different materials type tested. It can be seen that the corrosion length of the CEM I concrete specimens is lower than that of the CEM I mortar specimens. Additionally, the distribution of the corrosion products layer obtained by the optical microscopy analyses indicates the same difference observed for the corrosion length (Figure 6-4). It should be indicated that this difference is due to a dissimilarity in the carbonation length of concrete and mortar surrounding the rebars. Indeed, it can be seen in Figure 6-2 that the carbonation length in the steel/concrete interface is lower than the one measured in steel/mortar interface. This indicates that the length of damaged interface neighboring the mechanical crack is smaller for concrete binder than for mortar binder. This can be explained by the difference in the mechanical behavior between concrete and mortar due to the smaller amount of cement paste used and to the reduced interfacial transition zone in the concrete mix. In fact, limestone aggregates are used for concrete while sandstone aggregates are used for mortar. In study [5], it is indicated that the tensile strength of concrete containing limestone aggregates is higher than the one containing sandstone aggregates due to a probable chemical interaction between calcium hydroxide and calcareous aggregates providing additional hydration products and thus reducing the interfacial transition zone.

The corrosion length measured in (CEM I + slag) mortar specimens is lower than the one measured in CEM I mortar for the first two analyses (15, 30 raining/drying cycles). This observation is also visible in the optical microscopy results (Figure 6-4). Thereafter, for higher raining/drying cycles, the measured corrosion lengths of rebars embedded in (CEM I + slag) mortar increase while remaining slightly lower than those measured in rebars embedded in a CEM I mortar (Figure 6-1). However, the carbonation lengths measured along the steel/mortar interface of (CEM I + slag) mortar specimens is higher than those measured along the steel/mortar interface of both others materials (CEM I mortar and CEM I concrete) (Figure 6-2). Indeed, the amount of carbonatable materials based on (CEM I + slag) (amount of calcium) is lower than those present in materials based on CEM I (Table 2-2). For this reason, the carbonation rate is highest in (CEM I + slag) mortar which justifies the highest carbonation length measured along the steel/mortar interface. Furthermore, the length of the corrosion measured along the rebar embedded in the (CEM I + slag) mortar specimens seems to be lower than the carbonated length (Figure 6-3). In fact, corrosion in (CEM I + slag) mortar specimens may be limited by a cathodic control due to low oxygen flows to the cathodic area. The reason of the lack in oxygen may be linked to the small porosities and to the high specific surface area of (CEM I + slag) mortar. Additionally, it has been shown in Table 2-6 that the electrical resistivity of (CEM I + slag) mortar specimens is higher than that of materials based on CEM I. However, it is known that a complete electrical circuit between the anode and the cathode is needed for the corrosion. Therefore, corrosion may also be limited by the high resistivity of the medium that limits the diffusion of hydroxyl ions from the cathode to the anode.

To summarize, the macrocell corrosion mechanism may be restrained in (CEM I + slag) mortar specimens due to its high resistivity and/or to the limitation of the cathodic reactions by the lack of oxygen. Therefore, the main mechanism in this case is a microcell corrosion process and this could justify the limitation observed in the measured corrosion layer length.

This is consistent with the conclusion of Scott and Alexander [207] stating that the corrosion in SCM concretes is primarily controlled by resistivity of the system.

According to Figure 6-4, the amount of corrosion products (S) in (CEM I + slag) mortar specimens and in (CEM I) concrete specimens is lower than the one obtained in (CEM I) mortar specimens. This is confirmed with the observations noted previously. In fact, concerning the concrete, the length of the carbonated interface (i.e. zone in which steel is de-passivated) is small and thus corrosion could exit in a zone smaller than in CEM I mortar specimens. Concerning the mortar based on (CEM I + slag), the corrosion does not initiate over the entire carbonated interface due to the mortar resistivity.

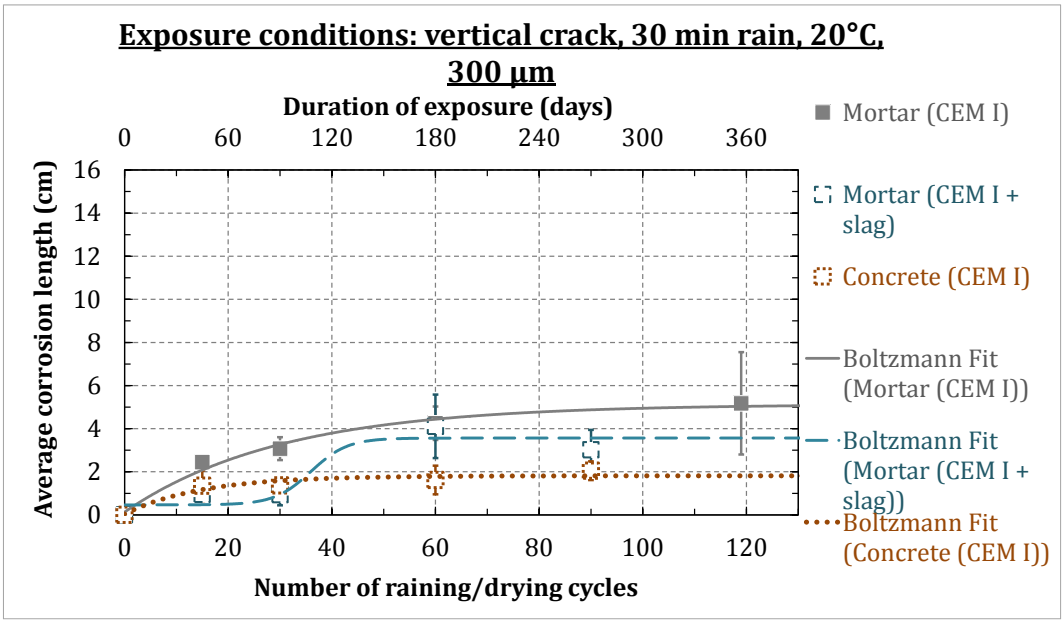

Figure 6-1: Corrosion length evolution with respect to raining/drying cycles and materials type (visual inspection)

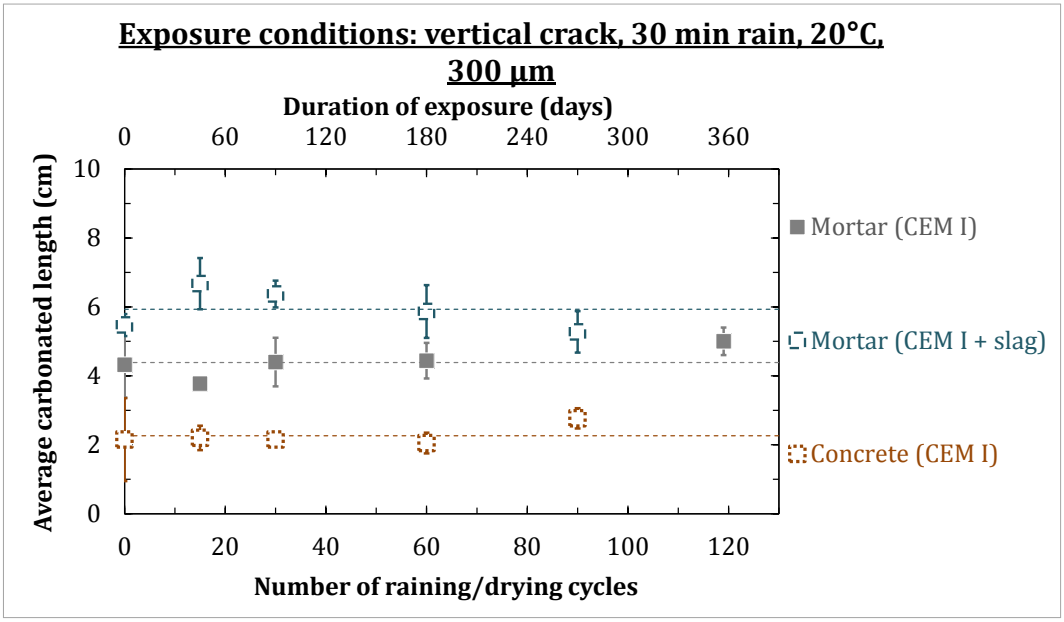

Figure 6-2 : Carbonation length evolution with respect to raining/drying cycles and materials type (visual inspection)

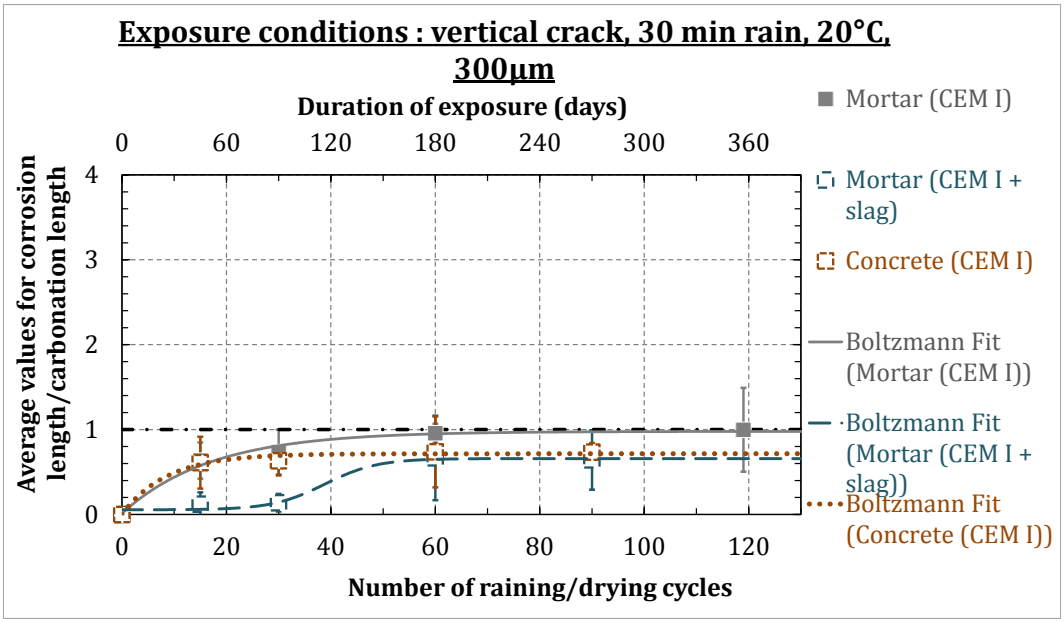

Figure 6-3 : Evolution of the corrosion over carbonation length ratio with respect to raining/drying cycles and materials type (visual inspection)

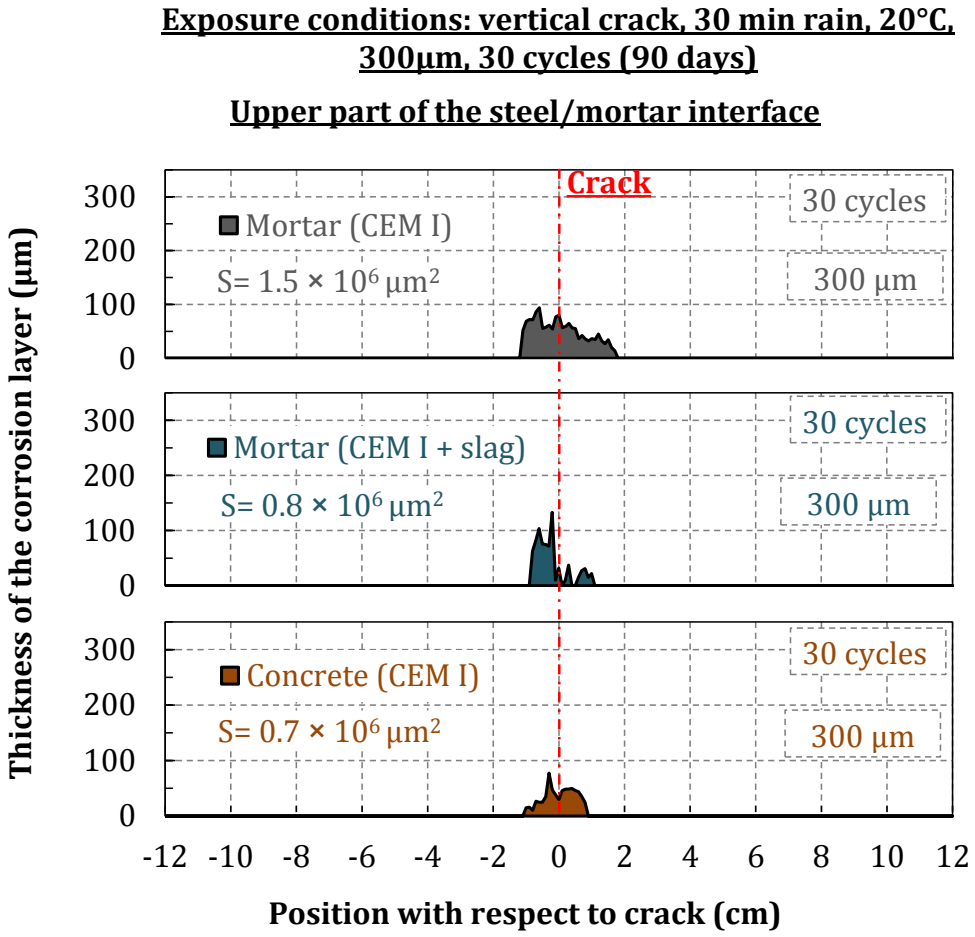

Figure 6-4: Corrosion products repartition obtained on specimens with different materials type (optical microscopy)

6.3 GRAVIMETRIC MEASUREMENTS

The evolution of the iron mass loss and the corrosion kinetics in specimens fabricated with different materials type are shown in Figure 6-5 and Figure 6-6. Similarly to the corrosion amount and for the same reasons explained previously, the iron mass losses measured on rebars embedded in (CEM I + slag) mortar and (CEM I) concrete specimens are smaller than those measured on (CEM I) mortar specimens. However, independently from the materials type, the iron mass losses tend to stabilize after 60 raining/drying cycles.

After 90 raining/drying cycles, no significant influence of the materials type on the corrosion kinetics can be noted. Moreover, independently from the materials type, the corrosion rate decreases. It should be reminded that the measured corrosion kinetics corresponds to the rate of the metal dissolution. As deduced in chapter 4, after several raining/drying cycles, corrosion products seal the crack and limit the access of water to the rebar. The corrosion kinetics is thus monitored by the corrosion products developed deep in the crack which will mask the influence of the materials type on the corrosion rate.

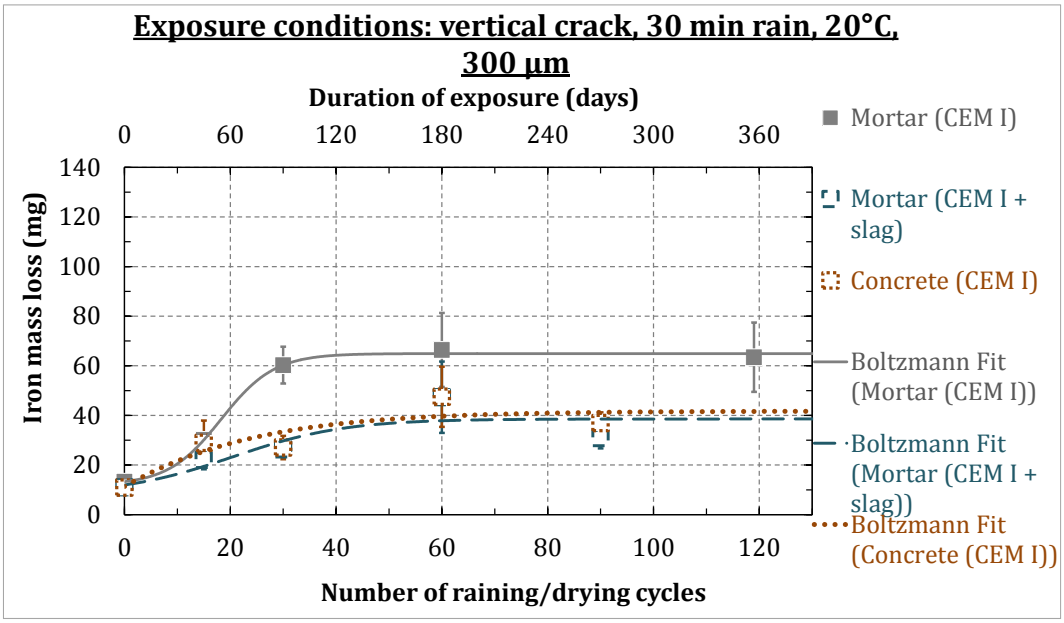

Figure 6-5: Iron mass loss evolution with respect to raining/drying cycles and materials type

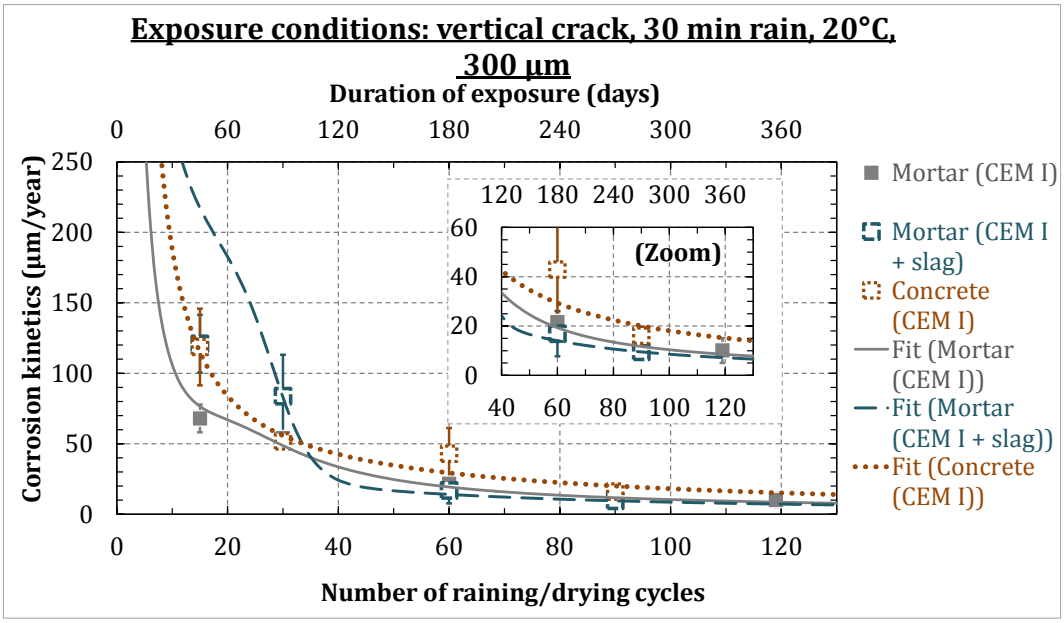

Figure 6-6: Corrosion rate evolution with respect to raining/drying cycles and materials type

6.4 CORROSION PRODUCTS TYPE

The corrosion layers developed along the upper part of the steel/mortar interface of (CEM I + slag) mortar specimens and (CEM I) concrete specimens are given in Figure 6-7 and Figure 6-8 respectively. Some typical Raman spectra are given in Figure 6-9.

Mortar (CEM I+ slag), verical crack, 300 µm residual crack opening, 30 minutes rain, 20°C, 60 cycles, 180 days

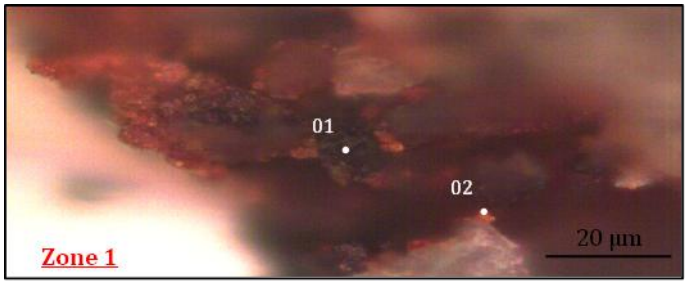

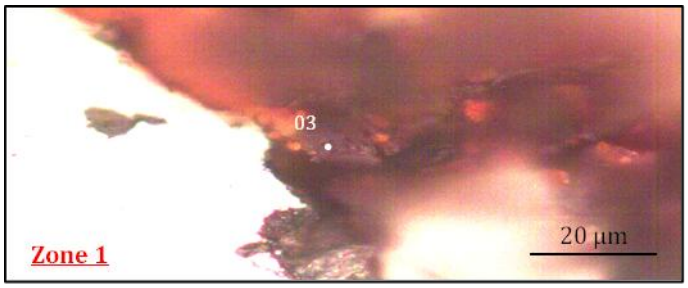

01 = Ferrihydrite

02 = Ferrihydrite

03 = Ferrihydrite

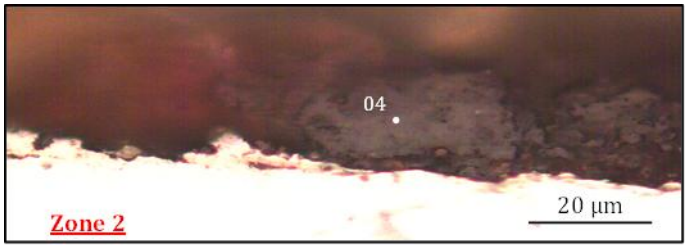

04 = Goethite

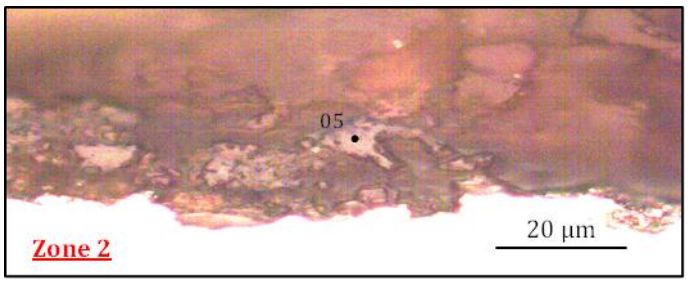

05 = Lepidocrocite + Ferrihydrite

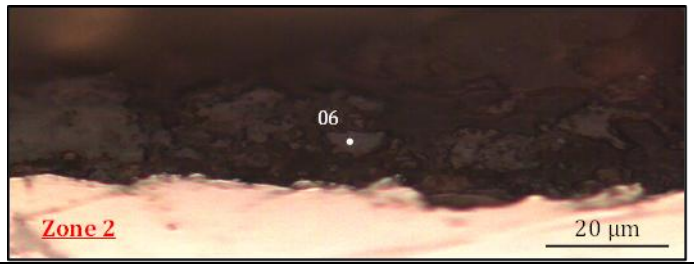

06 = Goethite + Ferrihydrite

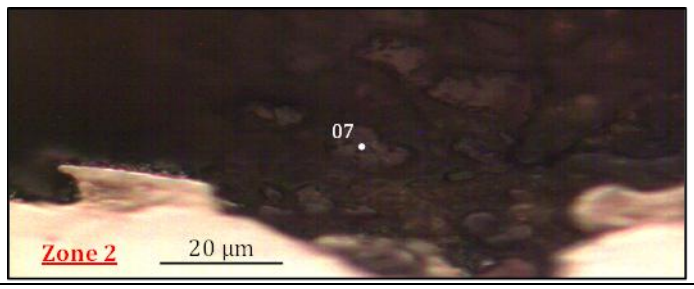

07 = Goethite + Ferrihydrite

Figure 6-7: Corrosion layer observed at steel/mortar interfaces located far from the crack and deep in the crack in (CEM I + slag) mortar specimens

Concrete (CEM I), verical crack, 300 µm residual crack opening, 30 minutes rain, 20°C, 60 cycles, 180 days

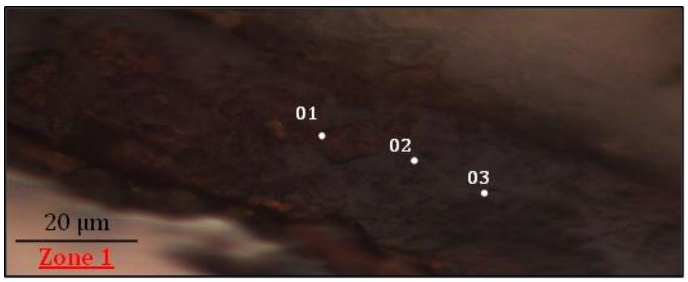

01 = Ferrihydrite + undetermined phase

02 = Ferrihydrite

03 = Ferrihydrite

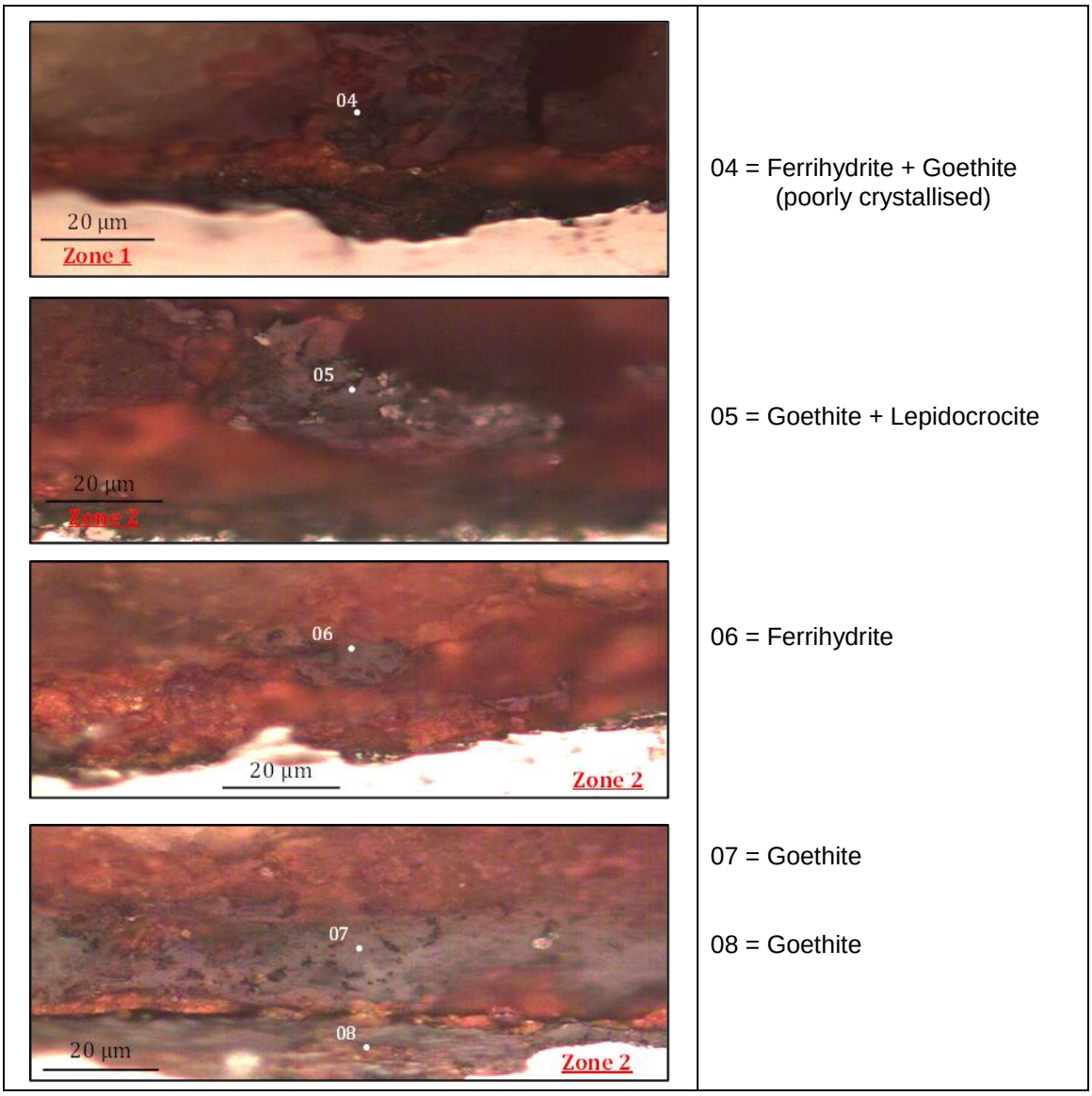

Figure 6-8 : Corrosion layer observed at steel/mortar interfaces located far from the crack and deep in the crack in (CEM I) concrete specimens

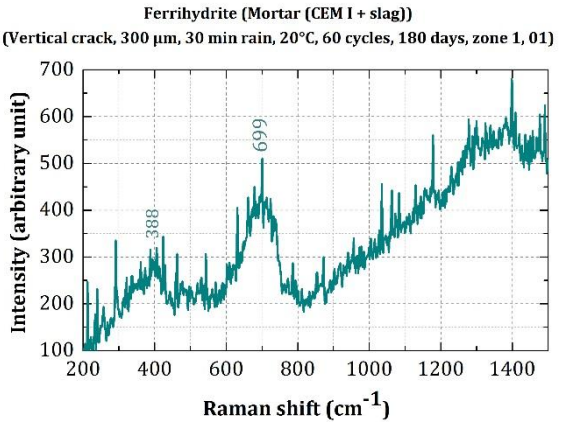

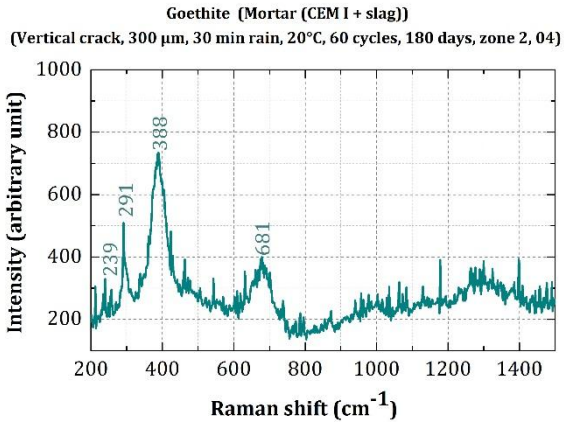

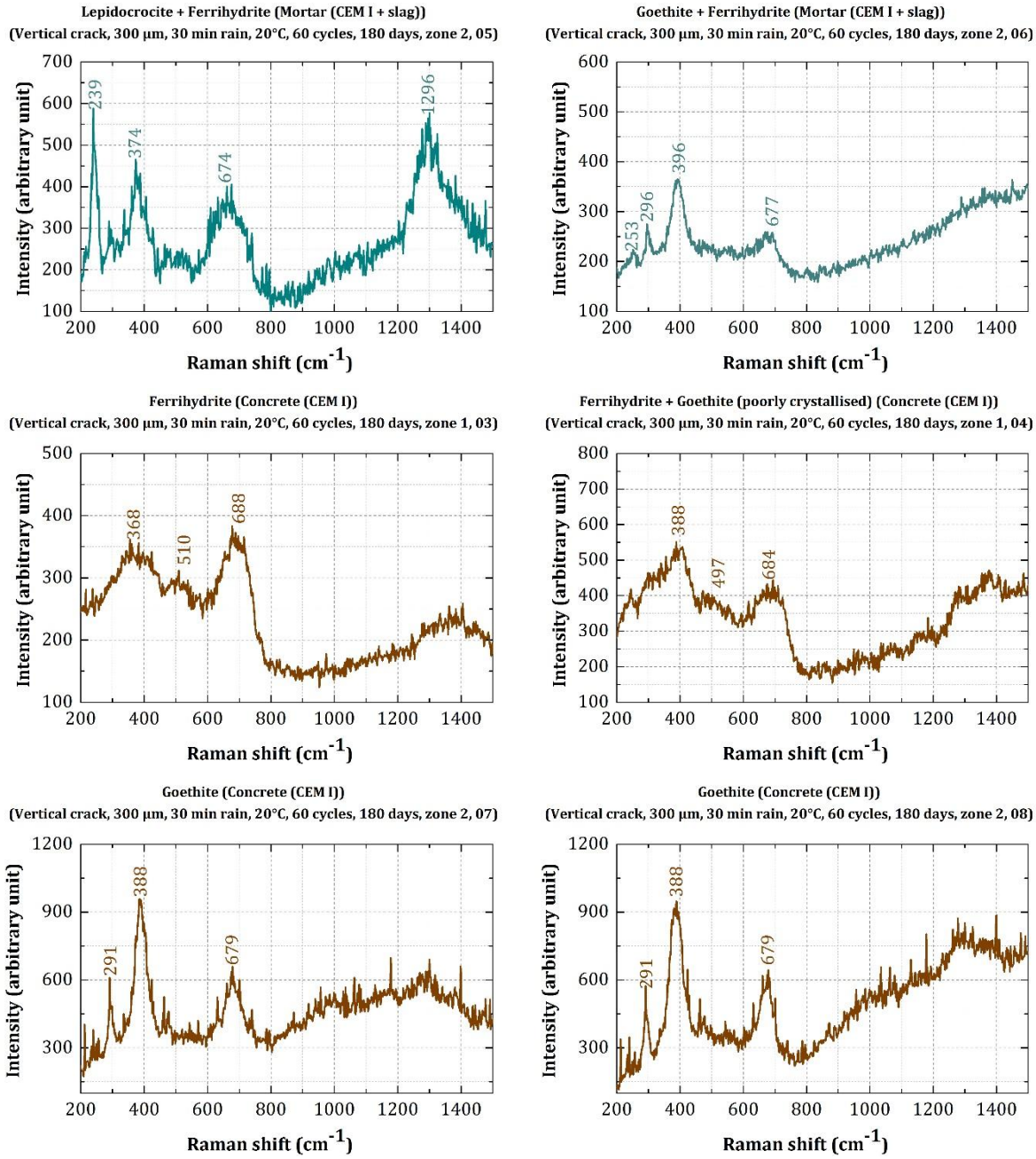

Figure 6-9 : Raman spectra of corrosion products identified in (CEM I + slag) mortar and (CEM I) concrete specimens

Figure 6-10 summarizes the corrosion patterns developed in different materials type. It can be seen that the corrosion patterns are similar independently from the binder. Mostly reactive phases are developed (ferrihydrite, Lepidocrocite, goethite, etc.). This observation corresponds to the study [208] in which the same corrosion phases were identified in the corrosion layer independently form the binders characteristics.

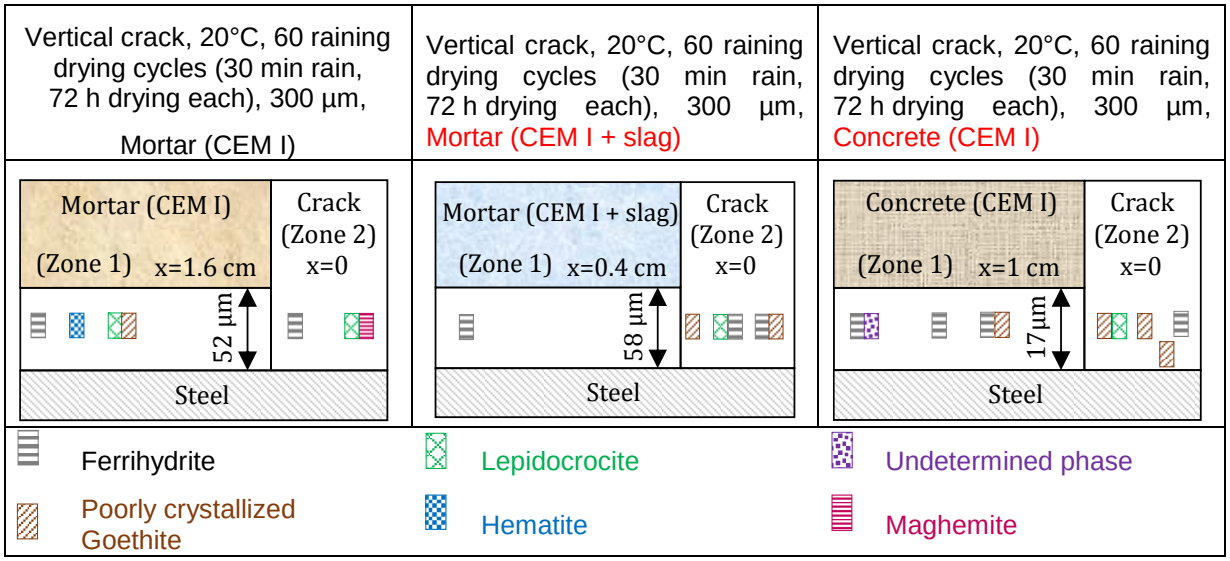

Figure 6-10: Summary of the corrosion products identified in specimens with different materials type

6.5 CONCLUSION

In this chapter, the effect of the materials type on the carbonation-induced corrosion in cracked concrete is inspected. The results indicate that the corrosion lengths in concrete based on CEM I and mortar based on CEM I + slag are lower than those in mortar based on CEM I. Concerning the concrete, the difference in the observed corrosion length is due to a difference in the mechanical behavior. While, for the (CEM I + slag) mortar specimens, the difference in the corrosion length may be due to a difference in the corrosion mechanism (limitation of the macrocell corrosion). Nevertheless, no difference can be noted in the corrosion kinetics measured in the three cementitious materials because corrosion products seal the crack after a certain number of raining/drying cycles and control the corrosion kinetics independently from the binder. Additionally, the corrosion products types are also independent from the binder.

CHAPTER 7. EFFECT OF THE STEEL/MORTAR INTERFACE QUALITY ON THE CORROSION DEVELOPMENT

Chapter 7. Effect of the steel/mortar interface quality on the corrosion development

7.1 INTRODUCTION

This chapter aims at testing the influence of the steel/mortar interface quality on carbonation-induced corrosion development. This parameter is tested on two specimen's dimensions: centimetric (prismatic specimens) and metric (concrete slabs).

In metric specimens, two layers of reinforcements are present and a comparison between the distribution of the corrosion products layer on the upper and lower rebars with respect to casting direction is performed after different raining/drying cycles. Additionally, the length of the carbonated steel/concrete interface measured on the upper rebar is compared with the one measured on the lower rebar.

On the other hand, the distribution of the corrosion products layer along the upper and the lower steel/binder interface of a unique rebar embedded in centimetric specimens is also investigated at different raining/drying cycles. Moreover, the influence of the steel/mortar interface quality on the carbonation-induced corrosion is inspected in centimetric specimens with respect to different materials type. Additionally, on centimetric specimens, a comparison between the corrosion products type developed on these two interfaces of the steel/binder is also performed.
Finally, the results are discussed and conclusion is drawn.

7.2 PRISMATIC SPECIMENS

In this section, prismatic specimens containing one deformed rebar of 6 mm diameter are inspected (§2.3.2).

7.2.1 CEM I mortar specimens

The distribution of the corrosion products layer on the upper part and the lower part of the steel/mortar interface of specimens corroded in the reference protocol for 30 and 60 raining/drying cycles are given in Figure 7-1 (a, b).

It is plain to see that the thickness of the corrosion products layer developed on the lower steel/mortar interface is mostly higher than that of the upper steel/mortar interface. It should be reminded that the upper and the lower steel/mortar interfaces are determined with respect to casting direction and are subjected to the same mechanical loading during the three point bending test. Based on the literature review presented in §1.4.3.4, the quality of the lower steel/mortar interface is poorer than the upper one which justify the thicker corrosion products layer on this interface.

Accordingly to Figure 7-1, it is visible that the corrosion products thicknesses measured on the upper steel/mortar interface increase with the residual crack opening. While on the lower part of the interface, the thickness of the corrosion layer is independent from the residual crack opening. Moreover, Figure 7-2 shows the difference between the corrosion thicknesses measured on the lower part of the steel/mortar interface and those measured on its upper part with respect to the residual crack opening. It can be noted that the difference between these both corrosion thicknesses decreases with the increase in the residual crack openings. In fact, mechanical loading induces microcracks along the both interfaces in the zone surrounding the mechanical crack. Consequently, a rapid carbonation may occur on the both interfaces of the rebar during the accelerated carbonation test. Once the steel/mortar interfaces are carbonated, the corrosion initiates. Its thickness on the upper interface should be dependent from the intensity of the mechanical damage. However, this is not the case on the lower part of the interface because the influence of microcracks on the corrosion thickness may be masked by the presence of porous materials induced by bleeding and settlement of mortar as reported in the studies [116], [122]. Therefore, the corrosion layer

thickness developed on the lower part of the interface is independent from the residual crack opening (mechanical damage).

Concerning the difference in the corrosion lengths measured on both part of the interface, they do not show any dependency from the residual crack opening (Figure 7-3). The corrosion length measured on the lower part of the interface is sometime lower and sometime higher than the one measured on the upper interface. This is dependent on the variability of the corrosion initiation and propagation process. No difference can be noted between the corrosion products layer length measured on the upper and the lower interfaces.

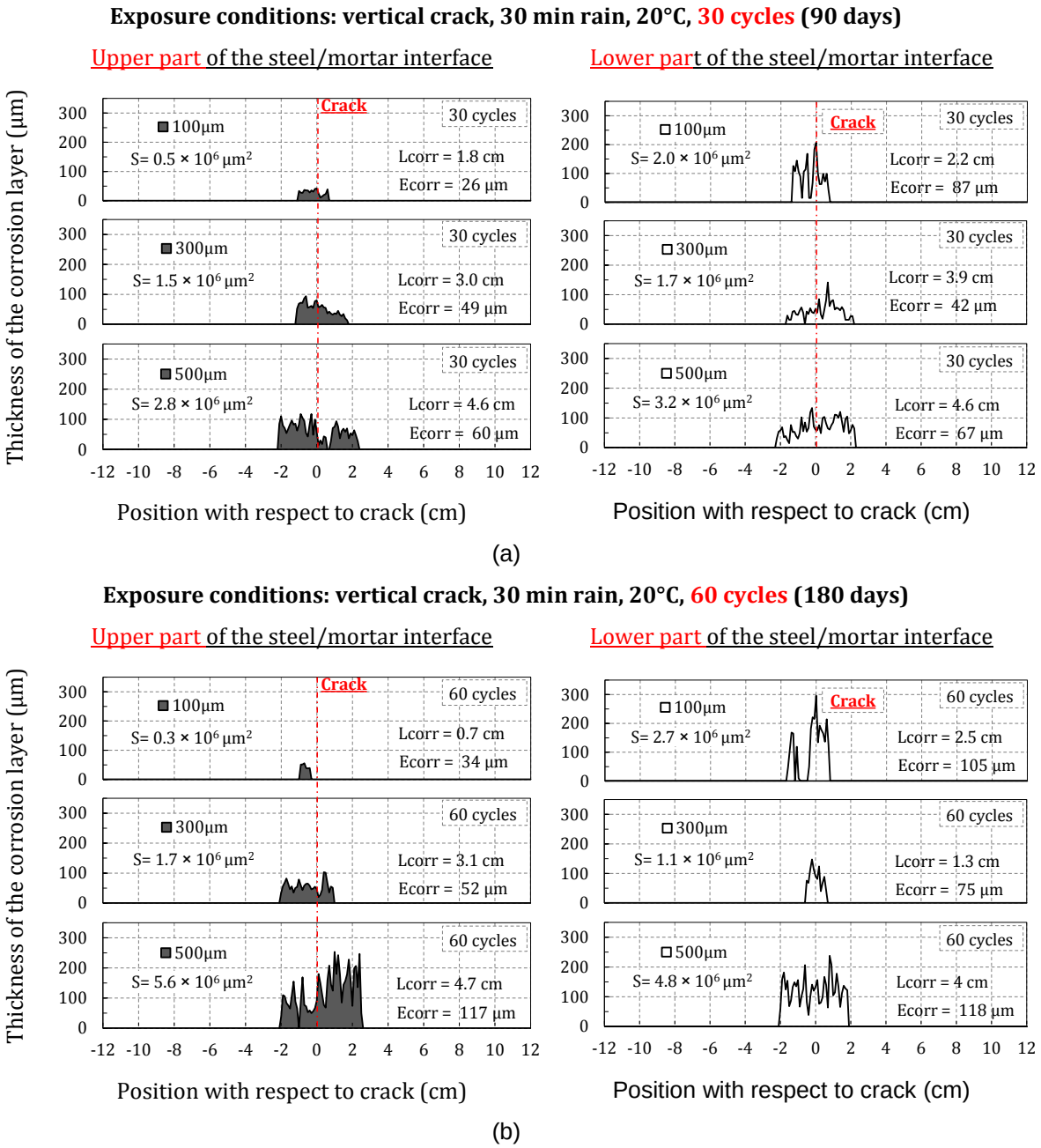

Figure 7-1 : Corrosion products repartition on the upper and the lower steel/mortar interfaces of specimens corroded in the reference test[5]

[5] In Figure 7-1, "Lcorr" corresponds to the corrosion products layer length. Its thickness is noted "Ecorr"

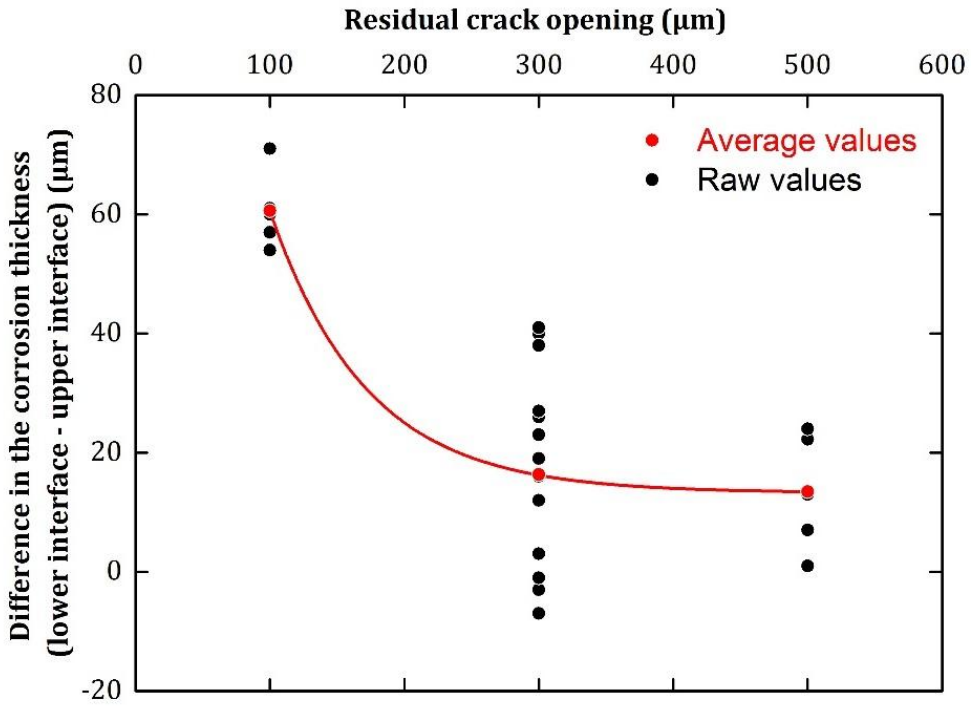

Figure 7-2 : Effect of the residual crack openings on the difference in the corrosion products layer thickness measured on the upper and the lower steel/mortar interfaces (optical microscopy)

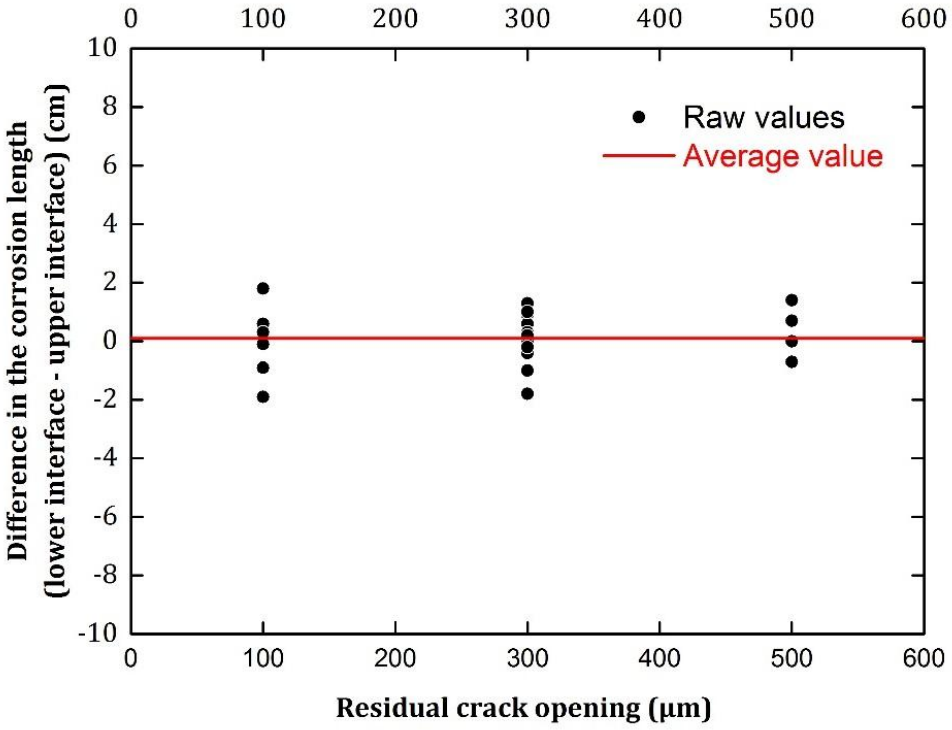

Figure 7-3 : Effect of the residual crack openings on the difference in the corrosion products layer length measured on the upper and the lower steel/mortar interfaces (optical microscopy)

7.2.2 Different materials type

This section aims at testing whether the influence of the steel/binder quality on the corrosion development depends on the type of binder. Tests are realized on centimetric specimens fabricated with (CEM I) mortar, (CEM I + slag) mortar and (CEM I) concrete mortar and showing one residual crack opening of 300 µm.

In Figure 7-4, it can be noted that independently from the material type, the thickness of the corrosion layer developed on the lower part of the steel/binder interface is higher than the one developed on the upper part of the interface due to the presence of a higher porosity on the lower part of the interface.

Only, for (CEM I + slag) mortar specimens, a difference between the corrosion lengths measured on the upper and lower part of the steel/binder interface may be noted. Indeed, in these specimens, the corrosion products layer has a greater length on the lower part of the interface than on its upper part (Figure 7-5).

In specimens containing slag, the corrosion rate is principally controlled by the resistivity of the system (binder) [207]. On the lower part of the interface, the poorer quality of the binder may lead to a decrease in the binder resistivity. This should explain the spread of corrosion for higher length on the lower part. This difference is not significant on the materials that do not contain slag because their resistivity is not high as much as the materials containing slag.

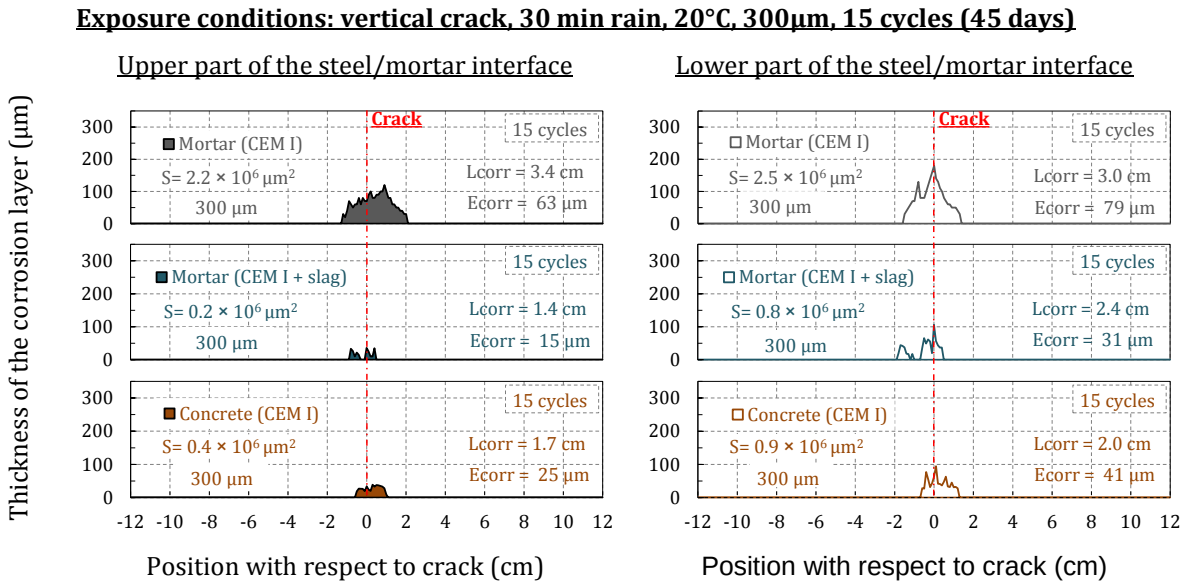

Figure 7-4 : Corrosion products repartition on the upper and the lower steel/mortar interfaces of specimens with different materials type (optical microscopy)

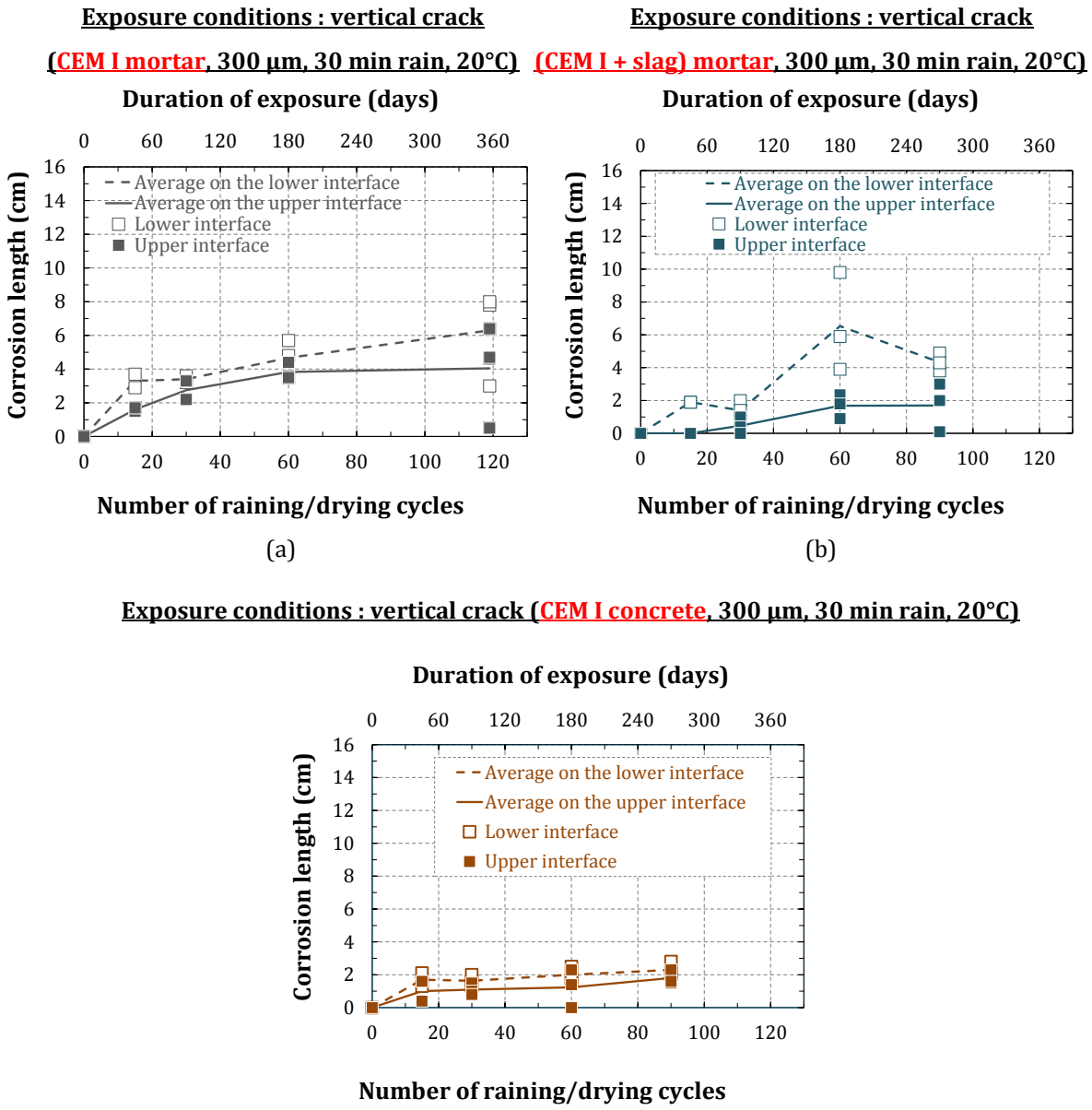

Figure 7-5 : Evolution of the corrosion length measured on the upper and the lower steel/mortar interfaces of specimens with different materials type (visual inspection)

7.3 CONCRETE SLABS

In this section, laboratory tests are performed on concrete slabs which are more representative of the cooling towers than the centimetric specimens. It is important to highlight that these concrete slabs contains two reinforcement layers (§2.3.1). First, the impact of steel/concrete interface quality on the carbonation spread is presented. Then its impact on the corrosion products layer distribution is investigated.

7.3.1 Steel/concrete interface carbonation

After the carbonation process, a sample is cut from the concrete slab as shown in Figure 2-50. It is then broken in two parts using the splitting test. Thereafter, reinforcements are extracted and two steel/concrete interfaces are subjected to the phenolphthalein pH indicator test. These interfaces correspond to the lower part of the upper longitudinal rebar and to the upper part of the lower longitudinal rebar with respect to casting direction (Figure 7-6). The spread of carbon dioxide along the remaining steel/concrete interfaces is not performed because of the presence of transversal rebars that inhibit the access to this information.

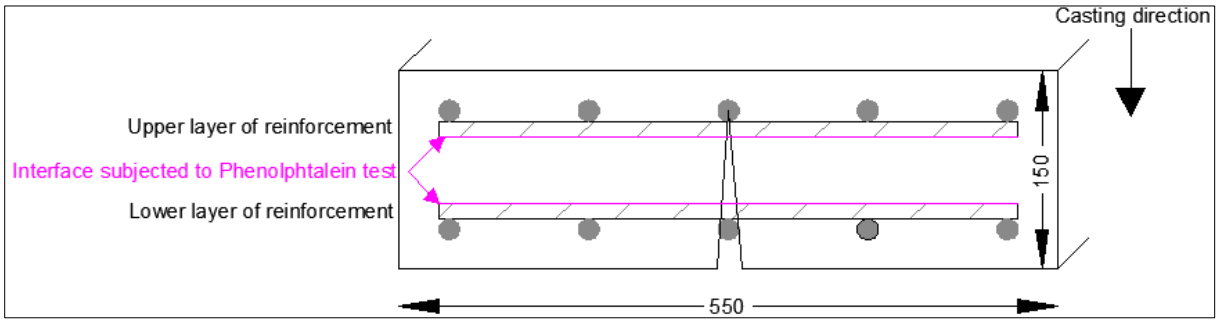

Figure 7-6: Schematic representation of the steel/concrete interfaces localization subjected to the phenolphthalein test (concrete slab)

Figure 7-7 shows a photograph of the tested interface after the phenolphthalein was sprayed. Carbon dioxide spread along the entire length of the lower steel/concrete interface of the upper reinforcement (Figure 7-7(a)). While, carbonation length remains limited to several cm along the upper part of the steel/concrete interface of the lower reinforcement despite the possible carbonation shrinkage that may occur due to the higher carbon dioxide concentration of 50% used during the carbonation test (Figure 7-7(b)). However, during the three point bending test, the upper rebar is subjected to a tensile stress lower than the one applied on the lower rebar. And, as shown in Figure 7-6, the width of the mechanical crack intercepting the upper rebar is lower than the one intercepting the lower rebar. Consequently, the mechanical damage should be smaller in the steel/concrete interface of the upper rebar than in the interface of the lower rebar. It could be concluded therefore that carbon dioxide spread along the lower part of the upper rebar for a length greater than the damaged one. This is due to the quality of this interface. Indeed, materials quantity under the upper rebar is higher than under the lower rebar. Consequently, settlement and water bleeding under the upper rebar is more important than under the lower rebar (Top bar effect). For this reason, significant defects and voids exists under the upper rebar and facilitates the carbon dioxide spread overall this interface.

Lower part of steel/concrete interface of the upper reinforcement rebar

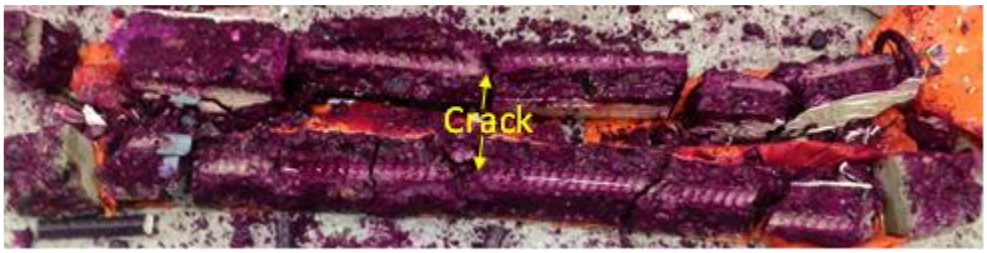

(a)

Upper part of steel/concrete interface of the lower reinforcement layer

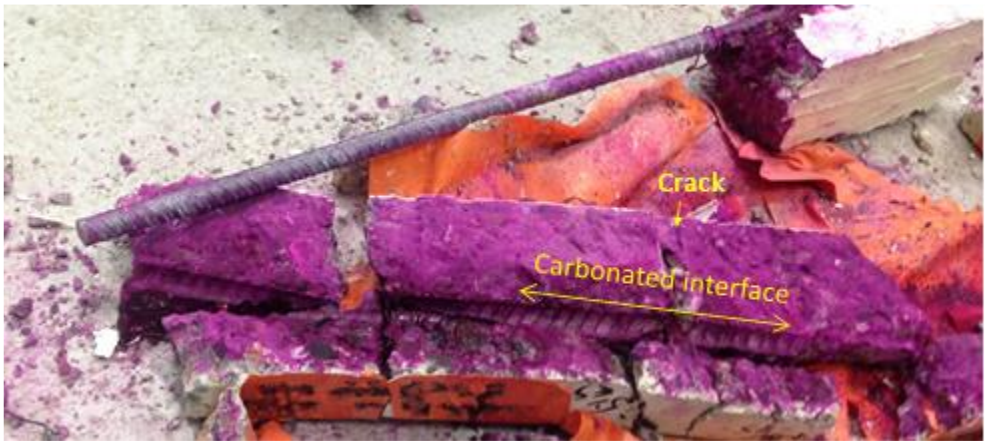

(b)

Figure 7-7: Photos of the carbonated interfaces in a concrete slab

7.3.2 Corrosion thickness

7.3.2.1 Optical microscopy observation

After 12 raining/drying cycles, another sample is cut in the direction shown in Figure 2-50. For the optical microscopy analysis, several transversal samples are cut and generated according to Figure 7-8. On the obtained samples, the entire perimeter of the rebar is shown. Samples are prepared as described in §2.7.2.1 and then optical microscopy analyses are performed.

Figure 7-10 provides local information on the corrosion layer distribution at different points located at either sides of the crack. It can be seen that the average corrosion thickness developed on the lower part of the upper rebar is slightly higher than the one measured on the lower part of the lower rebar (Figure 7-10(b)).

The same analysis is performed thereafter for a higher number of cycles equal to 24. During this analysis, the cutting way of the small samples is not similar and is performed as shown in Figure 7-9. In this cutting way, after polishing, the obtained samples are shown in Figure 2-52.

Sample 3 and 8 containing the upper and lower rebar respectively are analyzed using optical microscopy and the results are shown in Figure 7-11. These two samples are chosen to be analyzed because they contain the mechanical crack. Here again, the corrosion amount obtained on the lower part of the upper rebar is higher than the one obtained on the lower part of the lower rebar (Figure 7-11(b)).

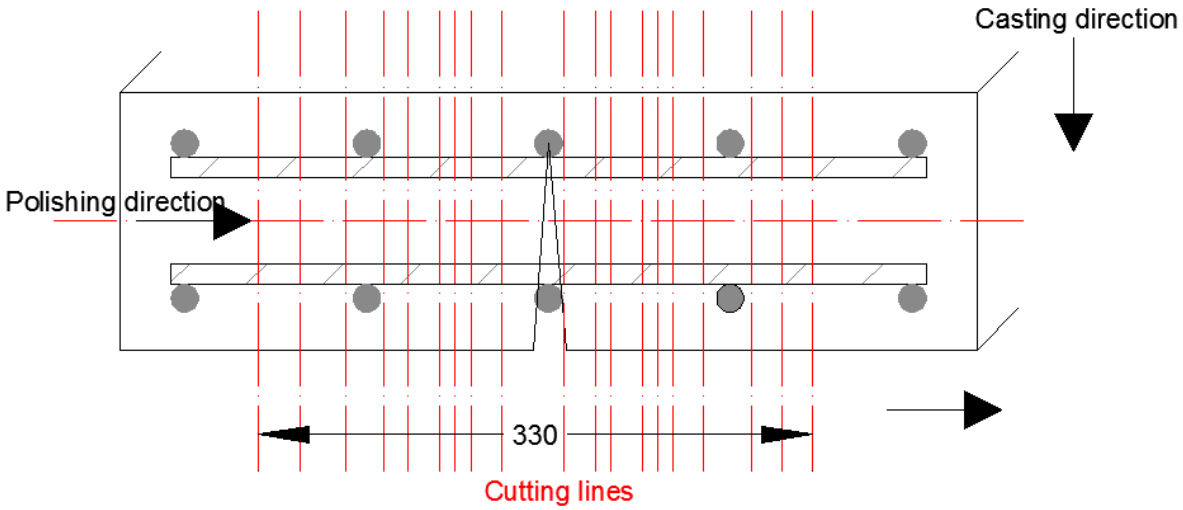

Figure 7-8: Transversal cutting localization on the sample extracted from a concrete slab subjected to 12 raining/drying cycles

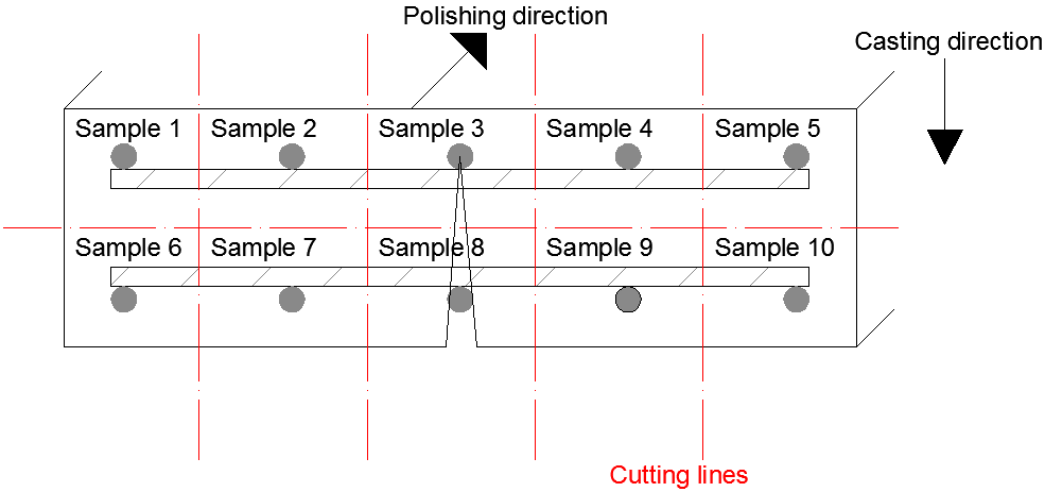

Figure 7-9: Cutting directions of samples from a specimen extracted from a concrete slab subject to 24 raining/drying cycles (similar to Figure 2-51)

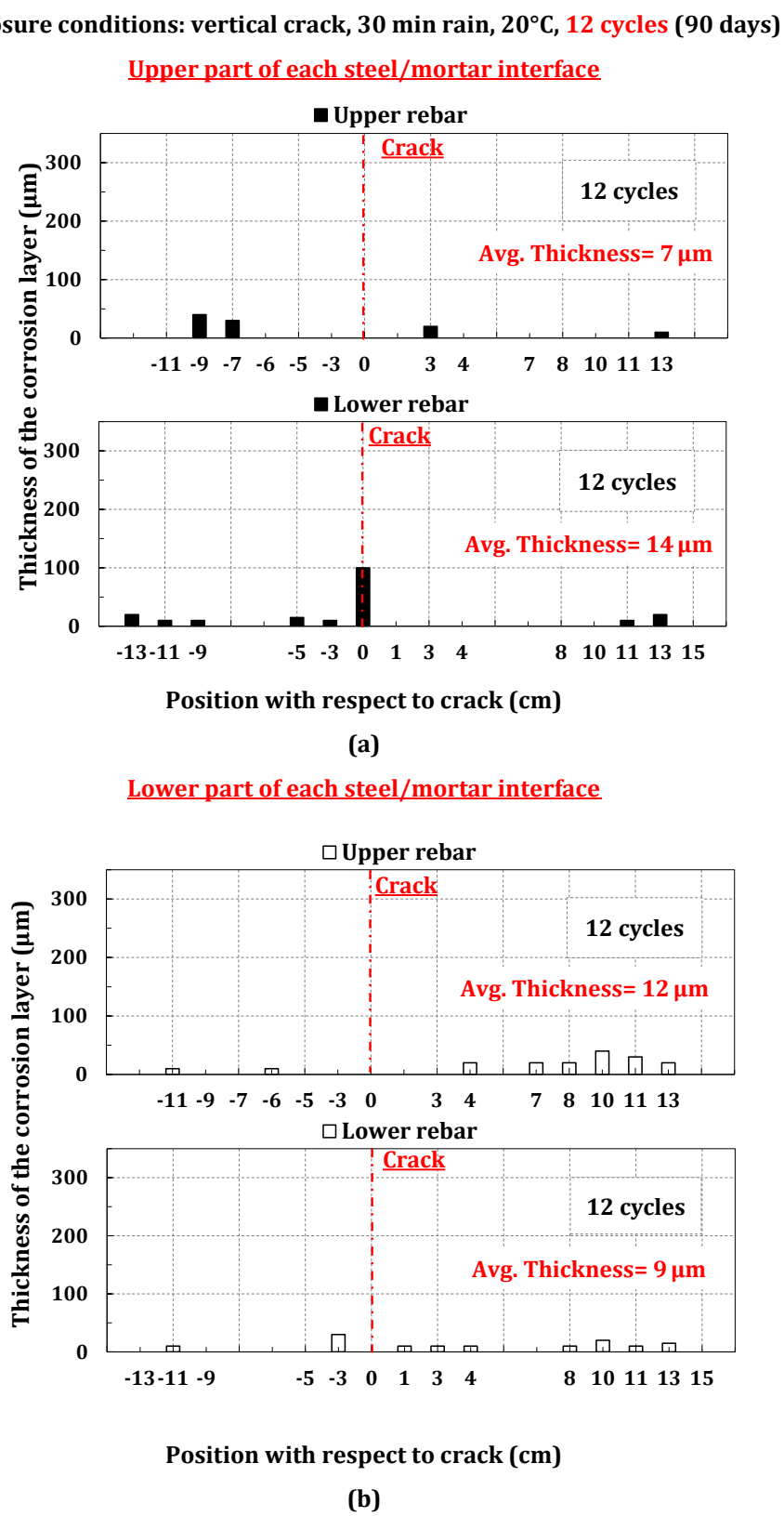

Figure 7-10: Corrosion products repartition on the upper and the lower steel/mortar interfaces of both reinforcement layers embedded in a concrete slab subjected to 12 cycles.

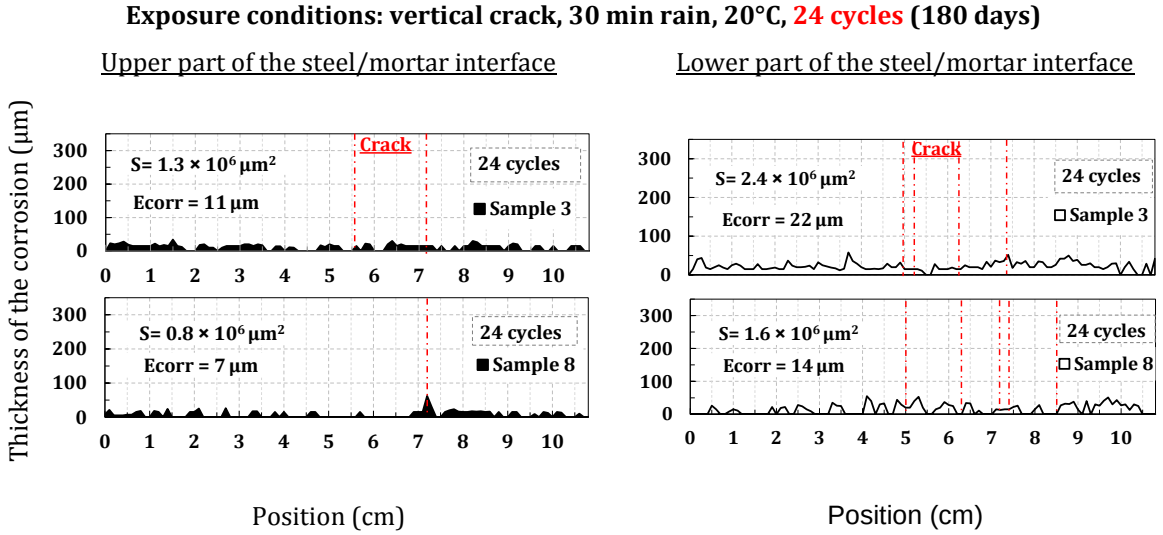

Figure 7-11 : Corrosion products repartition on the upper and the lower steel/mortar interfaces of both reinforcement layers embedded in a concrete slab subjected to 24 cycles.

Moreover, Figure 7-12 shows the corrosion layer on the transversal rebars existing in samples 3 and 8. For sample 3, located at the upper reinforcement layer with respect to casting direction, the corrosion appears mainly on the lower steel/concrete interface (Figure 7-12(a)). In sample 8, corrosion is localized near the crack location and is not visible over the entire lower part of the interface as shown for sample 3.

To summarize, corrosion is more developed along the lower interface of the upper rebars than along the lower interface of the lower rebar despite that the crack opening intercepting the lower reinforcement layer is larger than the one intercepting the upper reinforcement layer. This is due to the top bar effect (i.e., interface quality).

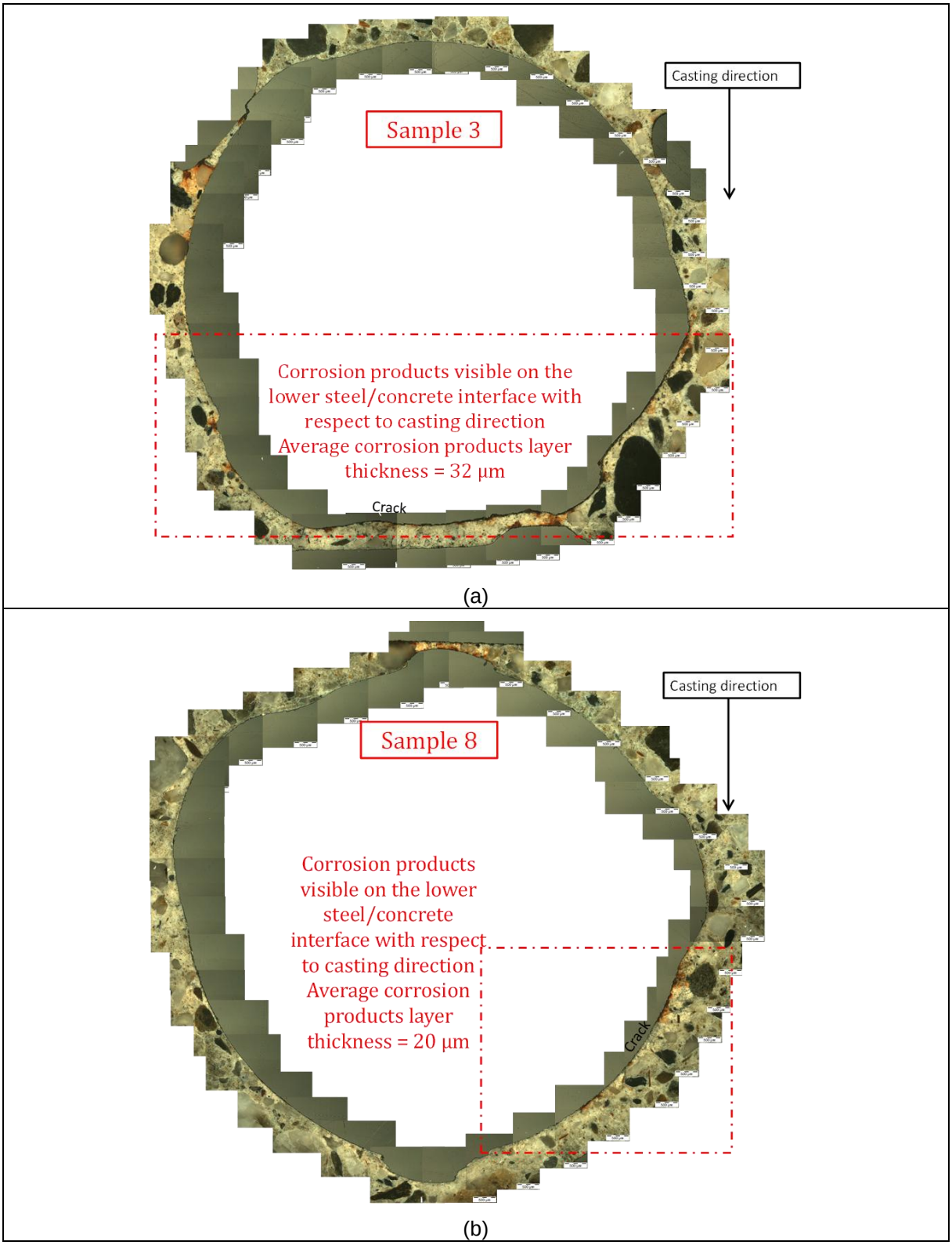

Figure 7-12: Thickness of the corrosion products layer along the transversal rebars extracted from specimens exposed to 24 cycles

7.4 CORROSION PRODUCTS TYPE

The corrosion products type are only analyzed on centimetric specimens reinforced by a unique rebar. A comparison between the corrosion products type developed on the upper and the lower steel/binder interface of the same rebar is performed in this section. To this end, prismatic specimens corroded in the reference test and showing 300 and 500 µm residual crack openings are used.

Figure 7-13 and Figure 7-14 show respectively the corrosion layer developed along the upper and lower steel/mortar interface of the rebar embedded in CEM I mortar specimen showing 500 µm residual crack opening. While Figure 7-15 shows only the corrosion layer along the lower interface of the rebar embedded in CEM I mortar specimen having 300 µm residual crack opening. The corrosion developed on the upper steel/mortar interface of the latter specimens is given in Figure 4-11Figure 4-12. All the obtained Raman spectra are reported in Appendix I.6.9. Figure 7-16 summarizes schematically the corrosion products type developed along the upper and lower analyzed interfaces. It can be deduced that the corrosion products are similar along both interfaces and are mainly composed of reactive phases.

Vertical crack, 500 µm residual crack opening, 30 minutes rain, 20°C, 15 cycles (30 days), upper steel/mortar interface

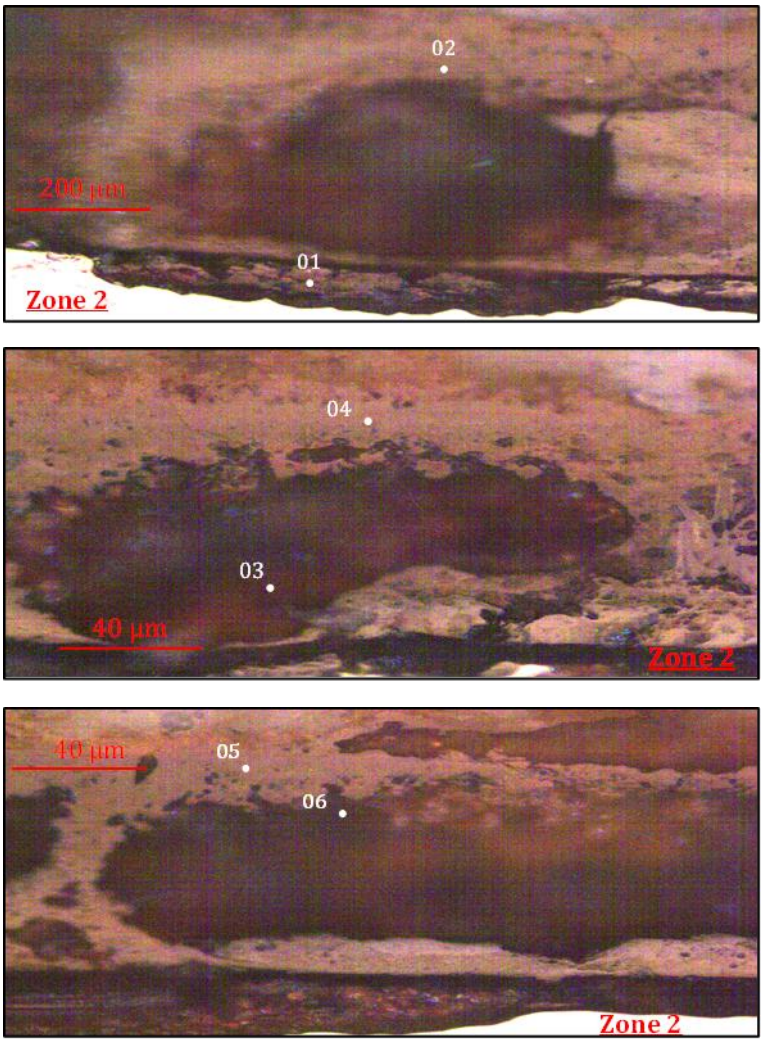

01 = Goethite + Ferrihydrite

02 = Goethite + Ferrihydrite

03 = Ferrihydrite

04 = Goethite + Ferrihydrite

05 = Goethite

06 = Goethite + Lepidocrocite + possible presence of Ferrihydrite

Figure 7-13: Corrosion layer observed at the upper steel/mortar interfaces located far from the crack and deep in the crack in specimens corroded in the reference test for 15 cycles (W_r = 500 µm)

Vertical crack, 500 µm residual crack opening, 30 minutes rain, 20°C, 15 cycles (30 days), lower steel/mortar interface

07 = Goethite + Lepidocrocite

Figure 7-14: Corrosion layer observed at the lower steel/mortar interfaces located far from the crack and deep in the crack in specimens corroded in the reference test for 15 cycles (W_r = 500 µm)

Vertical crack, 30 minutes rain, 72 hours drying, 20°C, 60 cycles, 180 days, 300 µm, lower steel/mortar interface

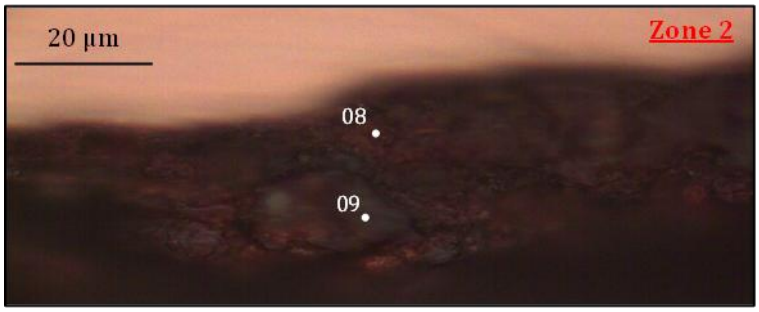

08 = Lepidocrocite + Ferrihydrite + undetermined phase

09 = Ferrihydrite

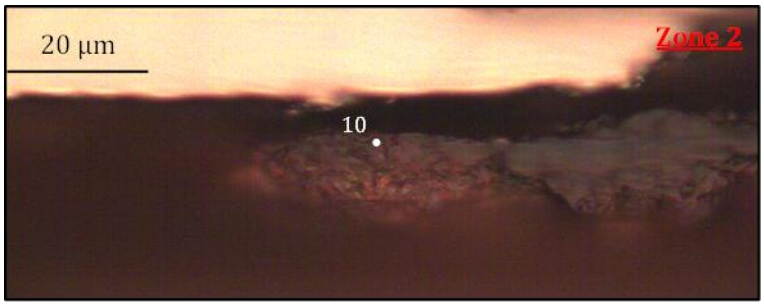

10 = Ferrihydrite + Lepidocrocite

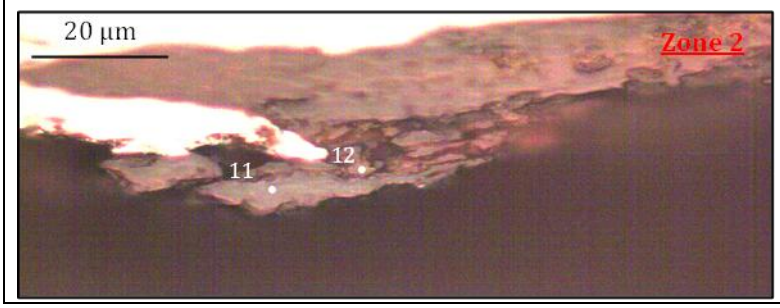

11 = Goethite + Lepidocrocite

12 = Goethite

Figure 7-15: Corrosion layer observed at the lower steel/mortar interfaces located far from the crack and deep in the crack in specimens corroded in the reference test for 60 cycles (W_r = 300 µm)

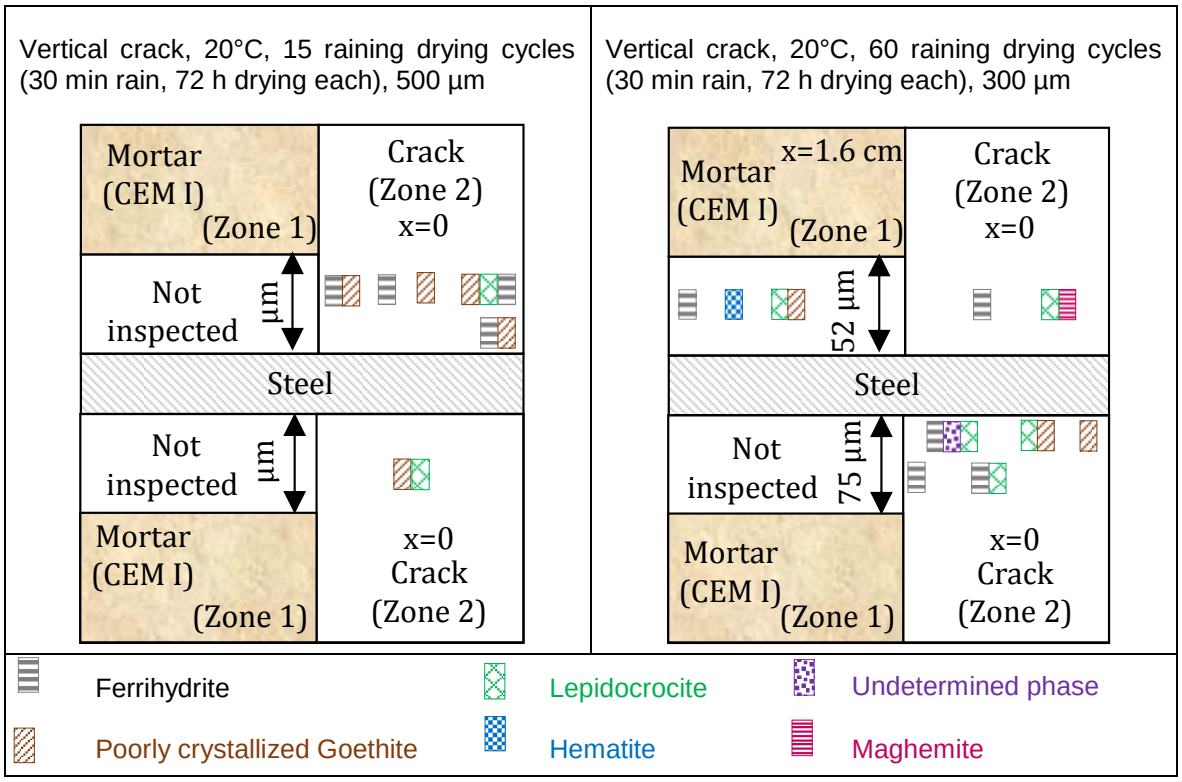

Figure 7-16: Summary of the corrosion products identified on the upper and lower steel/mortar interfaces of specimens corroded in the reference test.

7.5 DISCUSSION AND CONCLUSION

In this chapter, the effect of the steel/binder interface quality on the carbonation-induced corrosion is tested and analyzed.

The results indicate that in specimens containing only one rebar, the thickness of the corrosion products in the lower interface is higher than the one developed on the upper interface due to the higher porosity of the lower interface.
Additionally, it is observed that this difference in the corrosion thickness decreases with the increase in the mechanical loading. This is due to the fact that the thickness of the corrosion products on the lower interface is independent from the intensity of the mechanical damage which is not the case for the upper interface.
Moreover, for materials based on Portland cement, no difference can be noted between the corrosion length developed on the upper and the lower interface of the same rebar. However, in materials containing slags, the corrosion length is higher on the lower interface of the rebar than on its upper interface, and could be due to a difference in the resistivity of the binder. Indeed, this observation may be due to a smaller resistivity of the binder surrounding the lower interface comparing with the one surrounding the upper interface. Consequently, the macrocell corrosion process may not be limited on the lower interface as much as on the upper one.

In specimens containing two layers of reinforcements, the lower part of the upper reinforcement layer shows the highest spread of carbonation and the highest corrosion thickness even if it intercepts a thinner crack. These observations are due to the poorer quality of the lower part of the upper horizontal rebars induced by the top bar effect.

From all these results, it can be deduced that the steel/binder interface quality is more important to reinforcement corrosion issues than the surface crack width.

GENERAL CONCLUSION

The objective of this study is to investigate the carbonation-induced corrosion process in cracked concrete while varying several parameters such as the crack widths, crack orientations with respect to rain, rain durations, temperatures, materials type, location of the rebars in the specimens, etc. Since an industrial application is behind this project, the experimental program is defined in a manner to be the most representative for the cooling towers of EDF nuclear power plants.

The first fundamental step in this project is to find the suitable cracking protocol that leads to cracks similar to those found on the cooling towers. The first requirement is to define a suitable method for controlling the crack widths. The second and the most important factor is to limit and quantify the zone in which mechanical damages may occur along the steel/mortar interface.

Laboratory specimens of 70 × 70 × 280 mm are cracked by the mean of three point bending test. Loading/unloading cycles are realized to reach the three desired residual crack widths of 100, 300 and 500 µm which are measured using a Linear Variable Differential Transformer (LVDT) during the test. In addition, digital image correlation and X-rays computed tomography are also performed to identify the evolution of the crack width in the entire height of the specimen and in the zones close to the reinforcement steel. It is deduced that at a given height of the specimen, the residual crack opening deep in the specimen is approximately equal to the one measured on its surface. In addition, Thales' theorem can be used to determine the residual crack opening near the rebar with respect to its maximal value measured by the mean of the LVDT. The ratio between these two values of the crack widths is 44 ± 5%.

Accelerated carbonation is performed after cracking and the length of the carbonated steel/binder interface is used as an indicator for the damaged zone. However, the carbonation conditions should be well defined, especially the carbon dioxide concentration which may induce supplementary damages according to its value. In this study, it is proven that 50% of CO_2 concentration commonly used for this type of tests is non-appropriate because it induces high carbonation shrinkage along the steel/mortar interface and thus overestimate the length of the damaged zone. The carbonation protocol proven to be the most suitable is 30 days at 3% CO_2, 55% relative humidity and 25°C temperature. Using this protocol, the damaged steel/mortar interface is quantified and proven to be limited to several centimeters from either sides of the crack.

The accelerated carbonation procedure is used also to accelerate the rebar depassivation and is performed on all the prismatic specimens for one month duration before exposing them to corrosion conditions.

During the corrosion tests, the influence of the crack opening on the carbonation-induced corrosion process is tested on specimens subjected to corrosion under raining/drying cycles at 20°C for 30 minutes rain duration in each cycle. After a certain number of raining/drying cycles, a decrease in the corrosion rate is detected. This is attributed to rebar repassivation which is due to the corrosion products that seal the cracks and act as a protective layer for the rebar by limiting the access of aggressive agents. During the repassivation phase, the rate of the corrosion process is independent from the residual crack opening.

In addition, carbonation-induced corrosion rate is independent from the crack orientation with respect to rain and from the two raining durations tested (3 and 30 minutes). This is linked to

the corrosion products that develop in the crack and limit the access of water to the rebar masking therefore the influence of the raining/drying cycles on the corrosion process.
In fact, these two rain durations tested are supposed to represent two different sides of the cooling tower that may not receive the similar amount of water. Therefore, the obtained results confirm that these sides are corroded similarly and cannot be treated differently in the cooling towers maintenance program.

Some corrosion tests are performed under raining/drying cycles at 40°C instead of 20°C and aim to determine the impact of the temperature on the corrosion process. The same corrosion rate is found under these two temperatures because the drying phase at 40°C induces an increase in the mortar resistivity and limits the macrocell corrosion process. This will mask the increase in the corrosion rate that may be induced by the thermodynamic activation of the anodic and cathodic reactions at 40°C leading therefore to corrosion kinetics comparable to those found at 20°C. Consequently, independent from their locations, the cooling towers are expected to be corroded similarly and should thus be maintained similarly.

Some specimens are exposed to the natural environment of Saclay and aim to validate whether the developed experimental procedure of corrosion in the laboratory leads to corrosion results that are representative of the reality. Corrosion kinetics tends also to decrease with time which lead the author to deduce that the corrosion of rebar in specimens exposed to natural environments conditions follows the same mechanism than those corroded in the laboratory. Additionally, this experiment constitutes a test that may be used to validate the empirical model that will be developed later by EDF to evaluate the corrosion kinetics.

All the above described corrosion conditions are tested on CEM I mortar specimens. However, EDF cooling towers materials are performed with concrete based on (CEM I + slag) as communicated by EDF. For this reason, some (CEM I + slag) mortar and (CEM I) concrete specimens are prepared, cured, carbonated and corroded in the same manner as the CEM I mortar specimens under raining/drying cycles at 20°C for 30 minutes rain. The same corrosion rate tendency is visible for the three materials tested and this is linked to the corrosion products that seal the crack and control the corrosion evolution independently from the binder. However, it should be noted that the corrosion length in concrete and (CEM I + slag) mortar specimens is lower than the one measured in CEM I mortar specimens. In the concrete specimens, the observed difference in the corrosion lengths is due to a difference in the damaged zone lengths because concrete may have a higher tensile resistance than mortar.
Nevertheless, the difference noted in the corrosion lengths measured in specimens containing slag may be related to the high resistivity of the medium surrounding the rebar which limit the flow of hydroxyl ions from the cathodic zone to the anodic one. In addition, cathodic reactions may also be restrained because of the lack of oxygen due to the small porosities of materials containing slag. The general conclusion that could be drawn is that the rate of iron dissolution obtained in (CEM I) mortar specimens is the same in cracked concrete specimens and cracked mortar specimens that contain slag. However, the zone of the corroded area is smaller in concrete and (CEM I + slag) mortar specimens.

Finally, some concrete slabs of 550 × 300 × 150 mm with two reinforcement layers are fabricated in order to test the impact of the steel/concrete interface quality on the carbonation-induced corrosion. The results indicate that the upper rebar in the concrete slabs defined with respect to casting directions shows the highest corrosion thickness despite that it intercepts a crack with a smaller width than the lower rebar. This is due to the presence of defects and voids under the upper rebar which are the result of settlement and bleeding of the materials (“Top bar effect”). The same observation is noted for the 70 × 70 × 280 mm specimens containing a unique rebar. In fact, the thickness of the corrosion products layer is higher on the lower part of this rebar than on its upper part. This is due to the high porosity of

the materials under this horizontal rebar. Additionally the thickness of the corrosion products layer on this lower interface is shown to be independent from the intensity of the mechanical steel/mortar interface damage because the higher porosity of the lower interface promotes a higher corrosion layer thickness. The main conclusion that could be drawn in this case is that the steel/binder interface quality is more important to reinforcement corrosion issues than the surface crack width. Additionally, since gaps are induced by concrete settlement and water bleeding, the localization of the horizontal rebars in reinforced concrete structures is determinant for the steel/concrete quality. Indeed, the rebars subjected to higher corrosion may be localized at the highest part of each casted concrete block and on this rebar the corrosion diagnostic should be performed. This should be taken into account while the inspection of the cooling towers.

The corrosion products developed in all the above detailed exposure conditions are analyzed by Raman micro-spectroscopy. It can be deduced that the degree of saturation has the highest impact on the corrosion patterns. At low saturation (cycles under 40°C, cycles of 3 minutes rain duration, Saclay environment), amorphous corrosion products dehydrate and recrystallize to a more crystallized phase which are more stable and characterized by a small reactivity. This is not the case in exposure conditions inducing high saturation (30 minutes rain at each cycle, 90% relative humidity condition) for which the corrosion products are found to be more reactive with low crystallinity state. Additionally, it is also detected that the nature of the corrosion products type does not evolve during the duration of this study (120 raining/drying cycles corresponding to 12 months exposure duration).

A general observation could also be noted for all the above tested conditions which correspond to a decrease in the corrosion kinetics with respect to time in addition to an absence of corrosion cracks detection. This is an indicator of the presence of a retarding phase in the corrosion process. Moreover, this phase is detected in all the free corrosion potential measurements realized on some exposure conditions. Indeed, corrosion potential decreases at the beginning of the test where a macrocell and microcell corrosion process take place then increases after a certain number of raining/drying cycles and tends to reach the corrosion potential of a passivated rebar. During this second phase, the corrosion mechanism is a microcell process. All these observations lead the author to confirm the presence of corrosion-delaying effect (repassivation) which reduces the hazardous impact of corrosion on the structure durability. However, the sustainability of the structure may be threatened by the total carbonation of the concrete cover. The long term corrosion behavior is not studied in the frame of this project due to time constraint, however, phenomenological corrosion models aiming to predict the long term behavior are proposed for steel located in cracked and carbonated concrete. In the case of static cracks, basing on the results of this study, it can be predicted that structure sustainability will not be threatened by carbonation-induced corrosion deep in the crack.

It is important to insist that this conclusion does not apply to structures:

- Subjected to frost or chemical attacks where physical and chemical attacks are decisive for the durability more than carbonation-induced corrosion deep in the crack.

- Subjected to dynamic loading inducing a variation in the crack widths. Indeed, the variation in the crack width may inhibit the sealing effect of the corrosion products and inhibit thus the repassivation.

- Subjected to an environment containing chloride.

Consequently, the ambient environment impact the structure durability more than the mechanical cracks that may exist in the concrete cover.

Since the cooling towers could be subjected to crack width variation induced by a variation in the temperature, relative humidity and wind, it is of interest in a future work to monitor the corrosion rate evolution under this conditions. In order to simulate the crack width variation, cyclic loading may be performed on the specimens exposed to the corrosion environment at constant time intervals. A schematic representation for the experimental procedure that could be performed is given in (Figure 8-1). By the mean of a torque wrench, loading could be changed. Free corrosion potential measurements may be sufficient to indicate the evolution of the corrosion during the load variations cycles.

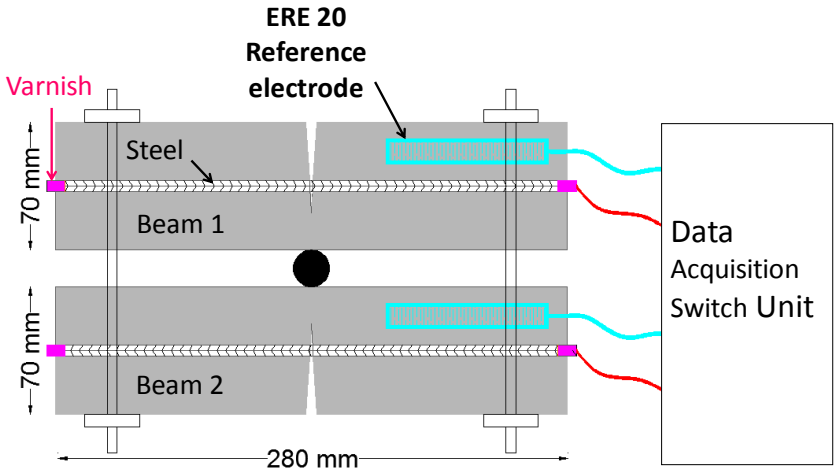

Figure 8-1 : Laoding system

In addition, it is important to investigate specimens from existing cooling towers for two reasons. The first is to have an estimation of the corrosion state and degree in the cooling towers. The second reason is to make a comparison with the laboratory results in order to verify if they are in accordance. These samples may be taken from the rebar located at the highest location in a casted concrete block because it will represent the most critical corrosion state

According to the degree of corrosion that will be found, it can be confirmed whether the cooling towers are threatened by corrosion deep in the crack or much more by the surrounding environment. And based on the observation that will be drawn, it could be decided whether a corrosion treatment is needed or a protection of concrete cover against degradation requested.

REFERENCES

[1] R. Francois and G. Arliguie, “Effect of micro-cracking and cracking on the development of corrosion in reinforced concrete members,” *Mag. Concr. Res.*, vol. 51, pp. 143–150, 1999.

[2] J. A. González *et al.*, “Some questions on the corrosion of steel in concrete. Part II: Corrosion mechanism and monitoring, service life prediction and protection methods,” *Mater. Struct.*, vol. 29, pp. 97–104, 1996.

[3] Y. F. Houst, “Carbonatation du béton et corrosion des armatures,” *Chron. des matériaux Constr.*, vol. 15, pp. 569–574, 1984.

[4] P. D. Tennis and H. M. Jennings, “A model for two types of calcium silicate hydrate in the microstructure of Portland cement pastes,” *Cem. Concr. Res.*, vol. 30, pp. 855–863, 2000.

[5] P. K. Mehta and P. J. Monteiro, *Concrete: Microstructure, Properties, and Materials*. 2006.

[6] V. Baroghel-Bouny, “Caractérisation microstructurale et hydrique des pâtes de ciment et des bétons ordinaires et à très hautes performances,” Thèse Ecole Nationale des Ponts et Chaussées, 1994.

[7] J. Stark and K. Bollmann, “Delayed Ettringite Formation in Concrete,” *Nord. Concr. Res.*, vol. 23, pp. 4–28, 2000.

[8] I.-S. Yoon, O. Çopuroğlu, and K.-B. Park, “Effect of global climatic change on carbonation progress of concrete,” *Atmos. Environ.*, vol. 41, pp. 7274–7285, 2007.

[9] S. Werner and J. J. Morgan, *Aquatic chemistry: chemical equilibria and rates in natural waters*. John Wiley & Sons, 2012.

[10] N. Hyvert, “Application de l’approche probabiliste à la durabilité des produits préfabriqués en béton,” PhD thesis, Université Paul Sabatier-Toulouse III, 2009.

[11] M. Thiery, “Modélisation de la carbonatation atmosphérique des matériaux cimentaires. Prise en compte des effets cinétiques et des modifications microstructurales et hydriques,” Thèse Ecole Nationale des Ponts et Chaussees, 2006.

[12] A. Dunster, “An investigation of the carbonation of cement paste using trimethylsilylation,” *Adv. Cem. Res.*, vol. 2, pp. 99–106, 1989.

[13] G. W. Groves, A. Brough, I. G. Richardson, and C. M. Dobson, “Progressive changes in the structure of hardened C3S cement pastes due to carbonation,” *J. Am. Ceram. Soc.*, vol. 74, pp. 2891–2896, 1991.

[14] M. Castellote, L. Fernandez, C. Andrade, and C. Alonso, “Chemical changes and phase analysis of OPC pastes carbonated at different CO2 concentrations,” *Mater. Struct.*, vol. 42, pp. 515–525, 2009.

[15] H. Weber, “Methods for calculating the progress of carbonation and the associated life expectancy of reinforced concrete components,” *Betyonwerk+Fertigteil-Technik*, vol. 8, pp. 508–514, 1983.

[16] P. Castro, M. . Sanjuán, and J. Genescá, “Carbonation of concretes in the Mexican Gulf,” *Build. Environ.*, vol. 35, pp. 145–149, Feb. 2000.

[17] V. G. Papadakis, M. N. Fardis, and C. G. Vayenas, “Hydration and carbonation of pozzolanic cements,” *ACI Mater. J.*, vol. 89, pp. 119–130, 1992.

[18] T. Chaussadent, *Etat des lieux et réflexions sur la carbonatation du béton armé*. Paris: Thèse Laboratoire Central des Ponts et Chaussees, 1999.

[19] D. Burden, “The Durability of Concrete Containing High Levels of Fly Ash.,” Thesis University of New Brunswick, 2006.

[20] E. Drouet, “Impact de la température sur la carbonatation des matériaux cimentaires - prise en compte des transferts hydriques,” PhD thesis, Ecole Normale Supérieure de Cachan, 2010.

[21] H.-W. Song, S.-J. Kwon, K.-J. Byun, and C.-K. Park, “Predicting carbonation in early-aged cracked concrete,” *Cem. Concr. Res.*, vol. 36, pp. 979–989, 2006.
[22] J. Alexandre and M. Vénuat, “De la carbonatation du béton-partie II,” *Rev. des matériaux Constr.*, vol. 639, pp. 469–481, 1968.
[23] P. A. M. Basheer, S. E. Chidiact, and A. E. Long, “Predictive models for deterioration of concrete structures,” *Constr. Build. Mater.*, vol. 10, pp. 27–37, 1996.
[24] R. François and J. C. Maso, “Effect of damage in reinforced concrete on carbonation or chloride penetration,” *Cem. Concr. Res.*, vol. 18, pp. 961–970, 1988.
[25] A. Castel, R. François, and G. Arliguie, “Effect of loading on carbonation penetration in reinforced concrete elements,” *Cem. Concr. Res.*, vol. 29, pp. 561–565, 1999.
[26] S. Alahmad, A. Toumi, J. Verdier, and R. François, “Effect of crack opening on carbon dioxide penetration in cracked mortar samples,” *Mater. Struct.*, vol. 42, pp. 559–566, 2009.
[27] L. Liu, J. Ha, T. Hashida, and S. Teramura, “Development of a CO2 solidification method for recycling autoclaved lightweight concrete waste,” *J. Mater. Sci. Lett.*, vol. 20, pp. 1791–1794, 2001.
[28] J. John, K. Hiari, and H. Mihashi, “Influence of environmental moisture and température on carbonation of mortar,” *Concr. Res. Technol.*, vol. 1, pp. 85–94, 1990.
[29] S. Poyet, “Experimental investigation of the effect of temperature on the first desorption isotherm of concrete,” *Cem. Concr. Res.*, vol. 39, pp. 1052–1059, 2009.
[30] S. Wong, T. Wee, S. Swaddiwudhipong, and S. Lee, “Study of water movement in concrete,” *Mag. Concr. Res.*, vol. 53, pp. 205–220, 2001.
[31] T. Mori, K. Shirayamaka, K. Kamimura, and A. Yoda, “Carbonation of blast-furnace slag cement,” in *Proceedings of the 26th annual meeting of cement assocation of Japan*, 1972, pp. 326–329.
[32] K. Yanagi and F. Tomosawa, “An experiment on the prediction of carbonating speed of concrete. Part II: Influence of various factors on carbonation,” in *Proceedings of Architectural Institute of Japan*, 1987, p. 247–248.
[33] V. G. Papadakis, C. G. Vayenas, and M. N. Fardis, “Fundamental modeling and experimental investigation of concrete carbonation,” *Mater. J.*, vol. 88, pp. 363–373, 1991.
[34] G. Villain, G. Croquette, and K. Ounoughi, “Transferts dans les bétons et Durabilités des Ouvrages. Optimisation des conditions d’essais pour la carbonatation accélérée des bétons.,” Bordeaux, 2000.
[35] S. P. Burg, *Postharvest physiology and hypobaric storage of fresh produce*. Miami, Florida, USA: CABI, 2004.
[36] G. J. Verbeck, “Carbonation of Hydrated Portland Cement,” *Cem. Concr. Spec. Tech. Publ.*, vol. 205, pp. 17–36, 1958.
[37] I. Galan, C. Andrade, and M. Castellote, “Natural and accelerated CO2 binding kinetics in cement paste at different relative humidities,” *Cem. Concr. Res.*, vol. 49, pp. 21–28, 2013.
[38] N. Hyvert, A. Sellier, F. Duprat, P. Rougeau, and P. Francisco, “Dependency of C-S-H carbonation rate on CO2 pressure to explain transition from accelerated tests to natural carbonation,” *Cem. Concr. Res.*, vol. 40, pp. 1582–1589, 2010.
[39] F. Matsushita, Y. Aono, and S. Shibata, “Microstructure Changes in Autoclaved Aerated Concrete during Carbonation under Working and Accelerated Conditions,” *J. Adv. Concr. Technol.*, vol. 2, pp. 121–129, 2004.
[40] G. Groves, D. Rodway, and I. Richardson, “The carbonation of hardened cement pastes,” *Adv. Cem. Res.*, vol. 3, pp. 117–125, 1990.
[41] C. M. Hunt and L. A. Tomes, “Reaction of blended Portland Cement Paste with Carbon- dioxide,” *J. Res. Natl. Bur. Stand. (1934).*, vol. 66A, pp. 473–481, 1962.
[42] E. Swenson and P. Sereda, “Mechanism of the Carbonation Shrinkage of Lime and Hydrated Cement,” *J. Appl. Chem.*, vol. 18, pp. 111–117, 1968.
[43] J. J. Chen, J. J. Thomas, and H. M. Jennings, “Decalcification shrinkage of cement paste,” *Cem. Concr. Res.*, vol. 36, pp. 801–809, 2006.

[44] P. Faucon, B. Gerard, J. Jacquinot, and J. Marchand, “Water attack of a cement paste: towards an improved accelerated test?,” *Adv. Cem. Res.*, vol. 10, pp. 67–73, 1998.
[45] Y. F. Houst and F. H. Wittmann, “Depth profiles of carbonates formed during natural carbonation,” *Cem. Concr. Res.*, vol. 32, pp. 1923–1930, 2002.
[46] H. Sadouki, “L’effet de paroi: son influence sur les propriétés du béton superficiel,” *Chron. des matériaux Constr. Constr.*, vol. 18, pp. 11–15, 1987.
[47] P. C. Kreijger, “The skin of concrete composition and properties,” *Matériaux Constr. Constr.*, vol. 17, pp. 275–283, 1984.
[48] J. M. Khatib and P. S. Mangat, “Porosity of cement paste cured at 45°C as a function of location relative to casting position,” *Cem. Concr. Compos.*, vol. 25, pp. 97–108, 2003.
[49] J. M. Khatib, S. Kenai, J. S. Zhang, S. Firat, and P. H. Harris, “Effect of sample location and curing on pore volume and threshold diameter of cement paste with and without Slag,” in *Second International Conference on Sustainable Construction Materials and Technologies*, 2010, p. 9.
[50] C. D. Atis, “Accelerated carbonation and testing of concrete made with fly ash,” *Constr. Build. Mater.*, vol. 17, pp. 147–152, 2003.
[51] J. P. Balayssac, C. H. Détriché, and J. Grandet, “Effects of curing upon carbonation of concrete,” *Constr. Build. Mater.*, vol. 9, pp. 91–95, 1995.
[52] N. I. Fattuhi, “Carbonation of concrete as affected by mix constituents and initial water curing period,” *Mater. Struct.*, vol. 19, pp. 131–136, 1986.
[53] D. Chen, E. Sakai, M. Daimon, and Y. Ohba, “Carbonation of low heat portland cement paste precured in water for different time,” *J. Univ. Sci. Technol. Beijing, Miner. Metall. Mater.*, vol. 14, pp. 178–184, 2007.
[54] C. Clear, “The effects of autogenous healing upon the leakage of water through cracks in concrete,” Buckinghamshire England, 1985.
[55] Y. F. Houst and F. H. Wittmann, “Retrait de carbonatation,” *Chron. des matériaux Constr.*, vol. 20, pp. 255–260, 1989.
[56] C. F. Chang and J. W. Chen, “Strength and elastic modulus of carbonated concrete,” *ACI Mater. J.*, vol. 102, pp. 315–321, 2005.
[57] M. Auroy *et al.*, “Impact of carbonation on unsaturated water transport properties of cement-based materials,” *Cem. Concr. Res.*, vol. 74, pp. 44–58, 2015.
[58] V. L’Hostis, D. Neff, L. Bellot-Gurlet, and P. Dillmann, “Characterization of long-term corrosion of rebars embedded in concretes sampled on French historical buildings aged from 50 to 80 years,” *Mater. Corros.*, vol. 60, pp. 93–98, 2009.
[59] A. Demoulin, C. Trigance, D. Neff, E. Foy, P. Dillmann, and V. L’hostis, “The evolution of the corrosion of iron in hydraulic binders analysed from 46- and 260-year-old buildings,” *Corros. Sci.*, vol. 52, pp. 3168–3179, 2010.
[60] K. Sagoe-Crentsil and F. Glasser, “Steel in concrete: Part IA review of the electrochemical and thermodynamic aspects,” *Mag. Concr. Res.*, vol. 41, pp. 205–212, 1989.
[61] N. T. Vu, “Contribution à l’étude de la corrosion par carbonatation du béton armé : approche expérimentale et probabilitiste,” Thèse Université de Toulouse, 2011.
[62] V. L’Hostis, E. Amblard, C. Blanc, F. Miserque, C. Paris, and L. Bellot-Gurlet, “Passive corrosion of steel in concrete in context of nuclear waste disposal,” *Corros. Eng. Sci. Technol.*, vol. 46, pp. 177–181, 2011.
[63] J. A. González, S. Feliú, P. Rodríquez, E. Ramírez, C. Alonso, and C. Andrade, “Some questions on the corrosion of steel in concrete- Part I : when, how and how much steel corrodes,” *Mater. Struct.*, vol. 29, pp. 40–46, 1996.
[64] L. Bertolini, B. Elsener, P. Pedeferri, E. Redaelli, and R. B. Polder, *Corrosion of steel in concrete: prevention, diagnosis, repair*. Wiley-VCH, 2005.
[65] B. Huet, V. L’Hostis, L. Tricheux, and H. Idrissi, “Influence of alkali, silicate, and sulfate content of carbonated concrete pore solution on mild steel corrosion behavior,” *Mater. Corros.*, vol. 61, pp. 111–124, 2010.

[66] G. S. Duffó, W. Morris, I. Raspini, and C. Saragovi, “A study of steel rebars embedded in concrete during 65 years,” *Corros. Sci.*, vol. 46, pp. 2143–2157, 2004.
[67] P. Bamforth, *Probalistic Performance based durability Design of Concrete Structures*. Management of concrete structures for long-term serviceability. Proceedings of the Int. Seminar. Sheffield, UK, 1997.
[68] K. Tuutti, *Corrosion of steel in concrete*. Cement and Concrete Research Institute, 1982.
[69] C. Arya and F. K. Ofori-Darko, “Influence of crack frequency on reinforcement corrosion in concrete,” *Cem. Concr. Res.*, vol. 26, pp. 345–353, 1996.
[70] N. S. Berke, M. P. Dallaire, M. C. Hicks, and R. J. Hoopes, “Corrosion of Steel in Cracked Concrete,” *Corros. Sci.*, vol. 49, pp. 934–943, 1993.
[71] O. Gautefall and O. Vennesland, “Effects of cracks on the corrosion of embedded steel in silica-concrete compared to ordinary concrete,” *Nord. Concr. Res.*, vol. 2, pp. 17–28, 1983.
[72] T. U. Mohammed, N. Otsuki, M. Hisada, and T. Shibata, “Effect of Crack Width and Bar Types on Corrosion of Steel in Concrete,” *J. Mater. Civ. Eng.*, vol. 13, pp. 194–201, 2001.
[73] P. Schießl and M. Raupach, “Laboratory Studies and Calculations on the Influence of Crack Width on Chloride-Induced Corrosion of Steel in Concrete,” *ACI Mater. J.*, vol. 94, pp. 56–61, 1997.
[74] P. Fidjestol and N. Nilson, “Field test of reinforcement corrosion in concrete,” *ACI Spec. Publ.*, vol. 65, pp. 205–217, 1980.
[75] K. Katawaki, “Corrosion of steel in the concrete exposed to seawater spray zone,” *Symp. Proc. Crack. Concr. Struct.*, pp. 133–136, 1977.
[76] G. Rehm and H. Moll, “Versuche zum studium des einflußes der rissbreite auf die rostbilding an der bewehrung von stahlbeton-bauteilen.,” in *Deutscher Ausschuss für Stahlbeton*, 1964, p. 169.
[77] P. Schießl, “Zur frage der zulassigen rissbreite und der enforderlichen betondeckung im stahlbetonbau unter besonderer berucksichtigung der karbonatisierung des betons,” in *Deutscher Ausschuss für Stahlbeton*, 1976, p. 255.
[78] E. F. O’Neil, “Study of reinforced concrete beams exposed to marine environment,” *ACI Spec. Publ.*, vol. 65, pp. 113–132, 1980.
[79] R. François and G. Arliguie, “Durability of loaded reinforced concrete in chloride environment,” *ACI Spec. Publ.*, vol. 145, pp. 573–596, 1994.
[80] R. Durton and A. Mommens, “Corrosion des armatures dans le béton armé,” 1964.
[81] B. Tremper, “The Corrosion of Reinforcing Steel in Cracked Concrete,” *J. Proc.*, vol. 43, 1947.
[82] E. Vesikari, “Corrosion of reinforcing steels at cracks in concrete,” *NASA STI/Recon Tech. Rep. N*, vol. 83, 1981.
[83] V. H. Dang, R. François, V. L’Hostis, and D. Meinel, “Propagation of corrosion in pre-cracked carbonated reinforced mortar,” *Mater. Struct.*, vol. 48, pp. 2575–2595, 2015.
[84] G. Markeset and R. Myrdal, “Modelling of reinforcement corrosion in concrete - State of the art,” Oslo, 2008.
[85] C. Andrade and J. Gulikers, “Advances in Modeling Concrete Service Life,” in *Proceedings of 4th International RILEM PhD Workshop*, 2010, p. 164.
[86] V. L’Hostis, A. Millard, S. Perrin, E. Burger, D. Neff, and P. Dillmann, “Modelling the corrosion-induced cracking of reinforced concrete structures exposed to the atmosphere,” *Mater. Corros.*, vol. 62, pp. 943–947, 2011.
[87] B. Huet, “Comportement à la corrosion des armatures dans un béton carbonaté . Influence de la chimie de la solution interstitielle et d ’une barrière de transport,” PhD thesis, Insitutat National des Sciences Appliquées de Lyon, 2005.
[88] V. L’Hostis, “Contribution to the study of Corrosion in Cementitious Media for the Phenomenological Modelling of the Long-term Behavior of Reinforced Concrete Structures,” HDR Thesis at Toulouse III University, 2010.
[89] L. Liu and R. W. Weyers, “Modelling the dynamic corrosion process in chloride

contaminated concrete structures," *Cem. Concr. Res.*, vol. 28, pp. 365–379, 1998.
[90] W. López, J. A. González, and C. Andrade, "Influence of temperature on the service life of rebars," *Cem. Concr. Res.*, vol. 23, pp. 1130–1140, 1993.
[91] V. Živica, "Significance and influence of the ambient temperature as a rate factor of steel reinforcement corrosion," *Bull. Mater. Sci.*, vol. 25, pp. 375–379, 2002.
[92] R. M. Cornell and U. Schwertmann, *The iron oxides: structure, properties, reactions, occurrences and uses*. Wiley-VCH, 2003.
[93] S. Goni, C. Alonso, and C. Andrade, *Relationship between resistivity, porosity and corrosion rate of rebars in concrete*. 1990.
[94] C. Plage, "Nature and properties of concrete in relation to reinforcement corrosion," *Corros. steel Concr. Aachen*, pp. 17–19, 1992.
[95] C. Andrade, C. Alonso, and J. Sarría, "Corrosion rate evolution in concrete structures exposed to the atmosphere," *Cem. Concr. Compos.*, vol. 24, pp. 55–64, 2002.
[96] D.-W. Ryu, J.-W. Ko, and T. Noguchi, "Effects of simulated environmental conditions on the internal relative humidity and relative moisture content distribution of exposed concrete," *Cem. Concr. Compos.*, vol. 33, pp. 142–153, 2011.
[97] R. Weydert, "Einfluss der Umgebungsbedingungen auf das Instandsetzungsprinzip W bei Korrosion infolge Karbonatisierung des Betons," *Mater. Corros.*, vol. 45, pp. 447–453, 2003.
[98] K. Kobayashi and K. Shuttoh, "Oxygen diffusivity of various cementitious materials," *Cem. Concr. Res.*, vol. 21, pp. 273–284, 1991.
[99] S. Goto and D. M. Roy, "The effect of w/c ratio and curing temperature on the permeability of hardened cement paste," *Cem. Concr. Res.*, vol. 11, pp. 575–579, 1981.
[100] S. Feliu, C. Andrade, J. Gonzalez, and C. Alonso, "A new method for in-situ measurement of electrical resistivity of reinforced concrete," *Mater. Struct.*, vol. 29, pp. 362–365, 1996.
[101] G. Balabanić, N. Bićanić, and A. Dureković, "The influence of w/c ratio, concrete cover thickness and degree of water saturation of the corrosion rate of reinforcing steel in concrete," *Cem. Concr. Res.*, vol. 26, pp. 761–769, 1996.
[102] P. S. Mangat and B. T. Molloy, "Factors influencing chloride-induced corrosion of reinforcement in concrete," *Mater. Struct.*, vol. 25, pp. 404–411, 1992.
[103] M.-T. Liang, W.-L. Jin, R.-J. Yang, and N.-M. Huang, "Predeterminate model of corrosion rate of steel in concrete," *Cem. Concr. Res.*, vol. 35, pp. 1827–1833, 2005.
[104] C. Alonso, C. Andrade, and J. A. González, "Relation between resistivity and corrosion rate of reinforcements in carbonated mortar made with several cement types," *Cem. Concr. Res.*, vol. 18, pp. 687–698, 1988.
[105] J. F. Lataste, "Evaluation non destructive de l'état d'endommagement des ouvrages en béton armé par mesures de résistivité électrique," thèse Université Bordeaux 1, 2002.
[106] M. Raupach, "Models for the propagation phase of reinforcement corrosion – an overview," *Mater. Corros.*, vol. 57, pp. 605–613, 2006.
[107] B. Huet, V. L'hostis, G. Santarini, D. Feron, and H. Idrissi, "Steel corrosion in concrete: Determinist modeling of cathodic reaction as a function of water saturation degree," *Corros. Sci.*, vol. 49, pp. 1918–1932, 2007.
[108] M. Raupach, "Effect of temperature on chloride induced steel corrosion in concrete," *Eur. Corros. Congr.*, vol. 1, pp. 431–438, 1997.
[109] Eurocode 2, "Design of concrete structures - Part 1-1 : General rules and rules for buildings, BS EN 1992-1-1," 2004.
[110] ACI Committee 224, "Control of Cracking in Concrete Structures Reported," 2001.
[111] New Zealand Standard, "Concrete structures standard, part 1- The design of concrete structures , NZS3101," 1995.
[112] S. Nelson, "Chloride Induced Corrosion of Reinforcement Steel in Concrete, Threshold Values and Ion Distributions at the Concrete-Steel Interface Department of Civil and Environmental Engineering Chloride Induced Corrosion of Reinforcement Steel in

Concrete," Thesis Chalmers University of Technology, 2013.
[113] A. T. Horne, I. G. Richardson, and R. M. D. Brydson, "Quantitative analysis of the microstructure of interfaces in steel reinforced concrete," *Cem. Concr. Res.*, vol. 37, pp. 1613–1623, 2007.
[114] A. Kenny and A. Katz, "Statistical relationship between mix properties and the interfacial transition zone around embedded rebar," *Cem. Concr. Compos.*, vol. 60, pp. 82–91, 2015.
[115] T. Soylev and R. François, "Quality of steel–concrete interface and corrosion of reinforcing steel," *Cem. Concr. Res.*, vol. 33, pp. 1407–1415, 2003.
[116] T. Mohammed, N. Otsuki, H. Hamada, and T. Yamaji, "Chloride-Induced Corrosion of Steel Bars in Concrete with Presence of Gap at Steel-Concrete Interface," *ACI Mater. J.*, vol. 99, pp. 149–156, 2002.
[117] B. J. Pease, "Influence of concrete cracking on ingress and reinforcement corrosion," Thesis, Technical University of Denmark, 2010.
[118] A. Michel, A. O. S. Solgaard, B. J. Pease, M. R. Geiker, H. Stang, and J. F. Olesen, "Experimental investigation of the relation between damage at the concrete-steel interface and initiation of reinforcement corrosion in plain and fibre reinforced concrete," *Corros. Sci.*, vol. 77, pp. 308–321, 2013.
[119] A. Castel, T. Vidal, R. François, and G. Arliguie, "Influence of steel – concrete interface quality on reinforcement corrosion induced by chlorides," *Mag. Concr. Res.*, vol. 55, pp. 151–159, 2003.
[120] J. S. Ryou and K. Y. Ann, "Variation in the chloride threshold level for steel corrosion in concrete arising from different chloride sources," *Mag. Concr. Res.*, vol. 60, pp. 177–187, 2008.
[121] W. H. Hartt and J. Nam, "Effect of Cement Alkalinity on Chloride Threshold and Time-to-Corrosion of Reinforcing Steel in Concrete," *Corros. Sci. Sect.*, vol. 64, pp. 671–680, Aug. 2008.
[122] T. A. Söylev and R. François, "Corrosion of Reinforcement in Relation to Presence of Defects at the Interface between Steel and Concrete," *J. Mater. Civ. Eng.*, vol. 17, pp. 447–455, 2005.
[123] L. Yu, R. François, and R. Gagné, "Influence of steel–concrete interface defects induced by top-casting on development of chloride-induced corrosion in RC beams under sustained loading," *Mater. Struct.*, pp. 1–13, 2016.
[124] D. J. Naus, *Primer on Durability of Nuclear Power Plant Reinforced Concrete Structures - A Review of Pertinent Factors*. United States: Oak Ridge National Laboratory, 2007.
[125] A. Al-Harthy, J. Mullard, and M. Stewart, "Cracking in concrete due to corrosion of steel reinforcement," in *Proceedings of the 5th international conference on concrete under severe conditions: environment & loading (CONSEC 07)*, 2007.
[126] C. Alonso, C. Andrade, J. Rodriguez, and J. M. Diez, "Factors controlling cracking of concrete affected by reinforcement corrosion," *Mater. Struct.*, vol. 31, pp. 435–441, 1998.
[127] L. Parrott, "Damage caused by carbonatation of reinforced concrete," *Mater. Struct.*, vol. 23, pp. 230–234, 1990.
[128] K. Stanish, R. Hooton, and S. Pantazopoulou, "Corrosion Effects on Bond Strength in Reinforced Concrete," *Struct. J.*, vol. 96, pp. 915–921, 1997.
[129] Y. Auyeung, P. Balaguru, and L. Chung, "Bond Behavior of Corroded Reinforcement Bars," *Mater. J.*, vol. 97, pp. 214–220, 2000.
[130] J. Rodríguez, L. Ortega, J. Casal, and J. Díez, "Corrosion of reinforcement and service life of concrete structures," *Int. Conf. Durab. Build. Mater. Components*, vol. 7, pp. 117–126, 1996.
[131] I. Khan, R. François, and A. Castel, "Prediction of reinforcement corrosion using corrosion induced cracks width in corroded reinforced concrete beams," *Cem. Concr. Res.*, vol. 56, pp. 84–96, 2014.
[132] A. Millard and V. L'Hostis, "Modelling the effects of steel corrosion in concrete,

induced by carbon dioxide penetration," *Eur. J. Environ. Civ. Eng.*, vol. 16, pp. 375–391, 2012.
[133] W.-J. Chitty, P. Dillmann, V. L'Hostis, and A. Millard, "Long-term corrosion of rebars embedded in aerial and hydraulic binders – Parametric study and first step of modelling," *Corros. Sci.*, vol. 50, pp. 3047–3055, 2008.
[134] V. H. Dang, "Initiation and propagation phases of re-bars corrosion in pre-cracked reinforced concrete exposed to carbonation or chloride environment," PhD thesis, Institut National des Sciences Appliquées de Toulouse, 2013.
[135] W. Zhang, X. Song, X. Gu, and S. Li, "Tensile and fatigue behavior of corroded rebars," *Constr. Build. Mater.*, vol. 34, pp. 409–417, 2012.
[136] A. A. Almusallam, A. S. Al-Gahtani, A. R. Aziz, and Rasheeduzzafart, "Effect of reinforcement corrosion on bond strength," *Constr. Build. Mater.*, vol. 10, pp. 123–129, 1996.
[137] H.-S. Lee, T. Noguchi, and F. Tomosawa, "Evaluation of the bond properties between concrete and reinforcement as a function of the degree of reinforcement corrosion," *Cem. Concr. Res.*, vol. 32, pp. 1313–1318, 2002.
[138] X. Fu and D. D. L. Chung, "Effect of corrosion on the bond between concrete and steel rebar," *Cem. Concr. Compos.*, vol. 27, pp. 1811–1815, 1997.
[139] P. S. Mangat and M. S. Elgarf, "Bond characteristics of corroding reinforcement in concrete beams," *Mater. Struct.*, vol. 32, pp. 89–97, 1999.
[140] J. G. Cabrera, "Deterioration of concrete due to reinforcement steel corrosion," *Cem. Concr. Compos.*, vol. 18, pp. 47–59, 1996.
[141] A. Castel, R. François, and G. Arliguie, "Mechanical behaviour of corroded reinforced concrete beams - Part 1 : Experimental study of corroded beams," *Mater. Struct.*, vol. 33, pp. 539–544, 2000.
[142] Norme NF EN 196-1, "Méthodes d'essais des ciments - Partie 1 : détermination des résistances mécaniques," p. 31, 2006.
[143] R. Witasse, "Contribution à la compréhension du comportement d'une coque d'aéroréfrigérant vieilli : définition d'un état initial, influence des effets différés sous chargements hydro-mécaniques," thèse INSA LYON, 2000.
[144] NF EN 12350-2, "Essais pour béton frais - Partie 2 : essai d'affaissement," 2012.
[145] NF EN 12390-3, "Essais pour béton durci - Partie 3 : résistance à la compression des éprouvettes," 2012.
[146] NF EN 12390-6, "Essais pour béton durci - Partie 6 : détermination de la résistance en traction par fendage d'éprouvettes," 2012.
[147] NF EN 12390-13, "Essai pour béton durci - Partie 13 : détermination du module sécant d'élasticité en compression," 2014.
[148] RILEM, "Bond test for reinforcing steel (Pull-Out Test)," *Matériaux Constr.*, vol. 3, pp. 175–178.
[149] Rilem TCS, "Determination of the fracture energy of mortar and concrete by means of three-point bend tests on notched beams," *Mater. Struct.*, vol. 18, pp. 285–290, 1985.
[150] E. W. Washburn, "The dynamics of capillary flow," *Phys. Rev.*, vol. 17, pp. 273–283, 1921.
[151] S. Diamond, "Mercury porosimetry: An inappropriate method for the measurement of pore size distributions in cement-based materials," *Cem. Concr. Res.*, vol. 30, pp. 1517–1525, 2000.
[152] A. S. El-Dieb and R. D. Hooton, "Evaluation of the katz-Thomson model for estimating the water permeability of cement-based materials from mercury intrusion porosimetry data," *Cem. Concr. Res.*, vol. 24, pp. 443–455, 1994.
[153] S. Stephant, "Étude de l'influence de l'hydratation des laitiers sur les propriétés de transfert gazeux dans les matériaux cimentaires," Thèse de l'Université de Bourgogne, 2015.
[154] E. M. J. Berodier, "Impact of the Supplementary Cementitious Materials on the kinetics and microstructural development of cement hydration," Thèse Ecole Polytechnique fédérale de Lausanne, 2015.

[155] G. Arliguie and H. Hornain, “Grandeurs associées à la durabilité des bétons,” *Press. l’Ecole Natl. des Ponts Chaussées*, 2007.
[156] X. P., P. Gu, X. Zhongzi, and J. . Beaudoin, “A rationalized a.c. impedence model for microstructural characterization of hydrating cement systems,” *Cem. Concr. Compos.*, vol. 23, pp. 359–367, 1993.
[157] T. Christensen, Bruce J Coverdale, R. A. Olson, S. J. Ford, H. M. Garboczi, Edward J Jennings, and T. O. Mason, “Impedance Spectroscopy of Hydrating Cement-Based Materials: Measurement, Interpretation, and Application,” *J. Am. Ceram. Soc.*, vol. 77, pp. 2789–2804, 1994.
[158] O. Francy, “Modélisation de la pénétration des ions chlorures dans les mortiers partiellement saturés en eau,” Thèse Université de Toulouse 3, 1998.
[159] L. Greenspan, “Humidity fixed points of binary saturated aqueous solutions,” *J. Res. Natl. Bur. Stand. (1934).*, vol. 81, pp. 89–96, 1977.
[160] M. Dupeux, *Aide Mémoire - Science des Matériaux*. 2005.
[161] J. Barralis and G. Maeder, *Précis de Métallurgie. 6è édition. Paris : AFNOR/Nathan*. 1993.
[162] C. Arvieu and I. Guillot, *Atlas de Métallographie. Université de Technologie de Compiègne*. 1997.
[163] D. François, “Essais mécaniques des métaux Détermination des lois de comportement,” *Essais dureté, Tech. l’ingénieur, Matériaux métalliques*, vol. 123, pp. 1–17, 2005.
[164] NF EN ISO 18265, “Metallic materials - Conversion of hardness values,” 2013.
[165] F. Paradis, “Influence de la fissuration du béton sur la corrosion des armatures. Caractérisation des produits de corrosion formés dans le béton,” thèse Faculté des sciences et de génie, Université de Laval, 2009.
[166] D. Trejo, P. J. Monteiro, B. C. Gerwick Jr, and G. Thomas, “Microstructural design of concrete reinforcing bars for improved corrosion performance,” *ACI Mater. J.*, vol. 97, pp. 78–83, 2000.
[167] G. Slama and B. . Michaud, “Use of Shot Peening to Improve the SCC Resistance of Vapor Generator Tubes of PWR Nuclear Plants,” in *9th National Days on Prestrain Shot Peening*, 1985.
[168] N. Ben Salah-Rousset, M. A. Chaouachi, and A. Chellouf, “Role of Surface Finishing on Pitting Corrosion of a Duplex Stainless Steel in Seawater,” *J. Mater. Eng. Perform.*, vol. 5, pp. 225–231, 1996.
[169] V. Lapointe, “Initiation et propagation de la corrosion dans un élement de béton,” thèse Université Laval, 2009.
[170] W. Zhong and W. Yao, “Influence of damage degree on self-healing of concrete,” *Constr. Build. Mater.*, vol. 22, pp. 1137–1142, 2008.
[171] S. Jacobsen, J. Marchand, and L. Boisvert, “Effect of cracking and healing on chloride transport in OPC concrete,” *Cem. Concr. Res.*, vol. 26, pp. 869–881, 1996.
[172] S. Alahmad, “Traitement des fissurations dans les ouvrages hydrauliques,” thèse INSA Toulouse, 2009.
[173] V. H. Dang, R. François, and V. L’Hostis, “Effects of pre-cracks on both initiation and propagation of re-bar corrosion in pure carbon dioxide,” *Int. Work. NUCPERF 2012 Long-Term Perform. Cem. Barriers Reinf. Concr. Nucl. Power Plant Radioact. Waste Storage Dispos. (RILEM Event TC 226-CNM EFC Event 351)*, vol. 56, pp. 1–11, 2013.
[174] Q. Zhou and F. Glasser, “Thermal stability and decomposition mechanisms of ettringite at <120°C,” *Cem. Concr. Res.*, vol. 31, pp. 1333–1339, 2001.
[175] B. Lothenbach, T. Matschei, G. Möschner, and F. P. Glasser, “Thermodynamic modelling of the effect of temperature on the hydration and porosity of Portland cement,” *Cem. Concr. Res.*, vol. 38, pp. 1–18, 2008.
[176] D. Lecompte *et al.*, “Quality assessment of speckle patterns for digital image correlation,” *Opt. Lasers Eng.*, vol. 44, pp. 1132–1145, 2006.
[177] M. Sutton, W. Wolters, W. Peters, W. Ranson, and S. McNeill, “Determination of displacements using an improved digital correlation method,” *Image Vis. Comput.*, vol.

1, pp. 133–139, 1983.
[178] M. Bornert, F. Vales, H. Gharbi, and D. Nguyen Minh, “Multiscale full-field strain measurements for micromechanical investigations of the hydromechanical behaviour of clayey rocks,” *Strain*, vol. 46, pp. 33–46, 2010.
[179] R. Gagné, R. François, and P. Masse, “Chloride penetration testing of cracked mortar samples,” *Concr. under Sev. Cond.*, vol. 1, pp. 198–205, 2001.
[180] “XP P18-458: essai pour béton durci - essai de carbonatation accélérée - mesure de l’épaisseur de béton carbonaté,” 2008.
[181] prBS 1881-131, “Testing hardened concrete — — Part XX : Determination of the potential carbonation resistance of concrete : Accelerated carbonation method,” no. November, pp. 1–15, 2011.
[182] T. A. Harrison, G. Khanna, S. Kandasami, M. D. Newlands, and M. R. Jones, “Experience of using the prTS 12390-12 accelerated carbonation test to assess the relative performance of concrete,” *Mag. Concr. Res.*, vol. 64, pp. 737–747, 2012.
[183] NF EN ISO 8407, “Corrosion des métaux et alliages - Élimination des produits de corrosion sur les éprouvettes d’essai de corrosion,” 2014.
[184] D. Landolt, *Corrosion and surface chemistry of metals*. CRC Press, 2007.
[185] D. Neff, S. Reguer, L. Bellot-Gurlet, P. Dillmann, and R. Berthelon, “Structural characterization of corrosion products on archeological iron: an integrated analytical approach to establish corrosion forms,” *J. Raman Spectrosc.*, vol. 35, pp. 739–745, 2004.
[186] D. Neff, P. Dillmann, L. Bellot-Gurlet, and G. Beranger, “Corrosion of iron archaeological artefacts in soil: characterisation of the corrosion system,” *Corros. Sci.*, vol. 47, pp. 515–535, 2005.
[187] M. Hanesh, “Raman spectroscopy of iron oxides and (oxy)hydroxides at low laser power and possible applications in environmental magnetic studies,” *Geophys. J. Int.*, vol. 177, pp. 941–948, 2009.
[188] F. Glasser and T. Matschei, “Interactions between Portland cement and carbon dioxide,” in *Proceedings of the 12th International Congress on the Chemistry of Cements*, 2007.
[189] L. Parrott and D. Killoh, “Carbonation in a 36 year old, in-situ concrete,” *Cem. Concr. Res.*, vol. 19, pp. 649–656, 1989.
[190] A. Rosenberg, C. Hansson, and C. Andrade, “Mechanisms of corrosion of steel in concrete,” *Mater. Sci. Concr.*, vol. 1, pp. 285–314, 1989.
[191] C. M. Hansson, “Comments on electrochemical measurements of the rate of corrosion of steel in concrete,” *Cem. Concr. Res.*, vol. 14, pp. 574–584, 1984.
[192] U. Cornell, Rochelle M Schwertmann, *The iron oxides: structure, properties, reactions, occurrences and uses*. Weinheim: John Wiley & Sons, 2003.
[193] U. Schwertmann and R. M. Cornell, *Iron oxides in the laboratory: preparation and characterization*. Weinheim: John Wiley & Sons, 2008.
[194] H. Antony, L. Legrand, L. Maréchal, S. Perrin, P. Dillmann, and A. Chaussé, “Study of lepidocrocite γ-FeOOH electrochemical reduction in neutral and slightly alkaline solutions at 25 °C,” *Electrochim. Acta*, vol. 51, pp. 745–753, 2005.
[195] H. Antony, S. Perrin, P. Dillmann, L. Legrand, and A. Chaussé, “Electrochemical study of indoor atmospheric corrosion layers formed on ancient iron artefacts,” *Electrochim. Acta*, vol. 52, pp. 7754–7759, 2007.
[196] J. Monnier *et al.*, “A corrosion study of the ferrous medieval reinforcement of the Amiens cathedral. Phase characterisation and localisation by various microprobes techniques,” *Corros. Sci.*, vol. 52, pp. 695–710, 2010.
[197] T. Misawa, K. Hashimoto, and S. Shimodaira, “The mechanism of formation of iron oxide and oxyhydroxides in aqueous solutions at room temperature,” *Corros. Sci.*, vol. 14, pp. 131–149, 1974.
[198] V. L’Hostis, L. Vincent, V. Praca, D. Neff, L. Bellot-Gurlet, and P. Dillmann, “Characterization of long-term corrosion of rebars embedded in concretes from French Historical Buildings aged from 50 to 80 years,” in *Eurocorr*, 2007, pp. 1–10.

[199] M. Stratmann and K. Hoffmann, “In situ Mössbauer spectroscopic study of reactions within rust layers,” *Corros. Sci.*, vol. 29, pp. 1329–1352, 1989.
[200] R. François and G. Arliguie, “Influence of Service Cracking on Reinforcement Steel Corrosion,” *J. Mater. Civ. Eng.*, vol. 10, pp. 14–20, 1998.
[201] O. Francy and R. François, “Modélisation du transfert couplé ions chlore-humidité dans les matériaux cimentaires,” *Rev. Française Génie Civ.*, vol. 5, pp. 377–396, 2001.
[202] B. Martin-Pérez, S. J. Pantazopoulou, and M. D. A. Thomas, “Numerical solution of mass transport equations in concrete structures,” *Comput. Struct.*, vol. 79, pp. 1251–1264, 2001.
[203] B. Bary and A. Sellier, “Coupled moisture - Carbon dioxide-calcium transfer model for carbonation of concrete,” *Cem. Concr. Res.*, vol. 34, pp. 1859–1872, 2004.
[204] B. Larbi, “Caractérisation du transport diffusif dans les matériaux cimentaires: influence de la microstructure des mortiers,” Thèse Université Paris-Est, 2013.
[205] W. Elkey and E. J. Sellevold, “electrical resistivity of concrete,” Norway, 1995.
[206] R. Battino, T. R. Rettich, and T. Tominaga, “The solubility of Oxygen and Ozone in Liquids,” *J. Phys. Chem. Ref. data*, vol. 12, pp. 163–178, 1983.
[207] A. Scott and M. Alexander, “The influence of binder type, cracking and cover on corrosion rates of steel in chloride-contaminated concrete,” *Mag. Concr. Res.*, vol. 59, pp. 495–505, 2007.
[208] W.-J. Chitty, P. Dillmann, V. L’Hostis, and C. Lombard, “Long-term corrosion resistance of metallic reinforcements in concrete - A study of corrosion mechanisms based on archaeological artefacts.,” *Corros. Sci.*, vol. 47, pp. 1555–1581, 2005.
[209] R. M. Cornell and U. Schwertmann, *The iron Oxides, Structure, Properties, Reactions, Occurences and Uses*, 2nd editio. 2003.
[210] B. Jegdić, S. Polić-Radovanović, S. Ristić, and A. Alil, “Corrosion Processes, Nature and Composition of Corrosion Products on Iron Artefacts of Weaponry,” *Sci. Tech. Rev.*, vol. 61, pp. 50–56, 2011.

APPENDIX

I.1 CORROSION INITIATION AND EVOLUTION

I.1.1 Experimental procedure

In this study, XRF is used to follow the migration of iron in the binder during the corrosion processes and particularly to detect the initiation of the corrosion. This test is performed on millimetric samples described in §2.3.3.

For this aim, the device developed at the Laboratory of Archeomaterials and Prediction of Alteration (CEA/DRF/IRAMIS/NIMBE/LAPA-IRAMAT) is used as illustrated in Figure I-1. In this device, a molybdenum anode (λ: 0.70932 Å) is used to generate X-rays. The X-ray beam is focused up to 50×30 µm^2 with a photon flux of 106 phs-1. X-rays hit the sample surface with an incident angle of 5° and thus the size of the sample surface impinged by X-rays is 600×30 µm^2.
Concerning the XRF analysis, the sample surface excited with a high-energy X-rays emits secondary X-rays which are collected and analyzed by energy. According to the energy measured, it is possible to determine the chemical composition. An example of an obtain spectrum at the steel/mortar interface after several humidification/drying cycle is given in Figure I-2. The range of energy collected for steel corresponds to Kα rays from 704 to 758 KeV (red vertical lines in Figure I-2) while the Kα rays collected for calcium show a range of energy from 410 to 442 Kev (blue vertical lines in Figure I-2).

An XRF analysis is performed every 3 humidification/drying cycles. At each analysis, the evolution of steel in the same zone of interest is studied. An optical microscopy is used to find this zone (Figure I-3). The points chosen to be analyzed cover the steel, the steel/mortar interface and the mortar. The distance between each point is 20 µm and the total analyzed distance is 500 µm (red rectangle in Figure I-3). The analysis begin at point “O” and one minute analysis duration is performed for each point.

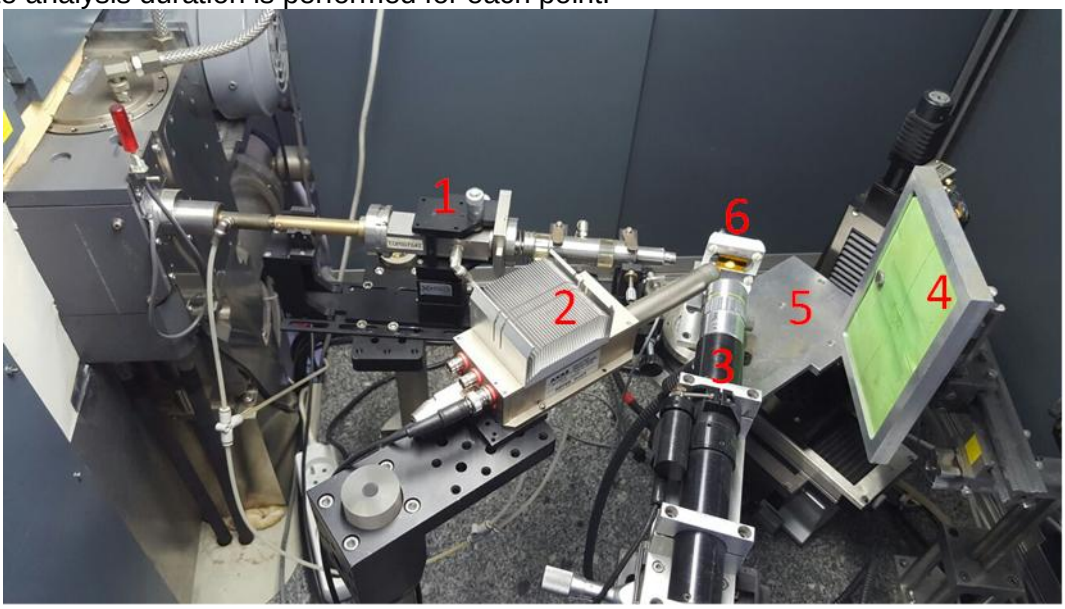

Figure I-1: Photograph of the assembly anode/XRD developed in LAPA (CEA/DSM/IRAMIS/SIS2M/LAPA) Legend: 1) X-Ray (Mo, λKα = 0,709 Å), 2) X-Fluorescence detector 3) Optical microscope, 4) image plate (Fuji), 5) moving stage, 6) sample

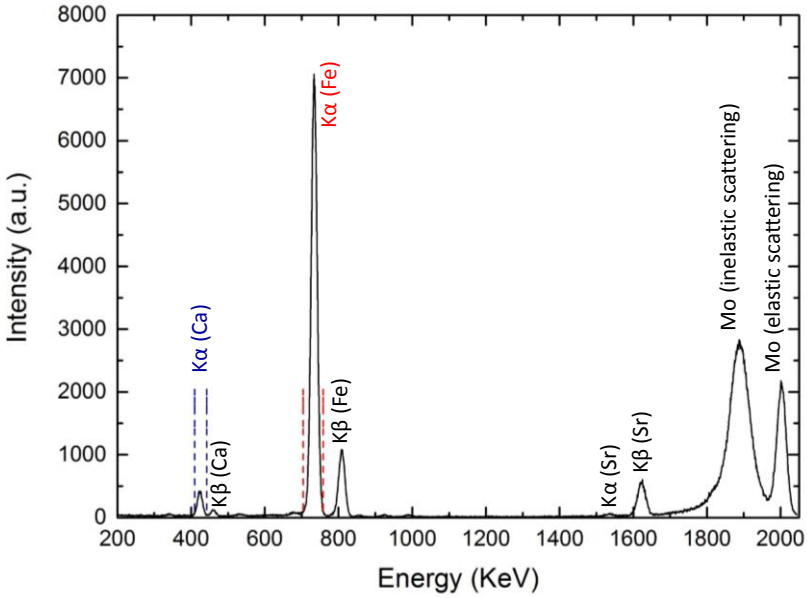

Figure I-2: XRF spectrum at the steel/mortar interface

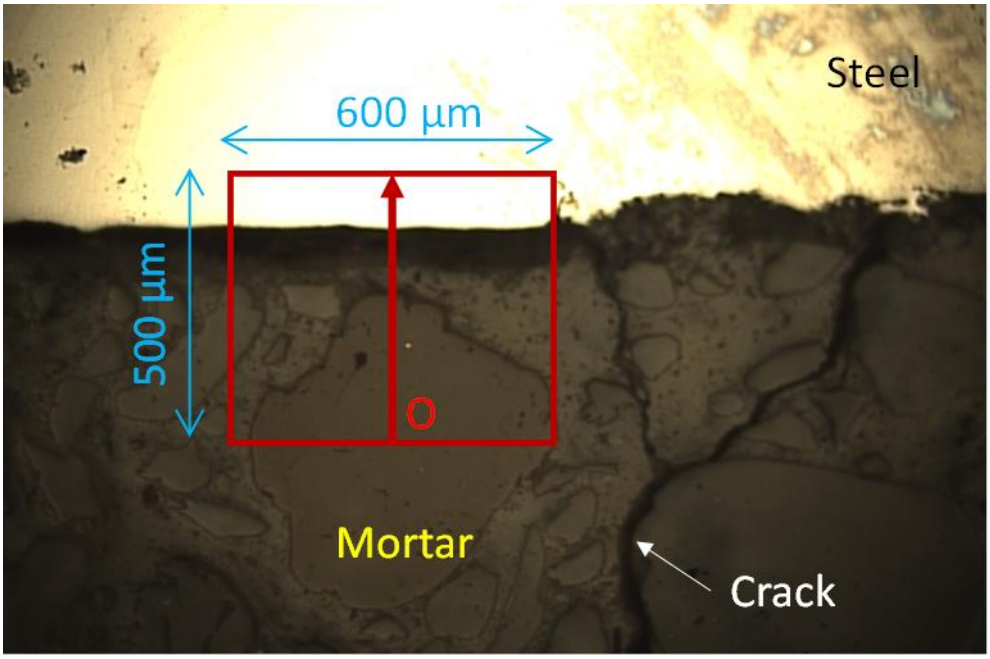

Figure I-3: Zone of interest in which corrosion development is monitored by x-ray fluorescence spectroscopy

I.1.2 Result

X-ray fluorescence profiles carried out in the areas selected near the crack using the optical microscopy are given in Figure I-4. The aim of these profiles is to track the evolution of iron migration inside the binder as well as the corrosion evolution in the steel/mortar interface. In Figure I-4, the iron profiles are given for different wetting/drying cycles. The intensity of the iron in the interface is slightly higher than the one measured in the mortar which could corresponds to corrosion products developed at the interface. However, even after 48

wet/dry cycles, no iron diffusion can be detected in the binder. This indicates that for this number of raining/drying cycles, if iron diffusion in mortar exists, its quantity is lower than the detection limit of the X-ray fluorescence detector. Therefore, the impact of this diffusion on the binder can be neglected.

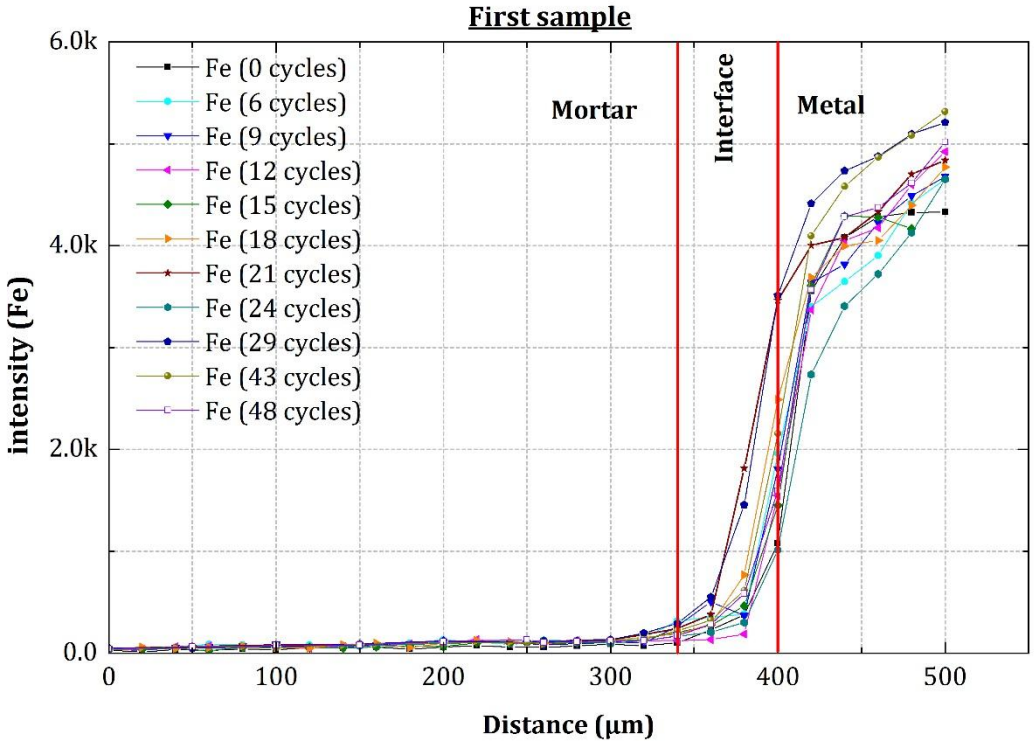

Figure I-4: Diffusion profiles of iron inside the binder obtained on millimetric sample by the X-ray

I.2 DISTRIBUTION OF THE CORROSION PRODUCTS LAYER

I.2.1 Exposure condition: horizontal crack, 30 min rain, 20°C

1) Corrosion length on the upper and lower part of the steel/mortar interface

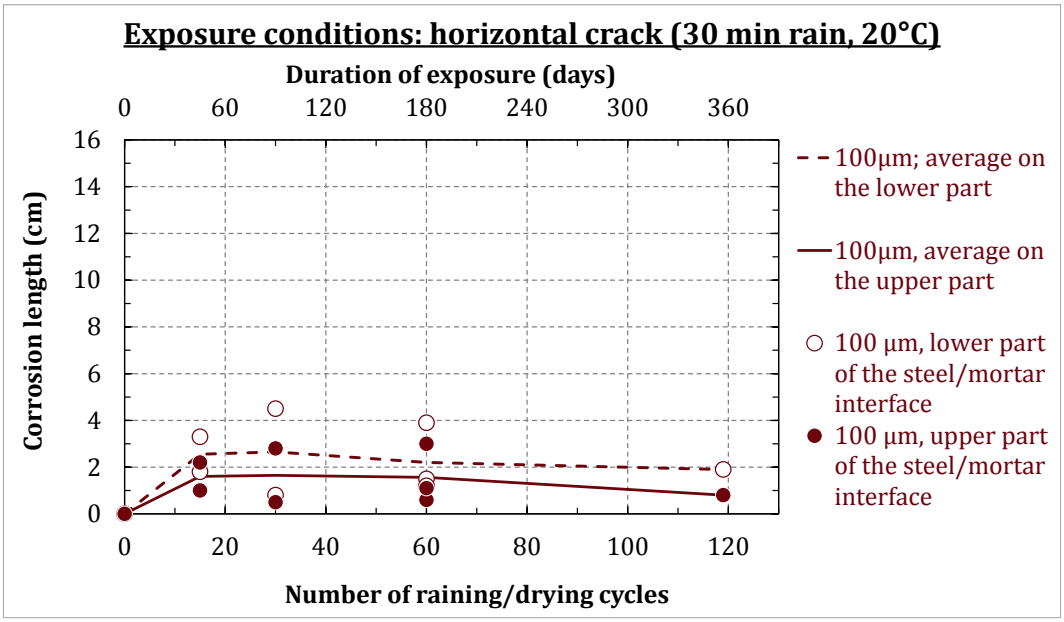

Figure I-5 : Corrosion length along the upper and the lower steel/mortar interface with respect to raining/drying cycles (horizontally oriented cracks, W_r = 100 µm)

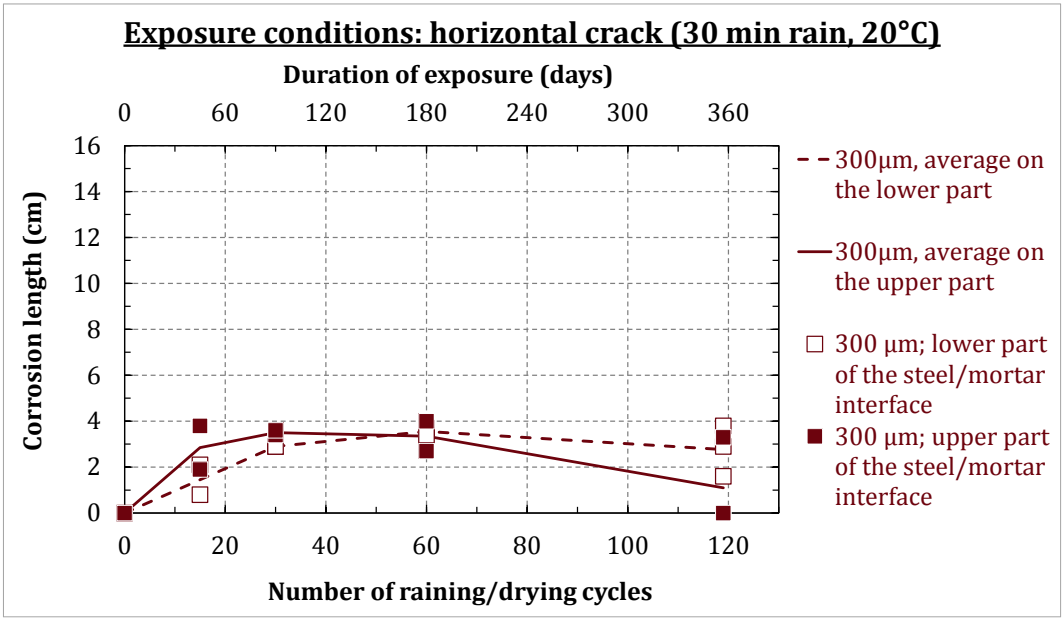

Figure I-6 : Corrosion length along the upper and the lower steel/mortar interface with respect to raining/drying cycles (horizontally oriented cracks, W_r = 300 µm)

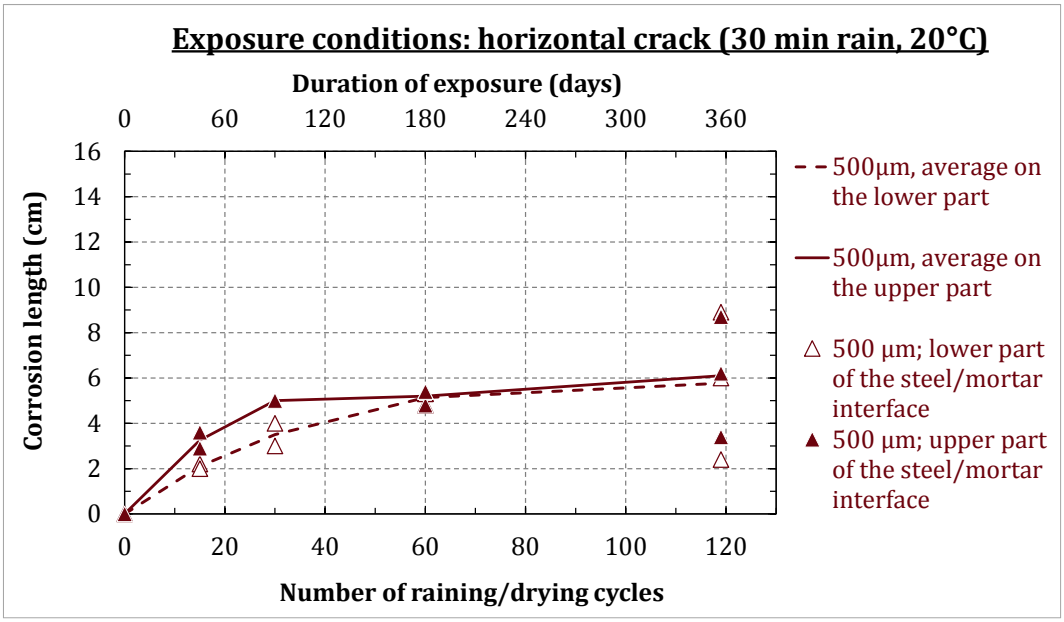

Figure I-7 : Corrosion length along the upper and the lower steel/mortar interface with respect to raining/drying cycles (horizontally oriented cracks, W_r = 500 µm)

2) Evolution of the corrosion products along the upper and lower part of the steel/mortar interface

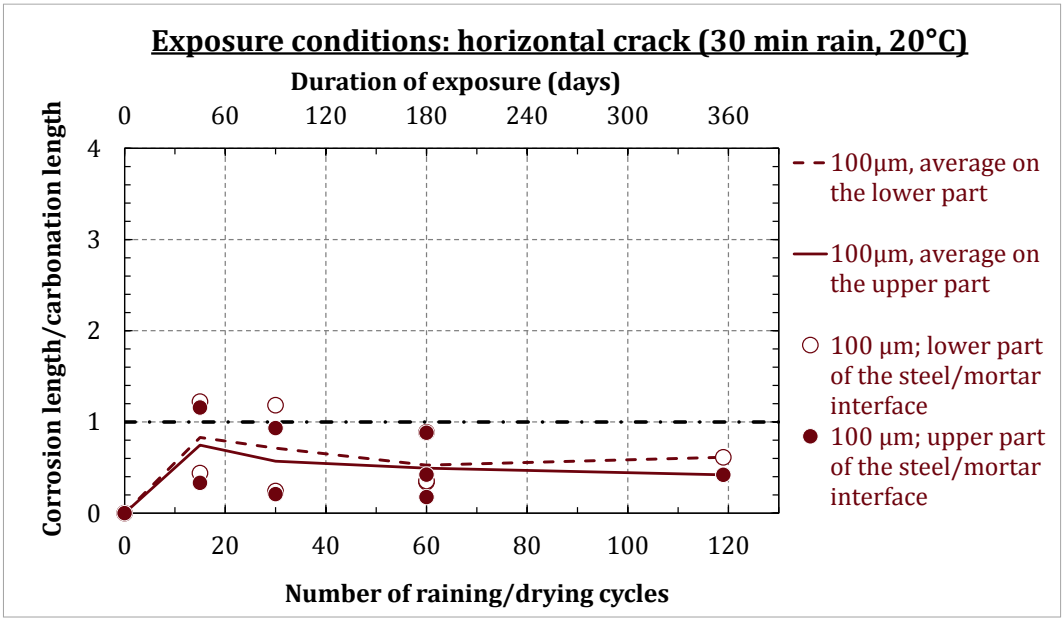

Figure I-8 : Evolution of the corrosion over carbonation length ratio measured on the upper and the lower steel/mortar interface with respect to raining/drying cycles (horizontally oriented cracks, W_r = 100 µm)

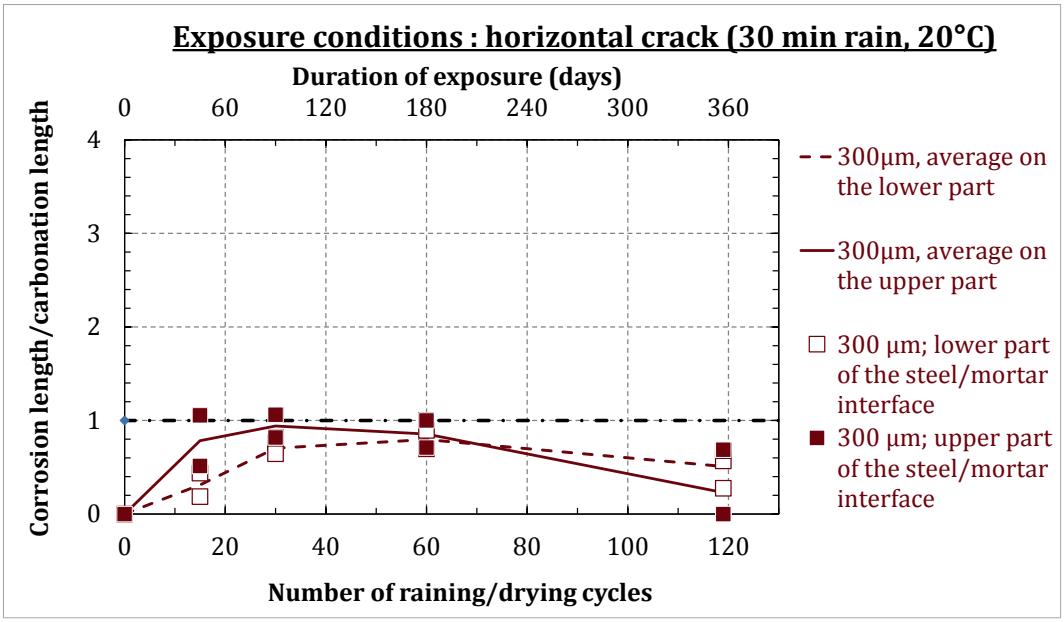

Figure I-9 : Evolution of the corrosion over carbonation length ratio measured on the upper and the lower steel/mortar interface with respect to raining/drying cycles (horizontally oriented cracks, W_r = 300 µm)

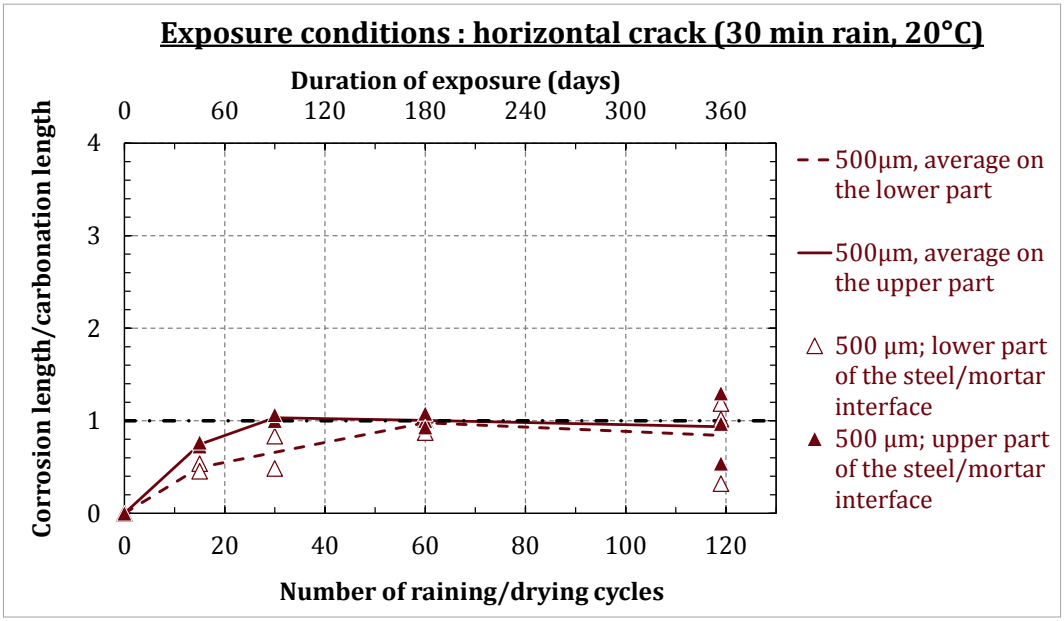

Figure I-10 : Evolution of the corrosion over carbonation length ratio measured on the upper and the lower steel/mortar interface with respect to raining/drying cycles (horizontally oriented cracks, W_r = 500 µm)

I.2.2 Exposure condition: vertical crack, 3 min rain, 20°C

1) Corrosion length on the upper and lower part of the steel/mortar interface

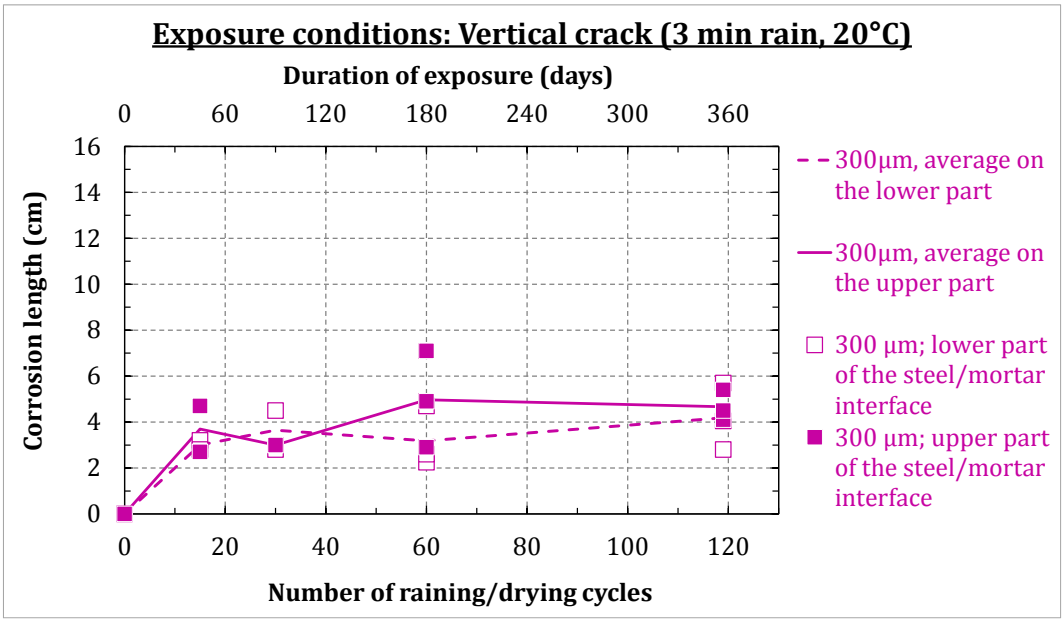

Figure I-11 : Corrosion length along the upper and the lower steel/mortar interface with respect to raining/drying cycles (3 min rain, W_r = 300 µm)

2) Evolution of the corrosion products along the upper and lower part of the steel/mortar interface

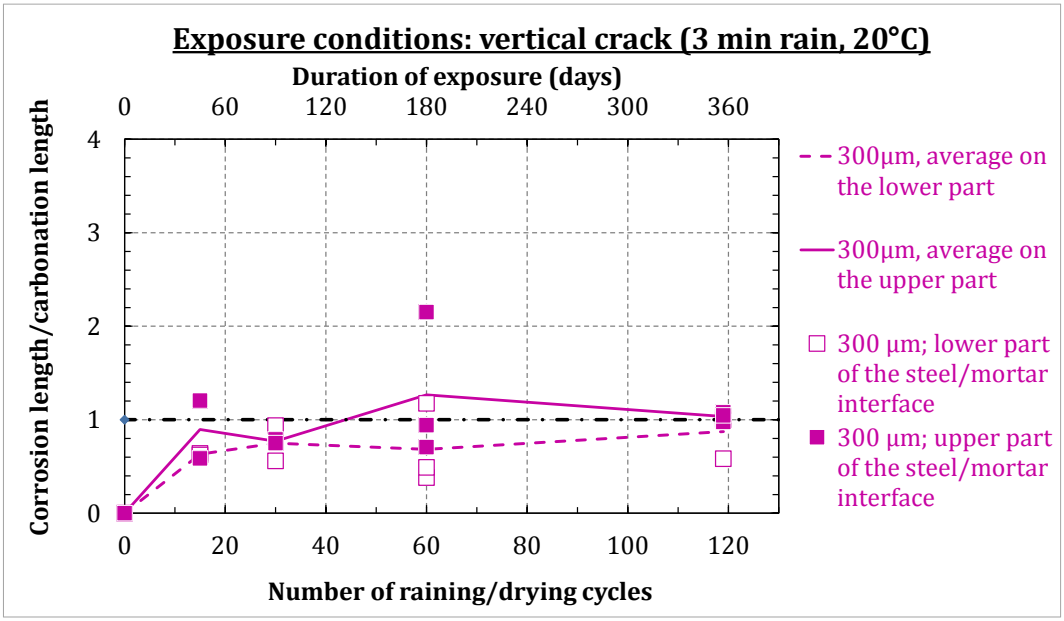

Figure I-12 : Evolution of the corrosion over carbonation length ratio measured on the upper and the lower steel/mortar interface with respect to raining/drying cycles (3 min rain, W_r = 300 µm)

I.2.3 Exposure condition: 90% RH, 20°C

1) Corrosion length on the upper and lower part of the steel/mortar interface

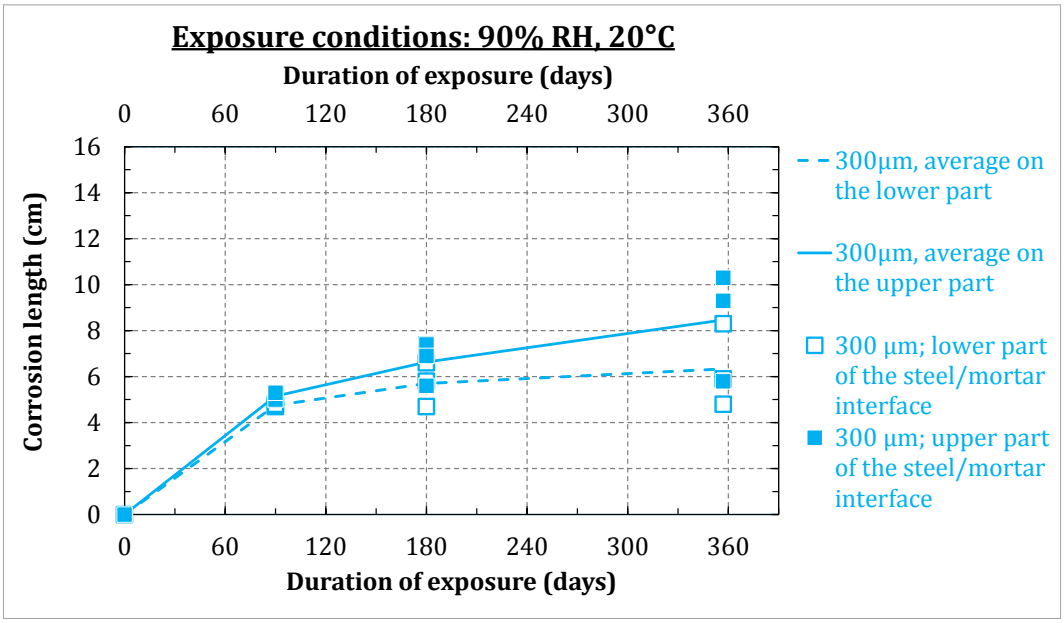

Figure I-13 : Corrosion length along the upper and the lower steel/mortar interface with respect to raining/drying cycles (90% RH, W_r = 300 µm)

2) Evolution of the corrosion products along the upper and lower part of the steel/mortar interface

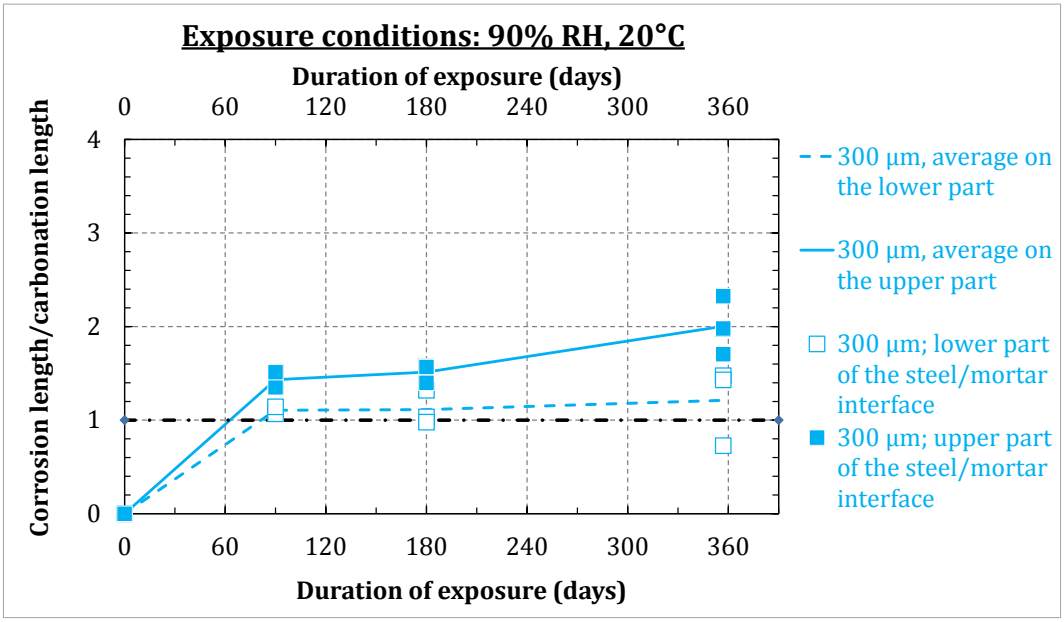

Figure I-14 : Evolution of the corrosion over carbonation length ratio measured on the upper and the lower steel/mortar interface with respect to raining/drying cycles (90%RH, W_r = 300 µm)

I.2.4 Exposure condition: vertical crack, 30 min rain, 40°C

1) Corrosion length on the upper and lower part of the steel/mortar interface

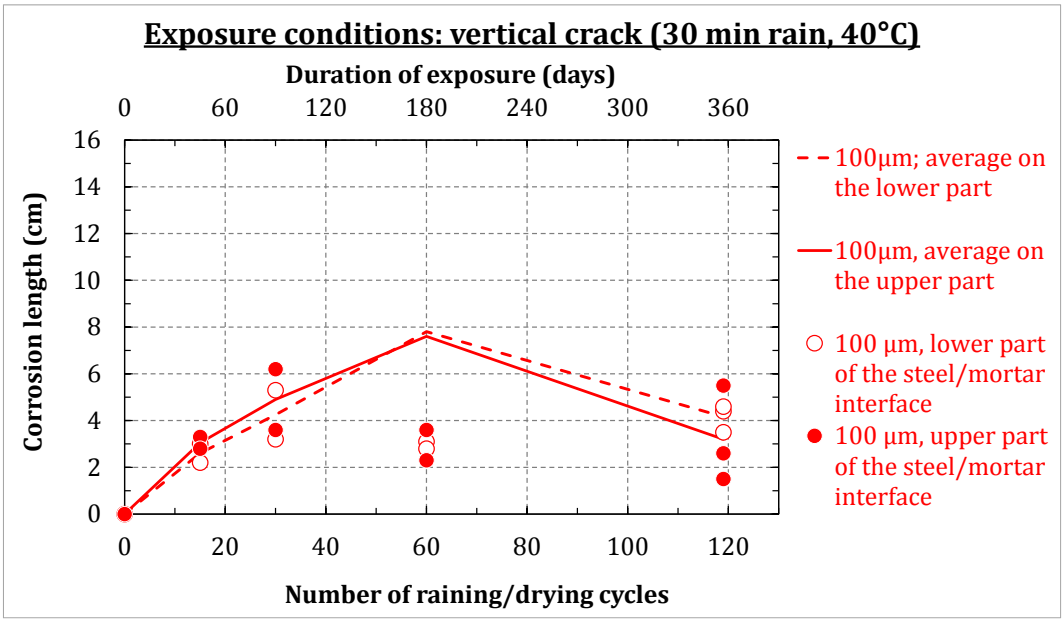

Figure I-15 : Corrosion length along the upper and the lower steel/mortar interface with respect to raining/drying cycles (40°C, W_r = 100 µm)

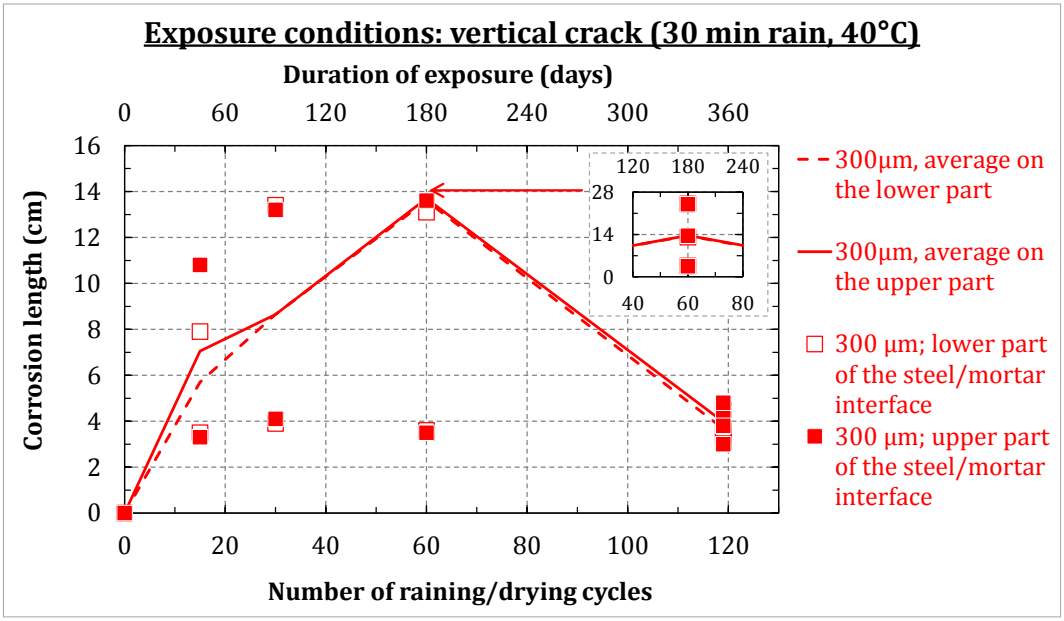

Figure I-16 : Corrosion length along the upper and the lower steel/mortar interface with respect to raining/drying cycles (40°C, W_r = 300 µm)

2) Evolution of the corrosion products along the upper and lower part of the steel/mortar interface

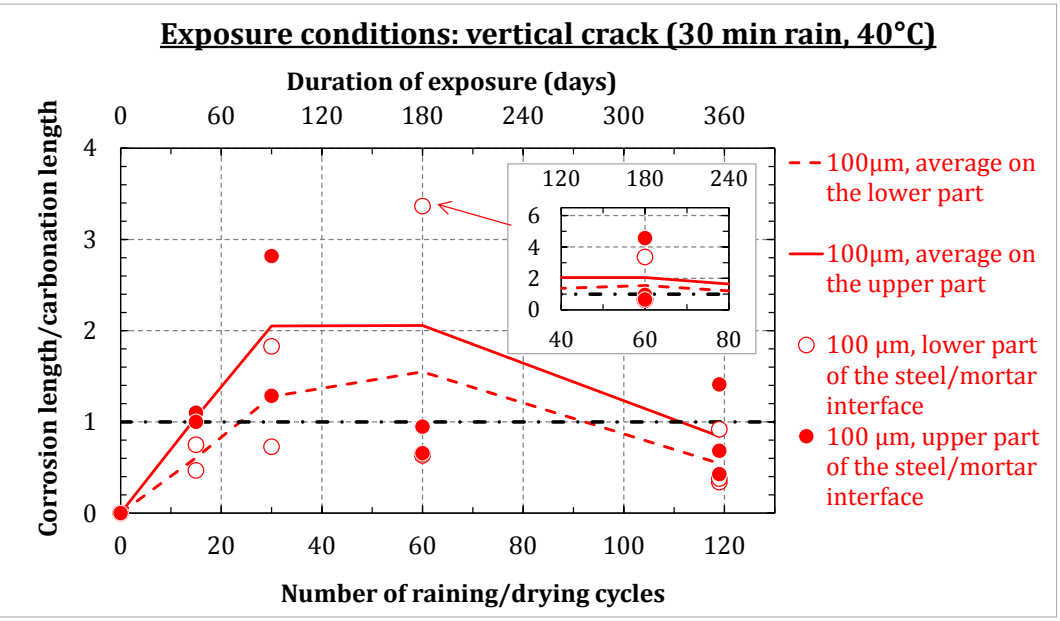

Figure I-17 : Evolution of the corrosion over carbonation length ratio measured on the upper and the lower steel/mortar interface with respect to raining/drying cycles (40°C, W_r = 100 µm)

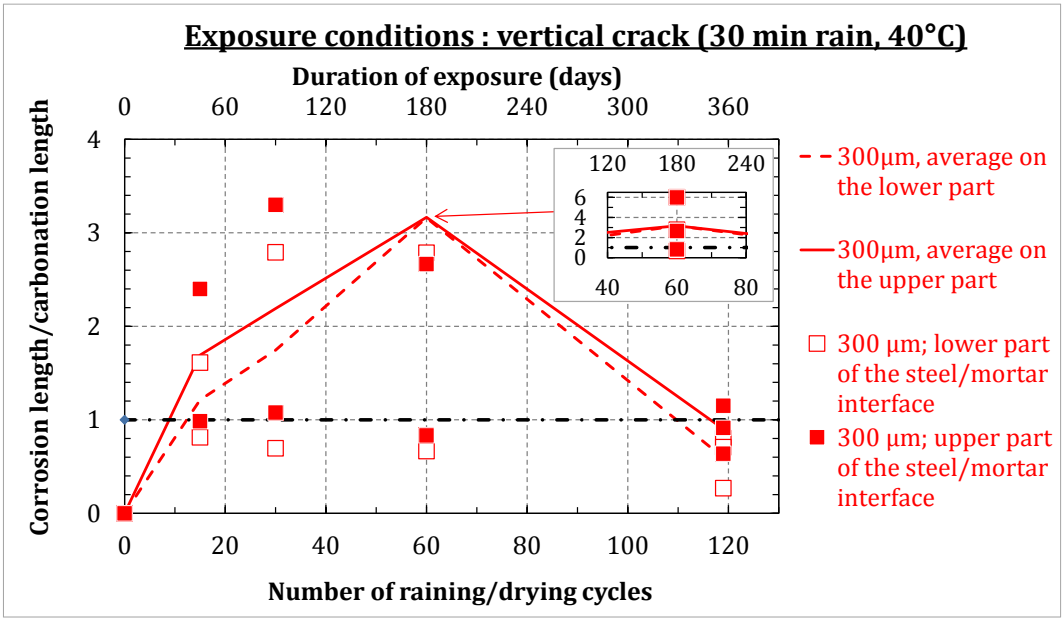

Figure I-18: Evolution of the corrosion over carbonation length ratio measured on the upper and the lower steel/mortar interface with respect to raining/drying cycles (40°C, W_r = 300 µm)

I.2.5 Exposure condition: Environmental conditions of Saclay

1) Corrosion length on the upper and lower part of the steel/mortar interface

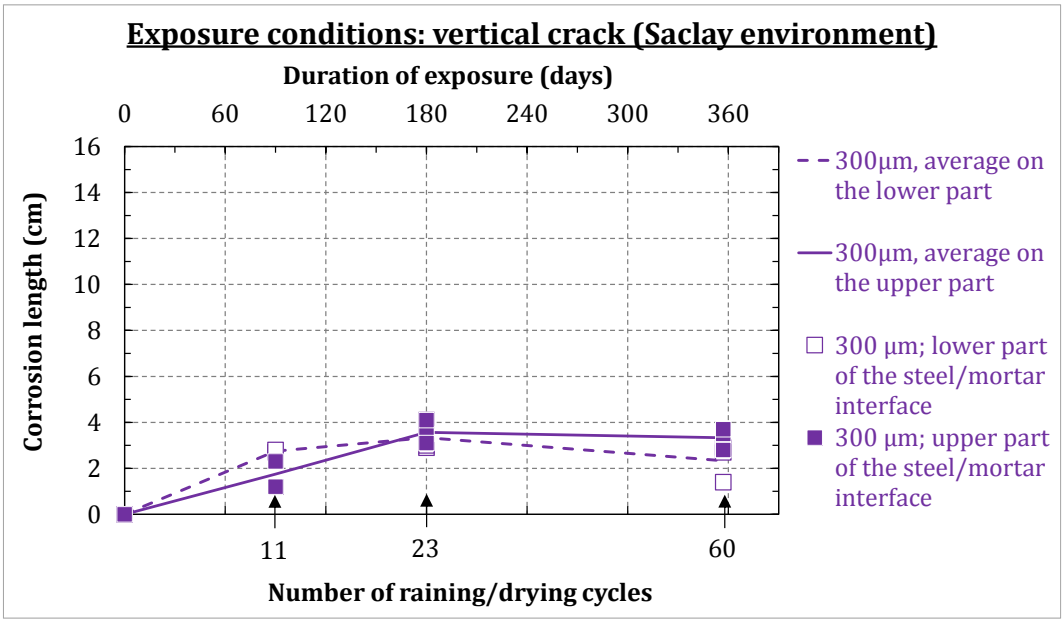

Figure I-19 : Corrosion length along the upper and the lower steel/mortar interface with respect to raining/drying cycles (Saclay, W_r = 300 µm)

2) Evolution of the corrosion products along the upper and lower part of the steel/mortar interface

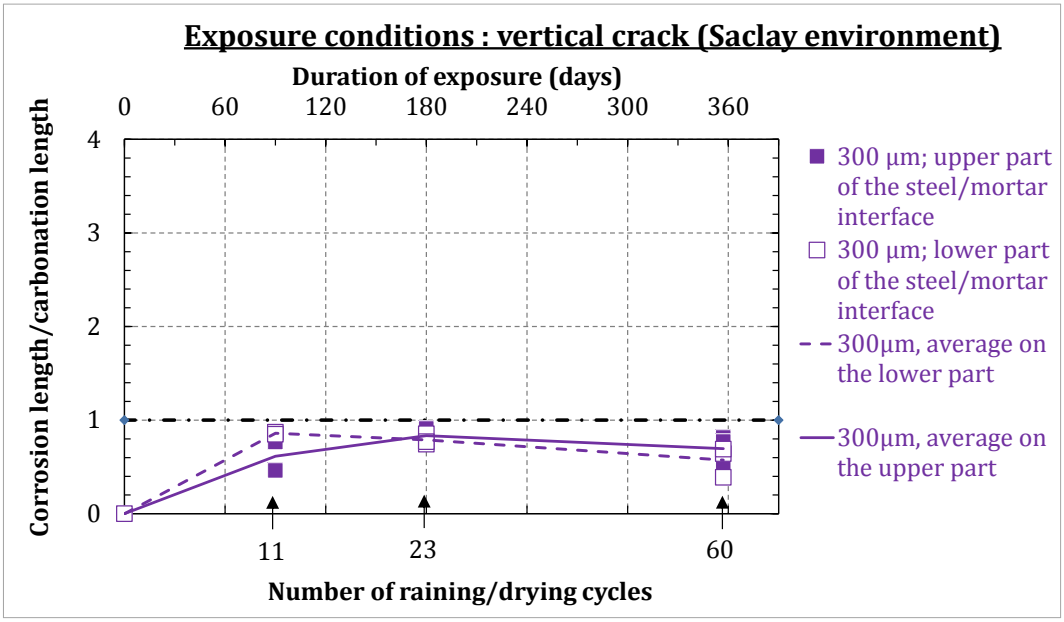

Figure I-20 : Evolution of the corrosion over carbonation length ratio measured on the upper and the lower steel/mortar interface with respect to raining/drying cycles (Saclay, W_r = 300 µm)

I.2.6 Materials type

1) Corrosion length on the upper and lower part of the steel/mortar interface

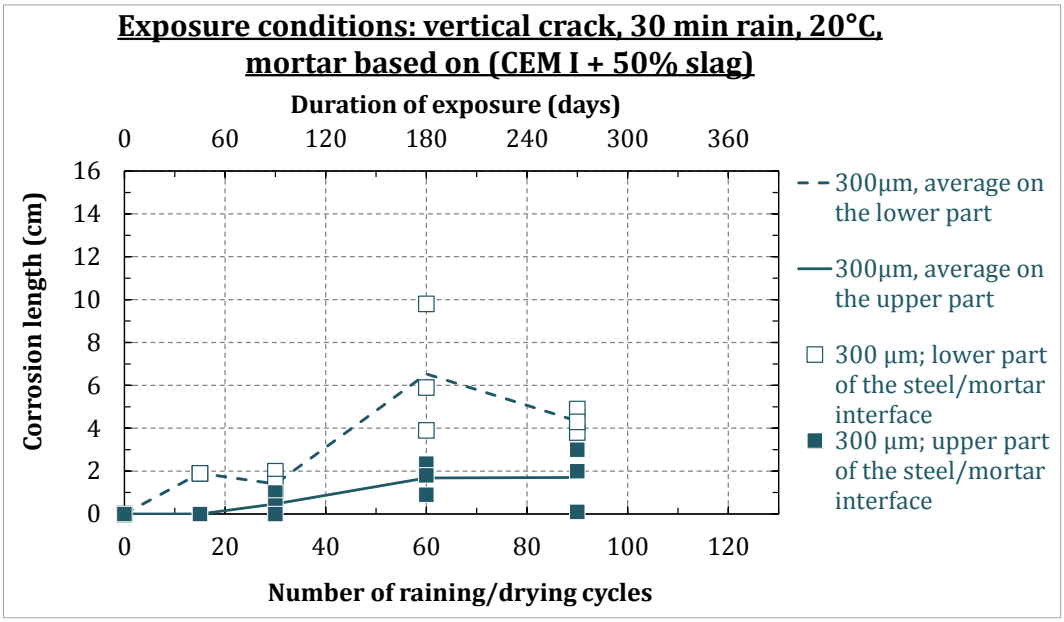

Figure I-21 : Corrosion length along the upper and the lower steel/mortar interface with respect to raining/drying cycles ((CEM I + slag) mortar, W_r = 300 µm)

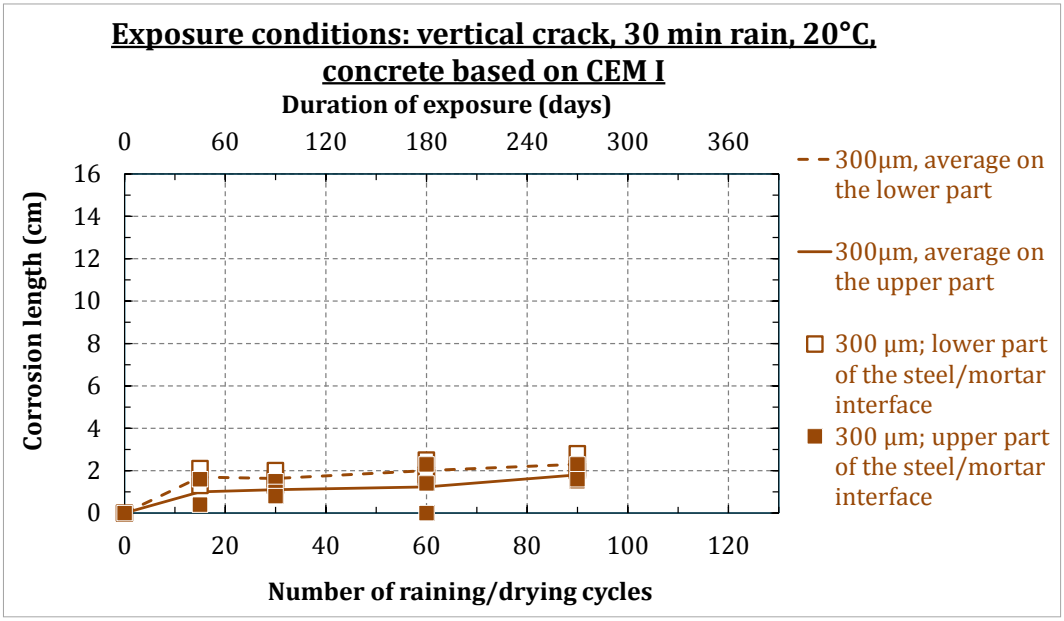

Figure I-22 : Corrosion length along the upper and the lower steel/mortar interface with respect to raining/drying cycles (CEM I concrete, W_r = 300 µm)

2) Evolution of the corrosion products along the upper and lower part of the steel/mortar interface

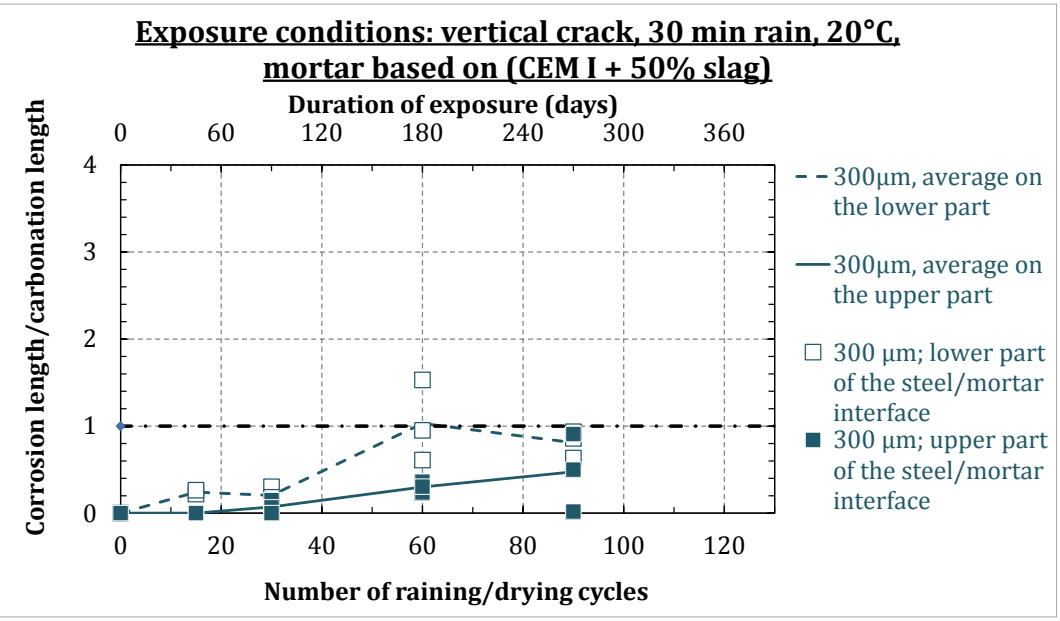

Figure I-23 : Evolution of the corrosion over carbonation length ratio measured on the upper and the lower steel/mortar interface with respect to raining/drying cycles ((CEM I + slag) mortar, W_r = 300 µm)

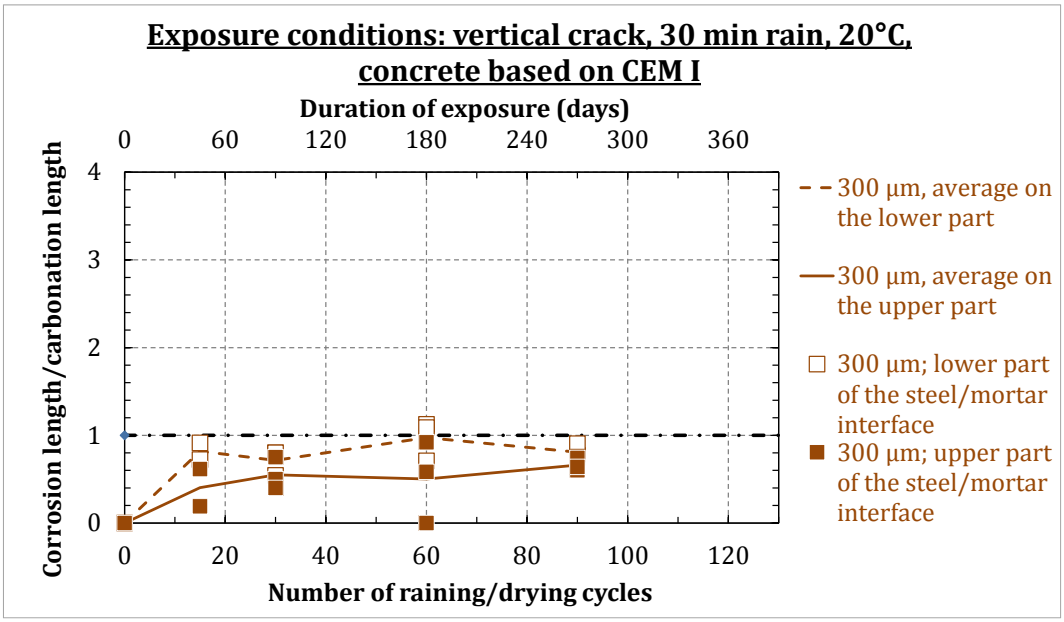

Figure I-24 : Evolution of the corrosion over carbonation length ratio measured on the upper and the lower steel/mortar interface with respect to raining/drying cycles (CEM I concrete, W_r = 300 µm)

I.3 EFFECT OF THE CRACK OPENING ON THE CORROSION DEVELOPMENT

1) Length of corrosion products layer

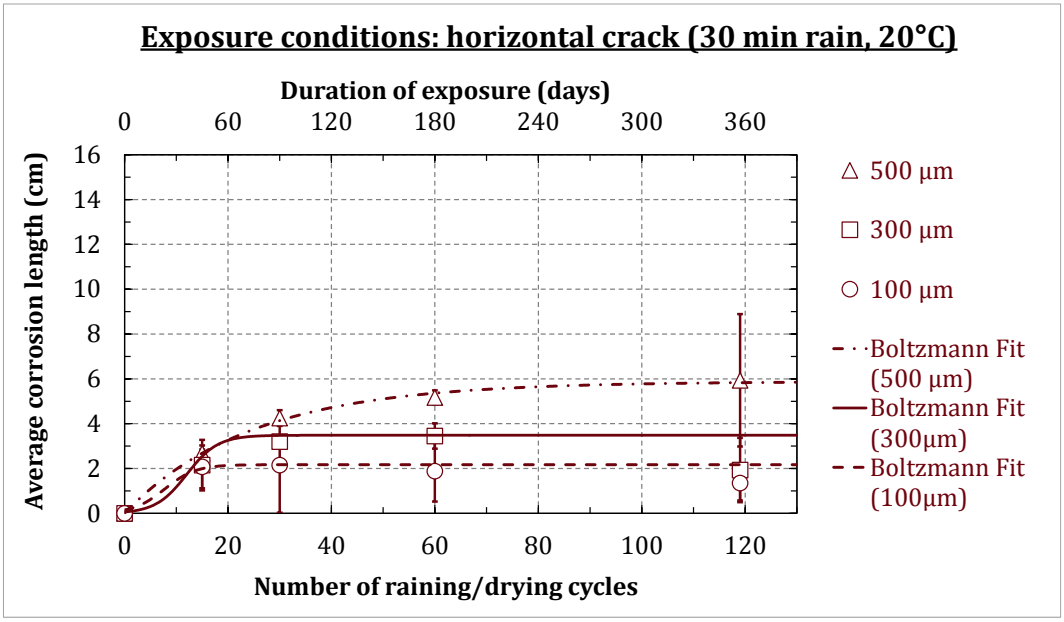

Figure I-25 : Corrosion length evolution with respect to raining/drying cycles and residual crack width (horizontally oriented cracks)

2) Corrosion products evolution

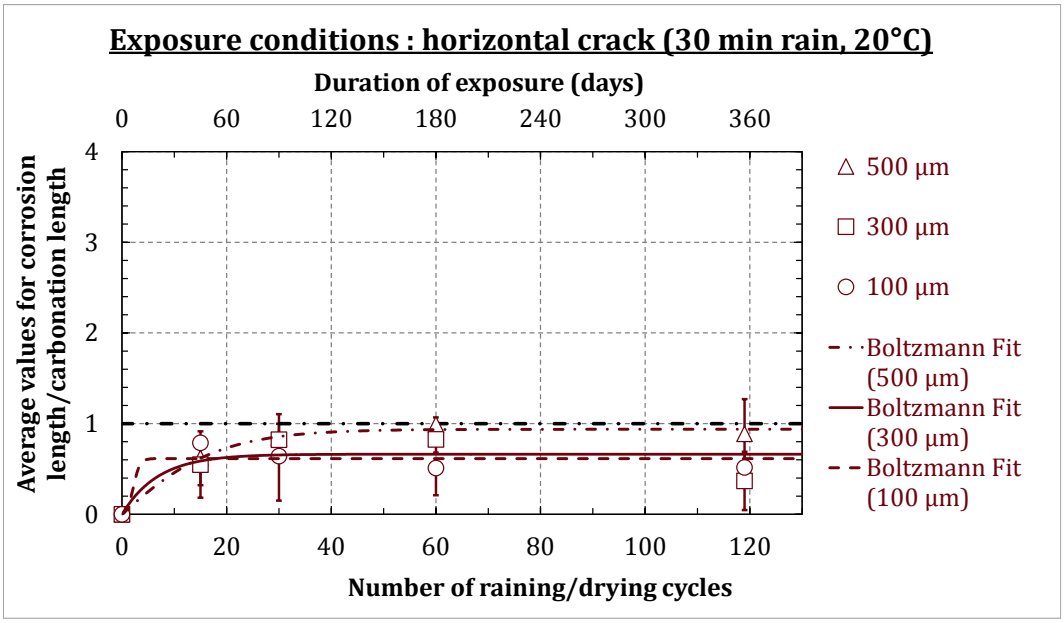

Figure I-26 : Evolution of the corrosion over carbonation length ratio with respect to raining/drying cycles and residual crack width (horizontally oriented cracks)

3) Thickness of the corrosion products layer

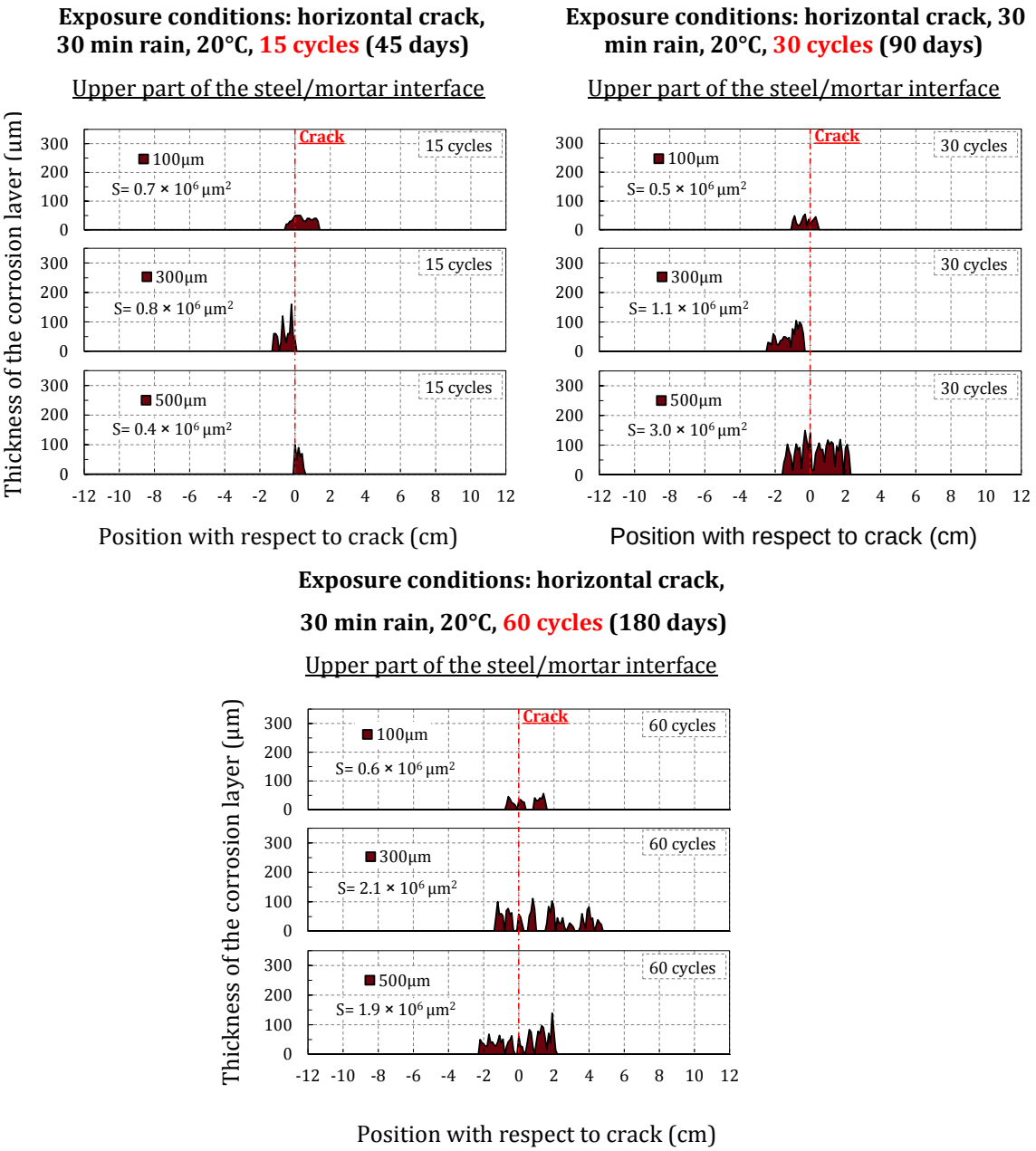

Figure I-27 : Corrosion products repartition obtained on specimens showing different residual crack openings and oriented horizontally with respect to rain

4) Gravimetric measurements

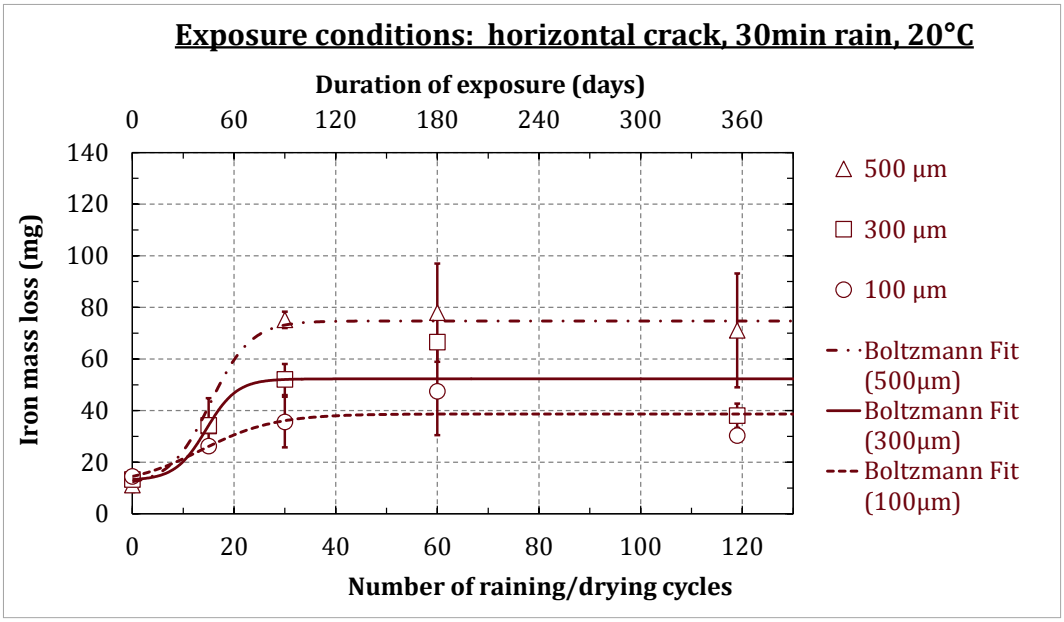

Figure I-28 : Iron mass losses in specimens having different residual crack openings with respect to raining/drying cycles (horizontally oriented cracks)

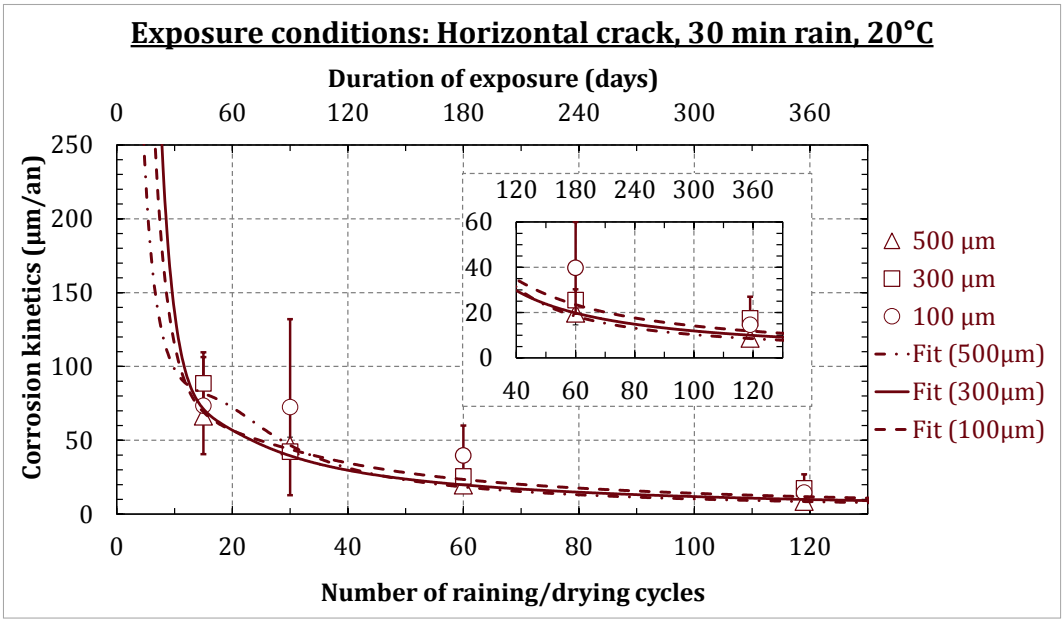

Figure I-29 : Corrosion rate evolution in specimens having different residual crack openings with respect to raining/drying cycles (horizontally oriented cracks)

I.4 EFFECT OF DIFFERENT CORROSION CONDITIONS ON CORROSION DEVELOPMENT

I.4.1 Crack orientation

1) Length of corrosion products layer

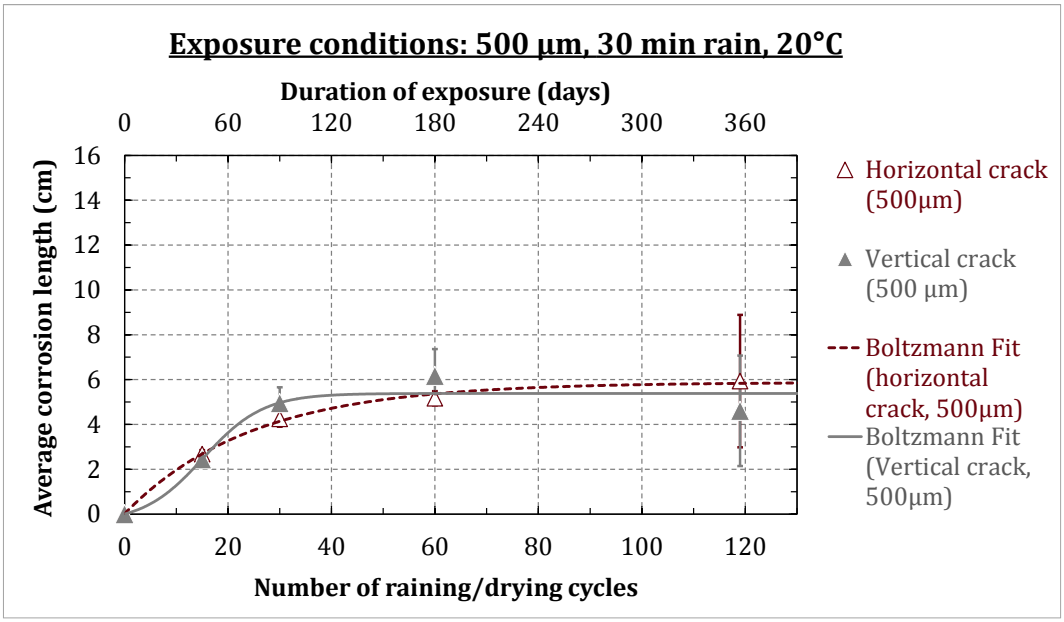

Figure I-30 : Corrosion length evolution with respect to raining/drying cycles and crack orientation (W_r = 500 µm)

2) Corrosion products evolution

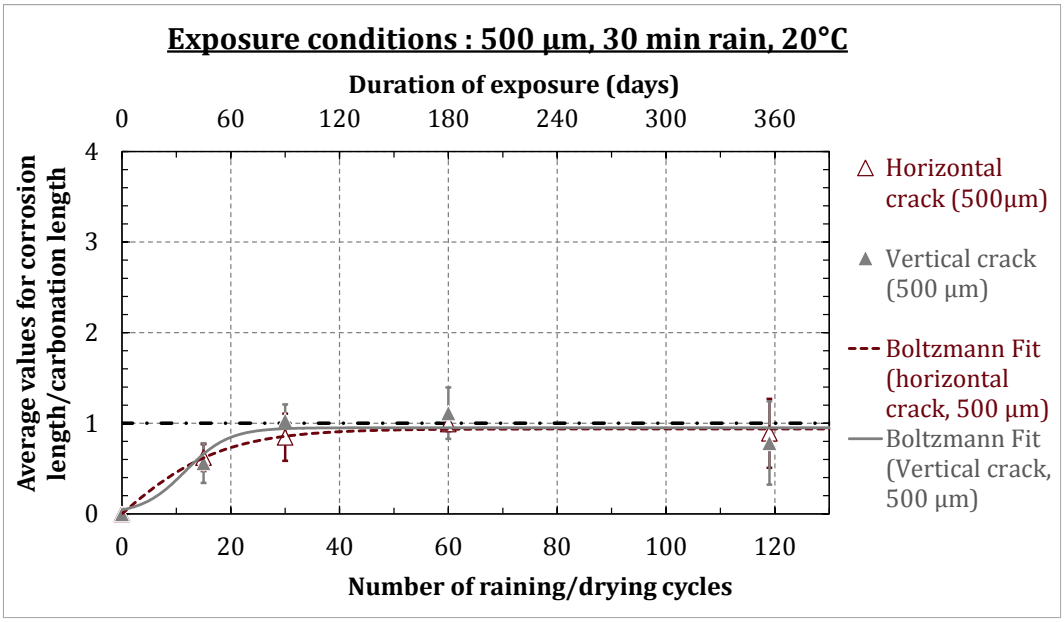

Figure I-31 : Evolution of the corrosion over carbonation length ratio with respect to raining/drying cycles and crack orientation (W_r = 500 µm)

3) Thickness of the corrosion products layer

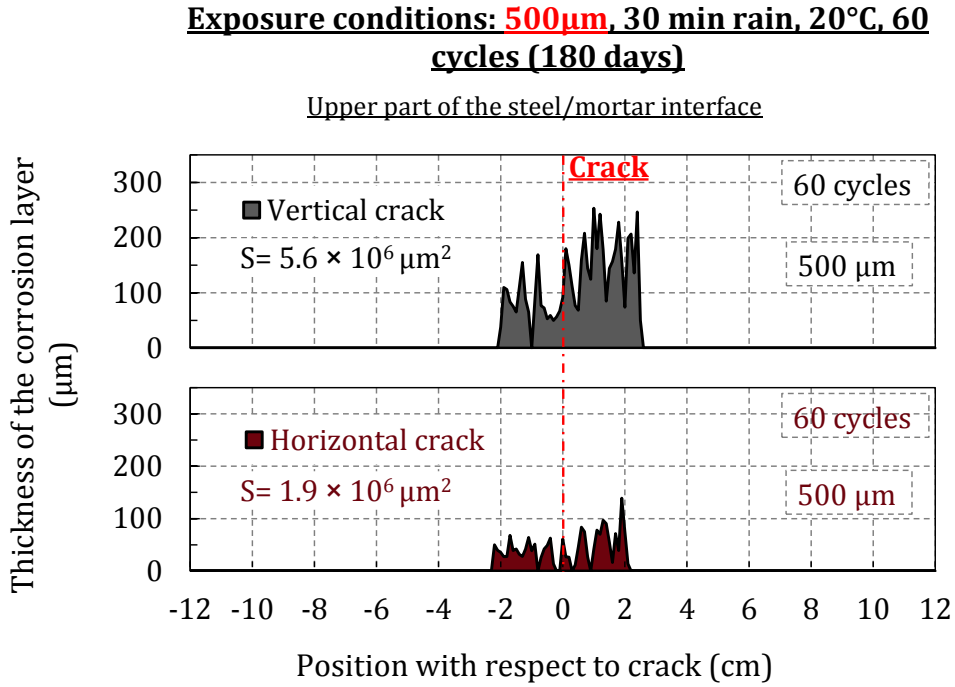

Figure I-32 : Corrosion products repartition obtained on specimens oriented differently with respect to rain (W_r = 500 µm)

4) Gravimetric measurements

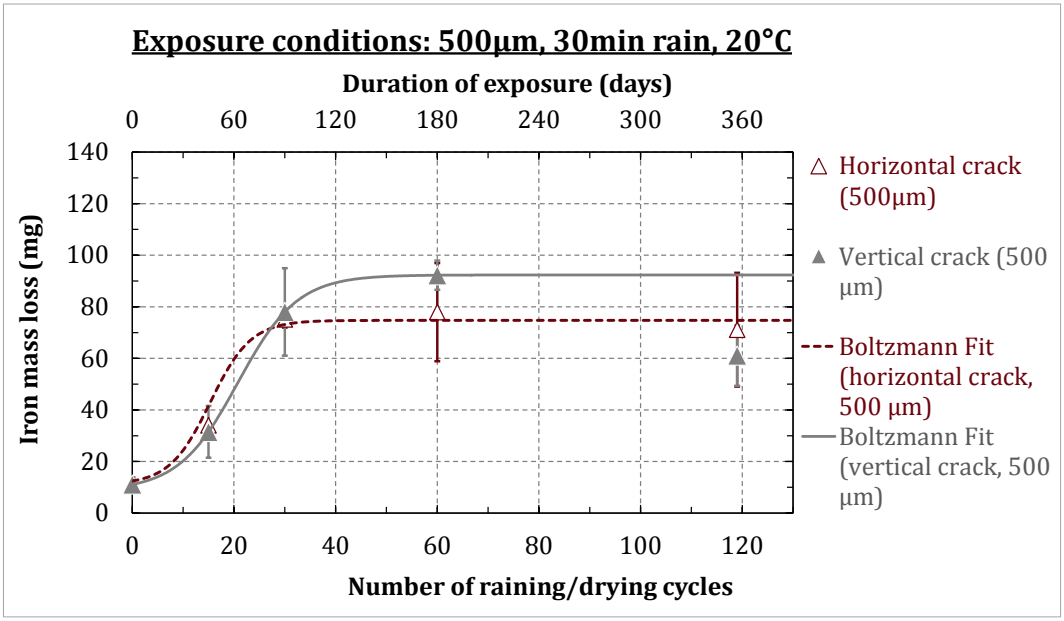

Figure I-33 : Iron mass losses in specimens having different crack orientations with respect to raining/drying cycles (W_r = 500 µm)

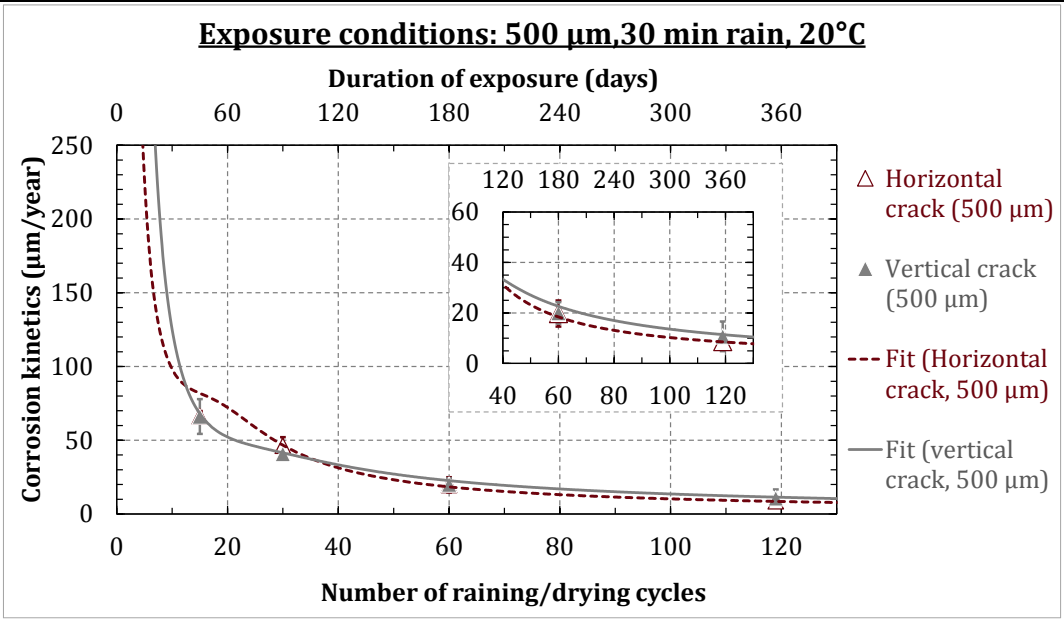

Figure I-34 : Corrosion rate evolution in specimens having different crack orientations with respect to raining/drying cycles

5) Free corrosion potential measurements

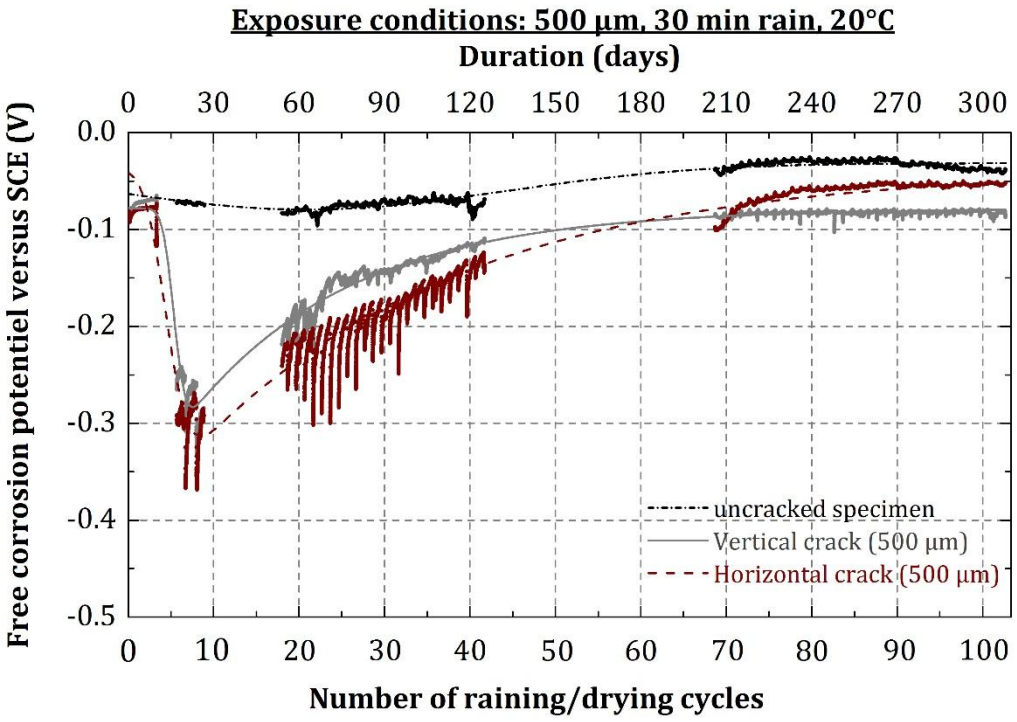

Figure I-35 : Free corrosion potential (versus SCE) measured in specimens showing 500 µm residual crack exposed in different directions with respect to rain

I.4.2 Rain duration

1) Free corrosion potential measurements

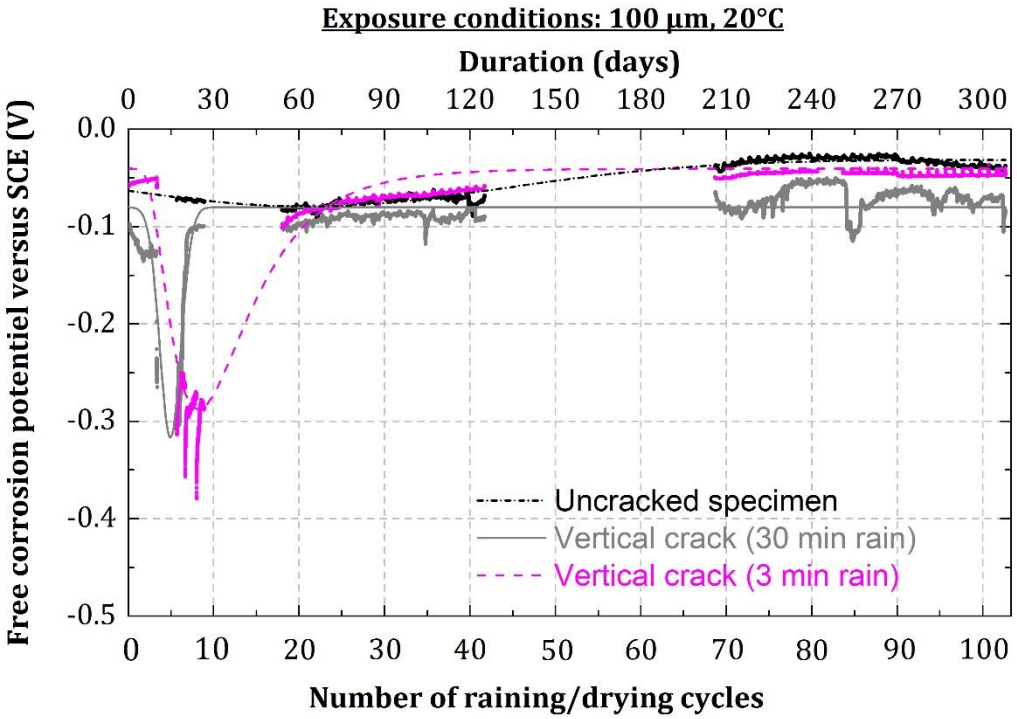

Figure I-36: Free corrosion potential (versus SCE) measured in specimens showing 100 µm residual crack width exposed to different raining durations

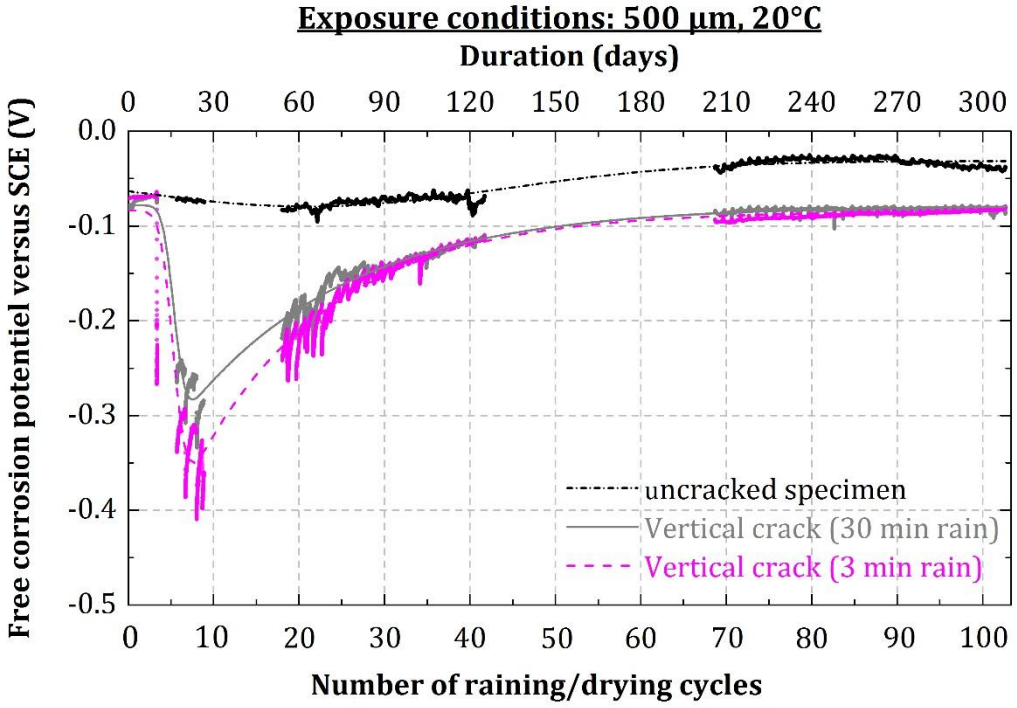

Figure I-37: Free corrosion potential (versus SCE) measured in specimens showing 500 µm residual crack width exposed to different raining durations

I.5 THICKNESS OF THE CORROSION PRODUCTS LAYER

I.5.1 Parameter tested: Effect of the crack opening

Exposure conditions: vertical crack, 30 min rain, 20°C, 30 cycles (90 days)

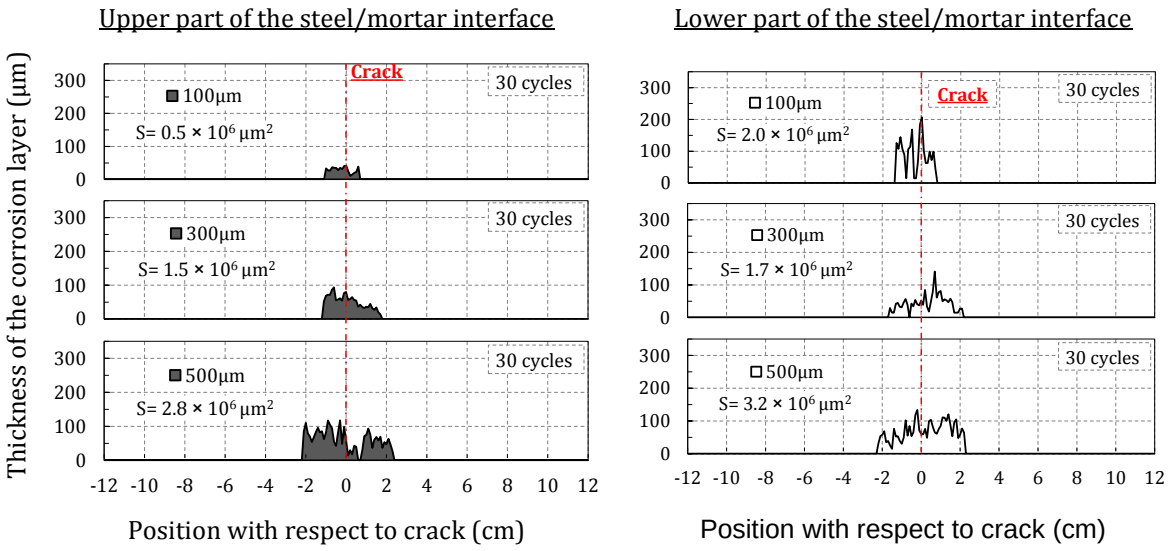

Exposure conditions: vertical crack, 30 min rain, 20°C, 60 cycles (180 days)

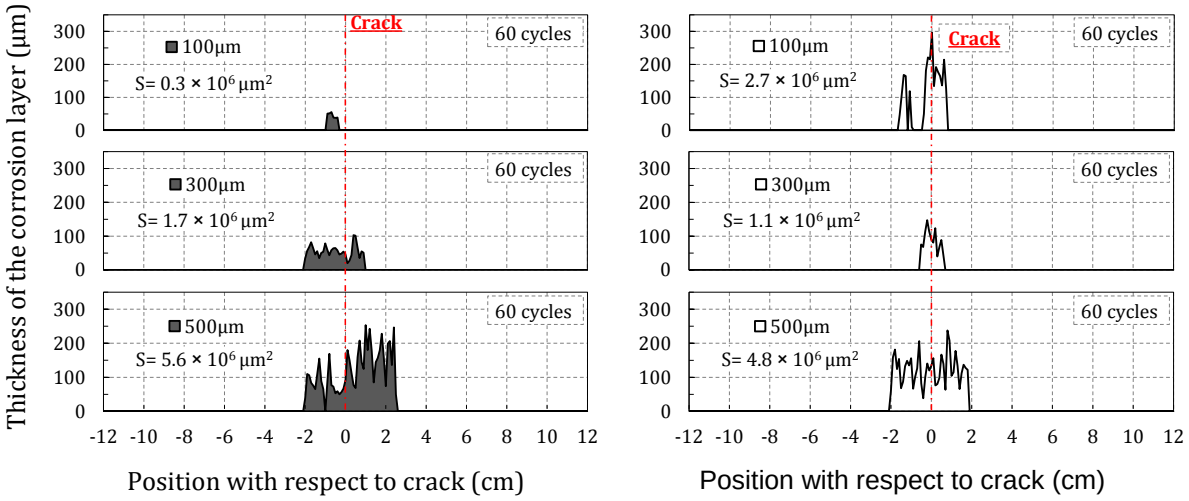

Figure I-38: Corrosion products repartition on the upper and the lower steel/mortar interfaces of specimens corroded in the reference test (30, 60 raining/drying cycles)

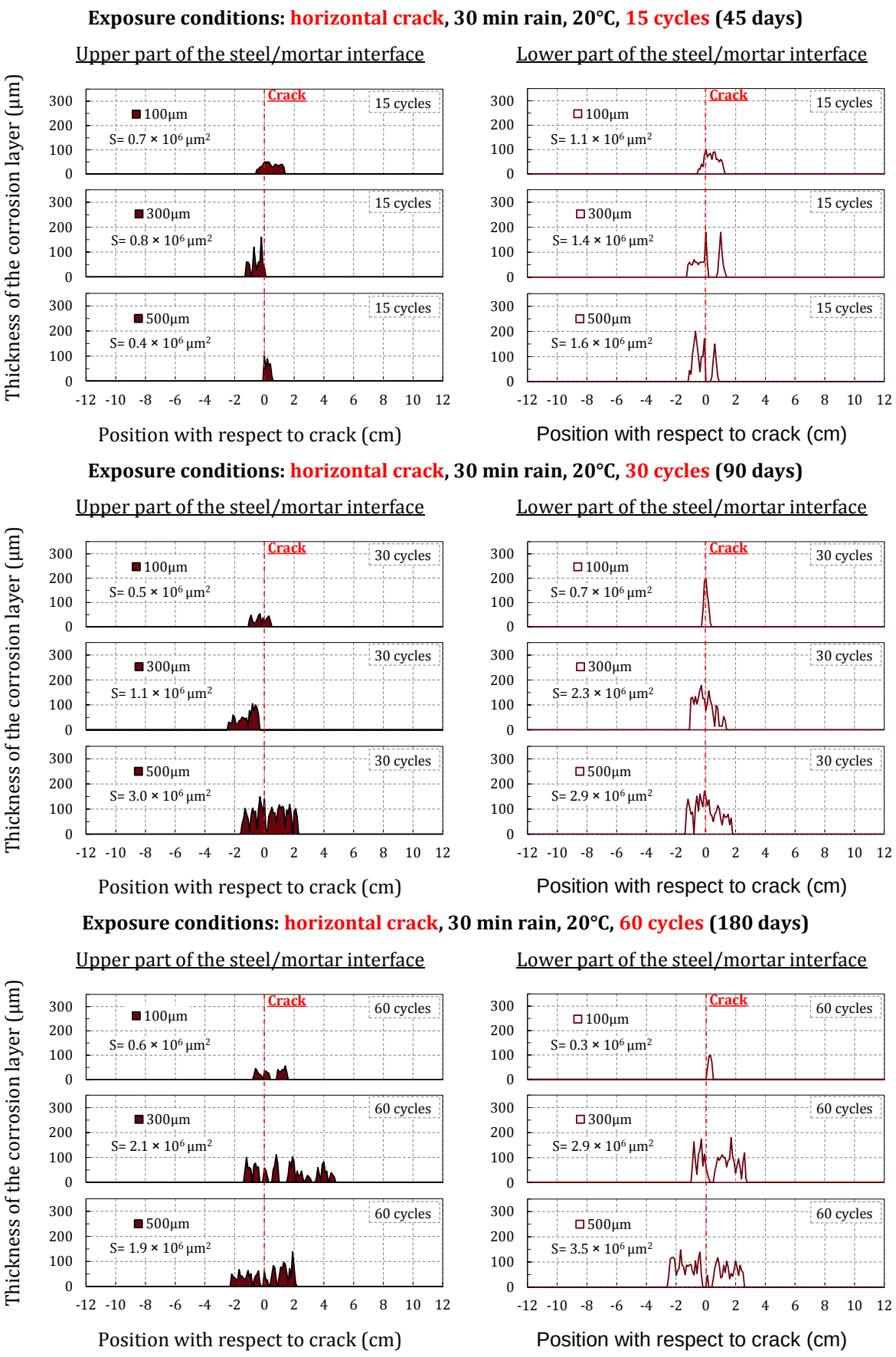

Figure I-39: Corrosion products repartition on the upper and the lower steel/mortar interfaces of specimens exposed horizontally with respect to rain (15, 30, 60 raining/drying cycles)

I.5.2 Parameter tested: effect of the crack orientation

Exposure conditions: 300µm, 30 min rain, 20°C, 15 cycles (45 days)

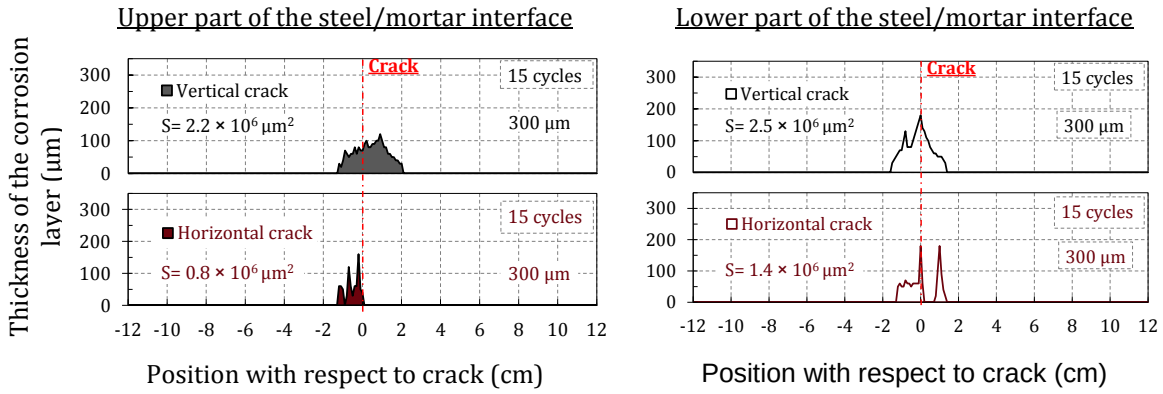

Figure I-40: Corrosion products repartition on the upper and the lower steel/mortar interfaces of specimens oriented differently with respect to rain (15 raining/drying cycles)

Exposure conditions: 100 µm, 30 min rain, 20°C, 30 cycles (90 days)

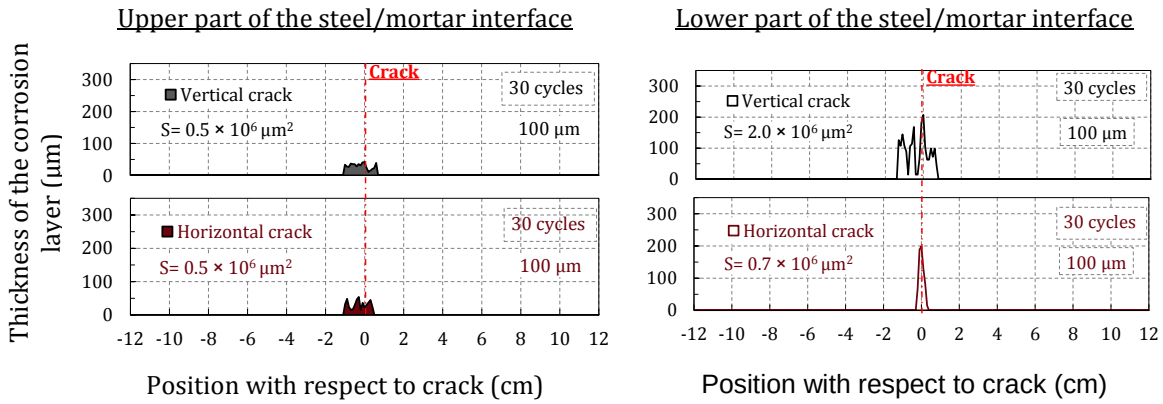

Exposure conditions: 300µm, 30 min rain, 20°C, 30 cycles (90 days)

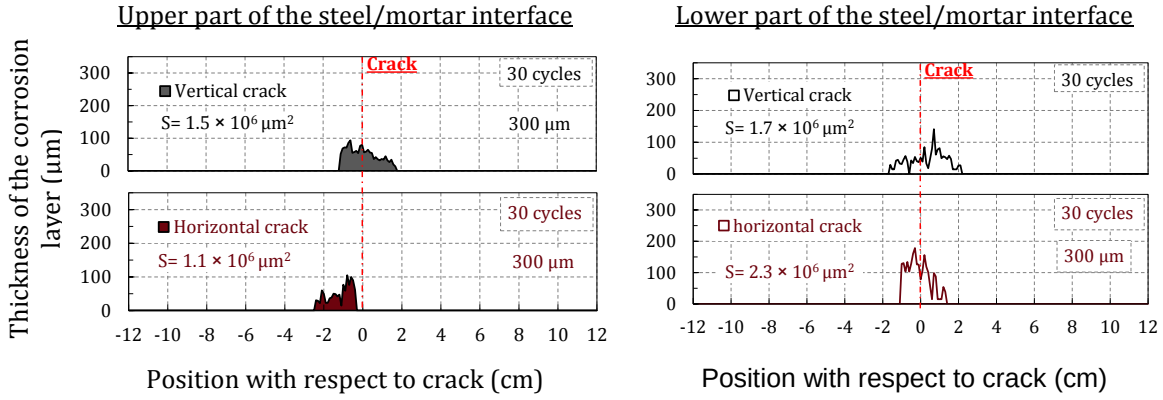

Exposure conditions: 500 µm, 30 min rain, 20°C, 30 cycles (90 days)

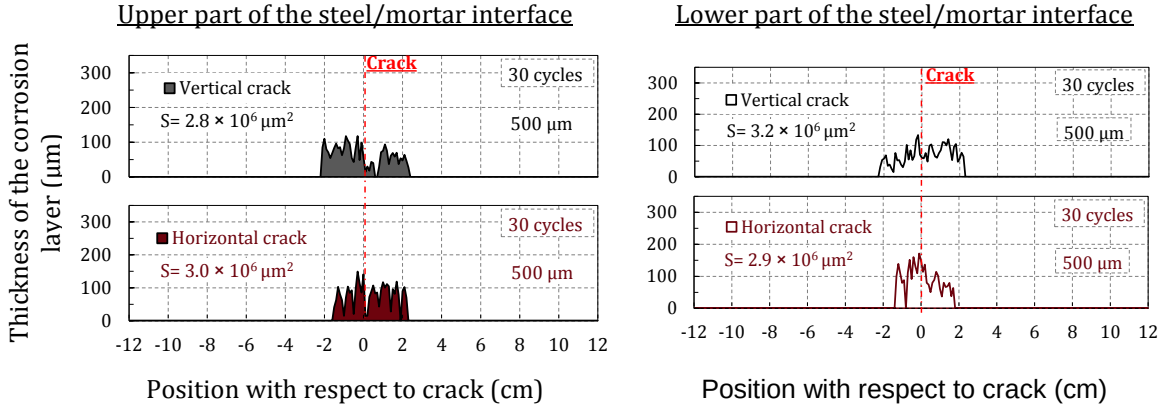

Figure I-41:Corrosion products repartition on the upper and the lower steel/mortar interfaces of specimens oriented differently with respect to rain (30 raining/drying cycles)

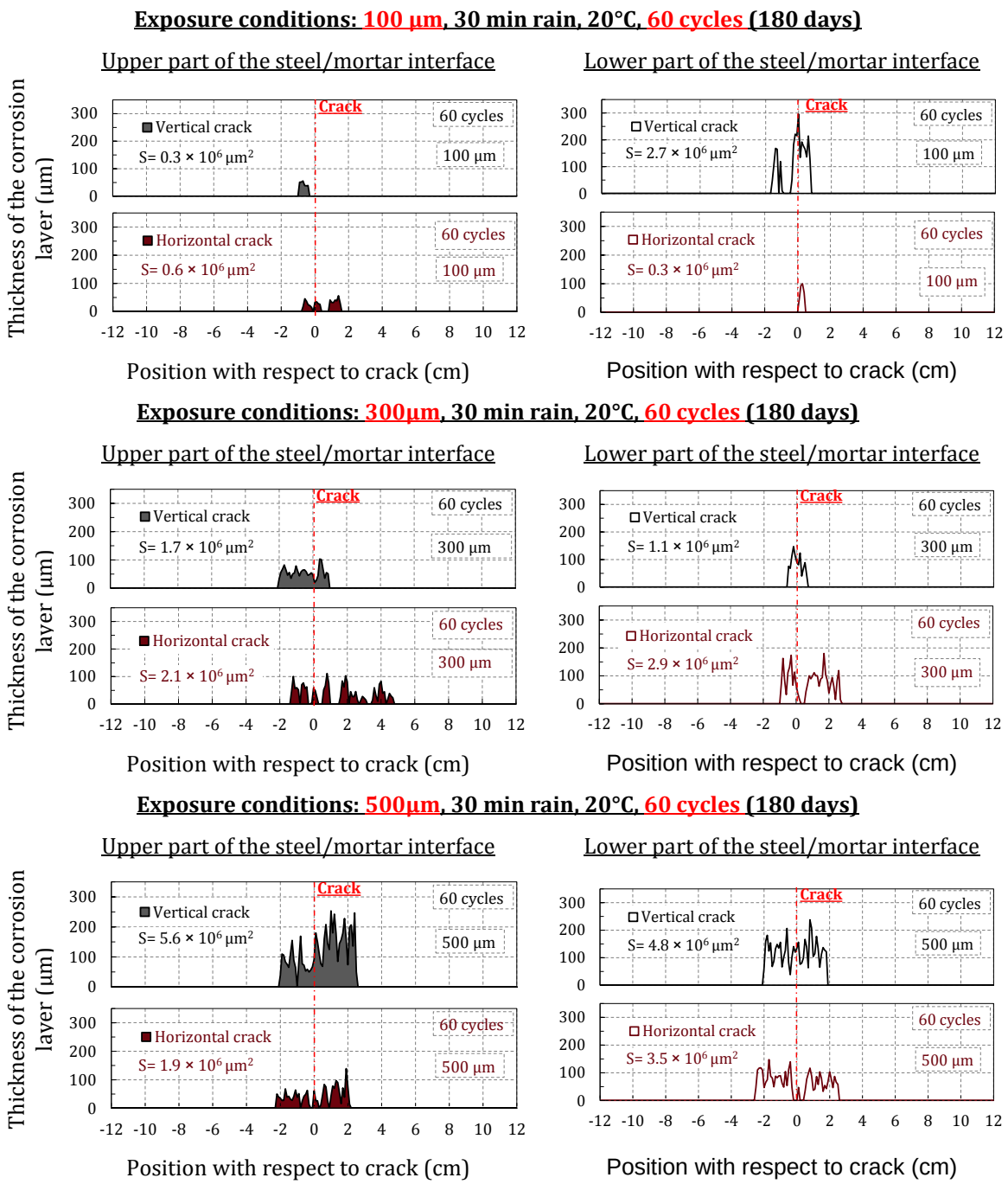

Figure I-42: Corrosion products repartition on the upper and the lower steel/mortar interfaces of specimens oriented differently with respect to rain (60 raining/drying cycles)

I.5.3 Parameter tested: effect of the rain duration

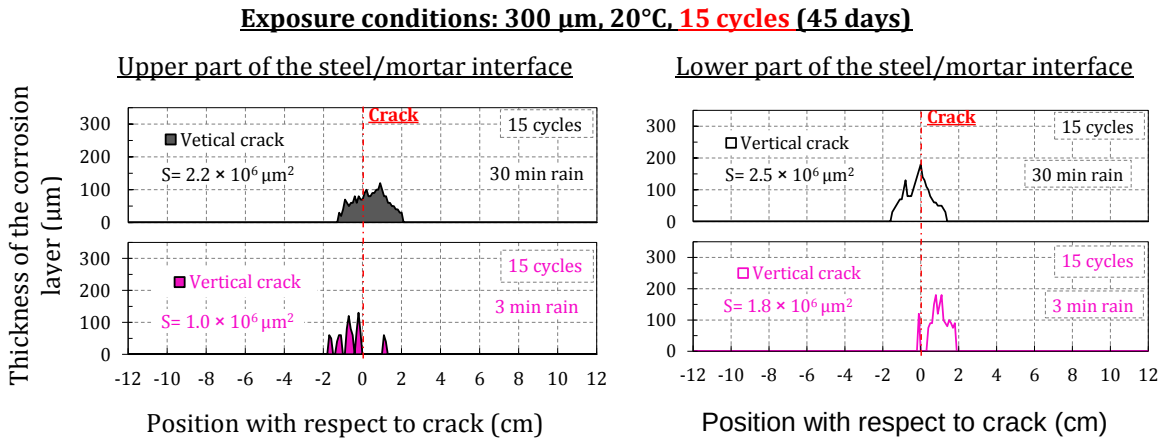

Figure I-43: Corrosion products repartition on the upper and the lower steel/mortar interfaces of specimens exposed to different rain durations (15 raining/drying cycles)

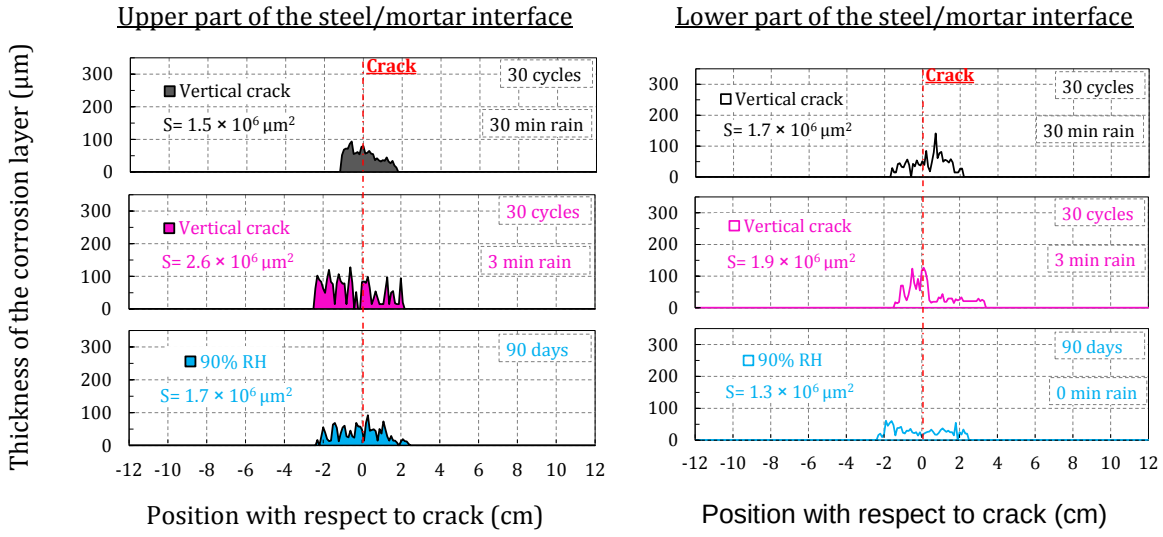

Figure I-44: Corrosion products repartition on the upper and the lower steel/mortar interfaces of specimens exposed to different rain durations (30 raining/drying cycles)

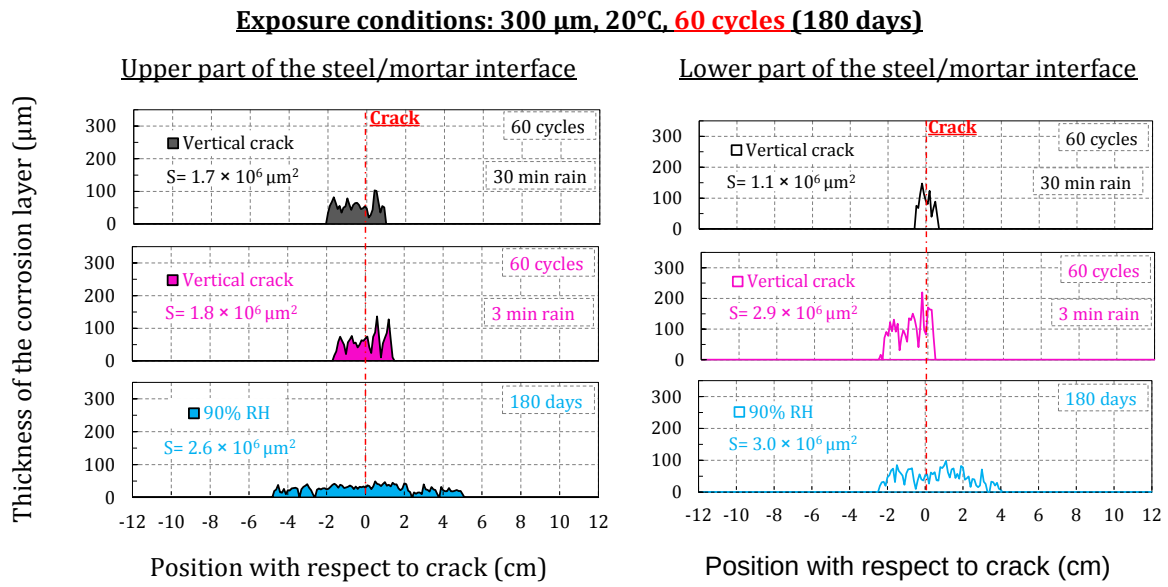

Figure I-45: Corrosion products repartition on the upper and the lower steel/mortar interfaces of specimens exposed to different rain durations (60 raining/drying cycles)

I.5.4 Parameter tested: effect of the temperature

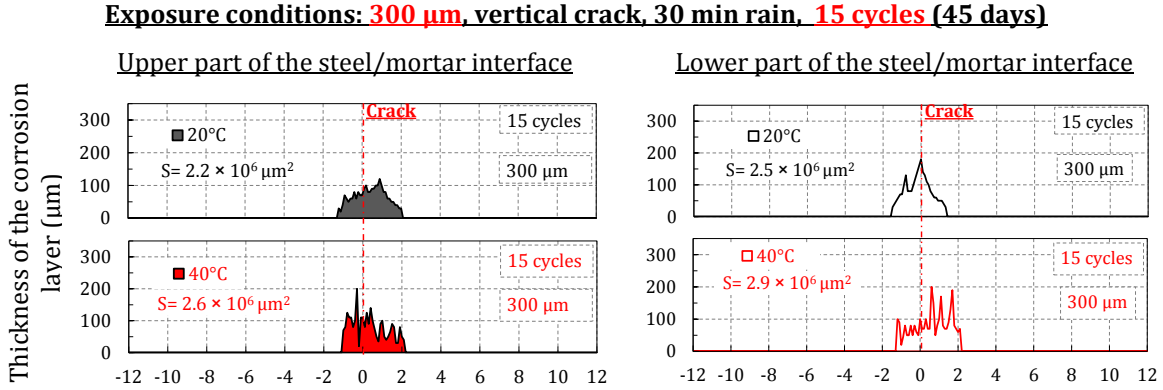

Figure I-46: Corrosion products repartition on the upper and the lower steel/mortar interfaces of specimens exposed to different temperatures (15 raining/drying cycles)

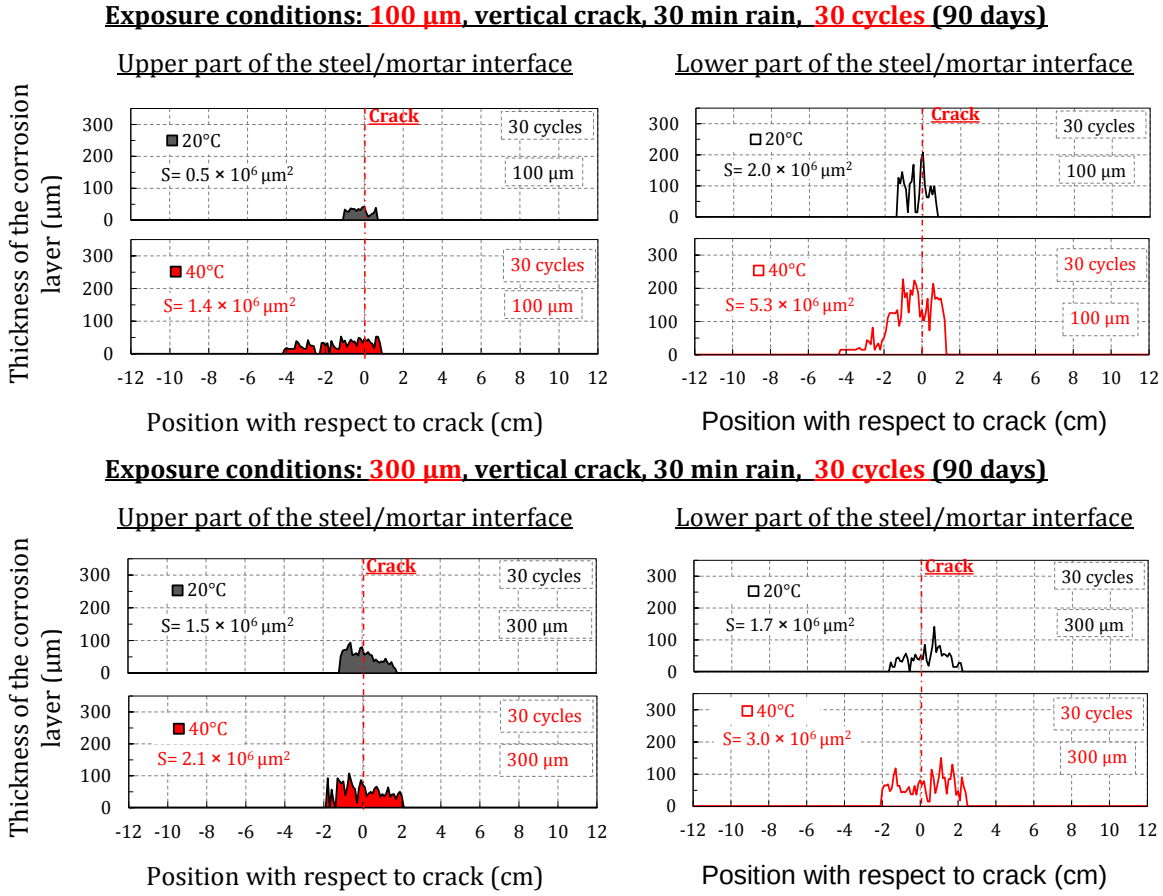

Figure I-47: Corrosion products repartition on the upper and the lower steel/mortar interfaces of specimens exposed to different temperatures (30 raining/drying cycles)

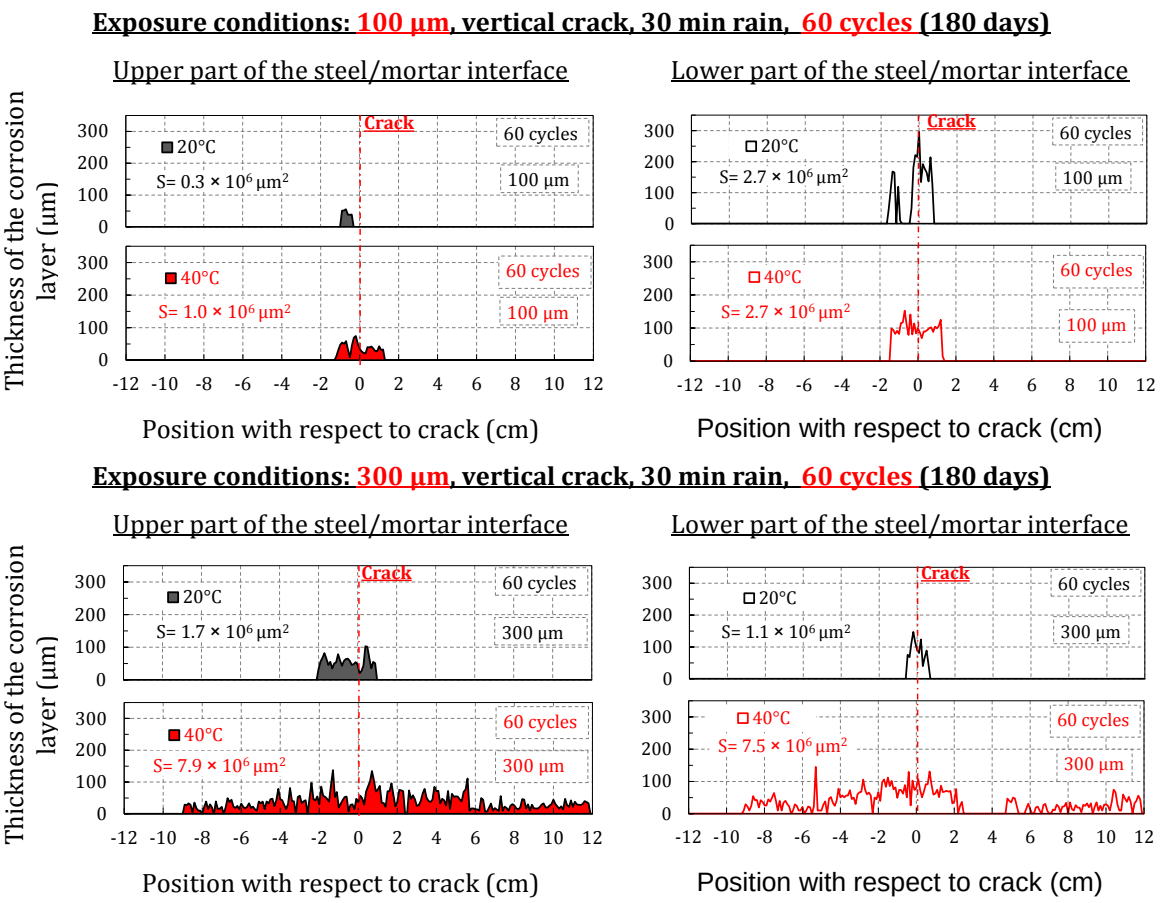

Figure I-48: Corrosion products repartition on the upper and the lower steel/mortar interfaces of specimens exposed to different temperatures (60 raining/drying cycles)

I.5.5 Exposure condition: Environmental conditions of Saclay

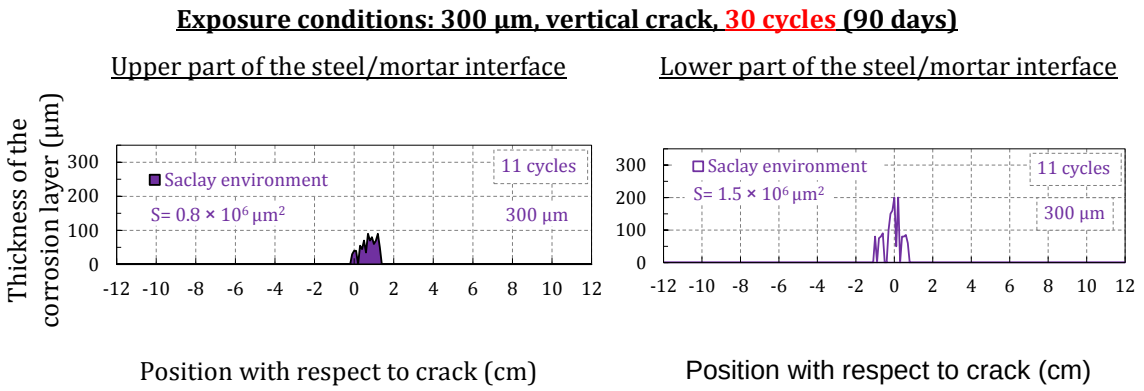

Figure I-49: Corrosion products repartition on the upper and the lower steel/mortar interfaces of specimens exposed to Saclay environment

I.5.6 Materials type

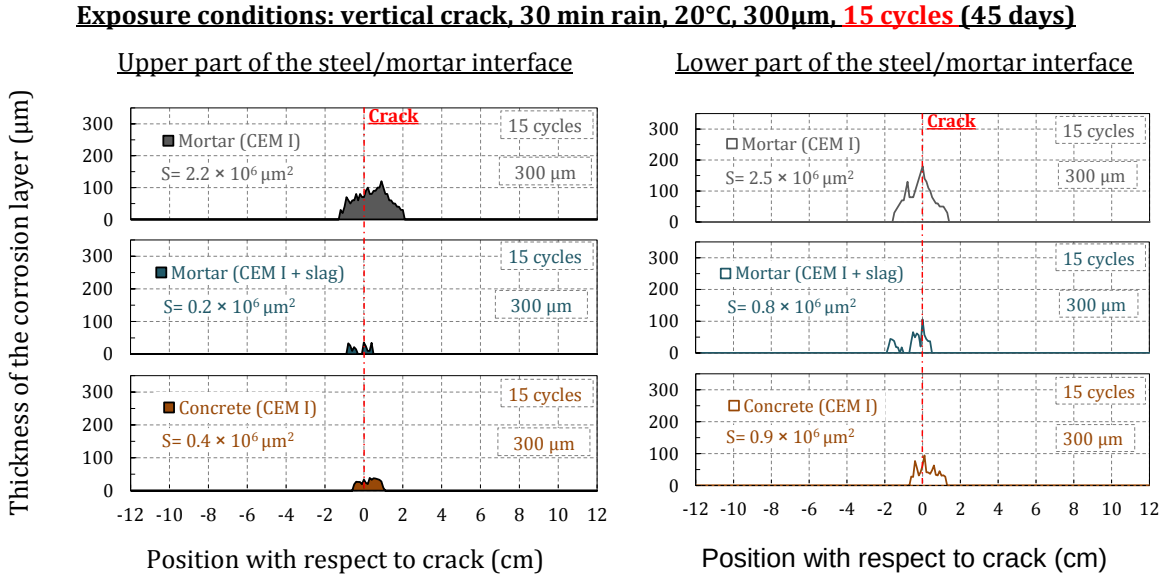

Figure I-50: Corrosion products repartition on the upper and the lower steel/mortar interfaces of specimens with different materials type (15 raining/drying cycles)

I.6 CORROSION PRODUCTS TYPE

I.6.1 Parameter tested: effect of the crack opening

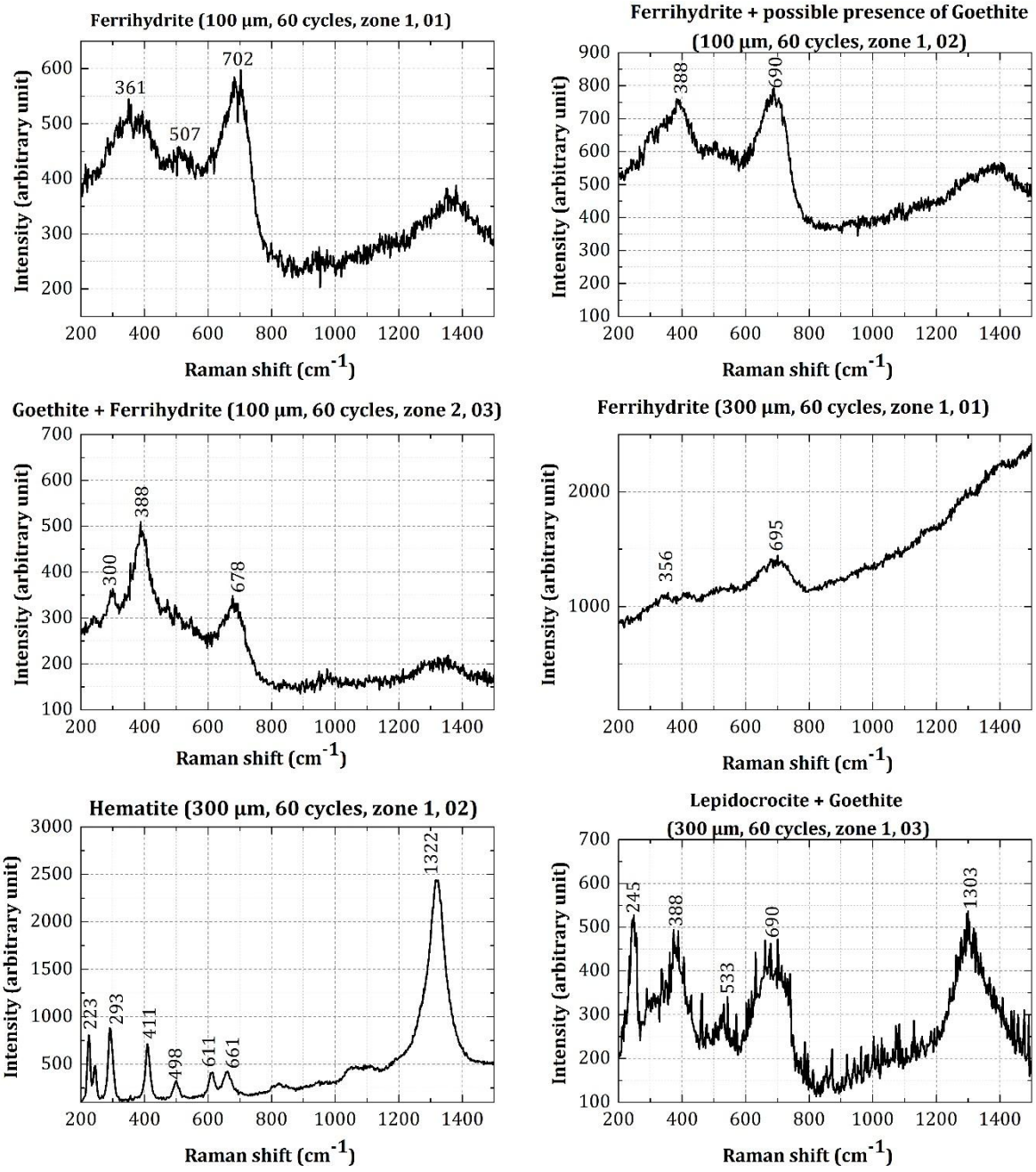

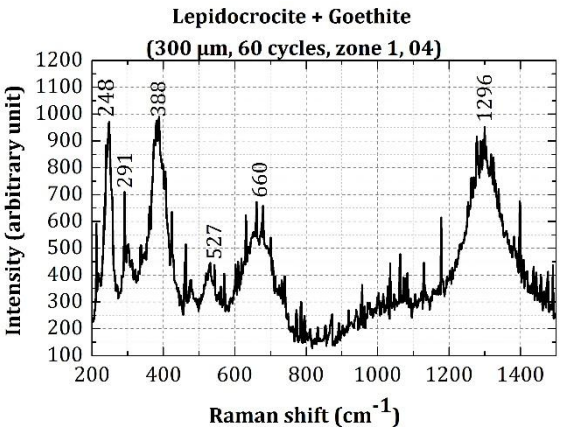
Lepidocrocite + Goethite
(300 µm, 60 cycles, zone 1, 04)
Intensity (arbitrary unit)
Raman shift (cm-1)
248
291
388
527
660
1296

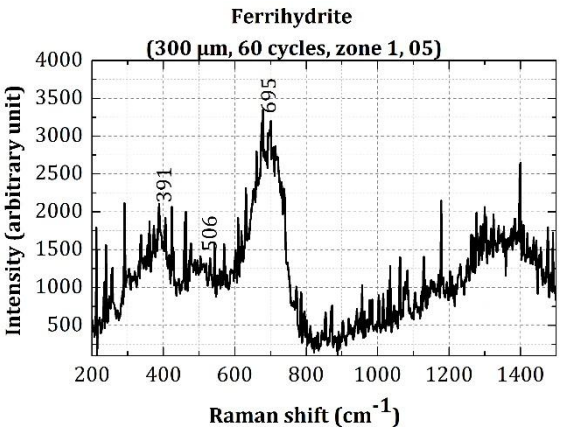
Ferrihydrite
(300 µm, 60 cycles, zone 1, 05)
Intensity (arbitrary unit)
Raman shift (cm-1)
391
506
695

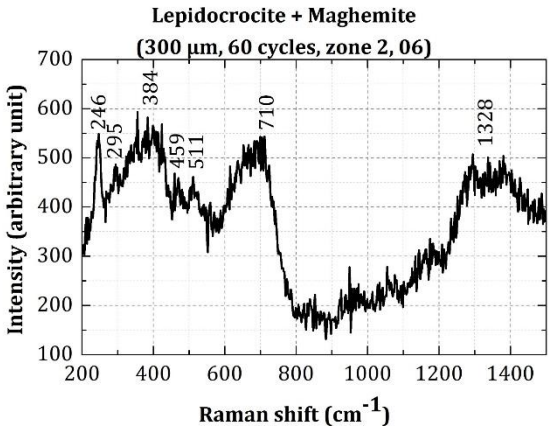
Lepidocrocite + Maghemite
(300 µm, 60 cycles, zone 2, 06)
Intensity (arbitrary unit)
Raman shift (cm-1)
246
295
384
459
511
710
1328

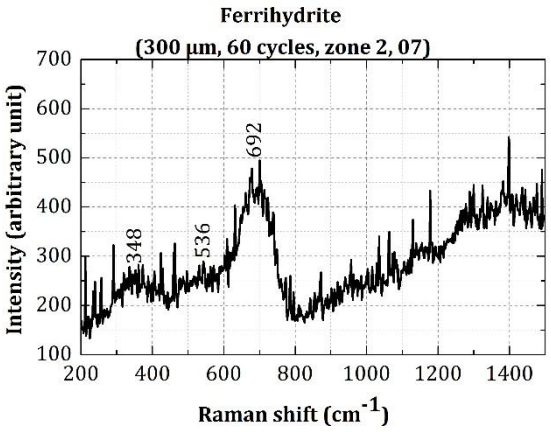
Ferrihydrite
(300 µm, 60 cycles, zone 2, 07)
Intensity (arbitrary unit)
Raman shift (cm-1)
348
536
692

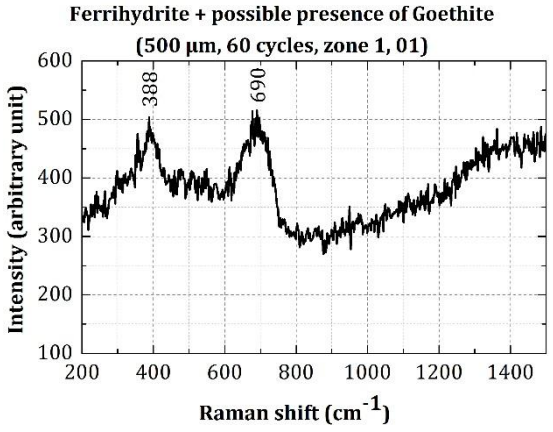
Ferrihydrite + possible presence of Goethite
(500 µm, 60 cycles, zone 1, 01)
Intensity (arbitrary unit)
Raman shift (cm-1)
388
690

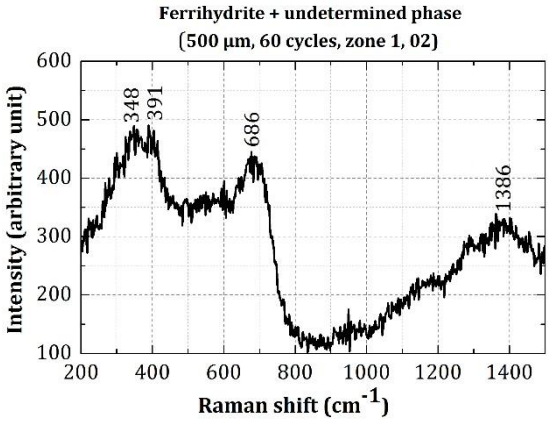
Ferrihydrite + undetermined phase
(500 µm, 60 cycles, zone 1, 02)
Intensity (arbitrary unit)
Raman shift (cm-1)
348
391
686
1386

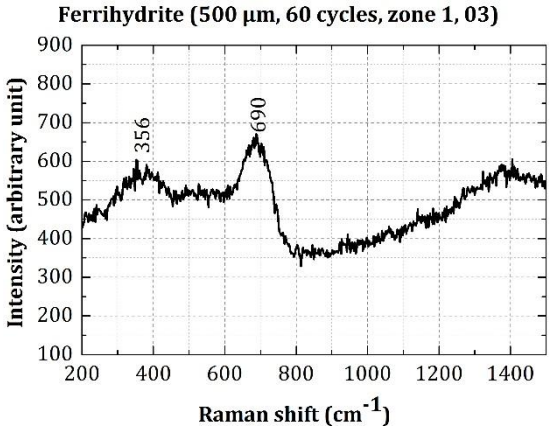
Ferrihydrite (500 µm, 60 cycles, zone 1, 03)
Intensity (arbitrary unit)
Raman shift (cm-1)
356
690

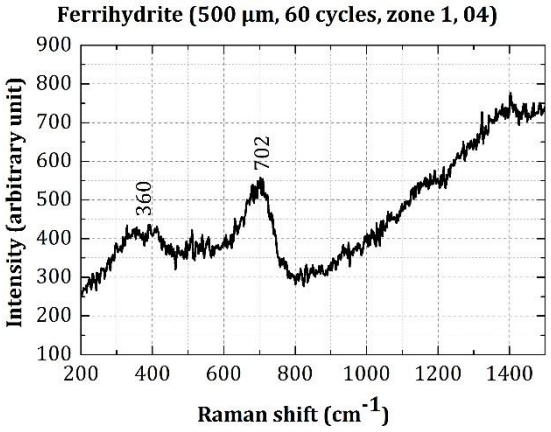
Ferrihydrite (500 µm, 60 cycles, zone 1, 04)
Intensity (arbitrary unit)
Raman shift (cm-1)
360
702

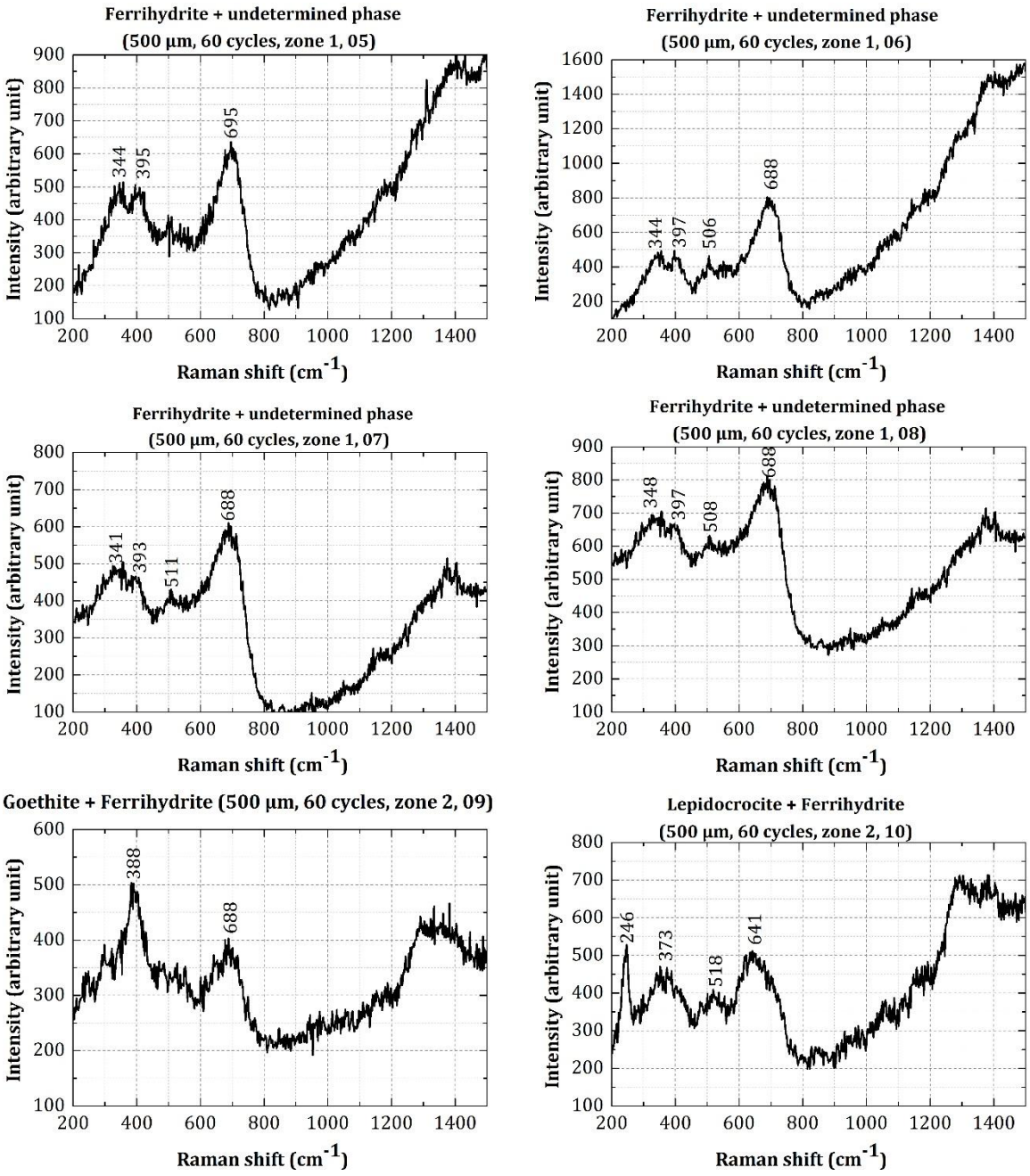

Figure I-51: All the Raman spectra of corrosion products obtained on specimens showing three different residual crack openings and corroded in the reference test

I.6.2 Parameter tested: effect of the crack orientation

Ferrihydrite
(Horz. crack, 300 µm, 30 min rain, 20°C, 60 cycles, zone 1, 01)

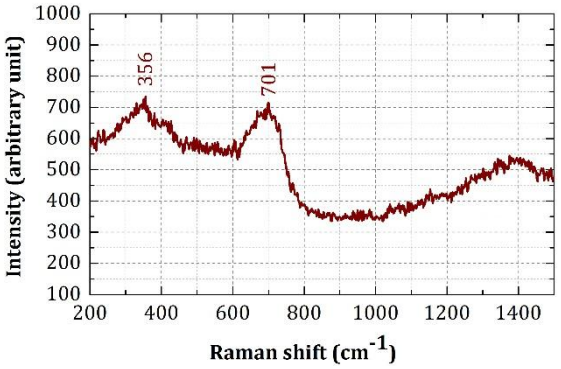

Ferrihydrite
(Horz. crack, 300 µm, 30 min rain, 20°C, 60 cycles, zone 1, 02)

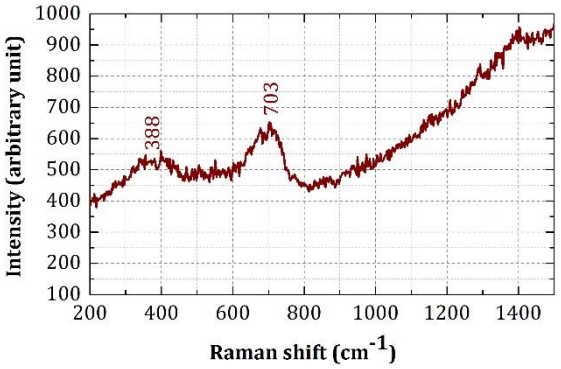

Goethite
(Horz. crack, 300 µm, 30 min rain, 20°C, 60 cycles, zone 1, 03)

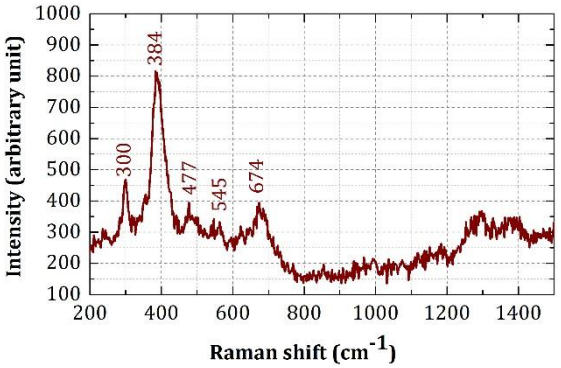

Goethite
(Horz. crack, 300 µm, 30 min rain, 20°C, 60 cycles, zone 1, 04)

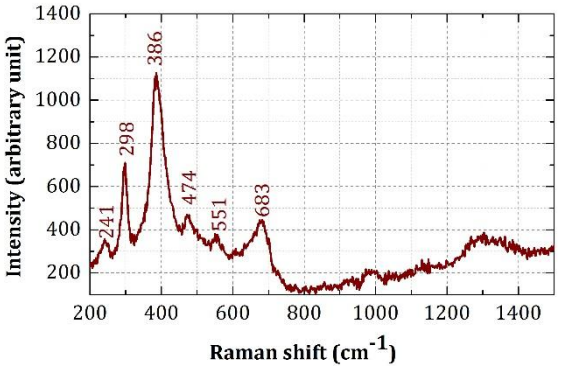

Ferrihydrite
(Horz. crack, 300 µm, 30 min rain, 20°C, 60 cycles, zone 1, 05)

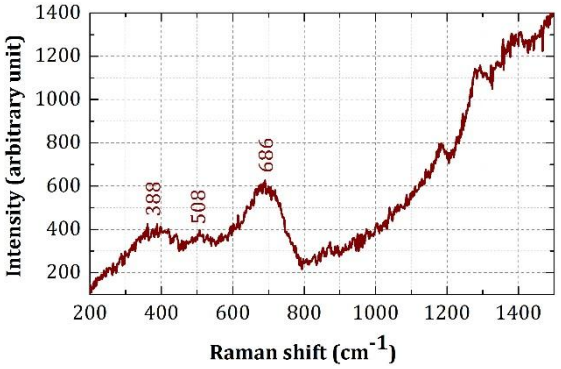

Lepidocrocite
(Horz. crack, 300 µm, 30 min rain, 20°C, 60 cycles, zone 1, 06)

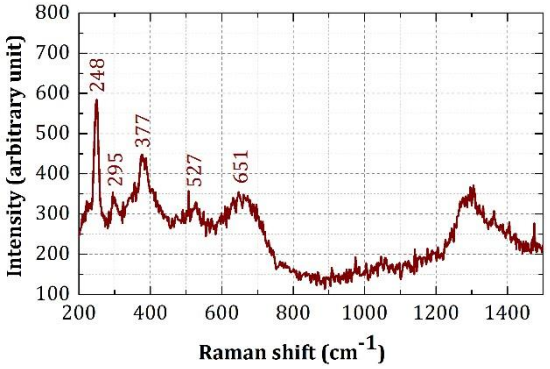

Ferrihydrite + undetermined phase
(Horz. crack, 300 µm, 30 min rain, 20°C, 60 cycles, zone 2, 07)

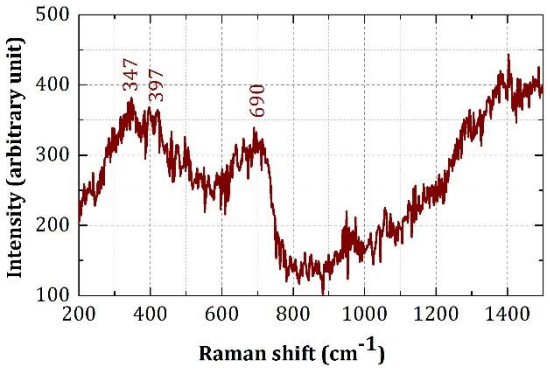

Ferrihydrite
(Horz. crack, 300 µm, 30 min rain, 20°C, 60 cycles, zone 2, 08)

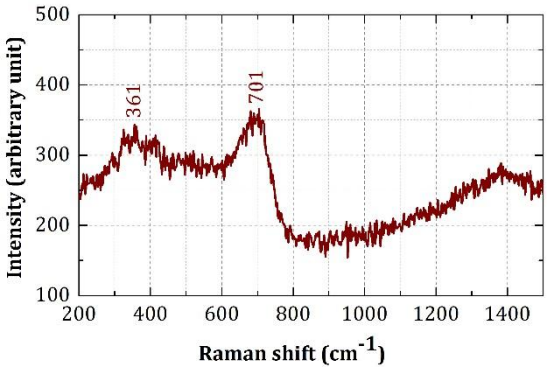

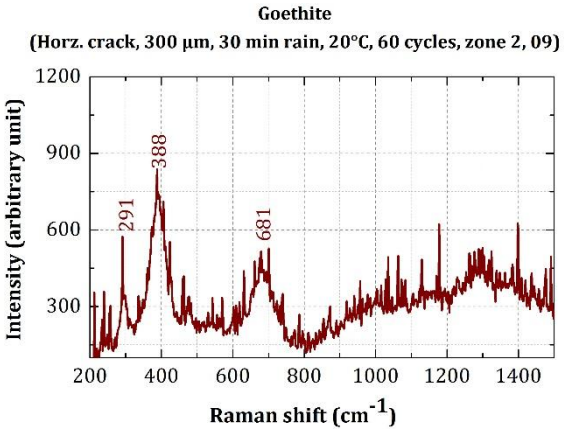

Figure I-52: All the Raman spectra of corrosion products obtained on specimens having 300 µm crack width oriented horizontally with respect to rain

I.6.3 Parameter tested: effect of the rain duration

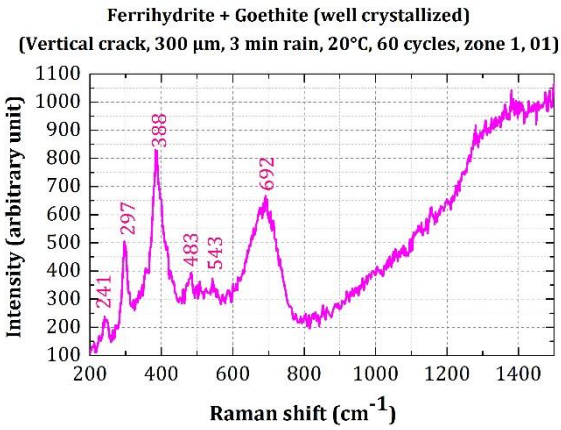

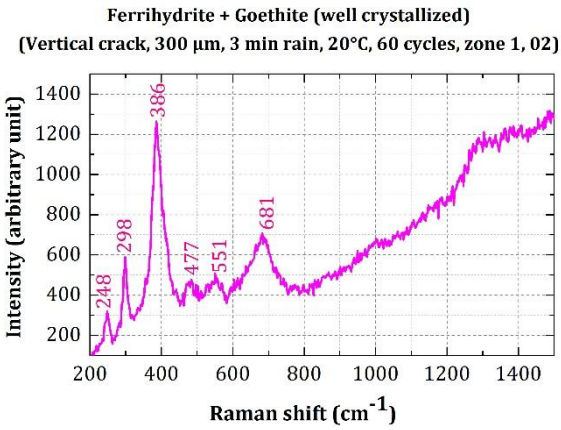

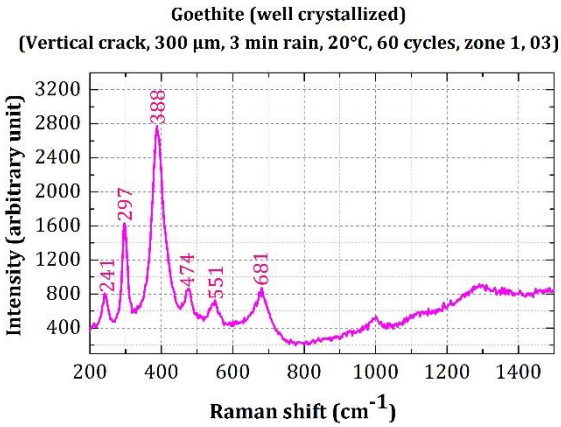

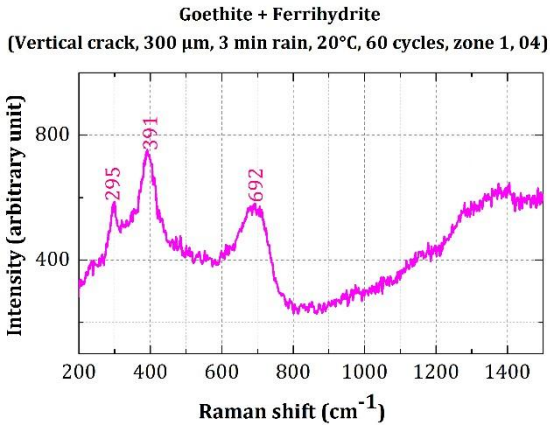

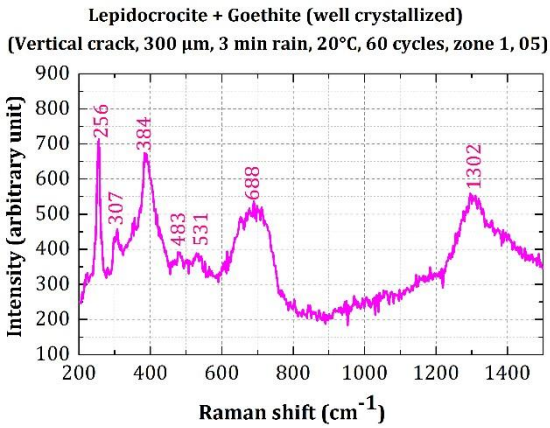

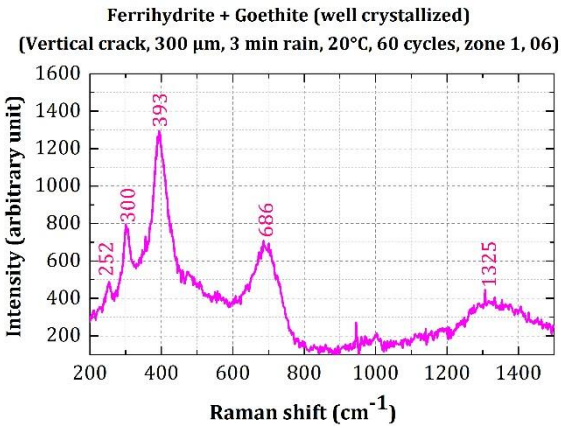

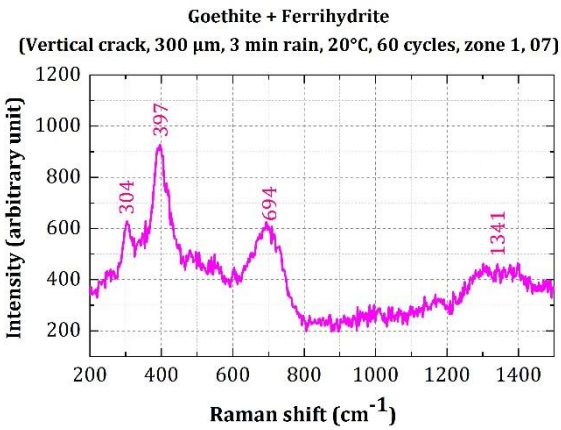

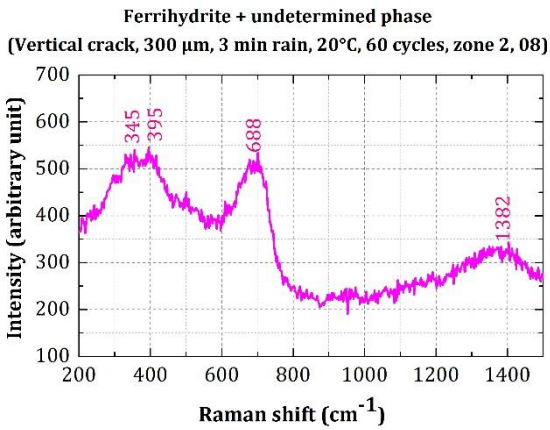

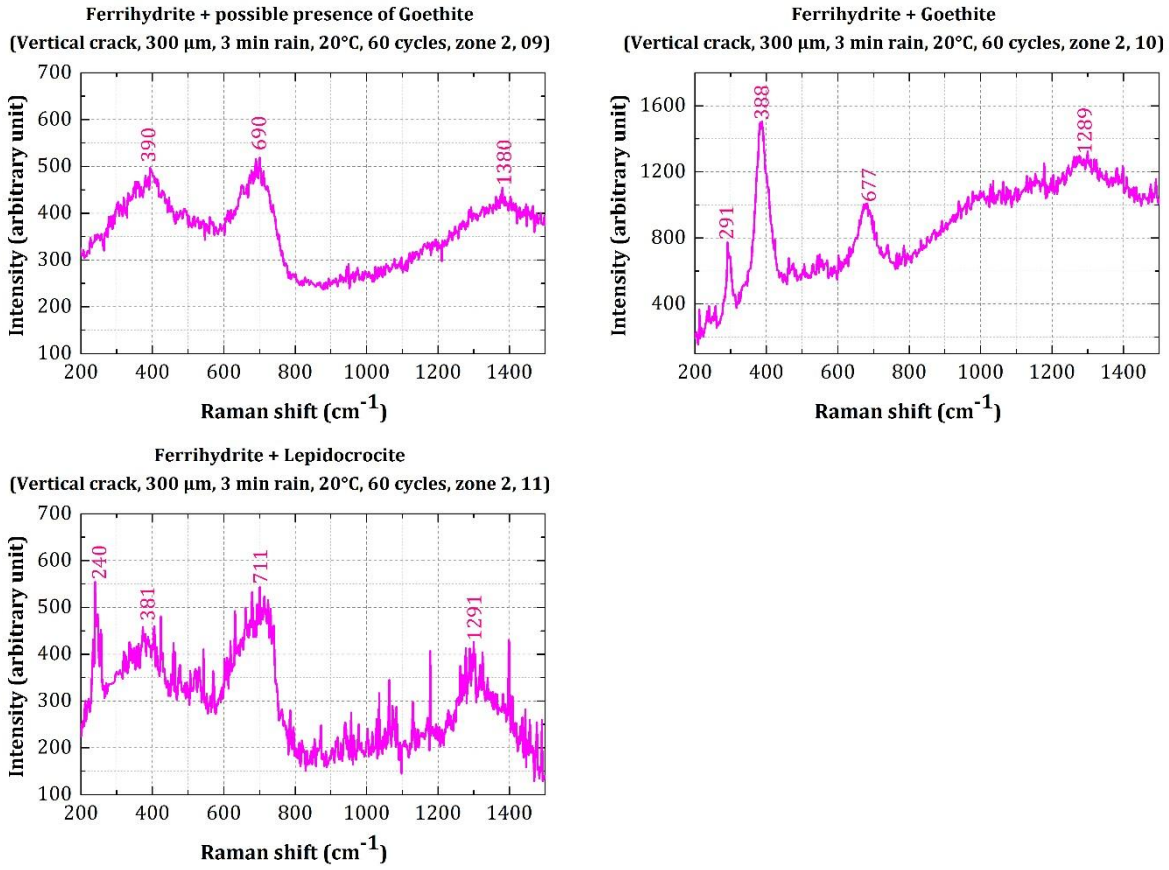

Figure I-53: All the Raman spectra of corrosion products obtained on specimens having 300 µm crack width and subjected to 3 minutes rain at each raining/drying cycle

I.6.4 Parameter tested: 90% RH

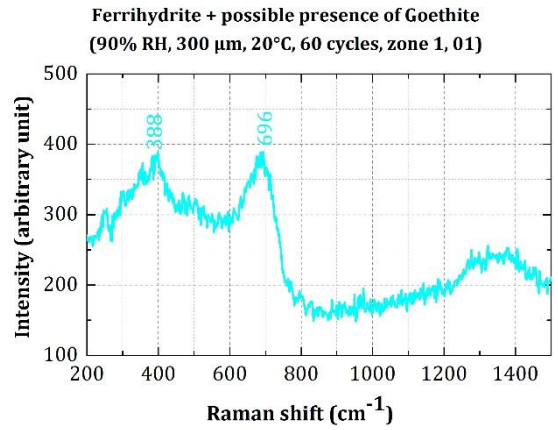

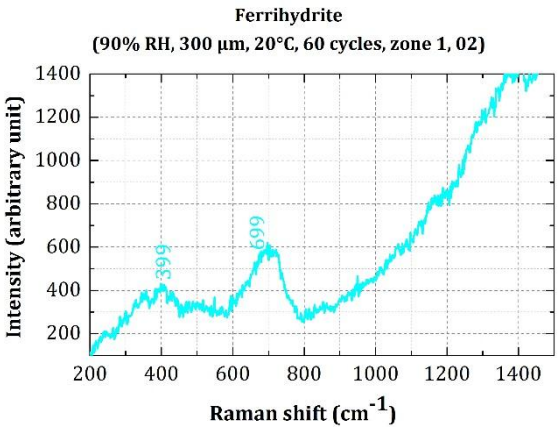

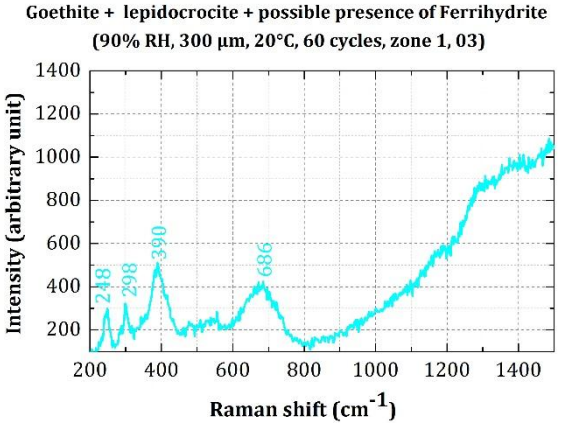

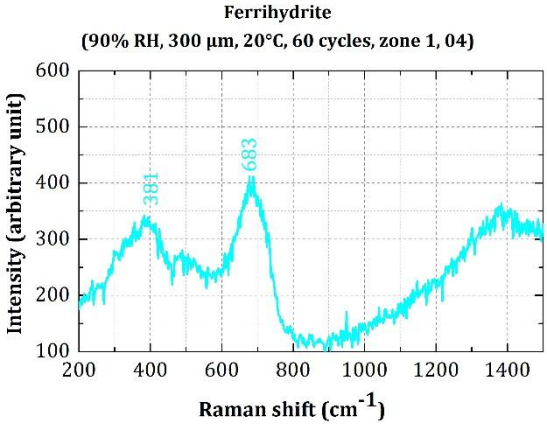

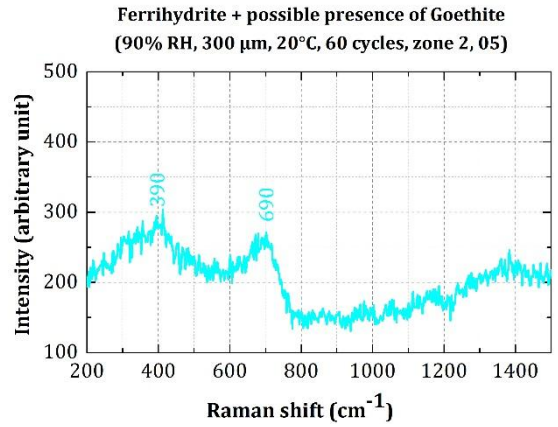

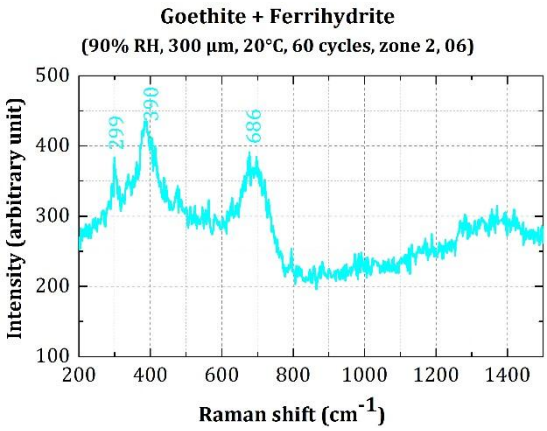

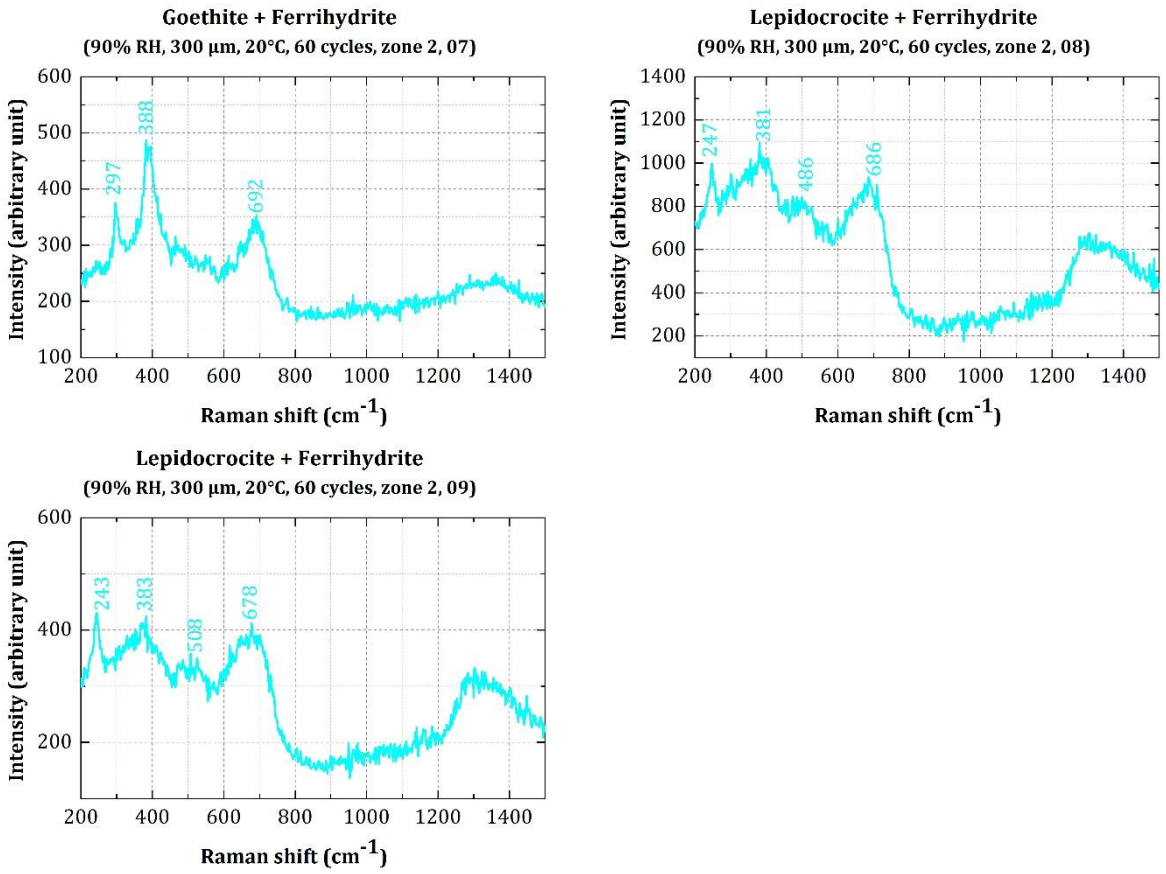

Figure I-54: All the Raman spectra of corrosion products obtained on specimens having 300 µm crack width and subjected continuously to 90% RH

I.6.5 Parameter tested: effect of the temperature

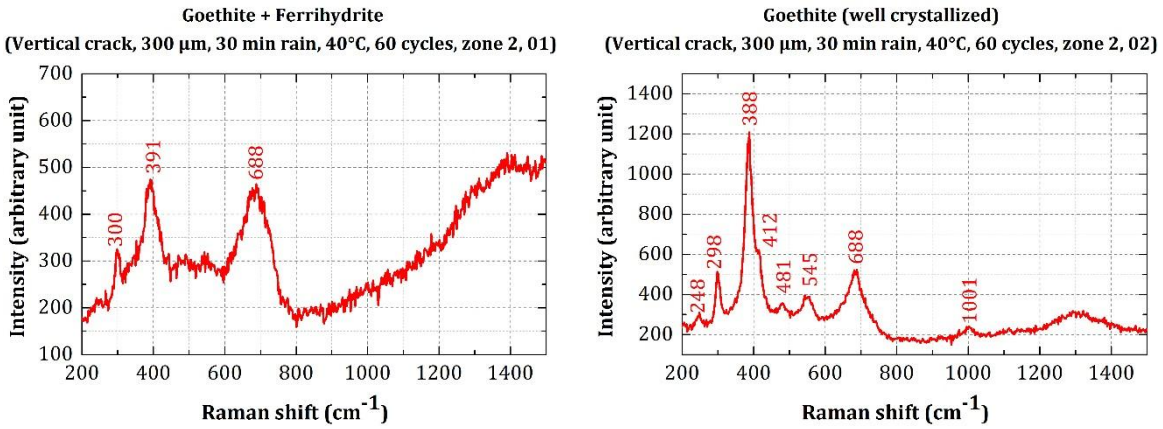

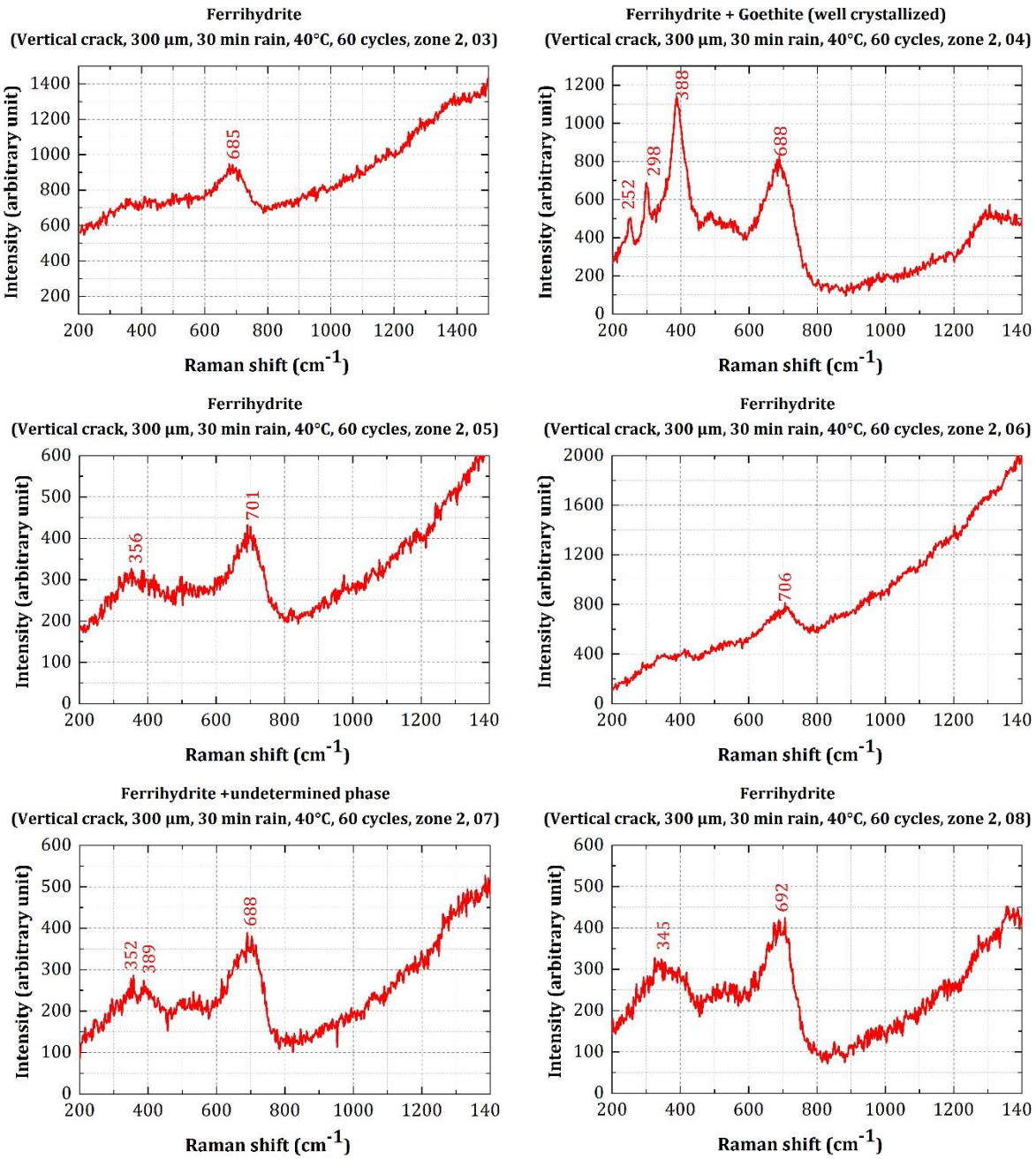

Figure I-55: All the Raman spectra of corrosion products obtained on specimens having 300 µm crack width and corroded at 40°C under raining/drying cycles of 30 minutes rain each (deep in the crack)

Vertical crack, 300 µm, 30 min rain, 40°C, 60 cycles, non-carbonated zone

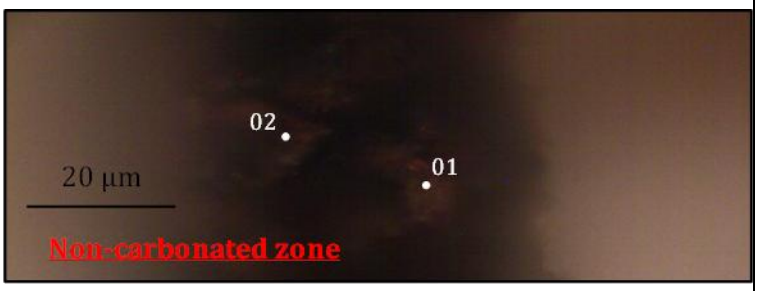

01 = Ferrihydrite

02 = Lepidocrocite

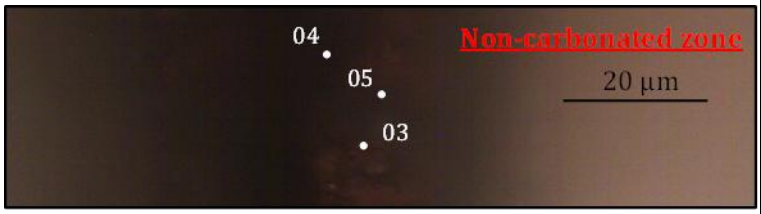

03 = Ferrihydrite

04 = Ferrihydrite

05 = Ferrihydrite

06 = Ferrihydrite + Goethite (well crystallized)

07 = Ferrihydrite + Goethite (well crystallized)

08 = Ferrihydrite

09 = Ferrihydrite

10 = Ferrihydrite

11 = Lepidocrocite + Goethite + possible presence of Ferrihydrite

12 = Lepidocrocite + Goethite + possible presence of Ferrihydrite

Figure I-56: Corrosion layer observed at steel/mortar interface located in the non-carbonated zone of specimens having 300 µm crack width and corroded under raining/drying cycles at 40°C

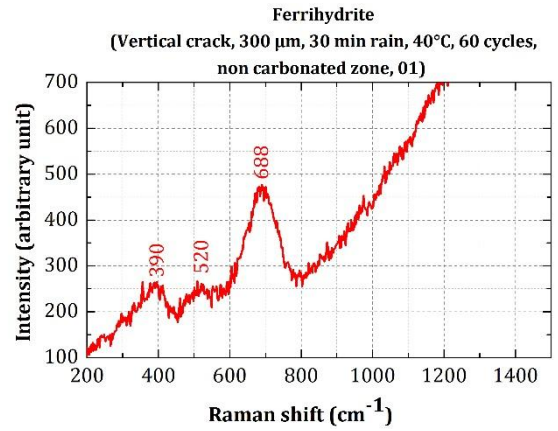
Ferrihydrite
(Vertical crack, 300 µm, 30 min rain, 40°C, 60 cycles,
non carbonated zone, 01)
Intensity (arbitrary unit)
Raman shift (cm-1)
390
520
688

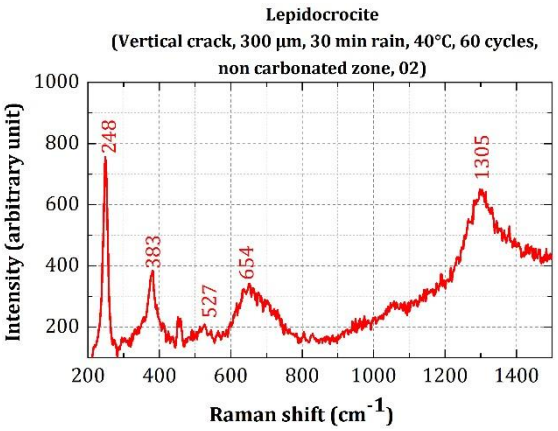
Lepidocrocite
(Vertical crack, 300 µm, 30 min rain, 40°C, 60 cycles,
non carbonated zone, 02)
Intensity (arbitrary unit)
Raman shift (cm-1)
248
383
527
654
1305

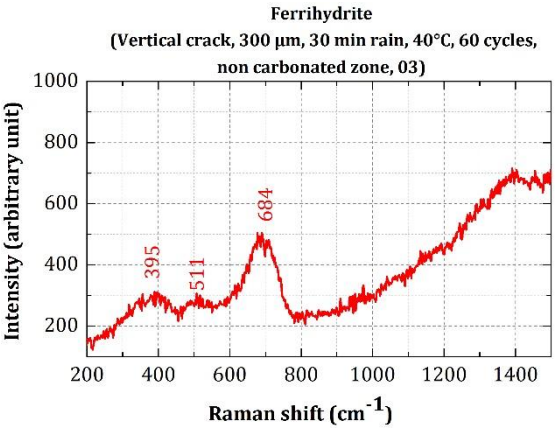
Ferrihydrite
(Vertical crack, 300 µm, 30 min rain, 40°C, 60 cycles,
non carbonated zone, 03)
Intensity (arbitrary unit)
Raman shift (cm-1)
395
511
684

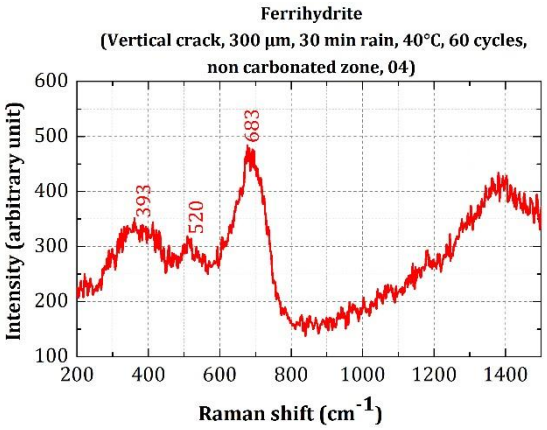
Ferrihydrite
(Vertical crack, 300 µm, 30 min rain, 40°C, 60 cycles,
non carbonated zone, 04)
Intensity (arbitrary unit)
Raman shift (cm-1)
393
520
683

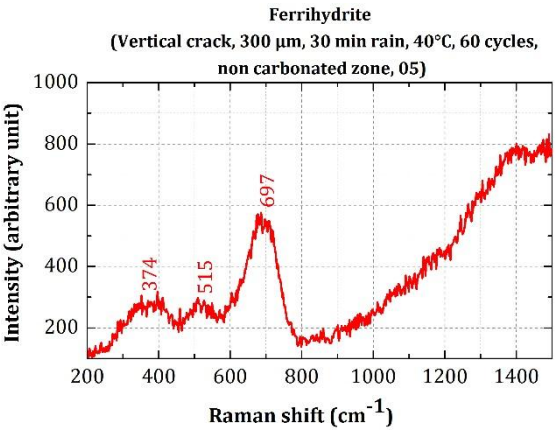
Ferrihydrite
(Vertical crack, 300 µm, 30 min rain, 40°C, 60 cycles,
non carbonated zone, 05)
Intensity (arbitrary unit)
Raman shift (cm-1)
374
515
697

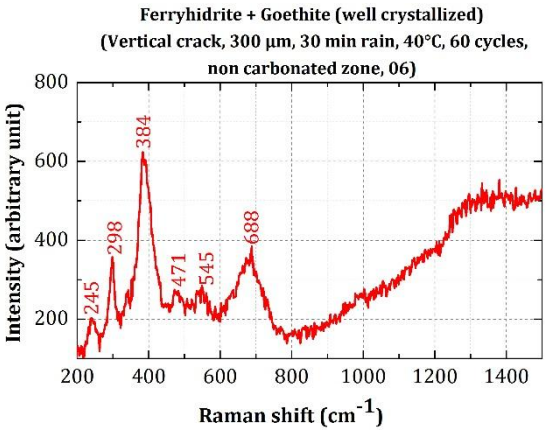
Ferryhidrite + Goethite (well crystallized)
(Vertical crack, 300 µm, 30 min rain, 40°C, 60 cycles,
non carbonated zone, 06)
Intensity (arbitrary unit)
Raman shift (cm-1)
245
298
384
471
545
688

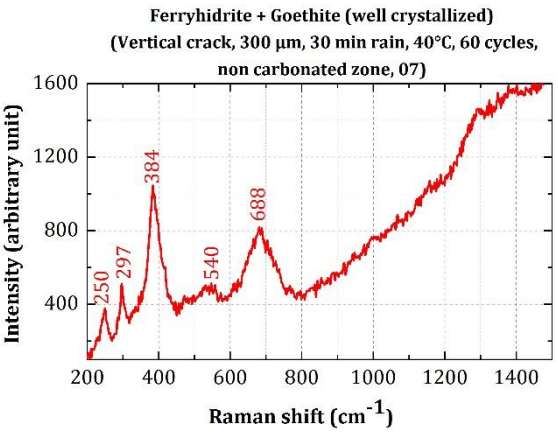
Ferryhidrite + Goethite (well crystallized)
(Vertical crack, 300 µm, 30 min rain, 40°C, 60 cycles,
non carbonated zone, 07)
Intensity (arbitrary unit)
Raman shift (cm-1)
250
297
384
540
688

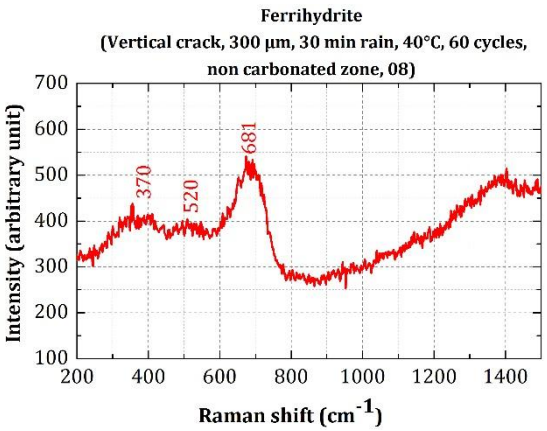
Ferrihydrite
(Vertical crack, 300 µm, 30 min rain, 40°C, 60 cycles,
non carbonated zone, 08)
Intensity (arbitrary unit)
Raman shift (cm-1)
370
520
681

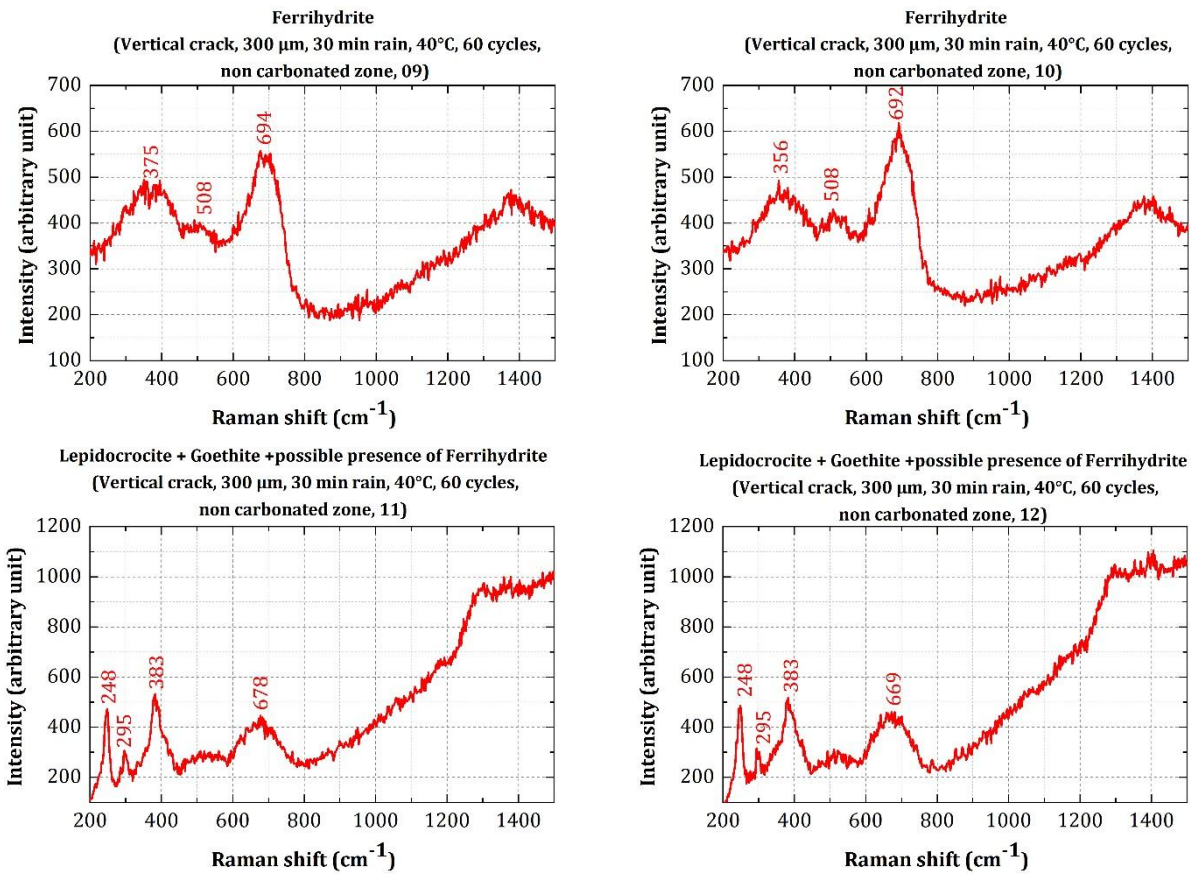

Figure I-57: All the Raman spectra of corrosion products obtained on specimens having 300 µm crack width and corroded at 40°C under raining/drying cycles of 30 minutes rain each (in the non-carbonated area)

I.6.6 Exposure condition: Environmental conditions of Saclay

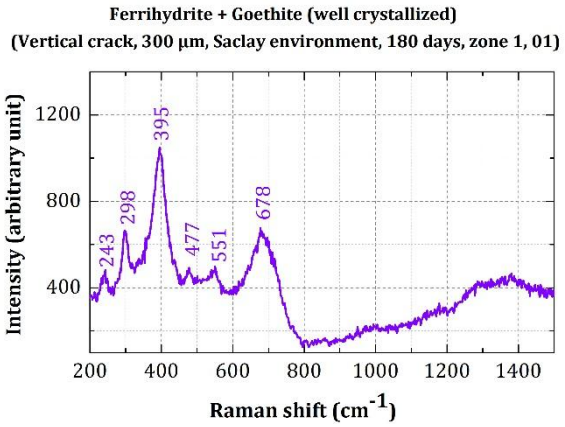

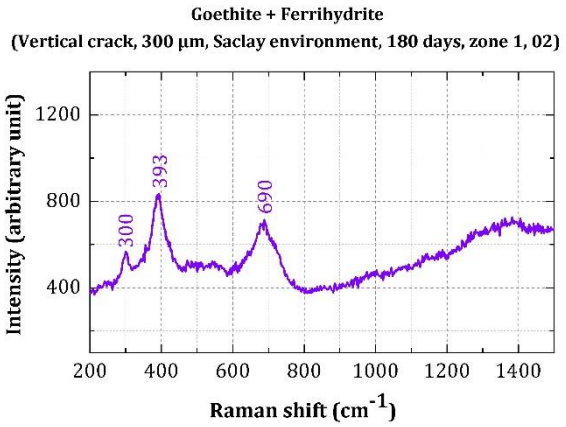

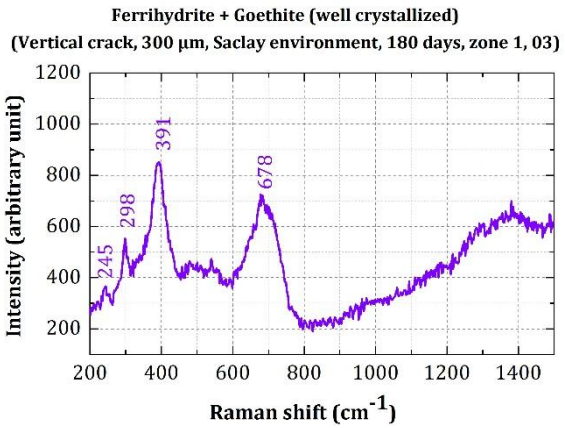

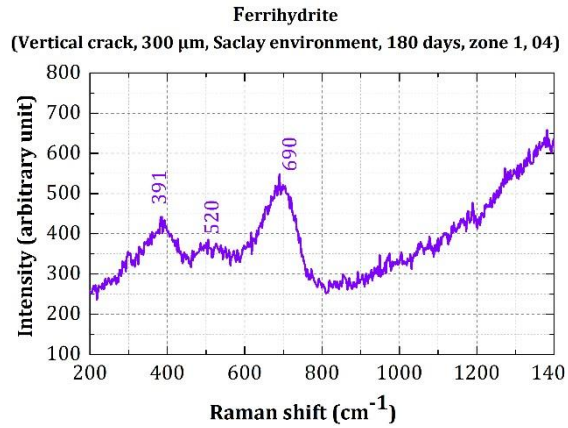

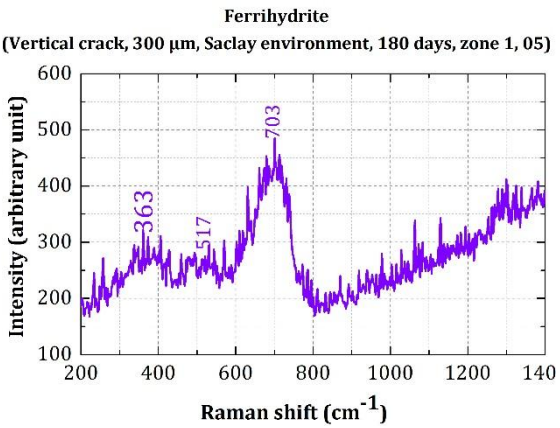

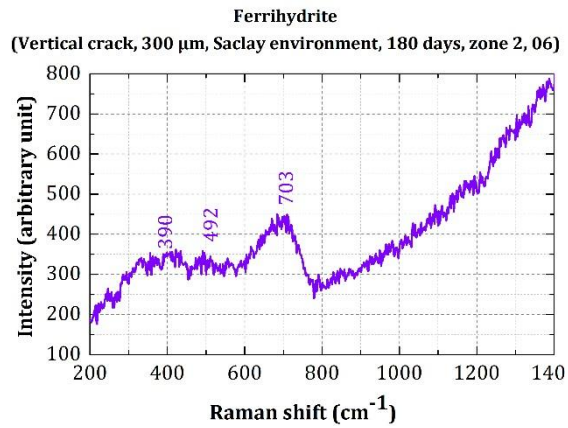

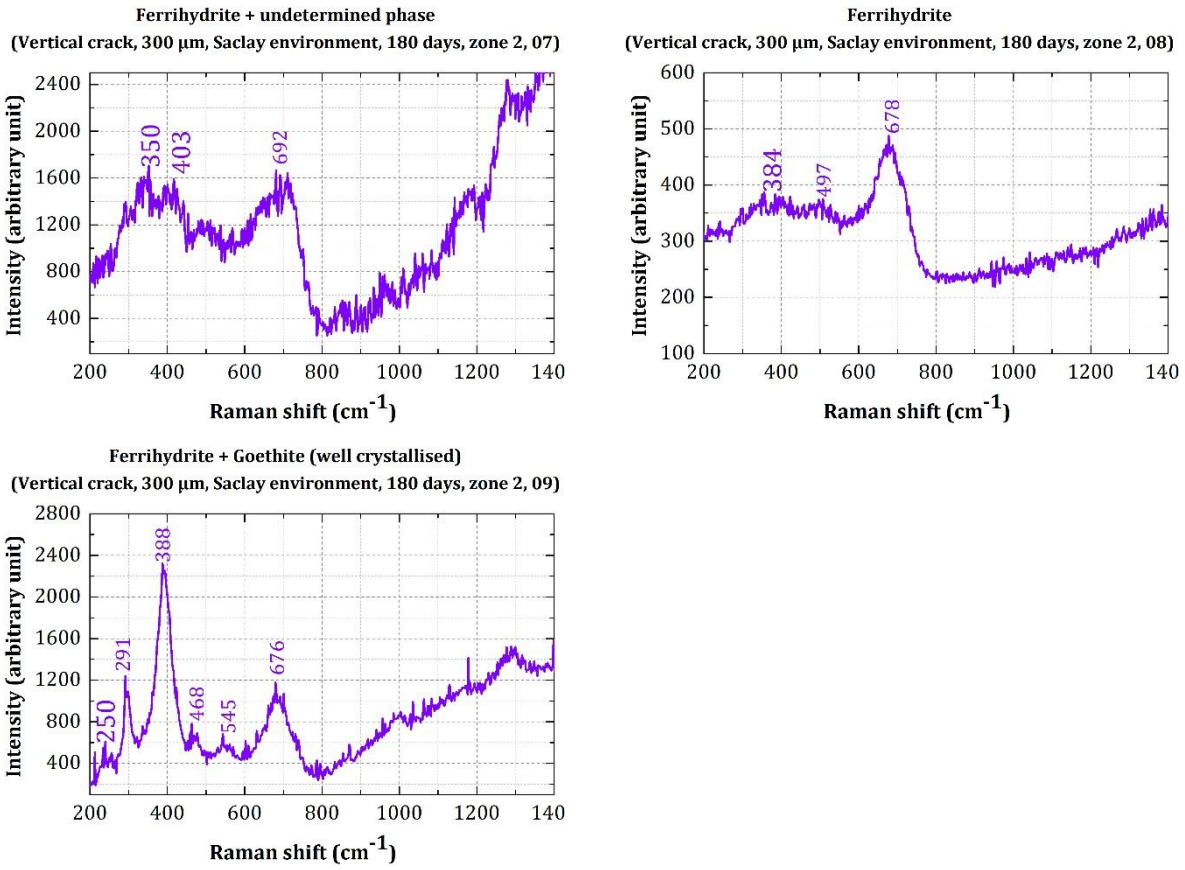

Figure I-58: All the Raman spectra of corrosion products obtained on specimens having 300 µm crack width and corroded in Saclay environment

I.6.7 Parameter tested: Evolution of the corrosion products

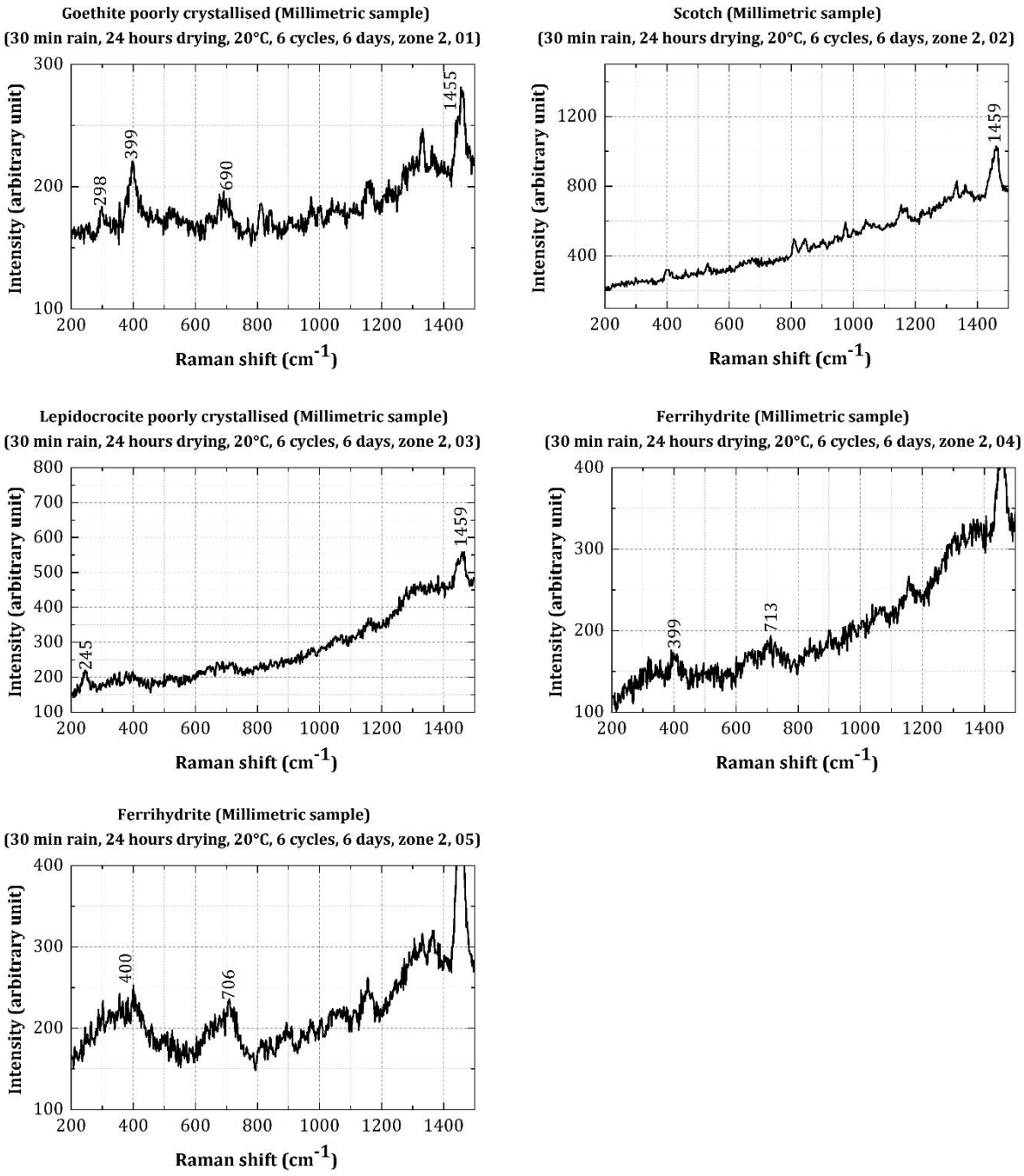

Figure I-59 : All the Raman spectra of corrosion products obtained on millimetric samples after 6 wetting/drying cycles

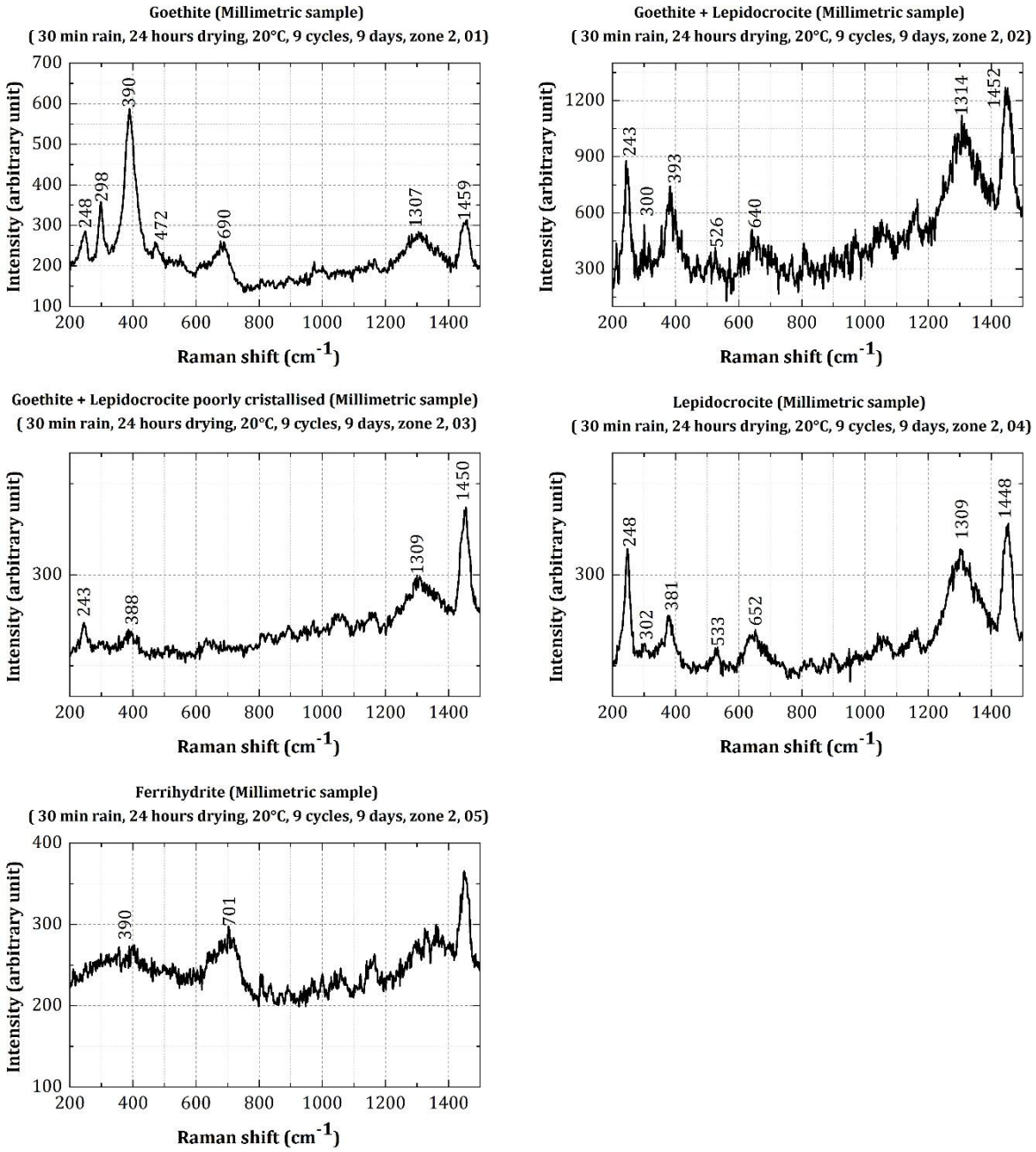

Figure I-60: All the Raman spectra of corrosion products obtained on millimetric samples after 9 wetting/drying cycles

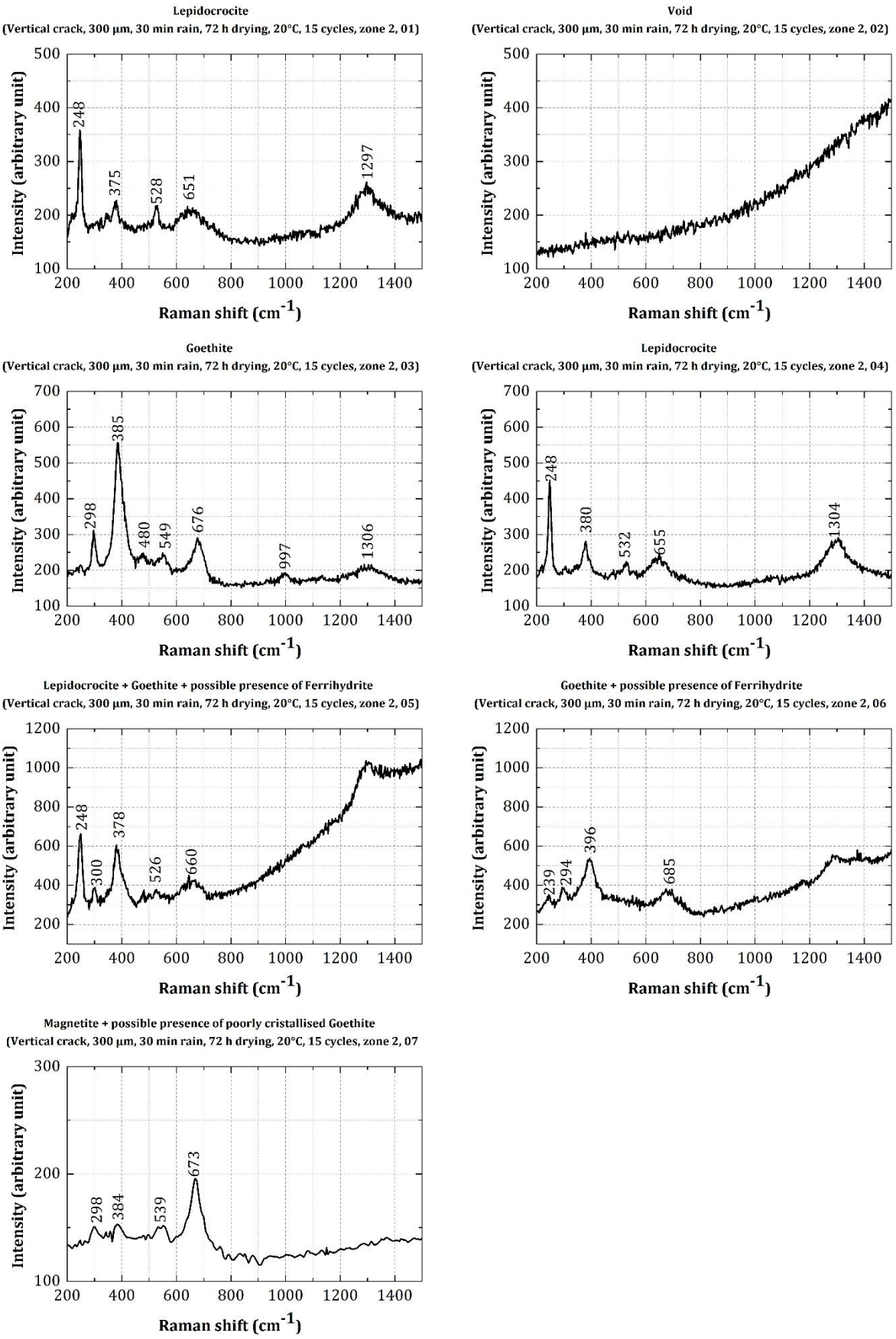

Figure I-61: All the Raman spectra of corrosion products obtained on centimetric samples after 15 raining/drying cycles

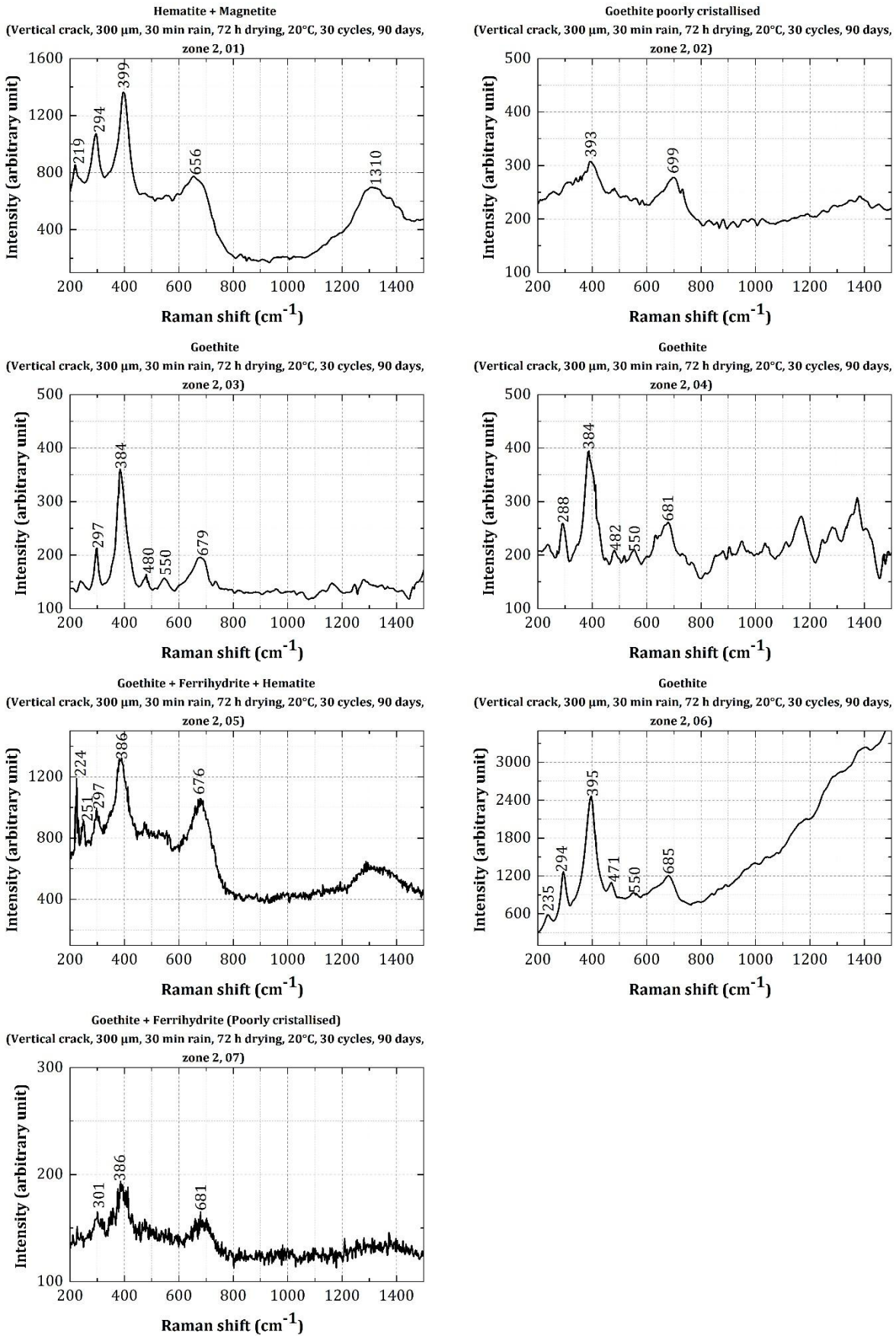

Figure I-62: All the Raman spectra of corrosion products obtained on centimetric samples after 30 raining/drying cycles

I.6.8 Parameter tested: materials type

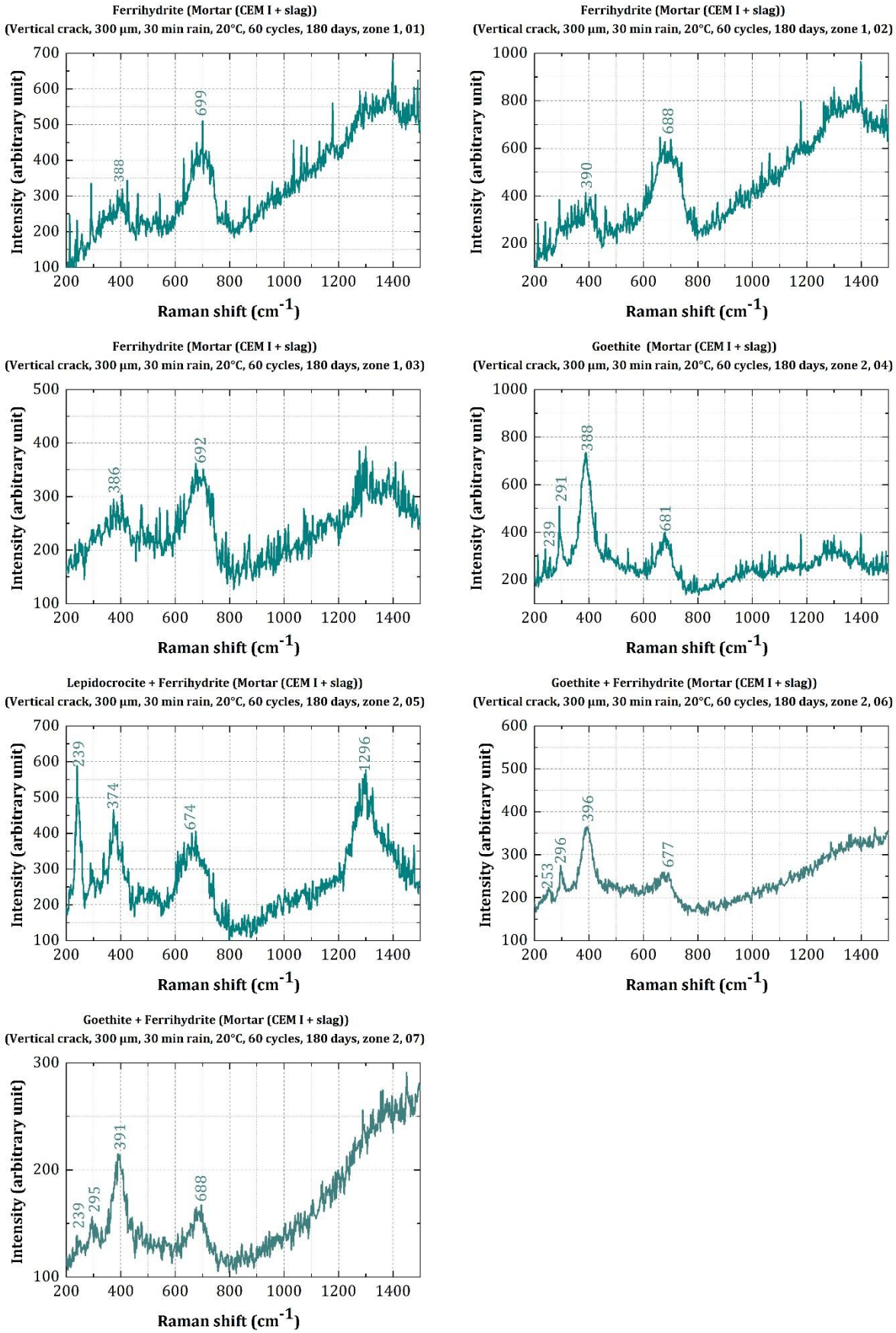

Figure I-63: All the Raman spectra of corrosion products identified in (CEM I + slag) mortar

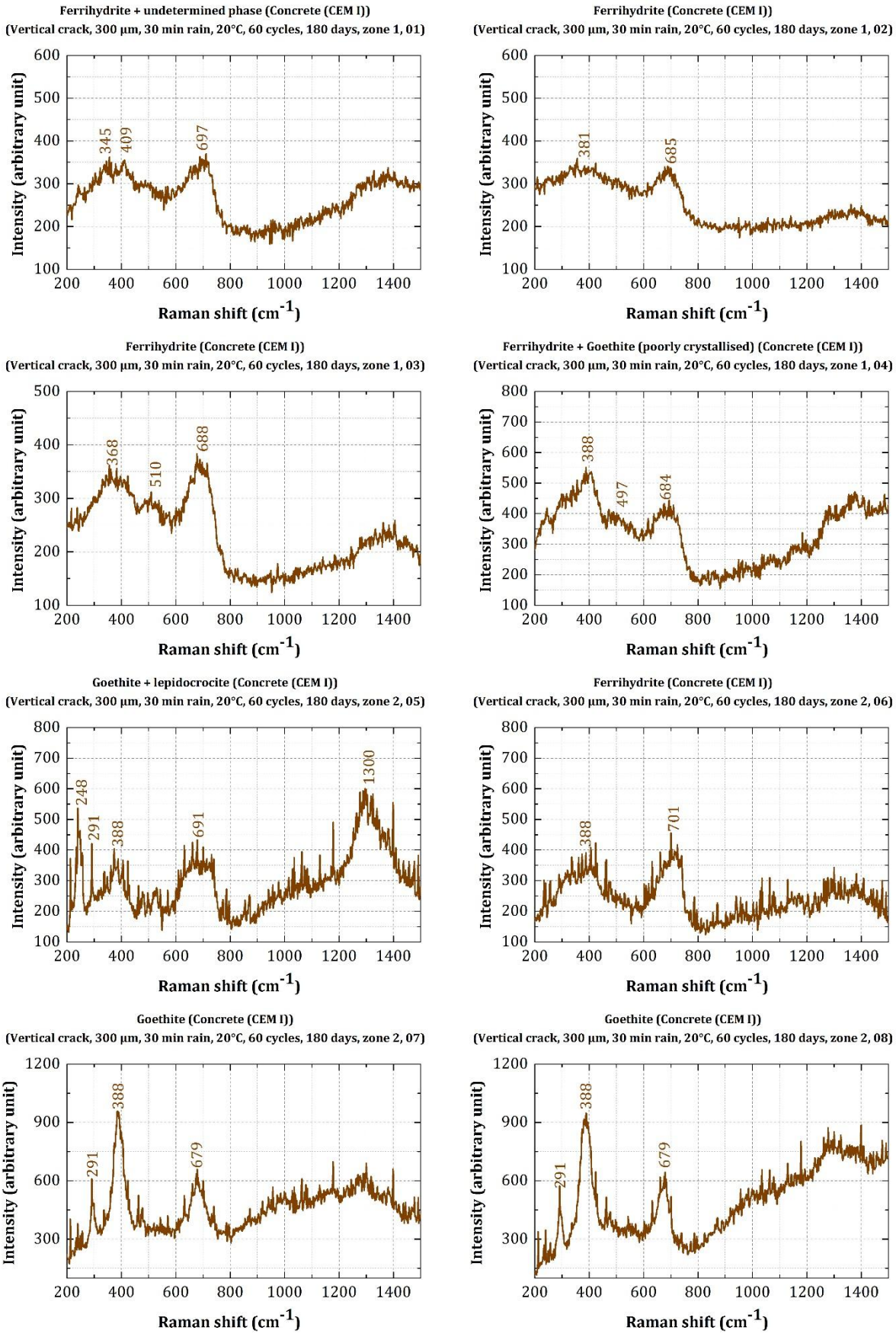

Figure I-64: All the Raman spectra of corrosion products identified in CEM I concrete specimen

I.6.9 Parameter tested: comparison of the corrosion products type developed on the upper steel/mortar interface with those on the lower steel/mortar interface

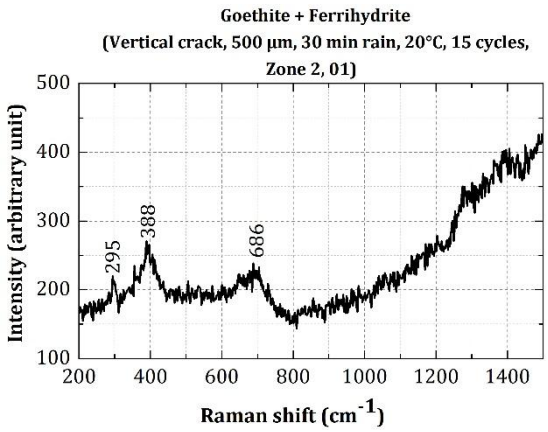

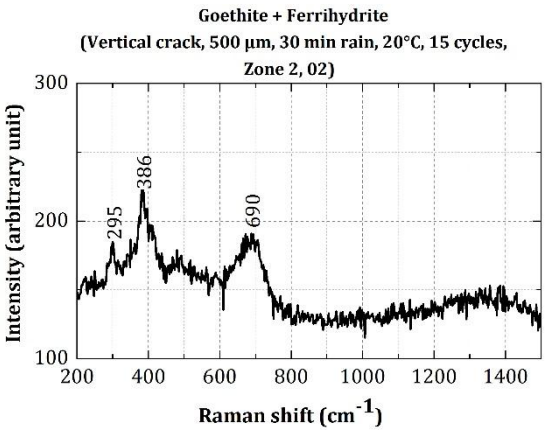

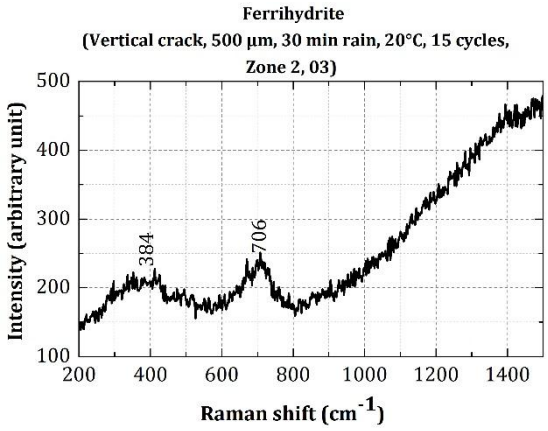

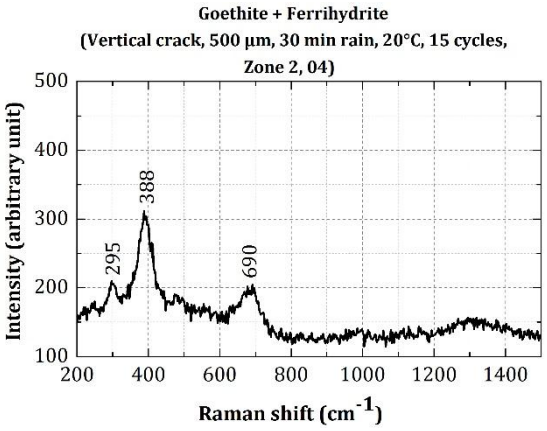

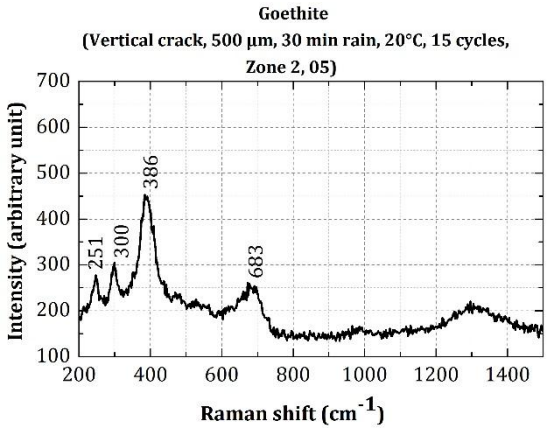

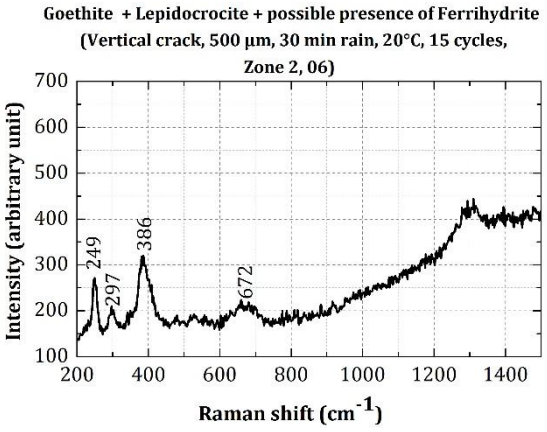

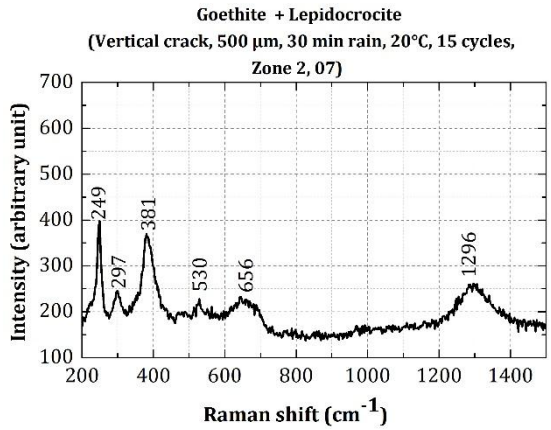

Figure I-65: All the Raman spectra of corrosion products identified on the upper and the lower interfaces of specimens having 500 µm residual crack width and corroded in the reference test (15 cycles)

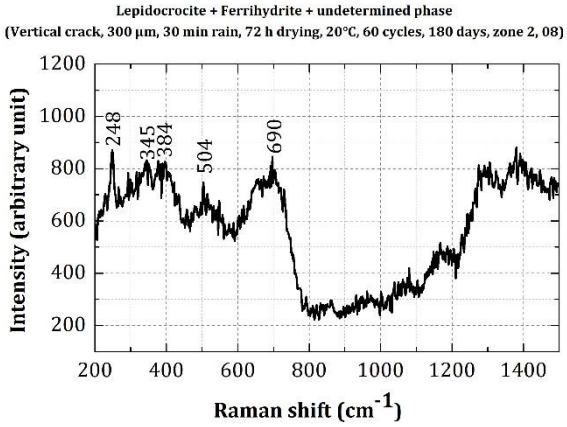

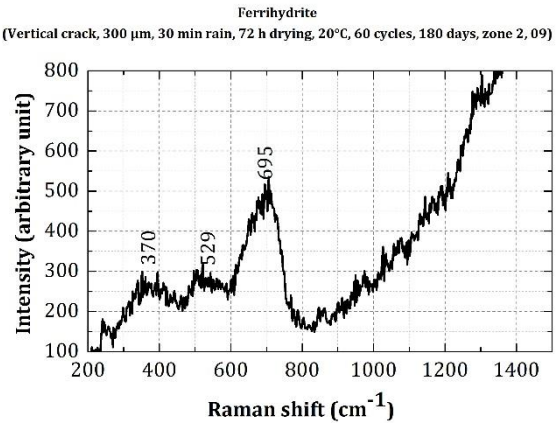

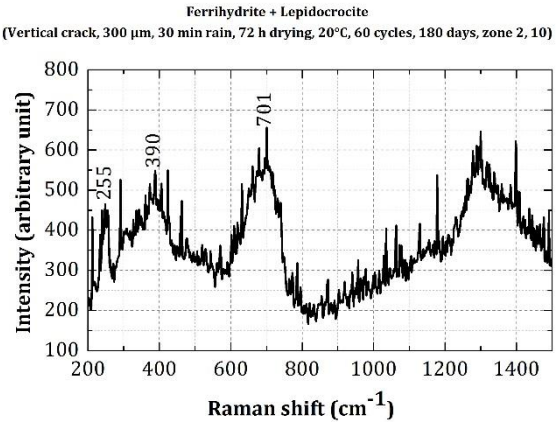

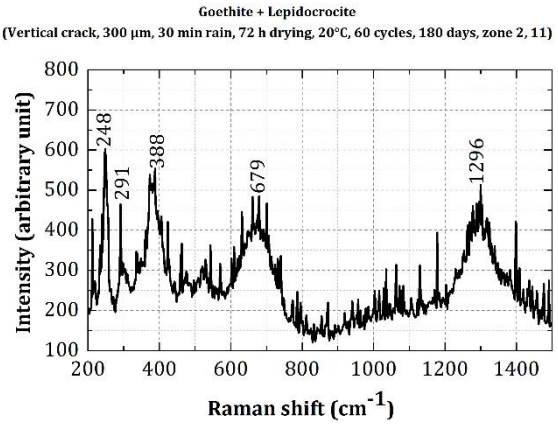

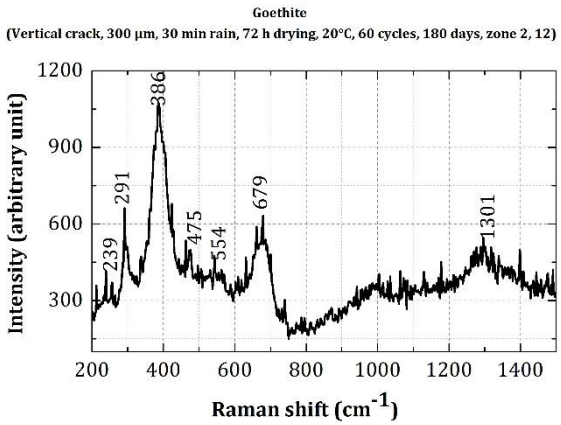

Figure I-66: All the Raman spectra of corrosion products identified on the lower interface of specimens having 300 µm residual crack width and corroded in the reference test (60 cycles)

I.7 EVOLUTION OF THE CARBONATION LENGTH

I.7.1 Parameter tested: Effect of the crack opening

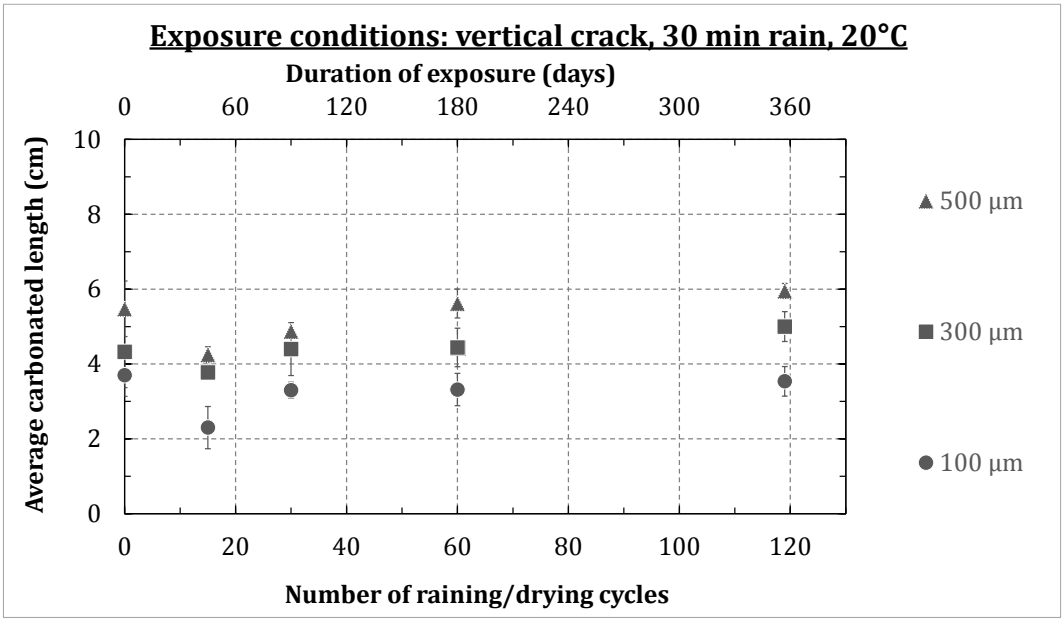

Figure I-67: Evolution of the carbonated steel/mortar interface length in specimens having different residual crack openings and corroded in the reference test

I.7.2 Parameter tested: effect of the crack orientation

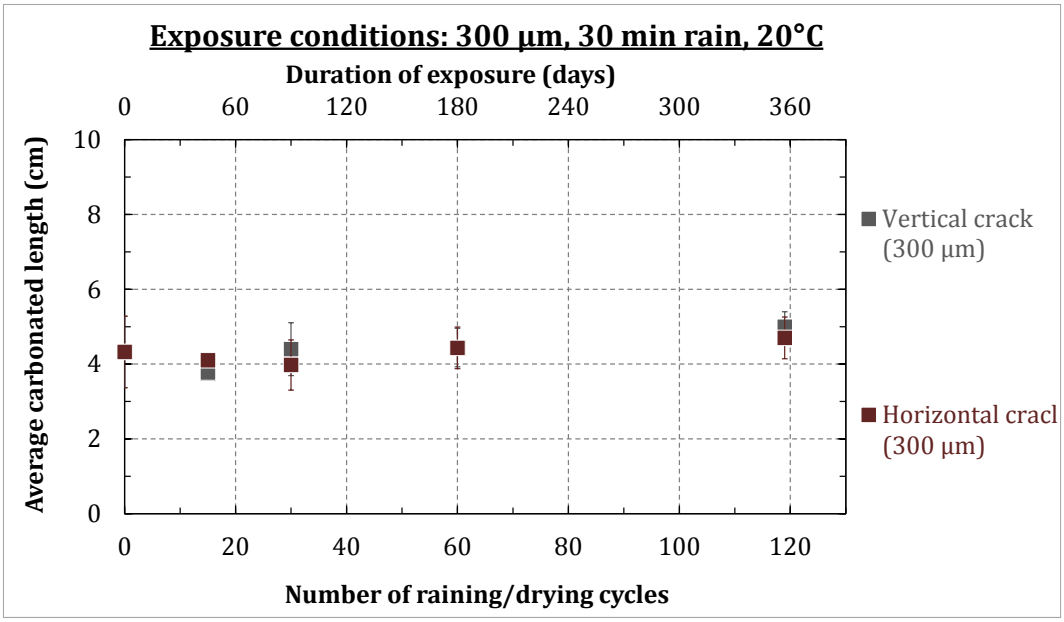

Figure I-68: Evolution of the carbonated steel/mortar interface length in specimens exposed differently with respect to rain

I.7.3 Parameter tested: effect of the rain duration

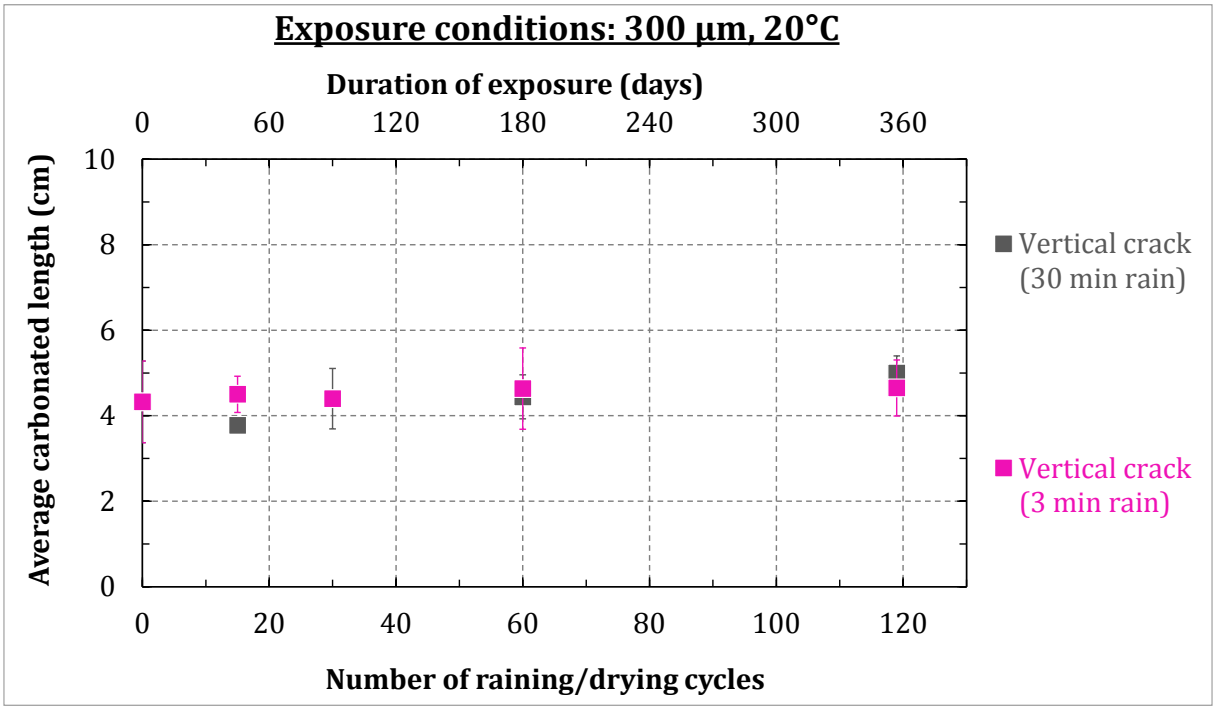

Figure I-69: Evolution of the carbonated steel/mortar interface length in specimens exposed to different rain durations

I.7.4 Parameter tested: 90% RH

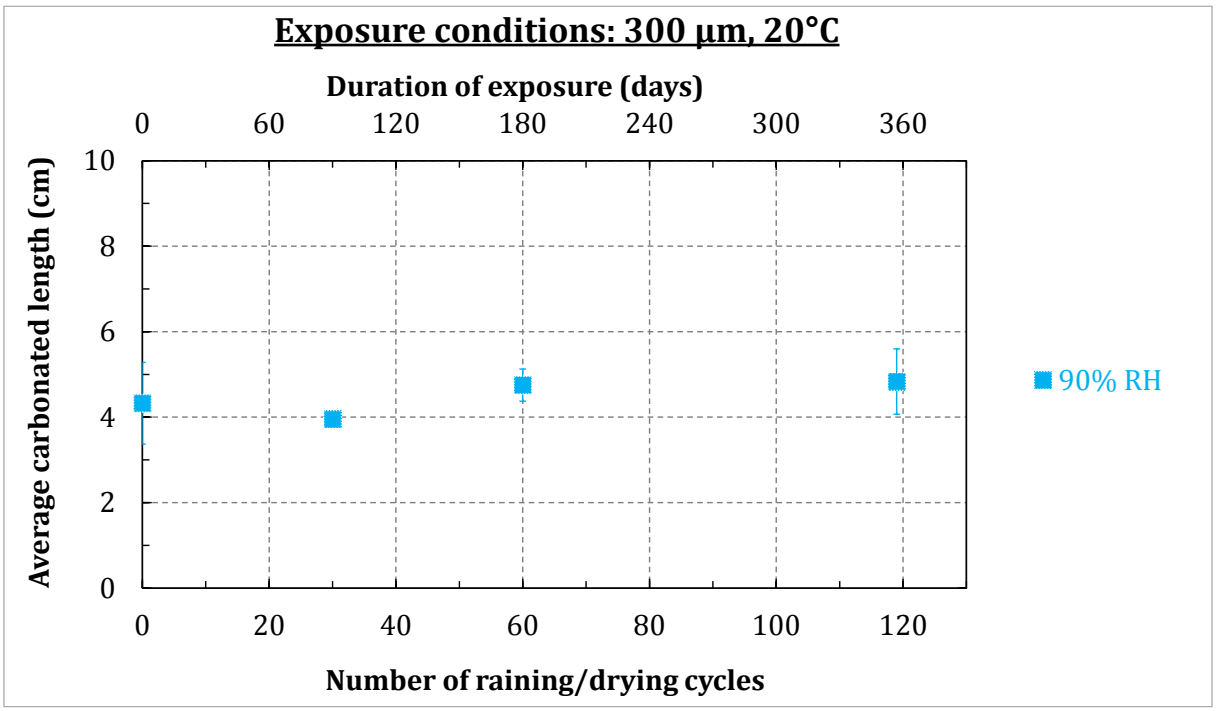

Figure I-70: Evolution of the carbonated steel/mortar interface length in specimens exposed continuously to 90% RH

I.7.5 Parameter tested: effect of the temperature

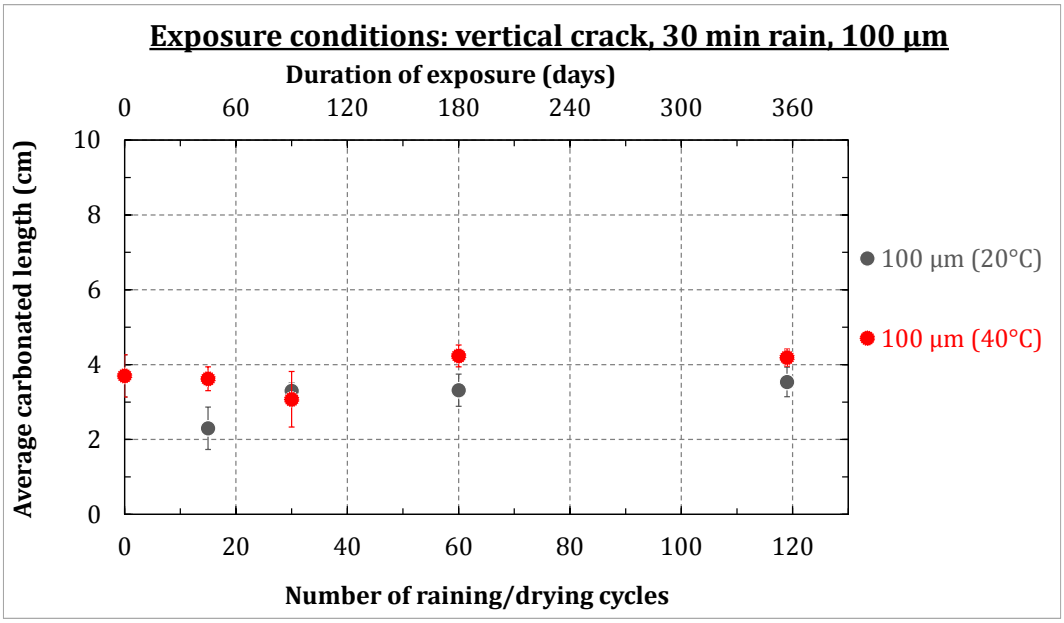

Figure I-71: Evolution of the carbonated steel/mortar interface length in specimens exposed to different temperatures (100 µm)

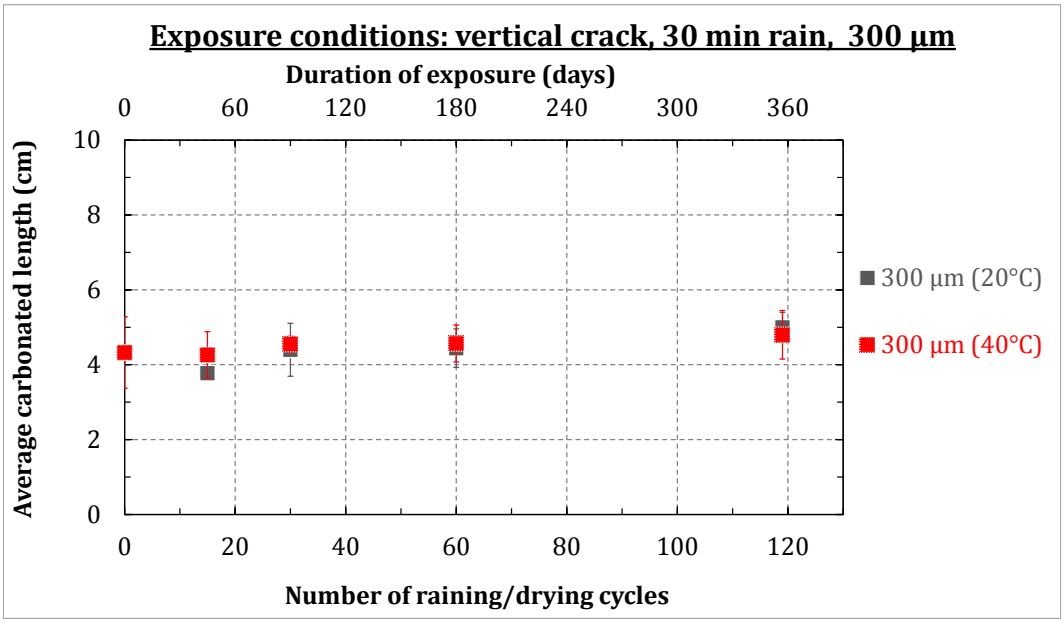

Figure I-72: Evolution of the carbonated steel/mortar interface length in specimens exposed to different temperatures (300 µm)

I.7.6 Exposure condition: Environmental conditions of Saclay

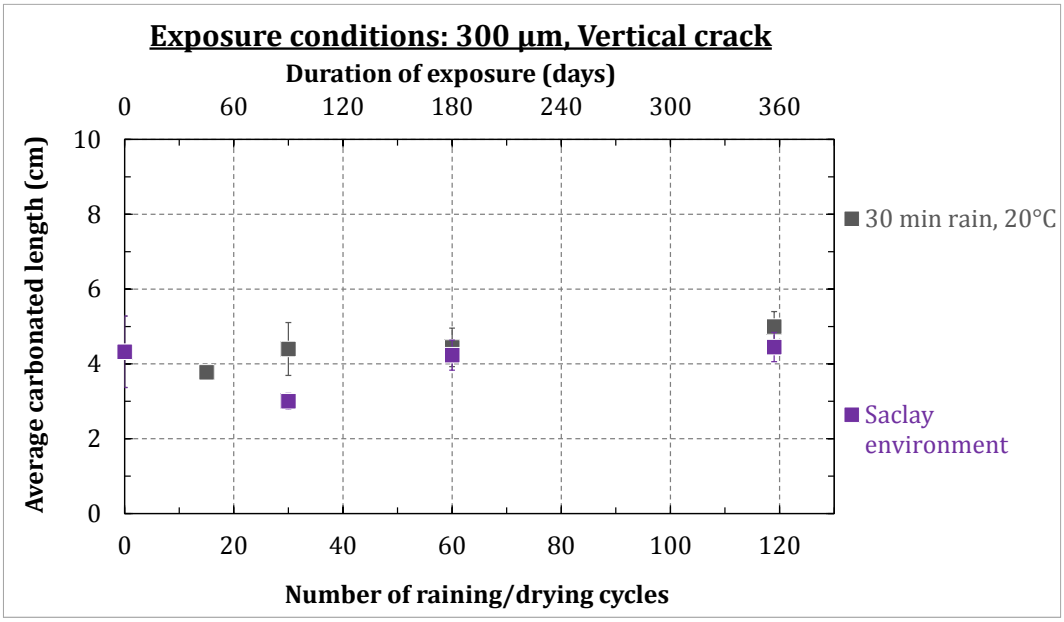

Figure I-73: Evolution of the carbonated steel/mortar interface length in specimens exposed to Saclay environment

I.8 CHEMICAL FORMULAS OF CORROSION PRODUCTS

Table I-1 : Characteristic of corrosion products [209], [210]

Chemical Name	Mineral name	Chemical formula	color
Iron (II) hydroxide		$Fe(OH)_2$	White→ greenish tinge due to oxygen
iron (III) hydroxide	Bernalite	$Fe(OH)_3$	Red brown
Iron oxy-hydroxide	Goethite	α-FeOOH	Yellow-brown
Iron oxy-hydroxide	Akaganeite	β-FeOOH	Red-brown
Iron oxy-hydroxide	Lepidocrocite	γ-FeOOH	Orange
Iron(II,III) oxide	Magnetite	Fe_3O_4	Dark gray
Iron(III) oxide	Hematite	Fe_2O_3	Black or sliver-gray, brown to reddish brown or red
Iron carbonate	Siderite	$FeCO_3$	Yellow-brown
Hydrated ferric iron oxide	Ferrihydrite	$5Fe_2O_3•9H_2O$	Dark brown, yellow-brown
Ferromagnetic iron oxide	Maghemite	γ-Fe_2O_3	Brown, bluish black; brown to yellow in transmitted light; white to bluish gray in reflected light.
Iron oxide	Wüstite	FeO	Greyish white to yellow or brown

I.9 CEMENT NOMENCLATURE

Table I-2: Cement nomenclature

Chemical notation	Cement nomenclature
CaO	C
SiO_2	S
Al_2O_3	A
Fe_2O_3	F
H_2O	H
SO_3	$\overline{S}$